Research Report

Behavior of Hot-Rolled Asymmetric Steel I-Beams

FINAL REPORT

AISC RESEARCH REPORT NO. AISC-MILEK-2025-01
DECEMBER 2024

Project Title:	**Behavior of Hot-Rolled Asymmetric Steel I-Beams**
Primary Investigator(s):	**Matthew Yarnold**
Research Organization(s):	**Auburn University**

DISCLAIMER

PREFACE

The American Institute of Steel Construction (AISC), headquartered in Chicago, is a non-partisan, not-for-profit technical institute and trade association established in 1921 to serve the structural steel design community and construction industry in the United States. As part of its technical activities, AISC actively funds and supports research related to structural steel design and construction. AISC members primarily come from the structural steel construction community, including producers, fabricators, and engineers.

Many AISC members are engineers, so much of our research supports the engineering community, including maintaining and updating our technical publications such as Design Guides, The Steel Construction Manual, and our Specifications and Provisions. We distribute our specifications free for their use. The primary goal of those specifications is the reliability of structures and, through that, the safety of the public.

AISC does not use the results of research for profit, nor do we sell reports of the research or derivatives from it. Our work is performed in the interest of public safety. As such, we fund projects to, in part, support the development of next-generation steel systems for enhanced performance, safety, sustainability, and economy.

It is reasonably common for AISC research projects to receive additional direct, indirect, or in-kind support from external organizations such as federal or state agencies or member companies . As such, the partial or complete contents of this Report may also reside in the public domain of these external funding agencies.

Behavior of Hot-Rolled Asymmetric Steel I-Beams

Matthew Yarnold[1], Chase Ottmers[2], Robel Alemayehu[3], Eric Stoddard[4], and Sheyenne Davis[5]

[1]Associate Professor & Director of the Advanced Structural Engineering Laboratory, Auburn University, Auburn, AL myarnold@auburn.edu
[2]Ph.D. Candidate, Texas A&M University, College Station, TX
[3]Postdoctoral Fellow, Auburn University, Auburn, AL
[4]Ph.D. Graduate, Texas A&M University, College Station, TX
[5]M.S. Graduate, Texas A&M University, College Station, TX

Presented to the American Institute of Steel Construction

December 2024

Table of Contents – Executive Report

Detailed Content:

Abstract

The presented study established hot-rolled asymmetric steel I-beam (or A-shape) cross-sectional dimensions for production in the United States (US) and future adoption in Part 1 of the AISC Steel Construction Manual. The primary motivation for hot-rolled A-shapes is to improve steel building economy, speed, and efficiency. Medium- to long-span floor systems in residential and commercial buildings have utilized shallow-depth steel-concrete composite construction to compete with flat concrete slabs. These shallow-depth composite floor systems typically use built-up asymmetric steel beams, along with other elements. A hot-rolled section using partial composite construction can provide a faster and more cost-effective solution. Extensive numerical and experimental research was performed to ensure the A-shapes could be efficiently rolled, while the structural performance met the construction and in-service demands for shallow-depth floor systems.

Research Goals

The primary research goal was to evaluate (numerically and experimentally) the behavior of hot-rolled asymmetric steel I-beams (or A-shapes) within shallow-depth composite floor systems. The next goal was to utilize that knowledge to establish recommended A-shape cross-sectional dimensions. Another goal was to leverage the in-depth understanding of A-shape composite floor system behavior for the development of design guidance in the form of a design example and design tables.

The long-term goal is for A-shapes to be regularly milled in the United States and utilized within building floor systems. As part of this, the goal is for A-shapes to be added to Part 1 of future AISC Steel Construction Manuals.

Motivation and Background

The principal motivation for hot-rolled A-shapes is to improve building floor system economy, speed, and efficiency. Flat slab construction is a relatively common floor system method that utilizes reinforced concrete or post-tensioned concrete (shown on the left side of Figure 1)). These systems yield a relatively shallow depth. However, they require extensive shoring and effort for reinforcement placement, making them relatively slow to construct. An alternative to flat slabs is conventional composite floor systems, which do not require shoring. Conventional composite floor systems consist of rolled steel beams integrated with a reinforced concrete slab. These systems commonly utilize doubly symmetric wide flange beams (typically W-shapes) and a cast-in-place concrete slab on steel decking (shown in the center of Figure 1). Shear studs are welded to the top flange of the beam to transfer longitudinal shear forces. A downfall of this floor system is the relatively large floor depths.

The alternative to the systems above is shallow-depth composite floor systems where stay-in-place formwork (either precast concrete panels or steel deep decking) is installed on the bottom flange of steel beams (shown on the right side of Figure 1). Following formwork placement, a concrete slab is cast-in-place, and the concrete encases the top flange and web of the steel beams. However, hot-rolled steel beams currently produced in the United States (US), such as W-shapes, do not allow formwork to be placed on the bottom flange easily due to top flange interference. Thus, asymmetric I-beams (or A-shapes) are desirable to allow for easy and rapid placement of formwork. A comparison of common multi-story residential and commercial building floor systems is shown in Figure 1.

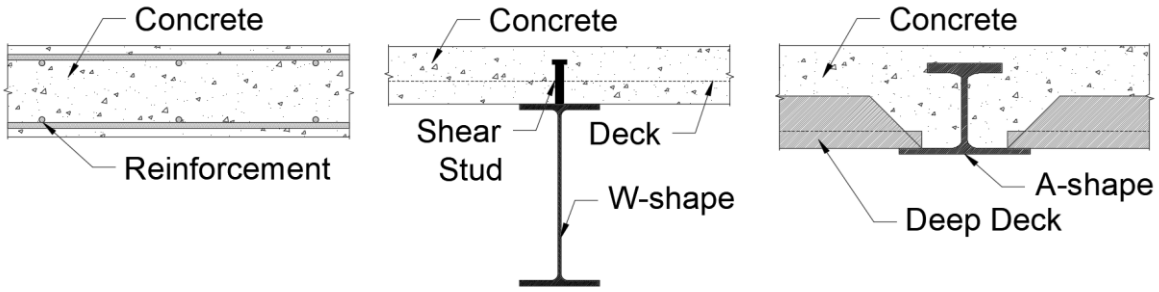

	Flat Slab	Conventional Composite	Shallow-Depth Composite
Speed		✓	✓
Depth	✓		✓

Figure 1: Overview of the Common Multi-Story Residential and Commercial Floor Systems

There are various built-up asymmetric I-beams utilized in building floor systems with stay-in-place formwork; however, they all require intensive fabrication work. Some of the beam systems include Girder-Slab®, Kloeckner Westok®, ArcelorMittal Slim-Floor, and ComSlab®. The Girder-Slab® system utilizes D-BEAMS®, which are fabricated by cutting the web of a W-shape in a castellated pattern and welding a flat bar to the top of the cut web. The Girder-Slab® floor system utilizes precast concrete panels placed on the bottom flange of the D-BEAM®. Kloeckner Westok® beams are analogous in that the beams are fabricated from two uncommonly sized W-shapes that are cut with a castellated pattern and are joined together to form an asymmetric cross-section. ArcelorMittal Slim-Floor and ComSlab® systems utilize a flat plate welded to the bottom of a W-shape, which supports steel deep decking. ArcelorMittal Slim-Floor also fabricates asymmetric I-beams that utilize a WT-shape and weld a flange plate to the web.

An alternative solution to built-up asymmetric I-beams, which require intensive fabrication work, is to hot roll them at a steel mill. Currently, there are no hot-rolled asymmetric I-beams at US steel mills, and there is limited production of hot-rolled asymmetric I-beams around the world. A floor system in the United Kingdom called Slimdek® utilizes hot-rolled asymmetric I-beams produced by British Steel and is built by Corus Construction and Industrial. British Steel hot rolls ten asymmetric steel beams, termed ASBs, on request. The Slimdek® floor system utilizes both precast concrete panels and steel deep decking that is supported by the ASB bottom flange.

Shallow-depth floor systems utilizing A-shapes and stay-in-place formwork do not use shear studs on the top flange of the beam to transfer longitudinal shear between the concrete and steel (as shown in Figure 2(a)). Shear studs are not utilized to increase the efficiency of building construction and to achieve minimal floor depths. Stay-in-place formwork placed on the bottom flange allows for the top flange and web to be encased in the concrete slab. As a result, longitudinal shear transfer will occur due to the bond shear that forms between the concrete and steel.

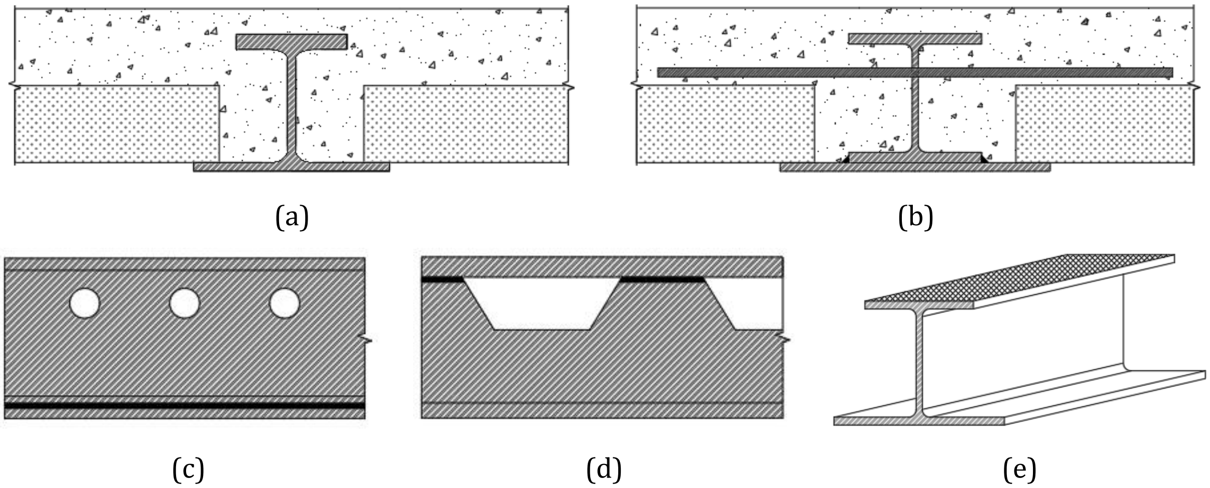
(a) (b)
(c) (d) (e)

Figure 2: Bond Transfer Systems: (a) Pure Bond in Shallow-Depth Floor System with A-shapes, (b) Dowel Reinforcement in Composite Slim-Floor Beams, (c) Composite Slim-Floor Beam with Dowel Reinforcement Holes, (d) Girder-Slab® D-BEAM® with Castellated Web Openings for Dowel Reinforcement, and (e) Embossed Top Flange

Composite flexural behavior for shallow-depth systems can be improved by having web openings, which helps the concrete lock onto the steel section. Fabricating the D-BEAM® achieves this by having a castellated pattern with openings in the web. Furthermore, including dowel reinforcement that goes through the web openings helps increase the amount of bond shear transfer and degree of composite action, which is utilized in the Girder-Slab® and ArcelorMittal Composite Slim-Floor systems (general illustration in Figure 2(b)). Openings in the web are introduced from drilling holes (see Figure 2(c)) or are inherent from cutting a castellated pattern in the web during fabrication (as shown in Figure 2(d)). Another alternative to improve the bond shear is to have an embossed pattern rolled into the top flange of the beam, as shown in Figure 2(e). The embossed pattern increases the roughness of the top flange, allowing for an improved bond shear between the concrete and steel. However, to keep the A-shape floor system as simple (and fast to construct) as possible, no additional mechanisms are used to increase the composite flexural behavior. The bond shear between the concrete and the A-shape steel surface is a reliable mechanism that provides composite flexural behavior. This is conservatively accounted for with a partial composite flexural design.

Research Approach and Timeline

The research approach to achieve the goals stated earlier was to study all stages in the "life" of future A-shape beams within shallow-depth composite floor systems. This began with the manufacturing of the sections and continued throughout the in-service performance. Figure 3 provides the research timeline for the primary phases of the study.

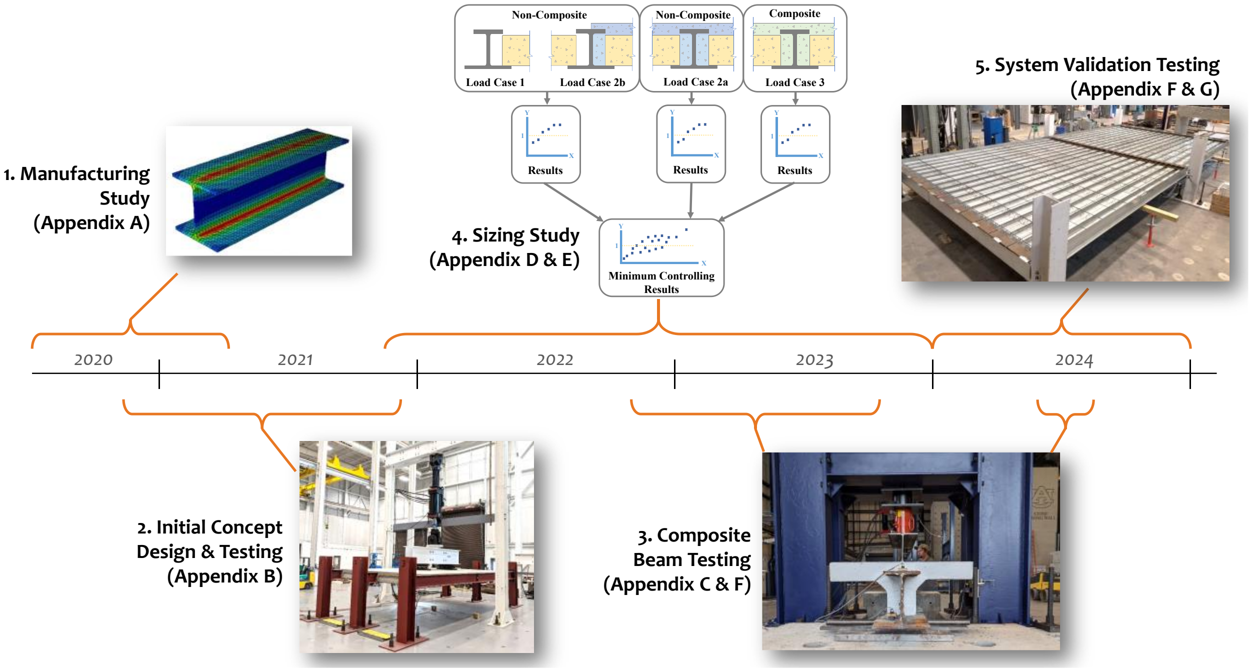

Figure 3: Research Timeline

The initial phase of the research focused on manufacturing future hot-rolled A-shapes. This work included numerical modeling to understand A-shape residual stresses and deformations from the milling process. In addition, interviews were conducted with the major US steel mills for geometric criteria aimed at rolling efficiency. The second research phase designed and conducted an early experiment using a prototype A-shape (from Nucor) within a composite floor system using precast hollow-core panels. Through this testing and other numerical work, the composite behavior was identified as an area with relatively high uncertainty. Therefore, the third research phase performed nine composite beam tests. The aim of the tests was to evaluate the composite behavior and the ductility of a composite section gained from bond interaction between the steel and concrete.

The fourth phase of research brought together the prior findings, along with information from the literature, to size future A-shape cross-sections. The sizing study consisted of analyzing the cross-section for 16 limit states to establish efficient beams. In addition, a numerical fire study was performed. The fifth phase of the research performed a significant system test using composite A-shapes with concrete cast on deep metal decking (from New Millennium). This included evaluation of construction behavior, vibration performance, and in-service flexural stiffness and strength. The final official phase of the research (not shown in Figure 3) developed generalized results and design guidance for engineers.

Research Summary

This section of the report provides high-level information for the six research phases. Detailed information (literature review, comprehensive results, references, etc.) on Phases 1 through 5 are provided in Appendices A through G. Each of these appendices (with the exception of Appendix G) are journal manuscripts that have or will be published separately. The design aids from Phase 6 are provided in Appendices H through J.

1. Manufacturing Study

The goal of the manufacturing portion of the research was to ensure the final A-shapes could be reasonably produced on a large scale. As a result, the research in this phase was comprised of three tasks. The initial two tasks evaluated the cooling process through numerical modeling and physical testing with proof-of-concept beams. The purpose was to evaluate residual stresses and deformations. The critical findings from these two tasks were:

- A flange width-to-thickness ratio (b/t), quantified as $(0.5b_f/t_f)$, limit of 17 was recommended to manufacture A-shapes with compressive residual stresses below 30% of the yield stress.
- No cross-sectional limit was recommended to satisfy the global deformation (camber) of A-shapes.

The third manufacturing study task was to obtain guidance from three US steel mills through meetings with key personnel. This guidance was incorporated within Phase 4 of the research (see below). The critical findings from this effort included the following:

- Proportion the A-shapes to have the top flange area equal to the bottom flange area.
- Provide a minimum A-shape web thickness of 0.50 in. and ensure the flange-to-web thickness ratio is no more than 2.0.
- Utilize A992, Grade 50, steel for A-shapes.

More detailed information on Phase 1 can be found in Appendix A.

2. Initial Concept Design and Testing

The purpose of this phase was a preliminary constructability assessment of a shallow-depth steel-concrete composite floor system utilizing A-shapes, along with a quantitative evaluation of the structural performance during construction and under service loading. An initial proof-of-concept test was performed to analyze the behavior (see Figure 4). The findings from this experimental research contributed to the A-shape sizing study as part of Phase 4 (discussed below). The primary takeaway from this work was that A-shapes supporting precast panels and a concrete deck is a viable option for building floor systems. The critical findings of the initial testing were:

- Shallow-depth floor systems are easy and fast to construct by placing precast concrete panels on the bottom flange of an A-shape and casting a deck slab that tops the panels and encases the steel beam.

- The non-composite A-shape performed well in terms of lateral-torsional buckling and torsional response due to loading the beams on the bottom flange, creating a stabilizing load-height effect.
- The floor system had a stiff response during service level loading, indicating that the moment of inertia of the gross composite section can be utilized for serviceability analysis.
- Significant partial composite strength was achieved through bond shear forming between the steel beam and concrete. The composite floor system failed at an equivalent load of 500 psf applied using four-point bending over the center beam.
- Due to the beam spacing (limited by laboratory constraints) and the concrete not encasing the entire edge beam, the edge beams failed first due to load distribution from the center to the edge beams. Therefore, component-level beam tests or full-scale system tests with wider beam spacings should be utilized to analyze the composite behavior developed through bond stress for shallow-depth composite floor systems.

Figure 4: Initial Proof-of-Concept Testing

More detailed information on Phase 2 can be found in Appendix B.

3. <u>Composite Beam Testing</u>

The purpose of Phase 3 was to evaluate the composite stiffness and strength of the shallow-depth steel-concrete composite floor system by conducting nine component-level beam tests (eight initially and one later validation). The tests were designed to gain a better understanding of the bond strength between the concrete and unpainted steel to address the uncertainty in composite action gained without the use of mechanical connectors. Furthermore, the predicted partial composite flexural capacity was analyzed using three methods: (1) linear interpolation between the steel and full composite moment capacity, (2) partial plastic stress distribution, and (3) strain compatibility. These methods were compared to the experimental composite strength to establish the best methodology to analyze partially encased composite beams.

The composite beam tests were performed in three main stages: (1) lower load levels to analyze elastic behavior, (2) main test cycle to define the partial composite strength, and (3) additional test cycles to analyze the ductility of the composite beams. Furthermore, the flexural stiffness of the composite section was analyzed at varying load levels. Figure 5 provides an illustration of a component test. The main conclusions drawn from the composite beam testing include:

- The flexural stiffness of the composite beams remained intact throughout the test, and the gross moment of inertia of the transformed section can be utilized for serviceability analysis.
- The component-level beams reached 74% to 83% of the full composite strength in stage two loading before minimal bond slip occurred or a large flexural crack formed.
- The beams were reloaded in stage three and reached 77% to 91% of the full composite strength due to the bond reengaging between the steel and concrete, proving the ductile behavior of the composite section.
- A bond stress of 100 psi undercuts most of the experimental results quantified with the maximum moment in the main test stage. The constant bond stress was assumed to act over a bond perimeter that is above the elastic neutral axis of the composite section. The maximum load transfer developed through bond shear is quantified using elastic shear transfer. The elastic shear transfer is calculated using the constant bond stress, assumed bond perimeter, and the effective length of the shear span.
- The partial composite strength can be conservatively calculated using the linear interpolation method with a bond stress of 100 psi (this approach is recommended for future design with unpainted steel). The partial plastic stress distribution and strain compatibility methods provide reasonable results but are unconservative when compared to the experimental capacity of stage two.

Figure 5: Example Initial Composite Beam Test under Loading

More detailed information on Phase 3 can be found in Appendices C and F. Appendix C includes the eight initial tests that were performed to quantify the bond strength and evaluate different methodologies to calculate the partial composite strength of shallow-depth composite floor systems. Appendix F includes the last component-level beam test that utilized a similar cross-section as the system validation testing (discussed below in Phase 5). This composite beam test was performed roughly a year after the initial eight tests.

4. Sizing Study

The primary goal of Phase 4 was to develop standardized A-shape cross-sectional geometry for residential and commercial building applications. The knowledge gained from Phases 1 through 3 was utilized in establishing A-shapes, which included manufacturing considerations from steel mills, structural stability improvement for construction load cases due to load height effect, and composite action gained from bond interaction between the steel and concrete. An extensive analytical sizing study was performed, and the main findings were:

- A robust sizing study framework was developed to establish efficient and effective A-shape cross-sections. The A-shapes achieve relatively long span lengths and wide beam spacings while maintaining minimum floor depths.
- Seven A-shapes were established that satisfied 16 limit states, which encompassed manufacturing constraints, all plausible construction load scenarios on the non-composite section, and in-service loading applied to the composite section.
- The sensitivity of the controlling limit states was evaluated to understand the impact of the primary building parameters. This included changing the concrete weight, depth, and strength, as well as the bond strength assumption concluded in Phase 3. Furthermore, the service live load was varied for the use of A-shapes in different facilities, and the established cross-sections were analyzed for varying beam lengths and spacings. The parametric studies indicated that composite strength is a controlling limit state in several grid layouts, which highlights the importance of the composite beam testing conducted in Phase 3.

The final A-shapes developed from this work are fully conveyed in Phase 6 below. The primary A8s are drawn to scale in Figure 6. The A8x52 is an ideal section for multi-story residential facilities.

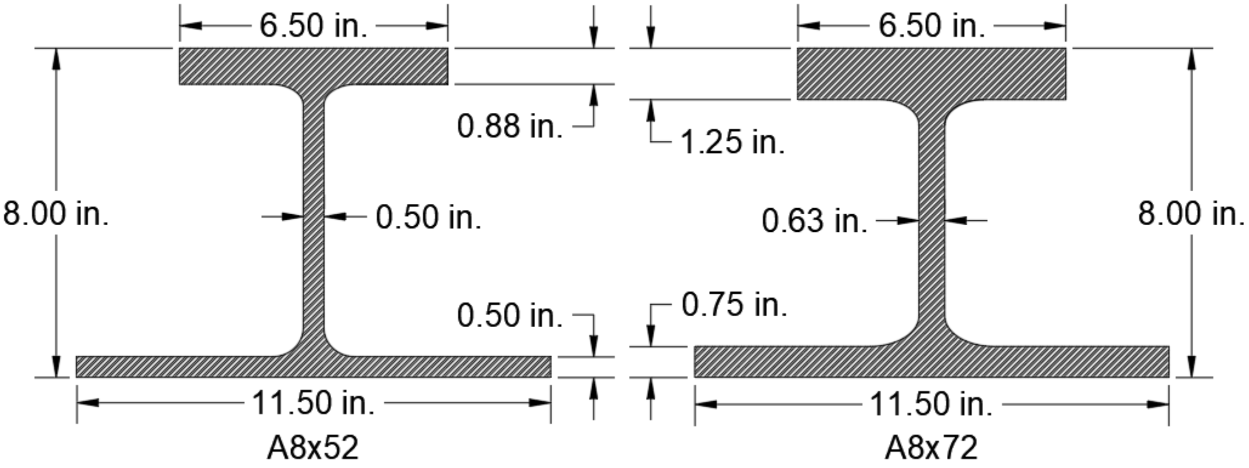

Figure 6: Primary A-Shapes Drawn to Scale

More detailed information on the Phase 4 sizing study can be found in Appendix D.

An important limit state for floor systems is fire resistance. Fire resistance was not included in the sizing study above. However, a supplemental study was conducted on the established A-shapes to analyze the fire resistance within shallow-depth floor systems of an unprotected beam. The steel beams of conventional composite floor systems (illustrated in Figure 1) are covered with spray-applied fire protection to reduce the temperature in steel beams. Experimental testing and numerical work in the literature have shown that shallow-depth composite floor systems have inherent fire resistance due to a significant temperature gradient occurring throughout the steel depth. The temperature gradient is attributed to only the bottom flange being exposed to the fire, with the remaining steel section being encased in concrete. This helps reduce the steel temperature compared to conventional systems.

The high temperatures in the bottom flange (if unprotected) can significantly reduce the strength contribution of the bottom flange. As a result, the fire resistance can be improved by increasing the web thickness or incorporating fire reinforcement near the web of the A-shape (shown in Figure 7). A numerical fire study was conducted based on research published in the literature for the established A-shapes with an unprotected bottom flange. The composite strength of shallow-depth floor systems was quantified using a partial plastic stress distribution with varying steel strength due to the temperature gradient. The main findings of the supplemental fire study were:

- The established cross-sections have an inherent fire resistance due to concrete encasement and satisfy the moment demand during a fire event for a wide range of building geometries.
- An increased web thickness improves the fire resistance; however, the weight of the sections increases with minimal benefit to the other limit states. Therefore, this is not recommended.
- Incorporating fire reinforcement near the bottom of the web of the A-shape is recommended because it significantly improves the fire resistance by increasing the tensile resistance.
- A-shape shallow-depth floor systems have an inherent fire resistance but should be experimentally fire tested if the bottom flange is not fire protected.

The fire resistance could be improved if the bottom flange is protected with spray-applied fire protection, gypsum board, or intumescent paint. These are examples of passive fire protection that reduce the temperature in the bottom flange, therefore increasing the flexural capacity of the composite section during fire. Note, the analysis conducted in the supplemental study utilizes an unprotected bottom flange.

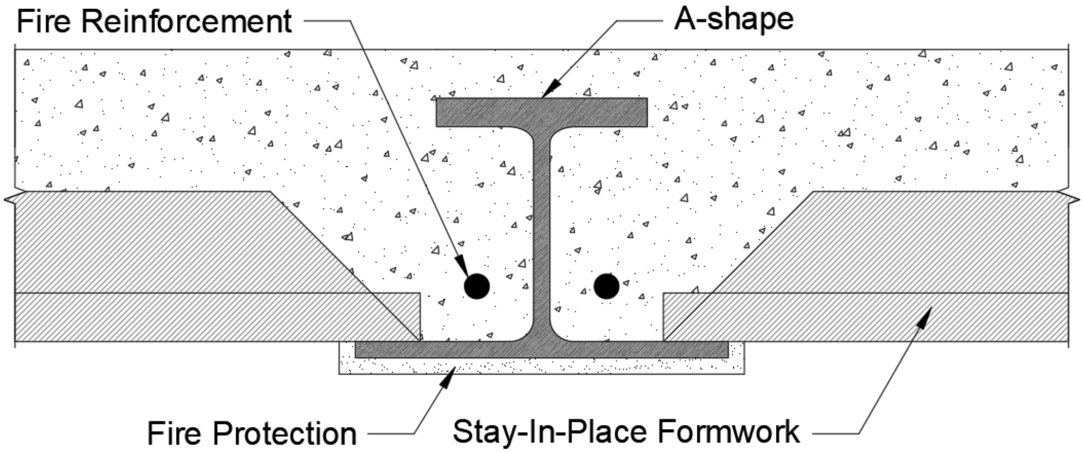

Figure 7: Shallow-Depth Composite Floor Systems with Fire Reinforcement

More detailed information regarding the supplemental fire study can be found in Appendix E.

5. System Validation Testing

A full-scale laboratory experiment was conducted in Phase 5 to further validate the use of A-shapes within shallow-depth composite floor systems in multi-story residential and commercial buildings. A prototype built-up plate girder of the A8x52 cross-section (shown in Figure 6) was utilized in a system test. The system test consisted of three unpainted A8x52 beams spanning between stub columns that were spaced 20 ft on center in both directions. New Millennium deep decking was utilized to span over 19 ft between the A8x52 beams (shown in Figure 8). A concrete slab was then cast monolithically to produce a 10.1 in. deep floor system that was 20 ft x 40 ft (center-to-center of the columns). A photo of the full-scale shallow-depth floor system is shown in Figure 9.

Figure 8: A-Shapes Supporting Deep Decking Prior to Rebar Placement and Deck Casting

Figure 9: Full-Scale System Testing

The A-shape behavior was evaluated throughout construction. This included the constructability of the system, along with the structural performance during the concrete slab pour. Next, vibration testing of the floor system was performed through heel drops, jumping, and walking scenarios. The floor system was then loaded in multiple service load locations to evaluate the stiffness. Finally, the center A-shape was loaded until failure to determine the ultimate flexural capacity. The main findings from the full-scale system testing included:

- The floor system was easy to construct, and the A-shape performed well structurally during construction. The deep decking was shored at midspan, per manufacturer requirements, which reduced the A-shape demands. The maximum strain measured during the slab pour corresponded to a stress of 7.0 ksi. Note that A-shapes were established in Phase 4 considering precast concrete panels (unshored construction), which induce higher torsional demands.
- Vibration testing was conducted in the constructed state to analyze the fundamental frequencies and mode shapes. The first two natural frequencies of the floor system were 8.1 Hz and 9.3 Hz and corresponded to the bending modes of the slab.
- Service level testing was conducted in four locations around the slab to analyze the serviceability. This included loading at two locations near the midspan of the decking, close to the edge beams, and near the center beam. For an 80 psf equivalent area load, the deflection of the floor system corresponds to L/690 when loaded at the center of the decking span. The floor system had a stiff response and further confirmed the gross moment of inertia should be utilized for shallow-depth composite floor systems stiffness calculations.
- The flexural stiffness and the ultimate capacity of the system-level test were analyzed by loading directly over the center beam. The composite beam had a flexural stiffness greater than the gross moment of inertia of the composite section quantified with two times the ANSI/AISC 360-22 specified effective width. Furthermore, the system-level test reached 125% of the full composite strength analyzed. The overstrength and increased stiffness are due to more concrete than the specified effective width being engaged in the composite section. This was verified by measuring significant concrete strain on the slab surface beyond two times the specified effective width.

More detailed information on Phase 5 can be found in Appendix F. A supplemental study for the vibration testing was conducted by Dr. Brad Davis and is included in Appendix G.

6. <u>Generalized Results and Design Guidance</u>

The final phase of the research was to produce generalized results and design guidance for the A-shape cross-sections established in Phase 4. The established cross-sections (shown in Figure 10), along with the section properties of each shape, are provided in Appendix H.

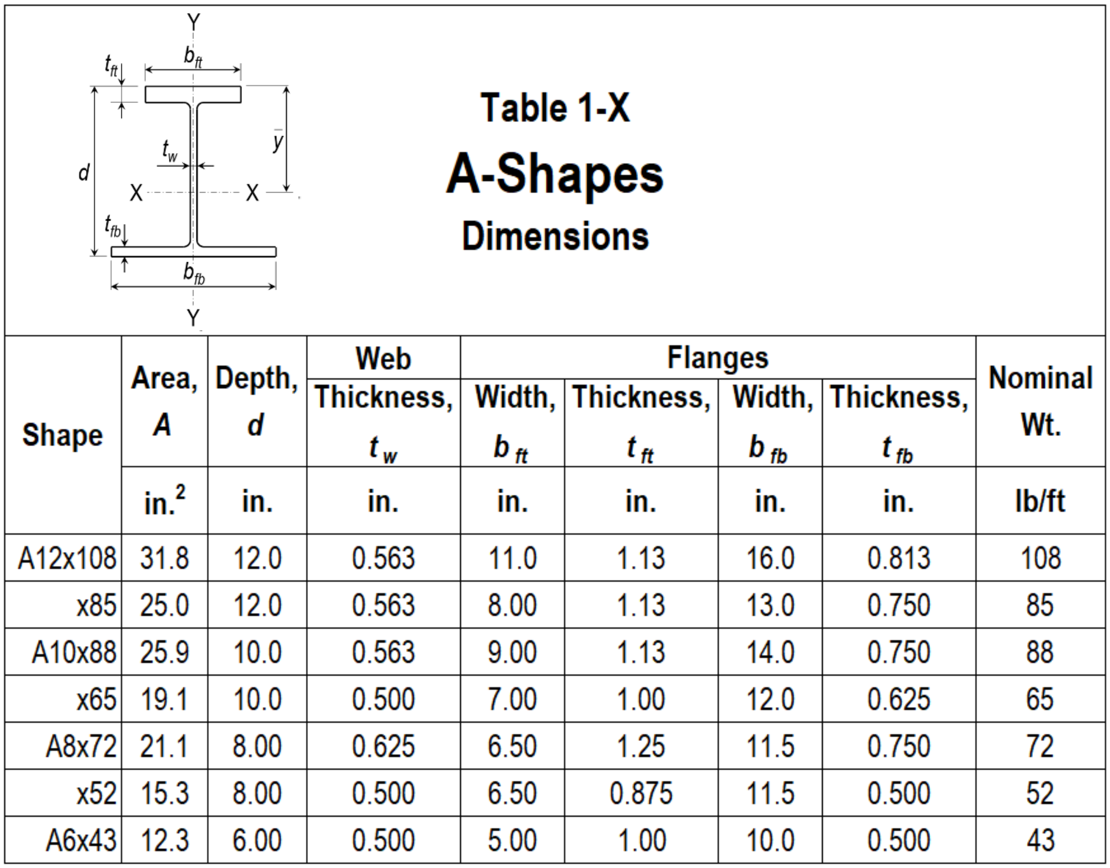

Table 1-X
A-Shapes
Dimensions

Shape	Area, A	Depth, d	Web Thickness, t_w	Flanges Width, b_{ft}	Flanges Thickness, t_{ft}	Flanges Width, b_{fb}	Flanges Thickness, t_{fb}	Nominal Wt.
	in.^{2}	in.	in.	in.	in.	in.	in.	lb/ft
A12x108	31.8	12.0	0.563	11.0	1.13	16.0	0.813	108
x85	25.0	12.0	0.563	8.00	1.13	13.0	0.750	85
A10x88	25.9	10.0	0.563	9.00	1.13	14.0	0.750	88
x65	19.1	10.0	0.500	7.00	1.00	12.0	0.625	65
A8x72	21.1	8.00	0.625	6.50	1.25	11.5	0.750	72
x52	15.3	8.00	0.500	6.50	0.875	11.5	0.500	52
A6x43	12.3	6.00	0.500	5.00	1.00	10.0	0.500	43

Figure 10: Recommended A-Shape Dimensions

A comprehensive ***design example*** (presented in Appendix I) was developed from the knowledge gained in Phases 1 through 5. This design example includes the primary calculations for the design of A-shapes within shallow-depth floor systems. Specifically, analysis during non-composite construction loading is performed, which incorporates a load height effect into the flexural capacity since the load is applied to the bottom flange. This includes torsional analysis (particularly important for large beam spacings). In-service composite analysis is provided, where composite action is developed through bond shear formation between the unpainted steel and concrete. No mechanical connectors, such as shear studs, are utilized for horizontal shear transfer. Serviceability criteria, both deflection and vibration, are also analyzed for the composite section. Finally, supplemental analysis is presented, which includes the fire resistance of A-shapes without a protected bottom flange.

Furthermore, ***design tables*** were developed and are provided in Appendix J to assist engineers in the design of shallow-depth floor systems with A-shapes. This includes:

- Steel A-shape flexural capacity tables for varying unbraced lengths. Note the stabilizing load height effect is incorporated in these calculations by including the lateral-torsional buckling modification factor that considers the load height effect (C_b^*).
- Steel A-shape torsional analysis tables for the maximum uniformly distributed eccentric loading (for construction load cases).
- Composite moment capacity tables using the linear interpolation method for partial composite flexural capacity.
- Capacity-to-Demand tables for A-shape selection within shallow-depth floor systems. An array of beam length and spacing combinations are provided for specific loading scenarios.

Conclusions and Future Work

The overarching motivation of this study was to improve building floor system economy, speed, and efficiency. Flat slab construction is a relatively common and shallow floor system method that utilizes reinforced concrete or post-tensioned concrete. However, flat slabs require extensive shoring and effort for reinforcement placement, making them relatively slow to construct. The alternative to flat slabs is shallow-depth composite floor systems where stay-in-place formwork (either precast concrete panels or steel deep decking) is installed on the bottom flange of steel beams. Following formwork placement, a concrete slab is cast-in-place, encasing the top flange and web of the steel beams. However, hot-rolled steel beams currently produced in the US are doubly symmetric; therefore, stay-in-place formwork cannot be placed on the bottom flange easily due to top flange interference. Thus, asymmetric I-beams (or A-shapes) are desirable to allow for easy and rapid placement of formwork.

An extensive numerical and experimental study was performed to quantitatively evaluate the behavior of hot-rolled A-shapes within shallow-depth composite floor systems. The research study was comprised of six phases. These phases of research covered all stages in the "life" of future A-shape beams within shallow-depth composite floor systems. This began with the manufacturing of the sections and continued throughout the in-service performance. The experimental testing program was comprised of an initial proof-of-concept test, nine composite beam tests, and a substantial building system test. The results from this testing were incorporated into the comprehensive numerical analysis. In the end, the knowledge gained from this study was utilized to establish recommended A-shape cross-sectional dimensions for production in the US and future adoption in Part 1 of the AISC Steel Construction Manual. In addition, practical design guidance was provided in the form of a complete design example and several design tables.

In closing, A-shapes can be utilized within shallow-depth composite floor systems following the guidance provided herein. The main areas of future research could include fire testing to avoid protection applied to the bottom flange. In addition, cross-laminated timber (CLT) panels could be explored as a decking alternative.

Acknowledgments

The authors would like to express gratitude to AISC for financially supporting this research through the 2020 Milek Fellowship. The authors thank the project industry panel (names listed in Table 1) for all their insight and support.

Table 1: AISC Project Industry Panel

Name	Affiliation	Company/ Institution	Role	E-Mail
Devin Huber	Co-Chair for COR/NFS	AISC	Director of Research	huber@aisc.org
Margaret Matthew	Co-Chair for COR/NFS	AISC	Senior Engineer	matthew@aisc.org
Chris Garrell	COR/AISC	AISC	Senior Bridge Engineer	garrell@aisc.org
Chia-Ming Uang	COR	UC-San Diego	Academic	cmu@ucsd.edu
Tom Sabol	COR	Englekirk	Academic and Practicing Engineer	tom.sabol@englekirk.com
Joe Zona	COR	Simpson Gumpertz & Heger	Designer/Practicing Engineer	jjzona@sgh.com
Ronnie Medlock	COR	High Steel	Bridge Fabricator	rmedlock@high.net
Duff Zimmerman	COR	Cooper Steel	Building Fabricator	duff@coopersteel.com
Robert Carter	Interested Party	Steel Dynamics	Sales Manager for Structural Shapes	robert.carter@steeldynamics.com
Paul Yengst	Interested Party	Steel Dynamics	National Accounts Manager	Paul.Yengst@steeldynamics.com
Richelle Wilson	Interested Party	Steel Dynamics	Metallurgical Services Engineer	richelle.wilson@steeldynamics.com
Tabitha Stine (Kim Olson)	Interested Party	Nucor	Director – Construction Solutions Services	tabitha.stine@nucor.com
Shane Vernon	Interested Party	Nucor	Metallurgist	shane.vernon@nucor-yamato.com
Chris Hoyt	Interested Party	Gerdau	Director of Sales – Construction	christopher.hoyt@gerdau.com
Scott Meaney	Interested Party	Gerdau	Director of Marketing	Scott.meaney@gerdau.com
Fernao A. O. Cesar	Interested Party	Gerdau	Director of Marketing	fernao.cesar@gerdau.com
Rafael Garcia	Interested Party	Gerdau	Product Line Manager – Construction	Rafael.garcia@gerdau.com

The authors would also like to thank Nucor for donating the material and their services to produce the proof-of-concept A-shapes that were used in the first three research phases. Specifically, we want to acknowledge Mike Thomas, Phil Bischof, and Ross Simmons. The numerical analysis conducted in the manufacturing phase of the research was performed with high-performance research computing resources provided by Texas A&M University (https://hprc.tamu.edu).

The authors thank New Millennium for providing the deep decking and their guidance during the design of the full-scale experiment in the fifth phase, specifically Alex Therien and Marty Williams. Alex and Marty's guidance on shallow-depth floor systems greatly impacted this research project. The authors thank Dr. Brad Davis for his guidance and analysis of the vibration data recorded for the full-scale test. The authors appreciate Joshua McLeod's time and effort in assisting with data collection for the vibration testing.

The authors appreciate and would like to thank the laboratory staff for their support in conducting the experimental testing in the second, third, and fifth research phases. A large experimental campaign was performed as part of this research study, which was made possible by several laboratory staff. The staff includes Dr. Peter Keating, Charlie Droddy, and Kirk Martin from the Texas A&M High-Bay Laboratory, who helped with testing in the second phase. Testing was performed in the third and fifth phases at the Advanced Structural Engineering Laboratory at Auburn University. The authors thank the laboratory staff and students, including Rob Crosby, Caleb Fleming, and George Cowles, for their support.

Disclaimer

Auburn University, Texas A&M University, the researchers, and industry panel (denoted as the Research Team) are not liable for building projects utilizing this report. The information and results presented were issued in good faith. Every reasonable care was taken to ensure that the findings were accurate. The Research Team does not accept responsibility for any matters arising or consequences from the further use of this report.

Any party using the findings of this report agrees to indemnify, defend, and hold the Research Team harmless from and against all losses, expenses, damages, and costs, including reasonable attorney fees arising out of or relating to any misuse of the content provided by the Research Team.

Appendix A – Manufacturing Study

Appendix A provides detailed information on the manufacturing study (Phase 1) to analyze residual stresses and global deformations. Extensive thermomechanical finite element modeling was performed to analyze the residual stresses that formed for an array of asymmetric I-beams. The finite element modeling was validated by recording the temperature of proof-of-concept beams as they cooled. As a result of this analysis, a flange width-to-thickness ratio was established, and global deformation was found not to be an issue.

Citation

The following work has been published by the American Society of Civil Engineer's Journal of Structural Engineering. The citation to the published journal article is:

> Stoddard, E., and M. Yarnold. 2022. "Residual Stress and Global Deflection Limits for Future Hot-Rolled Steel Asymmetric I-beams." *Journal of Structural Engineering*, 148(1). https://doi.org/10.1061/(ASCE)ST.1943-541X.0003204

The following work is expanded upon and supplemental information/results are provided in Eric Stoddard's Ph.D. Dissertation. The citation to Eric's dissertation is:

> Stoddard, E. A. 2022. "Behavior of Hot-Rolled Asymmetric Steel I-beams: Concept to Construction." Ph.D. Dissertation, Texas A&M University.

Residual Stress and Global Deflection Limits for Future Hot Rolled Steel Asymmetric I-Beams

Eric Stoddard and Matthew Yarnold

Abstract

Medium- to long-span floor systems in residential and commercial construction have commonly utilized steel-concrete composite construction. These composite floor systems have become more structurally efficient with the use of built-up asymmetric steel beam sections. While structural efficiency is important, a fast and cost-effective solution is paramount. Research presented herein is being conducted for the American Institute of Steel Construction (AISC) on hot rolled asymmetric I-beams (A-shapes) for potential future addition to the AISC Steel Construction Manual. The aim is to adequately proportion these hot rolled shapes so they match or improve built-up asymmetric beam structural efficiency, while increasing the speed and economy of steel-concrete composite floor systems. The initial focus has been placed on the steel behavior as a result of the manufacturing process, where residual stresses and deformations can be an issue due to uneven cooling. A better understanding of residual stresses is critical for accurate calculation of the lateral torsional buckling strength during deck casting/placement. In addition, the steel mills have expressed concern regarding global deformation of an asymmetric I-shape. As a result, an extensive thermomechanical finite element modeling approach, using nonlinear thermomechanical properties of steel, was devised to simulate the cooling process of hot rolled steel shapes. A single model requires up to 50 hours of processing time using the Texas A&M high performance computing center. The modeling procedure was validated against accepted residual stress experimental test measurements. Proof-of-concept (POC) A-shape beams were also produced by Nucor. The POC beams cooling profile were used as further validation. Then, a parametric study was executed that individually altered the top flange width and thickness of two different depth W-shapes. The parametric study identified a maximum flange width-to-thickness ratio to satisfy a reasonable residual compressive stress limit. The study also found that despite concerns, global deformations are not an issue for realistic proportions of future hot rolled asymmetric I-beams.

Keywords: Hot-Rolled, Asymmetric Beams, Residual Stresses, Composite Floor System

Introduction

The United States (US) market for hot rolled steel beams is limited to double symmetric I-shapes such as W, M, or HP shapes (AISC 2016). These beams are utilized (in some form) in a large percentage of steel building floor systems, which take advantage of composite construction (precast and cast-in-place). In precast concrete floor system applications, steel beams are used to support the concrete panels. For these beams the top flange can hinder panel installation and requires cutting a current rolled section or making a relatively expensive plate girder section. Illustrated in Figure A-1 are several current asymmetric I-beam fabrication approaches commonly utilized with precast floor system construction.

One of the more common precast floor systems in the US is the Girder-Slab®. This system uses a beam called a D-Beam® (Girder-Slab Technologies 2016) (Figure A-1(b)). The D-Beam® is made by cutting a "parent" beam down the web longitudinally. The top flange and bottom flange sections of the "parent" both become bottom flanges of the new D-Beam® after a plate, narrower than the original flange, is welded to the cut web of each piece (Figure A-1(b)). As an example, two DB8 beams are made from a single W12 section. A similar beam system is the Kloeckner Westok® which utilizes two separate sizes of hot rolled sections which are both cut down the web longitudinally in a castellated pattern (Kloeckner Metals 2020). The smaller section is welded to the top of the larger section making an asymmetric beam (Figure A-1(d)). Another system is the Slim-Floor® which utilizes either a welded plate on a cut web similar to the previous systems or an addition of a plate welded to the beams bottom flange to increase its flange width (Figure A-1(c)) (ArcelorMittal Commercial Sections 2019). All current systems are either labor or material and labor intensive to achieve the built-up asymmetric I-beam required.

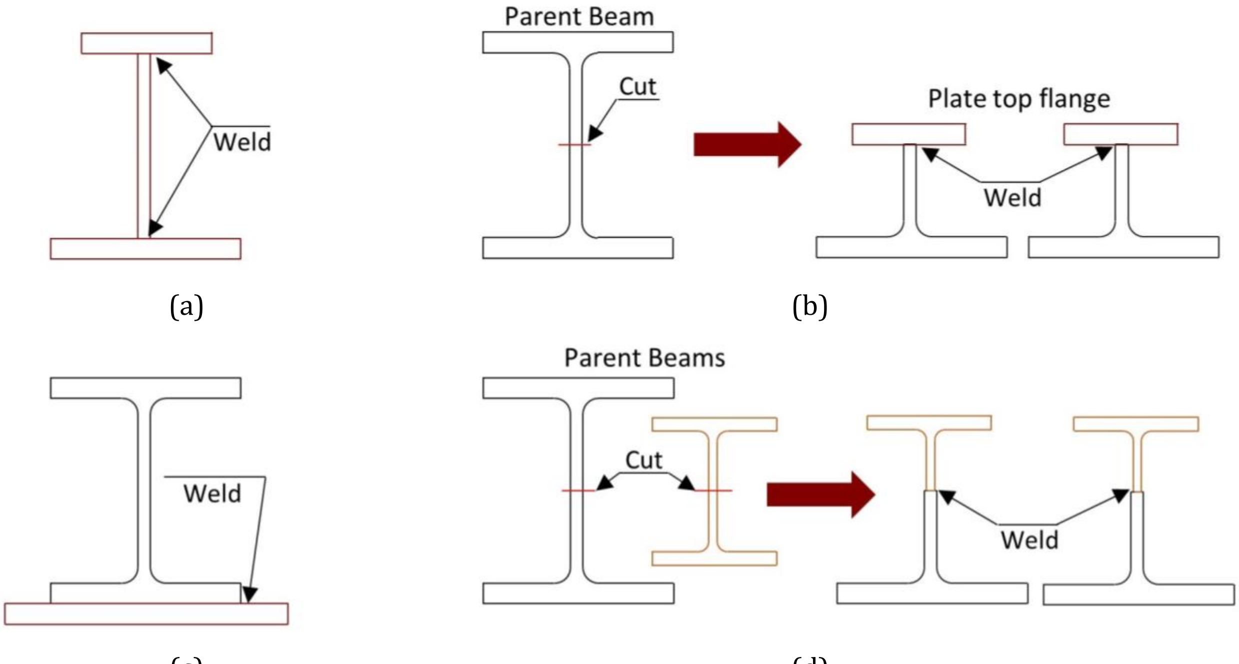

(a) (b)

(c) (d)

Figure A-1: Current Asymmetric Built-Up I-beams: (a) Plate Girder Section; (b) D-beam; (c) Plate Welded to Rolled Section; and (d) Kloeckner Westok

Conventional cast-in-place concrete floor systems are also widely utilized; these systems typically involve a deck slab cast on top of rolled steel beams. The concrete and steel are made composite through the use of welded shear studs. In composite floor systems the top flange of the steel beam does not have significant contributing strength or stiffness to the final floor system configuration. However, during construction it is an important factor. An asymmetric I-beam can be more structurally efficient, although the additional cost of fabrication typically outweighs the efficiency.

To improve the cost and speed of construction for pre-cast and cast-in-place floor systems, the manufacturing of hot rolled asymmetric I-beams (A-shape) is being studied (Yarnold and Stoddard 2020). AISC is researching faster construction methods as part of their new "need for speed" initiative. A-shapes are currently being researched to reduce fabrication and construction time for floor systems. Along with a savings in speed, the relative cost of floor systems may see a reduction if A-shapes become a viable rolled shape option. These A-shapes are comprised of a top flange that is relatively small compared to the bottom flange. Illustrated in Figure A-2 are the potential uses of A-shapes, with both cast-in-place and pre-cast floor systems. Currently, no major US steel mills produce A-shapes. There is also limited production of A-shapes around the world. This research is intended to improve the understanding of A-shape behavior from the hot-rolling process. Due to the extreme cost to manufacture a new rolled shape, numerical research is preferred. Future research will focus on the structural behavior during construction and the final configuration. AISC has invested (along with two major US steel mills) in the development of efficient A-shape cross-section dimensions. The goal is to include A-shapes in the AISC manual (AISC 2016) and have them regularly manufactured.

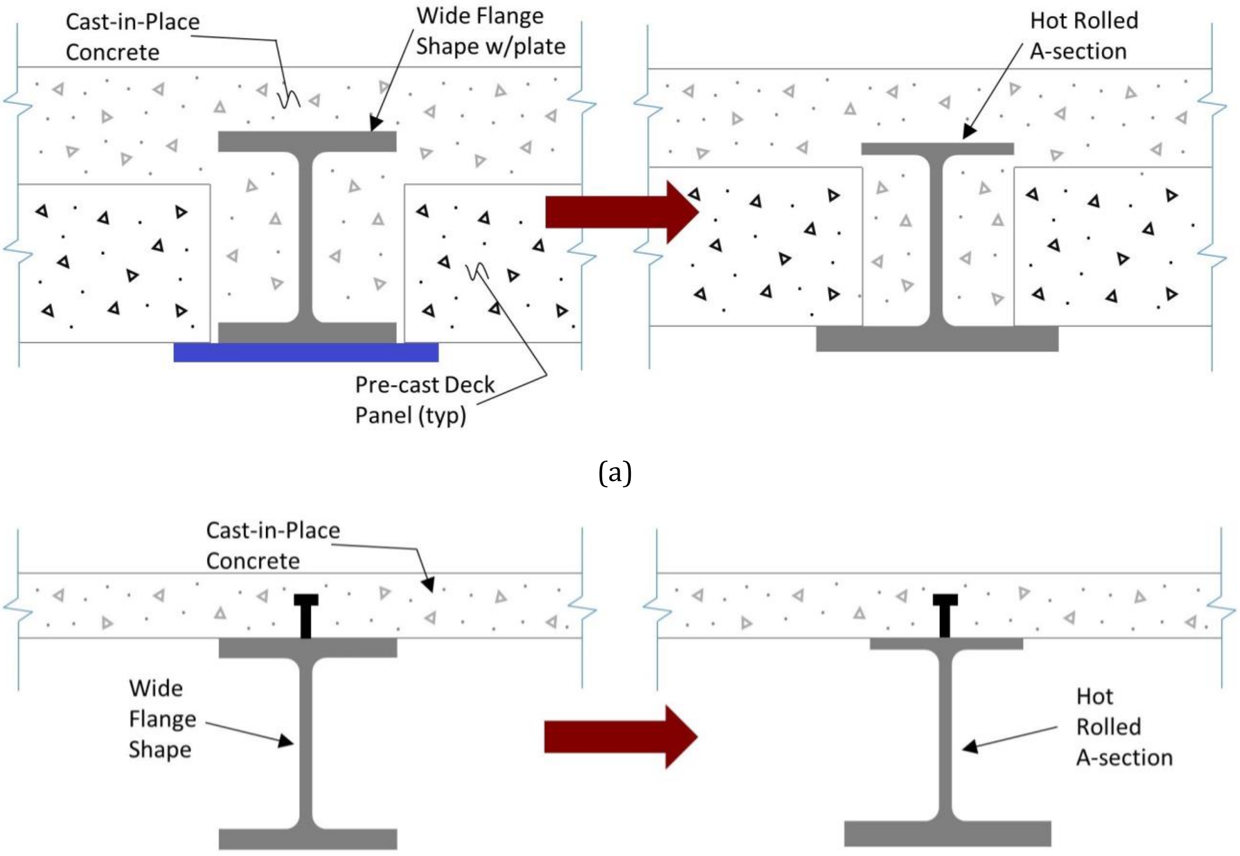

(a)

(b)

Figure A-2: Potential use of A-shapes in Floor Systems: (a) Precast Deck Floor Composite Floor Composite Floor System; and (b) Cast-In-Place Composite Floor Systems

Asymmetric hot rolled I-beams are not new to the steel industry. Steel members, known as Cross Tie Sections, have been rolled by custom mills and produced limited shapes going back to the early 1900's (Carnegie Steel Company 1923). British Steel rolls ten different asymmetric I-shapes (British Steel 2018). However, these I-shapes only include a minor reduction to the top flange width.

Current research on composite floor systems has not focused on hot rolled asymmetric I-beams. For example, recent research has been towards improvements in fire and vibration performance such as; component fire experiments of composite floor beams with various end support conditions (Choe et al. 2020), effects of load intensity and restraint on the fire resistance of composite beams (Alfawakhiri et al. 2016), control of vibrations induced by people walking on long-span composite floor decks (Varela and Battista 2011), and mitigating footfall-induced vibration in long-span floor systems (Nguyen et al. 2014). Another recent study investigated floor systems spanning up to 9 meters (30 feet) with minimal floor thickness up to 304mm (12 in.) (Huber et al. 2011). However, limited research has been performed on large-scale production of hot rolled A-shapes, to improve composite floor systems. With the increasing demand for asymmetric cross-sections from AISC and the steel industry, a better understating of the behavior and limits of hot-rolled asymmetric beams is needed.

The primary contribution of the presented research is the manufacturing limits for hot rolled A-shape cross-sectional geometry. Two main manufacturing concerns, during the cooling process, have been expressed by the steel community for future rolling of A-shapes. The first is excessive residual compressive stresses, which will impact the lateral torsional buckling resistance during construction. The second concern (expressed by the steel mills) is global deformations (or curvature). As a result, a comprehensive thermomechanical finite element (FE) modeling approach was developed to simulate the behavior of rolled shapes during the cooling process. This included heat-transfer analysis to identify the thermal behavior combined with stress analysis. The general analysis approach was applied to conventional doubly symmetric I-shapes for validation of the methodology. This was performed through a comparison of the results with several accepted stress distributions along with physical experiments and validated FE results. Proof-of-concept A-shape beams were also produced. Physical measurements of the cooling rates were used for further validation of the thermomechanical modeling results. A wide range of A-shape cross-sectional configurations were analyzed to identify the residual stresses and deformations (local and global). The main finding is a recommended flange width-to-thickness limit to satisfy the compressive stress limit. This limit will be used with future research (evaluating other limit states) to establish the specific A-shape cross-sections for the AISC manual. The other finding was that despite concerns, global deformations are not a concern for realistic proportions of future A-shapes. Further details on the methodology, validation, and parametric study are presented below.

Thermomechanical Modeling

3D thermomechanical FE analysis was selected for identification of the residual stresses and deformations imposed on hot rolled A-shapes as a result of cooling. ABAQUS/CAE software was chosen because of its robust nonlinear transient thermal and stress analysis capabilities. The FE modeling was performed with accepted and validated material properties along with FE methods (Quayyum and Hassan 2017) (described in detail in the Material Properties section). A coupled temperature-displacement analysis was chosen which utilized a 10-node thermally coupled tetrahedral element with second-order accuracy, trilinear displacement and temperature. The tetrahedral element was selected over the standard hexahedral element type to accurately model the complex geometry of fillets. The additional information for the modeling process is described in the following sections.

Geometry and Boundary Conditions

The cross-sectional geometry of the residual stress FE models was consistent throughout the study. A single tetrahedral element was used through the thickness of the flanges and web. Then the aspect ratio of the elements was set as close to unity as possible. Tetrahedral elements allowed for the fillets to be included, which improved the temperature distributions and resulting residual stress distributions. A typical meshing can be seen in Figure A-3.

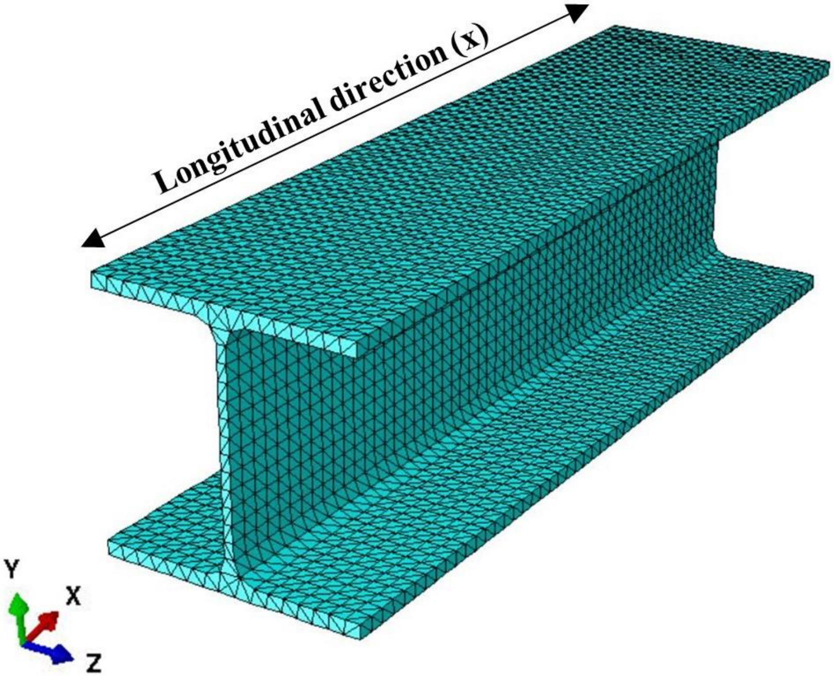

Figure A-3: Typical Beam Meshing (Residual Stress Analysis)

A sensitivity study was performed, which varied the mesh type and seed size. The mesh selected produces accurate results along with sufficient data resolution (validation shown below), while maintaining reasonable processing times. Sensitivity models, implementing hexahedral elements and tetrahedral elements, were studied with varying seed sizes up to 25 percent the validation flange thickness. Longitudinal stress measurements were compared in all cases. The sensitivity study also considered the stress variation through the flange thickness. Flange stresses were compared between the average and the outer fiber. A resulting difference of less than 1.8% was found acceptable and the outer fiber stresses were used for the remainder of the study. With processing times on the Texas A&M supercomputer of over 150 hours per model and negligible stress profile differences, the single element meshing was chosen.

The length of the beams analyzed varied based on the objective of the analysis and the depth of the cross-section. The residual stress models incorporated a length three times the depth, which has been shown in testing and theory (St. Venant Principle) to allow sufficient stresses to fully develop (Huber 1956). The reason for using a reduced length is to minimize the processing time, while still maintaining a sufficient number of nodes for adequate data resolution. For the deformation analysis, 9m (30ft) beams were analyzed. This was considered a reasonable length for hot rolled beam production based on tours of two different steel mills. A similar sensitivity study was performed for deformation analysis. An appropriate meshing was selected resulting in processing times of full-length beams up to 50 hours per model.

The beam boundary conditions were pinned or rolled in each corner to allow rotation and beam movement. The beams were not supported between corner conditions and gravitation affects were not applied. The modeled boundary conditions allowed the beams the ability to "shrink" when cooled without constraint. This was done to eliminate stresses induced by physical constraints.

Material Properties

A significant number of material properties needed to be identified and defined in the program to accurately perform the analysis. This included constant properties such as the steel density and temperature dependent properties such as thermal conductivity, elastic modulus, Poisson's ratio, thermal expansion, film coefficient, latent heat, specific heat, and plastic modulus. Past research on residual stress analysis resulting from uneven cooling has shown that many temperature dependent steel properties are needed for accurate results (Quayyum and Hassan 2017). Many properties of structural steel are similar for different ASTM grades having consistent composition and processing. The properties used were to model ASTM A992 steel, with 345 MPa (50 ksi) yield strength.

The thermal and mechanical analysis were coupled; however, the coefficients can mostly be grouped separately. The thermal modeling coefficients needed to solve Fourier's heat equation are density, specific heat, thermal conductivity, surface coefficient, and latent heat (Quayyum and Hassan 2017). The material was assumed to be isotropic and homogeneous. Density of the steel was modeled as constant with temperature with a magnitude of 7870 kg/m3 (490 lb/ft3) (AISC 2016). The specific heat (shown in Figure A-4(a)) was modeled with temperature (CEN 2005), where the significant spike at approximately 727 °C (1341 °F) indicates the phase change from solid-state α (Ferrite) to γ (Austenite) of the steel. Thermal conductivity also varies with temperature. Illustrated Figure A-4(b) is the bi-linear relationship utilized (CEN 2005). The surface coefficient (shown in Figure A-4(c)) is also a bi-linear relationship and can be explained as the temperature "loading" (Brickstad and Josefson 1998), which is expanded upon further below. Latent heat in this case is the energy released during the liquid to solid phase change. This was derived from the specific volumetric enthalpy (Wickström 1979) and was modeled over the phase change.

The mechanical coefficients needed for the coupled analysis were elastic modulus, Poisson's ratio, thermal expansion, latent heat, and plastic yield. The elastic modulus was varied with temperature as shown in Figure A-4(d). This relationship was taken from tests performed on coupons that were heated to different elevated temperatures and loaded at those elevated temperatures until fracture (Hu et al. 2009). Poisson's ratio was modeled as a bi-linear relationship (shown in Figure A-4(e)) (Andersson 1978). The linear coefficient of thermal expansion is provided in Figure A-4(f) (AISC 2016).

The plastic yield response is modeled with multiple stress-strain curves at different temperatures (Figure A-5). The plastic response was adapted for ABAQUS from past test values from steel test (Harmathy and Stanzak 2009). The yield plateau was slightly altered for compatibility with ABAQUS parameters. The plastic hardening is modeled as multilinear-kinematic hardening where the surface is defined by equivalent von Mises stresses. Equation (A-1) illustrates the calculations, which include the second-order stress tensor (σ), kinematic shift (α), deviatoric stress tensor (S), and deviatoric part of the back stress (α^{dev}).

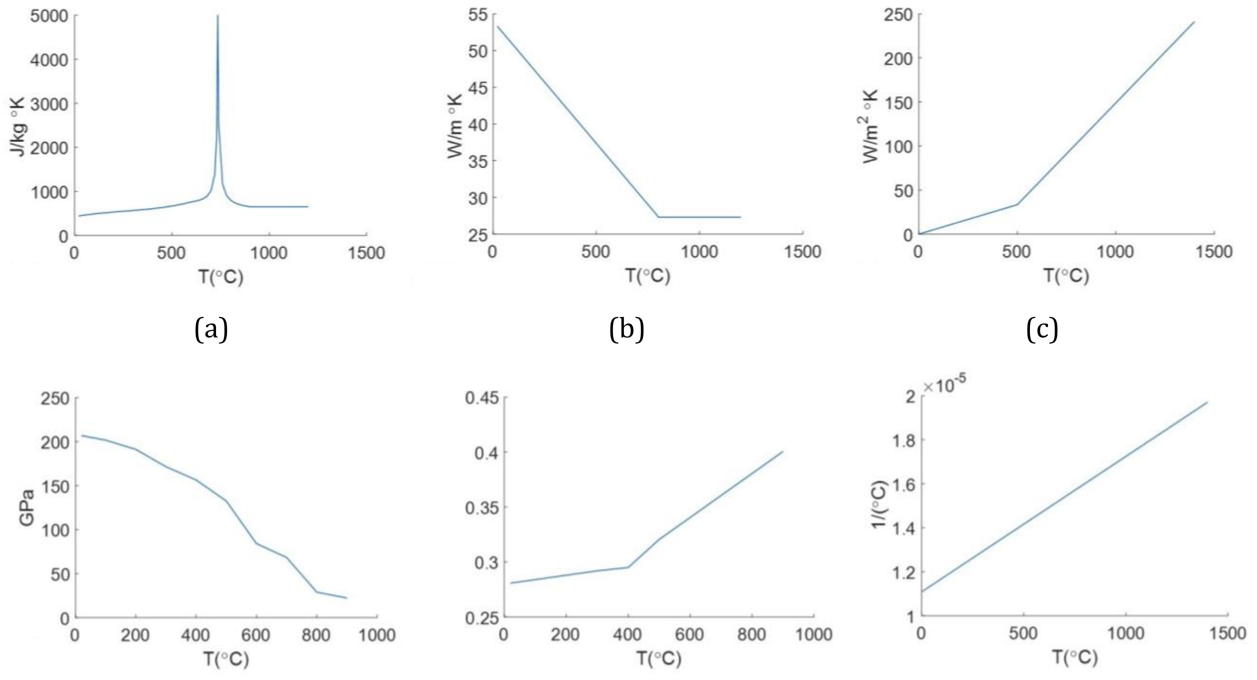

(a) (b) (c)

(d) (e) (f)

Figure A-4: Thermal and Material Coefficients: (a) Specific Heat (CEN 2005); (b) Thermal Conductivity (CEN 2005); (c) Film Coefficient (Brickstad and Josefson 1998); (d) Elastic Modulus (Hu et al. 2009); (e) Poisson Ratio (Andersson 1978); and (f) Thermal Expansion (AISC 2016)

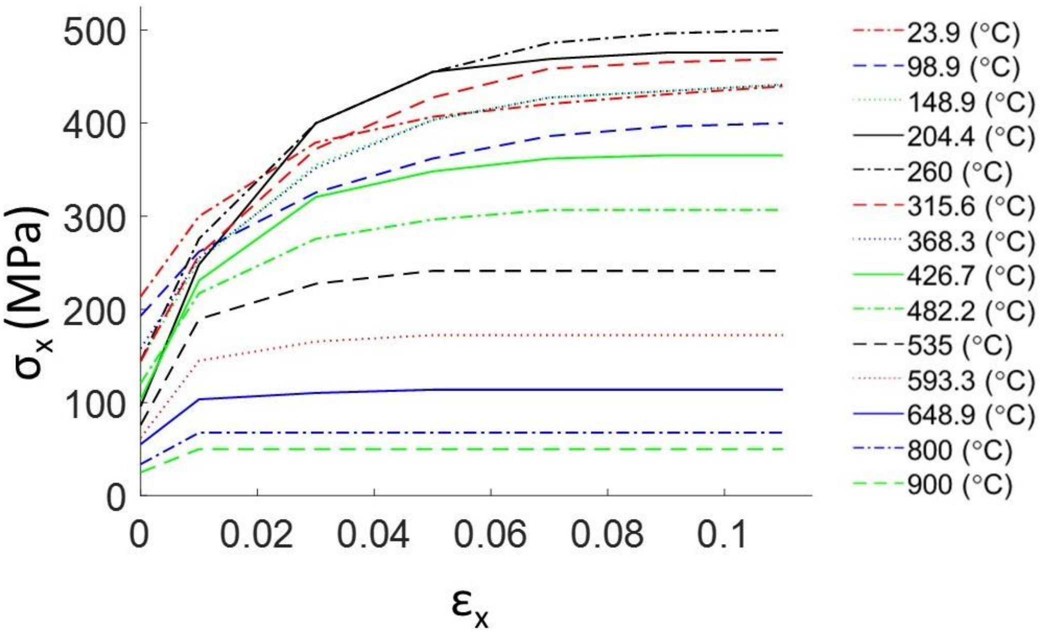

Figure A-5: Multilinear Kinematic Stress (σ_x) versus Strain (ε_x) Hardening Model Adapted from Test Data

$$f(\sigma - \alpha) = \sqrt{\frac{3}{2}(S - \alpha^{dev}) \; : \; (S - \alpha^{dev})} \qquad \text{(A-1)}$$

The model assumes the associated plastic flow shown in Equation (A-2). In this equation $\dot{\boldsymbol{\epsilon}}^{pl}$ represents the rate of plastic flow and $\bar{\dot{\epsilon}}^{pl}$ represents the equivalent plastic strain rate, which is provided in Equation (A-3).

$$\dot{\boldsymbol{\epsilon}}^{pl} = \frac{\partial f(\boldsymbol{\sigma} - \boldsymbol{\alpha})}{\partial \boldsymbol{\sigma}} \bar{\dot{\epsilon}}^{pl} \qquad \text{(A-2)}$$

$$\bar{\dot{\epsilon}}^{pl} = \sqrt{\frac{2}{3} \dot{\boldsymbol{\epsilon}}^{pl} \; : \; \dot{\boldsymbol{\epsilon}}^{pl}} \qquad \text{(A-3)}$$

The total strain rate ($\dot{\epsilon}$) equation includes the elastic strain rate ($\dot{\epsilon}^{el}$) and the plastic strain rate, as shown in Equation (A-4).

$$\dot{\epsilon} = \dot{\epsilon}^{el} + \dot{\epsilon}^{pl} \qquad \text{(A-4)}$$

Temperature “Loading”

The FE modeling initial conditions were 1300° C (2372° F) (Quayyum and Hassan 2017) to remove any appreciable stress. A temperature below the melting point was chosen and to mimic pre-rolling temperatures of steel beams. To cool the beam to an ambient air temperature of 20° C (68° F) an accepted film coefficient (Figure A-4(c)) for steel was modeled (Brickstad and Josefson 1998). The film coefficient was modeling simple cooling in still air. During the cooling, conduction, convection, and radiation all play a role to cool the section. The rate at which conduction, convection and radiation cool the beam are not constant and vary with temperature. To simplify modeling, since all three coefficients vary the speed at which the beam cools, the separate coefficients are combined into a single coefficient. The bi-linear film coefficient takes those cooling parameters into account in one modeled coefficient.

Thermomechanical Validation Study

Literature Comparison

The thermomechanical modeling process, described in the prior section, was used to analyze two separate beam cross-sections and the results were compared with experimental (and accepted numerical) results from the literature to validate the modeling process. The two cross sections chosen were the AISC W8x31 and W16x50. These two beam sizes were selected because there is ample residual stress test data available in the literature. The FE results for longitudinal residual stresses were compared to actual measured stresses along with accepted stress distributions. The finite element analysis (FEA) results were compared with sectioning results from Lehigh University (Huber 1958) for the W8x31 and sectioning results from Alpsten (Alpsten 1972) for the W16x50.

Along with physically measured results accepted stress patterns from, Young (Young 1975), ECCS (ECCS 1984), Galambos & Ketter (Galambos and Ketter 1959), and BSK99 (BSK (Blekinge Studentkar) 2003) were plotted. It should be noted that although more simplistic, the bi-linear distributions represent maximum compressive and tensile forces with reasonable accuracy. Accepted numerical results from Quayyan (Quayyum and Hassan 2017) were also presented for the W16x50. The plotted W8x31 stress comparison (Figure A-6(a)) and W16x50 (Figure A-6(b)) illustrates the comparison. The FEA results are within the accepted distributions. In addition, the outer fiber compressive stresses are relatively close to the literature values. Overall, the authors are confident that the FE modeling process produces reasonable results.

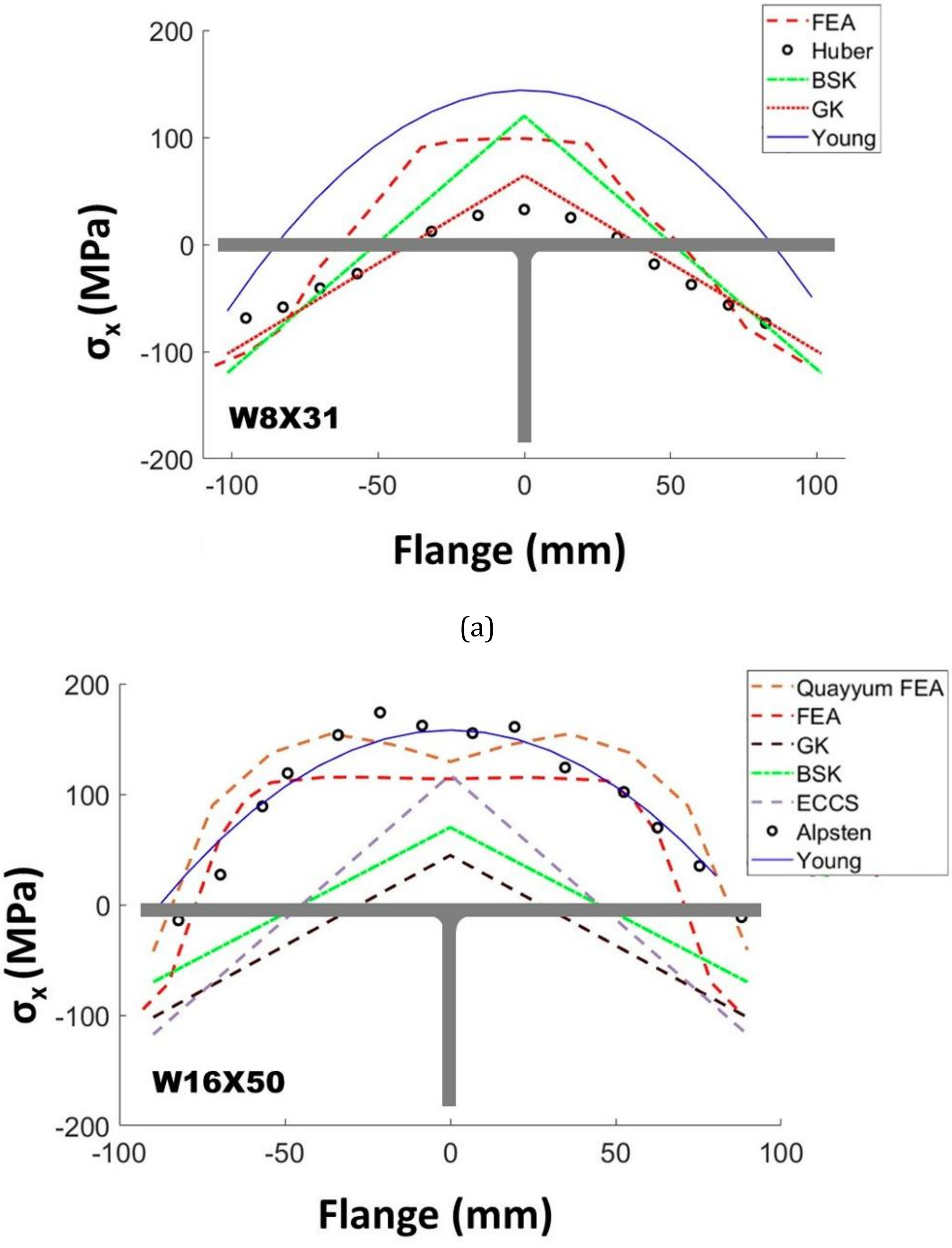

(a)

(b)

Figure A-6: Top Flange Residual Stresses for the (a) W8x31; and (b) W16x50.
Note: FEA indicates the results from this study.

Proof-of-Concept Beam Comparison

Proof-of-concept (POC) A-shape beams were devised by the authors and produced by Nucor to replicate a hot-rolled A-shape. The primary purpose for creating these beams is for future full-scale laboratory testing (discussed further in the Future Research section below). However, a secondary purpose was to utilize their cooling rates to further validate the thermomechanical modeling process.

The high cost of retooling rolling mill stands along with the lack of understanding for A-shape behavior, necessitated a creative solution to develop POC beams. Therefore, the general approach was to cut down (or narrow) the top flange of a W-shape, reheat the beam, and then let it cool in a similar manner to conventional rolled shapes (Figure A-7). This approach does not capture the correct grain structure, but was still considered sufficient for research purposes.

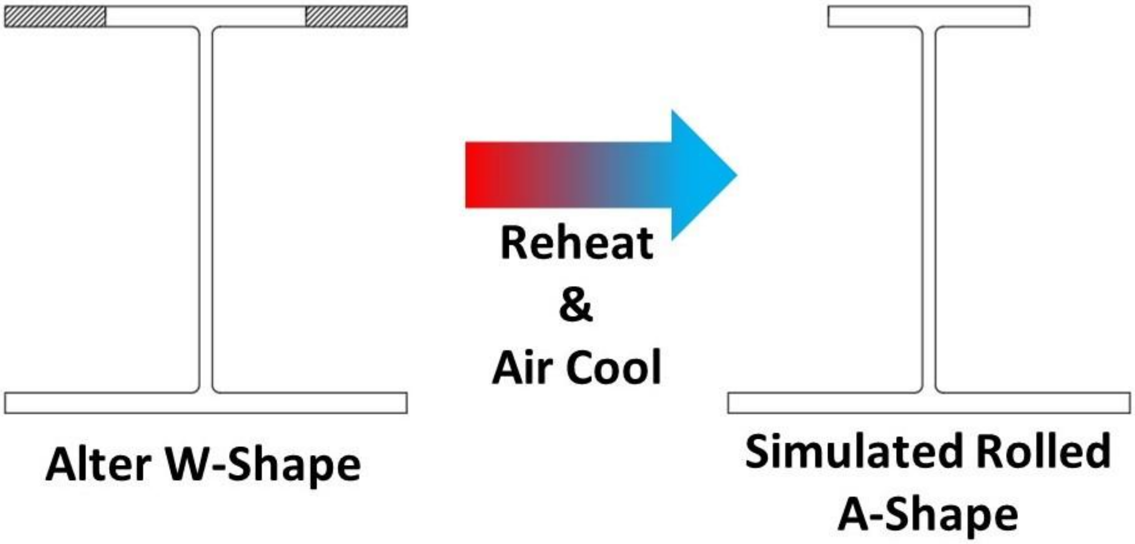

Figure A-7: Process to create Nucor POC Beams

The specific process to produce the POC beams initiated with donated W12x65 beams from the Nucor-Yamato Steel facility in Blytheville, Arkansas. The top flange of the W12x65 beams were cut longitudinally 7.62 cm (3 in) on each side, resulting in an asymmetric beam (labeled W12x65 0.50 b_f beam). The beams were then shipped to the Nucor facility in Longview, Texas where they were reheated to approximately 950ºC (1740 ºF). The reheated beam removal from the oven can be seen in Figure A-8. Again, the POC beams were produced to mimic rolled shapes without the extensive cost of having to retool an entire roll line.

Figure A-8: Reheated POC A-shaped Beams being Removed from the Oven

During the cooling process of the POC beams, non-contact temperature measurements were taken by the research team. These measured temperatures were compared to the FE model temperature distribution, as shown in Figure A-9. The percent differences ranged from 1.9% to 15.8%. The differences were attributed to challenges with conducting accurate temperature measurements along with aspects of the cooling process not included in the model (e.g., convective heat transfer from a slight wind). Overall, the research team believes the POC beam thermal behavior further validates the FE modeling approach.

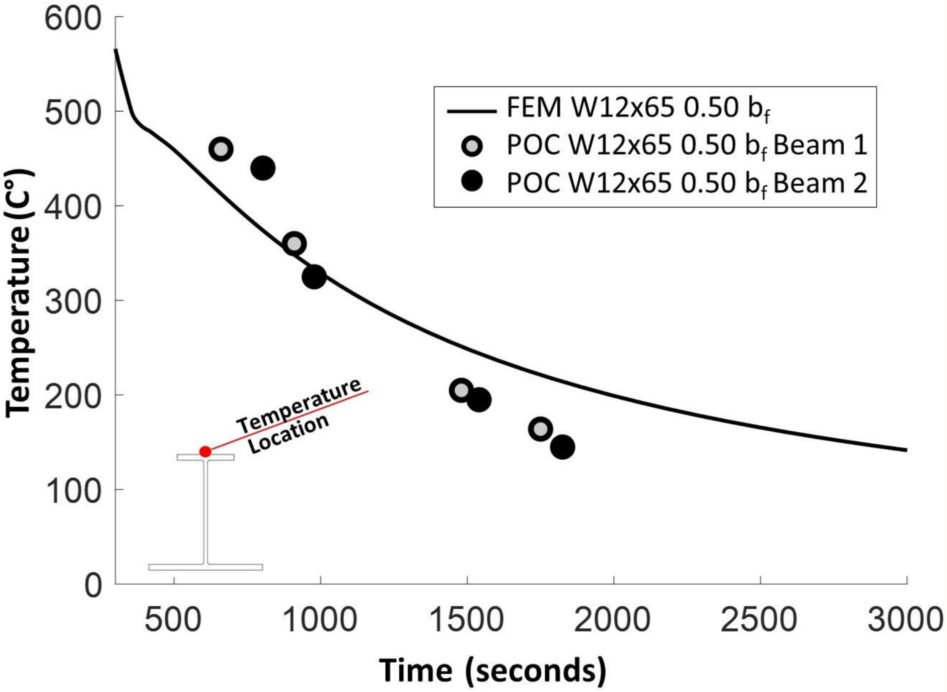

Figure A-9: POC W12x65 Temperature Distribution for Physical Beams and Validated FE Model

Parametric Study

A parametric study was devised to determine the cross-sectional limits for manufacturing of hot rolled A-shapes. These limits were based on the residual stresses and deformations of the beams after simulated cooling from manufacturing. The general approach was to perform thermomechanical FE modeling (described earlier) for different A-shape cross-sectional geometries. The specific geometries investigated, and the overall findings are provided below.

Cross-Section Geometry

The method for selecting the A-shape cross-sectional dimensions to be analyzed started with selection of two standard wide flange sections. The selection of the beam cross-sections was based on realistic shapes used for composite building floor systems. It was also desired to include two different depths. The beams chosen were the AISC W8x31 and W18x76. Next, the approach was to vary the width or thickness of the top flange, while holding all other dimensions constant. The resulting 30 unique cross-sections are shown in Figure A-10. The specific cross-section dimensions were linearly varied, the flange width and thickness were individually varied from 25% to 200% the original flange dimensions. Note that the limits produce unrealistic extreme cases that were included to determine the full spectrum of behavior. This included the standard W8x31 along with (7) W8x31 modified top flange width sections $\left(b_{ftMOD}\right)$ (1st row of Figure A-10) and (7) W8x31 modified top flange thickness sections $\left(t_{ftMOD}\right)$ (3rd row of Figure A-10). The remaining 15 sections include the standard W18x76 along with (7) W18x76 modified top flange width sections $\left(b_{ftMOD}\right)$ (2nd row of Figure A-10) and (7) W18x76 modified top flange thickness sections $\left(t_{ftMOD}\right)$ (4th row of Figure A-10) Note 1.00 b_f and 1.00 t_f are identical and original (non-altered) shapes.

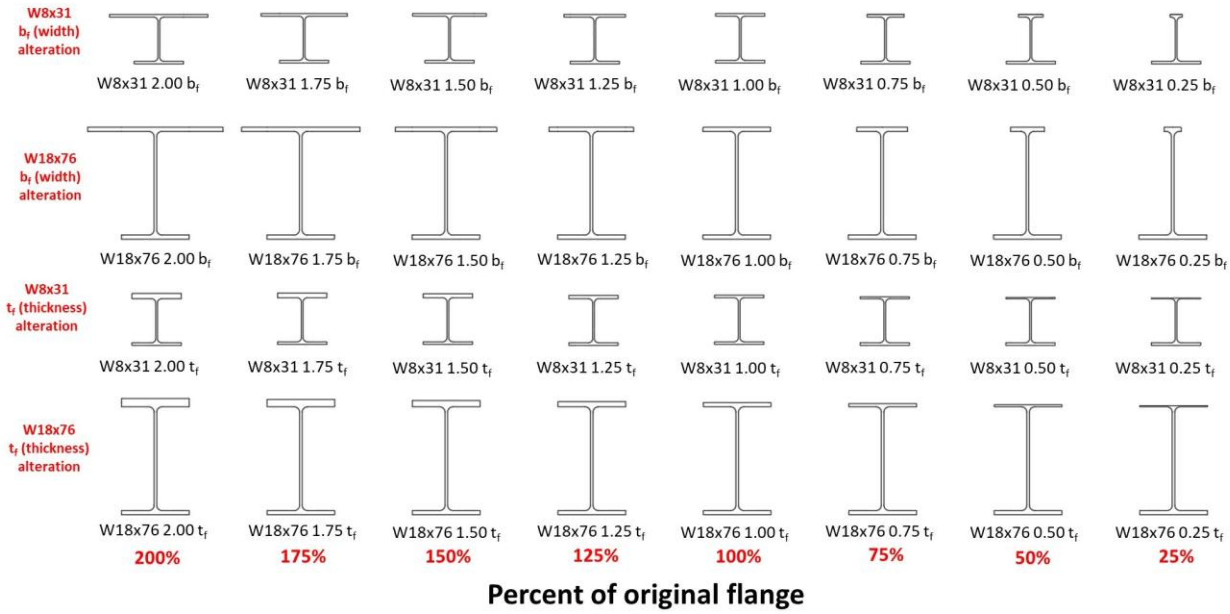

Figure A-10: Beam Modifications for Parametric Study

Finite Element Analysis

The thermomechanical FE analysis was performed for each A-shape cross-section mentioned in the prior section. In total 30 unique cross-sections were analyzed. The FE analysis began with the standard sections (W8x31 and W18x76). As expected, the uneven temperature variations in the flange during cooling causes a residual stress pattern to form. The temperature variation and resulting residual stress pattern for the W8x31 beam illustrated in Figure A-11. It can be observed how the outer fiber of the flanges cool faster than the middle where it meets the web. This typically produces compressive stress at the outer fibers of the flange where the flange is rapidly cooling and tensile stress in the middle where there is more steel and cooling is slowed. These temperature and stress distributions for doubly symmetric beams can be of significant magnitude. Altering a flange increases or decreases the flanges ability to cool, effecting the residual stress pattern. In addition, changes to only one flange produce unsymmetrical temperature variations along the height of the section, which induce deformations (results presented below).

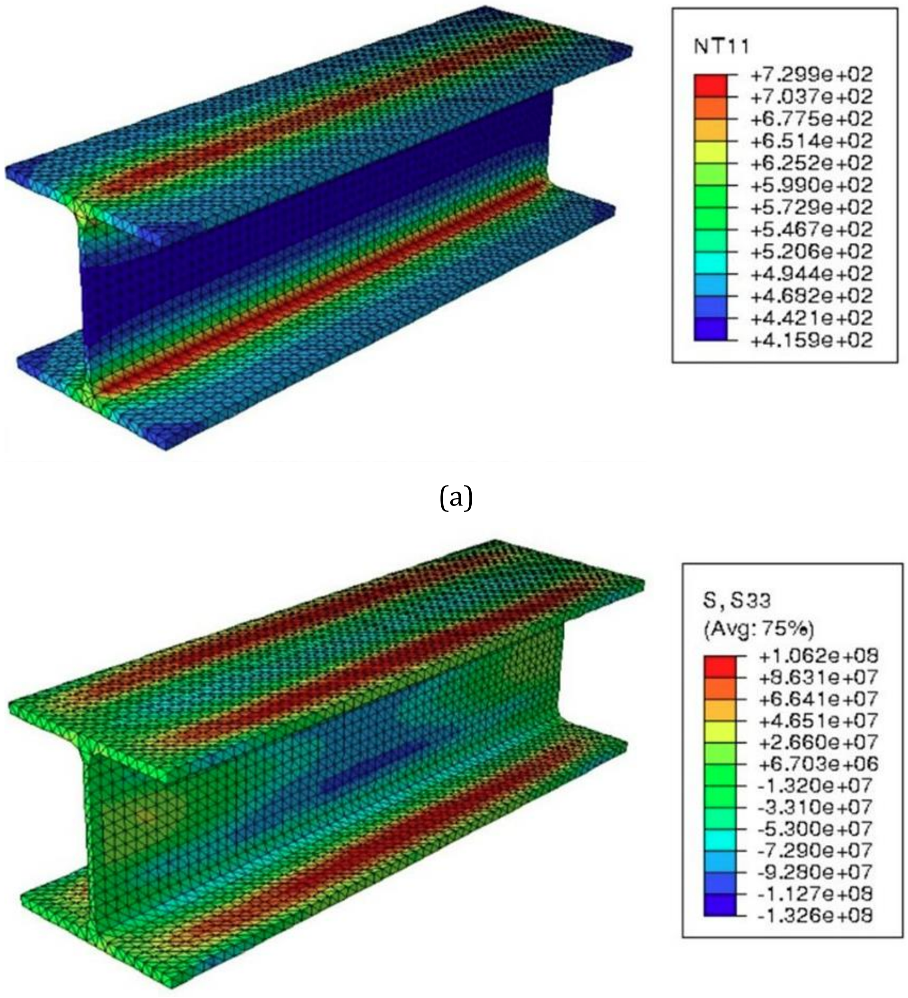

(a)

(b)

Figure A-11: (a) FE Model W8x31 Temperature Distribution at 300 s; and (b) FE Model W8x31 Longitudinal Stresses at 300 s. Units are in $^{\circ}C$ and Pa, respectively.

The FE residual stress results for the flange thickness changes are provided in Figure A-12. In both the W8x31 (Figure A-12(a)) and W18x76 (Figure A-12(b)) cases the highest compressive stresses at the flange outer fiber were seen in the very thin cases ($0.25t_{ft}$). This is due to the high width-to-thickness ratio of the flange, producing high temperature variations across the flange during cooling. The W8x31 altered beams showed a very consistent outer fiber stress of around 100 MPa (14.5 ksi). Even doubling of the flange thickness ($2.00t_{ft}$) did not affect the compressive outer fiber. The outer fiber of the $0.25t_{ft}$ W18x76 dipped below the 200MPa (29 ksi) of compression (Figure A-12(b)), again due to the relatively high ratio. For both the W8x31 and W18x76 cases the tensile stress at the web connection lowered (or stayed consistent) with increasing flange thickness (t_f).

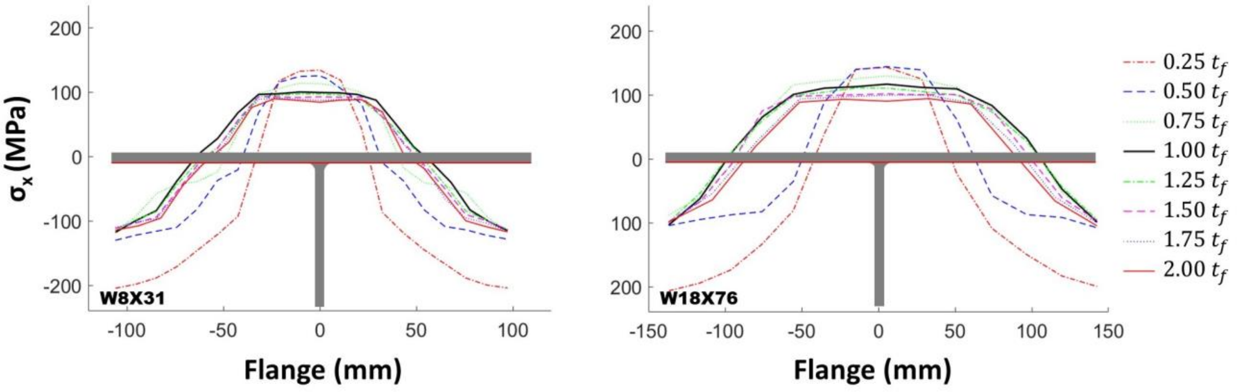

(a) (b)

Figure A-12: FE Stress Profiles for Top Flange Thickness Variations of the (a) W8x31 cases; and (b) W18x76 cases

The FE results for the flange width changes are provided in Figure A-13. The modification of width did not show extreme compression stresses forming as with the thickness changes. This is due to the relatively low width-to-thickness ratio's (and resulting temperature variations during cooling), even for the 2.00 b_{ft} case. Residual stresses stayed relatively consistent through the thickness of the flange. The thickest flange modeled was the W18x76 2.00b_f which had a b/t of 4 and thickness of 34.5 mm (1.36 in.). The W8x31 (Figure A-13(a)) and W18x76 (Figure A-13(b)) both show maximum compresssive stresses of approximatly 120MPa (17.4 ksi) at the outer fiber. A reduction in flange width ($0.25b_{ft}$) has a very low width-to-thickness resulted in tension at the outer fiber of the flange.

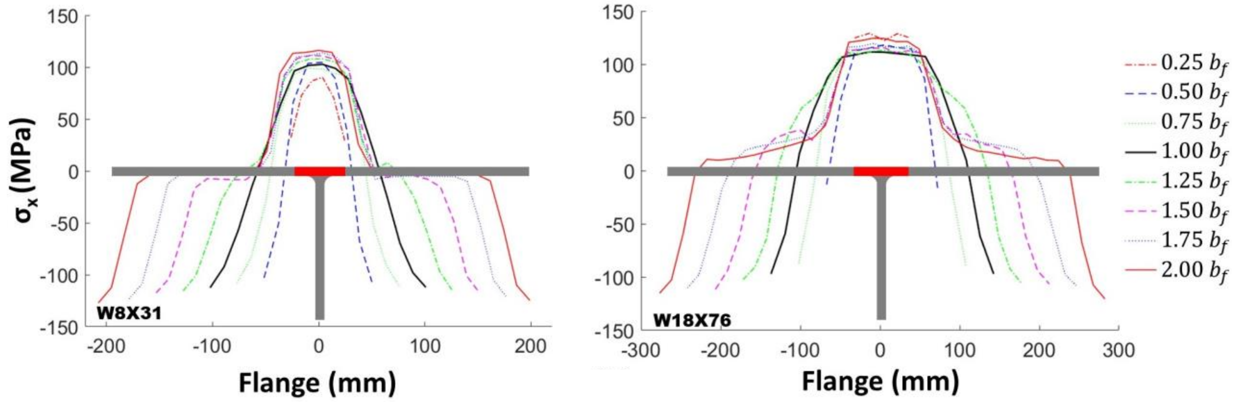

(a) (b)

Figure A-13: FE Stress Profiles for Top Flange Width Variations of the (a) W8x31 cases; and (b) W18x76 cases

Web residual stress profiles (Figure A-14) share interesting insight into how flange alterations influence residual stress profiles in the web. The changing of flange thickness (t_{ftMOD}) had the largest impact in the web causing a decrease in web compressive stresses at the thinnest profiles in both the W8x31 and W18x76.

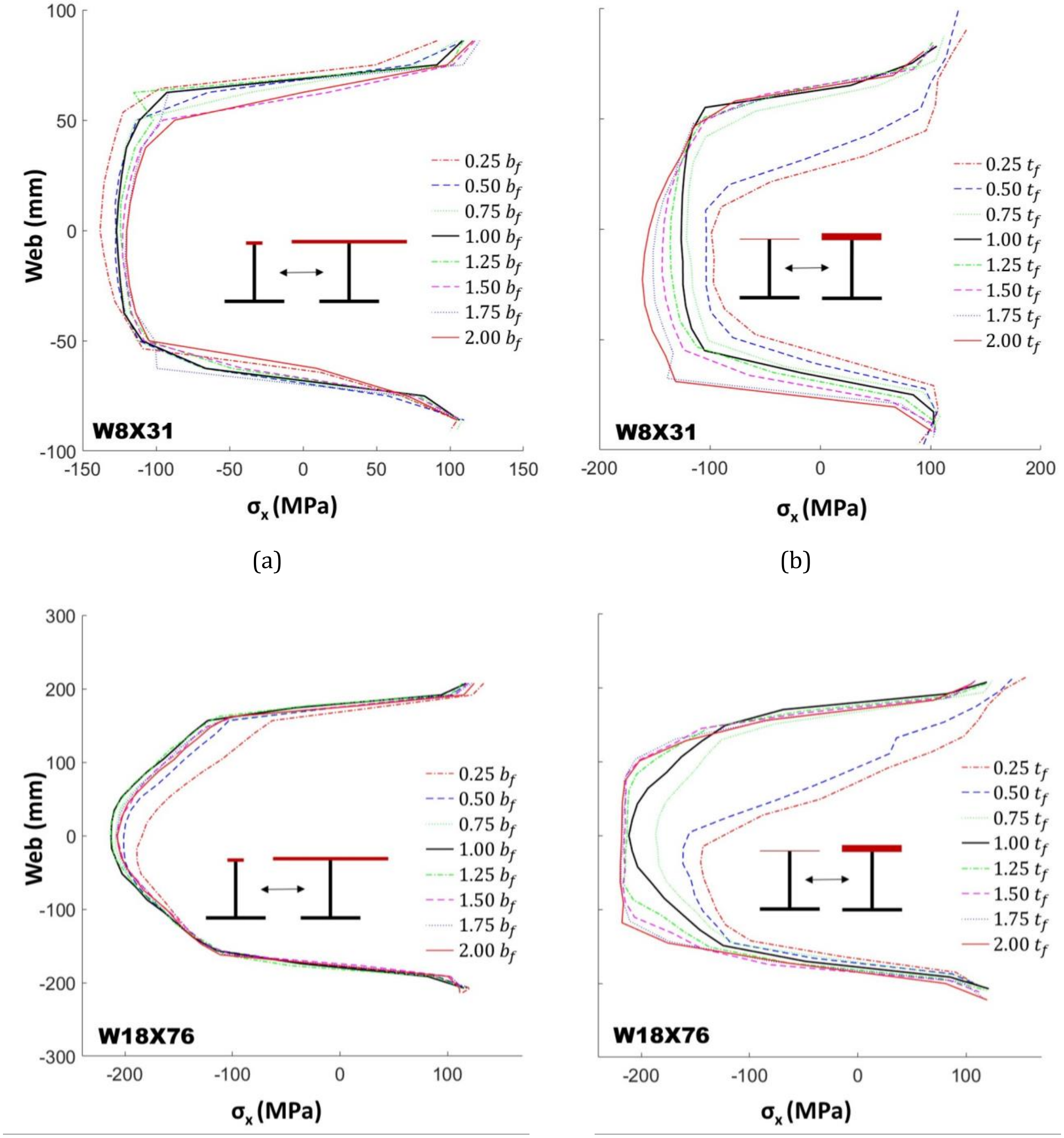

(a) (b)

(c) (d)

Figure A-14: Web Residual Stress Profiles for Width and Thickness Variations: (a) FE Stress Profiles for Top Flange W8x31 Width Variations; (b) FE Stress Profiles for Top Flange W8x31 Thickness Variations; (c) FE Stress Profiles for Top Flange W18x76 Width Variations; and (d) FE Stress Profiles for Top Flange W18x76 Thickness Variations

Findings

Residual Stresses

The goal of the parametric thermomechanical FE modeling study was to better understand A-shape residual stresses and deformations so that cross-sectional manufacturing limits could be established. Using the residual stress data obtained in the parametric study, many standard geometric properties were studied to find a correlation with the residual stress at the flange outer fiber. The outer fiber stresses were the focus because, as shown above, this is the location with the highest compressive stress. It is anticipated that most A-shapes will be utilized in composite floor systems where the top (reduced) flange is in compression. As a result, local and global stability is a concern. Residual stresses are a critical parameter for stability analysis. Note detailed stability analysis is identified as future research and explained below.

The geometric relationship that best correlates with flange outer fiber residual stress is the width-to-thickness (b/t) ratio of the flange, where the projected width (b) is defined as half the total width of the flange (consistent with AISC). Figure A-15 plots the normalized outer fiber stress (residual stress divided by yield stress) from each beam vs the b/t ratio of the modified flange. A 30% yield stress limit was also plotted on the graph, showing the current quantity used by AISC in many specification equations (AISC 2016). AISC applies a 30% reduction to the compressive flange yield stress to identify inelastic buckling. Using Figure A-15 for reference, a b/t limit of 17 was selected by the research team as the cross-sectional limit for manufacturing A-shapes.

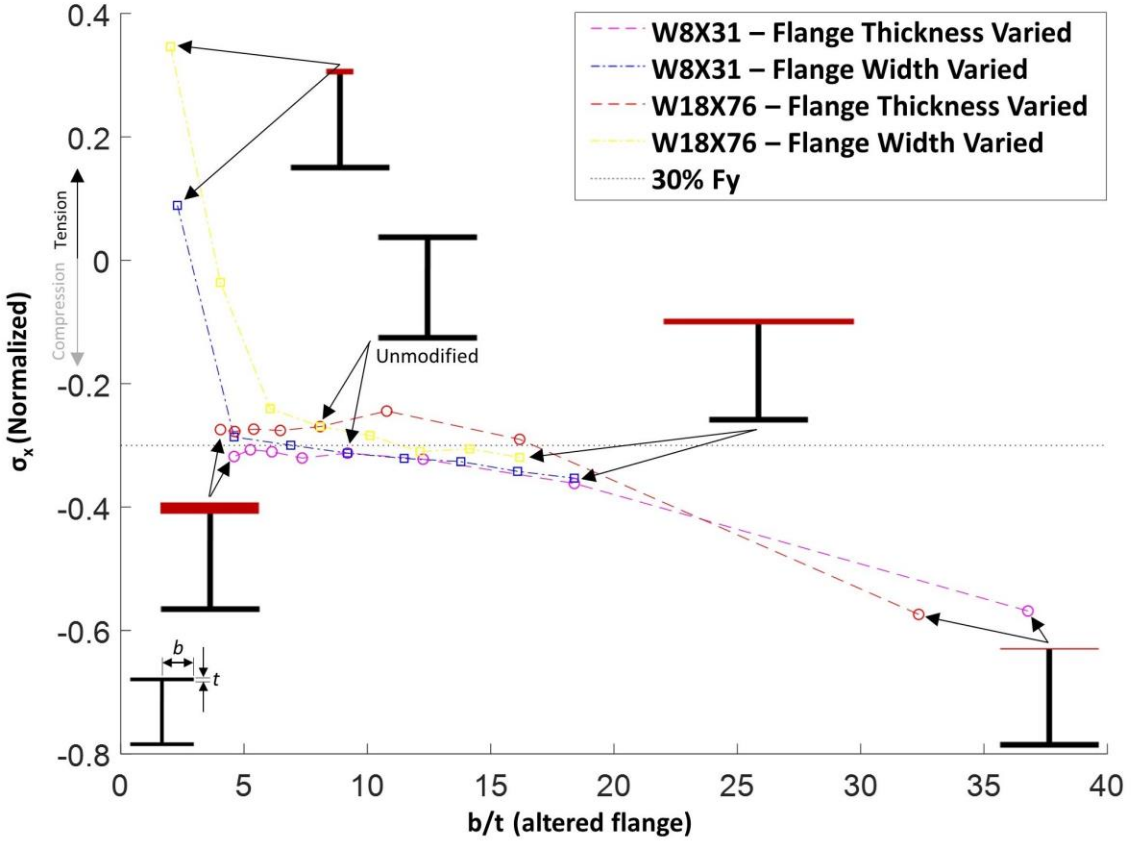

Figure A-15: Normalized Flange Outer Fiber Residual Stress versus b/t

Deformations

Local and global deformations were evaluated to anticipate potential future manufacturing issues. These deformations have been expressed as a concern by some in the steel industry. Manufacturing deformations can be fixed with rotary straightening. However, excessive deformations could make the beams more difficult to handle throughout the mill. In addition, the more severely deformed the beam, the more straightening is required, which can impact the cost and resulting future use.

To evaluate local and global deformations 9m (30ft) length beams were analyzed to mimic realistic manufactured lengths. The 9m (30ft) A-shapes were modeled using the parameters and boundary conditions presented previously. The local flange deformation of the cross section was analyzed for all the A-shapes modeled. Flange out of square limits (shown in Figure A-16(a)) were analyzed for each beam section. The most stringent T+T' limit was imposed by ASTM A6 (ASTM A6 / A6M-19 2019) for sections under 304 mm (12 in), allowing a max value of 6.35 mm (0.25 in). The worst case was the W8x31 with 0.25 t_f which has a T measurement of 0.0762 mm (0.003 in) making the maximum T+T' of 0.1524 mm (0.006 in) well within the ASTM A6 spec.

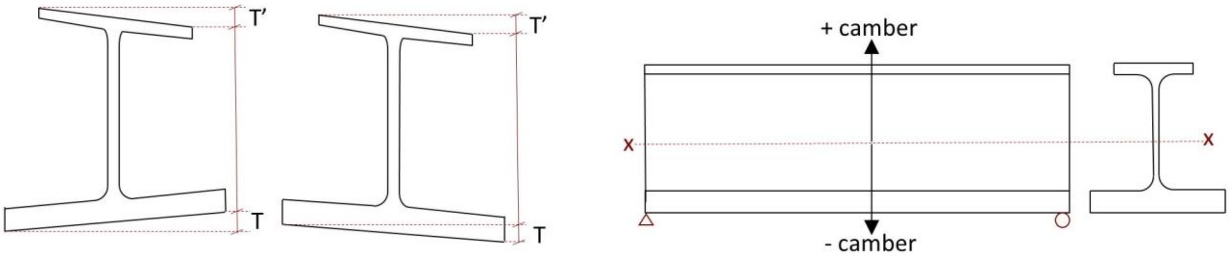

(a) (b)

Figure A-16: (a) ASTM A6 Flange Out of Square; and (b) Beam Camber Sign Convention

The global deformations (camber) were the primary focus and determined for all A-shapes. As a visual reference the modified W8x31 with 2.00 b_{ft} and 0.25 b_{ft} deflected shapes are provided in Figure A-17(a) and Figure A-17(b), respectively. Figure A-17(a) illustrates positive camber as defined by Figure A-16(b). The reason for the positive camber is the vertical temperature profile during cooling. The bottom of the beam cools faster causing greater contraction of this portion of the beam. The opposite situation (negative camber) arises for cases similar to Figure A-17(b).

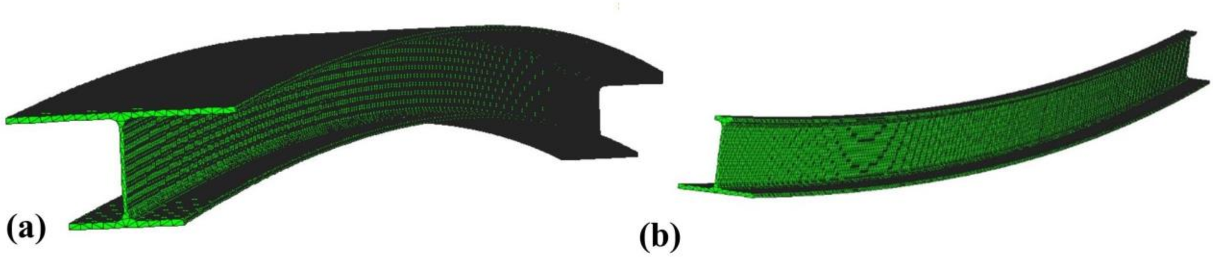

(a) (b)

Figure A-17: (a) 9 m FE Model of a W8x31 with $2.00b_{ft}$; and (b) 9 m FE Model of a W8x31 with $0.25b_{ft}$

The 9m (30ft) beams were first modeled without initial imperfections. This provided an understanding of deflection behavior for each case. Then, initial imperfections of L/125 or 7.32 cm (2.88 in) were extensively explored. The nodal input locations were altered creating a parabolic curvature. An extreme value of L/125 was imposed in the direction the beam tended to deflect due to the geometry. Worse case models of W8x31 0.25 b_f and W8x31 2.00 t_f were analyzed. The results showed that initial imperfections produced nearly the same cooling deformation as those without initial imperfections. As a result, all the displacement data shown is without initial imperfections and only represents the deformations as a result of cooling.

Figure A-18 provides the camber results for all cases. These results were compared to the ASTM A6 (ASTM A6 / A6M-19 2019) camber limit for channels since they are also asymmetric hot rolled sections. For 9m (30ft) beam lengths the limit is approximately 19 mm (0.75 in). In total, nine of the modeled sections did exceed the ASTM A6 channel limits. However, in all but one case the exceedance was relatively small. The largest global beam center displacement from the study was the W8x31 with 0.25 b_{ft}, which is an extreme case primarily included to capture the full range of behavior. Note for comparison, Figure A-18 also provides the ASTM A6 camber limit for W sections, which is equal to 9.5 mm (0.375 in). This limit would be overly stringent for a hot rolled asymmetric section and provided for context.

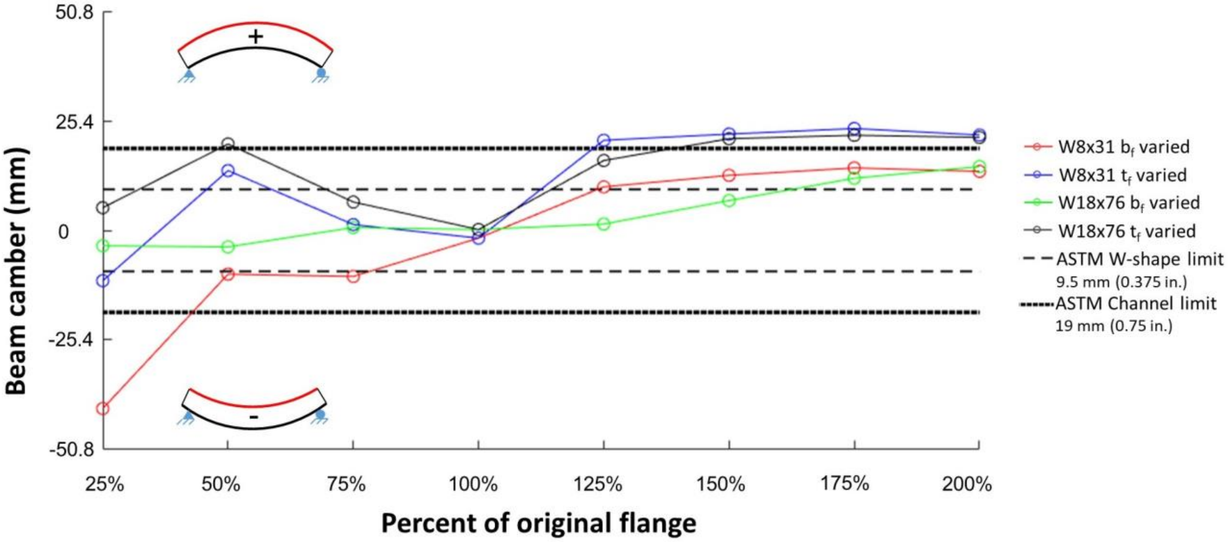

Figure A-18: Global Deflections

Conclusions

This study quantitatively determined manufacturing limits that are required for hot rolled A-shapes. The investigation focused on the induced residual stresses and deformations as a result of the cooling process. A comprehensive thermomechanical FE modeling procedure was developed to simulate the behavior of rolled shapes after the rolling process. This included heat-transfer analysis to identify the thermal behavior combined with stress analysis. Validation of the methodology was performed through comparison of the numerical results with accepted physical experiments from the literature and proof-of-concept beams. Then, using the validated methodology, a wide range of A-shape cross-sectional configurations were analyzed to identify the residual stresses and deformations (local and global). The primary findings include the following:

- A flange *b/t* limit of around 17 is recommended to manufacture A-shapes with compressive residual stresses below 30% the yield stress.
- No cross-sectional limit is recommended to satisfy local deformation of the A-shapes. All cases evaluated satisfied the ASTM A6 criteria for flange out of squareness.

- No cross-sectional limit is recommended to satisfy global deformation (camber) of A-shapes. Some cases exceeded the ASTM A6 camber criteria utilized. However, the magnitude of exceedance was sufficiently small enough to be corrected with rotary straightening.

The overarching goal of this line of research is to utilize the *b/t* limit established above along with future research identifying other cross-sectional limits (more details below). Once sufficient research (and the corresponding limits) has been performed, a table of A-shape cross-sections shall be recommended for Part 1 of the AISC manual.

Future Research

A comprehensive research program was developed and is currently underway to fully establish the future A-shapes. In general, the intent is to understand the behavior of A-shapes throughout manufacturing, construction, and the final configuration so that cross-section proportional limits can be developed. The primary behaviors to be evaluated include:

- Manufacturing: residual stresses and deformations due to asymmetric uneven cooling (results presented above)
- Construction: stability (lateral-torsional buckling and local buckling) and flange bending
- Final configuration: vertical deflection, ductility, floor frequency and local buckling

The future research methodology is to conduct extensive numerical simulation studies validated through full-scale laboratory experiments. Full-scale composite floor system testing will be performed using the POC beams described earlier. The stability evaluation shall be conducted for different construction scenarios. Prior research will be drawn upon for the investigation (Yura 2001) (El-Mahdy and El-Saadawy 2015; Helwig et al. 1997; Wang and Helwig 2008; Zhao et al. 2010). It is anticipated that eigenvalue buckling and large displacement analysis (including initial imperfections) using ABAQUS/CAE software will be performed. The resulting numerical simulation methods shall then be used for further parametric studies to determined additional cross-section proportional limits. The developed A-shape proportional limits that address manufacturing and structural behavior will be utilized for an optimization study to determine the final A-shape cross-sectional dimensions.

Data Availability Statement

Some or all data, models, or code that support the findings of this study are available from the corresponding author upon reasonable request.

Acknowledgements

The authors would like to express gratitude to AISC for financially supporting this research through the Milek Fellowship. Any opinions, findings, and conclusions or recommendations expressed in this material are those of the authors and do not necessarily reflect the views of AISC.

The authors also like to thank Nucor for donating the material and their services to produce the proof-of-concept A-shapes. Specifically, we would like to acknowledge Mike Thomas, Phil Bischof, and Ross Simmons. This research was conducted at Texas A&M College Station and partially funded through the Engineering Graduate Merit Fellowship. The numerical analysis of this research was conducted with high performance research computing resources provided by Texas A&M University (https://hprc.tamu.edu).

References

AISC (American Institute of Steel Construction). 2016. *Specification for Structural Steel Buildings*, ANSI / AISC 360-16. American Institute of Steel Construction.

Alfawakhiri, F., Carter, C. J., Berhinig, R. M., Zeeveld, P., Hervey, F. E., and Woods, L. C. 2016. "The effects of load intensity and restraint on the fire resistance of steel and composite beams." *Int. Conf. Structures in Fire.*, 9th, 484–491.

Alpsten, G. A. 1972. "Prediction of thermal residual stresses in hot- rolled plates and shapes of structural steel." *IABSE Ninth Congress*.

Andersson, B. A. B. 1978. "Thermal stresses in a submerged-arc welded joint considering phase transformations." *Journal of Engineering Materials and Technology, Transactions of the ASME*, 100(4), 356–362.

ArcelorMittal Commercial Sections. 2019. Electric arc furnace Rolling process Quenching and Self-Tempering (QST) process for HISTAR® steel.

ASTM A6 / A6M-19. 2019. Standard Specification for General Requirements for Rolled Structural Steel Bars, Plates, Shapes, and Sheet Piling. West Conshohocken, PA.

Brickstad, B., and Josefson, B. L. 1998. "A parametric study of residual stresses in multi-pass butt-welded stainless steel pipes." *International Journal of Pressure Vessels and Piping*, 75(1), 11–25.

BSK (Blekinge Studentkar). 2003. "Swedish design rules for steel structures."

Carnegie Steel Company. 1923. *Pocket Companion*. Pittsburgh.

CEN (European Committee for Standardization). 2005. "Design of steel structures. Part 1-2 General rules - Structural fire design.", Eurocode 3,EN1993-1-2,Brussels, Belgium.

Choe, L., Ramesh, S., Grosshandler, W., Hoehler, M., Seif, M., Gross, J., and Bundy, M. 2020. "Behavior and Limit States of Long-Span Composite Floor Beams with Simple Shear Connections Subject to Compartment Fires: Experimental Evaluation." *Journal of Structural Engineering (United States)*, 146(6), 1–14.

ECCS. 1984. "Ultimate Limit State Calculations of Sway Frames with Rigid Joints." 33.

El-Mahdy, G. M., and El-Saadawy, M. M. 2015. "Elastic and inelastic strength of singly symmetrical I-beams." *Structural Stability Research Council Annual Stability Conference 2015, SSRC 2015*, (2010), 1–12.

Galambos, T., and Ketter, R. 1959. "Columns Under Combined Bending and Thrust." *Transactions of the American Society of Civil Engineers*, 126(1), 1–23.

Girder-Slab Technologies, L. 2016. THE GIRDER-SLAB ® SYSTEM DESIGN GUIDE v3.3 ASSOCIATE The GIRDER-SLAB® System Design Guide v3.3 @GIRDERSLAB.

Harmathy, T. Z., and Stanzak, W. W. 2009. "Elevated-Temperature Tensile and Creep Properties of Some Structural and Prestressing Steels." *Fire Test Performance*, 186-186–23.

Helwig, T. A., Frank, K. H., and Yura, J. A. 1997. "Lateral-torsional buckling of singly symmetric I-beams." *Journal of Structural Engineering*, 123(9), 1172–1179.

Hu, G., Morovat, M. A., Lee, J., Schell, E., and Engelhardt, M. 2009. "Elevated temperature properties of ASTM A992 steel." *Proceedings of the 2009 Structures Congress - Don't Mess with Structural Engineers: Expanding Our Role*, 1067–1076.

Huber, A. W. 1956. "Residual stresses in wide-flange beams and columns." *Fritz Engineering Laboratory Report*, Paper 1498.

Huber, A. W. 1958. "Residual stresses in wide flange beams and columns . Lehigh University , (July 1956), revised." (July 1956).

Huber, D., Varma, A. H., Bowman, M. D., Connor, R. J., Liu, J., and Adams, D. E. 2011. "Development and validation of long span floor systems for multi-story residential structures." *Purdue University*.

Kloeckner Metals. 2020. The cellular beam pocket guide entrusted to design and deliver metal solutions.

Nguyen, T., Gad, E., Wilson, J., and Haritos, N. 2014. "Mitigating footfall-induced vibration in long-span floors *." 15(1).

Quayyum, S., and Hassan, T. 2017. "Initial Residual Stresses in Hot-Rolled Wide-Flange Shapes: A Computational Technique and Influence on Structural Performances." *Journal of Structural Engineering (United States)*, 143(5), 1–15.

British Steel. 2018. "Sections: Asymmetric Beams (ASB)."

Tebedge, N., Alpsten, G., and Tall, L. 1973. "Residual-stress measurement by the sectioning method." *Experimental Mechanics*, 13(2), 88–96.

Varela, W. D., and Battista, R. C. 2011. "Control of vibrations induced by people walking on large span composite floor decks." *Engineering Structures*, 33(9), 2485–2494.

Wang, L., and Helwig, T. A. 2008. "Stability bracing requirements for steel bridge girders with skewed supports." *Journal of Bridge Engineering*, 13(2), 149–157.

Wickström, U. 1979. "TASEF-2 - a computer program for temperature analysis of structures exposed to fire." (2).

Yarnold, M. T., and Stoddard, E. 2020. "Future Hot-Rolled Asymmetric Steel I-Beams." *Journal of Structural Engineering (United States)*.

Young, B. W. 1975. "Residual stresses in hot rolled members." *Proceedings IABSE Colloquium: On Column Strength.*, 23, 25–38.

Yura, J. A. 2001. "Fundamentals of beam bracing." *Engineering Journal*, 38(1), 11–26.

Zhao, Q., Yu, B., and Burdette, E. G. 2010. "Effects of cross-frame on stability of double I-girder system under erection." *Transportation Research Record*, (2152), 57–62.

Appendix B – Initial Concept Design and Testing

Appendix B provides detailed information on the initial large-scale experiment (Phase 2) conducted on shallow-depth composite floor systems. The experimental testing consisted of analyzing the A-shape behavior during Test 1: precast panel placement (multiple cases) and Test 2: the concrete slab pour. The composite behavior gained through the concrete-steel bond was analyzed through Test 3: actuator vertical loading. The experimental data from all three tests was compared with theoretical calculations that were bounded by pinned and fixed support connections.

Citation

The following work has been published by the American Society of Civil Engineer's Journal of Structural Engineering. The citation to the published journal article is:

> Davis, S., E. Stoddard, and M. T. Yarnold. 2023. "Full-Scale Floor System Testing for Future Hot-Rolled Asymmetric Steel I-beams." *Journal of Structural Engineering*, 149(2). https://ascelibrary.org/doi/10.1061/JSENDH.STENG-11610

The following work is expanded upon and supplemental information/results are provided in Sheyenne Davis's Thesis and Eric Stoddard's Ph.D. Dissertation. The citation to Sheyenne's thesis and Eric's dissertation are:

> Davis, S. 2022. "Full-Scale Floor System Testing for Future Hot-Rolled Asymmetric Steel I-beams." Master Thesis, Texas A&M University.
>
> Stoddard, E. A. 2022. "Behavior of Hot-Rolled Asymmetric Steel I-beams: Concept to Construction." Ph.D. Dissertation, Texas A&M University.

Full-Scale Floor System Testing for Future Hot-Rolled Asymmetric Steel I-Beams

Sheyenne Davis, Eric Stoddard, and Matthew T. Yarnold

Abstract

The presented study conveys the initial full-scale experimental study for future hot-rolled asymmetric steel I-beams, termed A-shapes. The primary use for these beams is residential building floor systems. Current systems commonly utilize concrete solutions, which achieve a shallow depth for optimal floor-to-floor heights. However, these floor systems are relatively slow to construct due to the amount of formwork, rebar/post-tensioning placement, and shoring needed. The shallow-depth steel-concrete floor system concept explored in this research aims to improve the speed and efficiency of residential building construction. This increase in speed is achieved through hot-rolled steel A-shapes, which reduce the fabrication time for beam production. These steel shapes have a wide bottom flange that can support precast concrete panels or deep metal decking. Therefore, a relatively easy to assemble, shallow depth system can be achieved. The research study presented herein includes the experimental feasibility testing of a full-scale shallow-depth steel-concrete floor system to further the knowledge of A-shape performance in such systems. The floor system concept evaluated consisted of three steel A-shapes, precast hollow-core concrete panels, and a cast-in-place concrete topping slab. The testing involved taking measurements during construction, service live loading, and loading of the system to failure. The major unknowns were constructability, stability during construction, live load performance, and composite behavior. This experiment revealed that the system was constructed easily and rapidly along with remained stable during construction. The system performed well under service live load, experiencing deflections equivalent to L/3000. The system failed due to the bond breaking between the concrete and painted steel, going non-composite after experiencing partially composite behavior. This occurred at an actuator load equivalent to five times the design service live load. All of this indicates that the floor system concept using A-shapes is a legitimate path forward to faster construction of residential facilities. This validates the need for the research toward standardized A-shapes in the United States, which may then be incorporated into the American Institute for Steel Construction Manual.

Keywords: Structural Steel, Hot Roll, Stability, Composite, and Floor System

Introduction

Research is being conducted on the potential large-scale production of a new hot-rolled steel section in the United States (U.S.). The new hot-rolled shape is an asymmetric I-beam where the top flange is narrower than the bottom flange (termed A-shape). The unique aspect of an A-shape is that it allows for rapid placement of stay-in-place formwork on top of the bottom flange (see Figure B-1). The formwork can consist of precast concrete panels or steel deep decking systems. Currently, a variety of residential building floor systems utilize a built-up asymmetric steel I-beam for this purpose. The major advantage of these systems is the speed and efficiency of construction. Some common built-up steel beam systems include Girder-Slab (GIRDER-SLAB 2016), SlimFlor (Mullett and Lawson 1993), and ComSlab (COMSLAB 2022), among others. Girder-Slab utilizes what is called a D-Beam. This steel beam is fabricated by cutting a wide-flange beam in half through the web in a castellated pattern, then a flat bar is welded on top of the castellated web creating the D-Beam's top flange. SlimFlor and ComSlab fabricate their steel beams by welding a cover plate to the bottom flange of a hot-rolled wide-flange section (similar to that shown in Figure B-1). While these floor systems are fast to construct, they are relatively slow to fabricate. A standard hot-rolled steel section, such as the proposed A-shape, could increase the speed from the completed design stage to the steel erection, reducing overall construction time. This is the primary purpose for research towards hot-rolled A-shapes.

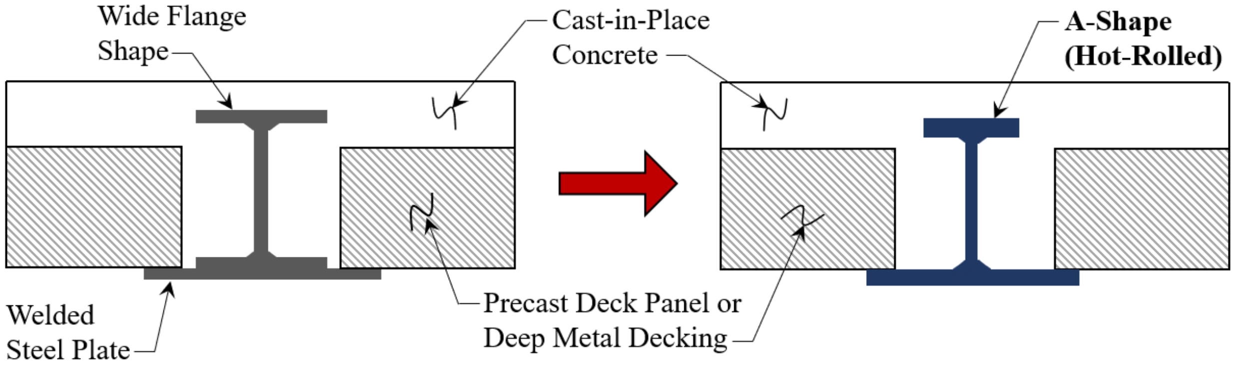

Figure B-1: Shallow-Depth Steel-Concrete Floor Systems using Hot-Rolled A-shapes

In the United Kingdom, Corus Construction Industries builds a floor system with hot-rolled asymmetric beams called Slimdek Beams (Corus 1999). The beams (termed ASBs) are produced by British Steel (British-Steel 2022). These sections have a limited production cycle and do not appear to be optimized for manufacturability or structural efficiency. The research team is currently conducting a study for the American Institute of Steel Construction (AISC) that creates an optimized U.S. version of these shapes (Yarnold and Stoddard 2020). As part of the study, there is an industry panel comprised of three major U.S. steel mills (Nucor, Steel Dynamics, and Gerdau), fabricators, erectors, designers, and members of AISC that provide semi-annual feedback.

The initial work for this research study focused on the manufacturability of A-shapes. Extensive thermal-mechanical modeling was performed to investigate potential issues with residual stresses or global deformations (curvature) during the cooling process (Stoddard and Yarnold 2022). In addition, interviews were conducted with the three U.S. steel mills and their roll-pass engineers, roll-pass designers, metallurgical engineers, roll mill supervisors, and product developers. Geometric proportional limits were established for the future numerical A-shape sizing study (discussed in the future research section). Overall, the prior research indicated that large-scale production of A-shapes in U.S. steel mills is feasible if these shapes are shown to be a viable structural option. As a result, the research team and industry panel commenced with an initial full-scale floor system feasibility experiment. The paper presented herein documents this research. This includes an evaluation of the constructability of the floor system concept as well as the structural performance during construction and in-service vertical loading up to failure. The research team drew upon an array of prior floor system testing studies. For example, Ju et al. (2009) performed floor system laboratory testing of built-up asymmetric steel sections with web openings. Sheehan et al. (2018) studied the flexural behavior of an asymmetric composite beam with a low degree of shear connection, assembled using unpropped construction. Hechler et al. (2016) also performed similar experimental testing of a related shallow depth steel-concrete composite floor system. In addition, Huber and Varma (2008) conducted experimental floor system testing of long-span floor systems for residential construction.

The primary contributions of this research were the constructability assessment of a shallow depth steel-concrete composite floor system utilizing A-shapes, along with the quantitative evaluation of the structural performance during construction and in service. The findings from this experimental research will contribute to the future A-shape numerical sizing study (discussed in the future research section). A full-scale floor system experiment was successfully performed that included an array of tests during the different stages of construction. The non-composite behavior was evaluated in detail. In addition, the composite in-service behavior was evaluated through service level vertical loading. The final test was the ultimate strength of the floor system. This identified the failure mechanism and reserve strength of the system. The overall research objectives for the study are provided in the next section.

Research Objectives

This research investigates shallow-depth steel-concrete composite floor systems utilizing hot-rolled A-shapes, with a focus on their use in residential buildings. This work addresses the knowledge gaps in such systems, which will aid in the future development of standardized A-shapes. The methods of this research are both experimental and numerical. A full-scale floor system was designed, built, and tested, and the results were compared with theoretical calculations. The information gathered from this research is measured per the following objectives.

1. Evaluate the ***constructability*** of the system for speed and ease of assembly for each of these stages: fabrication, steel erection, precast panel placement, and deck casting
2. Evaluate the ***system's structural performance during construction*** (panel placement and concrete pour) through characterization of A-shape stability, and the flexural and torsional behavior (stresses and deformations)
3. Evaluate the ***system structural performance under service live load*** to identify the flexural rigidity of the system and the composite behavior
4. Evaluate the ***ultimate strength of the system under vertical loading*** to determine the failure mechanism and quantify the ultimate capacity

Experiment Design

A full-scale floor system experiment was designed to realize the objectives stated above. It was decided by the research team and industry panel to explore precast panels for this first experiment and consider steel metal deep decking for future testing. The design approach for the entire experiment setup, as well as the instrumentation design, is explained in this section.

Experiment Setup

The design of the shallow-depth steel-concrete composite floor system (using precast hollow-core panels) was driven by several constraints and decisions, as is the case with any full-scale experimental testing. The first was the A-shape to be utilized for the laboratory floor system specimen. Prior work by Stoddard and Yarnold (2020) created proof-of-concept (POC) asymmetric I-beams with the support of Nucor steel mills. The high cost of retooling the rolling mill stands, along with the lack of known A-shape behavior, necessitated a creative solution to developing POC beams. Therefore, the approach was to cut down (or narrow) the top flange of a rolled W-shape (see Figure B-2). The altered beams were reheated to approximately 950ºC (1740 ºF) and then air-cooled in a similar manner to conventional hot-rolled shapes. This approach was used to capture the residual stresses and deformations of hot-rolled A-shapes but did not capture the correct grain structure. The A-shapes produced were termed A12x53s, which were originally W12x65s. The top flanges were reduced by 50%, as shown in Figure B-2. Note that future A-shapes will have a relatively thicker top flange to balance the top and bottom flange areas for manufacturability and structural efficiency. Also note that the A-shapes were painted, which reduces the concrete bond compared to unpainted steel.

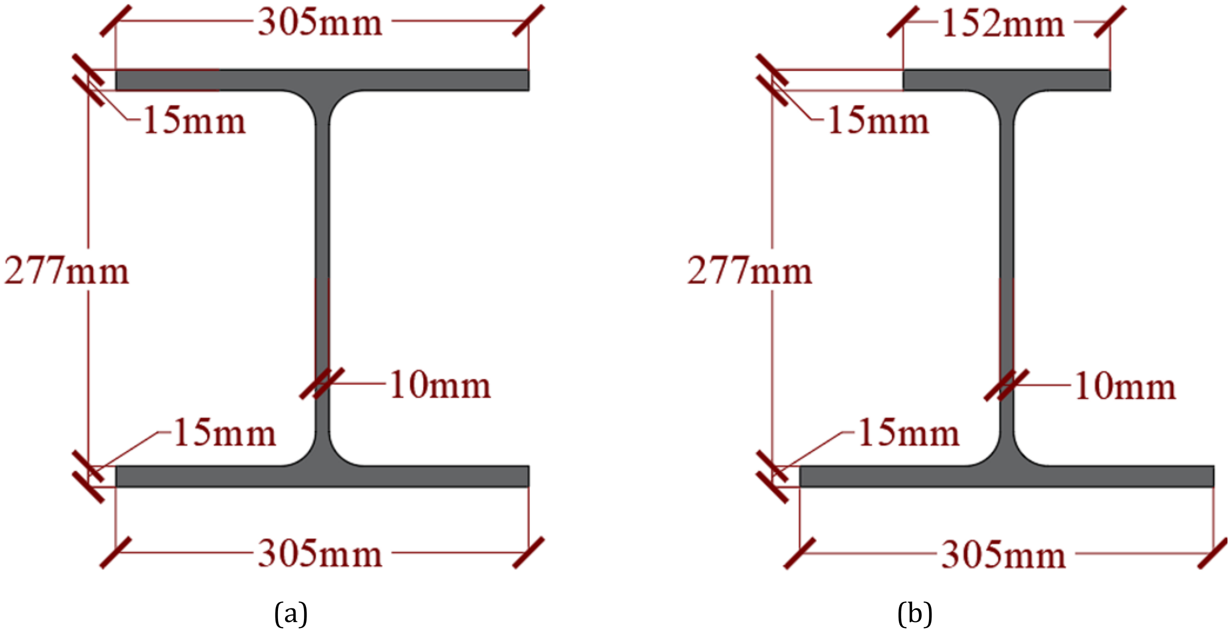

Figure B-2: (a) W12x65 shape; and (b) A12x53 shape

The common configuration for floor system testing is a two-bay system, either with or excluding edge beams. For this full-scale test, a two-bay floor system with three A-shapes was chosen. This allowed for studying the behavior of the A-shape under full loading (the center beam) in a more realistic floor system. In a standard building floor system, the edge beams would be larger to resist the considerable eccentric loading they will withstand. For this test, A-shapes were used for the edge beams because they provide more accurate view of the behavior of the middle beam. Excessively stiff edge beams would have attracted a relatively significant portion of the force. The selected configuration can be seen in Figure B-3.

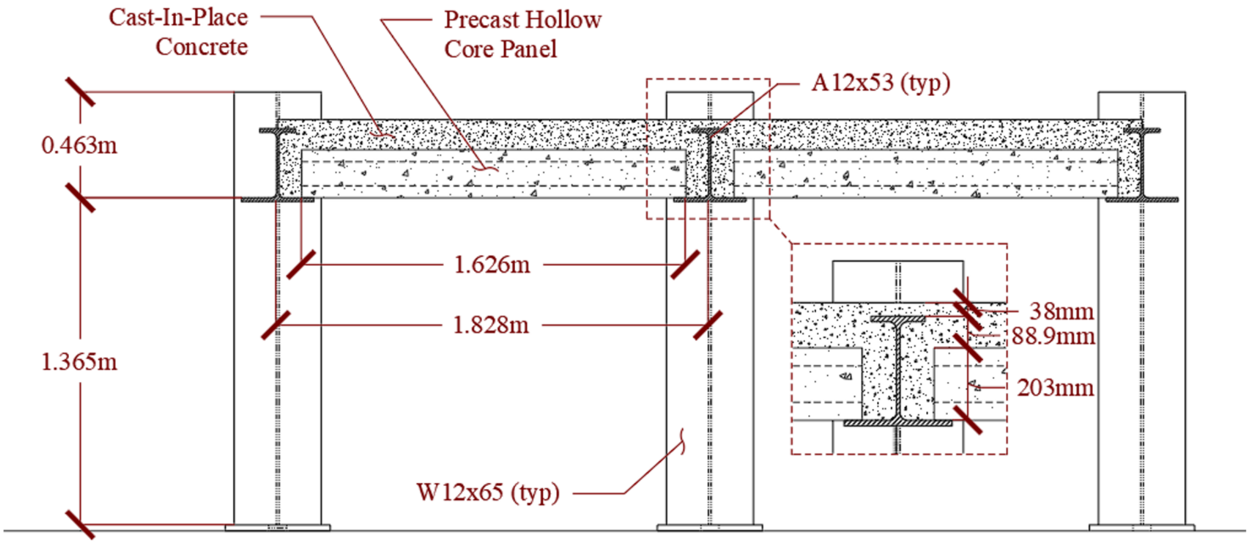

Figure B-3: Floor System Section View

The design of all other components of the experimental setup was such so that they would not control over the A-shapes. The columns were chosen to be W12x65 sections for simplicity in framing the A-shape beams and being a larger section than needed. To have easy access to the underside of the floor system and provide relatively stiff columns, the columns were chosen to be 1.83 m (6.0 ft) tall, with the beams framing in at roughly 1.37 m (4.5 ft). Simple shear (web only) connections were chosen to attach the center beams to the columns. To increase the torsional restraint at the ends of the edge beams, top and bottom angles were added to the connections (further discussed below).

The dimensions of the strong floor in the Texas A&M University High-Bay Laboratory presented some constraints for overall geometry. The tie-down holes in the floor are 0.91 m (3.0 ft) apart, meaning the baseplates for the columns had to adhere to that spacing. As a result, the beam spacing and span length were restricted to increments of 0.91 m (3.0 ft). The overall layout chosen is shown in Figure B-4. A beam spacing of 1.83 m (6.0 ft) was selected to be able to utilize the load frame header beams currently available in the laboratory. The spacing between columns was chosen as 7.32 m (24 ft), which made the beam span 6.98 m (22.9 ft) (center-to-center connection). In future floor systems of this type, the span length and beam spacing will be increased. This will necessitate stockier A-shape sections, which are currently under development (discussed in the future research section below).

The selected precast concrete panels had a width of 1.22 m (4 ft), so 10 panels were used. This exposed the steel connections for observation during testing. The panel length of 1.63 m (5.33 ft) was chosen to provide sufficient bearing seat width on the bottom flange of the beam. It should be noted that these panels can span much greater lengths, but as discussed earlier, the constraints of the laboratory limited the beam spacing. The difference between the bottom and top flange on one side of the beam was 76 mm (3.0 in), so a 51 mm (2.0 in) bearing seat was provided. This allowed for a 25 mm (1.0 in) tolerance on each side of the precast panels for lowering into place during installation. Precast hollow-core concrete panels with a 203 mm (8.0 in) thickness were selected. This thickness allowed for sufficient room between the top flange of the beam and the panels, making it easier to place wet concrete in the void between the panels and supporting A-shapes. The ends of the hollow-core panels were sealed to not allow concrete inside the panels themselves. The in-situ concrete topping slab was set to provide 38 mm (1.5 in) of cover over the beams to provide sufficient depth for reinforcement. This slab was lightly reinforced with 10 mm (#3) reinforcing bars (Grade 420 MPa (60 ksi)) spaced at 457 mm (18.0 in) on center in both directions. The concrete strength was 28.9 MPa (4.19 ksi), which was obtained from cylinder testing at 28 days.

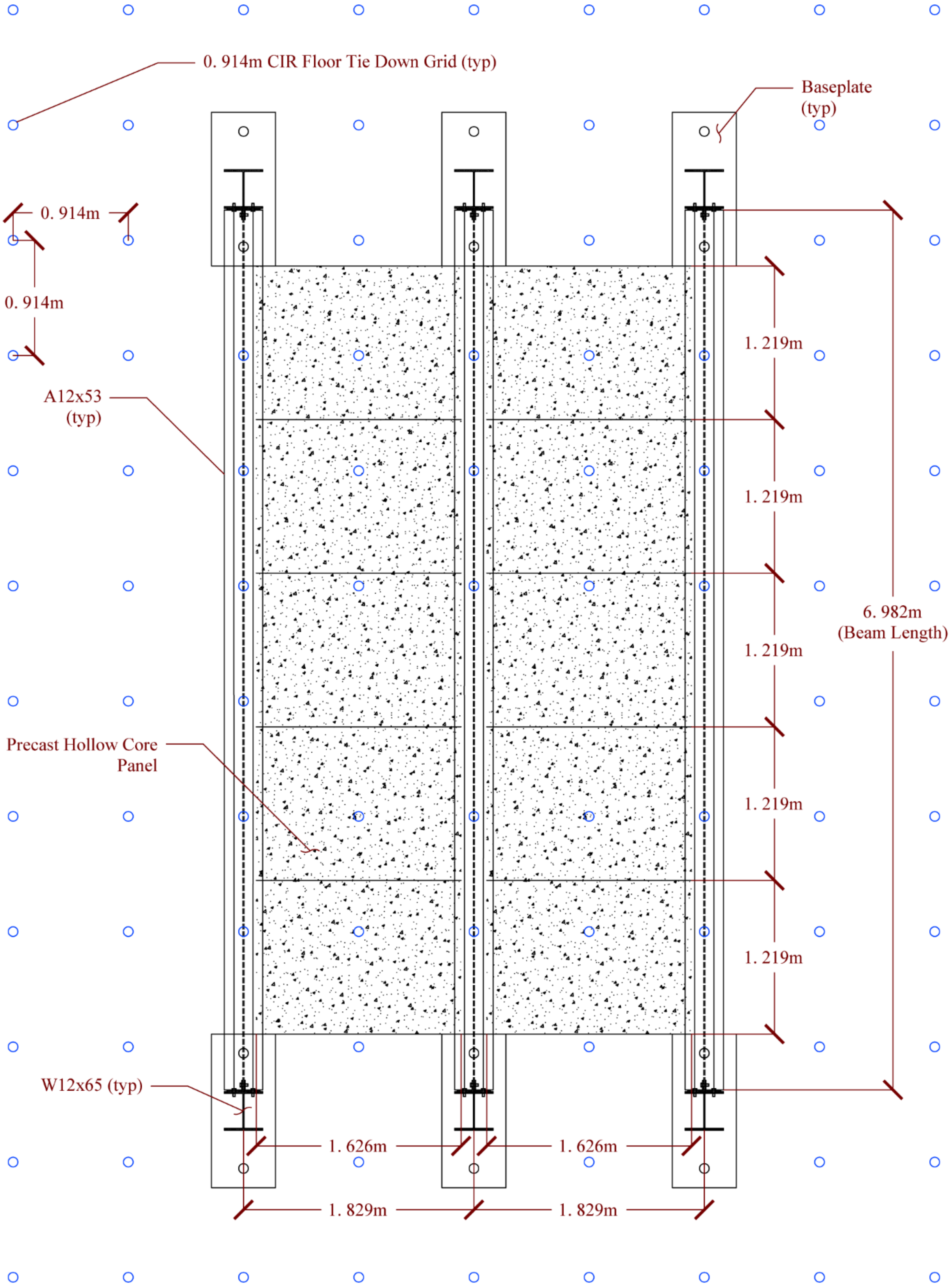

Figure B-4: Floor System Plan View

The chosen design was numerically evaluated using building codes and guidance documents. Primarily, the American Institute of Steel Construction (AISC) Steel Construction Manual (AISC 2017) and the AISC Design Guide 9 on Torsional Analysis of Structural Steel Members (Seaburg and Carter 2003) were utilized. The experiment design aimed to ensure the A-shapes would control during testing. Overall, the experiment was broken down into three separate tests that included Test 1: Precast Panel Placement, Test 2: Concrete Pour, and Test 3: Actuator Loading. From these tests, the following critical design stages needed to be checked, as shown in Figure B-5, Figure B-6, and Figure B-7.

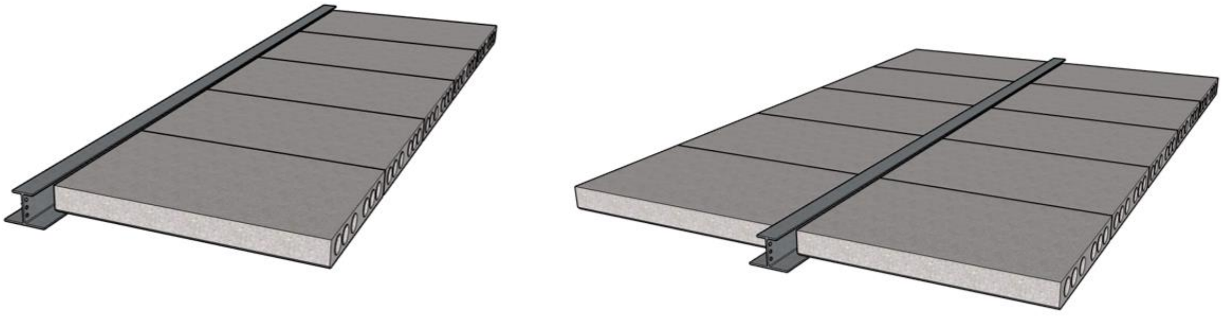

(a) (b)

Figure B-5: Test 1 Design Stage: (a) Precast Panels on One Side; and (b) Precast Panels on Both Sides (Stoddard 2022)

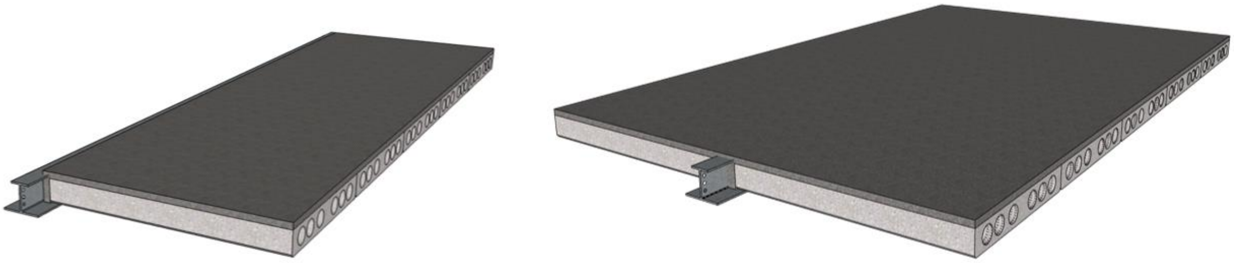

(a) (b)

Figure B-6: Test 2 Design Stage: (a) Precast Panels and Wet Concrete on One Side; and (b) Precast Panels and Wet Concrete on Both Sides (Stoddard 2022)

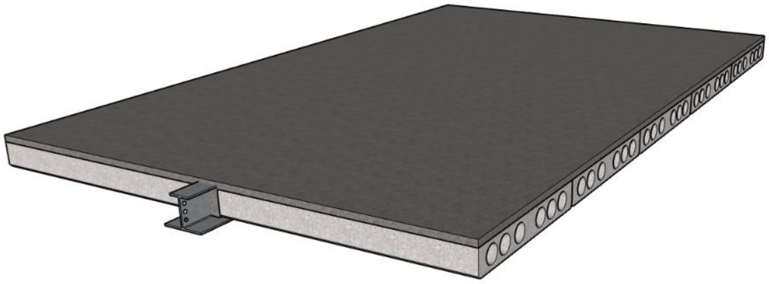

Figure B-7: Test 3 Design Stage: Live Load on Both Sides (Stoddard 2022)

The critical limit states were lateral-torsional buckling (LTB) and out-of-plane rotation of the edge beams during Tests 1 and 2. This was due to the eccentric loading. The critical limit state for Test 3 was yielding under normal stress (depending on the assumption of composite action). The numerical rotation of the edge beams was close to four degrees under the Test 2 loading plan. Out-of-plane rotational limits are not specified by code, but four degrees was decided to be a practical limit. Due to the anticipated edge beam rotation (assuming pin support behavior in bending and torsion), the initially designed shear connections (S) of the edge beams to the columns were changed to increase the rotational restrain (RR). The beam to column connection was stiffened by adding angles to the top and bottom flanges of the edge beams. The angles were bolted to the columns and welded to the beam flanges.

Instrumentation

To capture the structural behavior of the system during the testing, thirty-nine strain gauges were used within three cross-sections, and five displacement gauges were used within the midspan cross-section. The electrical resistance strain gauges (350 Ohm) were placed at midspan as well as 0.914 m (3.0 ft) in each direction. Displacement gauges (string potentiometers (SP)) were placed under each beam at midspan to measure the vertical displacements (V). Lateral displacement (L) gauges were placed at the top and bottom of Beam 1. This approach was used to measure lateral movement and out-of-plane rotation. Figure B-8 illustrates the locations of the strain gauges and displacement gauges at the midspan cross-section. The strain gauges were installed near the flange edges to capture in-plane bending and torsion. Each beam was instrumented with four strain gauges per cross-section, except for the center beam, which had an additional strain gauge at the center of its top flange. The two additional floor system cross-sections, located at a distance of 0.914 m (3.0 ft) from the midspan, have the same arrangement of strain gauges.

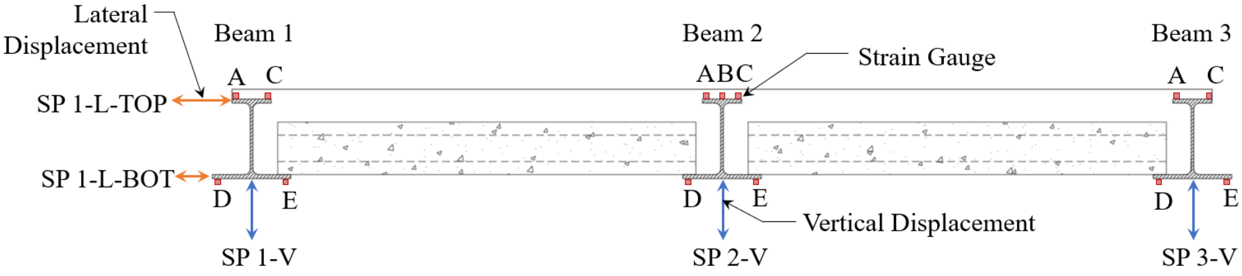

Figure B-8: Instrumentation at Midspan Cross-Section

System Testing Program

This section details the experimental laboratory testing performed in the study, which includes three primary tests. Tests 1 and 2 were construction loading during the floor system assembly. Test 3 was vertical loading to evaluate in-service behavior up to the ultimate strength. Typical experimental data from each test are presented below, along with the combined results.

Test 1: Precast Panel Placement

The first construction loading tests were placing the precast panels onto the bottom flanges of the beams. These tests were conducted by using a forklift to lift the panels above the system and lower them onto the beams' bottom flanges (this could have also been done using the overhead crane). Since the precast panels could be easily taken on and off the flanges by the forklift, three different loading cases were tested, as shown in Figure B-9. The purpose was to gain further insight into the A-shape beam behavior. The loading cases included (A) loading one bay entirely before proceeding to the next bay with the designed beam-column connections, (B) loading one bay with simple shear connections on the edge beam (the bolts connecting the top and bottom angles were removed), and (C) loading the bays alternately with the designed beam-column connections. Figure B-10 shows a photo of the floor system with panels fully installed.

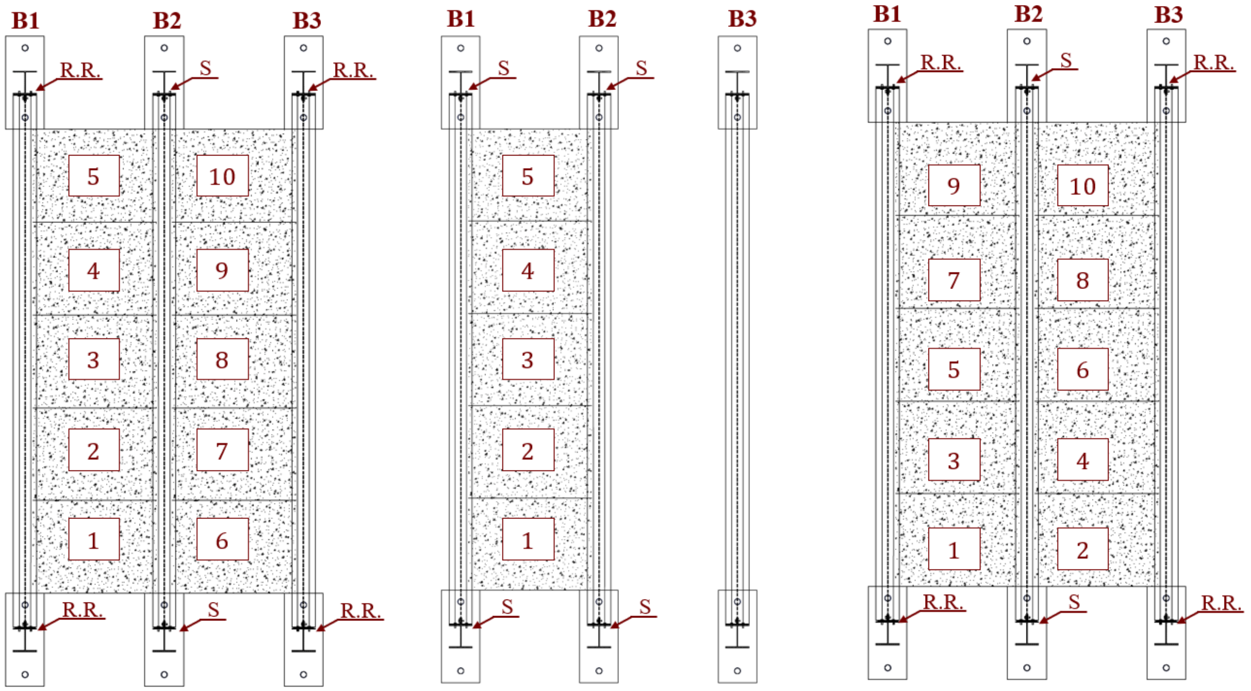

(A) (B) (C)

Figure B-9: Precast Panel Loading Cases (A), (B), and (C) with Shear (S) (web only) Connections or Rotationally Restrained (RR) (web and flange) Connections

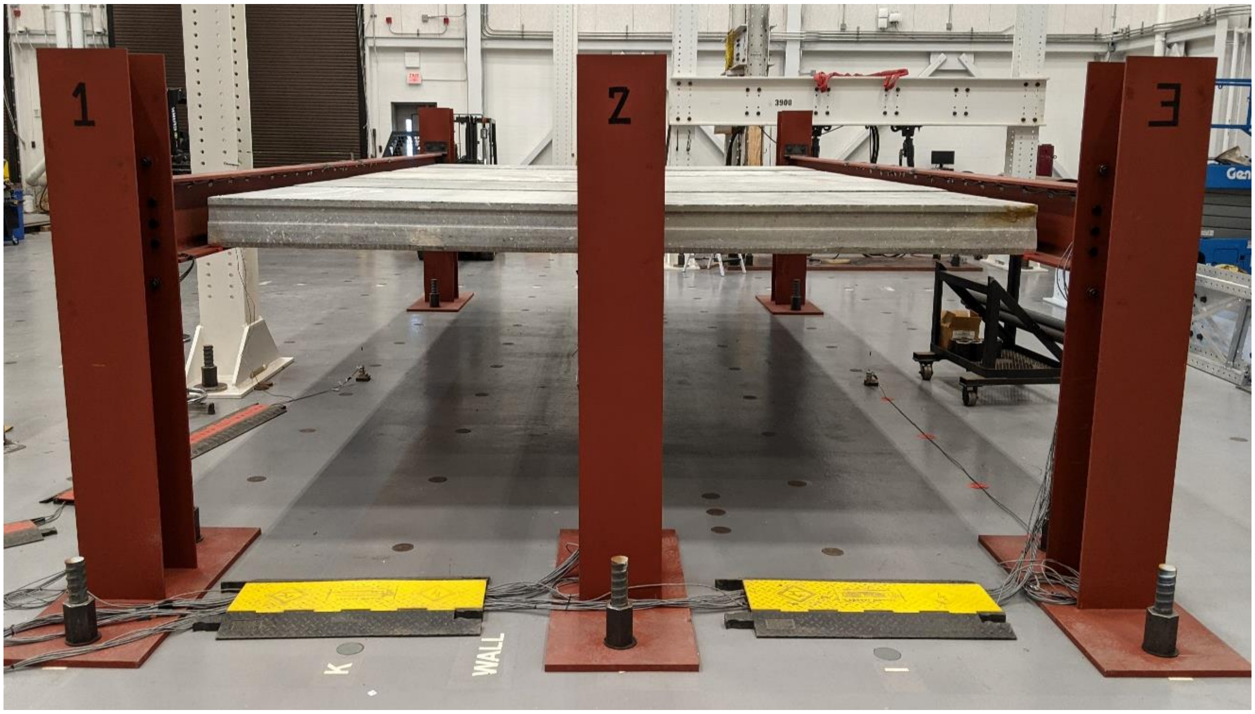

Figure B-10: Precast Panels Installed

The quality of the measurements throughout Test 1 was relatively good. The change in behavior from each panel placement could be observed through the local strains and global deformations (vertical displacement and rotation). Figure B-11 illustrates the raw data time history plots for Test 1, Case

(C), mid-span cross-section of Beams 1 and 2. The torsion from the eccentric load on Beam 1 can be clearly observed from the data (Figure B-11(a)) along with the order of magnitude of response. Similarly, the predominant in-place bending from the concentric load on Beam 2 can be observed from the data (Figure B-11(b)). Note the gauge notation is shown in Figure B-8.

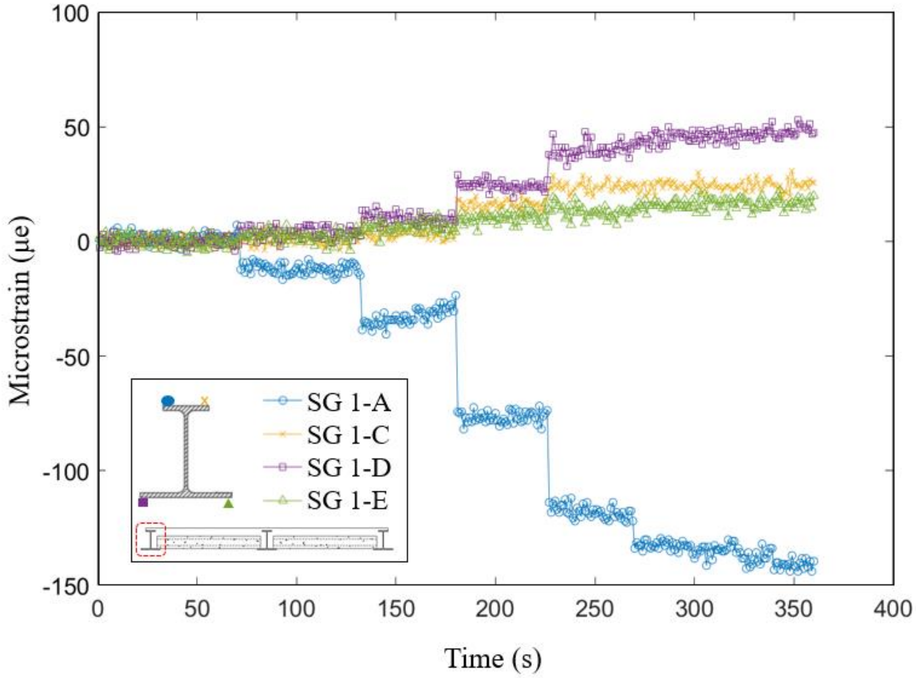

(a)

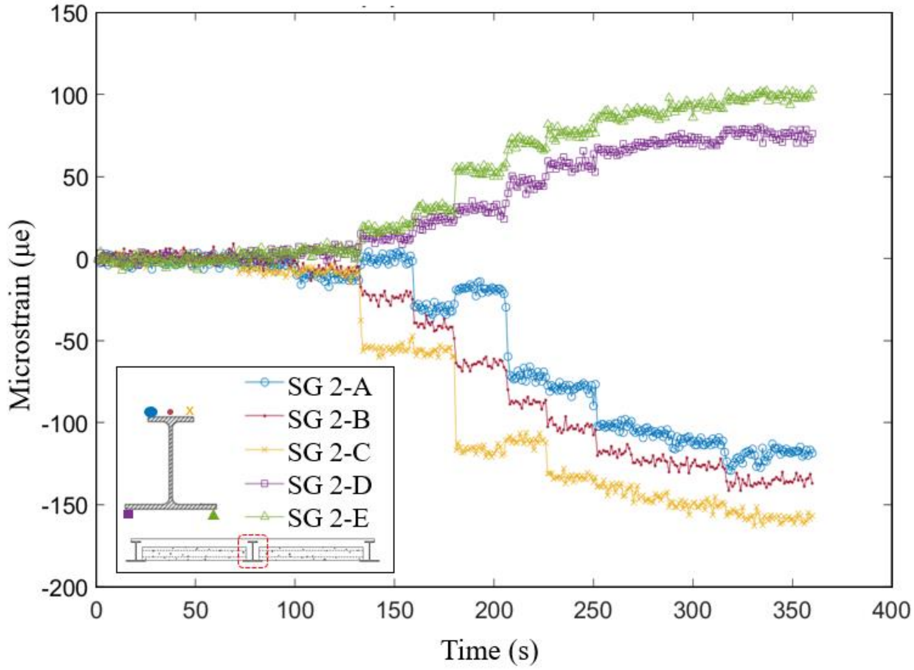

(b)

Figure B-11: Test 1 Case (C) Time History Results for (a) Beam 1; and (b) Beam 2

To better visualize the data, the peak response (placement of all panels) was plotted on cross-section views. Figure B-12 and Figure B-13 illustrate the midspan strain, displacement, and rotation data, respectively, for Test 1, Case (C). The other cases were not shown due to space limitations. These plots allowed for easier data interpretation. The primary findings from Test 1 included the following:

- Relatively good symmetry was observed in the data. Variations can be attributed to initial imperfections and inexact panel placement.
- The largest compressive stresses were observed in the outside top flange sensor of the edge beams. This was due to the combined in-plane bending and torsion. When compared to Cases (A) and (C), the magnitude of compressive strain increased slightly (13%) for Case (B) due to the softer connection.
- The displacements for Case (A) and (C) were relatively small, with Beam 2 experiencing roughly twice the magnitude as anticipated due to the additional load. For Case (B), the displacements for Beam 1 and 2 were essentially the same. Therefore, the top and bottom angles had a minimal impact on midspan displacements.
- The rotation of Beam 1 was approximately 1.45 degrees for all cases. There was a minimal increase in rotation (10%) for Case (B) with the removal of the top and bottom angles.

More detailed data analysis, including a comparison to theoretical calculations, is provided in the following sections. Also, for plots of all the data, please refer to Davis (2022).

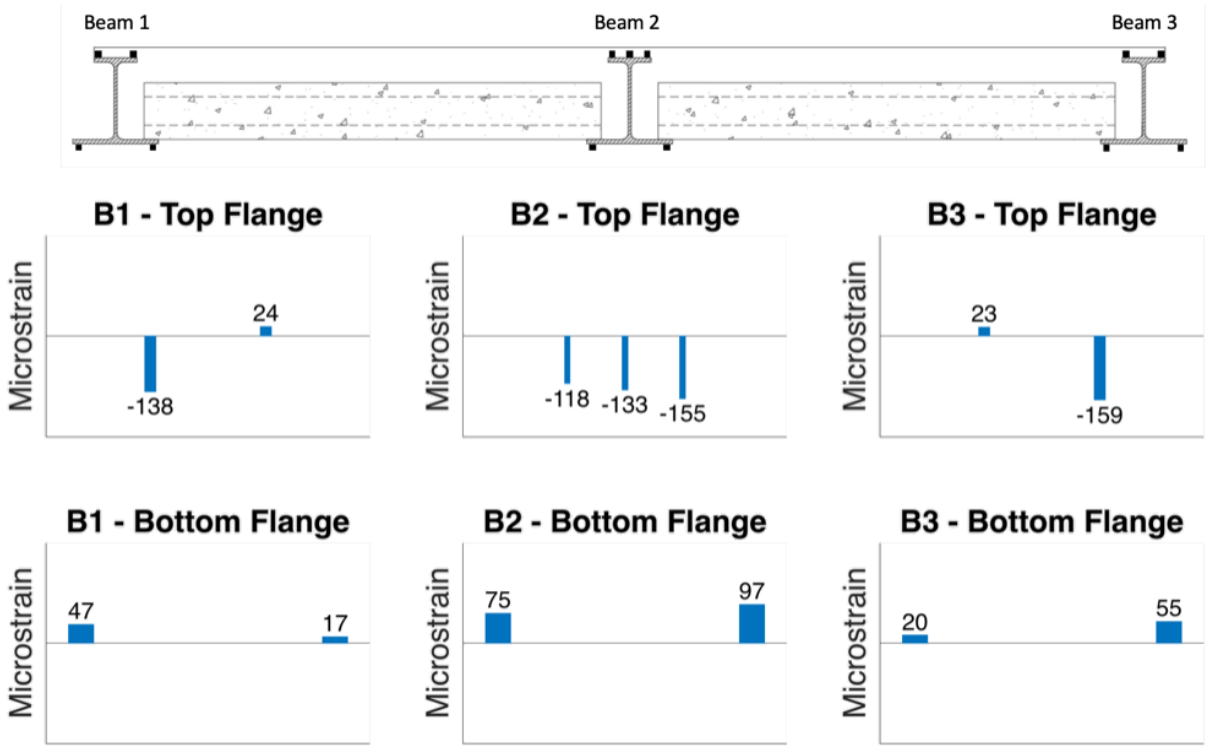

Figure B-12: Test 1 Case (C) Measured Strains at Midspan Cross-Section for Beam 1 (B1), Beam 2 (B2), and Beam 3 (B3)

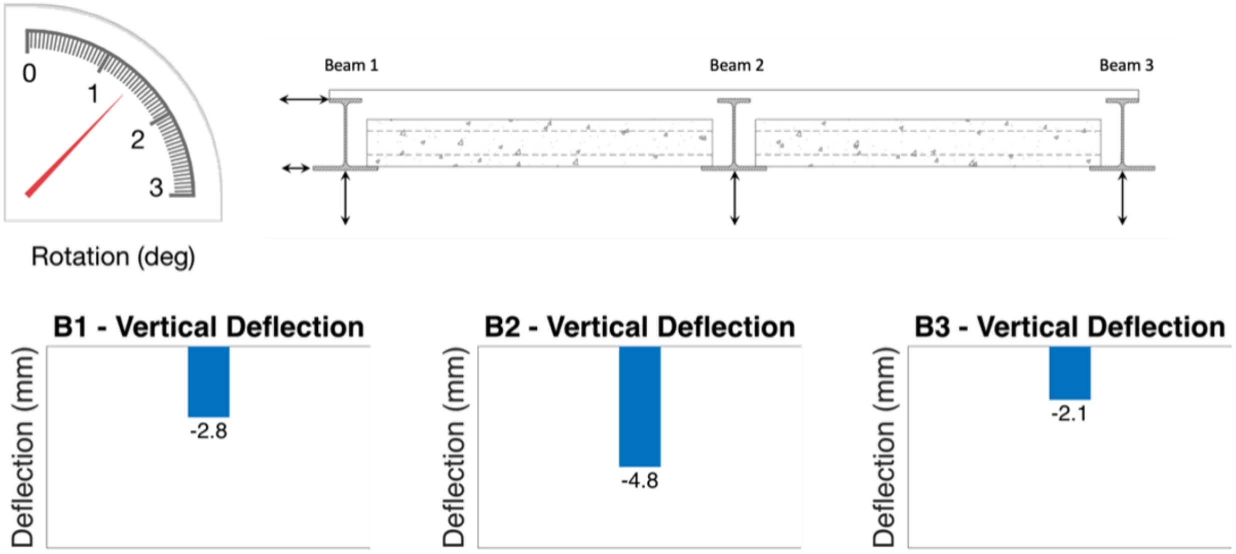

Figure B-13: Test 1 Case (C) Measured Displacements and Rotation at Midspan Cross-Section

Additional information collected during Test 1 included the subjective evaluation of constructability. The erection of the steel and precast panels went smoothly without any major issues. A seat width of 51 mm (2.0 in) was sufficient. After the placement of several panels, the speed of placement significantly increased, making the assembly relatively fast.

Test 2: Concrete Pour

The second construction loading test was during the pouring of the concrete topping slab. This test consisted of taking measurements throughout the concrete placement. Figure B-14 shows the strains at midspan for all three beams after the entire slab was placed. The strains shown are unique to Test 2 and only represent the loading during that test. The upper left gauge on Beam 2 (SG 2-A) was damaged during the concrete placement, so no measurement at this location is shown. The other four strain measurements along Beam 2 functioned properly. The primary findings from Test 2 included the following:

- The Beam 2 strains clearly show nearly all in-plane bending (no torsion), as expected.
- The magnitude of the Beam 2 strains was roughly 50% greater than from the panel loading.
- The peak compressive strains for Beams 1 and 3 were slightly less than those from the panel loading.
- The rotation of Beam 1 was only 0.65 degrees from the concrete pour (compared to nearly 1.45 degrees for the panel placement)

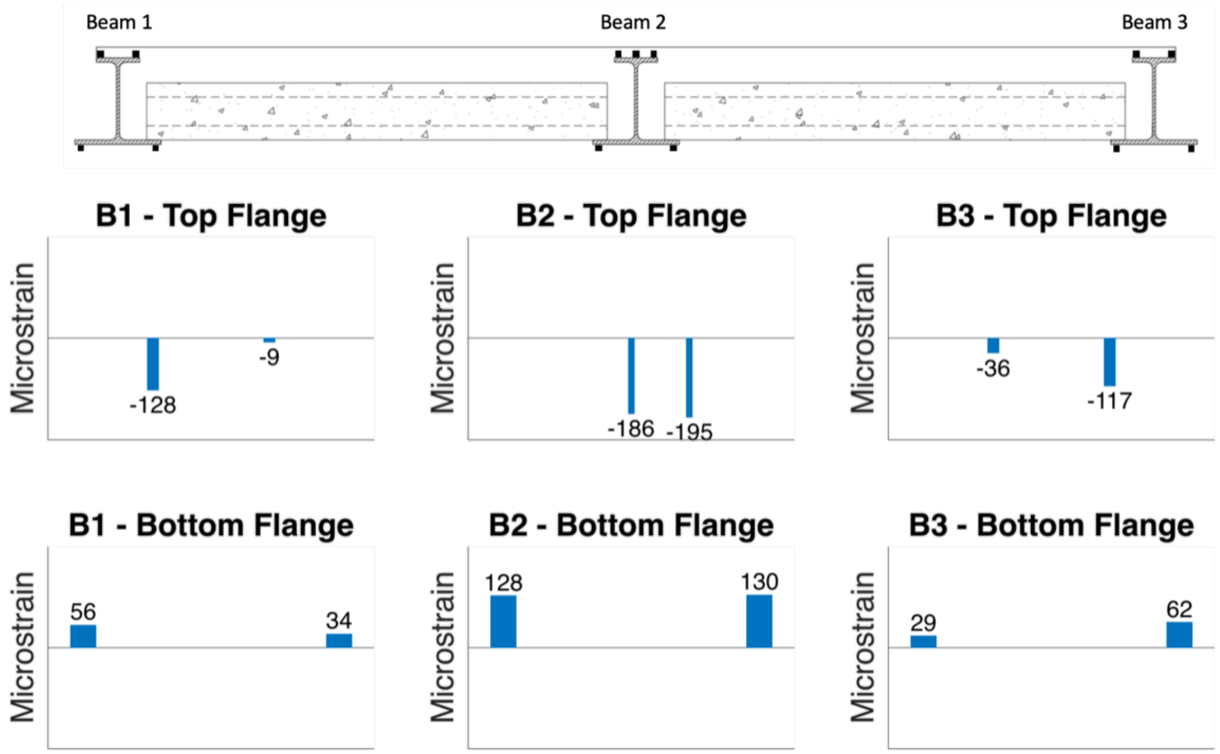

Figure B-14: Test 2 Measured Strains at Midspan Cross-Section

The superimposed Test 1 and 2 response after the concrete pour was important because the controlling limit state of the design was lateral-torsional buckling of the edge beams. The total combined Test 1 and 2 maximum measured top flange compressive response was 276 microstrain (55.2 MPa or 8.0 ksi), which was less than the predicted value of 397 microstrain (79.3 MPa or 11.5 ksi). Similarly, the combined Test 1 and 2 out-of-plane rotation at Beam 2 was 2.10 degrees, which was below the predicted value of 3.32 degrees. This was primarily due to the conservative design assumption of pinned connections. Further comparison of the experimental results with theoretical calculations is provided later.

As with Test 1, subjective observations were made about the concrete pour with A-shapes. The main concern was being able to sufficiently fill the gap around the web of the A-shape with wet concrete. This proved to not be an issue with 203 mm (8.0 in) precast panels and a 305 mm (12.0 in) steel section. However, if the A-shape is not as deep, the panels will either need to be shallower, or chamfers will need to be added to the top edges of the panels for sufficient concrete placement.

Test 3: Actuator Vertical Loading

The last test was conducted by using an 890 kN (200 kips) capacity MTS actuator in the configuration shown in Figure B-15. This testing occurred 54 days after Test 2. Despite designing floor systems for surface loads, most laboratory testing utilizes concentrated loading due to logistical reasons. For this experiment, four-point bending was chosen, with the actuator force distributed onto the system by a spreader beam and rockers. The spreader beam applied the loading 1.8 m (6.0 ft) apart (each 0.9 m (3.0 ft) from the midspan cross-section). Since the focus of the testing was Beam 2, the loading was centered over this beam. The actuator was programmed using force control for a variety of loading levels. The initial loading was a 1.7 kPa (35 psf) equivalent service loading (or 29 kN (6.6 kips)).

Additional vertical loading was applied and removed, and data was recorded. Finally, the system was gradually loaded until failure.

(a) (b)

Figure B-15: Actuator Loading Configuration: (a) Southeast View; and (b) Northwest View (Images by Matthew Yarnold)

The measured response for service level loading (4.8 kPa (100 psf) equivalent) was of good quality and illustrated linear behavior, as expected. Figure B-16 shows the measured strains for the 4.8 kPa (100 psf) service loading. Again, note that the upper left strain gauge on Beam 2 was damaged, so no value is reported. The vertical displacements for Beams 1, 2, and 3 were 1.5 mm (0.06 in), 2.3 mm (0.09 in), and 1.8 mm (0.07 in), respectively. Essentially, no rotation of Beam 1 was measured, as expected due to the concrete lateral restraint. The primary findings from service level testing include:

- The beam strains were approximately equal despite the loading positioned over the center beam.
- The stiffness of the composite section allowed for good lateral distribution of the loading.
- The magnitude of the service live load strains was relatively low compared to dead load strains. This was partly due to the closure pour producing a fully composite section under service level superimposed loads.
- The Beam 2 service level displacements were equivalent to L/3000, which is significantly better than the typical limit of L/360 for residential floor systems in the U.S.

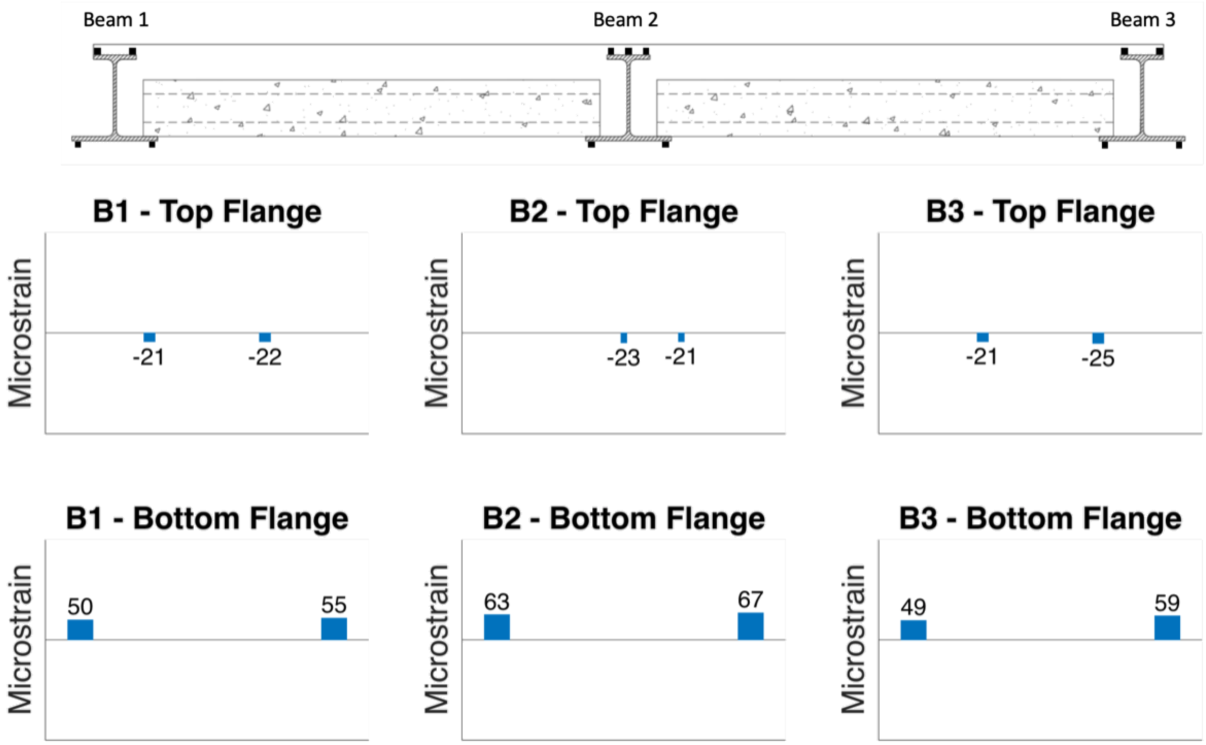

Figure B-16: Test 3 Measured Strain from 4.8 kPa (100 psf) Equivalent Loading (83 kN (18.6 kips) Actuator Load) at Midspan Cross-Section

The strain responses for the final loading to failure for Beams 1 and 2 are provided in Figure B-17 and Figure B-18, respectively. For all three beams, the strains gradually increase in magnitude in nearly a linear manner until a 23.9 kPa (500 psf) equivalent load was achieved. The plateaus in the data were due to periodic stops in the experiment to review the results. When the 23.9 kPa (500 psf) equivalent load (419 kN (94 kips)) was reached, an audible sound was heard, and the Beam 2 strains started to increase rapidly (Figure B-18). The actuator was abruptly stopped and held at this load level.

Failure of the system initiated with composite action breakdown of Beams 1 and 3. This was due to the fact that these beams were only partially encased providing limited bond surface. Also, the relatively close beam spacing resulted in relatively equal load sharing between the beams. Further description and a photograph of the failure mode are provided below.

After the composite action breakdown of Beams 1 and 3, the load was shed to Beam 2, which experienced a rapid increase in strain. However, soon after the bond break, the actuator load was held constant. The strains for Beams 1 and 3 held relatively constant until the load was removed and returned to zero after unloading. However, for Beam 2, the strains continued increasing after the initial failure.

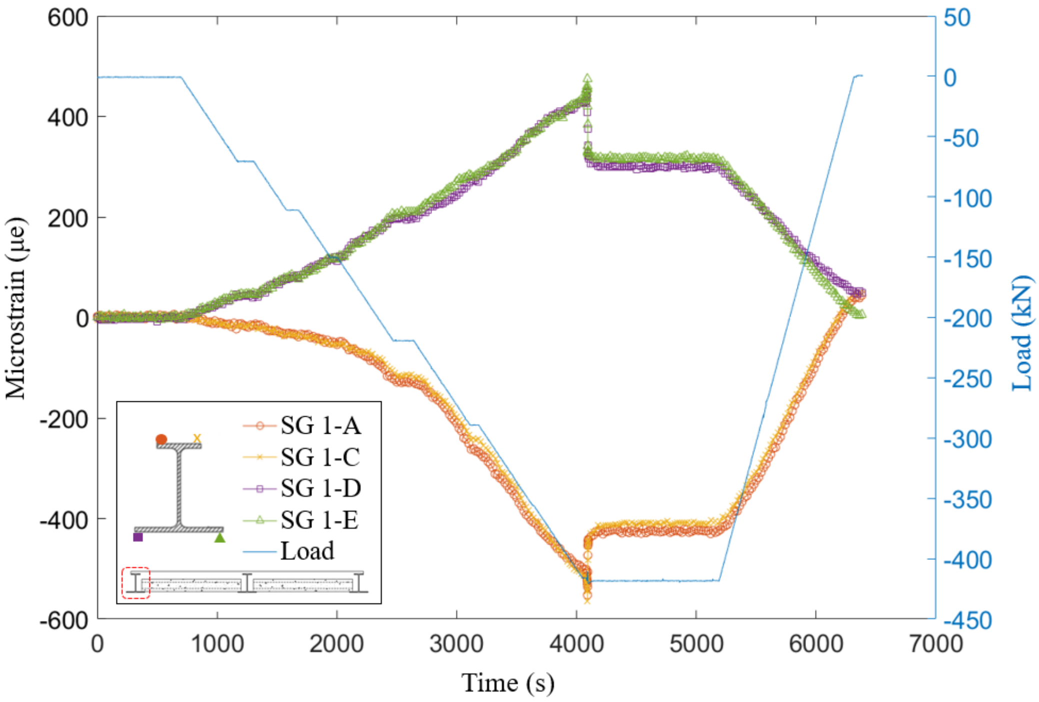

Figure B-17: Test 3 Ultimate Loading: Beam 1 Strain versus Time

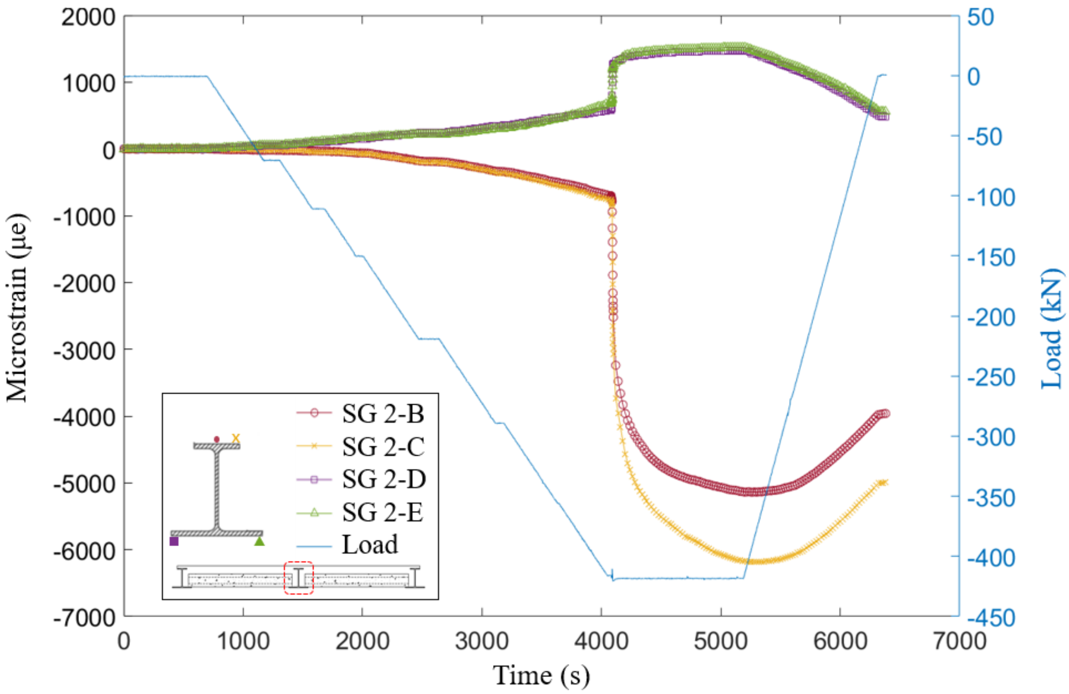

Figure B-18: Test 3 Ultimate Loading: Beam 2 Strain versus Time

Figure B-19 illustrates the load versus displacement relationship at Beam 1 and Beam 2. The failure of Beam 2 at 419 kN (94 kips) is clearly illustrated. The vertical displacement prior to failure was equivalent to L/260. However, after the failure load was reached, the actuator load was held constant for roughly 20 minutes and then unloaded. The permanent deformation at Beam 2 was 30 mm (1.2 in.). Beam 1 illustrates a similar trend in behavior up until the 419 kN (94 kips) loading, but with a lower magnitude of response. There was some residual deformation of Beam 1, but this was due to the load shedding from Beam 2 and not due to any plastic deformation. Beam 3 exhibited similar behavior to Beam 1 but is not shown for clarity.

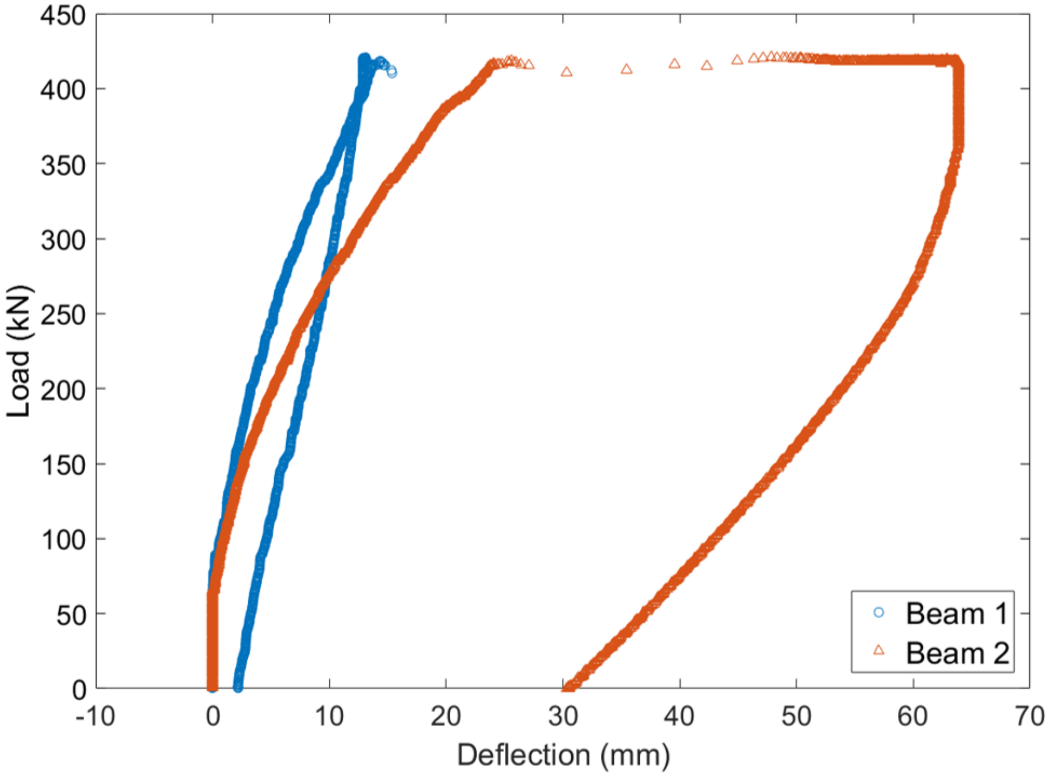

Figure B-19: Test 3 Ultimate Load versus Displacement for Beams 1 and 2

The failure was initiated with the composite action breaking between the painted steel and concrete for Beams 1 and 3 (only partially encased). This happened at 419 kN (94 kips). When this occurred, the load was shed to Beam 2, where the non-composite capacity (327 kN (73.4 kips) to reach the yield moment) was insufficient to carry the applied bending moment. Therefore, Beam 2 experienced plastic deformation, as shown in Figure B-20. This photo was taken after the loading was removed. The photo also shows the concrete slab separation from the edge beam that occurred. Overall, the primary findings from ultimate strength testing include:

- The lateral distribution of the load was relatively good. This was observed through the beam strains and the displacements.
- Failure of the floor system occurred at approximately 23.9 kPa (500 psf) equivalent loading (419 kN (94 kips) actuator load).
- The failure mode was the breakdown of composite action between the painted steel and concrete for Beams 1 and 3. After this occurred, the load was shed to the center beam (Beam 2), and the system remained stable. The failure was relatively ductile and held the peak load for 20 minutes prior to unloading.

Combined Experimental Results

The combined beam strains from Tests 1, 2, and 3 provided a comprehensive state of the beams prior to failure. Figure B-21 illustrates these strains for all three beams. The Beam 2 average top flange stress reached 1070 microstrain (214 MPa or 31.0 ksi) before the concrete bond was broken. Note that the yield strain for this steel is 1725 microstrain (345 MPa or 50.0 ksi). The Beam 2 vertical displacement (dead and live load) from Tests 1, 2, and 3 (100 psf) was 12.7 mm (0.5 in), which is equivalent to L/550.

Figure B-20: Center Beam Permanent Deformation and Steel-Concrete Separation (Image by Matthew Yarnold)

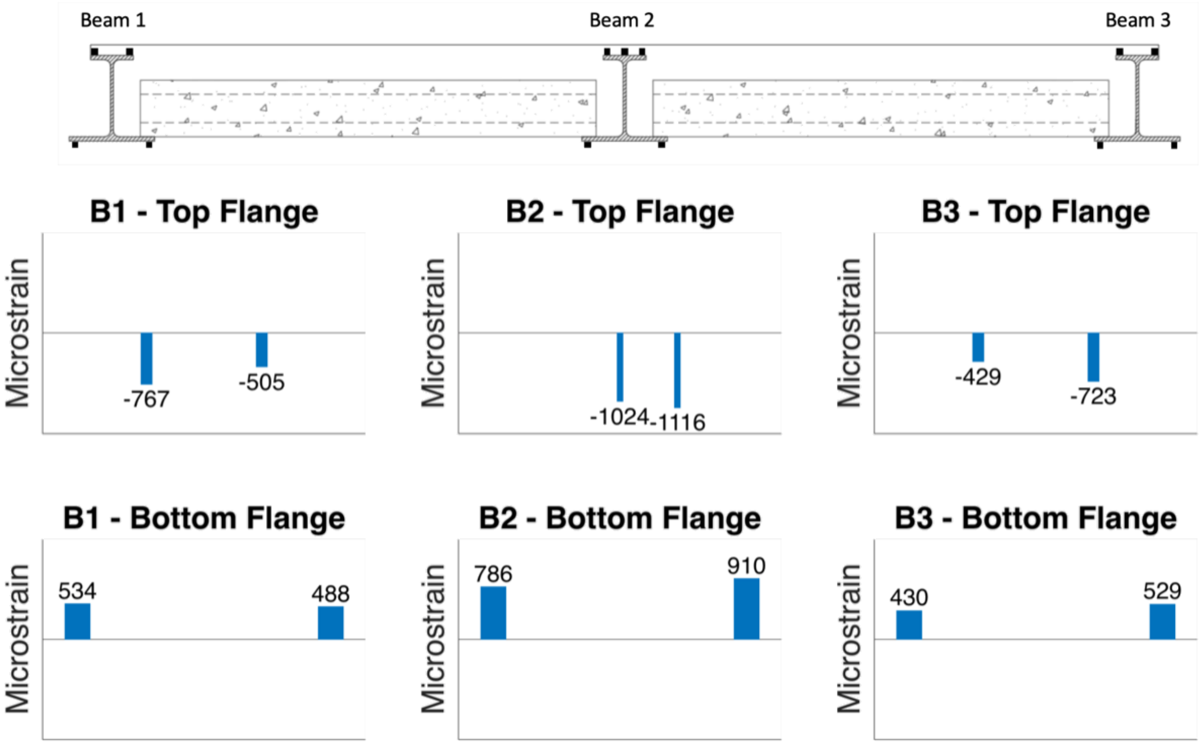

Figure B-21: Test 1, 2, and 3 Combined Strains prior to Failure

Data Analysis

This section presents a summary of the data analysis performed. A comparison of theoretical calculations with the experimental measurements was conducted. This includes an overall comparison of the measured responses. The flexural rigidity of the system is explored along with the composite behavior for the in-service system. In addition, the critical limit states are evaluated for the floor system tested along with discussion for future floor systems.

Theoretical vs. Experimental Comparison

Theoretical calculations were performed using beam analysis. Each beam was analyzed for the Test 1 Case (C), Test 2, and Test 3 (4.8 kPa (100 psf)) loading conditions. As discussed earlier, the beams were subjected to in-plane bending from concentric loads along with torsion from the eccentric loads. Therefore, quantification of the theoretical stresses requires the superposition of these demands, as illustrated in Figure B-22. Vertical displacements and rotations are calculated separately. A brief background of the theoretical basis is provided below, followed by the primary assumptions.

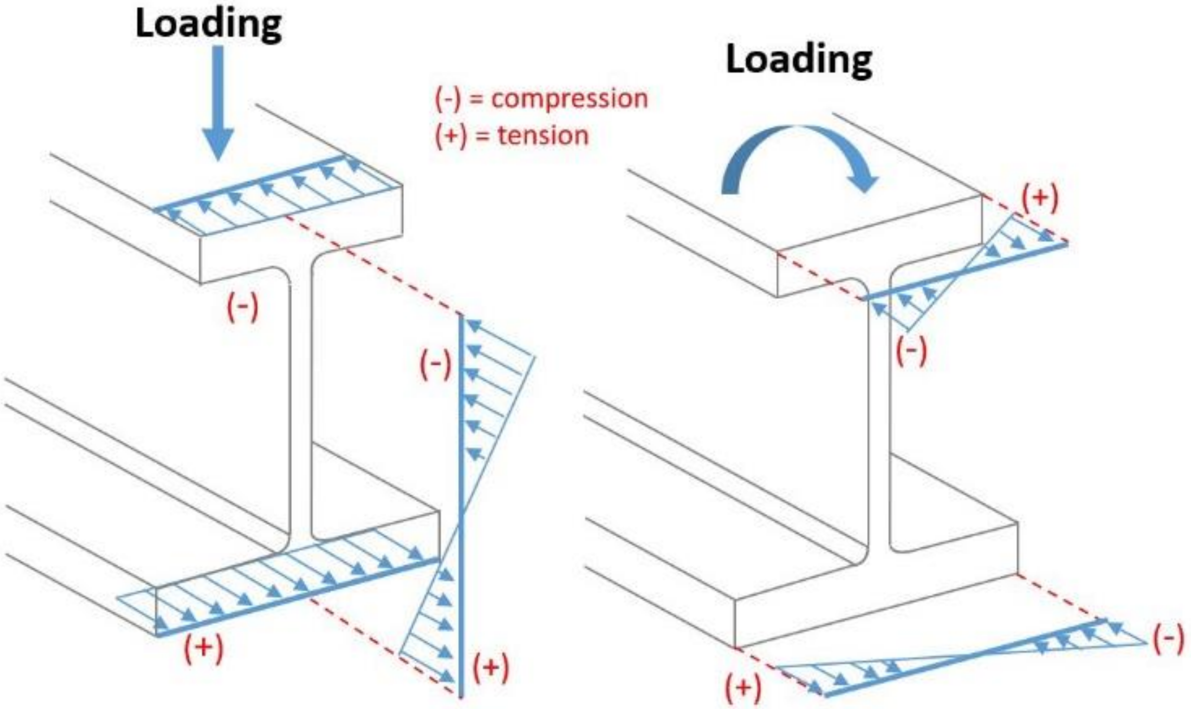

Figure B-22: Longitudinal Stress due to In-Plane Bending and Torsion

Theoretical Background

Calculation of the elastic in-plane bending stresses (σ_b) is relatively straightforward using Equation (B-1), which only requires the applied bending moment (M_u) and the elastic section modulus (S_x).

$$\sigma_b = \frac{M_u}{S_x} \tag{B-1}$$

The maximum midspan vertical displacements (δ) can also be easily quantified for a simply supported beam subjected to uniformly distributed load (ω), as shown in Equation (B-2). In this expression, the length, modulus of elasticity, and moment of inertia are represented by the variables l, E, and I, respectively.

$$\delta = \frac{5\omega l^4}{384EI} \tag{B-2}$$

For analysis of a beam due to torsion, it is best to start with the two torsional moments that are resisted by the cross-section. The first, expressed in Equation (B-3), is the torsional moment due to rotation of the section, also referred to as St. Venant Torsion (or pure torsion). The first derivative of the angle of twist per unit length (θ') is related to the torsional moment (T_t) using the shear modulus of elasticity (G) and a torsional constant (J).

$$T_t = GJ\theta' \tag{B-3}$$

For non-circular cross-sections, if axial deformation is unrestrained or allowed to rotate freely, only pure torsion exists. However, if longitudinal displacements due to torsion (termed warping) are restrained, a torsional moment due to restrained warping of the section (T_w) will be present. Equation (B-4) quantifies the torsion due to warping resistance (Seaburg and Carter 2003).

$$T_w = -EC_w\theta''' \tag{B-4}$$

During warping, shear forces in the flanges form a couple that resists the applied torque. Combining Young's modulus (E) with a warping constant (C_w) gives the warping rigidity of the section (EC_w). Equation (B-5) is a combination of the torsional resistance provided by the structural shape.

$$T = GJ\theta' - EC_w\theta''' \tag{B-5}$$

Ultimately, the angle of twist (θ) in the beam needs to be computed, allowing for the derivatives of twist to also be computed. The first step is to rearrange Equation (B-5) by dividing by the warping rigidity of the cross-section (EC_w), resulting in Equation (B-6). This effectively removes the constant from the θ''' term. To remove the constants from the θ' term, a separate definition shown in Equation (B-7) can be implemented to remove the warping rigidity (EC_w) and the pure torsional rigidity (GJ) from the right-hand side of Equation (B-6). Substituting Equation (B-7)'s results in Equation (B-6) yields Equation (B-8), which is for a constant torsional moment (T) applied to the beam.

$$\frac{T}{EC_w} = \frac{GJ\theta'}{EC_w} - \theta''' \tag{B-6}$$

$$a^2 = \frac{EC_w}{GJ} \tag{B-7}$$

$$\frac{T}{EC_w} = \frac{\theta'}{a^2} - \theta''' \tag{B-8}$$

This expression can be modified to analyze a uniformly distributed torsional moment (t), as shown in Equation (B-9) (Seaburg and Carter 2003). The solution for this differential equation is conveyed in Equation (B-10).

$$\frac{-t}{EC_w} = \frac{\theta''}{a^2} - \theta'''' \tag{B-9}$$

$$\theta = A + Bz + C\cosh\frac{z}{a} + D\sinh\frac{z}{a} - \frac{tz^2}{2GJ} \tag{B-10}$$

A further simplification can be made by applying pinned boundary conditions and solving the arbitrary constants ($A, B, C\ and\ D$), where l is the beam length, and z is the location on the beam where θ is evaluated. For this research, θ and θ'' are needed for the calculation of the beam rotation and stresses, respectively. Equations (B-11) and (B-12) provide the resulting equations.

$$\theta = \frac{tl^2}{GJ}\left[\frac{z}{6l} + \frac{a^2}{l^2}\left(\frac{\sinh\frac{z}{a}}{\sinh\frac{l}{a}} - \frac{z}{l}\right) - \frac{z^3}{6l^3}\right] \tag{B-11}$$

$$\theta'' = \frac{-a^2 t}{GJ}\left[\frac{1}{a^2} - \frac{\cosh\left(\frac{z}{a}\right)}{a^2} + \frac{\sinh\left(\frac{z}{a}\right)\tanh\left(\frac{al}{2}\right)}{a^2}\right] \tag{B-12}$$

The longitudinal warping stresses (σ_w) can be calculated using Equation (B-13). For this calculation, the normalized warping constant (W_{no}) is needed. For an asymmetric I-beam, this value is different with respect to the top and bottom flange. Equations (B-14) and (B-15) provide the normalized warping constant for the top flange (W_{not}) and bottom flange (W_{nob}) (Heins 1975). The required dimensional parameters shown in these equations include the location of the shear center from the centroid of the top flange (α), the distance between the centroid of the flanges (h_o), the width of the top flange (b_{ft}), and the width of the bottom flange (b_{fb}).

$$\sigma_w = E\, W_{no}\, \theta'' \tag{B-13}$$

$$W_{not} = \frac{\alpha\, b_{ft}}{2} \tag{B-14}$$

$$W_{nob} = \frac{(h_o - \alpha)}{2} b_{fb} \tag{B-15}$$

As mentioned earlier, to calculate theoretical stresses at any point along the beam cross-section, the in-plane bending stress (σ_b) and the warping stresses due to torsion (σ_w) must be accurately combined. The theoretical vertical displacements (δ) and rotations (θ) can be compared directly. The specific calculated values and the comparison to the experimental values are provided below.

Calculation Assumptions

As with any theoretical calculations, several uncertainties and assumptions were present in the calculation of the stresses, displacements, and rotations. The primary assumptions include:

- <u>Boundary Conditions</u>: The beam connections are semi-rigid for bending and torsion. The theoretical calculations were performed assuming pinned and fixed conditions to bound the behavior.
- <u>Longitudinal Load Distribution</u>: The longitudinal load distribution is assumed to be uniformly distributed for Tests 1 and 2. For Test 3, four-point bending is assumed.
- <u>Lateral Load Distribution</u>: The distribution of lateral load between the beams during Test 3 is complicated due to the setup, which includes different end connection types (stiffer outside beams). It is assumed that the lateral distribution is 25%-50%-25% for Beams 1, 2, and 3, respectively.
- <u>Load Position</u>: The load acting on the top of the bottom flange is assumed as a concentrated line load with the position at the center of the bearing.
- <u>Effective Width</u>: The effective width of the composite section in Test 3 (100 psf) is assumed to be the tributary width of each beam. This is justified by the relatively close spacing of the beams.
- <u>Composite Action</u>: The calculations for Test 3 (100 psf) assume the beams to act fully composite with the cast-in-place slab.
- <u>Material Properties</u>: The steel modulus of elasticity, shear modulus, and yield stress were assumed as 200,000 MPa (29,000 ksi), 77,000 MPa (11,200 ksi), and 345 MPa (50 ksi), respectively. The modulus of elasticity for the concrete was quantified from the concrete cylinder testing as 28.9 MPa (4.19 ksi).

<u>Overall Comparison</u>

The theoretical calculations were performed based on the equations and assumptions presented above. These calculations and the direct comparison to the measured experimental results are presented in Table B-1. The calculations are presented as essentially bounding values that include beam pinned end connections (bending and torsion) and fixed end connections (bending and torsion). This was chosen because the connection stiffness was the most sensitive parameter of the response. The true connections at the ends of the beams were semi-rigid. Further refinement of the calculations to identify longitudinal and rotational spring stiffnesses was explored but not selected for presentation herein. This was due to the nonlinearity of the response along with the influence of other parameters mentioned in the prior section.

Overall, the strain measurements fall within the theoretical bounds for all tests and all three beams. The results from Beam 2 clearly show that the behavior was semi-rigid. It was anticipated that with shear (web only) connections, the response would be closer to idealized pin behavior, but this was not the case. Beams 1 and 3 included further restraint at the ends (top and bottom angles), which can be observed in Table B-1. However, the behavior would still not be classified as fully restrained. One takeaway is that a future beam design assumption of pinned end conditions is conservative but also appropriate.

The displacements and rotation values mostly fall within the theoretical bounds. The Beam 1 rotation and Beam 3 displacement measurements are slightly outside the fixed boundary. The Beam 1 rotation measurement is essentially the same as the theoretical fixed value considering the resolution of the sensor. The Beam 3 displacements measurements may have been a data quality issue since only noise was recorded. Overall, the Beam 2 displacements indicate the in-plane bending behavior to be close to pinned conditions, as expected. For Beams 1 and 3, this was also the case, even with additional support connection restraint. The Beam 1 rotations from Test 1 and Test 2 indicate the rotational restraint to be closer to fixed but still semi-rigid.

Table B-1: Comparison of Theoretical Calculations with the Experimental (Exp.) Results

Beam	Measurement Type	Location	Test 1 (Case C)			Test 2			Test 3 (100 psf)		
			Theoretical		Exp.	Theoretical		Exp.	Theoretical		Exp.
			Pinned	Fixed		Pinned	Fixed		Pinned	Fixed	
1	Strain (micro)	A	-209	-116	-138	-188	-94	-128	-33	-12	-21
		C	2	47	24	-46	16	-9	-33	-12	-22
		D	94	44	47	93	40	56	74	27	50
		E	36	-1	17	54	9	34	74	27	54
	Displacement (mm)	-	2.8	0.5	2.8	3.0	0.5	0.5	1.8	0.3	1.5
	Rotation (deg)	-	1.98	0.98	1.45	1.34	0.66	*0.65*	-	-	-
2	Strain (micro)	A	-207	-69	-118	-	-	-	-	-	-
		B	-207	-69	-133	-234	-78	-186	-41	-15	-23
		C	-207	-69	-156	-234	-78	-195	-41	-15	-21
		D	130	43	75	147	48	128	120	44	63
		E	130	43	97	147	48	130	120	44	67
	Displacement (mm)	-	5.6	1.0	4.8	6.4	1.3	4.8	2.5	0.5	2.3
3	Strain (micro)	A	2	47	23	-46	16	-36	-33	-12	-21
		C	-209	-116	-159	-188	-94	-117	-33	-12	-25
		D	36	-1	20	54	9	29	74	27	49
		E	94	44	54	93	40	62	74	27	59
	Displacement (mm)	-	2.8	0.5	2.0	3.0	0.5	*0.0*	1.8	0.3	1.8

Note: The italic values represent an experimental result that was not bounded by the pinned or fixed theoretical condition.

Composite Behavior

The composite behavior for the floor system concept studied herein is essential to in-service performance. The composite action between the concrete and the encased steel section is only developed from the bond and friction (no mechanical connection). As stated earlier, the data clearly shows that the steel beams acted composite with the concrete under service level vertical loading. Further quantification of the composite action was performed.

Stress profiles were created for Beam 2 under different levels of vertical loading. For loading equivalent to 9.6 kPa (200 psf) (twice the typical design live load), the neutral axis (assuming a linear stress profile) was relatively close to the theoretical neutral axis for fully composite behavior. Figure B-23 illustrates the 9.6 kPa (200 psf) equivalent stress profiles and how the elastic neutral axis (ENA) is nearly the same. However, as the loading was increased, the ENA continued to drop due to the bond breaking between the steel and concrete. Figure B-23 also shows the stress profiles prior to failure (23.9 kPa (500 psf) equivalent loading). This behavior was observed gradually, meaning the bond breakdown at high load levels was relatively slow and ductile, producing partial composite behavior before reaching the ultimate strength of the bond.

The total level of composite behavior can be quantified by comparing the moment subjected to the composite beam at the failure to the moment capacity of the fully composite beam. The calculated fully composite flexural strength of Beam 2, after removal of the dead load demands, is 436 kN-m (322 kip-ft). This is using all the assumptions stated earlier. The applied bending moment at failure (from the actuator) was 237 kN-m (175 kip-ft). Therefore, failure occurred at 54% of the fully composite beam strength. The primary conclusions include:

- Additional strength could be obtained from the system if more bond was developed between the steel and the concrete through an increased surface bond or other mechanical means.
- Even with only 54% of the potential capacity used, the system failed at five times the service load, which is more than sufficient capacity for conventional residential floor systems.

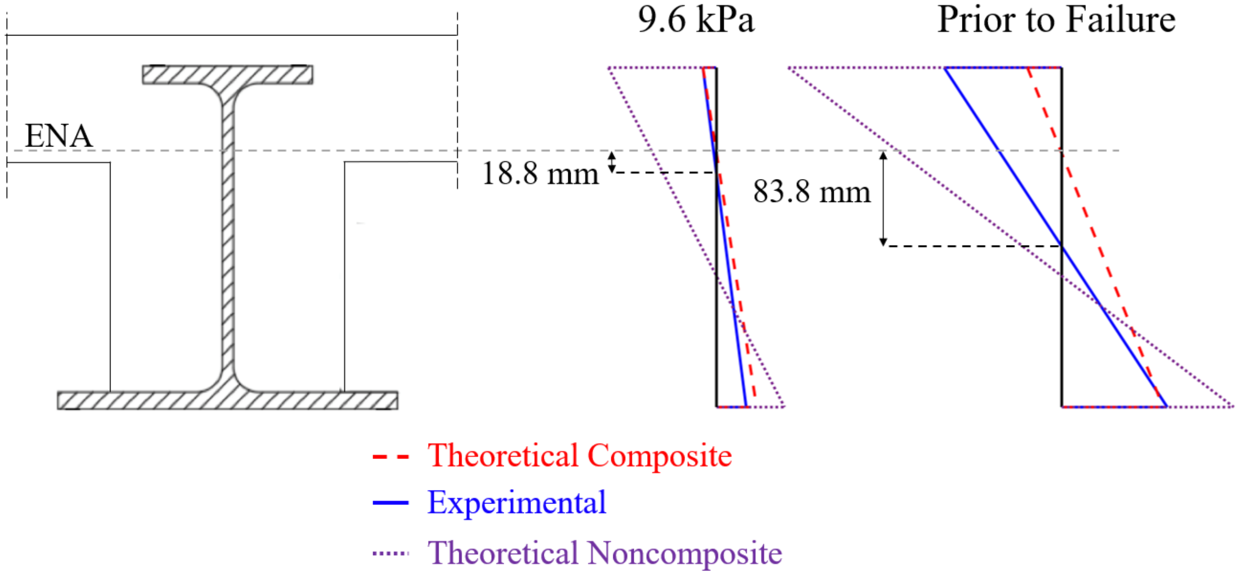

Figure B-23: Stress Profiles from Test 3 (9.6 kPa (200 psf)) and Test 3 Prior to Failure

Flexural Rigidity

The composite behavior of the floor system was further evaluated through the flexural rigidity and the resulting effective width of the center beam (Beam 2). The flexural rigidity is an important characteristic as it determines how well the system resists bending. This information is important for future design of in-service behavior, which includes live load deflections and vibrations.

The flexural rigidity (EI_x) values were calculated from the experimental deflections in Test 3 using Equation (B-16), which assumes pinned support conditions for the composite center beam. In this expression, P is the magnitude of one of the two concentrated loads, L is the length of the beam, a is the distance from the concentrated load to the end of the beam, b is the length of the beam minus a, and Δ is the experimental deflection. Pinned support conditions were utilized because the experimental deflection data (shown in Table B-1) for Test 3 (composite testing) were relatively close to the theoretical pin support deflections.

$$EI_x = \frac{Pa}{24\Delta}(3L^2 - 4a^2) \tag{B-16}$$

The flexural rigidity calculated from the experimental data was averaged for in-service loading up to 9.6 kPa (200 psf). This resulted in a magnitude of 1.04x10^{5} kN-m^{2} (2.51x10^{5} kip-ft^{2}). This was relatively close to the theoretical flexural rigidity, which assumed an effective width equal to the beam spacing (1.83 m (6.0 ft)) and used an experimentally determined modulus from concrete cylinder testing. The theoretical flexural rigidity was 1.02x10^{5} kN-m^{2} (2.47x10^{5} kip-in^{2}), which was a 2% difference. This further verified the composite behavior up through more than double the design live loading. In addition, the flexural rigidity calculations confirmed the effective width assumption utilized in this study. Note that future floor systems utilizing A-shapes may use wider beam spacing where the effective width will be less than the beam spacing.

Critical Limit States

The critical limit states that controlled the initial design of the floor system were explained earlier. This included LTB and rotation of the edge beams for Tests 1 and 2, along with yielding under normal stress for Test 3 (depending on the assumption of composite action). This was revisited using the experimental data after all three tests were completed.

The controlling limit state for the floor system tested was a rotation of the edge beams during the concrete pour (Test 2). The demand-to-capacity ratio was 0.53, which was better than that anticipated prior to testing. In future buildings, the edge beams will likely be stiffened to not control the beam design. Therefore, this limit state may not be of future interest. The controlling limit state for the center beam is of more importance for future systems. This limit state was LTB during the concrete pour (Test 2) with a demand-to-capacity ratio of 0.45. This is relatively low and shows the ability for further improvement of the A-shape design for future floor systems.

The ability of the system to behave as fully composite for twice the design live load rendered the Test 3 flexural capacity and service level deflections inconsequential. However, future A-shapes will likely be optimized to shallower depths of 200 mm (8 in) to 250 mm (10 in) and have wider beam spacings. In this case, these limit states could be an issue along with floor vibrations. These are indicated in the future research section below.

Conclusions

The overarching goal of this research was to experimentally evaluate a shallow-depth steel-concrete floor system utilizing hot-rolled steel A-shapes, with a focus on their use in residential buildings. This was done through full-scale system testing and comparison with theoretical calculations. The emphasis of this initial study was to address the primary knowledge gaps, which included the (1) constructability of the system, (2) system structural performance during construction (non-composite state), (3) system structural performance under service live load (composite state), and (4) ultimate strength of the system under vertical loading. The main conclusions from each are provided below.

(1) Constructability

The primary advantage of using hot-rolled steel A-shapes in this type of floor system, compared to other similar systems, is that it will be easier and faster to acquire steel sections on-site. Other systems require extensive fabrication to build up asymmetric steel sections. For this study, once the proof-of-concept beams were created (only required because this was a research study), the only fabrication for the interior beam was punching holes in the web at the ends for the beam-column connections. The erection of the steel was the same as standard construction. The placement of the panels went very well. The panels had plenty of clearance while lowered between the top flanges of the beams, and the seat width on the beam’s bottom flange was sufficient. The only challenge was ensuring the cast-in-place concrete fully filled the voided region around the beams. In this experiment, it was not an issue. However, for precast panels closer to the beam depth, it could become a challenge. One option to mitigate this issue would be to chamfer the ends of the panels or provide notches. Overall, the construction of the system went relatively easy, and it was accomplished quicker than if it had been constructed with built-up asymmetric steel shapes.

(2) Construction Performance

The performance of the A-shapes during construction is important because it is the stage where the steel beams do not have the additional lateral restraint from the concrete deck. Stability during construction was one of the concerns with this floor system. The controlling limit state for the floor system tested in this study was out-of-plane rotation of the edge beams during the concrete pour (Test 2). The demand-to-capacity ratio was 0.53, which was better than that anticipated. In future buildings, the edge beams will likely be stiffened to not control the beam design. Therefore, this limit state may not be a future concern. The controlling limit state for the center beam is of more importance for future systems. This was LTB during the concrete pour (Test 2) with a demand-to-capacity ratio of 0.45. This is relatively low and did not take into account the stabilizing load-height effect for forces acting on the bottom flange. As a result, there is potential for further improvement of the A-shape design for future floor systems.

(3) Service Level Performance

The floor system performed well under service level vertical loading. Fully composite behavior (through concrete-steel bond and friction) was observed for more than double the conventional design live loading. This was shown by the location of the neutral axis, which was relatively close to the theoretical location for the composite section. In addition, the measured steel strains were relatively low along with the vertical displacements, which were consistent with a fully composite system. For the equivalent design service live load (4.8 kPa (100 psf)), the deflections were equal to L/3000, which is well below the limit of L/360. These results indicate that future systems may be able to utilize the fully composite section for in-service deflection and vibration calculations. In addition, shallower sections may be sufficient.

(4) Ultimate Strength

The floor system failed at a vertical load equivalent to 23.9 kPa (500 psf), or five times the design service live load. The failure mode was the breakdown of composite action between the painted steel and concrete for Beams 1 and 3. After this occurred, the load was shed to the center beam, and the system remained stable. The failure was relatively ductile and held the peak load for 20 minutes before unloading. The failure load reached 54% of its composite capacity. This composite capacity was derived from the bond between the painted steel and concrete. Mechanical connection or increasing the bond (e.g., using unpainted beams) could be used to reach a higher capacity. However, one of the main advantages of this floor system is that it is easy and fast to assemble. Adding mechanical connections or further preparations to increase the bond would reduce the speed and efficiency. In future systems with longer spans, larger spacing, or shallower sections, strength may be more of an issue and could warrant such measures. However, for the configuration of this setup, the system failed at five times the design service live load, and more strength was not needed.

Summary

After this initial investigation presented herein, it was concluded that a shallow depth steel-concrete floor system utilizing A-shapes to support precast panels and a concrete deck is a viable option for residential floor systems. Overall, this floor system concept is relatively easy and fast to construct, and it can provide an adequate level of stability, stiffness, and strength for residential buildings. The A-shape performance was more than adequate, justifying a further reduction in A-shape depth and/or increase in span length and beam spacing. This study was part of a larger effort to develop standardized A-shapes. Details for the current and future research in this area are presented below.

Current and Future Research

Currently, research is being performed to develop standardized A-shapes for large-scale production in U.S. steel mills. This research builds off the experimental feasibility study outlined in this paper. The primary conclusions are being utilized along with manufacturing considerations from three major U.S. steel mills and other criteria specific to residential buildings. The approach is a large numerical study considering all feasible ranges in geometry. These geometric combinations are being analyzed for every conceivable limit state during construction and in-service. This includes the non-composite behavior due to eccentric construction loading, and the composite behavior is considering service level deflections, vibrations, etc. In addition, the ultimate strength and fire performance are being evaluated. The optimum cross-sections for residential buildings will be established for potential addition to Part 1 of the American Institute for Steel Construction Manual.

Future research includes a second full-scale laboratory experiment. The experiment design will focus on the areas of greatest importance and uncertainty identified from the numerical sizing study mentioned above. The limit states controlling typical residential floor system design will be explored in greater detail. This experiment will utilize one of the recommended A-shape cross-sections, which will likely be shallower than that used in the initial feasibility experiment. The experiment should provide further knowledge about A-shape behavior and the possibilities for future production.

Data Availability

Some or all data, models, or codes that support the findings of this study are available from the corresponding author upon reasonable request.

Acknowledgements

The authors are grateful to AISC for supporting this study through the Milek Fellowship. Any opinions, findings, conclusions, or recommendations expressed in this material are those of the authors and do not necessarily reflect the views of AISC.

The authors thank the project industry panel for all their insight and support. This panel is comprised of three U.S. steel mills (Nucor, Steel Dynamics, and Gerdau), fabricators, erectors, designers, and members of AISC (Devin Huber and Margaret Matthew). In addition, the authors appreciate the support from the Texas A&M High-Bay Laboratory, which includes Dr. Peter Keating, Charlie Droddy, and Kirk Martin.

References

AISC. 2017. *Steel Construction Manual*. 15th ed. Chicago, IL: American Institute of Steel Construction.

British Steel. 2022. "Sections Product Range: Asymmetric Beams (ASB)." Accessed February 1, 2022. https://britishsteel.co.uk/what-we-do/construction-steel/sections-product-range/.

COMSLAB. 2022. "Bailey Metal Products Ltd.: COMSLAB Long Span Concrete Floor System." Accessed February 1, 2022. https://www.bmp-group.com/products/comslab.

Corus. 1999. "Structural Sections." Corus Construction & Industrial, BS4: Part 1 and BS EN10056.

Davis, S. 2022. "Full-Scale Floor System Testing for Future Hot-Rolled Asymmetric Steel I-beams." Master Thesis, Texas A&M Univ.

GIRDER-SLAB. 2016. *The GIRDER-SLAB System Design Guide v3.3*. Cherry Hill, NJ: Girder-Slab Technologies.

Hechler, O., M. Braun, R. Obiala, U. Kuhlmann, F. Eggert, and G. Hauf. 2016. "CoSFB - Composite Slim-Floor Beam: Experimental Test Campaign and Evaluation." *Composite Construction in Steel and Concrete*, 7.

Heins, C. P. 1975. Bending and Torsional Design in Structural Members, Lexington Books.

Huber, D., and A. Varma. 2008. "Final Report for the AISC Fellowship Project." *Development of Long Span Floor Systems for Multi-Story Residential Structures*. AISC, Chicago, IL.

Ju, Y. K., S.-C. Chun, and S.-D. Kim. 2009. "Flexural Test of a Composite Beam using Asymmetric Steel Section with Web Openings." *Journal of Structural Engineering*, 135(4).

Mullet, D. L., and R. M. Lawson. 1993. *Slim Floor Construction Using Deep Decking. SCI P127*. Ascot, UK: The Steel Construction Institute.

Seaburg, P. A., and C. J. Carter. 2003. Steel Design Guide 9: Torsional Analysis of Structural Steel Members. Steel Design Guide Series. Chicago, IL: AISC.

Sheehan, T., X. Dai, and D. Lam. 2018. "Flexural Behavior of Asymmetric Composite Beam with Low Degree of Shear Connection." *Journal of Constructional Steel Research*, 141(Feb).

Stoddard, E., and M. Yarnold. 2022. "Residual Stress and Global Deflection Limits for Future Hot-Rolled Steel Asymmetric I-beams." *Journal of Structural Engineering*, 148(1).

Stoddard, E. A. 2022. "Behavior of Hot-Rolled Asymmetric Steel I-beams: Concept to Construction." Ph.D. Thesis, Texas A&M Univ.

Yarnold, M. T., and E. Stoddard. 2020. "Future Hot-Rolled Asymmetric Steel I-beams." *Journal of Structural Engineering*, 146(9).

Appendix C – Composite Beam Testing

Appendix C provides detailed information on the composite beam testing (Phase 3) conducted to analyze the composite behavior of shallow-depth composite floor systems. This includes a literature review on similar systems and background on quantifying the partial composite strength with three different methods. An experimental program was implemented and consisted of eight component-level beam tests to analyze the composite behavior, both strength and stiffness, developed through bond stress forming between the steel and concrete.

Citation

The following work has been published by Elsevier in the Engineering Structures journal. The citation to the published journal article is:

> Ottmers, C., R. W. Alemayehu, and M. Yarnold. 2025a. "Evaluating the Composite Behavior Developed through Bond in the Steel-Concrete Interface for Future Hot-Rolled Asymmetric Steel I-beams." *Engineering Structures*, 322. https://doi.org/10.1016/j.engstruct.2024.119185

The following work is expanded upon and supplemental information/results are provided in Chase Ottmers Ph.D. Dissertation. The citation to Chase's dissertation is:

> Ottmers, C. E. 2025. "Full-Scale Testing and Numerical Evaluation of Hot-Rolled Asymmetric I-beams in Shallow-Depth Composite Floor Systems." Ph.D. Dissertation, Texas A&M University.

Evaluating the Composite Behavior developed through Bond in the Steel-Concrete Interface for Future Hot-Rolled Asymmetric Steel I-beams

Chase Ottmers, Robel Wondimu Alemayehu, and Matthew Yarnold

Abstract

Conventional steel-concrete composite floor systems consist of hot-rolled steel beams with metal decking on the top flange that supports a concrete deck slab. An alternative to achieve shallower floor depths is to utilize stay-in-place formwork, either precast concrete panels or steel deep decking, placed on the bottom flange with a cast-in-place concrete slab. For ease of construction, an asymmetric section is needed for vertical placement of the precast panels or deep decking. However, there are no hot-rolled asymmetric steel I-beams (termed A-shapes) readily available in the United States. The purpose of this research is to evaluate the composite flexural behavior of a shallow-depth floor system for future large-scale production of A-shapes. To achieve minimal floor depths and increase the efficiency of steel building construction, shear studs (generally used in conventional composite floor systems) are not utilized to transfer longitudinal interface forces. The top flange and web of the steel member are encased in concrete, which will allow partial composite flexural behavior due to the formation of concrete-steel bond. The research presented herein includes eight experimental beam tests to understand the flexural strength and stiffness developed through concrete-steel bond shear. The eight tests performed well and achieved 74% to 83% of the full composite flexural strength before the bond started to slip, although only minimally. Following the initial slip, the shallow-depth beams were unloaded and reloaded to evaluate the robustness and ductility of the composite cross-section. The beams proved to be highly ductile and robust as they reached 77% to 91% of the full composite strength upon reloading due to reengaging of the bond after the occurrence of initial slip. The composite flexural stiffness of the beams was well intact under the service loading, indicating that the transformed moment of inertia of the cross-section can be utilized for serviceability analysis. A bond shear strength of 0.69 MPa (100 psi) was established since it undercuts most of the experiments with a bond perimeter assumed to be above the elastic neutral axis of the composite section. The partial composite strength was further evaluated utilizing three numerical methods: (1) linear interpolation between steel yield and full composite, (2) partial plastic stress distribution, and (3) strain compatibility. All methods predicted reasonable results but the method of linear interpolation was the most conservative one in relation to the bending moment that causes the initiation of bond slip.

Keywords: Structural Steel, Concrete-Steel Bond Stress, Asymmetric, Composite, and Floor System

Introduction

A common composite floor system utilized in buildings consists of rolled steel beams integrated with a reinforced concrete slab. These floor systems commonly utilize doubly symmetric wide flange beams and a concrete slab poured on top of a steel deck. Shear studs are generally attached to the top flange of the beam to transfer longitudinal shear forces between the concrete slab and steel beam to increase the strength and stiffness for in-service loading. A downfall of this floor system is the relatively large floor depths due to the concrete slab placed above the steel beam. An alternative to achieve shallower depths is to place stay-in-place formwork, either precast concrete panels or steel deep decking, on the bottom flange of steel beams. Following formwork placement, a concrete slab is cast-in-place, and the concrete encases the top flange and web of the steel beam. However, hot-rolled steel beams currently produced in the United States (US), such as doubly symmetric wide-flange beams (W-shapes) (AISC 2023), do not allow formwork to be placed on the bottom flange easily due to top flange interference. Thus, singly symmetric (or asymmetric) I-beams are desirable to allow for easy and rapid placement of formwork. A comparison of conventional composite and shallow-depth composite floor systems is shown in Figure C-1.

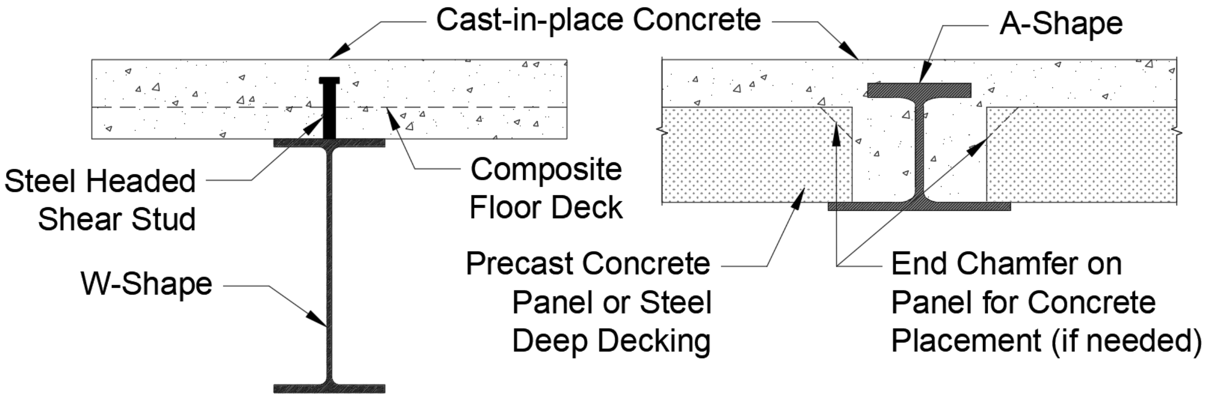

(a) (b)

Figure C-1: Overview of the Composite Floor Systems: (a) Conventional and (b) Shallow-Depth

There are various built-up asymmetric I-beams utilized in building floor systems with stay-in-place formwork; however, they all require intensive fabrication work. Some of the beam systems include Girder-Slab® (Girder-Slab Technologies 2016), Kloeckner Westok® (Kloeckner Metals 2020; Kloeckner Metals 2023), Slim-Floor (ArcelorMittal 2017; ArcelorMittal 2023b), and ComSlab® (Bailey Metal Products 2023). The Girder-Slab® system utilizes D-BEAMS®, which are fabricated by cutting the web of a W-shape in a castellated pattern and welding a flat bar to the top of the cut web. The Girder-Slab® floor system utilizes precast concrete panels placed on the bottom flange of the D-BEAM®. Kloeckner Westok® beams are analogous in that the beams are fabricated from two uncommonly sized W-shapes that are cut with a castellated pattern and are joined together to form an asymmetric cross-section. Slim-Floor and ComSlab® systems utilize a flat plate welded to the bottom of a standard doubly symmetric section which supports steel deep decking.

An alternative solution to built-up asymmetric I-beams, which require intensive fabrication work, is to hot roll them at a steel mill. Currently, there are no hot-rolled asymmetric I-beams at US steel mills, and there is limited production of hot-rolled asymmetric I-beams around the world. A floor system in the United Kingdom called *Slimdek*® (Lawson et al. 1997; Rackham et al. 2006) utilizes hot-rolled asymmetric I-beams produced by British Steel (2023), and is built by Corus Construction and

Industrial. British Steel hot rolls ten asymmetric steel beams, termed ASBs, on request. The *Slimdek®* floor system utilizes both precast concrete panels and steel deep decking that is supported by the ASB bottom flange.

Research is being conducted on the potential large-scale production of hot-rolled asymmetric I-beams (termed A-shapes) in the United States. This research is being performed in collaboration with the American Institute of Steel Construction (AISC) and is part of the AISC Milek Fellowship. In addition, this research is part of their Need for Speed (AISC 2024) initiative to increase the speed of building construction. There are many advantages to utilizing A-shapes and stay-in-place formwork placed on the bottom flange. Composite steel and concrete floor system depths can be decreased, which can increase floor-to-floor height or reduce the overall height of the structure. The fabrication cost is reduced compared to a built-up section as the steel beam would be rolled at a steel mill. Due to the spanning capabilities of precast concrete panels and steel deep decking, the number of steel beams required in a building is reduced, leading to faster construction times. These shallow-depth floor systems are advantageous due to the speed and efficiency of construction and will help to decrease the time required for steel construction.

The initial work of this research study consisted of a proof-of-concept full-scale floor testing (Davis 2022; Davis et al. 2023). The main goal of the preliminary testing was to examine the feasibility of A-shapes in shallow-depth floor systems. The constructability of the floor system was evaluated, and the structural performance of the A-shape was analyzed during construction and in-service. Additionally, the ultimate strength of the 3-beam floor system was quantified. Precast concrete panels were used as stay-in-place formwork between proof-of-concept beams developed in a residual stress study of an asymmetric I-beam (Stoddard and Yarnold 2022; Stoddard 2022). The experimental program consisted of various scenarios of precast concrete panel placement, slab casting, and vertical actuator loading to simulate in-service live load demands. The floor system was easy to construct, the non-composite proof-of-concept A-shape performed well in construction loading, and the composite section performed well for in-service loading (Davis 2022; Davis et al. 2023).

Following the knowledge gained from the proof-of-concept testing, an analytical sizing study was conducted to establish future A-shape geometry for residential construction (Ottmers et al. 2025b). Cross-sectional geometry limits were established through interviews conducted by the research team with three major US steel mills, Nucor, Gerdau, and Steel Dynamics, to increase the feasibility of manufacturing. The sizing study analyzed 65 different cross-sectional geometries (for a given beam depth) for 16 limit states during building erection and in-service loading. The limit states consist of non-composite flexure, shear, and torsion during building erection; composite flexure and serviceability criteria are checked for in-service. Efficient cross-sectional geometries were established for various beam depths and loading scenarios. Parametric studies were conducted using varying assumed parameters in the sizing study to investigate sensitive limit states. The established A-shape geometry was investigated for a wide range of beam lengths and beam spacing layouts, and composite flexural strength was the controlling limit state for multiple scenarios (Ottmers et al. 2025b). There is uncertainty in the parameters used to calculate the composite flexural strength, which initiated this research study (see the Background on Partial Composite Action section for further discussion). In addition, deflection due to service live load utilizing the composite flexural stiffness is a sensitive limit state and is critical or close to for various building geometries. Therefore, experimental analyses of the composite flexural behavior of partially encased composite beams are of main importance.

The proposed shallow-depth floor system utilizing A-shapes and stay-in-place formwork does not use shear studs on the top flange of the beam to transfer longitudinal shear between the concrete and steel (as shown in Figure C-2(a)). Shear studs are not utilized to increase the efficiency of building construction and to achieve minimal floor depths. Stay-in-place formwork placed on the bottom flange allows for the top flange and web to be encased in the concrete slab. As a result, longitudinal shear transfer will occur due to the bond shear that forms between the concrete and steel (Lawson et al. 1997; Rackham et al. 2006). However, the composite flexural behavior both for ultimate and serviceability states would be improved by having web openings, which helps the concrete lock onto the steel section. Fabricating the D-BEAM® achieves this by having a castellated pattern with openings in the web (Girder-Slab Technologies 2016). Furthermore, including dowel reinforcement that goes through the web openings helps increase the amount of bond shear transfer and degree of composite action, which is utilized in the Girder-Slab® (Girder-Slab Technologies 2016) and ArcelorMittal Composite Slim-Floor (ArcelorMittal 2017; ArcelorMittal 2023b) systems. A large experimental campaign was conducted consisting of push-out tests, shear beam tests, flexure beam tests, and beam tests to analyze the deflection and vibration of slim floor systems utilizing dowel reinforcement that pass through holes in the web of a steel section (Hauf and Kuhlmann 2015; Hechler et al. 2016; Kuhlmann et al. 2021; Lam et al. 2015; Schorr and Kuhlmann 2019; Sheehan et al. 2019). The experimental testing indicated that utilizing dowel reinforcement increases the composite strength by maintaining connection between the concrete and steel section when the concrete starts to slip (Kuhlmann et al. 2021). A general overview of a shallow-depth floor system with dowel reinforcement passing through web openings is shown in Figure C-2(b). Openings in the web are introduced from drilling holes (see Figure C-2(c)) or are inherent from cutting a castellated pattern in the web during fabrication (as shown in Figure C-2(d)). Another alternative to improve the bond shear is to have an embossed pattern rolled into the top flange of the beam (Lawson et al. 1997; Rackham et al. 2006) as shown in Figure C-2(e). The embossed pattern increases the roughness of the top flange, allowing for an improved bond shear between the concrete and steel. However, to keep the proposed floor system as simple as possible, no additional mechanisms are being used to increase the composite flexural behavior. The bond shear between the concrete and the hot-rolled steel surface is the only mechanism that provides composite flexural behavior for the proposed floor system (see the Background on Partial Composite Action section for further discussion).

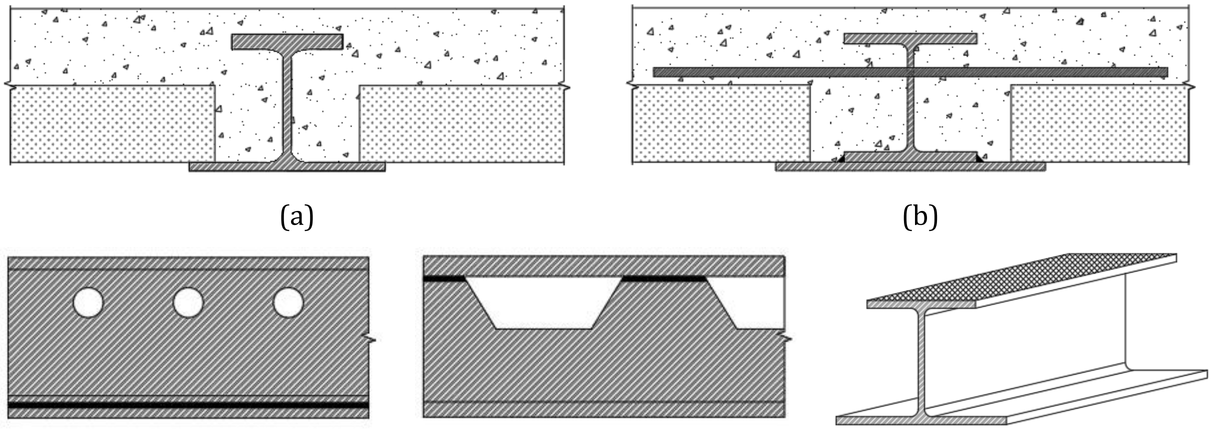

(a) (b)

(c) (d) (e)

Figure C-2: Bond Transfer Systems: (a) Pure Bond in Shallow-Depth Floor System with A-shapes, (b) Dowel Reinforcement in Composite Slim-Floor Beams (ArcelorMittal 2017; ArcelorMittal 2023b; Hauf and Kuhlmann 2015; Hechler et al. 2016; Kuhlmann et al. 2021; Lam et al. 2015; Schorr and Kuhlmann 2019; Sheehan et al. 2019), (c) Composite Slim-Floor Beam with Dowel Reinforcement Holes (ArcelorMittal 2017; ArcelorMittal 2023b; Hauf and Kuhlmann 2015; Hechler et al. 2016; Kuhlmann et al. 2021; Lam et al. 2015; Schorr and Kuhlmann 2019; Sheehan et al. 2019), (d) Girder-Slab® D-BEAM® with Castellated Web Openings for Dowel Reinforcement (Girder-Slab Technologies 2016), and (e) Embossed Top Flange (Lawson et al. 1997; Rackham et al. 2006)

The sizing study indicated that composite flexural behavior (either strength or stiffness) is the controlling limit state for various building geometries. A parametric study altering the assumed value for the bond strength varied the capacity-to-demand ratio of the composite flexural behavior limit states (Ottmers et al. 2025b). In this floor system concept, composite flexural behavior has a relatively high level of uncertainty in terms of in-service performance. Prior research has evaluated the bond stress between concrete and steel; however, different cross-section geometries were used. These include fully encased steel sections in beams (Weng et al. 2002) and columns (Roeder et al. 1999) or beams with web openings (Bandelt et al. 2019; Ju et al. 2009). In addition, there is a wide range of values in literature utilized for concrete-steel bond stress (see the Background on Partial Composite Action section for further discussion).

Due to composite flexural behavior being a controlling limit state in the prior analytical sizing study, experimental tests were conducted (and are presented herein) to evaluate the composite flexural behavior of shallow-depth floor systems using A-shapes. The primary contribution of this research was to reduce the uncertainty of composite flexural behavior developed through concrete-steel bond stress for partially encased beams. Adequate concrete-steel bond stress was determined for future engineers to use in composite flexural behavior calculations. In addition, the most appropriate methodology for the estimation of partial composite stiffness and strength was identified. Finally, the reserve capacity of these floor systems was evaluated. These contributions were accomplished by evaluating the composite flexural behavior of eight experimental component beam tests. The beam length and reinforcement layout were varied in the tests to examine the impact varying parameters had on the bond stress. Finally, the experimental results were compared to three different theoretical calculation methods to estimate the composite flexural behavior.

Background on Partial Composite Action

Evaluating composite flexural behavior accurately is important in a composite floor system to ensure sufficient strength and stiffness for in-service loading. Unlike conventional composite floor systems, the shallow-depth floor system with A-shapes does not utilize shear studs to transfer longitudinal shear forces between the concrete and steel parts of the beam. Additionally, there are no castellations or openings in the web nor increased roughness of the top flange. Composite flexural behavior with the A-shape is purely ensured by the bond stresses between the concrete and steel.

Bond Strength

The bond strength between steel and concrete is determined by various models in the literature, and there is some uncertainty. Some models quantify the bond strength as a percentage of the specified compressive strength of the concrete, specifically 3% (McCormac 1981). For instance, concrete with a compressive strength of 27.6 MPa (4000 psi) would have an allowable bond strength of 0.83 MPa (120 psi). However, other studies examining a multitude of experimental push-out tests show no correlation between the concrete compressive strength and the allowable bond strength (Roeder et al. 1999). However, a different bond strength model incorporates the ratio of the steel section area to the gross section area of the specimen (Roeder et al. 1999). Further studies have provided a constant value of 0.60 MPa (87 psi) for the bond strength with a bond perimeter around the top flange of the beam and the entire height of the steel web for shallow-depth beams (Lawson et al. 1997). Eurocode 4 ignores the effect of shear transfer from bond in composite beams but permits the use of a bond strength of 0.30 MPa (44 psi) for fully encased I-beams in columns and specifies greater values for concrete filled hollow sections (CEN 2004). The AISC Specification for Structural Steel Buildings (AISC 2022) allows for longitudinal shear transfer by direct bond interaction for filled composite members but not for encased composite members. The permitted allowable bond strength between concrete and steel depends on the wall thickness and width of the round and rectangular hollow steel section

(HSS). The maximum permitted value of the bond strength is 0.69 MPa (100 psi) for rectangular HSS cross sections and 1.38 MPa (200 psi) for circular HSS members (AISC 2022). Thus, there is a wide range of values in literature used for the bond strength and bond perimeter.

Composite Flexural Behavior

For considering the composite flexural behavior, the cross-sectional properties of the non-composite and composite sections are initially required. Due to the composite section consisting of concrete and steel, the concrete is transformed to an equivalent steel width using the modular ratio between Young's modulus of steel and concrete. The elastic neutral axis (ENA) of the composite section is determined for the transformed section using standard geometric decomposition. The composite moment of inertia can be quantified with properties of the non-composite and composite section utilizing the parallel axis theorem and the transformed cross-section. Further background is provided in the prior analytical sizing study publication (Ottmers et al. 2025b). The composite moment of inertia determined with the transformed cross section is assumed to be adequate and is utilized for the composite flexural stiffness. A few methods to determine the composite flexural strength are discussed in the following sections.

(1) Linear Interpolation with Bond Shear

To evaluate composite strength, a good starting point is to determine the full composite flexural capacity. A plastic stress distribution is utilized, implying the concrete is at 85% of the specified concrete strength (f'_c) and the entire steel section is at yield $\left(F_y\right)$. The portion of the A-shape below the plastic neutral axis (PNA) is the only component resisting tensile stresses because concrete below the PNA is ignored. Concrete and steel above the PNA contribute to the compressive resistance of the cross-section. The PNA is determined iteratively until the force resultants are in equilibrium, i.e., the total compressive force of the concrete (C_c) and steel (C_s) is equal to the tensile force of the A-shape (T).

Equations for each of the force components can be derived based on the location of the PNA. However, several cases are applicable depending on the cross-section geometry. The most common cases for the PNA are (1) in the top flange of the steel, (2) in the steel web above, or (3) below the height of the stay-in-place formwork. Two more PNA cases could occur if the stay-in-place formwork is in the depth of the top flange; these are where the PNA is in (4) the steel top flange or (5) the web. For each case, the centroid of each force component is derived using standard geometric decomposition to determine the fully composite flexural strength. For cases (3) through (5), the compressive strength of the precast concrete panel or the concrete in the deck ribs (non-continuous due to deck orientation) is ignored. The PNA could also be (6) above the steel in the concrete deck; however, this is unlikely.

An alternative method to deriving equations for all cases above is to use integrals to determine the force components of the cross-section. To achieve this, a width function of the concrete deck (b_c) and a width function of the steel section (b_s), both referenced from the top of the slab, must be utilized. These width functions are used in the integrals to calculate the force resistance of the concrete and the steel to ensure equilibrium of the cross-section. The depth of the PNA $\left(y_{pna}\right)$, referenced from the top of the slab, is iteratively adjusted until the summation of Equations (C-1) and (C-2) is in equilibrium with Equation (C-3). The nomenclature for a general composite section and the stress diagram and force resultants for the full composite moment case is shown in Figure C-3(a).

$$C_c = \int_{0}^{y_{pna}} 0.85f'_c b_c(y)dy \tag{C-1}$$

$$C_s = \int_{D_c}^{y_{pna}} F_y b_s(y)dy \tag{C-2}$$

$$T = \int_{y_{pna}}^{D_{tot}} F_y b_s(y)dy \tag{C-3}$$

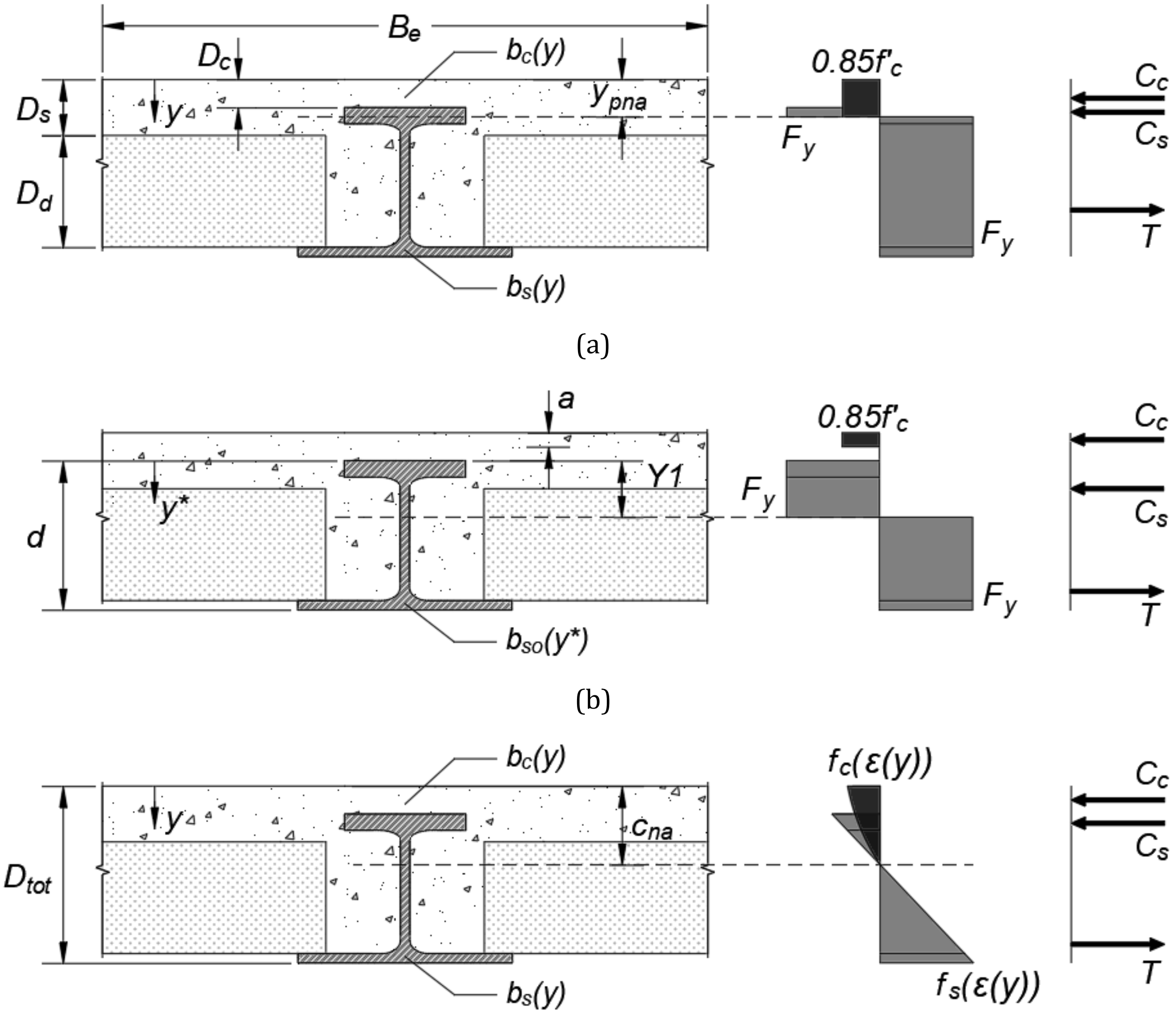

(a)

(b)

(c)

Figure C-3: Nomenclature for Composite Section, Cross-Sectional Stresses and Force Resultants for (a) Full Composite Moment, (b) Partial Plastic Stress Distribution, and (c) Strain Compatibility

The equations presented above do not require different cases depending on where the PNA falls within the cross-section. The width function for the steel considers the width of the top flange, web, and bottom flange. Similarly, the concrete width function must consider the width above the steel, in the steel top flange, web, and below the height of the stay-in-place formwork, respectively. Once the cross-section is in equilibrium by altering the depth of the PNA, the full composite moment capacity (M_{ncp}) can be determined with Equation (C-4).

$$M_{ncp} = \int_{0}^{y_{pna}} 0.85f'_c b_c(y)\left|y_{pna} - y\right|dy + \int_{D_c}^{D_{tot}} F_y b_s(y)\left|y_{pna} - y\right|dy \tag{C-4}$$

Due to no shear studs or additional mechanisms, such as web openings or an embossed top flange to enhance the concrete-steel bond shear, the full composite moment capacity in Equation (C-4) will likely not be achieved. A degree of partial composite action will be attained from the bond shear developed between the hot-rolled A-shape and the concrete slab due to the encasement of the top flange and the steel web. To quantify the degree of partial composite action, the maximum compressive force (F_{bs}) that can be transferred to the concrete deck through bond shear is quantified. The max compressive force is determined considering the elastic distribution of longitudinal bond shear, evaluated as the resultant area of the shear diagram for the assumed loading. The max compressive force that is allowed to develop is based on the assumed bond shear perimeter around the steel A-shape (p_{bs}) and the nominal bond shear stress (f_{bs}).

As discussed above, various assumptions are utilized for the bond shear perimeter. The bond perimeter is the amount of steel surface in the cross-section that is assumed to transfer a constant bond stress during bending of the composite beam. The shallow-depth composite cross-section with the A-shape will likely not be near the plastic state before the bond between the concrete and steel starts to slip. In addition, the strain and stress distributions will still be linear at this point, not reaching the plastic state. Therefore, the bond shear perimeter for the shallow-depth floor system with A-shapes is assumed to be only above the ENA of the composite section (y_{ec}) (see Equation (C-5) and Figure C-4(a)). The maximum compressive force transferred between the steel and concrete is dependent on the loading. For 4-point symmetrical loading (similar to the beam test discussed in the following section), a rectangular area between the support and the applied point load (a_{load}) would be used (see Figure C-4(b)). The maximum compressive force (F_{bs}) developed through bond shear for 4-point bending is quantified in Equation (C-6). Note that for uniformly distributed loading, a triangular area under the shear diagram would be utilized, which would replace the a_{load} term with the 25% of the beam length.

$$p_{bs} = 2\left(b_{ft} + y_{ec}\right) - t_w \tag{C-5}$$

$$F_{bs} = p_{bs} f_{bs} a_{load} \tag{C-6}$$

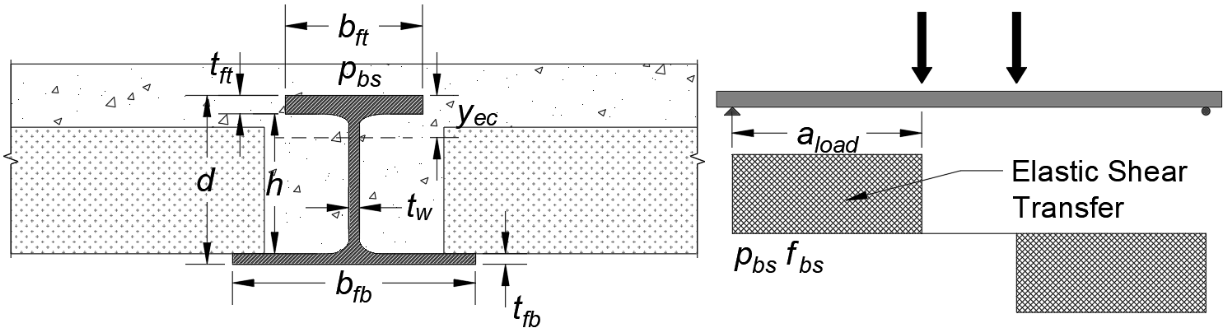

(a) (b)

Figure C-4: Bond Shear (a) Perimeter and (b) Elastic Shear Transfer (4-point loading)

To evaluate the partial composite moment capacity, linear interpolation is utilized between the steel-only yield moment (M_{sy}) and the full composite moment (M_{ncp}) (Lawson et al. 1997). The A-shape can reach the yield moment capacity in the completed state due to the concrete slab continuously bracing the top flange, omitting any issues with lateral-torsional buckling. The steel yield moment capacity is determined in Equation (C-7) using the elastic section modulus of the compression flange (S_{xc}). The elastic section modulus of the compression flange will control due to the asymmetry of the A-shape. The web plastification factor (R_{pc}) is also included per Section F4 (AISC 2022).

$$M_{sy} = R_{pc} F_y S_{xc} \tag{C-7}$$

The degree of composite action beyond the steel yield moment is dependent on the ratio of the max compressive force from bond shear (F_{bs}) to the compressive force in the concrete slab (C_c). Full composite action would be attained if the allowable force from the bond shear exceeded the compressive resistance of the concrete in the plastic analysis. The partial composite moment capacity (M_{nc}) using the linear interpolation method is determined using Equation (C-8) (Lawson et al. 1997).

$$M_{nc} = M_{sy} + \frac{F_{bs}}{C_c}\left(M_{ncp} - M_{sy}\right) \tag{C-8}$$

(2) Partial Plastic Stress Distribution

An alternative method to determine the partial composite strength, referred to as the partial plastic stress distribution, is similar to the full composite strength approach because a plastic stress distribution is utilized. However, the force that can develop in the concrete (C_c) is limited by the maximum compressive force that can develop through bond shear (F_{bs}) (see Equation (C-9)). The depth of the compression block in the concrete (a) is determined assuming the concrete is at 85% of the specified concrete compressive strength and the effective width (B_e) of the concrete slab is in accordance with the AISC specification for composite members (AISC 2022). The depth of the PNA for the partially composite section $(Y1)$, referenced from the top of the steel section, is iterated until the compressive (sum of Equations (C-9) and (C-10)) and tensile (Equation (C-11)) forces in the cross-section are in equilibrium. This approach is similar to the method used in the AISC specification for conventional composite floor systems with shear studs (AISC 2022). To determine the forces in the steel, a modified width function (b_{so}) is used which is referenced from the top of the steel section. The stress diagram, force resultants, and nomenclature for a partial plastic stress distribution is shown in Figure C-3(b).

$$C_c = F_{bs} = 0.85f'_c B_e a \qquad \text{(C-9)}$$

$$C_s = \int_0^{Y1} F_y b_{so}(y^*) dy^* \qquad \text{(C-10)}$$

$$T = \int_{Y1}^{d} F_y b_{so}(y^*) dy^* \qquad \text{(C-11)}$$

After establishing equilibrium, the partial composite flexural strength is determined with Equation (C-12). The first term is the moment contribution of the allowable force that can develop in the concrete about the partial PNA ($Y1$). The second term is the moment contribution from the entire steel section. The partial composite strength determined using Equation (C-12) is identical to the equation provided in the AISC specification commentary (Section I3.2a) for positive flexural strength (AISC 2022) but is in an alternative form.

$$M_{nc} = C_c \left(D_c - \frac{a}{2} + Y1\right) + \int_0^{d} F_y b_{so}(y^*)|Y1 - y^*| dy^* \qquad \text{(C-12)}$$

(3) Strain Compatibility

The final method considered for calculating the partial composite moment capacity utilizes strain compatibility, which is also allowed by the AISC specification (AISC 2022). The strain compatibility method assumes a linear distribution of strains (ε) over the entire depth of the composite cross section. Unlike in the previous methods, stress-strain models of concrete and steel are utilized in this procedure rather than utilizing a plastic stress distribution. The constitutive models selected for this study are an elastic perfectly plastic stress-strain relationship for steel (f_s) and the Hognestad concrete model (f_c). The strain values at the bottom flange and the concrete deck surface must be assumed to establish the depth of the neutral axis (c_{na}) and to check equilibrium in the cross-section (see Figure C-3(c) for nomenclature, stress profile, and force resultants). For the shallow-depth floor system, the strain at the bottom flange is assumed to be at yield, and the strain at the concrete deck surface will be iterated to ensure equilibrium in the cross-section. The width functions for steel (b_s) and concrete (b_c) reference the top of slab. The force components are calculated in Equations (C-13) through (C-15), and the partial moment capacity is determined using Equation (C-16) after equilibrium is satisfied.

$$C_c = \int_0^{c_{na}} f_c(\varepsilon(y)) b_c(y) dy \qquad \text{(C-13)}$$

$$C_s = \int_{D_c}^{c_{na}} f_s(\varepsilon(y))b_s(y)dy \tag{C-14}$$

$$T = \int_{c_{na}}^{D_{tot}} f_s(\varepsilon(y))b_s(y)dy \tag{C-15}$$

$$M_{nc} = \int_{0}^{c_{na}} f_c(\varepsilon(y))b_c(y)(c_{na} - y)dy + \int_{D_c}^{D_{tot}} f_s(\varepsilon(y))b_s(y)(c_{na} - y)dy \tag{C-16}$$

The three procedures resulting in Equations (C-8), (C-12), and (C-16) determine the partial moment capacity of the composite section and the predicted capacity is compared with the experimental results of eight experimental component beam tests discussed in the following section.

Experimental Program

An experimental program consisting of eight component beam tests was designed to gain an understanding of the composite flexural behavior of shallow-depth floor systems with A-shapes. The beam length and reinforcement layout were varied in the tests to evaluate the impact these parameters had on the bond shear stresses of the concrete-steel interface. The implemented instrumentation plan, the experimental setup and the results of the test specimens are discussed in this section.

Test Specimens

Experimental tests in a laboratory are subject to various constraints and selections, including the span length and dimensions of the specimens. After seeing a need for component testing of shallow-depth floor systems, several A-shapes must be obtained for the experiments. Due to the high costs of retooling and rolling an A-shape at a steel mill, acquiring rolled asymmetric sections would not be economical for experimental testing. Therefore, proof-of-concept (POC) asymmetric I-beams were created by Stoddard and Yarnold (2022) with the support of Nucor steel mills. The creative POC beams were made by cutting part of the top flange of a W-shape on both sides, narrowing the width. The narrowed top flange beams were reheated and allowed to cool to capture residual stresses and deformations of A-shapes. The POC beams utilized in the experiment were termed A8x26, which originally were W8x31 and Figure C-5 presents the dimensions for the cut-down beam. Several of the POC beams had defects, such as gradual horizontal curves or a twisted cross-section, due to uneven heating during the fabrication process and Table C-1 includes specific notes. The mill reports for the POC beams indicated that the yield strength of the steel section was 380 MPa (55 ksi).

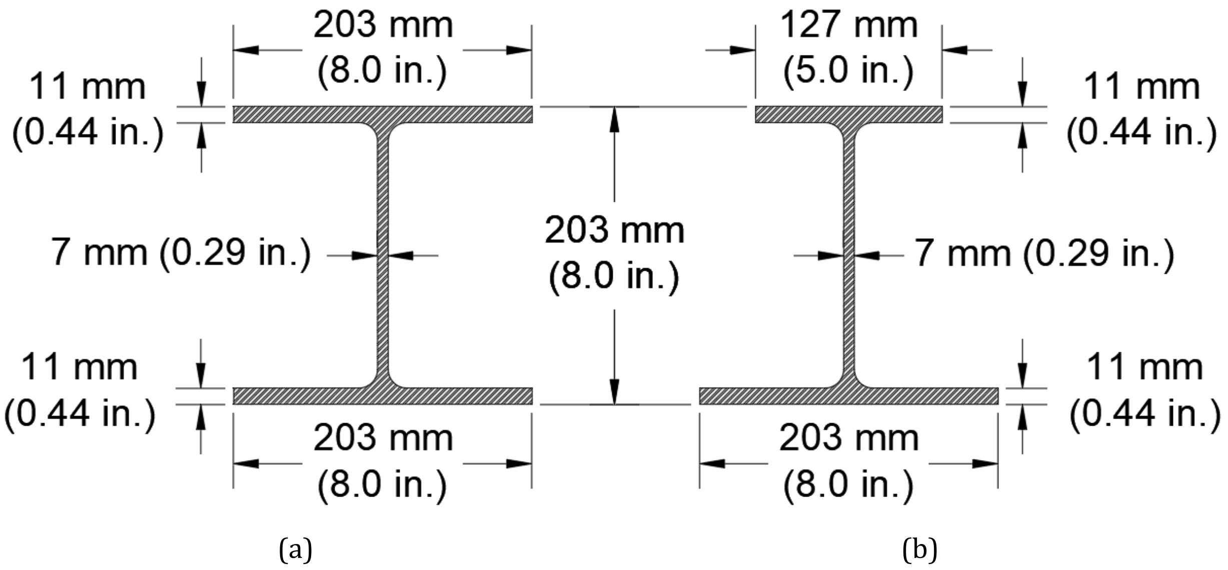

Figure C-5: Cross-Sectional Dimensions (a) W8x31 shape; (b) A8x26 shape

The POC beams were fabricated several years ago, and due to limited laboratory space, the beams were stored outside. The beams did not have paint or anything to protect them from weather effects, so surface rust formed on the POC beams. While the composite behavior is developed based on the bond stresses in the steel-concrete interface, a steel beam with surface rust would have improved bond strength with the concrete (see the Future Research section for possible additional testing on the impact of various surface conditions have on the composite strength). Therefore, the POC beams were sand blasted to get a conservative estimate for the composite flexural behavior and interface bond strength that resemble the properties of the steel beams delivered from a steel mill.

Further decisions had to be made on the length and width of the specimens (see Figure C-6 for the dimensions of the component beam). The POC beams from the residual stress study were 4.0 m (13 ft), 4.6 m (15 ft), or 5.2 m (17 ft) long. The available span lengths for the POC beams required the component beams to be either 3.7 m (12 ft) or 4.9 m (16 ft) to have sufficient bearing length on the supports and to work with the 0.6 m (2 ft) floor tie-down layout in the Advanced Structural Engineering Laboratory (ASEL) at Auburn University. To have ample clearance, the width of the concrete slab was 0.6 m (2 ft) due to the limitation of the test frame. Stay-in-place formwork was not utilized in the experiments due to the limited width of the beams. The test was designed to reduce uncertainty in the composite flexural behavior, so not utilizing stay-in-place formwork does not affect the objectives of the experiment. Instead, the location of the stay-in-place formwork was formed out of wood to create a void in the specimen. The void was formed with a chamfer at the edge to allow the concrete to flow more easily and encase the steel web and top flange. This chamfer would be cut into the edge of the precast concrete panels. The end of the steel deep decking can come chamfered from the factory, which would allow ample clearance. If this was not the case, the deck ribs would allow concrete to flow around the steel beam and encase the web and top flange.

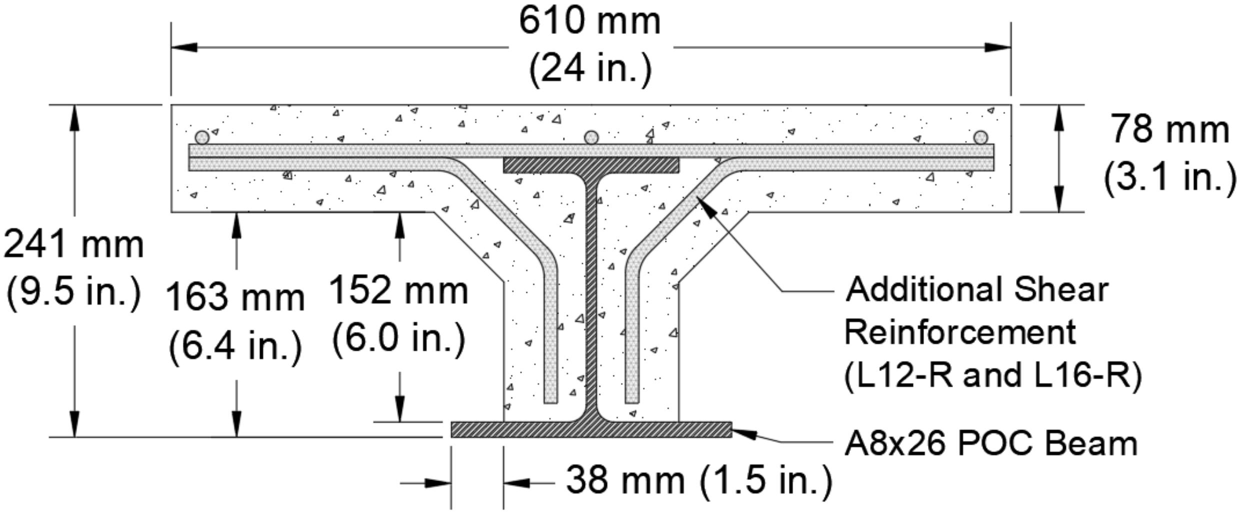

Figure C-6: Dimensions of the Component Beam

All specimens had temperature and shrinkage steel with 10 mm (#3) reinforcing bars, Grade 420 MPa (60 ksi), spaced at 305 mm (12 in.) centers in both directions. Half of the specimens had additional reinforcement, the same size and grade (see Figure C-6), that went across the chamfered region between the void and the top flange of the A-shape (L12-R and L16-R specimens only). The research team added the reinforcement across this region, as this was a location where cracks formed in the initial proof-of-concept testing (Davis et al. 2023). The additional reinforcement was added to the specimens to see if there was an improvement in the flexural capacity of the component beam. The additional reinforcement was placed at 152 mm (6 in.) on-center at the ends of the specimens for a quarter of the beam length, and at 305 mm (12 in.) in the middle half of the specimen. All specimens were cast on the ground in a single concrete pour, and the concrete strength was determined on the day of the test from three compressive test cylinders. The concrete mix design consisted of type 1L cement, sand, #57 stone aggregate, and water. The concrete was provided by a local ready-mix company and had a 17.8 cm (7 in.) slump. The author's requested the specific concrete mix, but it was not provided. The Future Research section discusses potential future testing to analyze the effect that varying mix designs have on the composite strength. Varying mix designs could impact the composite strength by affecting the bond performance in the concrete-steel interface. Casting the specimens on the ground resulted in conservative results as the beams would be cast in place in a structure, allowing the dead load to deflect and load the non-composite A-shape only. The dead load in the component beam tests, though minimal due to the size, loaded the composite beam. Table C-1 includes the naming nomenclature, average concrete strength, and notes about defects in the POC A-shape beams. As previously discussed, the only parameters that changed in the experimental tests are the span length and including additional reinforcement in half of the tests. The three L12-N specimens utilize the same cross-section and were repeated to get statistically significant results. The same is true for the three L12-R specimens and these specimens utilize the additional reinforcement.

Table C-1: Concrete Strength and Specimen Notes

Beam Specimen	Beam Length	Concrete Strength	Notes
	m (ft)	MPa (ksi)	
L12-N-A	3.7 (12)	27.0 (3.92)	Slight horizontal sweep along steel beam.
L12-N-B	3.7 (12)	27.8 (4.04)	Beam's flanges are out of square, slight horizontal sweep.
L12-N-C	3.7 (12)	27.6 (4.01)	Straight beam.
L12-R-A	3.7 (12)	29.0 (4.21)	Slight horizontal sweep along steel beam.
L12-R-B	3.7 (12)	28.5 (4.13)	Slight S-curve sweep along steel beam.
L12-R-C	3.7 (12)	27.4 (3.97)	Straight beam.
L16-N	4.9 (16)	29.6 (4.29)	Slight S-curve sweep along beam, beam end is raised.
L16-R	4.9 (16)	29.1 (4.22)	Slight horizontal sweep along steel beam.

Notes: The following abbreviations were used for beam specimen designation.
LXX = Beam Length; N = No Additional Reinforcement; R = Additional Shear Reinforcement;
A, B, and C = Test Letter for Multiple Specimens of Same Type

Instrumentation

To understand and capture the composite flexural behavior of the shallow-depth floor system, ten steel strain gauges were attached to the bottom and top flange of the steel A-shape. Half of the steel strain gauges (350 ohm) were located at midspan in the constant moment region, and the other half were placed 0.91 m (3 ft) off center. To analyze the distribution of strains in the concrete deck, six concrete strain gauges (120 ohm) were installed on the concrete surface above the strain gauges on the steel. Vertical displacement gauges (string potentiometers) were placed in the same locations with the two cross-sections of strain gauges. Horizontal displacement gauges were attached to the test frame to measure any lateral movement of the composite beam near the midspan. As expected, lateral movement of the beams was not an issue, even with defects in the straightness of the POC A-shapes. In addition, slip sensors were placed at both ends of the beam, top and bottom, to measure the relative longitudinal slip between the concrete and steel. The strain gauge and displacement instrumentation at midspan are shown in Figure C-7.

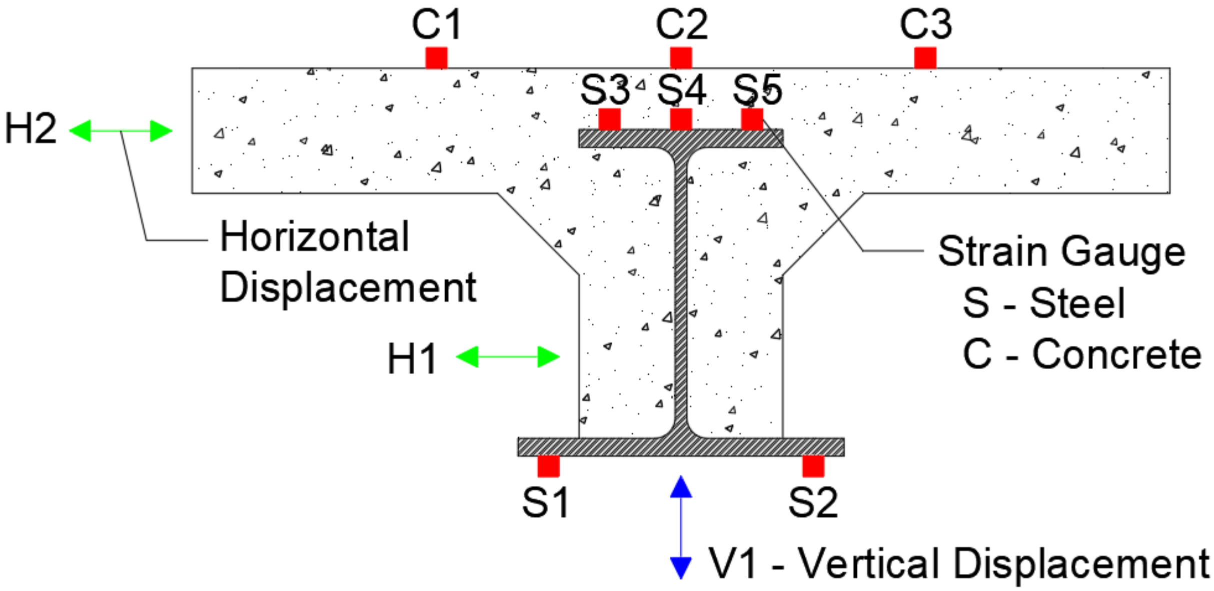

Figure C-7: Instrumentation at Midspan and 0.91 m (3 ft) from Midspan

Experimental Setup

The beams were tested using an 890 kN (200 kips) capacity Power Team actuator. Testing of the eight component beams occurred 20-30 days after the concrete pour. Four-point bending was selected for the experiments, and the actuator load was distributed with a 0.91 m (3 ft) spreader beam (load applied 0.46 m (1.5 ft) in both directions from the midspan) for all tests. The support conditions consisted of an idealized pin and roller. A piece of round bar stock was welded to a plate for the pin support, whereas the roller support consisted of a round bar stock sitting on a flat steel plate. The loading was applied quasi-statically, with incremental pauses to investigate any cracking in the concrete, compare experimental and theoretical strain values at varying load levels, and photograph the specimen (see Figure C-8 for test setup). Several load cycles were completed for each component beam test and they are explained in the following section.

Figure C-8: Photo of Beam Specimen and Test Setup (Image by Matthew Yarnold)

Experimental Results

Load-Time and Load-Displacement Histories

To fully understand the composite flexural behavior, the component beams were loaded in three stages. The first stage consisted of several cycles of low-magnitude loading to evaluate the linear elastic behavior of the composite beam. In addition, the repeatability of the data was checked during the initial loading to identify any anomalies. The second stage consisted of loading the beam slowly with pauses between the increments of loading. The loading was increased until sudden and loud cracking sounds were heard due to flexural-shear cracks forming in the concrete. Also, localized bond failure or minor concrete slipping in the bond interface occurred. As a result, there was a decrease in the actuator load due to the loss of stiffness of the composite beam. The sudden cracking of the concrete and dropping of load was defined as the "failure" moment (M_{fail}) and was utilized to evaluate the bond shear strength between the concrete and steel. The strain at the bottom flange of the beam was close to or exceeding yielding when "failure" occurred. The third stage of loading was conducted to evaluate the ductility and robustness of the shallow-depth floor system and it consisted of two additional loading cycles. The shallow-depth floor system had great ductility, and the concrete-steel bond was reengaged to allow the loading to get near, up to, or exceed the "failure" load in the second stage. The composite beam could still resist significant loading after the concrete had cracked, even with some relative slip between the concrete and steel, resulting in large deformations. The strain at the bottom flange exceeded yielding, and the concrete reached crushing at the top of the deck in some of the tests. The entire load time history of the L16-R test is shown in Figure C-9, with the three stages illustrated. In addition, the actuator load level causing yielding in the steel section

(M_{sy}), the plastic moment of the non-composite section (M_{sp}), and the full composite moment capacity (M_{ncp}) are shown to portray the magnitude of loading during the test.

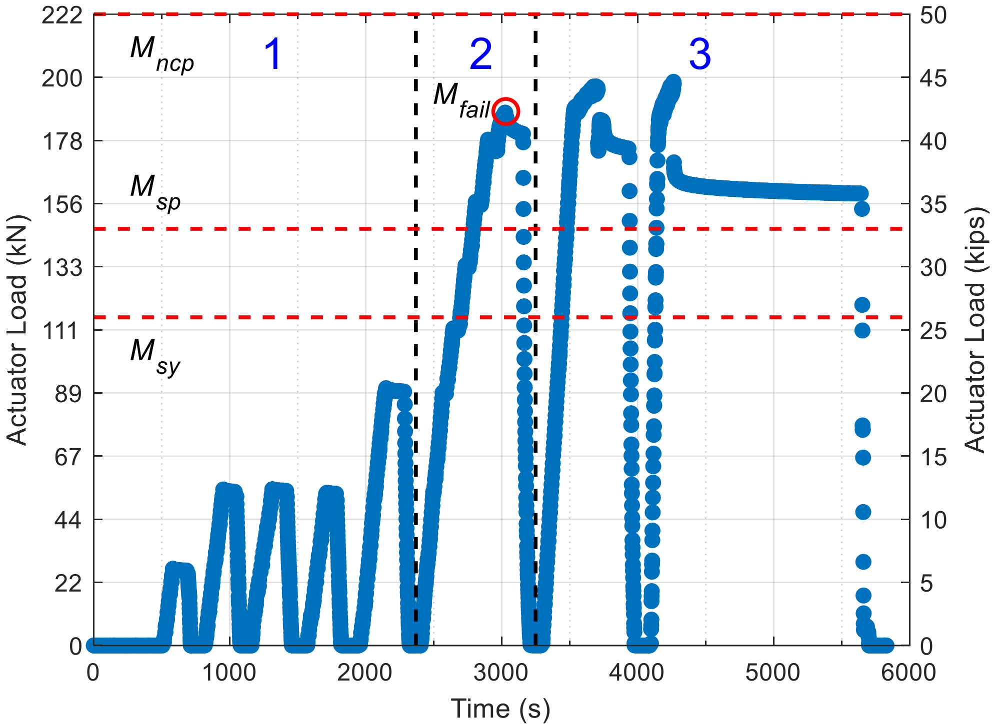

Figure C-9: Load-Time History for L16-R

The midspan deflection with the corresponding applied actuator load is shown in Figure C-10 for one of the component beam tests (L16-R). All eight experimental beam tests were conducted in a similar manner and produced comparable results. The linear elastic behavior of the initial low-magnitude loading in stage one can be observed by the repeatability and linearity of the load-displacement curve. The linearity indicates that there is no bond slippage at lower magnitude load levels for several load cycles. During stage two, the composite beam also stays linear elastic until the beam reaches the failure moment when the concrete develops flexural-shear cracks and minor relative slip between the concrete and steel occurs. Following this, the bottom flange of the A-shape exceeds the yield limit, causing minor plastic deformation observed when the load is released. In stage three, the composite beam follows a shifted linear behavior beyond the “failure” moment for two additional load cycles. Each load cycle causes additional plastic deformation due to the bottom flange steel strain going beyond yielding due to increasing slip between the concrete and steel. However, the component beam can still resist significant loading beyond the level that caused initial cracking and “failure” during stage two.

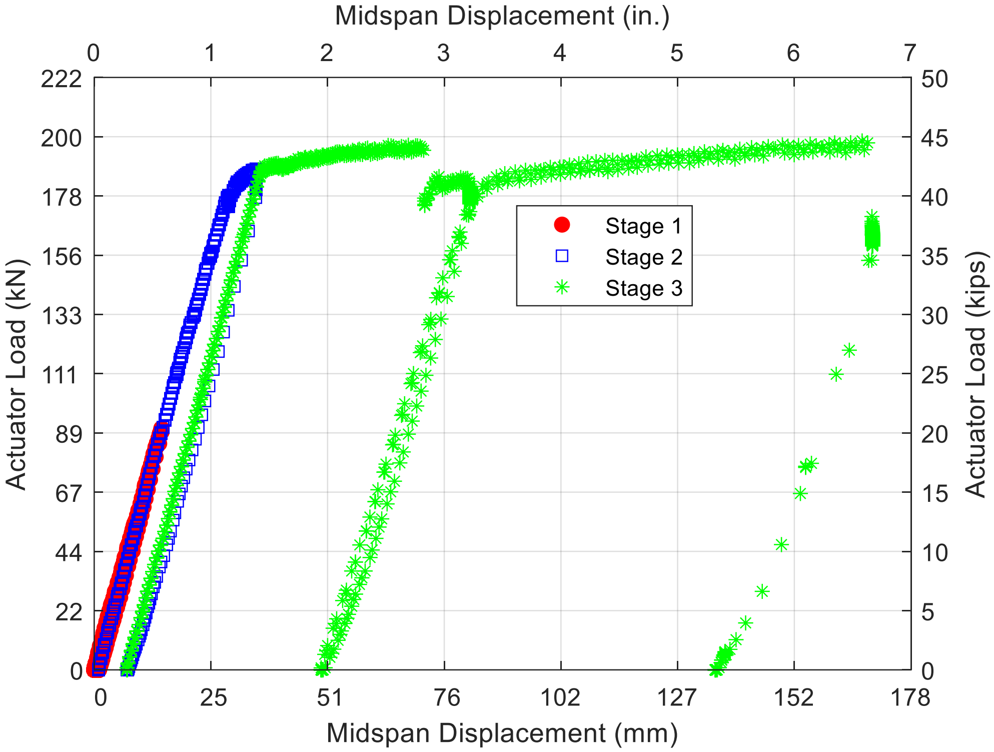

Figure C-10: Midspan Displacement for L16-R

Experimental Strain Analysis and Moment-Curvature Response

Experimental strain and deflection data from stage two were averaged over a short duration to evaluate the data at specific actuator load values during the incremental pauses. The corresponding bending response can be determined using 4-point symmetrical beam loading with a 0.91 m (3 ft) spreader beam. The experimental strain data from the bottom flange, top flange, and top of the concrete was investigated at single load levels. A best-fit line through all experimental strain data was compared to the theoretical distribution of strains using the composite section properties of the transformed cross-section. The theoretical and experimental strain data at midspan (for L16-R) for an actuator load of 178 kN (40 kips) is shown in Figure C-11. The actuator load level shown is near the "failure" moment for this beam test in stage two. The experimental strain data for the top of the concrete and steel top flanges compare well with the theoretical values. The experimental strains at the bottom flange are greater than the theoretical values, which makes the height (from the bottom flange) of the experimental neutral axis slightly higher than the theoretical value. The results ranged between 9.4 mm (0.37 in.) to 26 mm (1.04 in.), greater than the theoretical neutral axis for all tests. As a result, the beam acts compositely due to the bond shear stress between the concrete and steel, as seen in the distribution of strain in the entire depth of the cross-section.

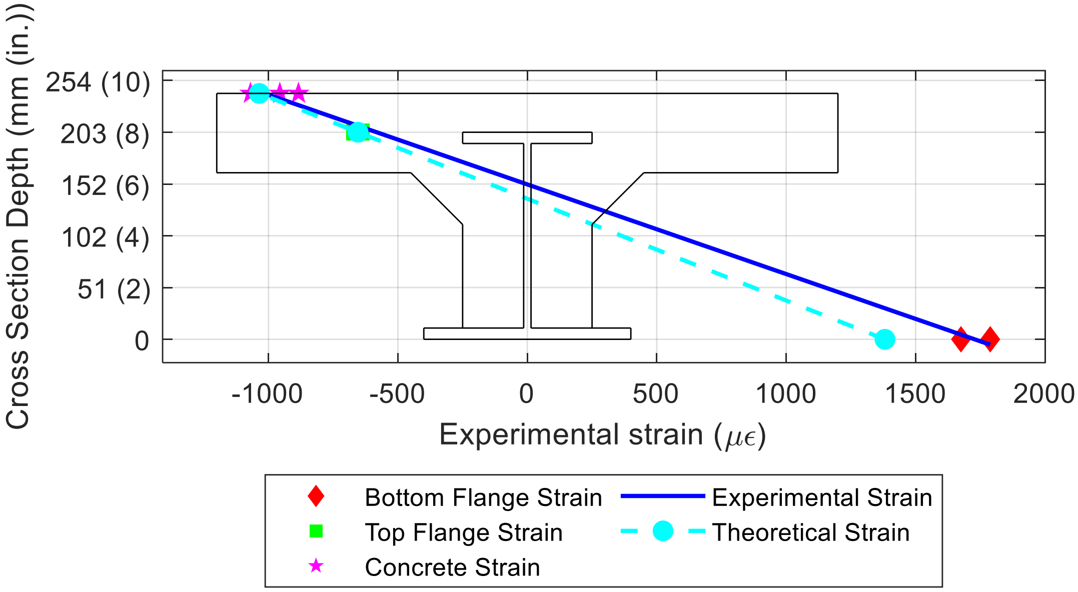

Figure C-11: Experimental Strains (L16-R) at Midspan, 178 kN (40 kips)

The process described above was completed for several specific load values to examine how the depth of the neutral axis varies. The experimental depth of the neutral axis has very minimal height change as the load is increased during the test (see Figure C-12). The depth of the theoretical fully composite plastic neutral axis (PNA), composite elastic neutral axis (ENA), and non-composite ENA are also shown to compare with the best-fit lines through the experimental strain. The depth of the theoretical composite ENA (from the top of concrete) is slightly lower than the experimental composite ENA. However, the experimental depth does not vary as the load is increasing, indicating that the beam is acting compositely throughout all of stage two. Similar results were observed for the other experimental tests.

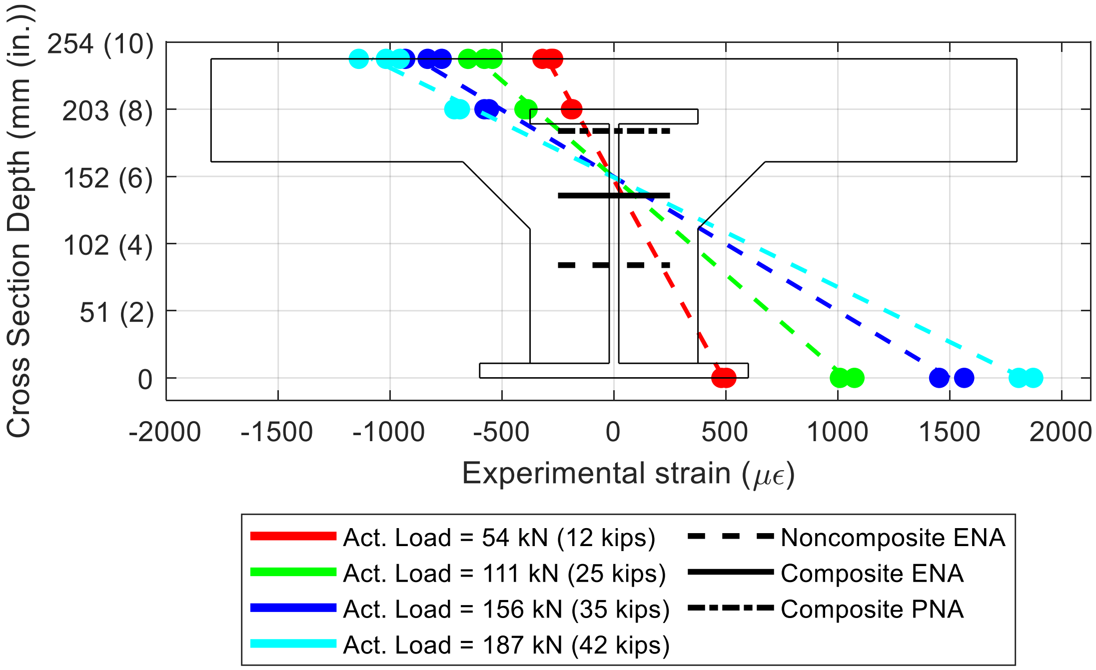

Figure C-12: Experimental Strains (L16-R) at Midspan, Varying Load Levels

Further comparison of the composite flexural behavior was completed with a moment-curvature analysis at specific actuator load levels. The flexural demands were evaluated through the strain profiles shown in Figure C-12. Utilizing the best-fit line through the experimental strain data, the beam curvature at the specific moment demand can be determined. This is achieved using the experimental strain data from the bottom flange and the height of the experimental neutral axis (determined with the best-fit line) from the bottom of the cross-section. The experimental flexural rigidity (EI) can be quantified with the moment demand and experimental beam curvature. The flexural rigidity of the composite beam is the slope of the moment-curvature diagram and affects the stiffness of the composite beam.

The analysis discussed above was completed for all eight component beam tests, and similar results were observed in all tests for midspan deflection, experimental strain data, and moment-curvature analysis. Due to testing different beam lengths, the actuator load differs for the two lengths to result in the same moment demand. Therefore, all eight tests can be compared at similar moments to the theoretical value using the moment-curvature analysis (see Figure C-13 for results from all tests). The experimental moment-curvature values of all the tests are comparable to the theoretical values determined with the transformed cross-section. The moment-curvature experimental values have a coefficient of determination (r^2) of 0.98. At higher moment demands, the experimental flexural rigidity is slightly lower than the theoretical value. When comparing the flexural rigidity at the level of ultimate moment, the experimental flexural rigidity ranges from 81% to 99% of the theoretical value for all eight tests. However, when calculating deflections at service load levels, the experimental and theoretical flexural rigidity are similar. For example, at 55% of the ultimate moment, the experimental flexural rigidity ranges from 91% to 104% when compared to the theoretical value. The experimental flexural rigidity ranges can be approximated for all tests at varying moment demand levels utilizing the dashed lines of 80%, 90%, and 110% of the theoretical value. Therefore, the composite flexural stiffness of shallow-depth floor systems can be estimated using the moment of inertia of the transformed composite cross-section.

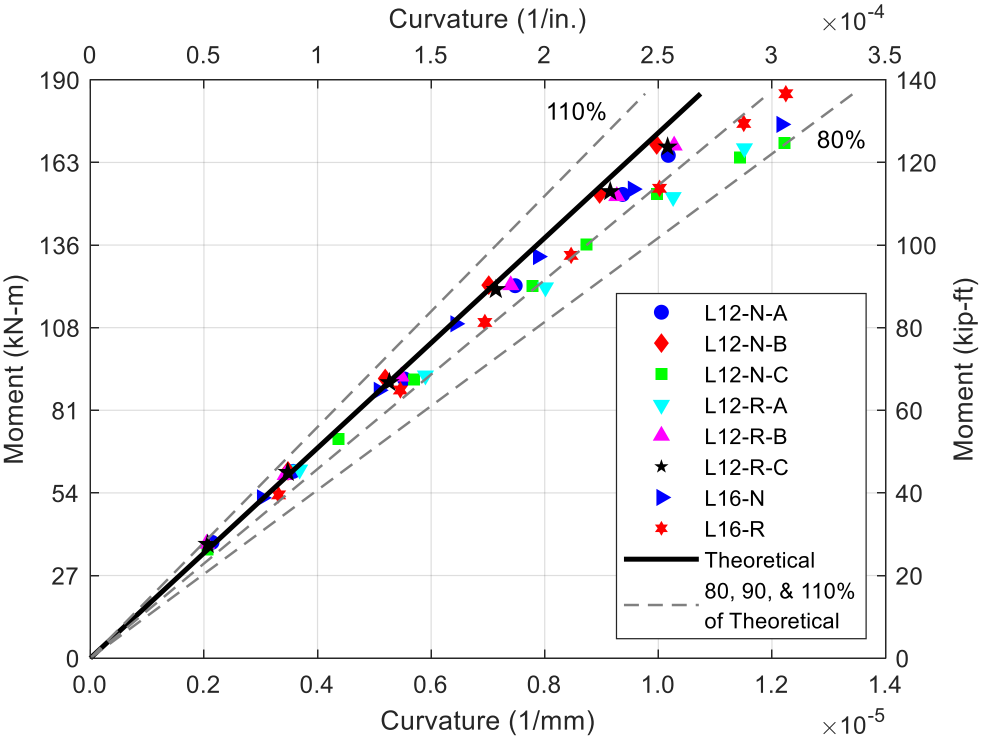

Figure C-13: Moment-Curvature Relationship at Midspan for All Tests

Analysis of Composite Flexural Strength

To understand the composite flexural strength of shallow-depth floor systems, the "failure" moment (M_{fail}) in stage two is utilized for each test. This is defined as the max moment in stage two and is utilized in Equation (C-8) as the nominal partial moment capacity (M_{nc}). Utilizing this equation, the maximum compressive force (F_{bs}) developed through bond shear is determined. Finally, the theoretical longitudinal bond shear stress (f_{bs}) developed in the test at the "failure" moment, with a bond perimeter (p_{bs}) above the theoretical composite ENA, is quantified. The maximum compressive force developed through elastic bond shear is quantified according to Equation (C-6) due to the experimental setup (4-point bending). The theoretical bond shear stress determined for each test is shown in Figure C-14. The additional reinforcement for shear in half of the tests (L12-R and L16-R) is not accounted for in the calculation of the longitudinal bond stress. However, the increase in the bond shear stress at failure indicates that the flexural strength in the beams with additional reinforcement was improved. The flexural strength had a 2% to 9% increase for the L12 specimens, whereas the L16 specimens only had a 1% increase. This improvement is due to the decrease in the width of the flexural-shear cracks, allowing for the beam to resist more load.

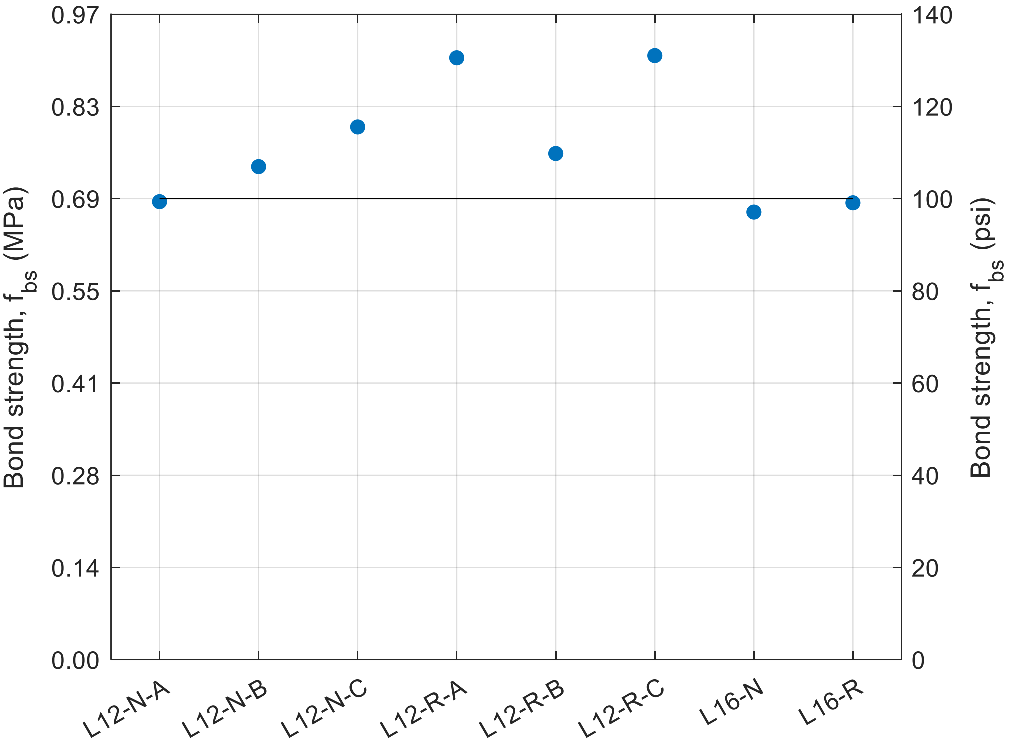

Figure C-14: Bond Strength at Max Moment in Stage 2

As discussed in the Bond Strength section, varying models exist for the value of the longitudinal bond strength. The results from the eight experimental beam tests also vary due to the additional reinforcement and length of the specimen. The bond strength for the L16 tests has a lower value at the "failure" moment in stage two. The calculated bond strength is dependent on the length (a_{load}) of the shear span between the support and the application point of the concentrated load. The same spreader beam was used for all tests, resulting in a longer length utilized in Equation (C-6) to determine the longitudinal bond strength for the L16 tests. Utilizing the concrete compressive strength for each test in Table C-1, the bond strength values range from 2.3% to 3.3%, indicating no clear correlation between the compressive strength of concrete and longitudinal bond strength of the concrete-steel interface. A bond shear strength of 0.69 MPa (100 psi) undercuts most of the experimental tests for the "failure" moment in stage two. As shown in the load-time history (Figure C-9), the composite beam resists more load in stage three; however, the beam reaches excessive deformations (Figure C-10) due to the bond slipping. In addition, uniformly distributed loads (UDL) are often assumed in the design for buildings. This will typically be the case as the A-shapes will likely be erected between columns due to the spanning capabilities of stay-in-place formwork (more discussion is provided in the prior publication (Ottmers et al. 2025b)). The partial composite strength quantified in Equation (C-8) is a function of the maximum compressive force (F_{bs}), which depends on the load distribution along the span (see Equation (C-6)). Due to the experimental setup, the maximum compressive force for a UDL is less than the value determined for 4-point loading utilized in the experiments. As a result, the partial composite strength determined for a UDL would be less than the partial strength determined for 4-point loading for the same cross-section. Since UDLs are often assumed in building design, a bond shear strength of 0.69 MPa (100 psi) is recommended to determine the nominal composite flexural strength developed through longitudinal bond shear in the steel-concrete interface.

The nominal partial composite moment capacity was evaluated utilizing the three numerical methods. This was completed to identify the most appropriate methodology for determining the nominal strength and to compare the experimental and theoretical values. The full composite moment capacity (M_{ncp}) using a plastic distribution (Equation (C-4)) was determined initially, which only depends on the cross-sectional geometry of the composite beam. The partial composite moment (M_{nc}) capacity using linear interpolation (Equation (C-8)) was determined using a bond shear strength of 0.69 MPa (100 psi). The partial composite moment capacity was also calculated using a plastic stress distribution (Equation (C-12)), but the concrete force was limited to the maximum compressive force resistance developed through a bond shear of 0.69 MPa (100 psi). The final method used to determine the partial composite moment capacity was the strain compatibility method (Equation (C-16)). The strain compatibility does not depend on the length of the specimen, nor the maximum compressive force resistance in the concrete. To determine the partial strength, the strain at the bottom flange was set at the yield value, which was observed at the "failure" moment in the experiments. The strain at the top of the concrete was iterated until equilibrium was satisfied. Worth noting, the required concrete strain to satisfy equilibrium was greater than the experimental strain data, and the compressive force in the concrete was greater than the maximum compressive force developed through bond shear. However, the strain compatibility method produces comparable results. The composite flexural strength determined for the L12 and L16 specimens using all methods are shown in Table C-2 for a concrete compressive strength of 27.6 MPa (4 ksi). The minor differences in the concrete strength for each test affect these moment values; however, the impact is minimal.

Table C-2: Analysis of Composite Flexural Strength

Beam Specimen	**Full Composite Strength: M_{ncp}, kN-m (kip-ft)**	**Partial Composite Strength: M_{nc}, kN-m (kip-ft)**					
		(1) Linear Interpolation		**(2) Partial Plastic**		**(3) Strain Compatibility**	
		Eq. (C-8)	**% Full**	**Eq. (C-12)**	**% Full**	**Eq. (C-16)**	**% Full**
L12	223 (165)	165 (122)	74%	201 (148)	90%	190 (140)	85%
L16	223 (165)	187 (138)	84%	215 (158)	96%	190 (140)	85%

The "failure" moment (M_{fail}) in stage two was compared to the full composite flexural strength to gain an understanding of how the composite beam performs with developing composite strength through bond shear only. The maximum moment in the entire test (M_{max}) was also compared to the full composite moment capacity to quantify the ductility of the composite beams. In addition, the three numerical methods to determine the partial moment capacity were compared to the "failure" moment to determine the best methodology to predict the composite flexural strength. A summary of the results, including average error and standard deviation is shown in Table C-3. The (1) linear interpolation method underestimates (indicated by values less than 1.0) the strength, whereas the (2) partial plastic stress distribution method and (3) strain compatibility method overestimate (indicated by values greater than 1.0) the partial composite strength. The linear interpolation method is the preferred methodology to determine the partial composite moment strength since the component beam is elastic (or just beyond) when "failure" occurs. This can be seen by the linear behavior of the load-displacement curve (Figure C-10) and the experimental neutral axis remaining at the same depth for varying load levels until "failure" (Figure C-12). For a selected bond strength value, the linear interpolation method yields the lowest composite strength. The specimens with the additional reinforcement have a greater "failure" and maximum moment in the test. Overall, the specimens performed very well, and significant composite strength was achieved through the longitudinal bond strength formed in the concrete-steel interface. The component beams are highly ductile and robust, as seen by loading the specimen beyond the "failure" load in stage two and achieving a higher maximum moment in stage three.

Table C-3: Summary of Test Results and Comparison of Methodologies

Beam Specimen	M_{fail}	M_{fail}/M_{ncp}	M_{max}	M_{max}/M_{ncp}	Theoretical/Experimental: M_{nc}/M_{fail}		
	kN-m (kip-ft)	% Full	kN-m (kip-ft)	% Full	Eq. (C-8)	Eq. (C-12)	Eq. (C-16)
L12-N-A	165 (122)	74%	177 (131)	79%	1.00	1.21	1.15
L12-N-B	169 (124)	75%	179 (132)	80%	0.98	1.19	1.13
L12-N-C	173 (128)	77%	173 (128)	77%	0.95	1.16	1.09
L12-R-A	180 (133)	80%	196 (144)	87%	0.92	1.11	1.05
L12-R-B	170 (125)	76%	198 (146)	88%	0.98	1.18	1.12
L12-R-C	180 (133)	81%	203 (150)	91%	0.92	1.11	1.05
L16-N	185 (136)	82%	200 (148)	89%	1.01	1.16	1.04
L16-R	186 (137)	83%	197 (145)	88%	1.01	1.15	1.03
Theoretical/Experimental (M_{nc} / M_{fail}) Average Error					0.97	1.16	1.08
Theoretical/Experimental (M_{nc} / M_{fail}) Standard Deviation					0.038	0.036	0.046

Conclusions

The main purpose of this research was to reduce the uncertainty of the composite flexural behavior of shallow-depth floor systems with A-shapes. To accomplish this, an experimental program was conducted that consisted of eight component beam tests to evaluate the composite strength and stiffness. A test matrix consisting of varying lengths, the addition of shear reinforcement, and varying concrete strength (minor) was utilized. The composite flexural behavior was achieved primarily through the mechanism of longitudinal bond strength due to the concrete encasement of the top flange and web of the steel section. The component beam tests were conducted in three stages to evaluate the linear elastic behavior during repeated low-magnitude loading. Secondly, to quantify the "failure" moment of the composite beam when a sudden loss of stiffness occurred due to forming of flexural-shear cracks and minor slip in the concrete-steel longitudinal shear interface. Finally, additional loading cycles were conducted to evaluate the ductility and robustness of the composite beam following initial "failure."

The distribution of strains throughout the depth of the shallow-depth floor system indicates that the beam acts compositely due to the longitudinal bond strength between the concrete and steel interface. Evaluation of the strain distributions at various load levels indicates that the location of the experimental neutral axis varies very little or not at all, which indicates that the composite action is sustained throughout stage two (up to initial "failure"). A moment-curvature analysis was performed to evaluate the composite flexural stiffness in the beam tests to the theoretical values determined with the transformed cross-section. The stiffness of the shallow-depth floor system under service loading is consistent with utilizing the full composite section. There are minimal differences in the flexural stiffness for all eight tests, showing repeatability in the data.

The eight experimental beam tests achieved 74% to 83% of the full composite strength at the "failure" moment in stage two. Partial composite action for shallow-depth floor systems is purely ensured by longitudinal bond stresses that form in the concrete-steel interface. The partial composite flexural strength was evaluated at the "failure" moment demand in stage two to quantify the nominal concrete-steel bond strength. The bond strength varied from 0.67 MPa (97 psi) to 0.90 MPa (131 psi), which was determined with 4-point bending for the maximum compressive force resistance and a bond perimeter above the elastic neutral axis of the composite section. The development length for the longitudinal bond shear interface was taken as the distance between the support and the application point of the concentrated load.

To evaluate the robustness and ductility of the composite section, the component beams were loaded again in stage three. The beams are relatively robust and ductile, even after the bond started to slip or the concrete started to crack. The applied actuator loading in stage three matched or exceeded the prior loading in stage two. The maximum moment in the entire test reached 77% to 91% of the full composite strength evaluated using a plastic analysis.

Finally, three numerical methods were utilized to evaluate the partial composite strength of the shallow-depth floor system. A bond strength of 0.69 MPa (100 psi) with a bond perimeter above the ENA of the composite section was utilized and is recommended when evaluating the partial composite strength. The composite strength determined with (1) linear interpolation between the steel yield and full composite moment capacity provides the most conservative results. Utilizing the (2) partial plastic distribution, which limits the force that can develop in the concrete, and the (3) strain compatibility method both provide reasonable results; however, the predicted composite strengths are non-conservative. Therefore, the authors recommend utilizing the linear interpolation method with a bond strength of 0.69 MPa (100 psi) to determine the composite flexural strength. Finally, the flexural stiffness of the full composite section moment is recommended for evaluating service level deflections.

Future Research

The research presented in this paper could be expanded upon in many forms to further the knowledge of shallow-depth floor systems. The composite behavior could be experimentally evaluated utilizing different concrete mix designs. Implementing different mix ratios will allow the engineering community to gain an understanding of the effects that the concrete mix ratios have on the bond performance between concrete and steel. Additionally, the surface roughness of steel sections from a steel mill should be tested to further the knowledge on the bond strength that forms between steel and concrete. The impact of altering the surface roughness of a steel section could be experimentally evaluated in component beam tests. Utilizing steel sections with varying levels of surface rust could provide knowledge on the effects that rust has on the bond performance.

Furthermore, a study could be conducted analyzing the effect that different bond enhancement transfer systems have on the composite behavior. These systems could include openings in the steel web and top flange, dowel reinforcement placed through openings in the steel web, and various embossed patterns in top flange to increase the surface roughness.

The final phase of this research will be to conduct a full-scale system-level laboratory experiment. The A-shape to be utilized in the experiment will have the same cross-section from the analytical sizing study (Ottmers et al. 2025b). The stay-in-place formwork will consist of deep decking spanning between three simulated A-shapes. The size of the experiment will resemble two bays in a building to gain an understanding of the behavior during construction and in-service. The ultimate strength of the composite section will be compared to the knowledge gained in this study.

Data Availability Statement

Some or all data, models, or codes that support the findings of this study are available from the corresponding author upon reasonable request.

Acknowledgments

The authors are grateful to AISC for supporting this study through the Milek Fellowship. Any opinions, findings, conclusions, or recommendations expressed in this material are those of the authors and do not necessarily reflect the views of AISC. The authors thank the project industry panel for all their insight and support. This panel is comprised of three US steel mills (Nucor, Gerdau, and Steel Dynamics), fabricators, erectors, designers, and members of AISC (Devin Huber and Margaret Matthew). Finally, the authors appreciate the support from the Advanced Structural Engineering Laboratory at Auburn University, which includes Rob Crosby and Caleb Fleming.

References

AISC. 2022. Specification for Structural Steel Buildings. ANSI/AISC 360-22. Chicago, IL: AISC.

AISC. 2023. Steel C*onstruction Manual*. 16th ed. Chicago, IL: AISC.

AISC. 2024. "Need for Speed." Accessed October 1, 2023. https://www.aisc.org/why-steel/innovative-systems/need-for-speed/.

ArcelorMittal. 2017. *Slim-Floor: An Innovative Concept for Floors*. Luxembourg: ArcelorMittal Commercial Sections.

ArcelorMittal. 2023b. "Slim Floor System." Accessed May 1, 2023. https://sections.arcelormittal.com/products_and_solutions/Our_Specialties/Slim_floor/EN.

Bailey Metal Products. 2023. "COMSLAB Long Span Concrete Floor System." Accessed May 1, 2023. https://www.bmp-group.com/products/comslab.

Bandelt, M. J., S. P. Gross, D. W. Dinehart, J. R. Yost, and J. D. Pudleiner. 2019. "Flexural Behavior of a Composite Steel and Precast Concrete Open Web Dissymmetric Framing System." *Engineering Structures*, 198.

British Steel. 2023. "Sections Product Range: Asymmetric Beams (ASB)." Accessed May 1, 2023. https://britishsteel.co.uk/what-we-do/construction-steel/sections-product-range/.

CEN. 2004. Design of Composite Steel and Concrete Structures, Part 1-1: General Rules and Rules for Buildings. Eurocode 4: EN 1994-1-1. Brussels, Belgium: European Committee for Standardization (CEN).

Davis, S. 2022. "Full-Scale Floor System Testing for Future Hot-Rolled Asymmetric Steel I-beams." Master Thesis, Texas A&M Univ.

Davis, S., E. Stoddard, and M. T. Yarnold. 2023. "Full-Scale Floor System Testing for Future Hot-Rolled Asymmetric Steel I-beams." *Journal of Structural Engineering*, 149(2).

Girder-Slab Technologies. 2016. *The GIRDER-SLAB System Design Guide v3.3*. Cherry Hill, NJ: Girder-Slab Technologies

Hauf, G., and U. Kuhlmann. 2015. "Deformation Calculation Methods for Slim Floors." *Steel Construction*, 8(2).

Hechler, O., M. Braun, R. Obiala, U. Kuhlmann, F. Eggert, and G. Hauf. 2016. "CoSFB - Composite Slim-Floor Beam: Experimental Test Campaign and Evaluation." *Composite Construction in Steel and Concrete*, 7.

Ju, Y. K., S.-C. Chun, and S.-D. Kim. 2009. "Flexural Test of a Composite Beam using Asymmetric Steel Section with Web Openings." *Journal of Structural Engineering*, 135(4).

Kloeckner Metals. 2020. The Cellular Beam Pocket Guide Entrusted to Design and Deliver Metal Solutions. Leeds, UK: Kloeckner Metals UK.

Kloeckner Metals. 2023. "Ultra Shallow Floor Beam." Accessed June 1, 2023. https://www.kloecknermetalsuk.com/en/westok/products/ultra-shallow-floor-beam.html.

Kuhlmann, U., R. M. Lawson, O. Vassart, D. Lam, R. Zandonini, and E. Hendrickx. 2021. "Slim-Floor Beams Preparation of Application rules in view of improved safety, functionality and LCA (SlimAPP)." Project No. RFSR-CT-2015-00020. European Union, Luxembourg.

Lam, D., X. Dai, U. Kuhlmann, J. Raichle, and M. Braun. 2015. "Slim-Floor Construction - Design for Ultimate Limit State." *Steel Construction*, 8(2).

Lawson, R. M., D. L. Mullet, and J. W. Rackham. 1997. *Design of Asymmetric Slimflor Beams using Deep Composite Decking*. *SCI P175.* Ascot, UK: The Steel Construction Institute.

McCormac, J. C. 1981. *Structural Steel Design*. 3rd ed. New York, NY: Jack C. McCormac.

Ottmers, C., E. Stoddard, and M. Yarnold. 2025b. "Establishment of Future A-Shape Geometry for Residential Construction." *Journal of Structural Engineering*.

Rackham, J. W., S. J. Hicks, and G. M. Newman. 2006. *Design of Asymmetric Slimflor Beams with Precast Concrete Slabs*. *SCI P342.* Ascot, UK: The Steel Construction Institute.

Roeder, C., R. Chmielowski, and C. Brown. 1999. "Shear Connector Requirements for Embedded Steel Sections." *Journal of Structural Engineering*, 125(2).

Schorr, J., and U. Kuhlmann. 2019. "Design of Slim-Floors and their Connections between Steel and Concrete." *The 14th Nordic Steel Construction Conference, September 18-20, 2019, Copenhangen, Denmark.*

Sheehan, T., X. Dai, J. Yang, K. Zhou, and D. Lam. 2019. "Flexural Behaviour of Composite Slim Floor Beams." *Structures*, 21.

Stoddard, E., and M. Yarnold. 2022. "Residual Stress and Global Deflection Limits for Future Hot-Rolled Steel Asymmetric I-beams." *Journal of Structural Engineering*, 148(1).

Stoddard, E. A. 2022. "Behavior of Hot-Rolled Asymmetric Steel I-beams: Concept to Construction." Ph.D. Thesis, Texas A&M Univ.

Weng, C. C., S. I. Yen, and M. H. Jiang. 2002. "Experimental Study on Shear Splitting Failure of Full-Scale Composite Concrete Encased Steel Beams." *Journal of Structural Engineering*, 128(9).

Appendix D – Sizing Study

Appendix D provides detailed information on the analytical sizing study (Phase 4) conducted to establish A-shape cross-sectional geometry. This includes literature review of similar systems, results of the sizing study, and parametric studies. The sizing study includes manufacturing and construction considerations as well as limit state analysis during construction and in-service. An overview of the manufacturing and construction considerations are provided. Likely structural load cases for shallow-depth floor systems are explained and used in the sizing study. Limit states analyzed in the sizing study are explained. Parametric studies are conducted altering assumed parameters to analyze sensitive limit states and the capabilities of A-shapes in shallow-depth composite floor systems.

Citation

The following work is currently in the publishing phase and was accepted by the American Society of Civil Engineer's Journal of Structural Engineering. After the journal is published, the citation to the journal article will be:

> Ottmers, C., E. Stoddard, and M. Yarnold. 2025. "Establishment of Future A-Shape Geometry for Residential Construction." *Journal of Structural Engineering*. https://ascelibrary.org/doi/10.1061/JSENDH/STENG-13726

The following work is expanded upon and supplemental information/results are provided in Chase Ottmers Ph.D. Dissertation. The citation to Chase's dissertation is:

> Ottmers, C. E. 2025. "Full-Scale Testing and Numerical Evaluation of Hot-Rolled Asymmetric I-beams in Shallow-Depth Composite Floor Systems." Ph.D. Dissertation, Texas A&M University.

Establishment of Future A-Shape Geometry for Residential Construction

Chase Ottmers, Eric Stoddard, and Matthew Yarnold

Abstract

Steel buildings utilizing steel-concrete composite construction typically have large floor depths due to the concrete deck cast above wide-flange beams. To achieve shallower composite floor systems, stay-in-place formwork is placed on the bottom flange. This formwork comprises either concrete precast panels or steel deep decking, which supports a concrete topping slab that encases the steel beam. The goal is to minimize the floor depth, reducing the building's overall height or increasing the floor-to-floor height. In the United States (US), there are currently no readily available hot-rolled steel shapes that allow for easy placement of stay-in-place formwork on the bottom flange. This necessitates intensive fabrication to create asymmetric beams, to facilitate rapid placement of stay-in-place formwork on the wider bottom flange. This study aims to develop standardized hot-rolled asymmetric steel I-beams (A-shapes) for potential large-scale production in the US. Utilizing A-shapes will decrease the required manufacturing time and will allow for increased speed and efficiency of residential building construction. The research presented herein includes beam sizing constraints established from interviews with three US steel mills. Utilizing the beam sizing constraints for manufacturing, a wide range of possible cross-sections were investigated for three structural load cases. Each cross-section iteration was analyzed for a total of 16 limit states to establish efficient and effective standardized A-shapes. Parametric studies were conducted to investigate sensitive limit states when altering assumed parameters. As a result of this study, two primary cross-sections, with a depth of 203 mm (8.0 in.) (A8s), were established for a 6.1 m (20 ft) square grid for a live load of 1.9 kPa (40 psf) and 4.8 kPa (100 psf). The heavier A8 cross-section (when supporting 1.9 kPa (40 psf) live loading) satisfies all limit states for a beam length of 6.1 m (20 ft) and spacing of 8.5 m (28 ft), which allows for large open spaces between columns. The methodology developed was also utilized to size four additional A-shapes (two A10s and two A12s) and can be used to size A-shapes for other facilities.

Keywords: Structural Steel, Hot Roll, Asymmetric, Composite, and Floor System

Introduction

Structural floor systems in steel buildings commonly utilize composite construction with hot-rolled steel beams and a concrete slab. To construct the floor system, stay-in-place formwork, either steel decking or concrete precast panels, is placed on the steel beams to support wet concrete. This formwork is placed on the top flange and is topped with a concrete slab, leading to relatively large floor depths. As an alternative, concrete precast panels or steel deep decking systems can be placed on the bottom flange to reduce the floor system depth (increasing the floor-to-floor height). Standard doubly symmetric wide-flange shapes in the United States, such as W-shapes (AISC 2023), do not allow for easy placement of formwork on the bottom flange due to top flange interference. As a result, fabricated asymmetric I-beams are built-up to allow for rapid placement of concrete precast panels or deep decking systems.

There are several steel fabricated asymmetric I-beam floor systems utilized today that use either precast concrete panels or deep decking. GIRDER-SLAB utilizes D-beams, which are asymmetric beams fabricated by cutting a castellated pattern in the web of a W-shape and welding a flat bar to the cut web. The GIRDER-SLAB floor system consists of concrete precast panels placed on the bottom flange that have a minimum bearing length of 51 mm (2 in.) (Girder-Slab Technologies 2016). Kloeckner Westok beams are similar in that the web of two uncommonly sized wide-flange beams are cut into a castellated pattern. The uncommon-sized cut beams are paired together to form an asymmetric cross-section that has a cellular pattern (Kloeckner Metals 2020; Kloeckner Metals 2023). Composite slim-floor beams (termed CoSFB) (ArcelorMittal 2017; ArcelorMittal 2023b) and COMSLAB are similar floor systems because they both utilize built-up asymmetric sections by welding a steel plate to the bottom of a standard wide-flange section. COMSLAB is a steel deep decking system that sits on the bottom plate of the built-up section, with a minimum bearing length of 51 mm (2 in.) (Bailey Metal Products 2023). The DELTABEAM is distinct because the cross-section is a built-up trapezoidal boxed beam, not an I-shape (Peikko 2023), and supports either precast concrete panels or cross-laminated timber (CLT) panels (DELTABEAM Technical Manual 2019). All the current asymmetric floor systems described above require intensive fabrication work. An alternative solution to built-up asymmetric shapes is to hot roll them at a steel mill. Research is being conducted and presented herein on a new hot-rolled asymmetric I-beam (termed A-shape) which has a wider bottom flange than the top flange.

Utilizing A-shapes will reduce fabrication time and cost and will also increase the speed of construction on a jobsite, which in turn, will help reduce the cost of steel buildings. This project is part of the American Institute of Steel Construction (AISC) “need for speed” initiative to increase the speed of steel construction. Furthermore, utilizing A-shapes will also reduce the floor-to-floor height of the composite floor system, leading to a reduction of the total building height (AISC 2024; Huber 2022). A general overview of a built-up (Figure D-1(a)) and a hot-rolled (Figure D-1(b)) shallow-depth composite floor system are shown in Figure D-1. The built-up cross-section consists of a steel plate that is welded to the bottom of a W-shape to allow for placement of stay-in-place formwork on the bottom portion of the asymmetric beam. Note, some built-up asymmetric systems utilize dowel reinforcement through openings in the web of the asymmetric beam but is not shown for simplicity. Dowel reinforcement is not utilized in the A-shape composite cross-section to increase speed of construction.

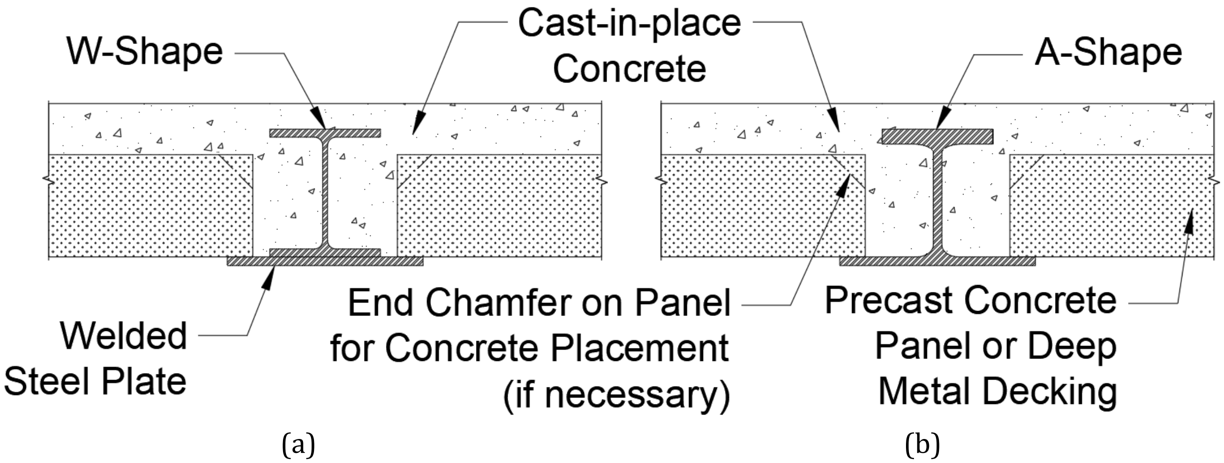

Figure D-1: Overview of (a) Built-Up and (b) Hot-Rolled Shallow-Depth Composite Floor Systems

Around the world, there is a limited production of rolled asymmetric I-shapes and currently, none are rolled at steel mills in the United States. A floor system in the United Kingdom called Slimdek (Lawson et al. 1997; Rackham et al. 2006) is built by Corus Construction and Industrial. The Slimdek floor system utilizes hot-rolled asymmetric steel beams, termed ASBs, that are produced by British Steel and are rolled on request. The dimension range for the cross-section depth, flange widths and thickness, and web thickness are provided in Table D-1. Note, that half of the cross-sections have a thicker web to improve the fire performance of ASBs. The Slimdek floor system consists of steel deep decking or precast concrete panels that have a minimum bearing length of 40 mm (1.6 in.) and 75 mm (3.0 in.), respectively (Lawson et al. 1997; Rackham et al. 2006).

Table D-1: ASB Dimension Range

ASB Parameters	Dimension Range (mm (in.))
Top Flange Width	175 (6.9) - 203 (8.0)
Bottom Flange Width	285 (11.2) - 313 (12.3)
Top and Bottom Flange Thickness	14 (0.6) - 40 (1.6)
Web Thickness	10 (0.4) - 40 (1.6)
Cross-Section Depth	272 (10.7) - 342 (13.5)
ASB Parameters	**Unit Weight Range (kg/m (lb/ft))**
Weight	74 (50) - 249 (167)

Source: Data from British Steel (2023).

Extensive research has been conducted on the ultimate capacity for a variety of shallow-depth concrete-steel composite floor systems. The ultimate capacity of shallow-depth composite cross-sections with vertical studs, horizontal studs, and dowel reinforcement was determined with a plastic analysis for slim-floor construction (Lam et al. 2015). Furthermore, the ultimate capacity was investigated for a composite slim-floor system with no shear connectors, headed stud connectors, and transverse steel bar connectors with experimental testing (Xia et al. 2021). An experimental study was conducted to evaluate the effect that time-dependent creep has on the ultimate load of a slim-floor system (Baldassino et al. 2019). Non-linear finite element modeling was utilized to compare the flexural stiffness and capacity of two shallow-depth composite floor systems: specifically, the CoSFB and ASB concepts (Borghi et al. 2021). The deformation for shallow-depth composite beams was investigated using an effective moment of inertia and an experimental investigation was conducted consisting of both single and two-span girders (Hauf and Kuhlmann 2015). The design approaches utilized for various shallow-depth composite floor systems around the world were analyzed (Ahmed and Tsavdaridis 2019). Additionally, research has been conducted on the ductility of the DELTABEAM floor system (Peltonen and Kyriakopoulos 2020), the load transfer mechanism between CLT panels and the DELTABEAM during ambient and fire temperatures (Camnasio 2022; West et al. 2023), and the performance of CLT panels and DELTABEAM due to human-induced floor vibrations (Yrjola and Salonen 2020). However, minimal research has been conducted on rolling asymmetric I-beams at steel mills and further understanding of structural behavior in all construction phases is needed.

In this research study, the initial work consisted of evaluating the manufacturability of A-shapes in the US. Potential issues with residual stress and global deformations were investigated utilizing extensive thermal-mechanical modeling (Stoddard and Yarnold 2022; Stoddard 2022). Beam sizing constraints were established considering the expert feedback from three US steel mills, Nucor, Gerdau, and Steel Dynamics (discussed further in the Manufacturing and Construction section below). Preliminary full-scale testing was conducted for a feasibility study of A-shapes (Davis 2022; Davis et al. 2023). Proof-of-concept beams developed in the residual stress study (Stoddard and Yarnold 2022; Yarnold and Stoddard 2020) were utilized in the full-scale test. The testing program evaluated the behavior during panel placement, concrete pour, and vertical loading (Davis et al. 2023). The information from these prior studies was utilized within the A-shape analytical sizing study presented herein.

The principal contributions of this research involve the development and implementation of a comprehensive analytical sizing study aimed at defining the prospective cross-sectional geometry of A-shapes. This research study is being performed in collaboration with AISC for the production of a new hot-rolled section in the US, which will then be added to Part 1 of the AISC Steel Construction Manual (AISC 2023). AISC, along with an industry panel comprised of consulting engineers, steel fabricators, and steel mills, provided guidance to the research team toward the initial implementation of A-shapes in residential building construction. The primary application lies in shallow-depth steel-concrete composite floor construction (see Figure D-1(b)), facilitating rapid placement of stay-in-place formwork onto the A-shapes bottom flange to achieve AISC's "need for speed" initiative (AISC 2024). An array of A-shape cross-sectional geometries were considered at specific depths that met dimensional constraints for manufacturability. Then, all possible cross-sections were evaluated for the behavior of the non-composite section during construction and the in-service limit states of the composite section.

Initially, two primary A-shape cross-sections were defined with a depth of 203 mm (8 in.). Subsequently, the study expanded to include four supplemental cross-sections. After establishing cross-sectional geometries, parametric studies were conducted to investigate sensitive limit states with altering critical parameters. These parameters include concrete strength, concrete weight, concrete topping depth above the A-shape (altering the total height of the floor system), service live load for various facilities, longitudinal bond shear between the concrete and steel, and the beam length and spacing of the grid layout. The parametric studies provided an understanding of the implications for future engineering design decisions. The study's research objectives are detailed in the following section.

Research Objectives

This research investigated future hot-rolled asymmetric steel I-beams (A-shapes) to be utilized in shallow-depth steel-concrete composite floor systems for residential buildings. The study aimed to understand the behavior of A-shapes and to develop standardized A-shape cross-sectional geometry. An extensive analytical sizing study was conducted to achieve the following objectives:

1. Develop a robust sizing study framework to establish efficient and effective A-shape cross-sections suitable for long-span lengths and large beam spacings in residential buildings, while achieving minimal floor depths.
2. Establish A-shapes that satisfy 16 limit states, which encompass manufacturing constraints, various construction load scenarios on the non-composite section, and in-service loading applied to the composite section.
3. Recommend a minimum number of cross-sectional geometries for potential large-scale production of new A-shapes in the United States.
4. Evaluate the sensitivity of the controlling limit states to discern the impact of the key building parameters.

Analytical Sizing Study

Overview

An analytical sizing study was conducted to establish A-shape cross-sectional geometry, encompassing both manufacturing and structural behavior (during construction and in-service). The manufacturing aspect involved interviews with industry experts complemented by a numerical modeling study. The structural behavior was numerically evaluated with 16 strength and serviceability limit states, considering both steel building erection and in-service condition. The sizing study considered 65 possible beam cross-sections (per beam depth). Each alternative cross-section geometry was evaluated for all limit states to understand the behavior of A-shapes across various load cases (discussed further below).

Initial beam cross-sectional sizing constraints were determined by expert building engineers, anticipating the future application of A-shapes in residential construction. As a result, the depth of the A-shape (d) was limited to 203 mm (8 in.) to allow for optimum floor-to-floor height. The goal was to achieve a total depth for the composite floor system (D_{tot}) of less than 254 mm (10 in.). In addition, four supplemental shapes (two 254 mm (10 in.) and two 305 mm (12 in.)) were developed for even further span length and beam spacing capabilities.

The range of beam cross-sectional geometries was established by adjusting the thickness and width of the top and bottom flanges, along with variations in the web thickness. Altering these dimensions allowed for a robust approach to establish efficient and economical cross-sectional geometry.

Manufacturing and Construction

An anticipated challenge for future asymmetric I-shapes (A-shapes) is their hot rolling process at steel mills. To increase the feasibility of manufacturing, the research team interviewed three major US steel mills, Nucor, Gerdau, and Steel Dynamics, to understand their anticipated concerns when hot rolling an A-shape. Expert feedback was provided from a wide breadth of knowledge from industry roll-pass engineers, roll-pass designers, metallurgical engineers, roll mill supervisors, and product developers.

Initially, bounds for the top flange thickness $\left(t_{ft}\right)$ and width $\left(b_{ft}\right)$ were established using engineering judgment. Steel mills mentioned during interviews that thin webs are challenging to roll with considerably thick flanges. Therefore, a minimum web thickness of 13 mm (0.5 in.) was established. In addition, the web thickness (t_w) was not allowed to be thinner than half the thickness of the thicker flange (which will always be the top flange due to the reasons stated below). In other words, the minimum web thickness was determined to be 13 mm (0.5 in.) but also no thinner than half of the top flange thickness.

An important constructability constraint was considered for establishing the bottom flange width. A bearing seat of 51 mm (2 in.) was utilized, and an additional 13 mm (0.5 in.) of clearance was included (developed from industry feedback and the literature of similar systems, as stated earlier). Therefore, the bottom flange width (b_{fb}) was set as 127 mm (5 in.) greater than the top flange width (b_{ft}). In addition, expert feedback provided that a 305 mm (12 in.) bottom flange on a 203 mm (8 in.) deep section should be achievable, but production might be limited to select mills. As a result, the bottom flange width was limited to 305 mm (12 in.) due to the consideration of manufacturing constraints, which also limits the possible widths of the top flange.

A critical manufacturing consideration was to provide balanced flange areas for A-shapes. Balanced flange areas are preferred by the steel mills since the steel is less likely to be overworked during rolling. As a result, the bottom flange thickness (t_{fb}) was quantified by equating the top and bottom flange areas. A summary of the beam sizing constraints and dimension ranges are shown in Figure D-2.

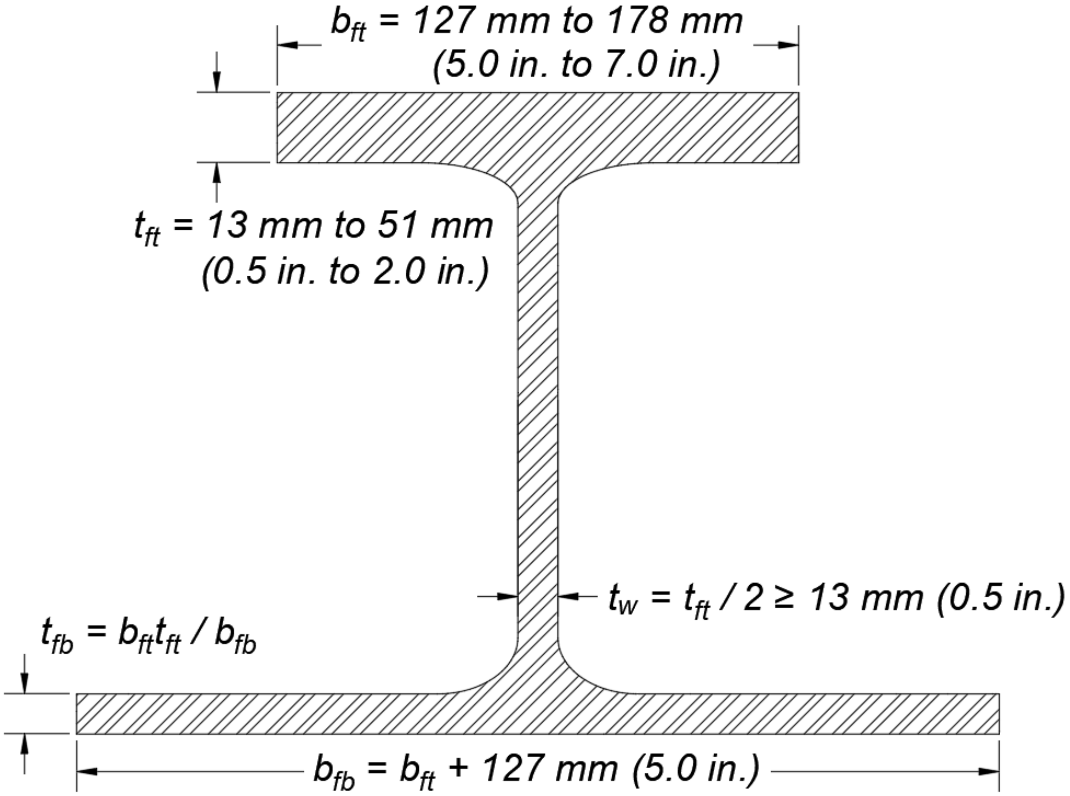

Figure D-2: Beam Sizing Manufacturing Constraints

Experts also expressed concerns about excessive residual stresses forming during the cooling process of A-shapes. Large residual stresses could impact the non-composite moment capacity, specifically lateral-torsional buckling, during the construction phases. A second concern raised was the possibility of excessive global deformations (curvature) that could increase the difficulty of handling the beams throughout the steel mill. To quantitatively evaluate these concerns, extensive thermal-mechanical finite element (FE) modeling was performed to simulate the cooling behavior of rolled asymmetric I-shapes. As a result of this prior study, a flange width-to-thickness (b/t) limit of

17 (Stoddard and Yarnold 2022) was established to satisfy the compressive stress 30% yield limit (AISC 2022). Global deformation (curvature) after cooling was determined not to be an issue.

Apart from beam cross-sectional constraints, defining material properties was necessary. The steel grade utilized was ASTM A992, with a steel yield strength $\left(F_y\right)$ of 345 MPa (50 ksi), which was another steel mill and engineer preference. Normal-weight concrete with a concrete compressive strength (f_c') of 27.6 MPa (4000 psi) was decided by the research team. A sensitivity study is included at the end of this paper to show the impact of these decisions.

Another important decision was the building geometry. The column line grid dimensions differ among projects; however, the research team decided on a 6.1 m (20 ft) by 6.1 m (20 ft) bay to set a beam length (L) and spacing (S) of 6.1 m (20 ft). A large beam spacing was utilized so the A-shapes span directly between columns to reduce the number of connections in a steel building. With the use of precast panels or deep decking, the beam spacing can be greater than a standard composite floor system due to the spanning capabilities. Again, a sensitivity study is presented at the end of this paper to illustrate A-shape capabilities for different grid layouts.

Boundary conditions for the A-shapes were chosen, opting for simple shear connections for flexure and torsion to reduce the floor system's complexity and expedite construction. Prior testing showed additional flexural and torsional restraint provided by these simple connections (Davis et al. 2023). However, the additional restraint was conservatively neglected during the analysis.

Structural Load Cases

Residential building construction and in-service conditions were considered to determine plausible loading scenarios to establish cross-sectional geometry. After the beams are erected, precast concrete panels are placed onto the bottom flange. After all panels are positioned, a concrete topping is poured on the precast panels and A-shape. The other common construction approach is to utilize deep metal decking supported on the bottom flange. Then, cast-in-place concrete is poured for the entire depth of the floor system. Note that temporary shoring is typically required. Therefore, the precast panel approach was considered the more critical method for A-shape sizing and was utilized for this study.

Three controlling load cases were established for A-shape cross-section sizing, which is graphically illustrated in Figure D-3. The first two cases are the critical construction conditions, where the A-shape is non-composite and supports all the load. It is worth noting that eccentric loading is applied to the A-shape in these load cases, which induces a torsional moment that must be adequately supported. The last load case is the in-service composite condition. For this case, serviceability criteria and ultimate capacity were considered. All three loading cases utilized for A-shape sizing are further explained below.

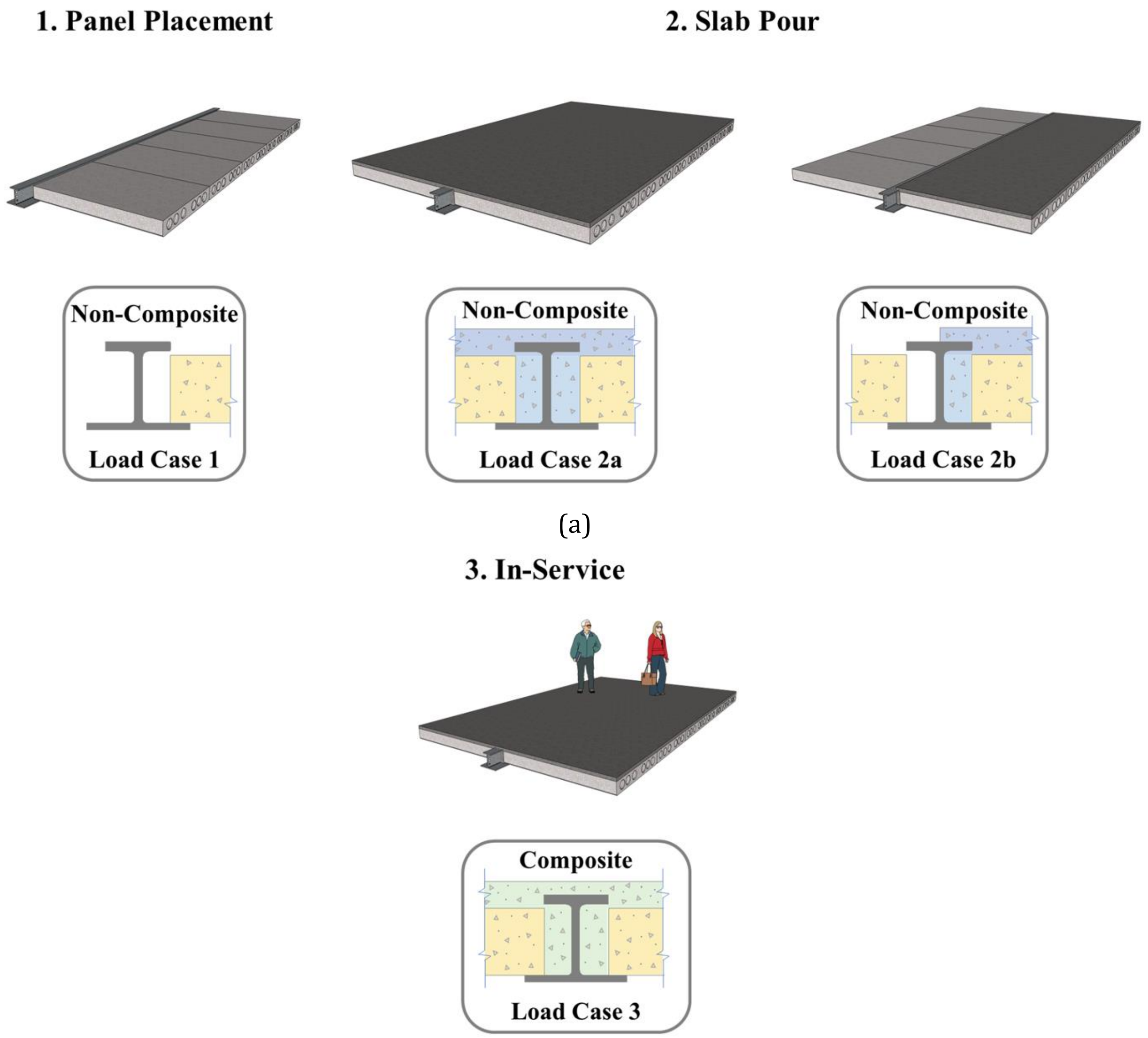

(a)

(b)

Figure D-3: Structural Load Cases: (a) Construction and (b) In-Service

Load Case 1 involves placing precast concrete panels on the bottom flange of the A-shape. Panel placement could occur in several different ways, such as alternating between the placement of panels on the left and right sides of the beam. This would primarily induce concentric loading (minimal torsion). A second option for panel placement is in a single line along the length of the building (as shown on the left side of Figure D-3). This option would produce an eccentric loading, inducing a torsional moment and out-of-plane rotation. The second option is more structurally demanding for the A-shape. Therefore, to conservatively size A-shapes, the second panel placement option was considered. Precast panels with a thickness (D_d) of 152 mm (6 in.) and a weight of 2.4 kPa (50 psf) were selected (Nitterhouse Concrete Products 2020). A construction live load of 0.96 kPa (20 psf) was included to account for construction workers walking around on the panels as they are being placed (ASCE 2014). The load combinations use a load factor of 1.4 for variable construction dead load, and a construction live load factor of 1.6 was utilized (ASCE 2014).

Load Case 2 captures the behavior during the pouring of the cast-in-place topping slab. This load case was split into two sub-cases (2a and 2b) since there are two critical scenarios for the concrete pour.

Load Case 2a examines the maximum concentric load that the A-shape will encounter to ensure the section has sufficient non-composite moment capacity. The dead load considered in this case is the panel weight on both sides of the beam and a concrete topping (D_c) of 38 mm (1.5 in.) over the steel section. This concrete topping depth was selected from prior research of the Slimdek system, which concluded a minimum of 30 mm (1.2 in.) of topping is required for adequate composite strength (Rackham et al. 2006). The concrete density utilized for normal-weight concrete was 2300 kg/m^3 (145 pcf). A construction live load of 0.96 kPa (20 psf) was also included in this limit state, as the construction workers will be finishing the topping slab. Load Case 2b considers concentric loading from the precast panels and eccentric loading for concrete poured on only one side of the A-shape (see Figure D-3). A concrete joint above the A-shape would not be ideal; however, a torsional load is likely to occur as the construction workers place the concrete. The dead and live loads for this case were consistent with Load Case 2a. The load factors for both Load Case 2a and 2b were consistent with Load Case 1.

The final load case, Load Case 3, focuses on in-service loading on the composite section and ensures serviceability and strength criteria are satisfied. Quantifying the composite flexural strength is discussed in depth in the Composite Flexure during Service Loading section below. The primary focus of this analytical sizing study was residential buildings; therefore, a live load of 1.9 kPa (40 psf) was utilized for private rooms in multifamily dwellings (ASCE 2022). A second live load value of 4.8 kPa (100 psf) was used for public rooms and corridors serving them (ASCE 2022). Residential and corridor live loads were reduced, and a nonreduced 0.72 kPa (15 psf) partition was included (ASCE 2022). In addition, a 0.48 kPa (10 psf) uniform distributed load was included for MEP. Therefore, two cross-sectional geometries were established for each live load condition. Live load was factored by 1.6, while dead load used a factor of 1.2 (ASCE 2022).

Limit State Analysis

To establish A-shape cross-sectional geometry, every geometric combination (within the constraints mentioned earlier) was considered. For each of these A-shape cross-sections, a total of 16 different limit states (four non-composite flexure, one shear, six torsion, two composite flexure, and three serviceability) were evaluated for the load cases discussed above. This allowed the research team to obtain normalized results (capacity versus demand) for every scenario. The results from each scenario were then combined. The purpose was to determine the controlling limit states and scenarios, followed by the identification of plausible cross-sections for residential buildings. The minimum area (and weight) of all cross-sections was utilized to select the most efficient cross-sectional geometry. A graphical overview of the analytical sizing study framework is shown in Figure D-4.

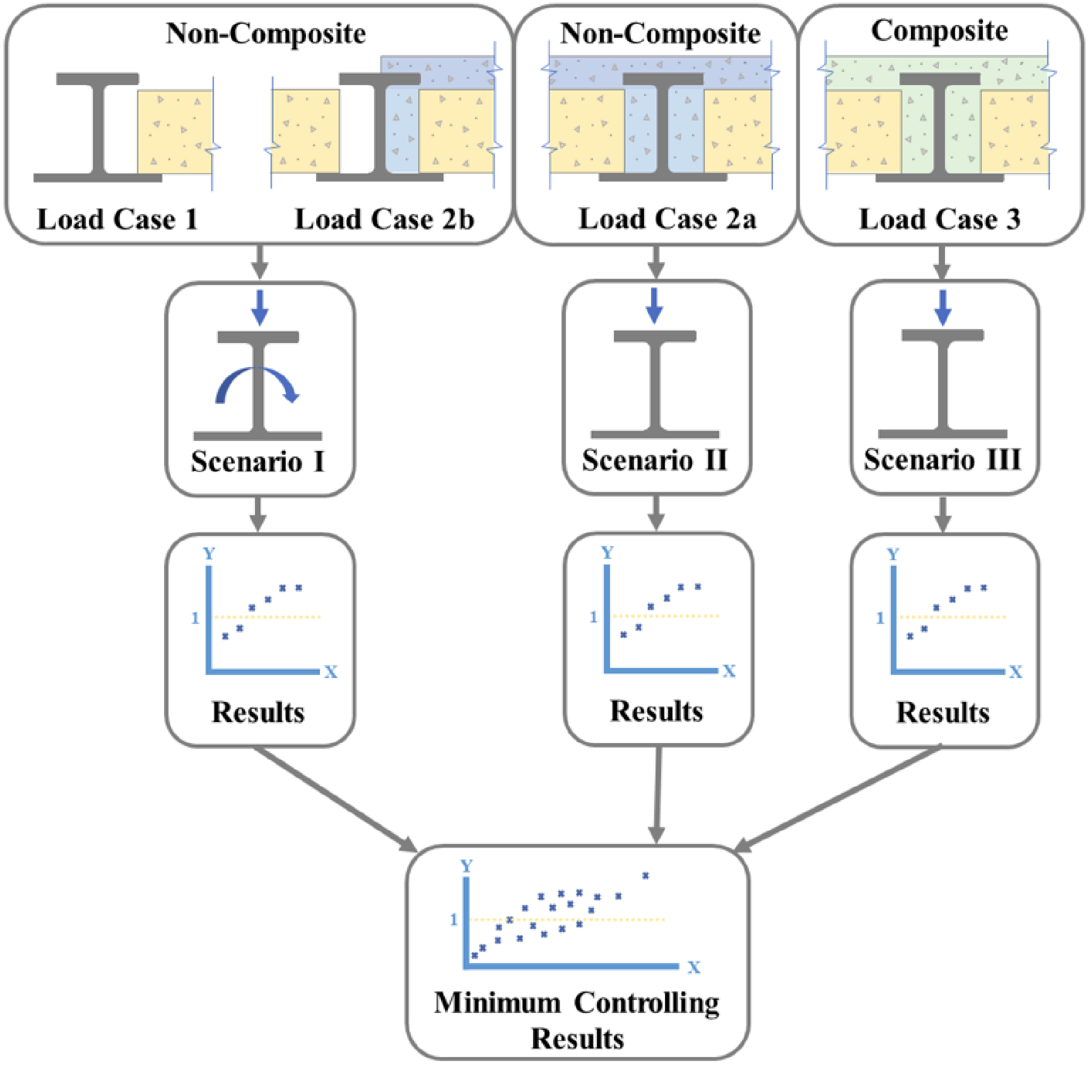

Figure D-4: Analytical Sizing Study Framework

Non-Composite Flexural Capacity in Construction Phase

Flexure criteria were considered for Load Cases 1, 2a, and 2b to ensure sufficient non-composite moment capacity. Load Case 2a results in the highest moment demand; however, the other two load cases are considered for completeness. The flexure capacity of a singly symmetric I-beam with a compact web is determined from Section F4 in the Specification for Structural Steel Buildings (AISC 2022). As a result of the web thickness manufacturing constraints (discussed earlier), the web was compact for all A-shape cross-sections considered. Therefore, the four limit states evaluated include compression flange yielding, tension flange yielding, compression flange local buckling, and lateral-torsional buckling.

The limit states for compression and tension flange yielding are relatively straightforward. They consider the elastic section modulus, yield stress of the steel, and a web plastification factor to determine the nominal moment capacity. This was calculated for every A-shape cross-section considered. Further details on the calculations are provided in the AISC Specification (AISC 2022). Compression flange local buckling does not apply to the A-shape cross-sections considered due to the width-to-thickness ratios of the top flange.

Lateral-torsional buckling (LTB) is defined as a lateral translation of a beam combined with a twist of the section about the tension flange. LTB capacity is highly dependent on the unbraced length. If sufficient bracing is provided, LTB does not apply. However, during the construction of residential buildings, the unbraced length can be relatively long, making inelastic or elastic LTB feasible. Elastic LTB capacity depends on the critical elastic lateral-torsional buckling stress, derived from the unbraced length (L_b), the LTB moment modification factor (C_b), and section properties of the cross-section. The full expressions are not provided due to space limitations but can be found in the AISC Specification (AISC 2022).

The equation for the critical elastic LTB stress is derived for a constant moment acting along the entire unbraced length. A constant moment is the worst case for LTB due to maximum compressive stress over the entire unbraced length (L_b). The critical elastic LTB stress is modified with the C_b factor for other moment distributions. Loading for A-shapes in residential buildings will be uniformly distributed over the entire length, which produces a parabolic moment distribution. The C_b value for this case, for no intermediate brace points, is 1.14 (AISC 2023).

For LTB, the formulas in the AISC Specification are derived for the load applied at the centroid. For many situations, the applied load is at the top of the beam; however, the beam is usually braced with metal decking in standard composite floor systems. If the load is applied to the top flange with large unbraced lengths, as the beam begins to buckle out-of-plane, a secondary moment is generated due to the rotation of the beam, resulting in an additional torsional moment in the direction of buckling (see Figure D-5(a)). However, if the load is applied to the bottom flange, a restoring moment is formed as the beam rotates, which is shown in Figure D-5(b). Since the primary use for A-shapes is to support precast panels or deep decking that bear on the bottom flange, the research team decided to take advantage of this improved loading condition.

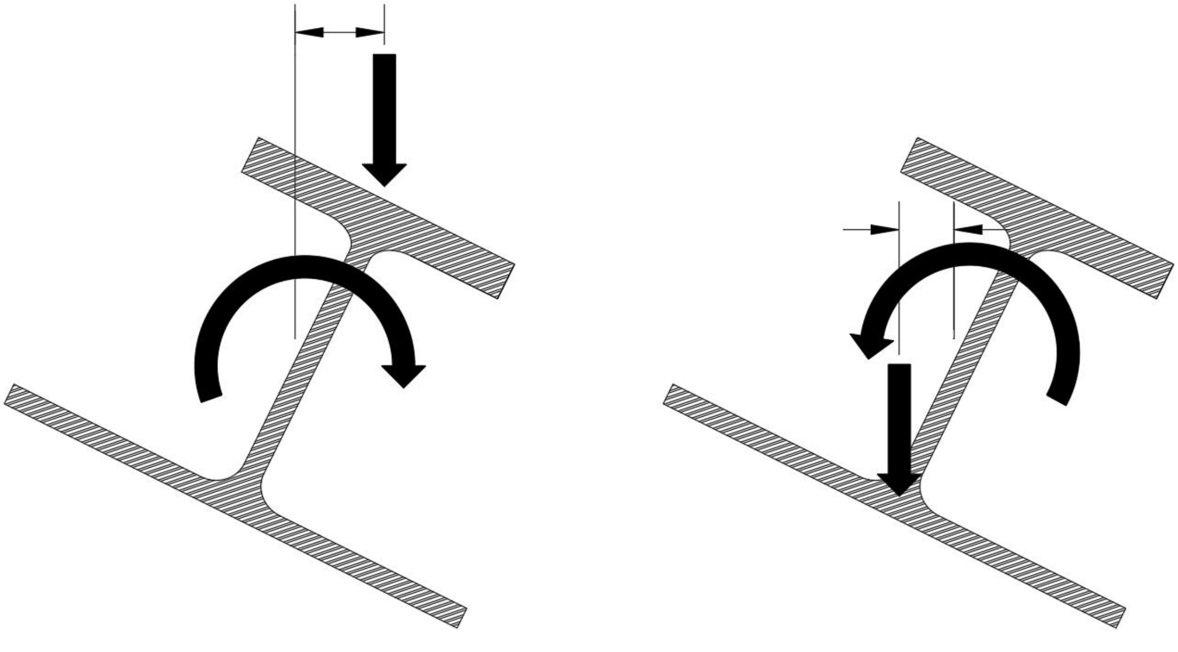
(a) (b)

Figure D-5: Load Height Effect for Loading Applied to (a) Top Flange and (b) Bottom Flange

An additional adjustment to C_b is made to account for the applied load height on the beam (also called the load height effect) through the load height modification factor (C_b^*) (Helwig et al. 1997). This factor is a function of the warping stiffness of the cross-section (W) and the type of loading. The warping stiffness parameter is evaluated in Equation (D-1) using the weak axis moment of inertia (I_y), the distance between flange centroids (h_o), the shear modulus (G), Young's modulus of the steel (E_s), and the polar moment of inertia (J). The parameter denoted as (B), considers the type of loading and the warping stiffness. Equation (D-2) is the equation utilized for uniformly distributed loads. The load height modification factor (C_b^*) with load applied on the bottom flange is expressed in Equation (D-3).

$$W = \frac{\pi}{L_b}\sqrt{\frac{E_s I_y h_o^2}{4GJ}} \tag{D-1}$$

$$B = 1 - 0.154W^2 + 0.535W \tag{D-2}$$

$$C_b^* = BC_b \tag{D-3}$$

This load height modification (C_b^*) increases C_b (equal to 1.14 for a uniformly distributed load without load height modification) by 10% to 35%, based on the geometry. This translates to a direct increase in the LTB capacity.

Vertical Shear Analysis for Construction Loading

The vertical shear capacity limit state of the A-shape is quantified utilizing Section G2.1 in the Specification for Structural Steel Buildings (AISC 2022). The nominal shear strength considers the shear area of the web, the yield stress of the steel, and the web shear strength coefficient. Vertical shear capacity of A-shapes was not a major concern due to the web thickness manufacturing limits. However, this limit state was included for completeness.

Torsion Analysis under Eccentric Loading during Construction

Eccentric loading due to concrete panel placement and pouring a topping slab over a single bay (Load Cases 1 and 2b, respectively) produce a significant torsional moment demand on the A-shape cross-section. During all construction load cases, due to wet concrete, there is no lateral or torsional bracing along the entire length of the beam. A torsional moment results in the beam wanting to twist; however, the cross-section is typically restrained at the ends with pinned-pinned connections. This induces torsional stresses and a stability concern. Tensile and compressive normal warping stresses, which vary along the width of the flange, form due to the bending of the flange under torsional load. In addition to the normal warping stresses, common flexural stresses due to plane bending are also present. Normal warping and flexural stresses are combined over the cross-section which results in the accumulation or reduction in total normal stress at certain corners of the cross-section. In addition to normal stresses, shear stresses form and accumulate due to warping restraint, pure torsional shear stress, and plane bending shear stress. A theoretical background on torsion was provided by the research team in the prior publication, Davis et al. (2023), and is not provided herein due to space limitations. Further, a more detailed background can be found in the AISC Design Guide 9 (Seaburg and Carter 2003).

Six limit states were evaluated for the A-shape subjected to torsion and torsion combined with in-plane bending. This included yielding of the cross-section under normal stresses and shear stresses. Both compression and tension flange yielding were considered due to the singly symmetric nature of the cross-section. Flange and web shear yielding were checked, and lateral-torsional buckling was also considered. In addition to stress checks, the cross-section rotations were verified to ensure that the torsional stiffness of the A-shape was large enough to not cause issues during construction.

Composite Flexure during Service Loading

To ensure sufficient flexural capacity for in-service loading, two limit states on the composite strength (partial or full) of a concrete-encased A-shape were included in the analytical study. The slab's effective width utilized for composite strength was determined with Section I3.1a from the Specification for Structural Steel Buildings (AISC 2022). The total effective width (B_e) of the slab, for a symmetric grid layout, is determined by the minimum of a quarter of the span length and the beam spacing.

Composite section properties are required to perform the flexural analysis. The nomenclature for the A-shape composite section is defined in Figure D-6. Due to the section comprising of two material types, the concrete is converted to an equivalent steel width using a modular ratio (n). The modular ratio is simply the ratio between the modulus of elasticity of the steel and concrete.

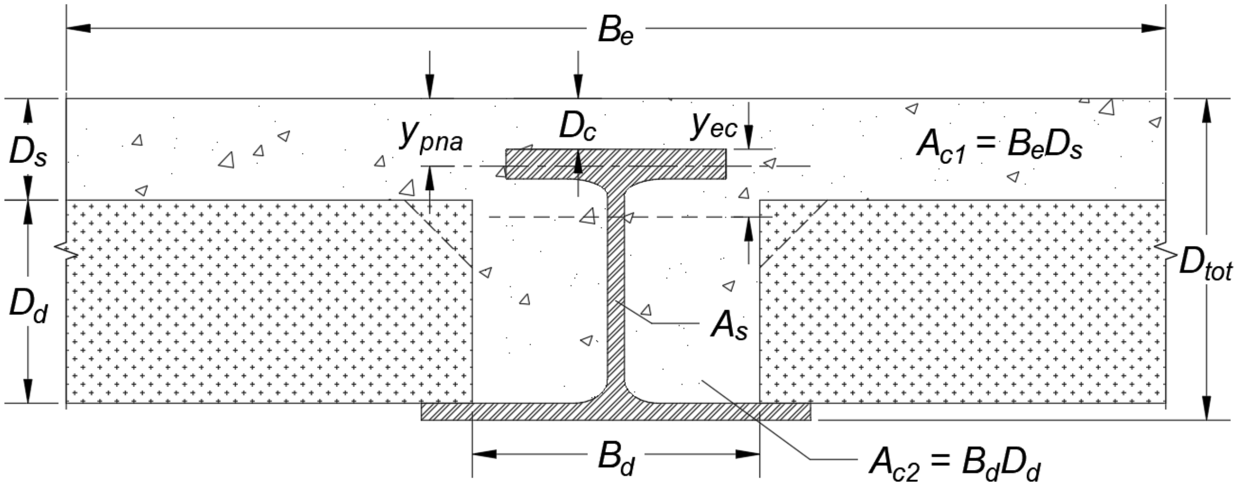

Figure D-6: Composite Section Nomenclature

The composite section is split into three areas to determine the elastic neutral axis (ENA) of the composite section (y_{ec}), referenced from the top of the steel section (Equation (D-4)). The three areas consist of the A-shape (A_s), the topping slab above the precast panels or the top of the deep decking (A_{c1}) and the beam encasement area (A_{c2}). The ENA of the A-shape (y_e) is determined with standard geometric decomposition. The moment of inertia of the A-shape (I_x) is determined using the cross-section properties of the A-shape and the parallel axis theorem. The moment of inertia for the composite section (I_{xc}) can be quantified with Equation (D-5).

$$y_{ec} = \frac{A_s y_e + \frac{A_{c1}}{n}\left(\frac{D_s}{2} - D_c\right) + \frac{A_{c2}}{n}\left(d - \frac{D_d}{2} - t_{fb}\right)}{A_s + \frac{A_{c1}}{n} + \frac{A_{c2}}{n}} \tag{D-4}$$

$$I_{xc} = I_x + A_s(y_e - y_{ec})^2 + \frac{A_{c1}D_s^2}{12n} + \frac{A_{c1}}{n}\left(\frac{D_s}{2} - D_c - y_{ec}\right)^2 + \frac{A_{c2}D_d^2}{12n} + \frac{A_{c2}}{n}\left(d - \frac{D_d}{2} - t_{fb} - y_{ec}\right)^2 \quad \text{(D-5)}$$

The full composite moment capacity is determined utilizing a plastic stress distribution. The steel A-shape is the only component that is considered to resist tensile stresses. The compressive stresses are resisted by the A-shape above the PNA and the concrete area from the topping slab, which has an effective width (B_e) and depth (D_s). The compressive resistance of the precast panel is conservatively not taken into consideration, even if the plastic neutral axis (PNA) is below the top of the precast panel. The PNA is established by ensuring that the combination of compressive forces in the concrete (C_c) and steel (C_s) is in equilibrium with the net tensile force (T) in the steel A-shape cross-section below the PNA.

The equations utilized to determine the compressive and tensile force resultants are dependent on the PNA location. There are five possible cases for the PNA. The first three cases are when the top of the precast panels or deep decking is below the bottom of the top flange. The PNA is either located in (1) the steel top flange, (2) in the steel web above the top of precast panels/deep decking, or (3) in the steel web but below the top of precast panels/deep decking. The final two cases consider if the top of precast panels/deep decking is above the bottom of the top flange. These cases consist of the PNA located in the (4) steel top flange or (5) the web.

The PNA generally falls into the steel top flange (Case 1), which means not all the topping slab is in compression (see Figure D-6). This is attributed in part to the minimum web thickness requirements discussed earlier for manufacturing. The concrete compressive force (assuming a rectangular stress block) and the steel compressive and tensile forces are determined using Equations (D-6) through (D-8). The depth of the PNA (y_{pna}) is determined by iteratively solving the equations below until equilibrium is satisfied (essentially the sum of the compressive forces is equal to the net tensile force).

$$C_c = 0.85f_c'\left[B_e D_c + \left(B_e - b_{ft}\right)\left(y_{pna} - D_c\right)\right] \quad \text{(D-6)}$$

$$C_s = F_y b_{ft}\left(y_{pna} - D_c\right) \quad \text{(D-7)}$$

$$T = A_s F_y - C_s \quad \text{(D-8)}$$

The centroidal locations of the three forces are determined after the PNA is identified. Centroids of the concrete and steel compressive forces and the tension force in the steel are found using standard geometric decomposition. For the other plausible PNA locations, similar equations were derived for the force components and locations of the forces. The full composite plastic moment capacity (M_{ncp}) is determined in Equation (D-9), which is the summation of moments due to the compressive forces in the concrete and steel about the tensile force centroid, with a moment arm of d_c and d_s, respectively.

$$M_{ncp} = C_c d_c + C_s d_s \quad \text{(D-9)}$$

To reduce fabrication/construction time and minimize the total depth of the floor system, no steel-headed stud anchors are used to transfer the longitudinal shear between the concrete and steel. Therefore, the full composite moment capacity determined with Equation (D-9) will likely not be achieved. However, partial composite action will form due to the bond between the steel and the concrete from encasement. This bond transfer is assumed to act around the top flange and steel web above the ENA of the cross-section with a uniform stress distribution, see Figure D-7(a) (Lawson et al. 1997). The cross-section will likely not reach the plastic state due to localized bond failure. Therefore, the stress distribution will be close to linear, and the bond surface that will transfer the longitudinal shear is assumed to be above the ENA only.

The first composite flexure limit state must determine the maximum compressive force that can be transferred between the concrete and steel from the bond shear (F_{bs}). Elastic shear flow is utilized for beams subjected to uniformly distributed load. See Figure D-7(b) for an illustration of the force that is transferred due to the formation of bond shear.

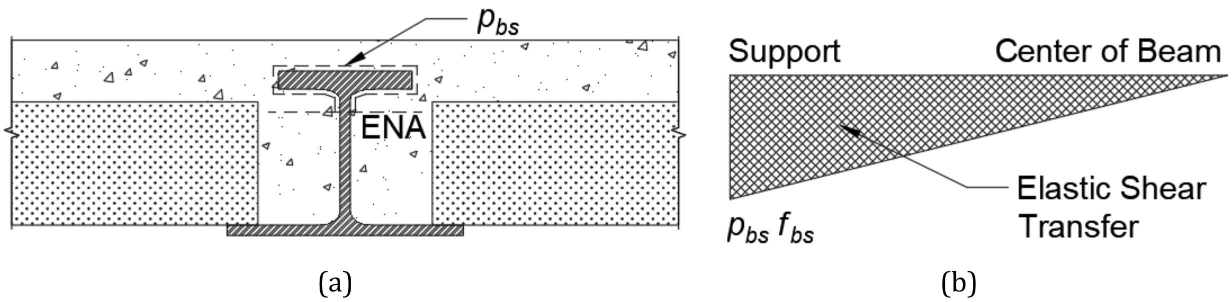

(a) (b)

Figure D-7: Bond Shear Action (a) Perimeter; (b) Elastic Shear Transfer

The bond shear capacity is dependent on the bond shear perimeter (p_{bs}) around the top flange and upper portion of the steel web, as calculated in Equation (D-10). The capacity is also a function of the allowable bond shear stress (f_{bs}). The allowable bond shear stress selected for this analytical sizing study is a constant value of 0.69 MPa (100 psi). The research team adopted this allowable bond stress which is a maximum value for filled composite members with rectangular cross sections (AISC 2022). In literature, there is a broad range of models and values for the allowable bond shear, some of which change with the concrete compressive strength (McCormac 1981). However, experimental push-out tests show that there is no distinct correlation between the allowable bond shear and the concrete compressive strength (Roeder et al. 1999). Further discussion on f_{bs} is provided at the end of this section. The maximum compressive force resistance (F_{bs}) is determined by calculating the resultant force that is transferred over half of the length of the beam, see Equation (D-11) and Figure D-7(b).

$$p_{bs} = 2(b_{ft} + y_{ec}) - t_w \qquad \text{(D-10)}$$

$$F_{bs} = p_{bs} f_{bs} \frac{L}{4} \qquad \text{(D-11)}$$

The partial composite moment capacity is linearly interpolated between the steel-only yield moment (M_{sy}) and the full composite moment capacity (M_{ncp}). Irrespective of the determined flexural capacity for the non-composite (steel-only) section during the construction limit states, the steel-only yield moment is implemented as the lower bound. This is the case because stability is not of concern once the concrete has cured because there is constant bracing of the section. Therefore, the steel can reach the minimum yield moment capacity of the compression or tension flange. For A-shapes, the compression flange yield moment, determined with the steel yield strength (F_y) and the elastic section modulus of the top flange (S_{xc}), will control due to the asymmetry. Furthermore, the web plastification factor (R_{pc}) is also included per Section F4 in the Specification for Structural Steel Buildings (AISC 2022). The lower bound compression flange yield moment is defined in Equation (D-12).

$$M_{sy} = R_{pc} F_y S_{xc} \tag{D-12}$$

The percentage of composite action is determined by evaluating the maximum allowable compressive force resistance from bond shear (F_{bs}) to the concrete compressive force (C_c) that forms in the slab if full composite action is achieved. See Equation (D-13) for the linear interpolation utilized to determine the partial composite moment capacity (M_{nc}) (Lawson et al. 1997).

$$M_{nc} = M_{sy} + \frac{F_{bs}}{C_c}\left(M_{ncp} - M_{sy}\right) \tag{D-13}$$

The second limit state evaluated for the composite flexural capacity is regarding a different failure mode of the longitudinal shear force transfer between the concrete and steel. The failure mode considered was from the precast panel to the edge of the top flange (line 1-2), across the width of the top flange (line 2-3), and down to the precast panel edge on the other side of the beam (line 3-4), shown by the dashed line in Figure D-8. The longitudinal shear force in the cross-section is transferred by the allowable bond stress between the concrete and steel (0.69 MPa (100 psi)) and the allowable concrete shear stress in Equation (D-14) (McCormac 1981). The longitudinal shear capacity, per unit length, is quantified with Equation (D-15).

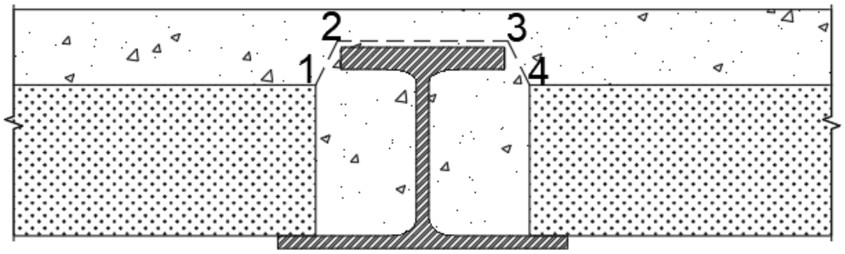

Figure D-8: Longitudinal Shear Transfer

$$f_{cs} = 0.12 f'_c \tag{D-14}$$

$$v_{bs} = 2 f_{cs} d_{1-2} + f_{bs} b_{ft} \tag{D-15}$$

The longitudinal shear limit state ensures that the force developed in the concrete does not crack due to in-service loading. The loading demand utilized is dependent on whether the floor system is shored during construction. For floor systems that utilize precast panels, unshored construction is likely to be utilized due to the panel span capabilities. Therefore, the load demand resisted by the longitudinal shear for unshored construction is only due to the in-service live load.

To evaluate the longitudinal shear demand per unit length (v_d), the maximum shear flow due to the load demand is obtained. The shear flow is dependent on the maximum vertical shear force (V) due to live (and possibly dead) loads. The first moment of area (Q) of the concrete above line 1-2-3-4 in Figure D-8 and the moment of inertia of the composite section (I_{xc}) (Equation (D-5)) are also utilized.

$$v_d = \frac{VQ}{I_{xc}} \tag{D-16}$$

In conclusion, both limit states evaluating the composite flexural strength are highly dependent on the allowable bond shear stress (f_{bs}). This bond shear stress has relatively high uncertainty. There is an array of prediction models for f_{bs} in the literature, producing a wide range of results. A parametric study addressing the wide range of results is conducted in the Analyzing the effect that Varying Bond Shear has on the Composite Analysis section below. In addition, the Future Research section provides plans to address this uncertainty.

Serviceability Checks

The final limit states (two deflection and one vibration) ensure the comfort of residents who are occupying the building. Deflections of the floor system are dependent upon the type of construction that is used. Evaluating deflections for unshored construction is the most complex because construction dead loads are supported by the A-shape alone. The dead load (w_1) deflection is evaluated with the A-shape moment of inertia (I_x) while the live load (w_2) is evaluated with the composite moment of inertia (I_{xc}). Both terms utilize the Young's modulus of steel (E_s) since the concrete was converted to an equivalent steel width. The combination of the deflection in Equation (D-17) yields the total deflection for the floor system at the midspan of an unshored system (AISC 2023). If shored construction is utilized, the concrete will cure in the shored position; therefore, the deflection due to live load and dead load is determined with composite section properties. Therefore, in Equation (D-17), the w_1 term is zero, and both the dead (DL) and live load (LL) are included in w_2.

$$\delta = \frac{5w_1L^4}{384E_sI_x} + \frac{5w_2L^4}{384E_sI_{xc}} \tag{D-17}$$

A common industry practice is to camber steel beams to satisfy the deflection criteria. Cambering the beams also produces a floor that is flatter in the final constructed state, which will improve the comfort of the residents. Specifying camber is accomplished with approximately 80% of the dead load to ensure the camber is removed from the beam. However, a minimum camber of 19 mm (0.75 in.) is commonly required by fabricators. The deflection quantified with Equation (D-17) will be decreased by the specified camber. To ensure resident comfortability, deflections from dead and live loads shall be less than the beam span length (L) divided by 240 and live load deflection shall be less than the span length divided by 360 (IBC 2018).

Vibrations in steel floor systems can cause discomfort to residents depending on their activity. For instance, people working in an office or at their home are more sensitive to movement than people at a shopping mall or on pedestrian bridges (Murray et al. 2016). To satisfy the vibration limit state, the ratio of the peak floor acceleration to gravity (a_p/g) of the floor system due to loading must be below the tolerant vibration levels for human comfort (a_o/g) (Murray et al. 2016).

The composite elastic neutral axis and moment of inertia, calculated with Equations (D-4) and (D-5), respectively, are adjusted for dynamic analysis. The modulus of elasticity of concrete (E_c) is increased by 35% which modifies the modular ratio for vibration (n_v) (Murray et al. 2016). The modular ratio for vibration (n_v) replaces the modular ratio (n) in Equations (D-4) and (D-5) to quantify the increase in stiffness of the concrete deck during dynamic loading compared to static loading (Murray et al. 2016).

The natural frequency (f_n) is estimated based on the deflection of the floor system in Equation (D-18). Vibrations are usually the most severe when the floor is lightly loaded; therefore, expected day-to-day dead and live loads are utilized (Murray et al. 2016). Loadings consist of the structural dead load, an additional 0.19 kPa (4 psf) for mechanical and ceiling installations, and 0.29 kPa (6 psf) for live load in a residence (Murray et al. 2016). The deflection for vibration (δ_v) is quantified with Equation (D-17) for the expected day-to-day loading in w_2, w_1 is set to zero, and the vibration altered composite moment of inertia $\left(I_{xc,v}\right)$ is utilized.

$$f_n = 0.18\sqrt{\frac{g}{\delta_v}} \tag{D-18}$$

The loading type producing the most severe dynamic response is a result of the natural frequency of the floor system. For low-frequency floors, $f_n < 9\ Hz$, the dynamic response is governed by the floor undergoing resonance from continuous footsteps. For high-frequency floors, $9\ Hz < f_n < 15\ Hz$, impulse response due to single footsteps governs the dynamic response. Floor systems with a natural frequency above 15 Hz are not known to be prone to excessive vibration (Murray et al. 2016).

The normalized peak floor acceleration response $\left(a_p/g\right)$ due to resonance is quantified in Equation (D-19). The amplitude of the driving force (P_o) is a constant value of 29.5 kg (65 lbs) (Murray et al. 2016). A damping ratio (β) of 3% was assumed considering the structural system, ceiling and ductwork, furniture in the residence, and possible partitions (Murray et al. 2016). The effective panel weight $\left(W_p\right)$ supported by the A-shape is also needed.

$$\frac{a_p}{g} = \frac{P_o e^{-0.35 f_n}}{\beta W_p} \tag{D-19}$$

Peak floor acceleration response $\left(a_p/g\right)$ due to impulse is quantified in Equation (D-20) utilizing the damping ratio (β), natural floor frequency (f_n), and the effective panel weight $\left(W_p\right)$. The footstep frequency $\left(f_{step}\right)$ is determined based on the step frequency harmonic matching the natural frequency (h_s) (Murray et al. 2016).

$$\frac{a_p}{g} = \left(\frac{154}{W_p}\right)\left(\frac{f_{step}^{1.43}}{f_n^{0.3}}\right)\sqrt{\frac{1 - e^{-4\pi h_s \beta}}{h_s \pi \beta}} \tag{D-20}$$

The peak floor acceleration response, either from resonance or impulse, is quantified and evaluated to the tolerant vibration levels for human comfort (a_o/g) (Murray et al. 2016). The vibration limit state was included in the analytical sizing study to investigate conventional residential facilities. However, a building-specific vibration analysis should be performed.

Final A-Shapes

A-shape cross-sectional geometries were established, ensuring the limit states above were satisfied, which considers manufacturing, construction, and in-service conditions for residential buildings. As desired by the steel mills, the number of established cross-sections was kept to a minimum. Two primary 203 mm (8.0 in.) A-shape cross-sections (A8s) were developed from the devised methodology. As stated earlier, a live load for private rooms and corridors, 1.9 kPa (40 psf) and 4.8 kPa (100 psf), respectively, were used to establish the two cross-sectional geometries for a 6.1 m (20 ft) square grid. In addition, two 254 mm (10.0 in) and two 305 mm (12.0 in) A-shapes (A10s and

A12s, respectively) were developed (using the same live loading) in the event slightly deeper sections were desired. The A10s were established for a 7.0 m (23 ft) square grid, whereas the A12s were established for a 7.9 m (26 ft) square grid. Due to space limitations, only the A8s are further explained below and utilized for the parametric sensitivity study in the following section.

The most efficient beam cross-sectional geometry that satisfied all limit states for each live load case was selected. The established cross-section for live load in private rooms, deemed A8 light, was selected from a minimum limit state plot, as shown in Figure D-9. Points with a capacity-to-demand ratio greater than 1.0 satisfy all limit states previously discussed. The controlling limit state for the A8 light cross-section is the composite flexural capacity of the A-shape (Load Case 3). The cross-sectional geometry for corridor loading, deemed A8 heavy, was established in a similar manner, which is controlled by composite flexural capacity (Load Case 3). In addition, sizing the A10s and A12s utilized the same approach and had the same controlling limit states. Further information on the controlling limit states for different beam lengths and spacings is provided within the parametric studies in the following section.

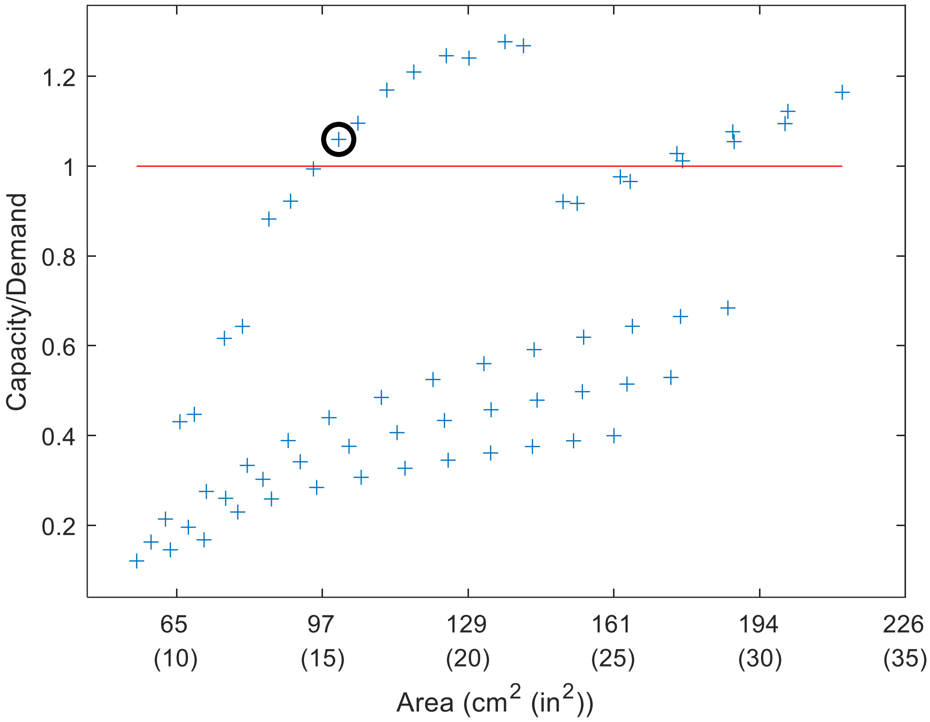

Figure D-9: Minimum Limit States – 1.9 kPa (40 psf) Live Load

The minimum limit state plots were utilized to establish efficient and effective cross-section geometries. The dimensions of the cross-section with the least area (also weight) that satisfied all limit states were altered slightly for standard dimensioned flanges. The two primary A8 established cross-sections are shown to scale in Figure D-10. Figure D-11 provides the cross-sectional geometry and section properties of all established cross-sections, both in English and SI units for each cross-section.

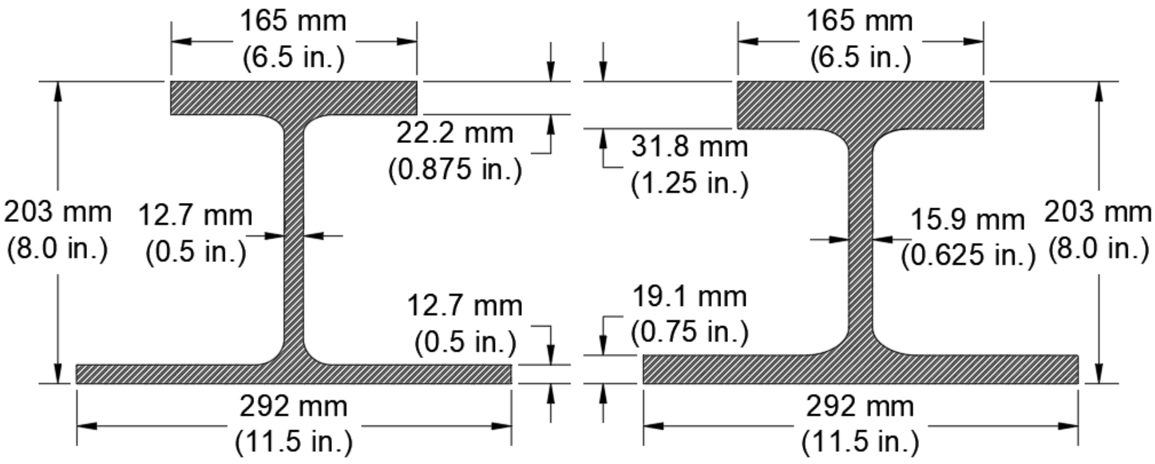

(a) (b)

Figure D-10: Established A8 Cross-Sections: (a) A8x52 and (b) A8x72

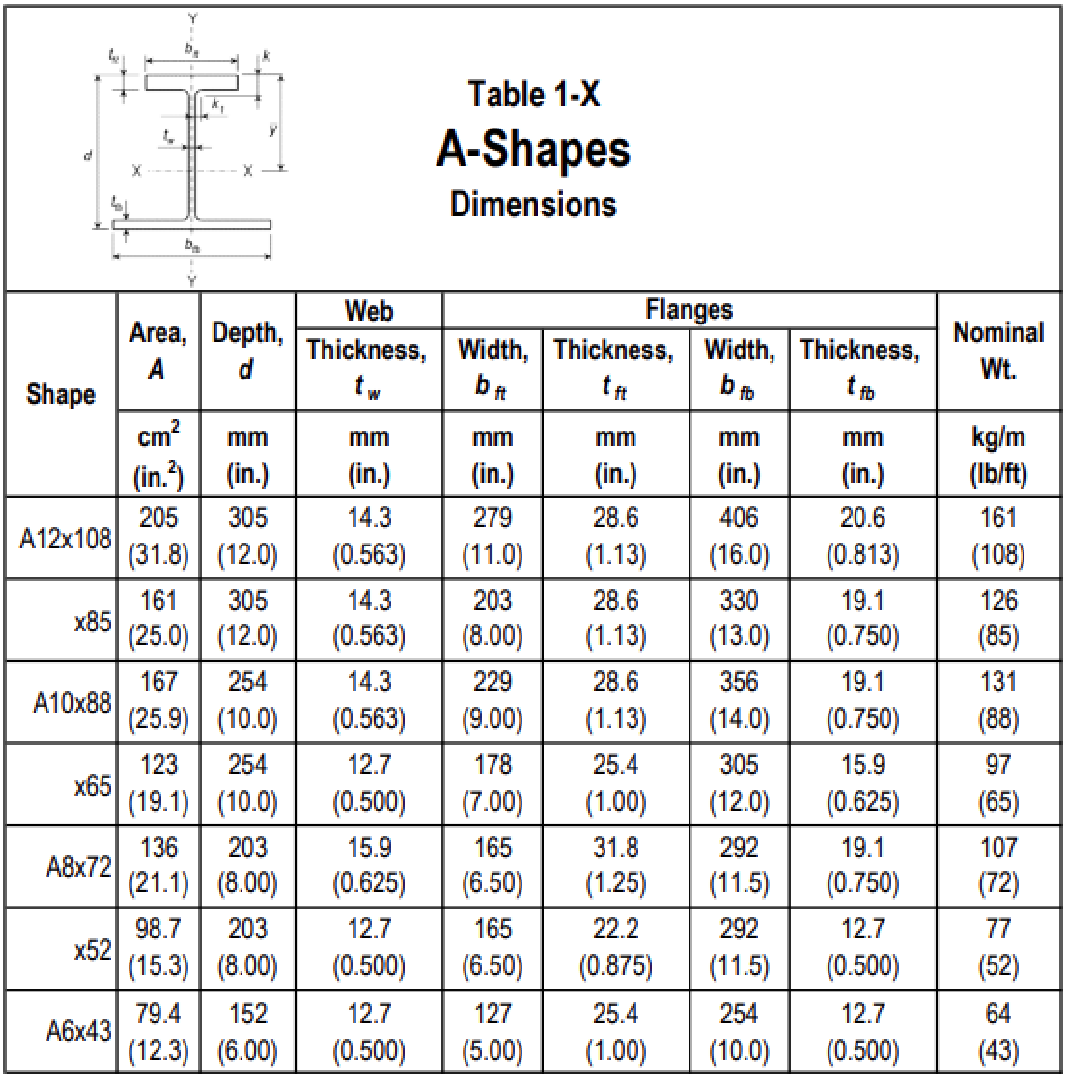

Table 1-X

A-Shapes

Dimensions

Shape	Area, A	Depth, d	Web	Flanges				Nominal Wt.
			Thickness, t_w	Width, b_{ft}	Thickness, t_{ft}	Width, b_{fb}	Thickness, t_{fb}	
	cm^2 (in.^{2})	mm (in.)	mm (in.)	mm (in.)	mm (in.)	mm (in.)	mm (in.)	kg/m (lb/ft)
A12x108	205 (31.8)	305 (12.0)	14.3 (0.563)	279 (11.0)	28.6 (1.13)	406 (16.0)	20.6 (0.813)	161 (108)
x85	161 (25.0)	305 (12.0)	14.3 (0.563)	203 (8.00)	28.6 (1.13)	330 (13.0)	19.1 (0.750)	126 (85)
A10x88	167 (25.9)	254 (10.0)	14.3 (0.563)	229 (9.00)	28.6 (1.13)	356 (14.0)	19.1 (0.750)	131 (88)
x65	123 (19.1)	254 (10.0)	12.7 (0.500)	178 (7.00)	25.4 (1.00)	305 (12.0)	15.9 (0.625)	97 (65)
A8x72	136 (21.1)	203 (8.00)	15.9 (0.625)	165 (6.50)	31.8 (1.25)	292 (11.5)	19.1 (0.750)	107 (72)
x52	98.7 (15.3)	203 (8.00)	12.7 (0.500)	165 (6.50)	22.2 (0.875)	292 (11.5)	12.7 (0.500)	77 (52)
A6x43	79.4 (12.3)	152 (6.00)	12.7 (0.500)	127 (5.00)	25.4 (1.00)	254 (10.0)	12.7 (0.500)	64 (43)

Figure D-11: Established A-Shape Geometry

Parametric Sensitivity Studies

The analytical sizing study employed various parameters that might vary for specific buildings. Parametric studies were conducted to investigate the impacts these assumptions have on sensitive limit states of the established cross-section geometries. Each study involved adjusting a specific parameter while keeping other parameters constant at their assumed values. Bar charts are included for each parametric study with sensitive limit states to investigate the sensitivity to a specific parameter. The ensuing parametric studies discussed herein were conducted on the A8 light cross-section (A8x52), except for the length and spacing study. Similar trends can be observed for the other A-shapes.

Utilizing Varying Concrete Strengths

An examination was conducted on the impact of using concrete topping slabs with varying strengths, both below and above the analytical sizing study value of 27.6 MPa (4000 psi). Concrete strengths ranging from 20.7 MPa (3000 psi) to 41.4 MPa (6000 psi) were investigated for typical concrete strengths. Figure D-12 displays the critical limit states affected by changes in concrete strength. It should be noted that other limit states have capacity-to-demand ratios that are slightly above 1.0. However, they are omitted from this analysis as they are not sensitive to changing concrete strengths. These limit states encompass non-composite flexure and compression flange yielding. For example, the vibration limit state has a capacity-to-demand ratio of approximately 1.1 for 20.7 MPa (3000 psi) concrete. Increasing the concrete strength to 27.6 MPa (4000 psi) increases the capacity-to-demand ratio to approximately 1.2, indicating a direct relationship between the vibration limit state and increasing concrete strength.

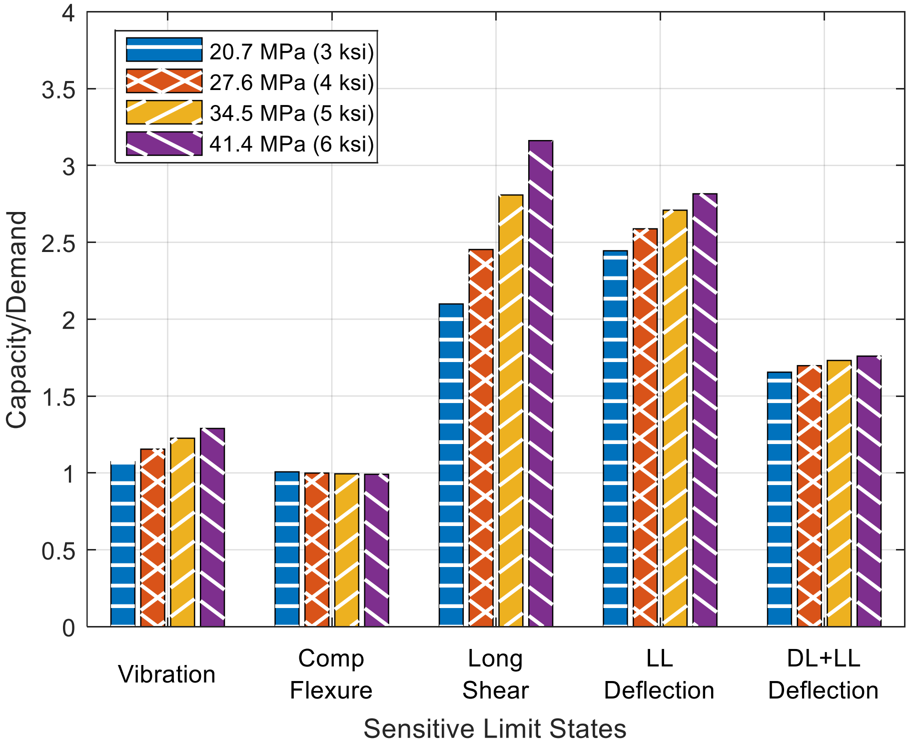

Figure D-12: Concrete Strength Sensitivity Study

Deflection limit states show improved performance (higher capacity-to-demand ratio) with increasing concrete strength due to increased stiffness. The modular ratio between steel and concrete decreases with increasing concrete strength, consequently enlarging the equivalent width of steel that was converted from concrete, thereby increasing the composite moment of inertia. Live load deflection has a percentage change from the base case of approximately 5% per 6.9 MPa (1.0 ksi). Dead load plus live load deflection is less sensitive and has roughly a 2% change per 6.9 MPa (1.0 ksi).

The vibration limit state is dependent on the natural frequency of the floor system. The natural frequency is inversely proportional to the deflection, which implies that the frequency is directly proportional to the stiffness. Vibration in the floor, quantified by a peak acceleration due to walking, decreases with increasing natural frequency. Therefore, as the stiffness of the floor system increases, the vibration capacity-to-demand ratio also increases. The vibration limit state has a percentage change of approximately 6% per 6.9 MPa (1.0 ksi).

Due to the assumed constant value for concrete-steel bond strength, composite (Comp) flexure does not directly depend on concrete strength. There are minimal differences, around 0.5% change per 6.9 MPa (1.0 ksi), in the capacity-to-demand ratio as the concrete strength varies. It should be noted if the bond strength was assumed to be a function of the concrete strength, the capacity-to-demand ratio for composite flexure would increase as the concrete strength is increased. The longitudinal (Long) shear limit state is dependent on the concrete strength (see Equation (D-15)). Elevated concrete strength leads to increased longitudinal shear strength, resulting in a higher capacity-to-demand ratio. However, the bond shear between steel and concrete remains sensitive and uncertain, observed in a variety of models used in literature. The longitudinal shear limit state is the most sensitive to varying concrete strengths and the capacity-to-demand ratio has a 14% change per 6.9 MPa (1.0 ksi). Refer to Future Research for more on this topic and plans to address the uncertainty.

Impact of using Light and Normal-Weight Concrete

The effect of employing a lighter concrete weight was explored, contrasting the analytical sizing study's use of normal-weight concrete. This examination encompassed two concrete types: lightweight (LWC) and normal-weight concrete (NWC). LWC has a density of 1800 kg/m^3 (110 pcf) compared to NWC, which has a density of 2300 kg/m^3 (145 pcf). This parametric study yielded interesting results, as seen in Figure D-13.

Limit states for non-composite (NC) flexure, compression flange (CF) yielding due to a torsional moment, and composite (Comp) flexure have an increasing capacity-to-demand ratio when utilizing LWC. The percentage change when using LWC rather than NWC is 9% for non-composite flexure, 3% for compression flange yielding due to torsion, and 6% for composite flexure. The reduced demand for the A-shape and composite section is attributed to the lighter concrete density.

Utilizing LWC, the vibration limit state is the opposite and does not pass the tolerable level for human comfort. Vibrations have the greatest magnitude when the floor system is lightly loaded; therefore, utilizing LWC contributes to the inadequate limit state. The stiffness of the composite floor system decreases when utilizing LWC since the modulus of concrete is reduced. As previously discussed, the capacity-to-demand ratio for vibration is directly proportional to the stiffness. Further, the vibration limit state has a 20% decrease when LWC is utilized compared to NWC.

The reduction in stiffness also contributes to the dead and live load deflection capacity-to-demand ratio, which is the most sensitive limit state and has a 22% decrease when LWC is utilized. The composite section is less stiff; therefore, the deflection from service live load increases (which leads to a decreasing capacity-to-demand ratio). A second factor is the amount of camber that can be applied to the A-shape when utilizing LWC due to the magnitude of dead load deflection.

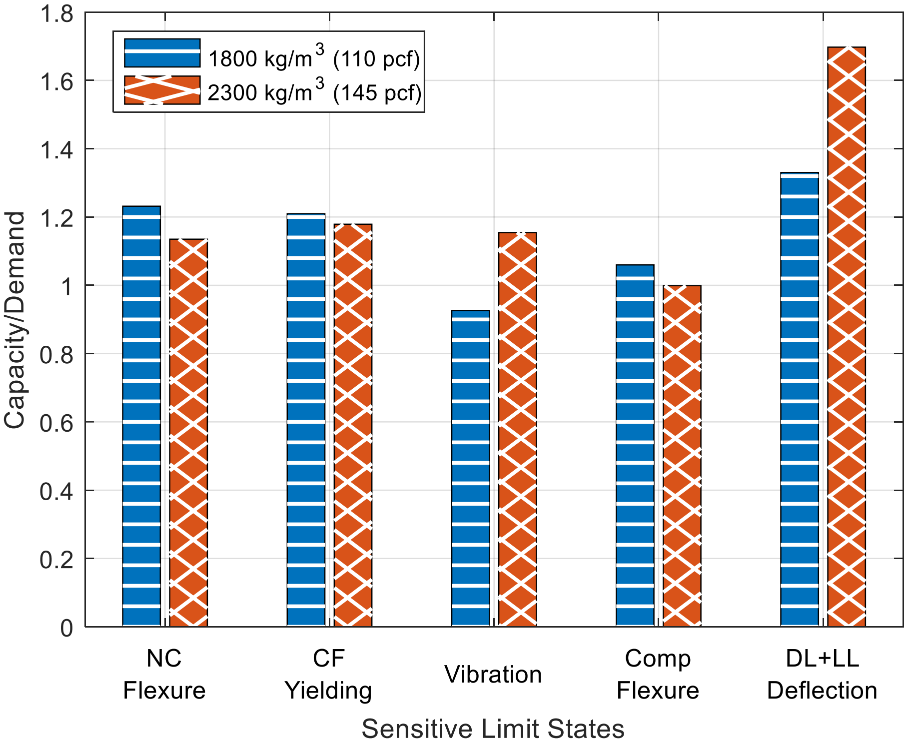

Figure D-13: Concrete Weight Sensitivity Study

Adjusting the Thickness of the Concrete Topping Slab

A parametric study was conducted on the depth of the concrete topping above the steel A-shape; hence, altering the total height of the floor system. The topping thicknesses above the A-shape considered were 38.1 mm (1.5 in.) (utilized in the analytical sizing study), 50.8 mm (2 in.), and 63.5 mm (2.5 in.). Increasing the thickness above the steel increases strength and stiffness; however, the dead load is also increased which diminishes the effectiveness. The parametric sensitivity study is shown in Figure D-14. A topping thickness of 25.4 mm (1 in.) was not investigated, as the minimum topping thickness to consider composite action is 30 mm (1.2 in.) (Rackham et al. 2006) and to allow for temperature and shrinkage steel to be placed on top of the beam. The subsequent discussion focuses on the sensitive limit states and observed trends.

The limit states involving non-composite (NC) flexure, compression flange (CF) yielding due to a torsional moment, composite (Comp) flexure, and dead (DL) plus live load (LL) deflection have similar trends as observed in the case of different concrete types. This similarity arises from the increased demand for the A-shape and composite section with a thicker concrete topping, resulting in a decreased capacity-to-demand ratio. When the total cross-section height is increased by 13 mm (0.5 in.), the percentage decrease for non-composite flexure is roughly 5%, approximately 2% for compression flange yielding due to torsion, around 3% for composite flexure, and is about 9% for dead plus live load deflection. However, in terms of the vibration limit state, the capacity-to-demand ratio improves appreciably as there is more dead load applied. Vibration is the most sensitive limit state to modifying the topping slab thickness (total height of the cross-section) and the capacity-to-demand ratio has a 17% increase per 13 mm (0.5 in.) of total floor depth.

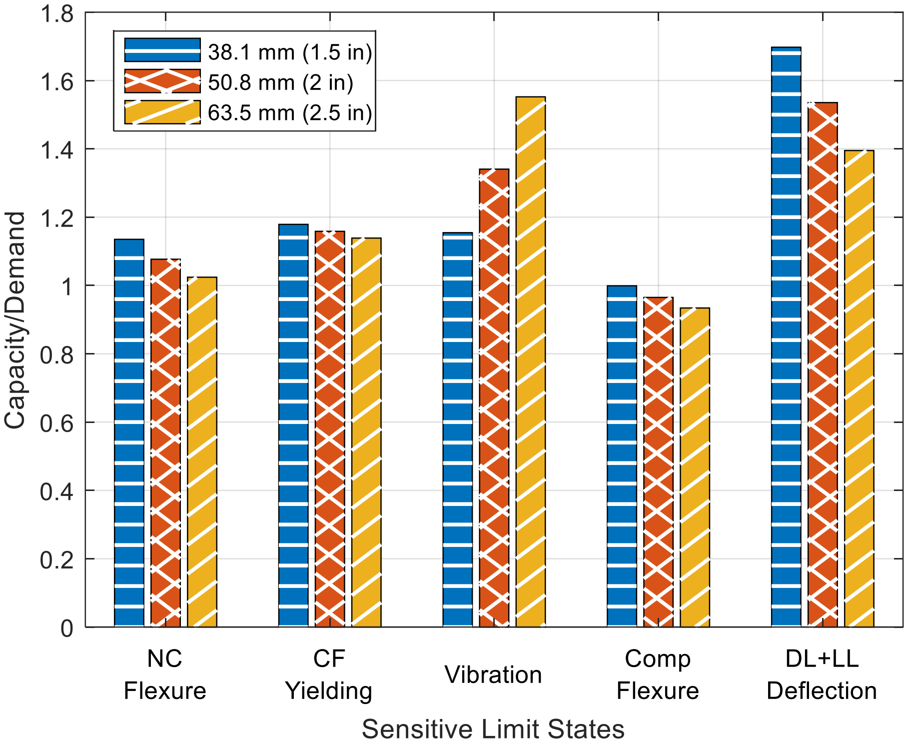

Figure D-14: Concrete Topping Sensitivity Study

Service Live Load for Various Facilities

A study was conducted to assess the beam's performance under increased service live loads for various facilities. Live loads of 1.9 kPa (40 psf) for residential buildings, 2.4 kPa (50 psf) for office buildings, and 2.9 kPa (60 psf) for operating rooms in a hospital were applied (ASCE 2022). As depicted in Figure D-15, the A8 light cross-section is satisfactory for all limit states under only the 1.9 kPa (40 psf) live loading. The limit states were evaluated across all service live loads for a 6.1 m (20 ft) square grid. However, the A8 light cross-section would be satisfactory for higher service loads for other grid layouts (refer to the Length and Spacing Analysis for Various Grid Layouts section for further discussion). The sensitive limit states are composite (Comp) flexure, longitudinal (Long) shear, and both deflection checks. With increasing service live loads, each limit state showed a decreasing capacity-to-demand ratio. Longitudinal shear and live load deflection are much more sensitive to changing the live load. Note that non-composite flexure and compression flange yielding limit states are not sensitive to varying live load, but the capacity-to-demand ratio is close to 1.0. Composite flexure has a percentage decrease of about 6% per 0.48 kPa (10 psf) of live loading, whereas dead plus live load deflection has a 9% decrease per 0.48 kPa (10 psf). Longitudinal shear and live load deflection are the most sensitive with roughly an 18% decrease when the live load is increased by 0.48 kPa (10 psf).

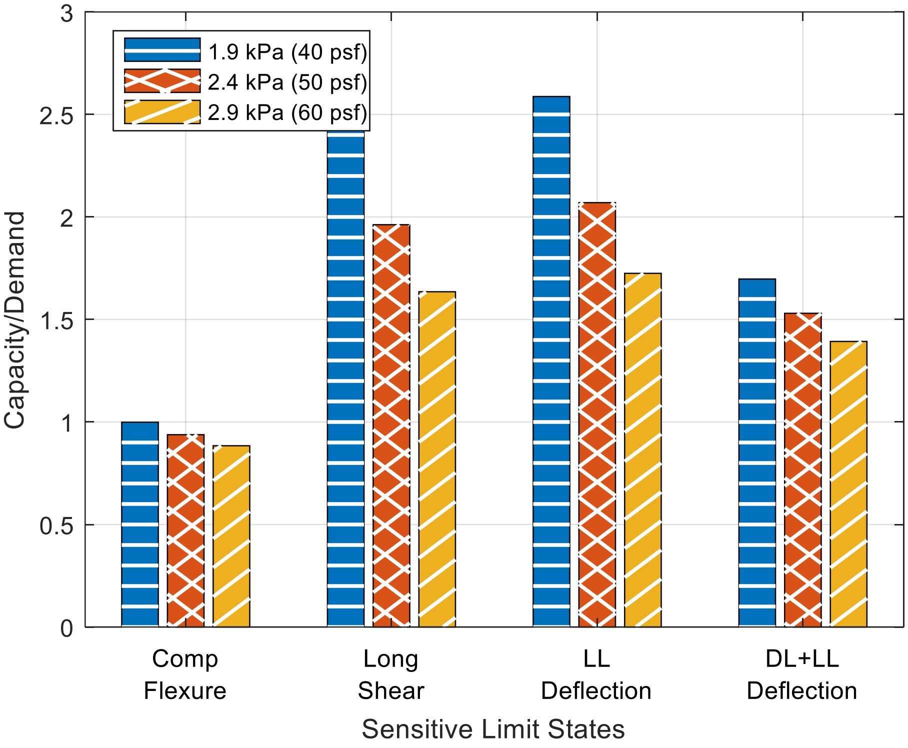

Figure D-15: Service Live Load Sensitivity Study

Analyzing the effect that Varying Bond Shear Strength has on the Composite Analysis

A parametric study examined the bond shear strength between concrete and steel to assess its impact on the critical limit states. The sizing study utilized a constant bond strength of 0.69 MPa (100 psi); however, various analytical models in the literature yield different values. In addition, the bond shear stress can be improved due to enhanced surface preparations, such as embossments on the top flange to increase the roughness or having web openings in the cross-section. However, to keep the shape as simple as possible, no additional mechanisms other than natural concrete-steel bond shear are being utilized to develop composite action. Bond shear strengths ranging from 0.41 MPa (60 psi) to 0.83 MPa (120 psi) were employed in the parametric study to investigate the impact that the assumed constant value has on the composite analysis. The bond strength was assumed to be independent of the compressive strength, and the bond strength was altered. Only two limit states were sensitive to changing the bond strength: composite (Comp) flexural capacity and longitudinal (Long) shear.

The partial composite flexural capacity is a function of the bond strength. As explained in the Composite Flexure during Service Loading section, the partial composite flexural capacity is linearly interpolated between the steel yield moment and the full composite moment capacity. The degree of composite action is quantified by the resultant of the longitudinal shear formed by the bond shear between the concrete and steel. Therefore, as the bond strength decreases, the degree of partial composite action also decreases. Though the sensitivity is minimal for this limit state and with a relatively low bond strength, the A8 light capacity-to-demand ratio is slightly under 1.0 for lower bond stress values. The capacity-to-demand ratio has a percentage change of about 1.5% when the bond shear strength is varied by 0.14 MPa (20 psi).

The longitudinal shear limit state ensures that the concrete and bond shear strength along a plausible failure plane – from the edge of the precast concrete panel, along the top flange, and back down to the precast panel – can withstand the loading on the composite section. As seen in Figure D-16, the longitudinal shear limit state is more sensitive than the composite flexural capacity and varies by 6% when the bond shear strength has a 0.14 MPa (20 psi) change. However, it is not the controlling limit state for the A8 light section. Note that non-composite flexure and compression flange yielding have a capacity-to-demand ratio near 1.0; however, they are not sensitive to varying bond shear strength.

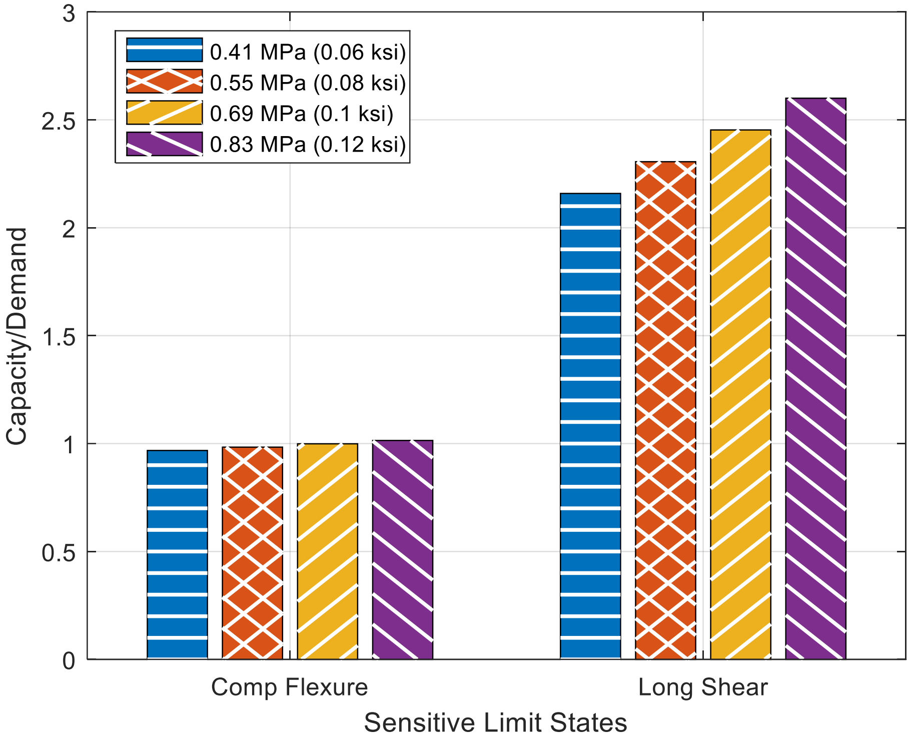

Figure D-16: Bond Shear Sensitivity Study

Length and Spacing Analysis for Various Grid Layouts

The final parametric study investigated a multitude of grid layouts by varying the length and spacing of the A-shape. The grid layout was altered to examine the effectiveness of the established A-shape geometry for a wide range of grid layouts, as the grid layout of structures will vary from the assumed square grid layout of 6.1 m (20 ft). The analysis conducted assumes that the beams are framed into columns directly and supports the entire tributary load. The beam lengths were altered between 3 m (10 ft) and 7.6 m (25 ft), and the beam spacings were altered between 3 m (10 ft) and 9.1 m (30 ft), both values altered in 0.3 m (1 ft increments). All limit states for small grid layouts are likely to be sufficient since the cross-sectional geometry was established for a 6.1 m (20 ft) by 6.1 m (20 ft) grid layout. However, the smaller grid dimensions were included to investigate a longer length with a smaller spacing and vice versa. Figure D-17 utilizes the assumed parameters for the A8 light (service live load of 1.9 kPa (40 psf)).

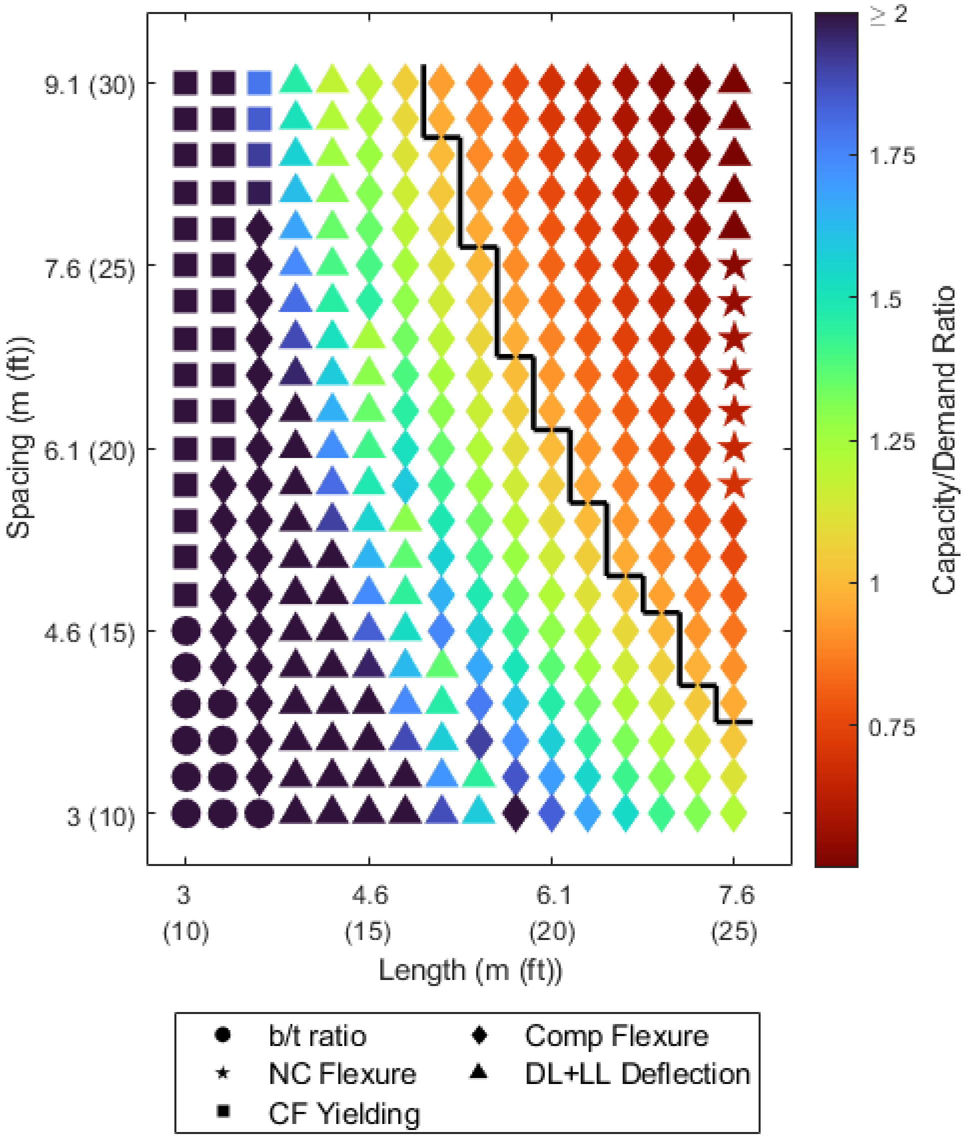

Figure D-17: A8 Light 1.9 kPa (40 psf) - Length versus Spacing

The established A8 light section performs satisfactorily for numerous grid layouts. The non-satisfactory grid layouts are above and to the right of the pass/fail threshold line in Figure D-17. The controlling limit state (the minimum capacity-to-demand ratio) is identified for each of the grid layouts with varying shapes. For example, Figure D-17 demonstrates the cross-section's adequacy for grid dimensions with a length of 7.6 m (25 ft) and spacing of 3.4 m (11 ft). The A-shape is also satisfactory for wider beam spacings with shorter lengths, such as a spacing of 9.1 m (30 ft) if the length is 4.6 m (15 ft). For both grid layouts mentioned above, the controlling limit state is composite flexure as indicated by the square symbol.

The A8 heavy cross-section (A8x72) was also investigated to examine the grid layout capability for a service live load of 1.9 kPa (40 psf), despite being originally sized for a 4.8 kPa (100 psf) live load. The beam lengths varied between 4.6 m (15 ft) to 9.1 m (30 ft) with the same beam spacing as the prior study since the cross-section was established for corridor loading with both a length and spacing of 6.1 m (20 ft). As seen in Figure D-18, the A-shape is suitable for much larger grid layouts. The A8 heavy can achieve a grid layout with a length and spacing of 6.1 m (20 ft) and 8.5 m (28 ft), respectively. As the length increases, the satisfactory grid dimensions stairstep downwards as the spacing decreases. The controlling limit state of grid layouts on the threshold line utilizing the A8 heavy is the flexural capacity of the composite cross-section during service loading (Load Case 3).

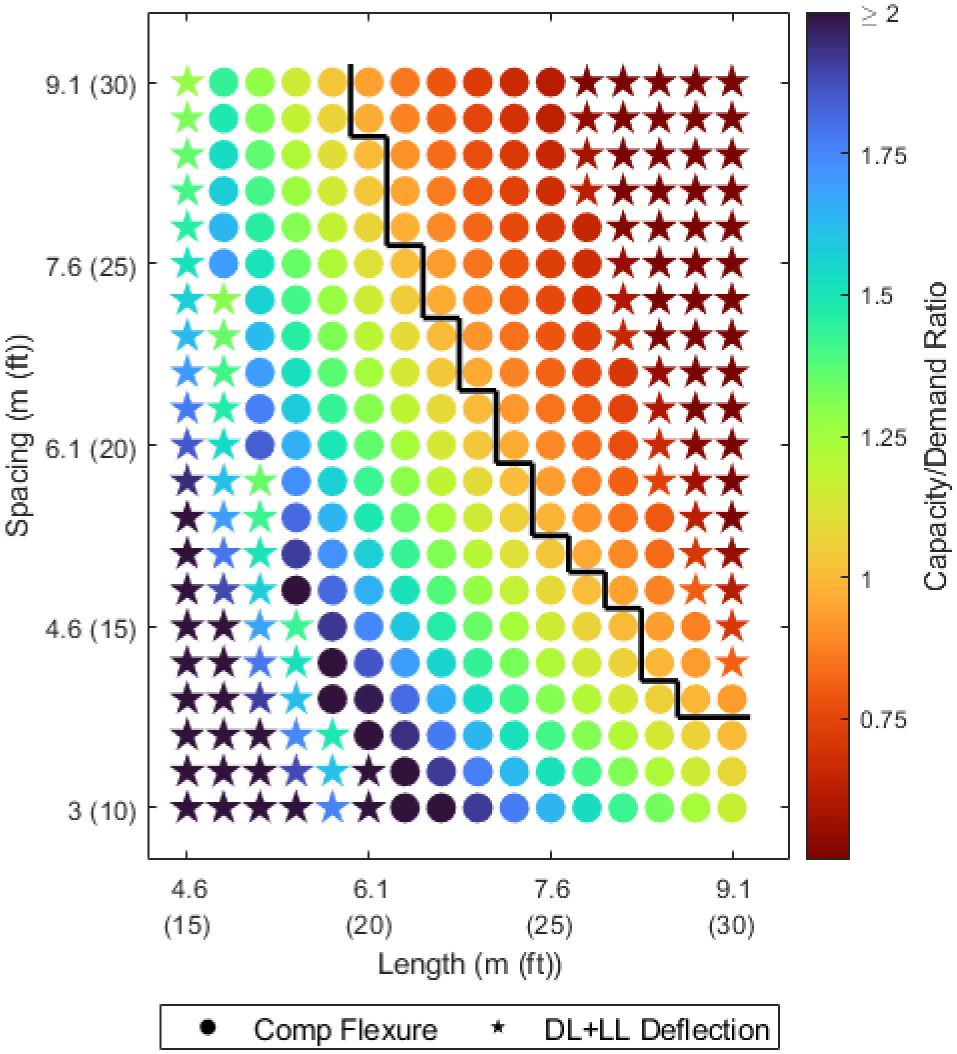

Figure D-18: A8 Heavy 1.9 kPa (40 psf) - Length versus Spacing

To fully understand the capabilities of the A8 heavy cross-section, corridor loading of 4.8 kPa (100 psf) was investigated over grid dimensions ranging from 3 m (10 ft) to 9.1 m (30 ft) (see Figure D-19). The A-shape has satisfactory limit states for a multitude of grid layouts. Layouts with lengths and spacings of 5.2 m (17 ft) and 9.1 m (30 ft), respectively, to a length of 7.3 m (24 ft) with a 4.3 m (14 ft) spacing are satisfactory. The controlling limit states when considering corridor loading is the composite moment capacity (Load Case 3) for grid layouts on the threshold line.

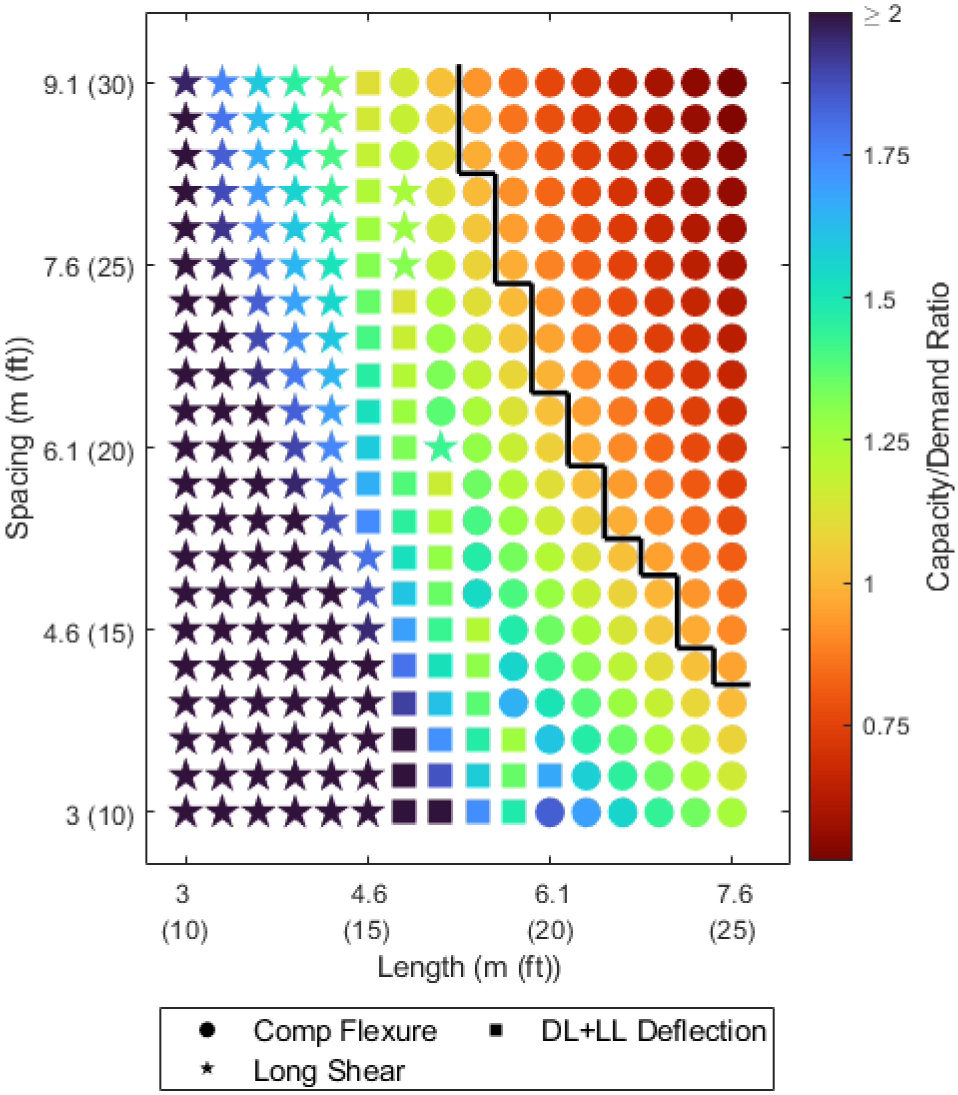

Figure D-19: A8 Heavy 4.8 kPa (100 psf) - Length versus Spacing

Conclusions

The overarching contribution of this research was the development of standardized A-shapes for large-scale production in US steel mills. The cross-sectional geometry of the A-shapes was established considering manufacturing considerations gained from expert feedback through interviews with three major steel mills. Previous investigations encompassing residual stress analysis and a full-scale feasibility experiment substantially informed the analytical sizing study. A multitude of cross-sections were investigated to establish efficient cross-sections. This comprehensive exploration led to the scrutiny of 65 viable A-shape geometries (per beam depth) across 16 crucial limit states that considered construction and in-service behavior for residential buildings. The study involved simulated construction loads, rigorously testing structural integrity and feasibility for the possible use in residential buildings. Employing A-shapes, that are hot-rolled at a steel mill, in structural systems is significant because it will help reduce fabrication time compared to built-up asymmetric beams. Reducing time will help lead to cost savings for steel buildings and help achieve AISC's "need for speed" initiative (AISC 2024). Furthermore, utilizing shallow-depth composite floor systems will help reduce the floor-to-floor height and could reduce the total height of a structure.

A robust framework was developed to establish A-shape cross-sections for the previously mentioned considerations. This framework was conducted to establish two primary A8 cross-sections suitable for residential applications, complemented by additional A10 and A12 variants. The established A8 cross-sections were investigated in parametric sensitivity studies to evaluate the impact if parameters other than those within the analytical sizing study were used (e.g., lightweight versus normal-weight concrete). This exploration unveiled sensitive limit states and enhanced comprehension regarding the impact of parameter adjustments.

The main findings from the parametric studies for the established A8 cross-sections underscore the heightened sensitivity of the longitudinal shear criterion and the pivotal importance of precisely gauging the bond shear strength between concrete and steel. See the following section for future experimental testing to investigate the bond shear strength. Both established A8 cross-sections have a wide range of grid layouts that can be achieved for a cross-section that was established for a 6.1 m (20 ft) square grid. Specifically, the A8 heavy cross-section demonstrated satisfactory performance with a beam length of 6.1 m (20 ft) and a spacing of 8.5 m (28 ft) for a live load of 1.9 kPa (40 psf), meeting all stipulated limit states under specific load and dimensional residential conditions, reinforcing its versatility for varied applications. The completed sizing and parametric study could be utilized to include potential implementation in commercial or industrial settings.

Future Research

Future research will include component beam tests to investigate the composite behavior of the partially encased shallow-depth steel-concrete composite floor system. The tests are designed to gain a better understanding of the bond strength between the concrete and steel to address the uncertainty and sensitivity of the longitudinal shear limit state. Furthermore, the predicted partial composite flexural capacity (previously discussed) will be compared to the experimental composite strength to further validate the methodology. The component beam tests will also indicate the degree of ductility in the floor system when loaded until failure. Finally, the failure mechanism of the component beam tests will be investigated.

In addition to the component beam tests, a full-scale laboratory experiment will be conducted. The experiment will utilize one of the A8 cross-sections established in this study and steel deep decking. The full-scale experiment will provide further knowledge during construction, in-service performance, and the ultimate composite strength of the shallow-depth composite floor system.

Data Availability Statement

Some or all data, models, or codes that support the findings of this study are available from the corresponding author upon reasonable request.

Acknowledgments

The authors are grateful to AISC for supporting this study through the Milek Fellowship. Any opinions, findings, conclusions, or recommendations expressed in this material are those of the authors and do not necessarily reflect the views of AISC. The authors thank the project industry panel for all their insight and support. This panel is comprised of three US steel mills (Nucor, Gerdau, and Steel Dynamics), fabricators, erectors, designers, and members of AISC (Devin Huber and Margaret Matthew).

References

Ahmed, I. M., and K. D. Tsavdaridis. 2019. "The Evolution of Composite Floor Systems: Applications, Testing, Modelling and Eurocode Design Approaches." *Journal of Constructional Steel Research*, 155.

AISC. 2022. Specification for Structural Steel Buildings. ANSI/AISC 360-22. Chicago, IL: AISC.

AISC. 2023. *Steel Construction Manual*. 16th ed. Chicago, IL: AISC.

AISC. 2024. "Need for Speed." Accessed October 1, 2023. https://www.aisc.org/why-steel/innovative-systems/need-for-speed/.

ArcelorMittal. 2017. *Slim-Floor: An Innovative Concept for Floors*. Luxembourg: ArcelorMittal Commercial Sections.

ArcelorMittal. 2023b. "Slim Floor System." Accessed May 1, 2023. https://sections.arcelormittal.com/products_and_solutions/Our_Specialties/Slim_floor/EN.

ASCE. 2014. Design Loads on Structures During Construction. ASCE/SEI 37-14. Reston, VA: ASCE.

ASCE. 2022. Minimum Design Loads and Associated Criteria for Buildings and Other Structures. ASCE/SEI 7-22. Reston, VA: ASCE.

Bailey Metal Products. 2023. "COMSLAB Long Span Concrete Floor System." Accessed May 1, 2023. https://www.bmp-group.com/products/comslab.

Baldassino, N., G. Roverso, G. Ranzi, and R. Zandonini. 2019. "Service and Ultimate Behaviour of Slim Floor Beams: An Experimental Study." *Structures*, 17.

Borghi, T. M., L. A. M. Oliveria, and A. L. H. C. E. Debs. 2021. "Numerical Investigation on Slim Floors: Comparative Analysis of ASB and CoSFB Typologies." *Revista IBRACON de Estruturas e Materiais*, 14(4).

British Steel. 2023. "Sections Product Range: Asymmetric Beams (ASB)." Accessed May 1, 2023. https://britishsteel.co.uk/what-we-do/construction-steel/sections-product-range/.

Camnasio, E. 2022. "DELTABEAM with Hybrid Timber Floors - Load Transfer Tests." *Peikko White Paper*.

Davis, S. 2022. "Full-Scale Floor System Testing for Future Hot-Rolled Asymmetric Steel I-beams." Master Thesis, Texas A&M Univ.

Davis, S., E. Stoddard, and M. T. Yarnold. 2023. "Full-Scale Floor System Testing for Future Hot-Rolled Asymmetric Steel I-beams." *Journal of Structural Engineering*, 149(2).

DELTABEAM Technical Manual. 2019. *DELTABEAM Slim Floor Structure*. Lebanon, PA: Peikko.

Girder-Slab Technologies. 2016. *The GIRDER-SLAB System Design Guide v3.3*. Cherry Hill, NJ: Girder-Slab Technologies

Hauf, G., and U. Kuhlmann. 2015. "Deformation Calculation Methods for Slim Floors." *Steel Construction*, 8(2).

Helwig, T. A., K. H. Frank, and J. A. Yura. 1997. "Lateral-Torsional Buckling of Singly Symmetric I-beams." *Journal of Structural Engineering*, 123(9).

Huber, D. 2022. "Increasing Speed through Research." *Modern Steel Construction*, 62(12), 112-117.

IBC. 2018. *International Building Code*. Country Club Hills, IL: International Code Council.

Kloeckner Metals. 2020. The Cellular Beam Pocket Guide Entrusted to Design and Deliver Metal Solutions. Leeds, UK: Kloeckner Metals UK.

Kloeckner Metals. 2023. "Ultra Shallow Floor Beam." Accessed June 1, 2023. https://www.kloecknermetalsuk.com/en/westok/products/ultra-shallow-floor-beam.html.

Lam, D., X. Dai, U. Kuhlmann, J. Raichle, and M. Braun. 2015. "Slim-Floor Construction - Design for Ultimate Limit State." *Steel Construction*, 8(2).

Lawson, R. M., D. L. Mullet, and J. W. Rackham. 1997. *Design of Asymmetric Slimflor Beams using Deep Composite Decking*. *SCI P175.* Ascot, UK: The Steel Construction Institute.

McCormac, J. C. 1981. *Structural Steel Design*. 3rd ed. New York, NY: Jack C. McCormac.

Murray, T. M., D. E. Allen, E. E. Ungar, and D. B. Davis. 2016. Steel Design Guide 11: Vibrations of Steel-Framed Structural Systems due to Human Activity. Steel Design Guide Series. Chicago, IL: AISC.

Nitterhouse Concrete Products. 2020. *NiCore Plank Load Tables*. Chambersburg, PA: Nitterhouse Concrete Products.

Peikko. 2023. "DELTABEAM Slim Floor Structure for Open Spaces." Accessed June 1, 2023. https://www.peikko.com/products/deltabeam-slim-floor-structures/overview/.

Peltonen, S., and P. Kyriakopoulos. 2020. "Ductility Project - DELTABEAM Slim Floor System." *Peikko White Paper*.

Rackham, J. W., S. J. Hicks, and G. M. Newman. 2006. *Design of Asymmetric Slimflor Beams with Precast Concrete Slabs*. *SCI P342.* Ascot, UK: The Steel Construction Institute.

Roeder, C., R. Chmielowski, and C. Brown. 1999. "Shear Connector Requirements for Embedded Steel Sections." *Journal of Structural Engineering*, 125(2).

Seaburg, P. A., and C. J. Carter. 2003. Steel Design Guide 9: Torsional Analysis of Structural Steel Members. Steel Design Guide Series. Chicago, IL: AISC.

Stoddard, E., and M. Yarnold. 2022. "Residual Stress and Global Deflection Limits for Future Hot-Rolled Steel Asymmetric I-beams." *Journal of Structural Engineering*, 148(1).

Stoddard, E. A. 2022. "Behavior of Hot-Rolled Asymmetric Steel I-beams: Concept to Construction." Ph.D. Thesis, Texas A&M Univ.

West, S.-M., E. Camnasio, and S. Peltonen. 2023. "DELTABEAM with Timber Floor Joints - Load Bearing Capacity at Ambient Temperature and in Fire Situation." *World Conference on Timber Engineering*.

Xia, Y., C. Han, D. Zhou, Y. Wang, and P. Wang. 2021. "Ultimate Flexural Strength Analysis of Composite Slim Floor Beam." *Advances in Structural Engineering*, 24(10).

Yarnold, M. T., and E. Stoddard. 2020. "Future Hot-Rolled Asymmetric Steel I-beams." *Journal of Structural Engineering*, 146(9).

Yrjola, J., and J. Salonen. 2020. "Performance of DELTABEAM - CLT Floors in Human-Induced Vibration." *Peikko White Paper*.

Appendix E – Fire Study

Appendix E provides detailed information on a supplemental study to the analytical sizing study (Phase 4). Shallow-depth composite floor systems have an inherent fire resistance due to the bottom flange only being exposed to fire. This results in a significant temperature gradient throughout the depth of the steel section, which has been observed in experimental testing of these floor systems. Detailed information is provided on quantifying the temperature gradient based on an analytical method provided in the literature. An analytical method to quantify the partial composite strength with varying steel strength is presented. Parametric studies are conducted to analyze the performance of increasing web thickness and fire reinforcement.

Citation

The following work has not been submitted to a journal at this time.

The work is expanded upon and supplemental information/results are provided in Chase Ottmers Ph.D. Dissertation. The citation to Chase's dissertation is:

> Ottmers, C. E. 2025. "Full-Scale Testing and Numerical Evaluation of Hot-Rolled Asymmetric I-beams in Shallow-Depth Composite Floor Systems." Ph.D. Dissertation, Texas A&M University.

Fire Resistance of Shallow-Depth Composite Floor Systems

Chase Ottmers, Robel Wondimu Alemayehu, and Matthew Yarnold

Abstract

Structural floor systems must retain strength during a fire event to allow occupants to escape the building. Generally, conventional composite beams are protected with spray-applied fire protection to limit the temperature in the steel beam. Conventional composite beams have poor fire resistance if the beam is unprotected due to fire exposure on three sides. The poor resistance is a result of steel properties being significantly affected at higher temperatures due to steel's high thermal conductivity. On the contrary, the bottom flange in shallow-depth floor systems is the only part of the steel beam exposed since stay-in-place formwork is placed on the bottom flange. Furthermore, the web and top flange of the beam are encased in concrete, which helps absorb heat from the steel beam. Experimental fire tests and numerical analyses of shallow-depth systems in literature have shown a significant temperature gradient throughout the beam depth. A temperature gradient presented in the literature was established from experimental results and is implemented to evaluate the fire resistance of shallow-depth composite floor systems using hot-rolled asymmetric I-beams (termed A-shapes). Composite action is gained in this floor system through bond shear interaction between the steel and concrete. Due to the significant temperature gradient, the steel at the bottom of the section has a large reduction in strength. A partial plastic stress distribution with varying steel strength is implemented to quantify the fire resistance of shallow-depth floor systems. Parametric studies were conducted by increasing the web thickness and incorporating fire reinforcement close to the web of the A-shape. Increasing the web thickness improves the fire resistance by increasing the tensile resistance of the cross-section since the strength of the bottom flange is reduced. However, an increased web thickness is not practical because other standard limit states are not drastically improved. Incorporating fire reinforcement near the bottom of the A-shape web also improves fire resistance and is more practical for these systems. Including fire reinforcement is recommended for these floor systems. The parametric studies conducted show that there is an inherent fire resistance for shallow-depth floor systems.

Keywords: Fire Resistance, Shallow-Depth Composite Floor Systems, Asymmetric I-beam, Structural Steel, Composite Action

Introduction

Unfortunately, there are many building fires in the United States (US) each year. As a result, structural systems must retain capacity during a fire event to allow ample time for residents to escape. An important limit state to consider when designing floor systems is the fire resistance of the cross-section. Many floor systems are utilized in the building industry, including wood systems, concrete slabs, and composite floor systems. Commonly, composite floor systems consist of a concrete slab that is supported by the top of steel beams. An alternative option incorporates the steel beam within the concrete slab to create a shallow-depth composite floor system. Conventional and shallow-depth composite floor systems are compared in Figure E-1.

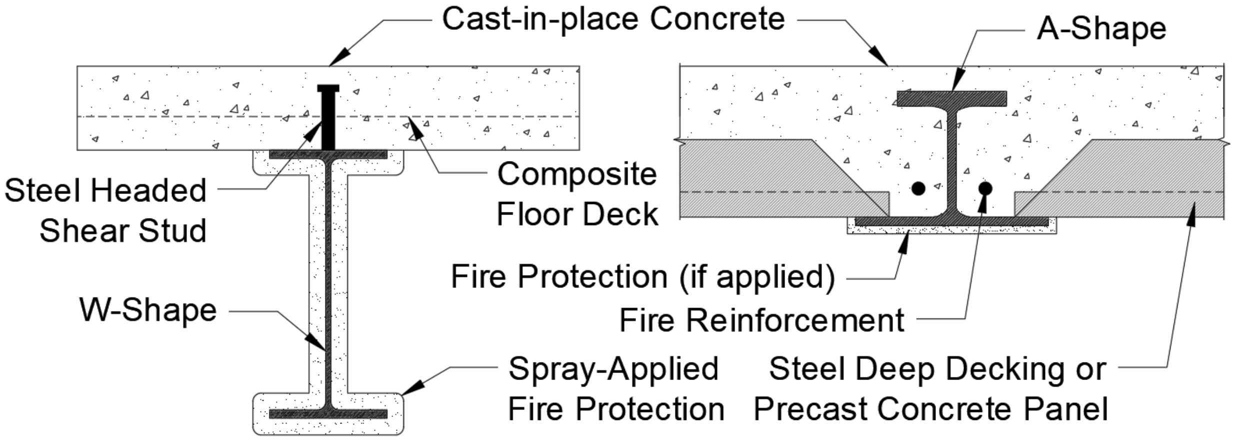

Figure E-1: Conventional and Shallow-Depth Composite Floor Systems

When structural beams are subjected to high temperatures, the strength of both steel and concrete degrades. The reduction in strength for steel and concrete affects the flexural capacity of the member, which could lead to structural failure. In addition, high temperatures reduce the stiffness of the cross-section, which could result in significant deflection during a fire. Both the strength and stiffness of a floor system need to be considered when analyzing the fire performance.

Knowledge of how various floor systems perform during a fire event has been gained through experimental testing and numerical evaluations. Thermal material properties, such as thermal conductivity and specific heat, affect the fire resistance of structural beams and depend on the temperature of the material (ASCE 2018). Steel has a greater thermal conductivity value than concrete, which means that steel will gain heat faster than concrete. The thermal conductivity affects the fire resistance because the strength of the material diminishes with increasing temperature. Reduction factors for the material properties of steel at elevated temperatures are provided in Appendix 4 of the *Specification for Structural Steel Buildings* (AISC 2022), and similar values are published in Eurocode 4 (CEN 2005). The strength of steel is not affected if the temperature remains below 400°C (752°F), as shown in Figure E-2. The strength reduction factor is multiplied by the ambient strength to determine the steel strength at increased temperatures.

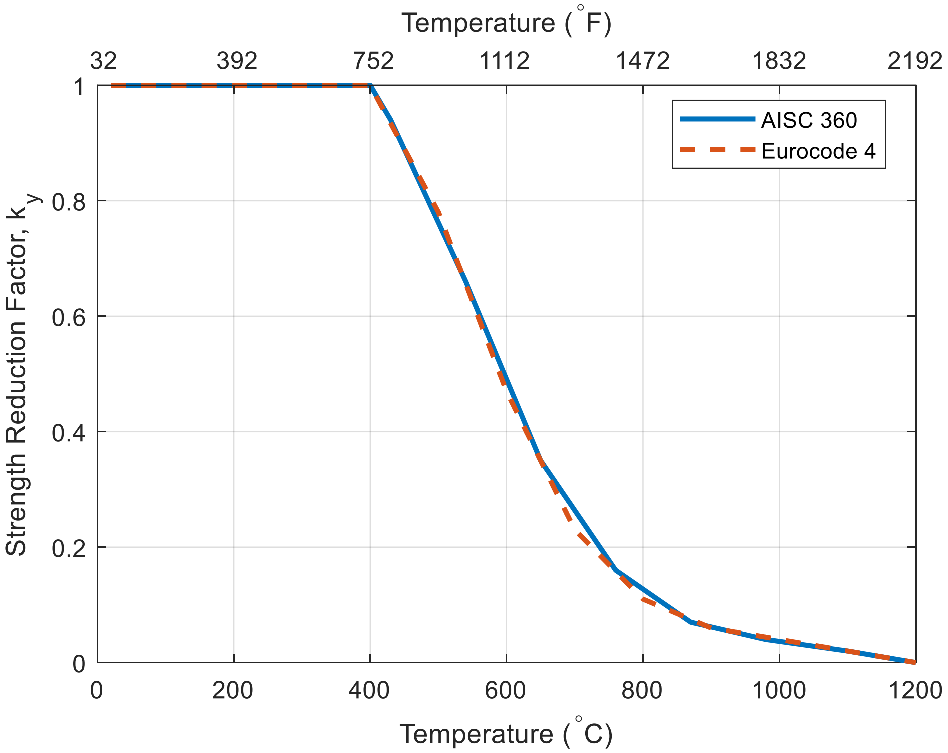

Figure E-2: Strength Reduction Factor for Steel (AISC 2022; CEN 2005)

The fire resistance of unprotected conventional steel-concrete composite floor systems is poor due to the rapid degradation of stiffness and strength of the steel beam when subjected to high temperatures. The poor behavior of unprotected conventional composite floor systems can be attributed to fire exposure on three sides of the beam. As a result, the steel beam heats up evenly, reducing the strength of the entire cross-section. An experimental fire test on an unprotected conventional composite beam had a fire resistance of less than 0.5 hours (Ahn and Lee 2017).

To improve the fire resistance, spray-applied fire protection (shown in Figure E-1) is implemented on structural beams to protect the steel from elevated temperatures (ASCE 2005; IBC 2018). An alternative method to improve the fire resistance is to encase the web and top flange of the beam with concrete, reducing the number of exposed sides. Ahn and Lee (2017) performed tests on three partially encased and one fully encased composite beam. The partially and fully encased beams are identical to a conventional composite system, but concrete protects the web and top flange of the W-shape. The web of the partially encased beam was surrounded by concrete cast flush with the flanges. Therefore, the bottom side of the bottom flange was the only steel exposed to the fire. The fully encased beam has concrete surrounding the entire section with a clear cover of 50 mm (2 in.).

The experimental study conducted by Ahn and Lee (2017) showed that the fully encased beam performed the best. This is attributed to the concrete having a lower thermal conductivity, which shields the steel beam from high temperatures. Reinforced concrete (RC) beams have an inherent fire resistance due to this reason. Fire experiments of RC beams have shown that increasing the concrete cover and the longitudinal reinforcement ratio improves fire resistance. The temperature of the steel reinforcement was reduced, and the tension capacity of the beam was increased (ASCE 2005; Wang et al. 2023b).

The partially encased conventional composite beams also performed well during the fire experiments but not as well as the fully encased section. Concrete surrounding the web of the steel beam helped reduce the temperature in the cross-section. Concrete absorbs heat from the steel, allowing parts of the steel beam to still have higher strengths. However, partially and fully encased conventional composite beams would be difficult to construct in the field. Therefore, spray-applied fire protection would still likely be utilized.

As previously discussed, an alternative to conventional composite floor systems is shallow-depth floor systems (see Figure E-1). Reducing the number of exposed sides is a lot easier with shallow-depth floor systems since stay-in-place formwork is placed on the bottom flange. A concrete slab is then cast, meaning that the bottom flange is the only exposed side to the fire, and the web and top flange are encased in concrete. Three shallow-depth composite beams were also tested by Ahn and Lee (2017). The performance of the shallow-depth floor systems was similar to the partially encased section. The temperature gradient measured over the depth of the shallow-depth floor system varied significantly due to heat being absorbed by the concrete. The significant temperature gradient allows the composite section to gain flexural strength during the fire event.

In the experimental study by Ahn and Lee (2017), two of the three shallow-depth composite floor beams had additional fire reinforcement close to the web of the asymmetric shape, which improved the fire resistance. Due to encasement and the thermal properties of concrete, the fire reinforcement remained at a reduced temperature during testing, retaining most of its strength. Therefore, as the bottom flange's temperature increased, the fire reinforcement was able to help resist tensile forces in the cross-section, which increased the flexural capacity and stiffness of the section.

The eight fire tests by Ahn and Lee (2017) were used to validate a numerical finite element model created by Wang et al. (2023a) in Abaqus to conduct a parametric study on varying the thickness of the web, among other parameters. As the web thickness increased, the fire resistance improved. The strength of the steel in the bottom flange is reduced due to its high temperatures from direct exposure to fire. This means that the web is the main component of the steel shape resisting the tensile forces of the cross-section. Therefore, increasing the web thickness leads to a greater flexural capacity during a fire event.

Additional experimental studies have been conducted on shallow-depth composite floor systems due to the interest in the United Kingdom. Newman (1995) and Wainman (1996) investigated the fire resistance of shallow-depth floor systems using an asymmetric steel beam (ASB) produced by British Steel (2023). In these tests, the composite beams experience a significant temperature gradient over the depth of the cross-section which contributes to the inherent fire resistance of the cross-section. The temperature gradient allows the upper portions of the steel to retain most of its strength and contribute to the flexural capacity during a fire. The fire resistance of shallow-depth floor systems was experimentally and numerically evaluated with an end plate connection (Bailey 1999; Bailey 2003). The end plate connection resulted in a fire resistance improvement due to an increased stiffness of the connection.

Alam et al. (2021) analyzed the fire resistance of composite slim-floor beams (termed CoSFB) with and without fire reinforcement in experimental tests. The fire resistance rating of beams with reinforcement was improved by an hour compared to the beams without reinforcement. In addition to the experiments, Alam et al. (2021) and Albero et al. (2019) conducted parametric studies with finite element software to analyze the effects of varying the size and location of the fire reinforcement. In addition, the size, spacing, and shape of the web holes were varied to analyze the improvement in the behavior of the composite section. The fire resistance improved with increasing the size of the fire reinforcement. As the distance between the top of the bottom flange and the center of the fire reinforcement increased, the temperature of the reinforcement decreased. However, the lever arm between the neutral axis and the reinforcement also decreased, which plateaued the improvement of the fire resistance.

Other shallow-depth floor systems used around the world have been experimentally and numerically evaluated. The innovative, technical, economical, and convenient hybrid (termed iTECH) beam was evaluated in six experimental tests (Kim et al. 2007). The fire resistance of unprotected ultra-shallow floor beams (abbreviated as USFBs) (Maraveas et al. 2017) and the DELTABEAM (Maraveas 2017) were evaluated using numerical investigations. Experimental fire tests are conducted at Underwriters Laboratories (UL) to validate and certify the fire resistance rating of a specific cross-section. Various conventional composite floor systems with spray-applied fire protection have been tested and have a UL fire rating. Similarly, UL fire testing has been conducted on the shallow-depth floor system using a D-BEAM (UL Design K912 2021) and DELTABEAM (UL Design N906 2021). The Girder-Slab system using the D-BEAM achieved a 3-hour fire rating but had to use spray-applied fire protection or gypsum board to protect the bottom flange. Large fire reinforcement is added in the trapezoidal box section of the DELTABEAM, which allowed the composite section to gain a fire rating of 4-hours with no protection.

To fully understand the behavior of new floor systems in fire conditions, fire resistance experimental testing should be completed. However, fire testing is expensive, and gaining an understanding of how a floor system will perform during a test beforehand is paramount. Complex numerical analysis with finite element software can be completed. However, the finite element model must be experimentally validated, which takes a lot of time and resources to complete due to the complexity of the models. Therefore, an ideal place to start is to use an analytical model to predict the fire resistance.

An analytical model was developed as part of the presented study. The analytical model utilizes a temperature gradient from the literature for a steel section in a shallow-depth floor system. A partial plastic stress distribution was utilized to analyze the fire resistance of a shallow-depth composite section with varying steel strength. The temperature gradient is a conservative estimate of experimental temperature data from a shallow-depth composite beam fire test in the literature. A parametric study was performed to analyze the effects on the fire resistance when the web thickness was increased and fire reinforcement was incorporated in the composite section using a plastic analysis. The details are explained in the following sections.

Temperature Gradient of Shallow-Depth Floor Systems

To predict the fire resistance of a shallow-depth composite floor system, determining the temperature gradient over the cross-section depth is paramount. There are a variety of ways this can be accomplished, from simplified analytical tools in literature to more complex approaches using finite element software. Multiple finite element software tools can be utilized, some of which are more generalized and others that were developed specifically for fire analysis of floor systems (ASCE 2018). Regardless of the finite element program, the general procedure is similar.

First, a fire model needs to be selected, which is generally a standard fire design curve, either ASTM (2022) in the US or ISO (1999) in Europe. Alternatively, a fire curve simulating a structure fire with a decay phase, such as a slow or fast fire growth (also known as a flashover) (Garlock 2016; ProfilARBED 1999; Ruddy et al. 2003) or the Cardington fire curve (Newman 1999) could be used. A structure fire model depends on the room geometry and the amount of fuel, which will affect the duration and the amount of heat generated. The standard fire test curves from ASTM E119 and ISO 834, as well as an example of a flashover fire curve, are shown in Figure E-3. The standard fire curve, according to ASTM E119, is used in the US to validate a cross-section during UL fire testing.

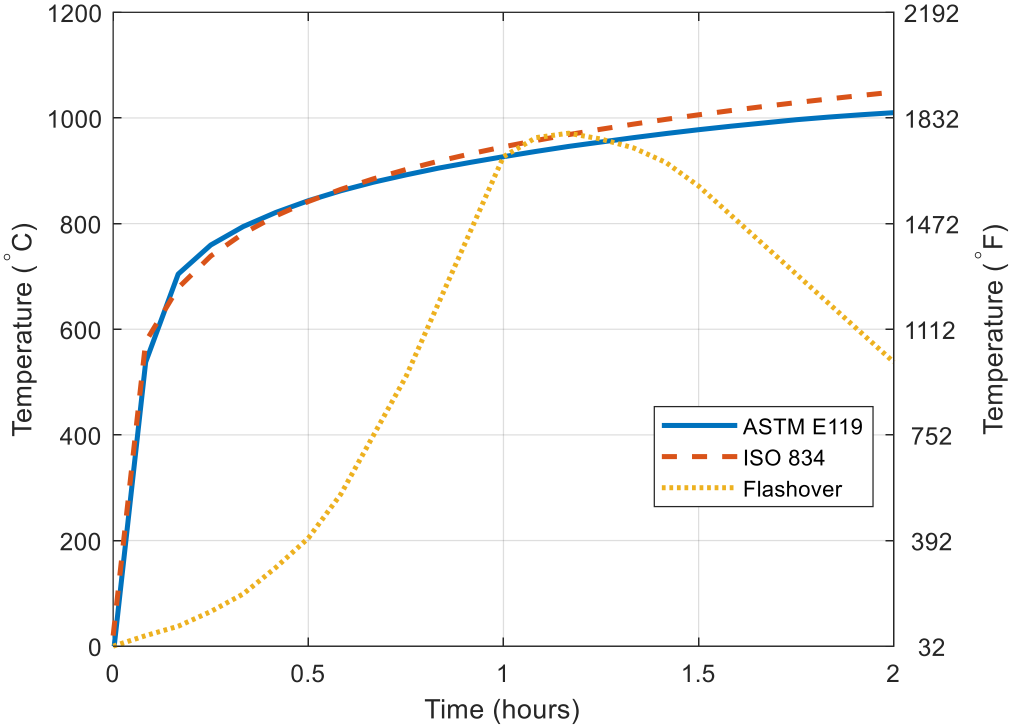

Figure E-3: Fire Temperature Curves

Following the selection of a fire model, a heat transfer analysis is performed to obtain the temperature profile over the depth of the cross-section. Finally, the temperature profile can be applied to a nonlinear finite element model to analyze the cross-section when exposed to fire. Due to the complexity of the finite element models, temperature gradients have been suggested in literature and specifications. A minimal temperature gradient is suggested for conventional composite floor systems based on test results conducted by UL. The slight variation is due to the concrete deck dissipating heat away from the steel beam, and the gradient is explained in AISC (2022) and Ruddy et al. (2003).

On the contrary, the temperature gradient observed in experimental tests of shallow-depth floor systems is significant due to encasing the beam in concrete. The concrete acts as a retardant for the web and top flange and dissipates heat throughout the depth of the web. In addition, the bottom flange is only exposed to fire, altering the temperature gradient. Due to the exposed bottom flange, the heat will transmit upwards through the depth but will be reduced by the concrete, which introduces challenges in predicting the gradient.

An analytical method was proposed by Zaharia and Franssen (2012) to quantify the temperature gradient of a steel section in a shallow-depth composite floor system. The models were established using experimentally validated numerical simulations of composite sections exposed to the ISO 834 fire curve (which is very similar to the ASTM E119 curve) for four fire ratings, specifically 0.5, 1, 1.5, and 2 hours. In the numerical simulations, the bottom flange thickness was varied to analyze the effect on the temperature. A second-order best-fit function was established in the form of Equation (E-1) to estimate a constant bottom flange temperature (Zaharia and Franssen 2012). The temperature of the bottom flange $\left(T_{fb}\right)$ is in $°C$ and the bottom flange thickness $\left(t_{fb}\right)$ is in mm. The coefficients A_i, B_i, and C_i are provided in Table E-1 and depend on the fire resistance rating (Zaharia and Franssen 2012).

$$T_{fb} = A_i t_{fb}^2 + B_i t_{fb} + C_i \tag{E-1}$$

The temperature of the web was also analyzed by Zaharia and Franssen (2012) for varying bottom flange thicknesses and four fire resistance ratings to examine how the temperature varied throughout the depth of the cross-section. Zaharia and Franssen (2012) concluded that the temperature in the web is mainly affected by the height measured from the top of the bottom flange. Exponential functions were established for the web temperature gradient and are calculated using Equation (E-2), per Zaharia and Franssen (2012). The temperature of the web (T_w) is in $°C$ and the bottom flange thickness $\left(t_{fb}\right)$ and the height from the top of the bottom flange (z) are in mm. The coefficients A_w, B_w, C_w, and D_w are dependent on the fire resistance rating and are provided in Table E-1 (Zaharia and Franssen 2012).

$$T_w = \left(A_w \ln t_{fb} + B_w\right) e^{\left(C_w \ln t_{fb} + D_w\right) z} \tag{E-2}$$

A simplified model is utilized by Zanon et al. (2021), which assumes that the temperature of the web is constant throughout the depth. The temperature of the web in Zanon et al. (2021) was established at 25% of the web height (h) above the top of the bottom flange. Therefore, the height from the bottom flange (z) in Equation (E-2) was set to a constant value of $0.25h$. This simplification was made for an easier analytical model.

Another simplified model is Romero et al. (2019), which splits the web into an upper and lower section. The height of the split depends on when the steel strength is not affected by the temperature, i.e., when the temperature of the web is less than 400°C (752°F) (as shown in Figure E-2). The temperature for the lower web portion is an average value between the temperature at the bottom of the web $(z = 0)$ in Equation (E-2) and 400°C (752°F). The upper web portion can simply be any value less than or equal to 400°C (752°F).

The temperature of the top flange is assumed to be less than 400°C (752°F) due to the concrete encasement (Duma et al. 2022; Zanon et al. 2021), and the top flange does not have any strength reduction. Furthermore, the contribution of the concrete below the top of the top flange is neglected for fire resistance capacity (Duma et al. 2022; Zanon et al. 2021). Due to the low temperature of the concrete above the top flange, the concrete resistance is not affected either (Duma et al. 2022; Zanon et al. 2021). Additionally, the plastic neutral axis of shallow-depth composite cross-sections is likely in the top flange due to strength reduction in the bottom portion of the steel section.

Longitudinal reinforcement in shallow-depth composite floor systems examined in experimental and numerical analyses improves the fire resistance. As a result, the temperature gradient throughout the depth of the concrete and the longitudinal reinforcement was analyzed by Zaharia and Franssen (2012). Predicting the temperature of the longitudinal reinforcement was improved upon by Hanus et al. (2017), but was altered slightly by Zanon et al. (2021), considering a corrigendum communicated to them by Hanus et al. (2017). The altered equation for the temperature of the longitudinal reinforcement is in Equation (E-3). The temperature of the rebar (T_r) is in $°C$ and the equivalent rebar distance $\left(u_{eq}\right)$ is in mm (see Equation (E-4)). An equivalent rebar distance is used for simplification and conservativeness to estimate the temperature in the rebar. The coefficient k_{cbf} is dependent on if the top of the bottom flange is fully covered by concrete. If the entire top surface of the bottom flange is covered, the k_{cbf} coefficient is 0.5; otherwise, the coefficient is 1.0 (Duma et al. 2022). For the application of shallow-depth composite floor systems supporting stay-in-place formwork on the bottom flange, the k_{cbf} coefficient will always be 1.0. The coefficients A_r, B_r, and C_r

are dependent on the fire resistance rating and are provided in Table E-1 (Duma et al. 2022; Hanus et al. 2017; Zanon et al. 2021).

$$T_r = A_r u_{eq}^2 + B_r u_{eq} + C_r \tag{E-3}$$

$$u_{eq} = min\left(45\ mm, 25\ mm + \frac{t_{fb}}{2}\right) + \frac{5\ mm}{k_{cbf}} \tag{E-4}$$

Table E-1: Simplified Analytical Method Coefficients (Hanus et al. 2017; Zaharia and Franssen 2012)

Coefficient	Fire Resistance (hours)			
	0.5	**1**	**1.5**	**2**
A_i	0.113	0.130	0	0
B_i	-12.80	-11.80	-2.60	-1.25
C_i	760	980	990	1025
A_w	-140.70	-103.80	-108.60	-70.44
B_w	832.42	968.60	1146.70	1124.40
C_w	0.00317	0.00232	0.00198	0.00158
D_w	-0.0230	-0.0182	-0.0154	-0.0134
A_r	0	0.0954	0.0548	0.0381
B_r	0	-19.254	-15.130	-12.797
C_r	300	1105.4	1135.9	1138.1

A comparison of the temperature gradients for a 1-hour fire rating is shown in Figure E-4 for an A8x52, which was established in Ottmers et al. (2025b) for general limit states at ambient conditions. The top of the bottom flange and the bottom of the top flange locations are distinguished with dashed lines in Figure E-4. Significant heat dissipation will occur in the web due to concrete encasement in a shallow-depth floor system. The assumption made by Zanon et al. (2021) for the temperature gradient is a lot simpler and close to the average temperature of the web determined with the gradient by Zaharia and Franssen (2012). The temperature gradient by Romero et al. (2019) captures the significant temperature gradient slightly better but still is a simplification. The temperature in the top flange remains at a low value due to the concrete encasement; therefore, it is unaffected by fire. Temperature gradients for 0.5, 1, 1.5, and 2 hours of fire exposure determined by Zaharia and Franssen (2012) are shown in Figure E-5 for the A8x52 cross-section.

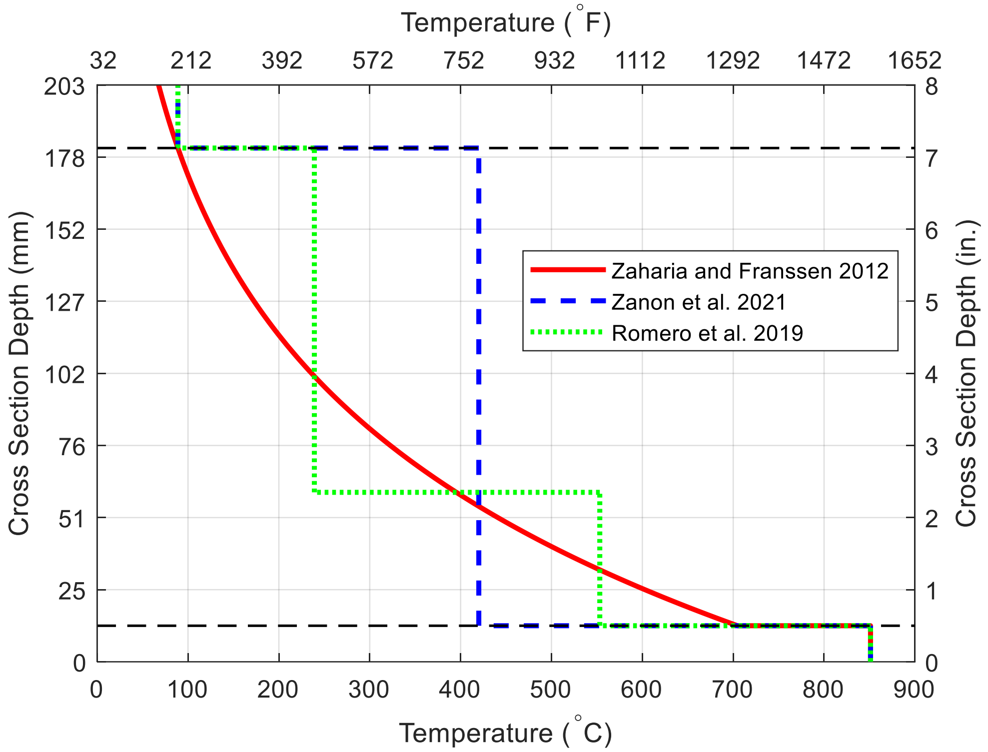

Figure E-4: Temperature Gradients for A8x52 at 1 hour

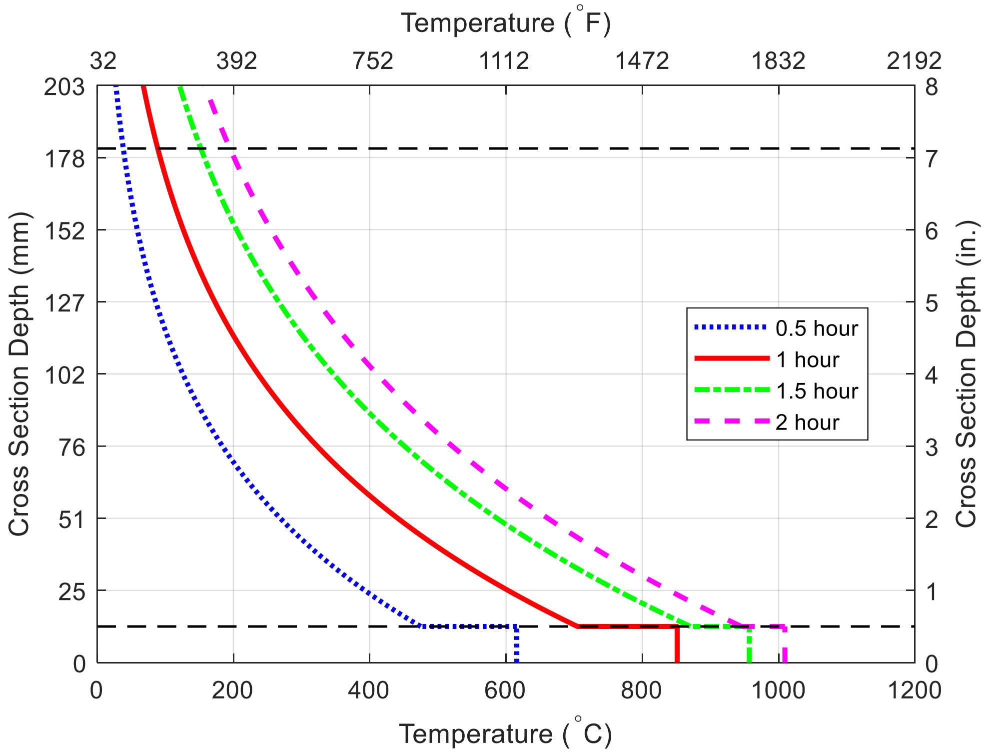

Figure E-5: Temperature Gradients for A8x52 at 0.5, 1, 1.5, and 2 hours

The temperature gradient for shallow-depth composite floor systems established by Zaharia and Franssen (2012) was compared to a finite element model created by Romero et al. (2019). Romero et al. found that the calculated temperature of the bottom flange with the analytical temperature model compared well to the model. Furthermore, the gradient of the web temperature determined by Zaharia and Franssen (2012) overestimated the temperature in the web compared to the finite element model. As a result, the flexural capacity was underestimated with the simplified temperature gradient model by 9% (Romero et al. 2019). Determining the flexural capacity of a shallow-depth floor system is discussed in the following section.

The experimental results from Alam et al. (2021) compare well with the predicted temperature gradient using Zaharia and Franssen (2012). The beam had a bottom plate welded to a W-shape; however, the temperature gradient is still very similar. As shown by the thermocouple data from the experiment, there is a significant temperature gradient from the bottom flange to the top flange due to concrete encasement. Similarly, the experimental temperature gradient in the shallow-depth composite floor beam tests by Ahn and Lee (2017) is less than the predicted gradient by Zaharia and Franssen (2012). However, the predicted gradient still provides analogous results to the experimental test. The temperature gradient was determined using a finite element program, TACS-FIR, and examined for a shallow-depth floor system (Makelainen and Ma 2000). The temperature gradient throughout the depth of the steel section at one hour is very similar to the gradient determined with the analytical temperature model by Zaharia and Franssen (2012).

Furthermore, the temperature gradient compares well to the experimental data recorded during a fire test of a shallow-depth floor system using an ASB at the Warrington Fire Research Center, test number WFRC 66162 (Wainman 1996). The shallow-depth cross-section utilized a 280 ASB 100 and steel deep decking, and the cross-section is shown in Figure E-6. Steel deep decking was placed on the bottom flange of the beam, and normal-weight concrete with a strength of 30 MPa (4.4 ksi) was cast monolithically, encasing the web and top flange of the beam. The 4.5 m (15 ft) long, simply supported beam was loaded with four concentrated loads as it was subjected to the standard ISO 834 fire curve. The cross-section failed the fire resistance criteria slightly before 2 hours when the deflection exceeded five percent of the span length, or 225 mm (8.9 in.) (Wainman 1996). Thermocouples near the midspan of the beam recorded temperature throughout the test, and the analytical model described above predicts the measured values very well. A comparison of the experimental temperatures and the theoretical temperature gradient after an hour is shown in Figure E-7.

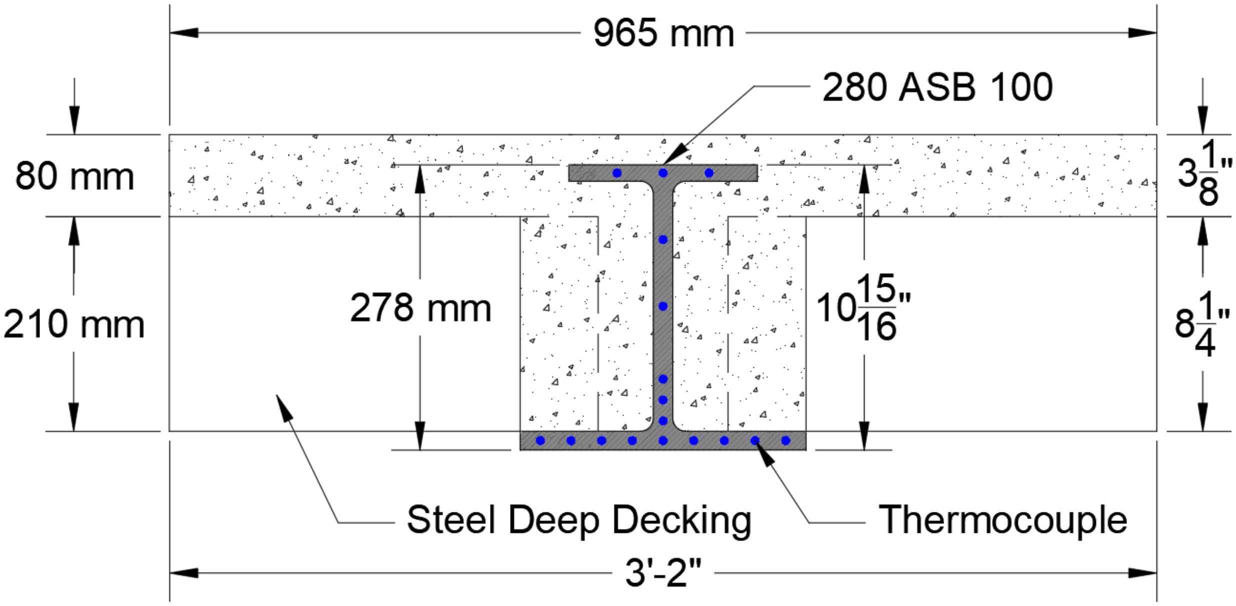

Figure E-6: Cross-Section in WFRC 66162 Fire Experiment (Wainman 1996)

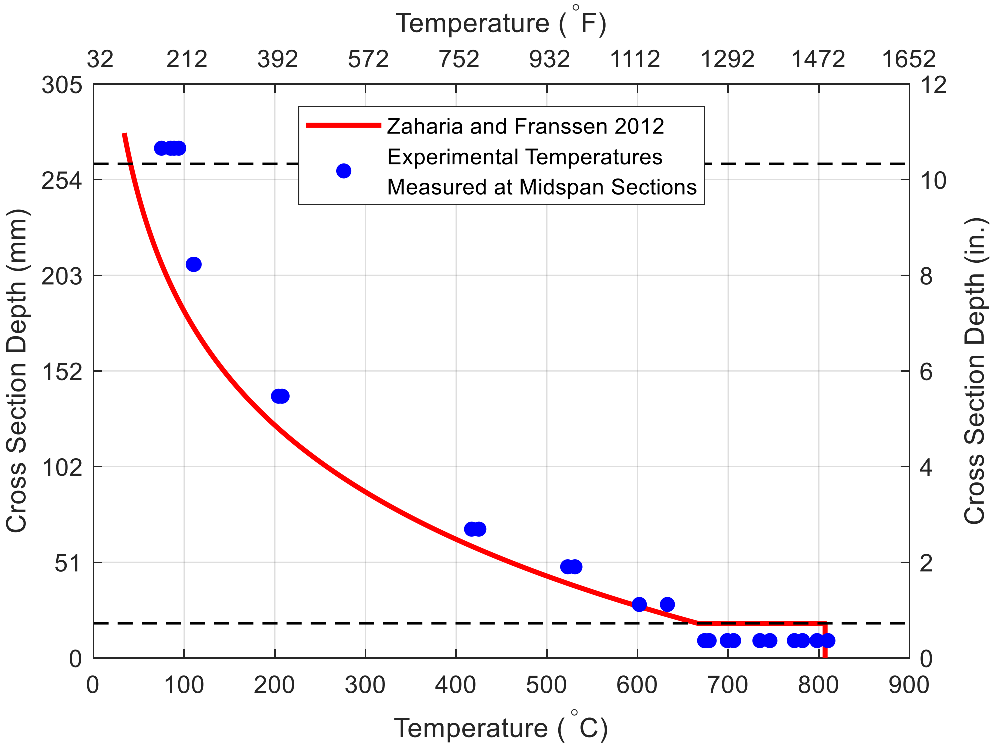

Figure E-7: Comparing Experimental and Theoretical Temperature Gradient

Flexural Composite Strength during Fire

There are various simplified approaches in standards and design guides to determine the flexural capacity for a fire resistance rating. Some of these include AISC 360 Appendix 4 (AISC 2022), SCI P175 (Lawson et al. 1997), and Eurocode 4 (CEN 2005). Other design guides, such as AISC Steel Design

Guide 19 (Ruddy et al. 2003) and ASCE/SEI 29 (ASCE 2005), alter the thickness of spray-applied fire material in UL fire-tested assemblies for similar beam details utilized in buildings.

For conventional composite floor systems, the nominal flexural strength of composite beams exposed to fire can be calculated with two methods in AISC 360 Appendix 4 (AISC 2022). The first method calculates the flexural capacity using a plastic analysis. The strength of the steel section is quantified by obtaining strength reduction factors (previously shown in Figure E-2) for the beam depth based on the assumed temperature gradient. The second method applies a retention factor based on the temperature of the bottom flange to the nominal flexural capacity determined for ambient temperatures (AISC 2022). Conventional composite systems have a less significant temperature gradient; therefore, the method utilizing the retention factor likely provides reasonable results and is simple. However, this method will significantly underestimate the moment capacity of a shallow-depth composite floor system due to direct bottom flange exposure. As shown in the temperature gradients, the bottom flange has a high temperature, but there is a significant gradient over the beam depth.

The temperature gradient discussed in the previous section for a shallow-depth composite floor system is used to quantify the flexural strength after a specific duration of fire exposure using a plastic analysis. SCI P175 and Eurocode 4 utilize a similar process with strength reduction factors for composite beams based on the temperature gradient of the cross-section. SCI P175 specifies a temperature gradient in a shallow-depth floor system after the beam has been exposed to fire for one hour. If prolonged periods of fire resistance are needed, SCI P175 suggests that the bottom flange be protected with conventional gypsum boards, spray-applied fire protection, or intumescent fire coatings to reduce the temperature of the bottom flange (Lawson et al. 1997).

Various analytical models have been developed in the literature to determine the moment capacity of the shallow-depth composite section exposed to fire (Braun et al. 2017; Lawson and Brekelmans 1999; Romero et al. 2019; Romero et al. 2015; Zanon et al. 2021). These models utilize the temperature gradient models established by Hanus et al. (2017) and Zaharia and Franssen (2012), as explained in the previous section. The models were developed for shallow-depth composite cross-sections with a doubly symmetric I-beam, such as a W-shape, and a plate welded to the bottom flange to support stay-in-place formwork.

The model developed by Zanon et al. (2021) was validated against experimental fire tests, and a large parameter study was conducted. The analytical model utilized a simpler temperature gradient by using the average temperature of the web for the entire height rather than the more accurate exponential prediction from Zaharia and Franssen (2012) (see Figure E-4 for a comparison of the temperature gradients). The parameter study was conducted for four fire resistance ratings of 0.5, 1, 1.5, and 2 hours, consisting of a total of 1240 simulations (Zanon et al. 2021). The simulations consisted of altering the dimensions of the steel section, the concrete topping thickness above the steel section, the strength of the steel and concrete, and the size and location of the fire reinforcement (Zanon et al. 2021).

The scope of the analytical model was expanded upon by Duma et al. (2022) to include other asymmetric shapes without the use of a welded bottom plate, such as a hot-rolled asymmetric I-beam (termed A-shape). A parametric study involving a total of 648 simulations was conducted by Duma et al. on the same four fire resistance ratings in SAFIR (Franssen 2005). Similarly, the study altered the steel geometry, the strength of steel and concrete, and the span length, among other parameters (Duma et al. 2022). The scope of application for the analytical model examined by Duma et al. (2022) and Zanon et al. (2021) is shown in Table E-2. The nomenclature of the composite section exposed to fire is shown in Figure E-8.

Table E-2: Analytical Model Scope (Duma et al. 2022; Zanon et al. 2021)

Steel Section			Concrete Slab	Reinforcement
12 mm (0.5 in.)	≤ t_{fb} ≤	40 mm (1.6 in.)	30 mm (1.2 in.) ≤ D_c ≤ 150 mm (5.9 in.)	$u_r \geq$ 25 mm (1.0 in.)
10 mm (0.4 in.)	≤ t_{ft} ≤	40 mm (1.6 in.)	$h_2 \geq$ 20 mm (0.8 in.)	$u_c \geq$ 30 mm (1.2 in.)
0.7	≤ t_{ft}/t_{fb} ≤	2.4	$b_{bw} \geq$ 40 mm (1.6 in.)	$u_w \geq$ 30 mm (1.2 in.)
6 mm (0.24 in.)	≤ t_w ≤	30 mm (1.2 in.)	b_{ft} + 60 mm (2.4 in.) ≤ B_d	$h_r \leq h - 2u_r$
135 mm (5.3 in.)	≤ h_1 ≤	450 mm (18 in.)		$A_{fr} \leq 0.5 b_{fb} t_{fb}$
160 mm (6.3 in.)	≤ b_{fb} ≤	500 mm (20 in.)		$A_{fr} \leq 0.05 B_d (h_1 + D_c)$
110 mm (4.3 in.)	≤ $b_{fb} - b_{ft}$ ≤	250 mm (9.8 in.)		$A_{fr} \leq 2 B_e D_c (f'_c / F_y)$

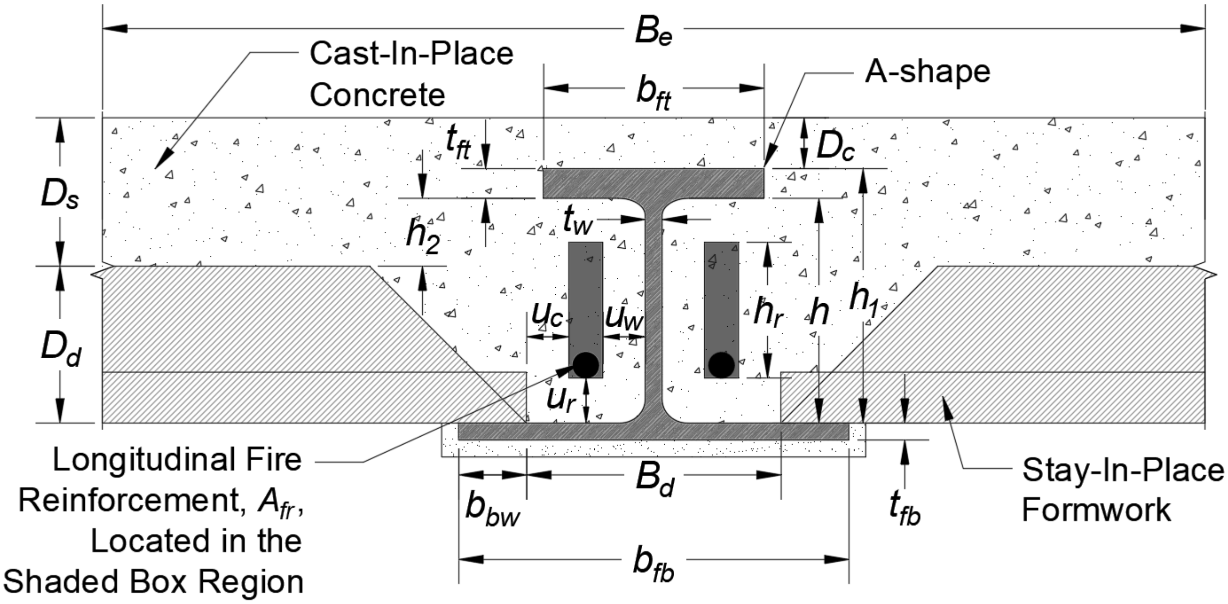

Figure E-8: Composite Beam Nomenclature for Fire

A partial plastic stress distribution is utilized to quantify the composite strength during a fire event (see Figure E-9). As mentioned above, the strength reduction factors are determined based on the temperature gradient, either Zaharia and Franssen (2012), Zanon et al. (2021), or Romero et al. (2019) for a shallow-depth floor system. After the strength reduction factors are obtained, the cross-section will have a varying steel strength. The varying steel strength is used in the partial plastic stress distribution for fire analysis and is illustrated in Figure E-9 for the Zaharia and Franssen (2012) temperature gradient.

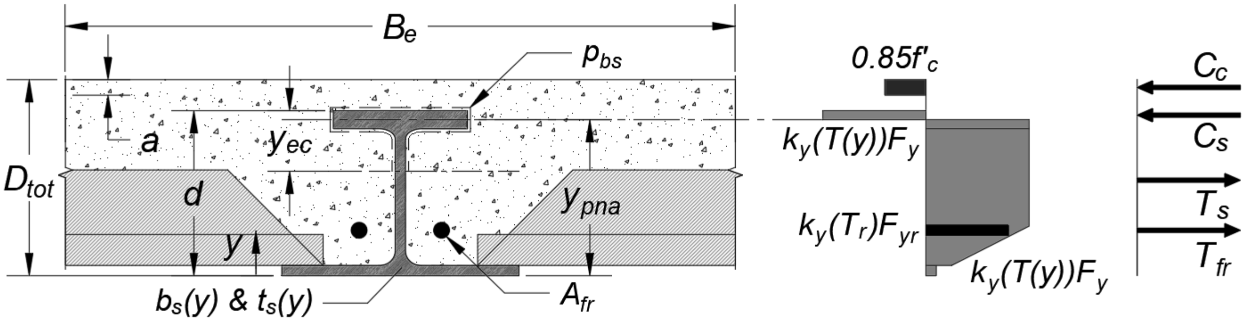

Figure E-9: Partial Plastic Stress Distribution for Fire Analysis

In a partial plastic stress distribution, the force that can develop in the concrete (C_c) is limited by the maximum load transfer between the steel and concrete. In shallow-depth composite floor systems, this load transfer is calculated based on the elastic bond shear transfer. Determined through experimental testing of shallow-depth floor systems during ambient conditions, the bond shear stress (f_{bs}) that formed around an assumed perimeter (p_{bs}) above the elastic neutral axis was determined to be 0.69 MPa (100 psi) (Ottmers et al. 2025a). The bond perimeter and the elastic shear transfer for a uniformly distributed load (UDL) are expressed in Equations (E-5) and (E-6), respectively. The elastic shear transfer for a UDL corresponds to the bond shear forming for a quarter of the span length (L). The depth of the compression block in the concrete (a) is determined assuming the concrete is at 85% of the specified concrete compressive strength (f'_c) and the effective width (B_e) of the concrete slab is in accordance with the AISC specification for composite members (AISC 2022).

$$p_{bs} = 2\left(b_{ft} + y_{ec}\right) - t_w \tag{E-5}$$

$$C_c = p_{bs} f_{bs} \frac{L}{4} = 0.85 f'_c B_e a \tag{E-6}$$

The compressive (C_s) and tension (T_s) forces that develop in the steel are determined by splitting the beam into several fibers with a thin height. Fiber width (b_s) and thickness (t_s) functions are required for the steel beam, which references the bottom of the steel beam. The beam temperature (T) is evaluated at the centroid of each fiber (y_c) to quantify the varying strength reduction factors $\left(k_y\right)$ over the beam depth. The varying strength is quantified by multiplying the strength reduction factors by the yield strength $\left(F_y\right)$ at ambient conditions. If fire reinforcement is utilized, the strength reduction factor is determined based on the temperature in the reinforcement (T_r). The reinforcement temperature is a conservative value based on an assumed equivalent rebar distance, but the height of the reinforcement (z_r) from the bottom of the steel beam is needed to determine the moment capacity. The tension force that develops in the fire reinforcement $\left(T_{fr}\right)$ depends on the rebar yield strength $\left(F_{yr}\right)$ and the total area of the fire reinforcement $\left(A_{fr}\right)$. The depth of the PNA $\left(y_{pna}\right)$, referenced from the bottom of the steel, is adjusted until the summation of Equations (E-6) and (E-7) is in equilibrium with the sum of Equations (E-8) and (E-9). After establishing equilibrium, the composite strength $\left(M_{cf}\right)$ during a fire event is determined with Equation (E-10).

$$C_s = \sum_{y=y_{pna}}^{y=d} k_y\big(T(y)\big)F_y t_s(y) b_s(y) \tag{E-7}$$

$$T_s = \sum_{y=0}^{y=y_{pna}} k_y\big(T(y)\big)F_y t_s(y) b_s(y) \tag{E-8}$$

$$T_{fr} = k_y(T_r)F_{yr}A_{fr} \tag{E-9}$$

$$\begin{aligned} M_{cf} = C_c\left(D_{tot} - \frac{a}{2} - y_{pna}\right) + \sum_{y=0}^{y=d} k_y\big(T(y)\big)F_y t_s(y) b_s(y)\left|y_c - y_{pna}\right| \\ + k_y(T_r)F_{yr}A_{fr}\big(y_{pna} - z_r\big) \end{aligned} \tag{E-10}$$

Parametric Studies

The procedure discussed above to quantify the flexural strength of a shallow-depth composite floor system was implemented for an A8x52 for one hour of fire exposure. The load combination for an extraordinary event uses a load factor of 1.2 for the dead load and 0.5 for the live load (ASCE 2022). The reduced factor for live load is utilized during a fire event to analyze the floor system for expected day-to-day load levels. Residential buildings were selected for this study; therefore, the assumed live load was a reducible 1.9 kPa (40 psf), and a nonreduced 0.72 kPa (15 psf) partition load was included (ASCE 2022). The dead load consisted of precast panels with a thickness (D_d) of 152 mm (6 in.) and a weight of 2.4 kPa (50 psf) (Nitterhouse Concrete Products 2020). A concrete topping (D_c) of 38 mm (1.5 in.) over the steel section was utilized for a total structure weight of 4.1 kPa (86 psf), assuming a normal-weight concrete density of 2300 kg/m^3 (145 pcf). In addition, a 0.48 kPa (10 psf) uniform area load was included for superimposed dead load.

Common material properties were utilized in the parametric studies. The steel A-shape was assumed to have a yield strength (F_y) of 345 MPa (50 ksi), and the fire reinforcement was assumed to be Grade 420 MPa (60 ksi). The concrete had a compressive strength (f_c') of 27.6 MPa (4000 psi). The benchmark temperature gradient that was utilized was from Zaharia and Franssen (2012), as it matched experimental results the best (see Figure E-7).

A parametric study was conducted by varying the beam length and spacing to analyze the fire resistance capabilities of an unprotected A8x52. The moment capacity was quantified for each grid layout and was compared to the moment demand determined for the load combination discussed above to quantify a capacity-to-demand ratio. A value greater than one means that the grid layout has sufficient strength for a fire duration of one hour. Values less than one indicate that the flexural strength is less than the demand; therefore, the beam needs to be protected. Additionally, a pass-fail threshold line is shown to further illustrate the performance. The length and spacing parametric study utilizing the Zaharia and Franssen (2012) temperature gradient after one hour for an unprotected A8x52 is shown in Figure E-10. The other two temperature gradients, Zanon et al. (2021) and Romero et al. (2019) do not significantly alter the capacity-to-demand ratios in Figure E-10. The Zanon et al. (2021) temperature gradient is slightly less conservative and moves the pass-fail threshold line up and to the right compared to the Zaharia and Franssen (2012) gradient. The pass-fail threshold line for the Romero et al. (2019) temperature gradient overlays the threshold line shown in Figure E-10.

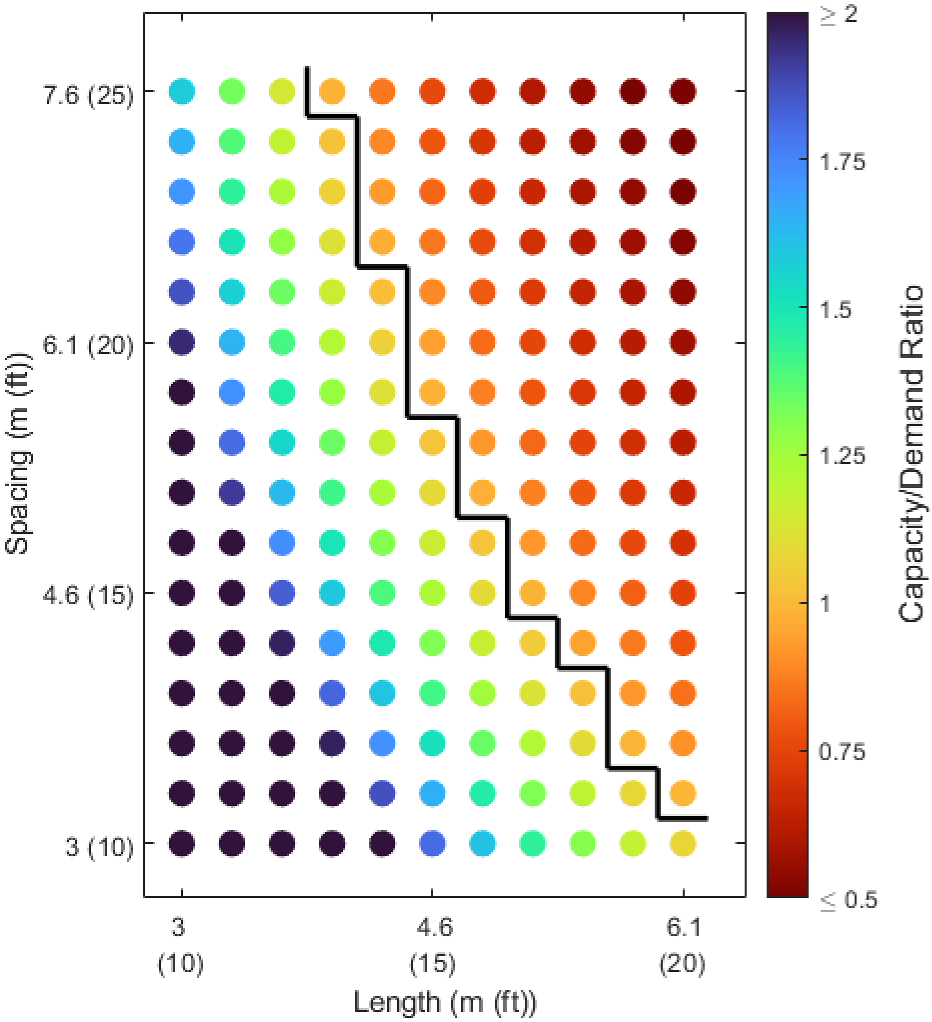

Figure E-10: Length vs Spacing A8x52 Fire Resistance for 1 hour

Parametric studies in the literature have shown that increasing the web thickness improves the fire resistance. As discussed above, the tensile resistance of the bottom flange is diminished significantly due to the high bottom flange temperature from direct exposure to fire. As a result, the web is one of the main components that resist tensile demand during bending. The length vs. spacing analysis was conducted for three web thicknesses: (1) the base web thickness for the A8x52, 13 mm (0.5 in.), and increased web thicknesses of (2) 16 mm (0.625 in.), and (3) 19 mm (0.75 in.). The Zaharia and Franssen (2012) temperature gradient was utilized for one hour for all analyses. The length vs. spacing with varying web thickness is shown in Figure E-11. The capacity-to-demand ratios shown correspond to the base case in Figure E-10. The pass-fail threshold line moves up and to the right when the web thickness is increased.

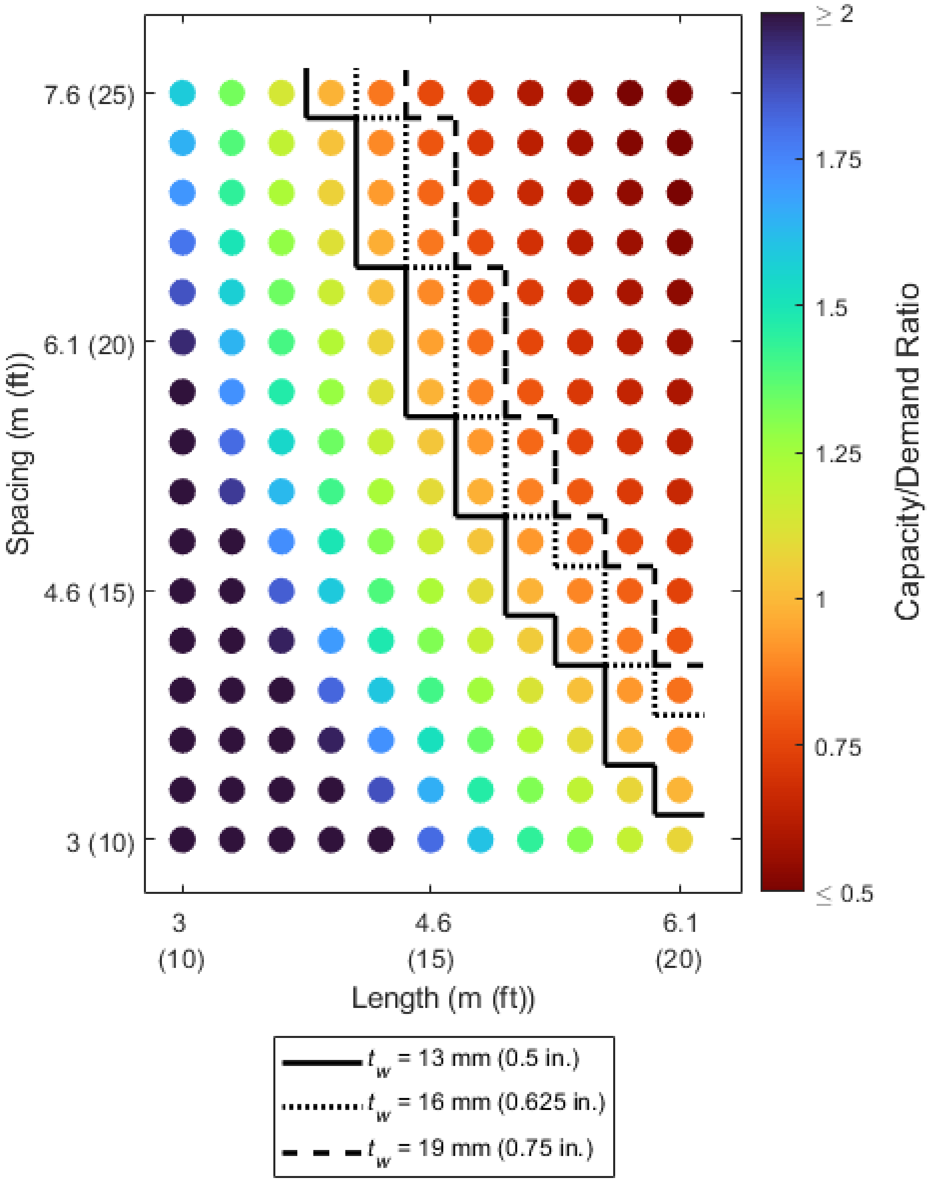

Figure E-11: Length vs Spacing for Varying Web Thickness

The parametric study conducted above is insightful; however, increasing the flexural capacity by including fire reinforcement is much more practical. Increasing the web thickness would increase the weight and cost of the steel beam. Furthermore, limit states at ambient conditions would not significantly be improved with a thicker web. The fire reinforcement stays at a reduced temperature due to the concrete encasement absorbing heat, which will help increase the tension capacity of the beam. Implementing fire reinforcement in the shallow-depth beam is analyzed in Figure E-12 for (1) no reinforcement (the base case), (2) two 19 mm (#6) rebar, and (3) two 25 mm (#8) rebar. A large improvement was observed with the implementation of fire reinforcement for a standard A8x52, analyzed with the Zaharia and Franssen (2012) temperature gradient.

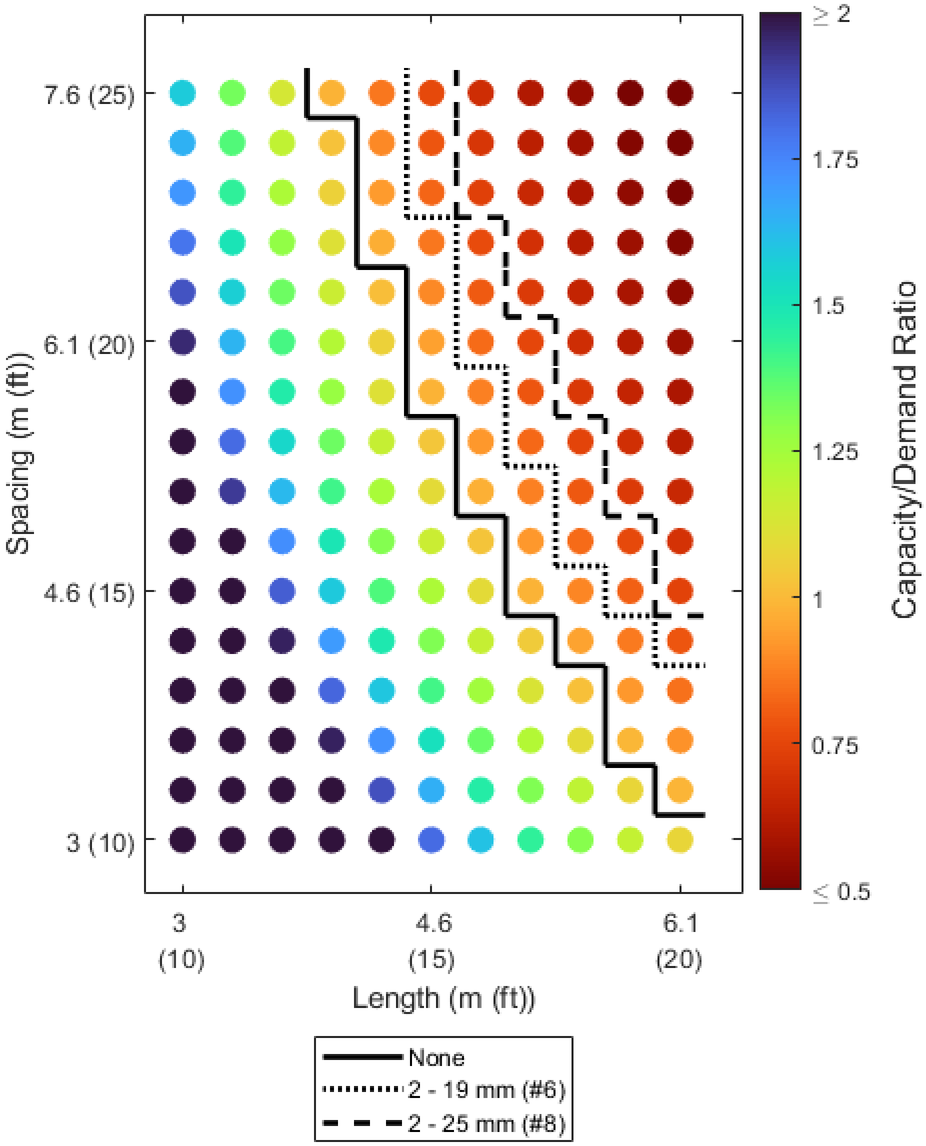

Figure E-12: Length vs Spacing with Fire Reinforcement

The parametric studies conducted above indicate that there is an inherent fire resistance for shallow-depth floor systems. Improvement can be made by increasing the web thickness or including fire reinforcement near the bottom of the section. The method discussed above could be implemented for other established A-shape cross-sections and analyzing the beams for a longer fire duration. However, the bottom flange might have to be protected to reduce the temperature in the bottom flange. In doing so, this will allow the beam to resist larger moment demands due to the beam length and spacing combinations.

The bottom flange of the A-shape could be protected with various methods of passive fire protection. The aim of passive fire protection is to reduce the temperature of the steel so the floor system can retain most of its capacity. Examples of passive fire protection include spray-applied fire protection or gypsum board. Alternatively, the bottom flange could be painted with intumescent paint to provide fire protection. These options would allow the bottom flange to remain at a lower temperature during a fire event, increasing the fire resistance of the composite section. A general cross-section of a protected bottom flange is shown in Figure E-13.

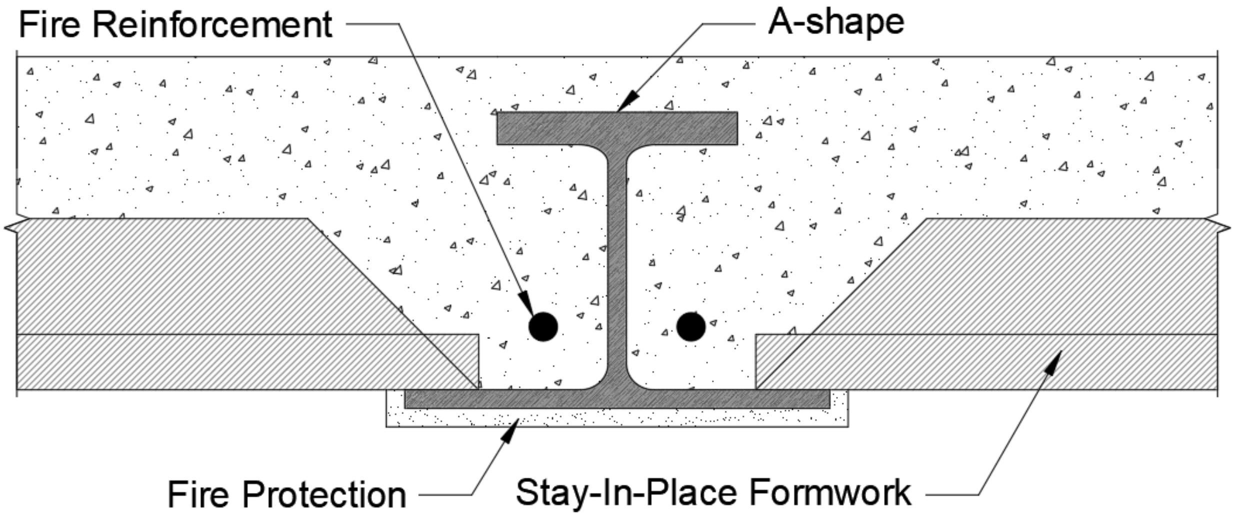

Figure E-13: Shallow-Depth Floor System with Protected Bottom Flange

Conclusions and Future Research

An important limit state to consider for a floor system is the fire resistance. Spray-applied fire protection is commonly applied to conventional composite floor systems to limit the temperature of the steel beam. However, experimental fire tests and numerical analyses of shallow-depth floor systems have shown an inherent resistance with an unprotected beam. This is attributed to concrete encasing the steel beam, and the bottom flange is the only component exposed to the fire. Significant temperature gradients are observed in the asymmetric steel beam due to the concrete absorbing heat from the steel section. Simpler analytical approaches to more complex finite element models can be utilized to obtain the temperature gradient. A temperature gradient was developed by Zaharia and Franssen (2012) for shallow-depth floor systems that matches experimental data very well. Obtaining an accurate temperature gradient is paramount in determining the flexural strength during a fire. The concrete force is limited by the elastic shear transfer that will occur between the steel and concrete through bond interaction. The steel beam has varying steel strength, which is quantified by determining strength reduction factors for the selected temperature gradient. Finally, the composite strength is quantified using a partial plastic stress distribution with varying steel strength.

The composite strength for a shallow-depth floor system using A-shapes was analyzed for varying length and spacing combinations. The benchmark case consisted of analyzing an A8x52 using the Zaharia and Franssen (2012) temperature gradient after one hour of fire exposure (no fire reinforcement). Parametric studies were conducted by increasing the web thickness of the A8x52 and adding fire reinforcement alongside the web of the A-shape. Improvement was observed for both studies; however, adding fire reinforcement is more practical. Increasing the size of the fire reinforcement can drastically improve the fire resistance of a shallow-depth floor system. Including fire reinforcement in shallow-depth composite floor systems with A-shapes is recommended to increase the moment capacity during a fire event.

The analytical method to quantify the fire resistance of shallow-depth floor systems shows promising performance. Literature has shown that these methods can be conservative in estimating the capacity and fire rating. Therefore, more complex finite element modeling and experimental fire testing of A-shapes in shallow-depth composite floor systems should be completed to further understand the performance of this system. Furthermore, UL fire testing of this system should be conducted to certify the response during a nationally recognized fire test.

Data Availability Statement

Some or all data, models, or codes that support the findings of this study are available from the corresponding author upon reasonable request.

Acknowledgements

The authors are grateful to AISC for supporting this study through the Milek Fellowship. Any opinions, findings, conclusions, or recommendations expressed in this material are those of the authors and do not necessarily reflect the views of AISC. The authors thank the project industry panel for all their insight and support. This panel is comprised of three US steel mills (Nucor, Gerdau, and Steel Dynamics), fabricators, erectors, designers, and members of AISC (Devin Huber and Margaret Matthew).

References

Ahn, J.-K., and C.-H. Lee. 2017. "Fire Behavior and Resistance of Partially Encased and Slim-floor Composite Beams." *Journal of Constructional Steel Research*, 129.

AISC. 2022. Specification for Structural Steel Buildings. ANSI/AISC 360-22. Chicago, IL: AISC.

Alam, N., A. Nadjai, F. Hanus, C. Kahanji, and O. Vassart. 2021. "Experimental and Numerical Investigations on Slim Floor Beams Exposed to Fire." *Journal of Building Engineering*, 42.

Albero, V., A. Espinos, E. Serra, M. L. Romero, and A. Hospitaler. 2019. "Numerical Study on the Flexural Behavior of Slim-Floor Beams with Hollow Core Slabs at Elevated Temperatures." *Engineering Structures*, 180.

ASCE. 2005. Standard Calculation Methods for Structural Fire Protection. ASCE/SEI 29-05. Reston, VA: ASCE.

ASCE. 2018. Structural Fire Engineering ASCE Manuals and Reports on Engineering Practice No. 138. Reston, VA: ASCE.

ASCE. 2022. Minimum Design Loads and Associated Criteria for Buildings and Other Structures. ASCE/SEI 7-22. Reston, VA: ASCE.

ASTM. 2022. Standard Test Methods for Fire Tests of Building Construction and Materials. ASTM E119. West Conshohcocken, PA: ASTM.

Bailey, C. G. 1999. "The Behavior of Asymmetric Slim Floor Steel Beams in Fire." *Journal of Constructional Steel Research*, 50.

Bailey, C. G. 2003. "Large Scale Fire Test on a Composite Slim-Floor System." *Steel and Composite Structures*, 3(3).

Braun, M., D. Xaganelli, F. Hanus, R. Obiala, L.-G. Cajot, and A. Peirce. 2017. "Simplified Analytical Determination of the Temperature Distribution and the Load Bearing Resistance of Slim-Floor Beams." *ce/papers*, 1(2).

British Steel. 2023. "Sections Product Range: Asymmetric Beams (ASB)." Accessed May 1, 2023. https://britishsteel.co.uk/what-we-do/construction-steel/sections-product-range/.

CEN. 2005. Design of Composite Steel and Concrete Structures, Part 1-2: General Rules - Structural Fire Design. Eurocode 4: EN 1994-1-2. Brussels, Belgium: European Committee for Standardization (CEN).

Duma, D., R. Zaharia, D. Pintea, I. Both, and F. Hanus. 2022. "Analytical Method for the Bending Resistance of Slim Floor Beams with Asymmetric Double-T Steel Section under ISO Fire." *Applied Sciences*, 12(2).

Franssen, J. M. 2005. "SAFIR: A Thermal/Structural Program for Modeling Structures under Fire." *Engineering Journal*, 42.

Garlock, M. "T.R. Higgins Lecture: Get Fired Up: What Structural Engineers should know about Fire Design [N79]." *Proc., NASCC, The Steel Conference*, AISC.

Hanus, F., D. Zaganelli, L.-G. Cajot, and M. Braun. 2017. "Analytical Methods for the Prediction of Fire Resistance of "Reinforced" Slim Floor Beams." *ce/papers*, 1(2).

IBC. 2018. *International Building Code*. Country Club Hills, IL: International Code Council.

ISO. 1999. *Fire Resistance Tests - Elements of Building Construction*. *ISO 834.* Geneva, Switzerland: International Standards Organization.

Kim, M.-H., S.-D. Kim, and S.-D. Kang. 2007. "Behavior of iTECH Composite Beam in Fire - Experimental Study." *Fire Science and Technology*, 26(2).

Lawson, R. M., and J. W. P. M. Brekelmans. 1999. "Design Recommendations for Shallow Floor Construction to Eurocodes 3 and 4.". European Commission.

Lawson, R. M., D. L. Mullet, and J. W. Rackham. 1997. *Design of Asymmetric Slimflor Beams using Deep Composite Decking*. *SCI P175.* Ascot, UK: The Steel Construction Institute.

Makelainen, P., and Z. Ma. 2000. "Fire Resistance of Composite Slim Floor Beams." *Journal of Constructional Steel Research*, 54.

Maraveas, C. 2017. "Fire Resistance of DELTABEAM Composite Beams: A Numerical Investigation." *Journal of Structural Fire Engineering*, 8(4).

Maraveas, C., K. D. Tsavdaridis, and A. Nadjai. 2017. "Fire Resistance of Unprotected Ultra Shallow Floor Beams (USFB): A Numerical Investigation." *Fire Technology*, 53.

Newman, G. 1995. "Fire Resistance of Slim Floor Beams." *Journal of Constructional Steel Research*, 33.

Newman, G. 1999. "The Cardington Fire Tests." *Proceedings of the North American Steel Construction Conference*. AISC, Chicago, IL.

Nitterhouse Concrete Products. 2020. *NiCore Plank Load Tables*. Chambersburg, PA: Nitterhouse Concrete Products.

Ottmers, C., R. W. Alemayehu, and M. Yarnold. 2025a. "Evaluating the Composite Behavior developed through Bond in the Steel-Concrete Interface for Future Hot-Rolled Asymmetric Steel I-beams." *Engineering Structures*, 322.

Ottmers, C., E. Stoddard, and M. Yarnold. 2025b. "Establishment of Future A-Shape Geometry for Residential Construction." *Journal of Structural Engineering*.

ProfilARBED. 1999. "Competitive Steel Buildings through Natural Fire Safety Concept."

Romero, M. L., V. Albero, A. Espinos, and A. Hospitaler. 2019. "Fire Design of Slim-Floor Beams." *Stahlbau*, 88(7).

Romero, M. L., L.-G. Cajot, Y. Conan, and M. Braun. 2015. "Fire Design Methods for Slim-Floor Structures." *Steel Construction*, 8(2).

Ruddy, J. L., J. P. Marlo, S. A. Ioannides, and F. Alfawakhiri. 2003. Steel Design Guide 19: Fire Resistance of Structural Steel Framing. Steel Design Guide Series. Chicago, IL: AISC.

UL Design K912. 2021. "Girder-Slab D-BEAM - Design No. K912." Accessed February 13, 2024. https://productiq.ulprospector.com/en.

UL Design N906. 2021. "Peikko DELTABEAM - Design No. N906." Accessed February 1, 2024. https://productiq.ulprospector.com/en.

Wainman, D. E. 1996. "Preliminary Assessment of the Data Arising from a Standard Fire Resistance Test Performed on a Slimflor Beam at the Warrington Fire Research Center on February 14, 1996: Test Number WFRC 66162." British Steel, Rotherham, UK.

Wang, W., B. Jiang, F.-x. Ding, Y. Wang, and X.-m. Liu. 2023a. "Numerical Study of the Fire Behavior of Encased and Slim-Floor Composite Beams." *Journal of Performance of Constructed Facilities*, 37(6).

Wang, Y., Z. Liu, S. Qu, J. Gong, and X. Lyu. 2023b. "Fire Resistance of Reinforced Concrete Beams: State of the art, Analysis and Prediction." *Construction and Building Materials*, 409.

Zaharia, R., and J. M. Franssen. 2012. "Simple Equations for the Calculation of the Temperature within the Cross-Section of Slim Floor Beams under ISO Fire." *Steel and Composite Structures*, 13(2).

Zanon, R., S. Yildiz, R. Obiala, and M. Braun. 2021. "Shallow Composite Floor Beams - Proposal of a Simplified Analytical Method for Standard Fire Rating." *ce/papers*, 4.

Appendix F – System Validation Testing

Appendix F provides detailed information on the full-scale system validation testing (Phase 5) conducted on an established A-shape (built-up A8x52). The full-scale testing analyzed the behavior of the A-shape during construction and in-service. Several service load locations were performed to analyze the displacement field of a shallow-depth floor system when loaded in various areas on the slab. Vibration testing was also conducted and is expanded upon further in Appendix G. The ultimate capacity of a shallow-depth floor system on the system level was also analyzed. In addition to the system-level test, a component-level beam test was conducted with a similar cross-section to compare to the system-level response.

Citation

The following work has been submitted to the American Society of Civil Engineer's Journal of Structural Engineering and is currently under review.

The work is expanded upon and supplemental information/results are provided in Chase Ottmers Ph.D. Dissertation. The citation to Chase's dissertation is:

> Ottmers, C. E. 2025. "Full-Scale Testing and Numerical Evaluation of Hot-Rolled Asymmetric I-beams in Shallow-Depth Composite Floor Systems." Ph.D. Dissertation, Texas A&M University.

Full-Scale System Testing for Asymmetric Steel I-beams in Shallow-Depth Composite Floor Systems

Chase Ottmers, Robel Wondimu Alemayehu, and Matthew Yarnold

Abstract

The aim of shallow-depth composite floor systems is to reduce the total depth while still meeting all limit states. This is achieved by placing deep decking (or precast concrete panels) on the bottom flange of a steel beam. A concrete slab is then cast, which encases the steel beams. For ease of construction, an asymmetric I-beam is needed to allow the decking to be dropped vertically onto the bottom flange. There are several built-up asymmetric cross-sections in the world and a limited number of hot-rolled sections in Europe. Hot-rolled asymmetric I-beams (termed A-shapes) are being researched for future large-scale production in the United States. The purpose of the research presented herein was to evaluate the behavior of A-shapes through a full-scale system test. To achieve this, a 6.1 m x 12.2 m (20 ft x 40 ft) shallow-depth composite floor system was constructed. The A-shapes spanned between stub columns, while New Millennium deep decking spanned between the beams. The floor system had a total depth of 257 mm (10.1 in.). In addition to the system test, a component-level beam test, with a finite slab width, was performed to compare to the system-level response. Testing of the floor system included monitoring the A-shape behavior during construction and analyzing the torsional response. Vibration testing was performed on the constructed floor system by conducting heel drop and walking tests. The natural frequencies of the first two modes were 8.1 Hz and 9.3 Hz. The serviceability of these floor systems was further evaluated by conducting service live load testing in locations around the slab. The floor system performed well, with a deflection corresponding to L/690 for a 3.8 kPa (80 psf) equivalent live load. Finally, the ultimate capacity of the floor system was quantified by loading the center beam to failure. The shallow-depth floor system gained significant composite strength and exceeded 125% of the full composite flexural capacity determined with a standard effective concrete width. The flexural rigidity of the floor system had a stiffness greater than the gross moment of inertia using twice the standard effective width. The overstrength and increased stiffness are a result of more concrete being engaged in the composite section, which was verified by measuring concrete strain on the slab surface. The full-scale testing conducted on shallow-depth floor systems with A-shapes indicated that it is a viable option for building floor systems.

Keywords: Structural Steel, Concrete-Steel Bond, Composite Action, Asymmetric I-beam, Shallow-Depth Floor Systems

Introduction

A new steel and concrete composite floor system is being evaluated to help reduce the overall depth of the floor system and to increase the speed of construction. In a conventional composite floor system, the steel beam is below the depth of the concrete slab, and the materials are mechanically connected using steel shear studs. Steel beams used in floor systems are generally I-beams, such as a W-shape (AISC 2023), due to their efficiency. The behavior of conventional composite floor systems is well understood, and these systems are used throughout the building industry. However, due to the concrete slab being above the steel beam, large floor depths are required for conventional composite floor systems. The overall depth of the composite floor system can be reduced by placing the steel beam within the depth of the slab for shallow-depth composite floor systems. To achieve this, precast concrete panels or steel deep decking are placed on the bottom flange of a steel beam to serve as stay-in-place formwork for a concrete slab. For ease of constructability, an asymmetric section is required to allow the formwork to be placed vertically down onto the section. Due to concrete encasement of the steel section, composite action will occur due to the bond that forms between steel and concrete. Conventional and shallow-depth composite floor systems are compared in Figure F-1.

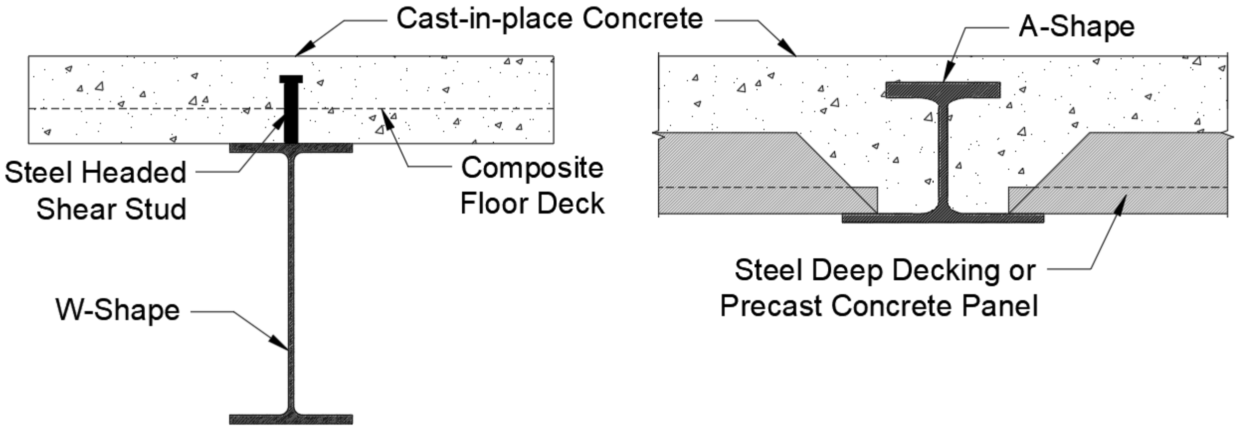

Figure F-1: Comparison of Conventional and Shallow-Depth Composite Floor Systems

Currently, there are no asymmetric I-beams rolled in the United States, and there is limited production around the world. As a result, various built-up sections have been developed for use in shallow-depth floor systems. These sections include simple plate girders, cutting doubly symmetric I-beams along the web and welding a steel plate or flat bar stock on the cut T-section, and fabricating other asymmetric sections. Plate girders have a lot of flexibility due to plate steel with different thicknesses and strengths. Doubly symmetric I-beams can be cut in various patterns to make an asymmetric section. Examples include cutting the web in a straight line (ArcelorMittal 2017; ArcelorMittal 2023b), a castellated pattern with straight lines (Girder-Slab Technologies 2016), or a castellated circular pattern (Kloeckner Metals 2020; Kloeckner Metals 2023). Other asymmetric sections are fabricated using channels, a steel plate, and threaded rod (ArcelorMittal 2017; ArcelorMittal 2023b) or using plate steel in a trapezoidal boxed section (DELTABEAM Technical Manual 2019; Peikko 2023). As an alternative, a limited number of hot-rolled asymmetric I-beams are rolled on request in Europe and are used in a floor system called Slimdek® (Lawson and Brekelmans 1999; Lawson et al. 1997; Lawson et al. 1998; Rackham et al. 2006).

Fabricating built-up asymmetric sections allows a lot of flexibility to make an efficient cross-section for varying scenarios. However, the asymmetric sections discussed above involve intensive fabrication which requires a lot of time. Rolling asymmetric sections at a steel mill would decrease the time needed for fabrication/manufacturing. As a result, research is being conducted on a new type of hot-rolled asymmetric I-beam (referred to as A-shapes) to help increase the speed of all phases of construction for steel buildings in the United States. This research is part of the American Institute of Steel Construction's (AISC) "Need for Speed" initiative (AISC 2024) and is funded by the AISC Milek Fellowship. Shallow-depth floor systems using A-shapes have several advantages due to increasing speed of construction, reducing the overall floor depth, and having large beam lengths and spacings due to the spanning capabilities of stay-in-place formwork.

Prior research in this project has consisted of both experimental and numerical work. Proof-of-concept (POC) testing was conducted at the beginning of the project to ensure that shallow-depth floor systems are a viable option for building floor systems (Davis 2022; Davis et al. 2023). POC asymmetric beams were utilized in the testing, which were initially developed for a residual stress study. The residual stress study analyzed the temperature variations of an asymmetric section as it cooled (Stoddard and Yarnold 2022; Stoddard 2022; Yarnold and Stoddard 2020). The POC testing consisted of analyzing the system during panel placement, slab pour, and vertical actuator loading to evaluate the system during construction and in-service. The testing showed that shallow-depth floor systems are feasible.

An analytical sizing study was performed to determine cross-sectional geometries for future production of A-shapes in the United States (US) (Ottmers et al. 2025b). To increase the viability of A-shape production, manufacturing considerations were determined by interviewing three major US steel mills: Nucor, Gerdau, and Steel Dynamics, to establish geometry limits. Structural load cases include both construction and in-service conditions to evaluate the A-shape and composite section for 16 limit states. To establish cross-sections, engineering judgement was used to determine common building grid layouts for residential buildings. Assumed parameters were varied in parametric studies to evaluate the sensitivity of controlling limit states. The controlling limit state for several scenarios in the parametric studies was the composite behavior, either strength or stiffness. However, there is uncertainty in the composite behavior of shallow-depth floor systems because no mechanical connectors are used to transfer load between the concrete and A-shape other than the bond stress that forms between the materials.

To reduce the uncertainty of the composite behavior, component-level testing was performed using POC asymmetric beams. Eight composite beams were tested to analyze the composite strength and stiffness of shallow-depth floor systems (Ottmers et al. 2025a). The composite beams performed well and gained significant composite strength, gained purely through the bond interaction between the steel and concrete. The eight tests included several redundant tests to gain a better understanding of the behavior and have a larger sample size. The partial composite strength was evaluated using three methods to determine the most conservative methodology. Furthermore, a bond stress was quantified for use in the partial strength calculations. The composite stiffness was evaluated for all eight tests to draw conclusions on the flexural rigidity of shallow-depth floor systems.

In order to fully understand the behavior of a shallow-depth composite section, a full-scale test was conducted (and is presented herein) to evaluate the system behavior of A-shapes in shallow-depth floor systems. The full-scale system test was conducted with guidance from prior floor system studies. These include system tests of an asymmetric section with web openings in Ju et al. (2009) and Bandelt et al. (2019). Long-span floor systems were studied by Huber and Varma (2008) for residential buildings. A full-scale component-level test with a wide effective width and a low degree of shear connection was conducted by Sheehan et al. (2018). A large experimental campaign was conducted to evaluate the performance of composite slim-floor beams (Hechler et al. 2016; Kuhlmann et al. 2021; Schorr and Kuhlmann 2019; Sheehan et al. 2019).

The research team also gained knowledge from several vibration studies on full-scale floor systems (Fahmy and Sidky 2012; Hicks et al. 2012; Sanchez et al. 2011). Vibration analysis can be completed using impact tests using an instrumented hammer, and more complex tests can be done using a shaker (Hanagan et al. 2003; Liu and Davis 2015). However, a much more cost-effective and simpler method to determine the vibration characteristics of a floor is outlined in Davis et al. (2014). In summary, heel-drop tests are performed to determine the fundamental frequencies of the floor system. Then, walking tests are performed at a normal walking pace to a harmonic of the dominant frequency, i.e., the step frequency multiplied by an integer (the harmonic) is equal to the dominant frequency (Davis et al. 2014).

The primary contributions of this research were to understand the behavior of the A-shape and the composite section at a system-level. The design methodologies utilized in the analytical sizing study were analyzed through all stages of a floor system. The constructability of these floor systems was assessed, and the structural behavior of the non-composite A-shape was analyzed during construction. Furthermore, the composite behavior was analyzed during service level loading and vibration testing. Additionally, the ultimate capacity of a shallow-depth floor system was evaluated. A full-scale component-level test was also conducted with similar cross-section geometry and properties to compare the component and system-level results. These contributions were accomplished by constructing two square bays of a building, each 6.1 m x 6.1 m (20 ft x 20 ft). The shallow-depth floor system had an overall floor depth of 257 mm (10.1 in.) with 203 mm (8 in.) prototype A-shapes. The research objectives for the experiments are outlined in the following section.

Research Objectives

Full-scale testing was conducted to quantify the behavior of shallow-depth composite floor systems utilizing A-shapes. A component-level test was performed, along with a system test that included relatively long beam lengths and wide beam spacing for residential buildings. The behavior of the floor system was analyzed during construction and in-service and was compared to theoretical results. The following research objectives were accomplished by designing, building, and testing a full-scale composite beam and two bays of a building floor system.

1. Evaluate the constructability of shallow-depth floor systems in terms of speed and assembly for steel erection, deep decking placement, and casting the slab.
2. Assess the serviceability by conducting several service live load scenarios to quantify the flexural rigidity and to analyze the degree of cracking due to a negative transverse moment across interior beams.
3. Examine the vibration serviceability of shallow-depth floor systems by conducting heel drop and walking tests to measure dominant floor frequencies and experimental mode shapes.
4. Analyze the ultimate capacity of a composite section gained through concrete-steel bond and quantify the reserve capacity of shallow-depth floor systems.
5. Compare the full-scale system and component-level response to analyze variability in the composite behavior.

Full-Scale Component-Level Testing

Prior to analyzing the full-scale system-level behavior, a component-level test was conducted to analyze the composite behavior of an established cross-section from the analytical sizing study (Ottmers et al. 2025b). The full-scale component-level test was conducted in a similar manner to the eight beam tests performed in Ottmers et al. (2025a). The component test presented herein was performed to analyze the same cross-section with a finite slab width that was used in the system-level test (discussed in the following section). The experimental setup, instrumentation, and results of the component-level test are discussed in this section.

Experimental Setup

The A-shape used in the full-scale testing was a prototype built-up plate girder of one of the established cross-section geometries. A plate girder was used instead of a hot-rolled asymmetric I-beam due to economic considerations for an experimental test. Rolling a handful of new structural steel shapes at a steel mill is not feasible for experimental testing. The built-up plate girder was a prototype for the A8x52, which is the lightest cross-section from Ottmers et al. (2025b), and the plate girder dimensions are shown in Figure F-2. Two different plate thicknesses were used in the shape, and the mill report indicated a different strength for each plate. The bottom flange and web had an average yield strength of 407 MPa (59 ksi), whereas the top flange had an average yield strength of 474 MPa (69 ksi). The steel plates were welded along the length of the beam using a fillet weld on both sides of the plate. The steel beams had a surface condition that was similar to a beam from a steel mill, and no paint was applied to the bare surface. The concrete used for this test was a pea gravel mix that included sand, pea gravel, type 1L cement, and water, which had a test day concrete strength of 21.4 MPa (3.1 ksi).

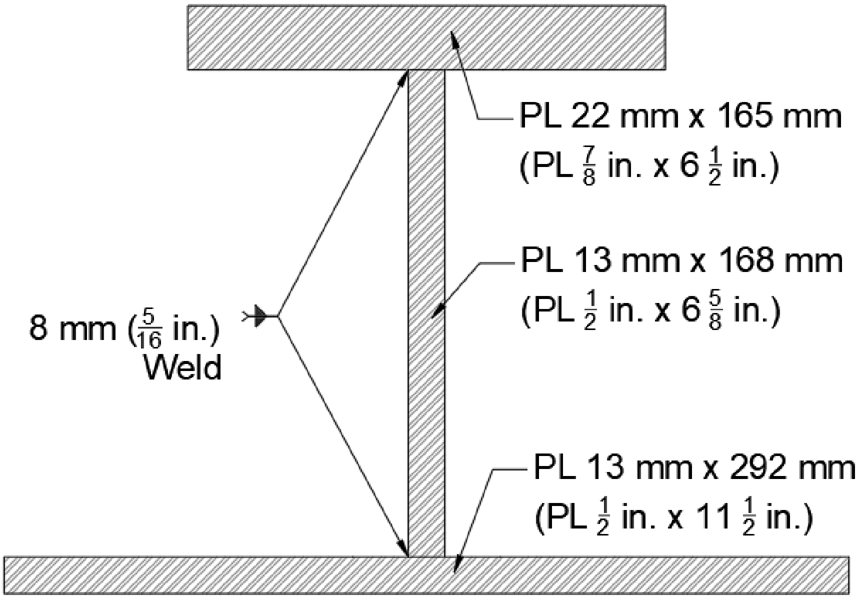

Figure F-2: Built-Up A-shape Plate Girder (prototype for the A8x52)

The width of the specimen was limited by the available test frame in the laboratory, so only a 0.9 m (3 ft) wide slab could be used for the composite section. The testing was performed at the Advanced Structural Engineering Laboratory at Auburn University. The length of the composite section was limited by the steel beam length to have sufficient bearing on the supports. The length of the concrete slab and the distance between the pin and roller supports was 5.5 m (18 ft). The stay-in-place formwork was constructed out of wood to create a void in the beam but was built using similar dimensions to the New Millennium steel deep decking (which was used in the system-level testing and is discussed in the Full-Scale System-Level Testing section). The wood formwork was removed after the concrete had cured and did not affect the results because composite action is gained through bond between the steel and concrete. Furthermore, the concrete would be non-continuous in the deep decking (void space in the component-level test) due to the ribbed pattern in the deck profile. Temperature and shrinkage steel reinforcement was placed directly on the top flange of the beam and consisted of 10 mm (#3), Grade 420 MPa (60 ksi) bars that were roughly spaced at 457 mm (18 in.) centers in both directions. No additional mechanical connection was provided between the steel and concrete other than the concrete encasing the steel section, which resulted in bond stress forming between the concrete and steel. A diagram of the composite section used in the full-scale component-level test is shown in Figure F-3.

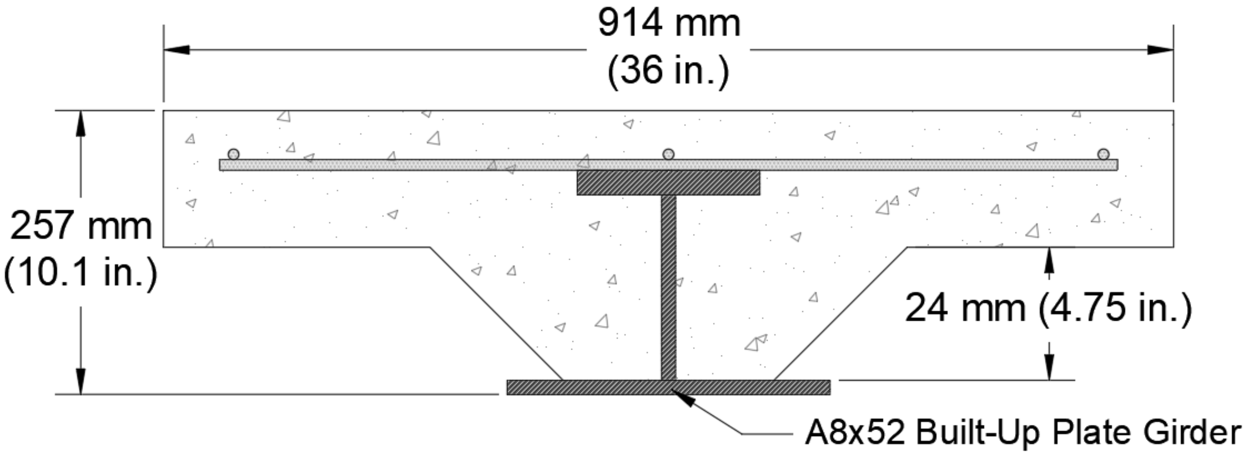

Figure F-3: Dimensions of the Component-Level Full-Scale Test Specimen

The composite beam was tested using a 2670 kN (600 kip) capacity Power Team actuator. The actuator load was spread out using a 1.8 m (6 ft) spreader beam to load the beam in four-point bending at the third points. The beam was supported at the ends by an idealized pin and roller, which consisted of a grooved and smooth plate, respectively, and both supports used a piece of round bar stock. The load was slowly increased using an air controlled hydraulic pump. A picture of the test setup is shown in Figure F-4.

Figure F-4: Photo of Test Specimen and Experimental Setup (Image by Chase Ottmers)

The composite behavior was measured using six steel strain gauges, three installed on the top flange, one on the web, and two on the bottom flange at the midspan of the beam. Five concrete strain gauges were installed on the concrete deck surface above the steel strain gauges at midspan to measure strain across the entire cross-section width. Inclinometers were utilized to measure rotation at the supports and at the location where the loads were applied in four-point bending. In total, five vertical displacement gauges (string potentiometers) were used to measure deflection throughout the test. Three of the string potentiometers were at midspan; one was under the steel section, and two were attached to the flat concrete surface in the voided area. Attaching the string potentiometers to the concrete could indicate if there was any twist of the section. The last two string potentiometers measured displacement underneath the applied point loads. Furthermore, slip sensors were installed on the steel beams at the supports to measure relative movement between the steel and concrete. The instrumentation utilized at midspan is shown in Figure F-5.

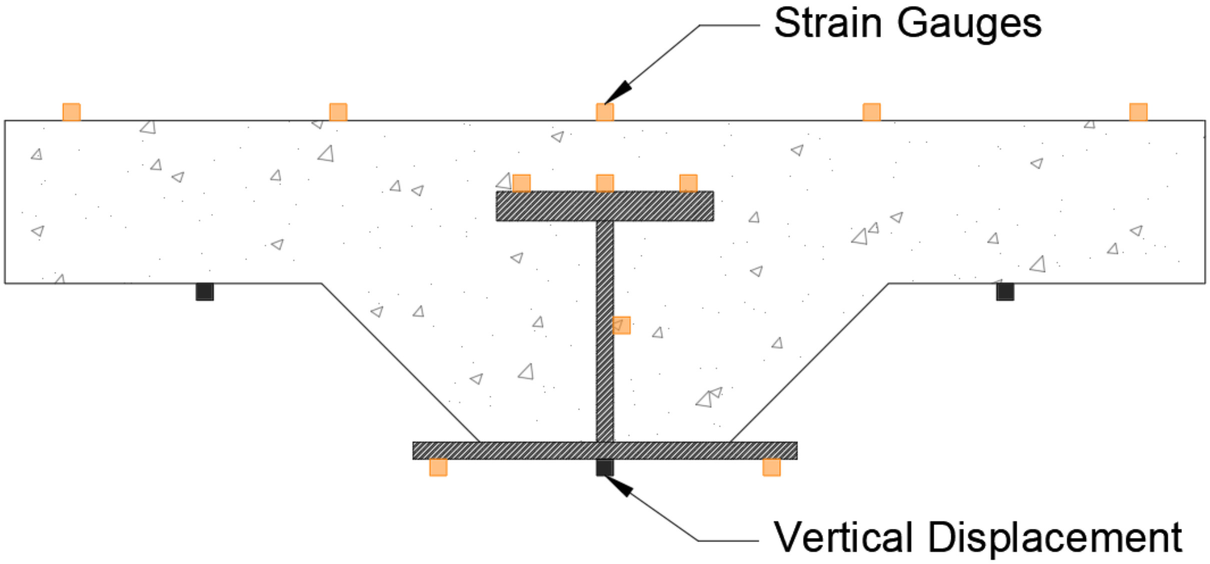

Figure F-5: Instrumentation at Midspan

Experimental Results

The component-level beam testing consisted of three loading stages. Stage one performed lower magnitude loading to investigate the linear elastic behavior. The load was slowly increased during stage two until the deflection reached 140 mm (5.5 in.). During stage two, there were two sudden cracks that reduced the stiffness of the composite section. These cracks occurred when the bottom flange strain was close to yielding. As a result, the section properties of the composite section were altered, and the bottom flange started to yield further. The third stage consisted of a reload cycle until the load began to plateau with a maximum midspan displacement of 213 mm (8.4 in.) before the test ended. The composite beam experienced great ductility and was able to develop significant composite action throughout the test. To understand the magnitude of the applied moment, the plastic moment of the A-shape (M_{sp}), the partial composite strength (M_{nc}) based on linear interpolation between the steel and full composite strength (recommended for design), and the full composite strength (M_{ncp}) are indicated with horizontal dashed lines in Figure F-6. A detailed discussion on the composite strength analysis for shallow-depth composite floor systems is given in Ottmers et al. (2025a).

The experimental strain for varying moment demands was examined to understand how the composite section performs throughout the test. A best-fit line was established through the recorded strain data over the depth of the cross-section. The moment demands selected in Figure F-7 are prior to the two sudden cracks that occurred when the bottom flange started to yield. A few load levels were included to analyze if the depth of the experimental neutral axis varies throughout the test. As seen in Figure F-7, the neutral axis depth does not vary throughout the beginning part of the test.

Furthermore, the depth of the neutral axis aligns with the theoretical composite elastic neutral axis (ENA). The theoretical composite ENA is determined using the gross moment of inertia of the transformed composite section. The plastic neutral axis (PNA) was determined for the full plastic composite strength.

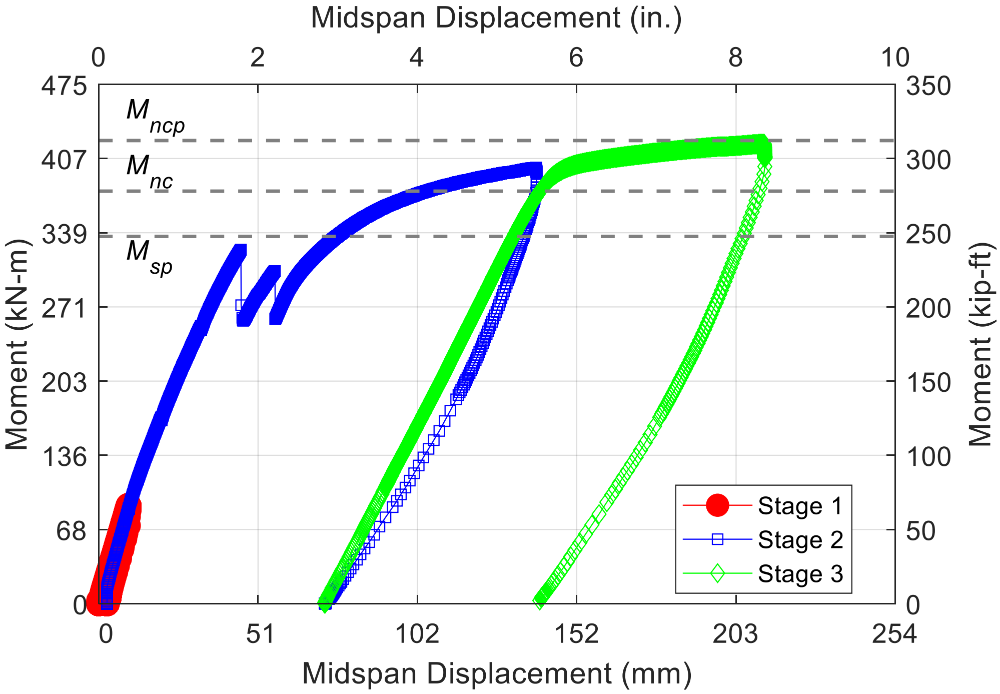

Figure F-6: Moment-Displacement Time History

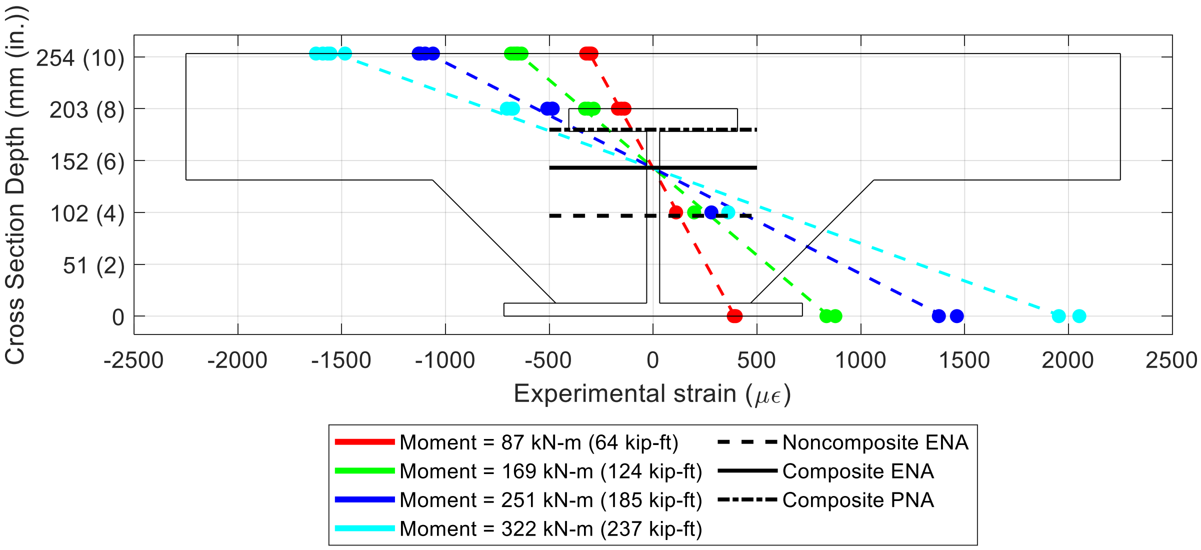

Figure F-7: Experimental Strains at Midspan

The inclinometer data in the experiment was utilized to quantify the moment-curvature relationship at midspan. The experimental strain data was also used and was similar to the inclinometer data before significant yielding occurred. However, strain gauges measure more of a localized result, whereas the inclinometer is more of a global response. The moment-curvature relationship using the inclinometer experimental data is shown in Figure F-8. The flexural rigidity of the component-level beam test was compared to three different theoretical values. The three values use (1) the gross moment of inertia of the composite section (I_{gross}), (2) the cracked moment of inertia ignoring concrete in tension below the neutral axis $(I_{cracked})$, and (3) an equivalent moment of inertia which interpolates between the steel and the gross moment of inertia of the composite section (I_{equiv}) (AISC 2022). The gross moment of inertia transforms all the concrete in the cross-section to an equivalent steel width. The cracked moment of inertia transforms concrete above the neutral axis to steel of an equivalent width. The degree of the flexural rigidity for the equivalent moment of inertia in AISC (2022) depends on the ratio of the maximum load that can be transferred through bond to the force that can develop in the concrete for the full composite cross-section. This method is similar to the linear interpolation method for partial composite strength discussed in Ottmers et al. (2025a).

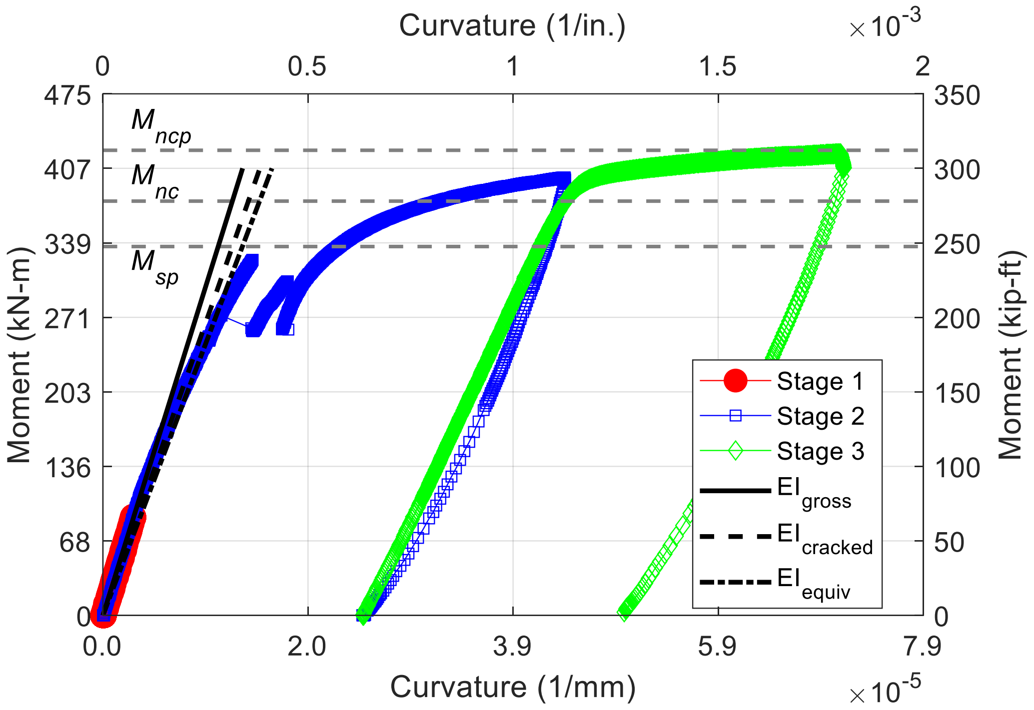

Figure F-8: Moment-Curvature Relationship at Midspan

The full-scale component-level test gained significant composite action and reached 99% of the full composite strength. Shallow-depth composite beams have significant ductility, and the beam in this experiment was able to resist load until a deflection of 213 mm (8.4 in.) was reached (Figure F-6). Analyzing the experimental strain profile (Figure F-7), the depth of the neutral axis did not change throughout the test before significant yielding occurred in the bottom flange. The partial composite strength quantified with the linear interpolation method provides a conservative analysis of the composite strength gained through bond formation between the steel and concrete.

The three methods used to quantify the composite moment of inertia all result in reasonable theoretical values (Figure F-8). The flexural rigidity of the composite beam is most conservative using the equivalent method in AISC (2022). However, there is not a major difference between the three methods. When comparing the theoretical and experimental curvature (or deflection) at service load levels, all three values provide conservative estimates.

A component-level test is great for understanding the composite behavior of these systems. However, there is still uncertainty with the system-level behavior. As a result, two bays of a building were constructed that used the same prototype A-shape, New Millennium steel deep decking, and a concrete slab. The full-scale system-level test is discussed in the following section.

Full-Scale System-Level Testing

To further understand the behavior of shallow-depth composite floor systems, two square bays of a building were constructed and tested. The beams spanned between the columns, and deep decking spanned between the beams. New Millennium Deep-Dek® (New Millennium 2019; New Millennium 2021a) was used in this test as precast concrete panels were previously implemented in Davis et al. (2023). The experimental setup, instrumentation utilized, and the testing program employed for the full-scale system-level test are discussed in this section.

Experimental Setup

Three prototype built-up A-shapes (discussed in the prior section and shown in Figure F-2) were used in the system-level test. The established A-shapes have approximately equal flange areas and have a total depth of 203 mm (8 in.). The bottom flange is 127 mm (5 in.) wider than the top flange to allow ample clearance during construction and bearing of the steel deep decking on the bottom flange. A detailed discussion of the manufacturing considerations for rolling A-shapes at a steel mill is provided in Ottmers et al. (2025b). The beams spanned between W12x65 stub columns that were spaced 6.1 m (20 ft) on center. The location of the stub columns was controlled by the 0.6 m (2 ft) on center tie-down holes at the Advanced Structural Engineering Laboratory at Auburn University. A simple shear connection using double clip angles connected the beams and columns together, roughly 0.9 m (3 ft) above the strong floor. The beam's span length between the bolted connection was about 5.6 m (18.5 ft) due to the column depth.

Steel deep decking panels were provided by New Millennium and were roughly 114 mm (4.5 in.) deep, 305 mm (12 in.) wide, and 1 mm (18 gage) thick. The panels had a length of 5.9 m (19.3 ft) to span between the A-shapes and had a 51 mm (2 in.) bearing seat on the bottom flange. A pneumatic crimper tool was utilized to crimp the deck panels together along their length at approximately 406 mm (16 in.) on centers. The deck panels were attached to the steel beams using a powder-actuated fastener tool; however, puddle welds could also be used. A plan view of the floor system is shown in Figure F-9.

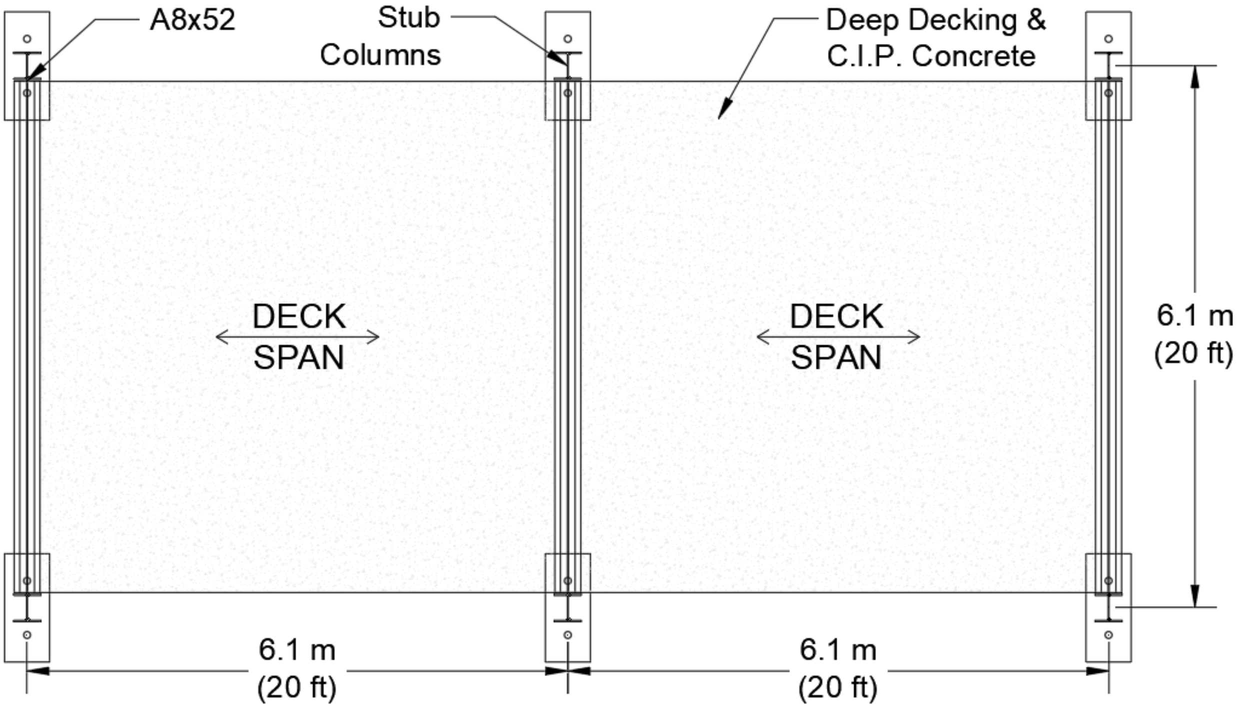

Figure F-9: Floor System Plan View

Following deck placement, a single mat of temperature and shrinkage reinforcement was installed near the top of the slab. The reinforcement consisted of 10 mm (#3), Grade 420 MPa (60 ksi) bars, spaced at 457 mm (18 in.) centers in both directions. The spacing of the transverse bars across the center beam was decreased to 152 mm (6 in.) to control cracking due to tension forming in the concrete slab when the midspan of the decking is loaded. The reinforcement sat directly on the steel A-shape, and no mechanical connectors were used to connect the A-shape to the concrete slab. A 127 mm (5 in.) deep concrete slab above the top of the deck was poured over the entire 6.1 m x 12.2 m (20 ft x 40 ft) floor system. As a result, the steel beams were encased in concrete, and the depth of the concrete above the steel section was 54 mm (2.1 in.). The shallow-depth composite floor system had a total floor depth of 257 mm (10.1 in.). The concrete consisted of type 1L cement, sand, #57 stone aggregate, and water and had a 178 mm (7 in.) slump. The concrete strength was determined on each test day using three compressive test cylinders per ASTM C39. Testing occurred between 15 and 22 days after the concrete pour, and the average strength ranged from 25.5 MPa (3.7 ksi) to 28.3 MPa (4.1 ksi). During the concrete pour, the midspan of the decking had to be shored per manufacturer requirements. Section views looking at the length of the beam and cross-sections of the floor system are shown in Figure F-10 and Figure F-11, respectively. The finished constructed floor system before the concrete pour is shown in Figure F-12.

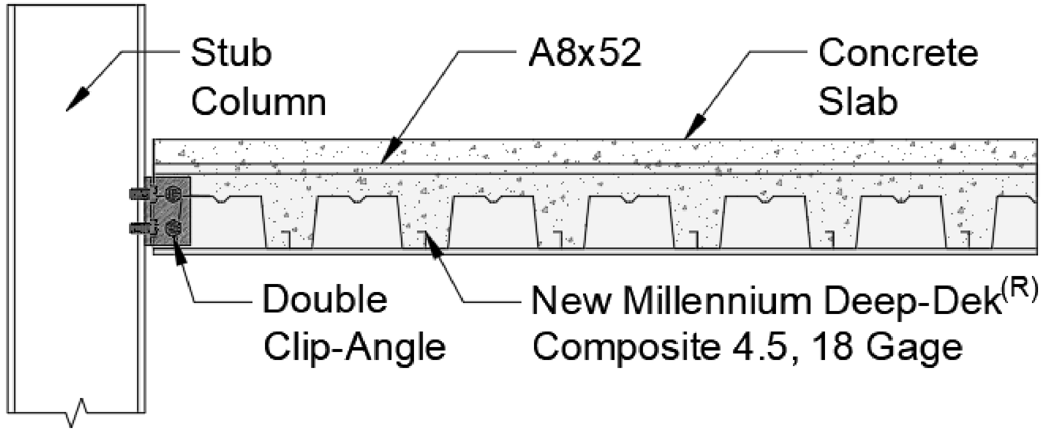

Figure F-10: Section Detail of the Floor System

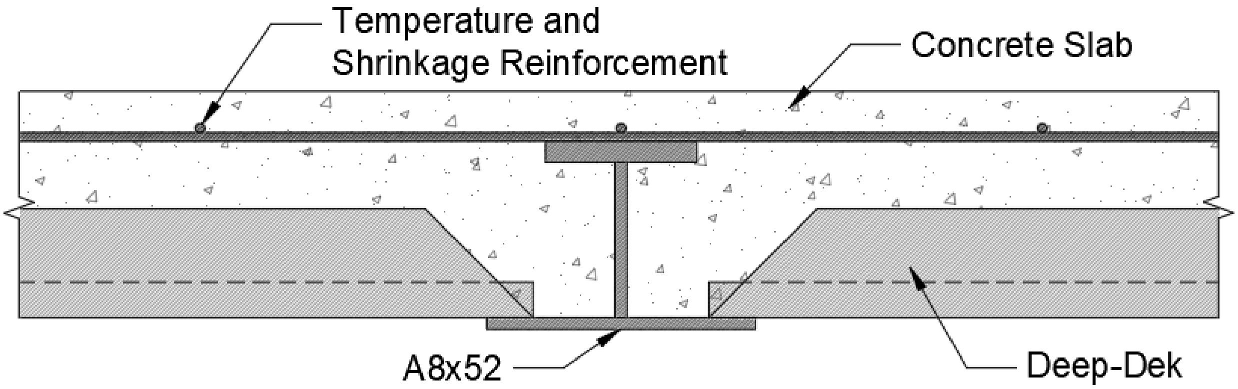

(a)

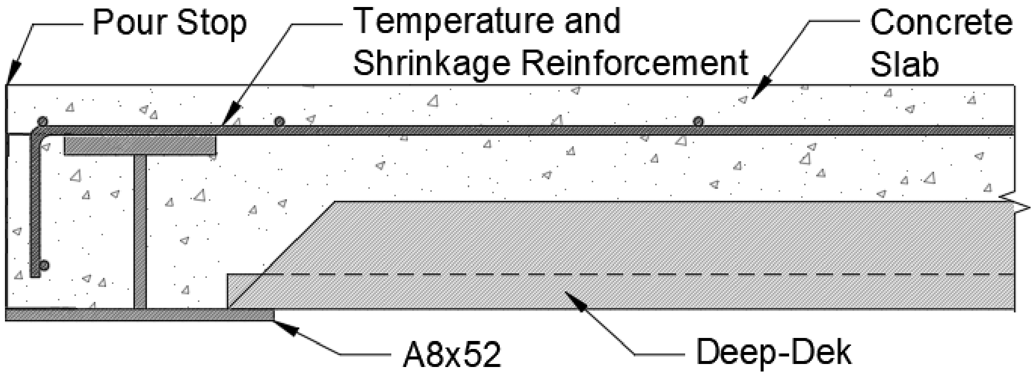

(b)

Figure F-11: Cross-Section Views of the (a) Center Beam and (b) Edge Beam

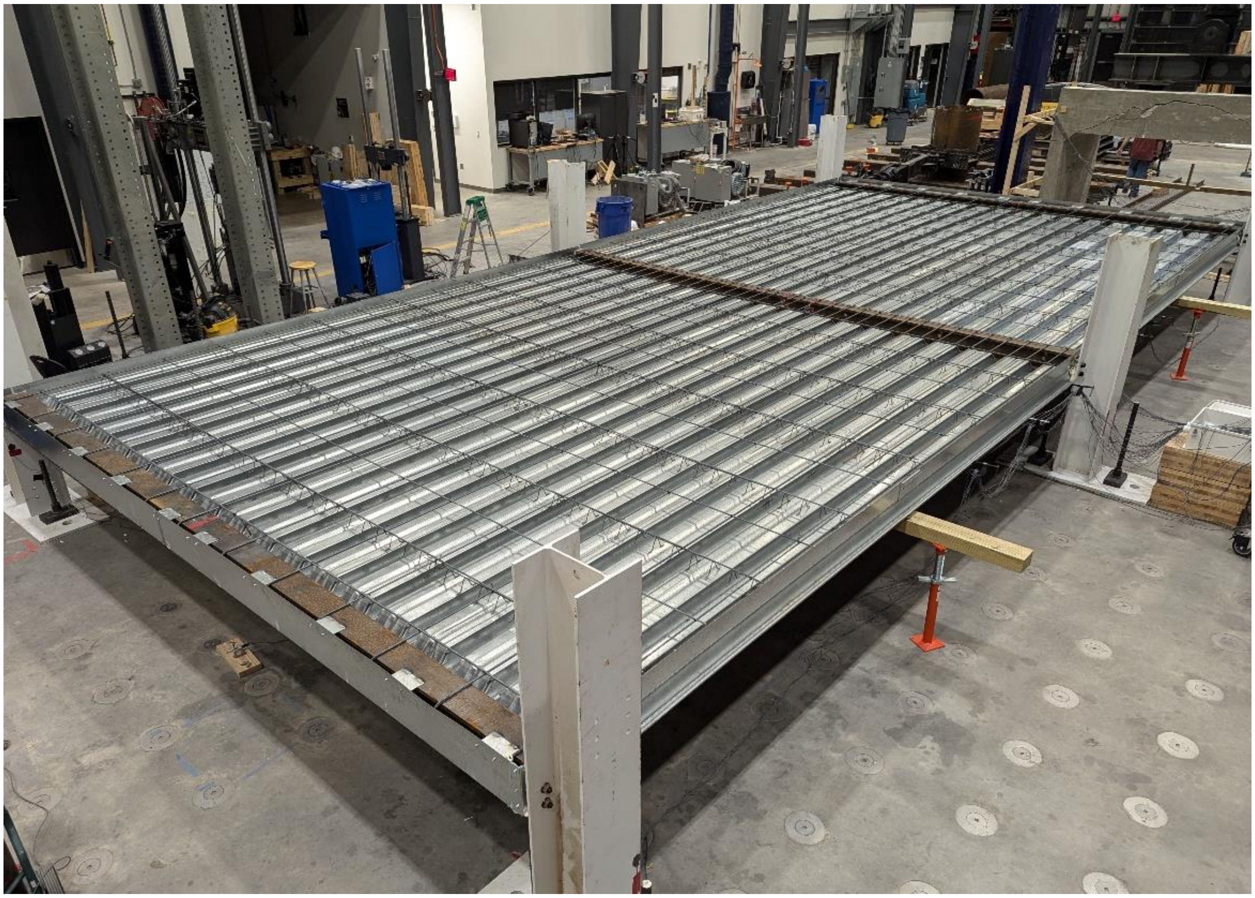

Figure F-12: Completed Floor System before Slab Pour (Image by Chase Ottmers)

Instrumentation

Similar instrumentation was utilized in the full-scale system-level test as the component-level test. Steel strain gauges were installed on the top flange, web, and bottom flange of all beams at midspan, and an additional set was installed on the center beam, which was 305 mm (1 ft) from midspan. Concrete strain gauges were positioned in the longitudinal direction above the steel strain gauge locations and in the transverse direction along the length of the center beam to measure tensile strain on the concrete slab surface during service load scenarios.

Inclinometers were mounted on the bottom flange of the beam to measure rotation at the supports and 0.9 m (3 ft) from midspan in both directions on the center beam. A grid of vertical displacement string potentiometers was installed underneath the slab to quantify the displacement field during loading. Finally, string potentiometers were included horizontally at the columns to measure if a sudden slip occurred between the steel and concrete at the ends of the beam. A plan view of the instrumentation implemented during the testing, which included over 100 sensors, is shown in Figure F-13.

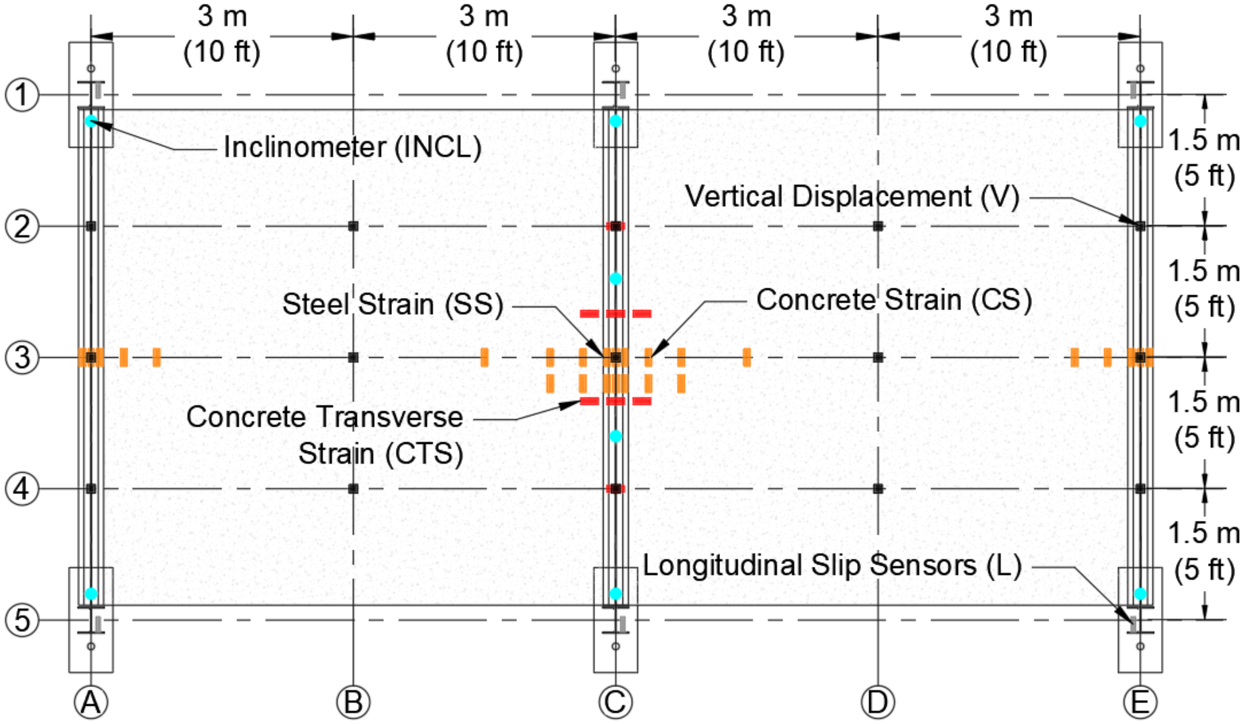

Figure F-13: Instrumentation Plan View

Testing Program

The floor system was tested in several configurations to understand the non-composite and composite behavior of shallow-depth floor systems. The behavior of construction loading during the concrete pour is analyzed in this section. Serviceability is often a controlling limit state for floors, and vibration could be an issue with shallow-depth floor systems. To address this concern, vibration testing was performed, which consisted of heel drop and walking tests. Serviceability deflection was also analyzed during several service loading scenarios in multiple locations around the slab. The final test consisted of loading the center beam to failure to examine the ultimate capacity of a system-level test. Experimental results from each of the tests are shown and discussed in this section.

Construction Loading

The construction loading for the shallow-depth floor system only consisted of the concrete pour. The deep decking panels are much lighter than precast concrete panels; therefore, the A-shape has minimal loading during the steel deck placement. The slab was cast starting from grid A5 (grids are shown in Figure F-13), and the pour moved across the slab. This can be observed in Figure F-14, which shows the deflection time history of the three A-shapes during the concrete pour. As a result, the A-shapes had to resist torsional loading during construction. The decking was shored at midspan, which means that the center beam only had to resist a tributary width of 1.5 m (5 ft) of wet concrete on each side of the beam. Displacement was only measured at the beam's midspan for the edge beams and was measured at midspan and 1.5 m (5 ft) from midspan in each direction for the center beam. The theoretical maximum displacement of the center beam at midspan (C3-V) is 11 mm (0.44 in.) and was determined using a concrete area load of 3.8 kPa (79 psf), per New Millennium (2021a), and a 3 m (10 ft) width due to shoring along Grids B and D. The theoretical displacement overestimates the experimental data by 5% and the experimental data is equal to L/505 when normalized by the length.

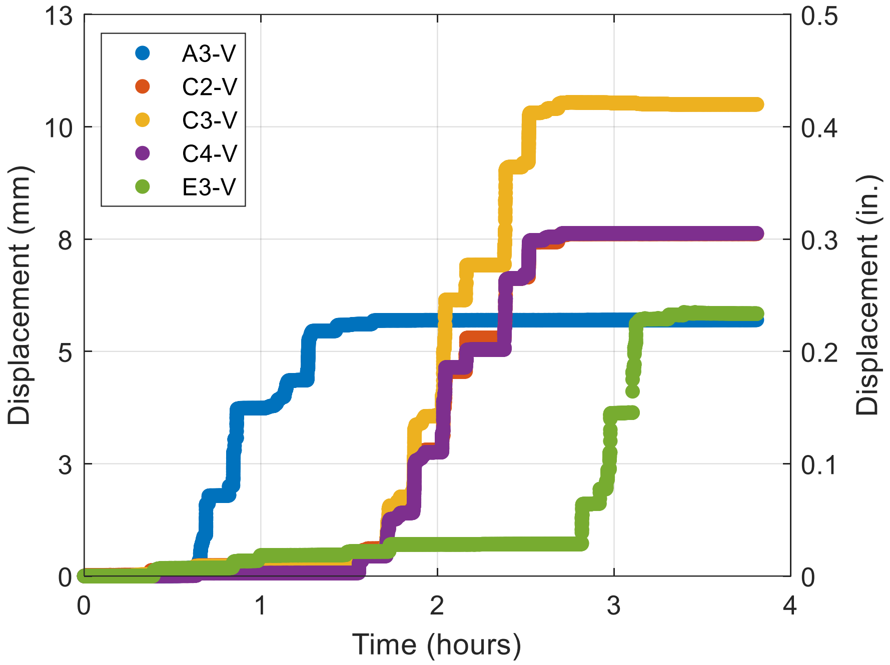

Figure F-14: Deflection Time History during Slab Pour

The edge beams and center beam had to resist a torsional moment during the slab pour. A torsional analysis was performed on the center beam when concrete was cast only on one side. Due to the decking being shored at midspan, torsion is not a major concern for A-shapes in this experiment. If precast concrete panels were utilized rather than deep decking, construction would be unshored, and torsion might be a controlling limit state if there were large beam spacings. With this in mind, the A-shapes were initially sized for unshored construction in Ottmers et al. (2025b). A detailed discussion on torsional analysis for A-shapes is provided in a prior publication by Davis et al. (2023), and further detail can be found in AISC's Design Guide 9 (DG9), *Torsional Analysis of Structural Steel Members* (Seaburg and Carter 2003).

The experimental strain on the top and bottom flange were compared to theoretical values using DG9. The theoretical values were determined for a uniformly distributed load that was quantified with a 3.8 kPa (79 psf) concrete area load and a 1.5 m (5 ft) tributary width. The uniform load was assumed to act at the center of the deep decking bearing width, which was 25 mm (1 in.) from the edge of the bottom flange. The theoretical and experimental strain values are compared in Figure F-15. The theoretical values are shown in parentheses, and they correspond to the combined bending and torsional strain at the gauge locations. The experimental strain indicates that there is less torsion in the cross-section because the experimental strains on the flanges do not have significant variation across the width of the flange. The maximum measured value was 245 microstrain, which corresponds to a stress of 49 MPa (7.1 ksi), indicating relatively low torsional demand. The difference could be attributed to the fact that the theoretical values assume the supports are pinned for both bending and torsion; however, double clip angles were utilized in the experiment which are semirigid connections. Torsional analysis assuming fixed-end and pinned connections was performed by Davis et al. (2023) to examine the degree of rigidity of simple shear connections. The behavior proved to be semirigid; however, assuming pinned connections is conservative and appropriate. Additionally, there could be imperfections in the steel beams, and the concrete placement might not have been exactly a 1.5 m (5 ft) width applied to the center beam.

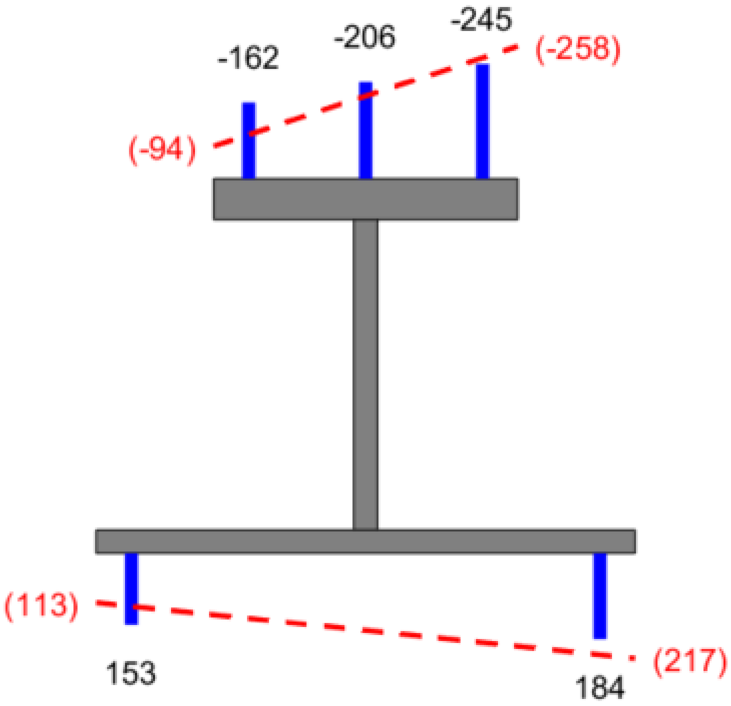

Figure F-15: Torsional Analysis for the Center Beam during the Slab Pour

Vibration Testing

Humans are susceptible to vibrations at varying levels depending on the activity they are performing (Murray et al. 2016). Utilizing shallow-depth floor systems and maximizing the beam length and spacing has a lot of architectural advantages; however, vibration issues could arise. To analyze the vibration characteristics of these floor systems, vibration tests were performed on the constructed system with no finishes. Acceleration data was recorded using seven uniaxial PCB Model 352 A24 accelerometers produced by PCB Piezotronics, Inc., and the sampling frequency was 2048 Hz.

Testing consisted of 52 heel drops to analyze the fundamental frequencies of the floor system. The heel drops were performed at various locations around the slab, and the accelerometers were moved to different locations. Included in those tests were conducting heel drop tests at a single location while roving five of the seven accelerometers across the slab surface. This was completed to quantify experimental mode shapes for the shallow-depth floor system. In addition, 66 walking and max excitation (running and jumping on the slab) tests were performed in random and straight paths across the slab. The walking tests were performed at a random pace or walking in rhythm with a metronome at a specific pace. During the walking tests, one, two, and four people walked on the slab. Furthermore, tests were performed to cause max excitation, where four and ten people were running around and jumping on the slab randomly.

When analyzing the acceleration data, a high pass filter was used to eliminate noise in the lab less than 2 Hz. After analyzing the frequency spectrum, there were two dominant frequencies for the first two modes that are of interest. There were higher modes present, which are torsional modes of the floor system and localized modes. The first mode of the floor system is an overall bending mode where the floor system was moving all as one system, and the frequency was 8.1 Hz. The two floor system bays moved in opposite directions in the second mode, and the frequency was 9.3 Hz. A 3D and plan view of the normalized modal shapes for the first two bending modes are shown in Figure F-16. These mode shapes were obtained by performing a heel drop in a single location and roving the accelerometers across the slab. Reference accelerometers were used to stitch the data together to analyze the mode shape for the entire floor system. The black points in the figure correspond to the normalized mode value analyzed for each accelerometer location. Dr. Brad Davis from the University of Kentucky, along with the authors, are conducting a further study of the vibration testing to analyze the vibration characteristics of shallow-depth floor systems with A-shapes (see Appendix G).

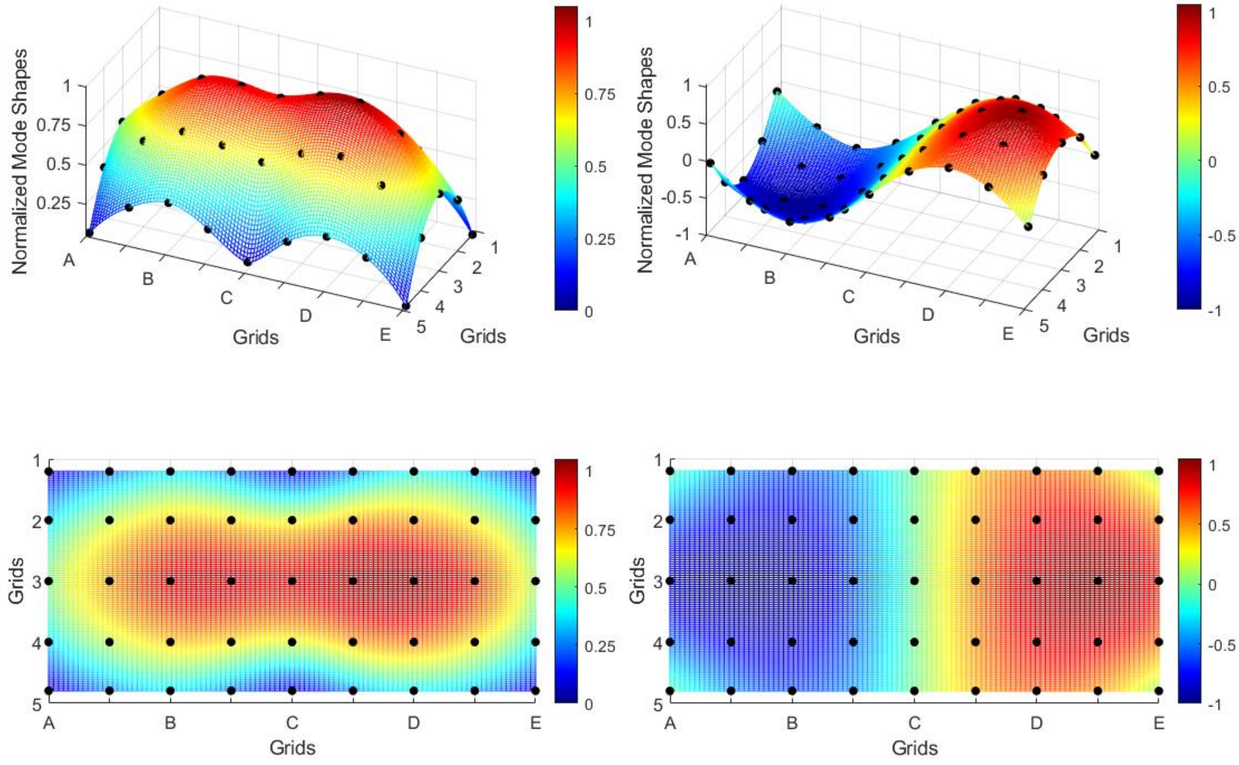

(a) (b)

Figure F-16: Experimental Mode Shapes: (a) Mode 1 (8.1 Hz) and (b) Mode 2 (9.3 Hz)

As discussed in AISC's Design Guide 11, *Vibrations of Steel-Framed Structural Systems due to Human Activity*, nonstructural components such as the ceiling and ductwork, furniture in the building, and partition walls contribute to the damping ratio (Murray et al. 2016). Therefore, the tested state of the floor system has minimal to no damping ratio. The mass of the structure also varies in each building stage, which affects the vibration characteristics. This was shown during vibration testing of a shallow-depth floor system during three stages: after steel erection, the concrete pour, and adding finishes. The natural frequency of the floor system varied significantly between the constructed state after the concrete pour and the finished building (Ju et al. 2004). The vibration testing conducted in this study provides valuable information to understand the vibration characteristics; however, various factors can alter the results that were measured.

Service Loading

Multiple load cycles were performed in various locations around the slab to further analyze the serviceability of shallow-depth floor systems. The loading was applied using two 1780 kN (400 kip) capacity Power Team actuators that were attached to two large test frames. Spreader beams were attached to the actuators to apply the loads 1.8 m (6 ft) apart. The loads were applied to the slab on 406 mm x 610 mm (16 in. x 24 in.) steel plates, which sat on rubber pads. Loading the floor system with an area load, such as using sand or water, would be more applicable for buildings. However, this was not practical for this experiment.

The loading scenarios included loading the slab at the midspan of the decking (Tests 1-4), at the edge beams (Tests 5-6), and the center beam (Tests 7-8). The last loading condition combined the test frames together to load directly over the center beam and is discussed in the following section (Test 9). The loading locations for the tests are shown in Figure F-17. The loading sequence consisted of loading one bay at a time (e.g., Tests 1A and 1B) and then loading both bays (e.g., Test 2) together. Load was applied using a pneumatic-driven hydraulic pump to increase load at a slow rate. During the tests, load was stopped at various levels to analyze the floor system for cracks in the concrete slab, take pictures of the floor system, and check the experimental data. The load levels with brief pauses consisted of equivalent area loads of 1.9 kPa (40 psf), 2.9 kPa (60 psf), and 3.8 kPa (80 psf). However, it should be mentioned again that the loading locations are localized due to practical reasons for experimental testing. An image of the experimental setup for Tests 1 and 2 is shown in Figure F-18.

Service loading performed in Test 2 was used to examine the performance of shallow-depth floor systems. The other tests provided similar information; however, they are not shown due to space limitations. Refer to Ottmers (2025) for further analysis and figures of other service loading locations. A good starting point for understanding system-level behavior is to analyze the measured displacements. The grid of displacement string potentiometers underneath the slab was utilized to create a displacement field of the floor system. To achieve this, 3-D interpolation was completed between the measured values. In addition to the measured displacements, the supports were assumed to have zero displacement. An example of the displacement field for Test 2 is shown in Figure F-19 for an equivalent 3.8 kPa (80 psf) live loading. The equivalent area load was applied at the four locations labeled with 1A, 2 and 1B, 2 in Figure F-17 and consisted of an applied load of 71 kN (16 kips) on each steel plate.

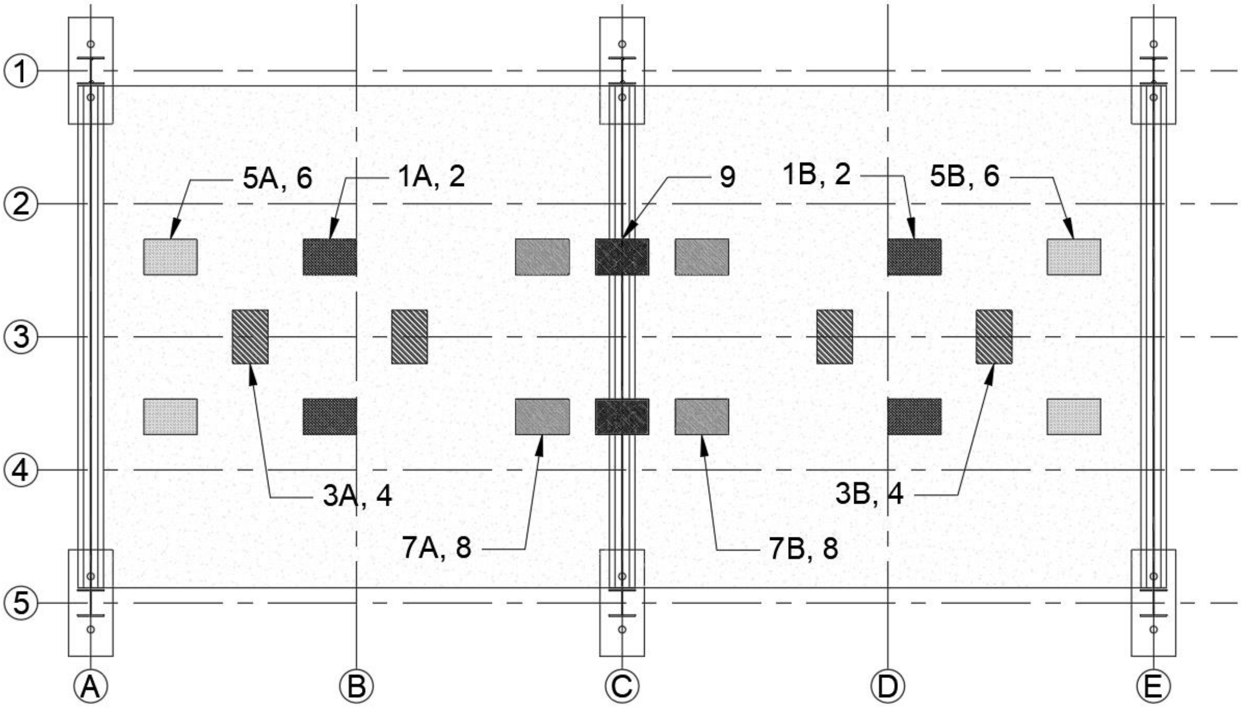

Figure F-17: Actuator Loading Locations

Figure F-18: Photo of Experimental Setup for Tests 1 and 2 (Image by Chase Ottmers)

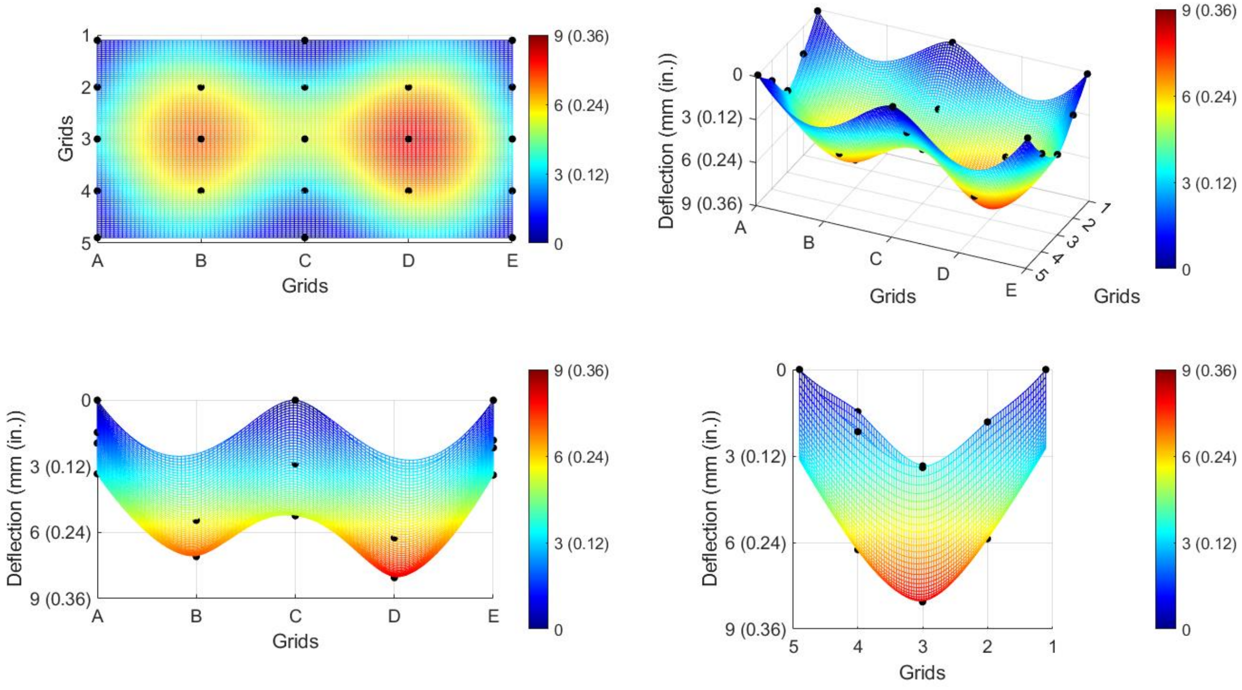

Figure F-19: Displacement Field for an Equivalent 3.8 kPa (80 psf) Live Loading

As shown in Figure F-19, the floor system had minimal deflections at this load level. The theoretical load distribution to the three beams would be 25%-50%-25%. Examining the maximum displacements at the midspan of each beam, the load distribution to the center beam is approximately 48%. This value was determined by comparing the displacement of the center beam to the sum of the midspan displacements. However, the load is applied slightly closer to the edge beams due to laboratory constraints (location of tie-down holes), which explains some of this discrepancy. This indicates that the load was distributed to the edge and center beams relatively equally during Test 2.

The maximum deflection in each bay occurs near the decking midspan (Grids B and D), and the A-shapes have less deflection than the decking. According to the International Building Code, the acceptable deflection limit for service live loading is L/360 (IBC 2018). The beam spacing is 6.1 m (20 ft), therefore the deflection of the decking must be less than 17 mm (0.67 in.). Whereas the beam length is roughly 5.6 m (18.5 ft), meaning that the maximum deflection during service can only be 16 mm (0.62 in.). As shown in Figure F-19, the live load deflection for the A-shape and deep decking are acceptable, and the normalized decking displacement is roughly L/690.

For a concrete and steel composite section, the total effective width of the concrete slab is assumed to be the minimum of a quarter of the span length and the beam spacing, per AISC (2022). The effective width of the composite section affects the composite strength and stiffness calculations. For this floor system, the theoretical effective width is controlled by a quarter of the span length and is 1.4 m (4.6 ft). To examine how much concrete width is contributing to the shallow-depth composite cross-section, strain gauges on the concrete slab were installed up to an effective width of 3 m (10 ft) centered over the A-shape. The measured longitudinal concrete strain values for an equivalent 3.8 kPa (80 psf) live loading are shown in Figure F-20, and vertical lines denote the theoretical effective width. The strain gauges indicate that a large portion of the concrete is engaged in shallow-depth cross-sections, which implies that the theoretical effective width assumption is conservative.

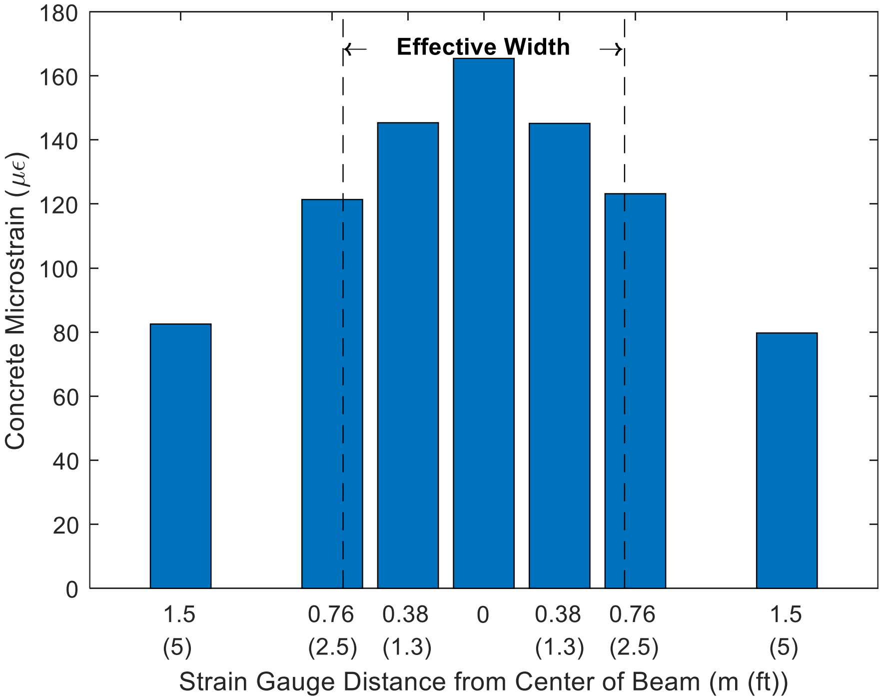

Figure F-20: Concrete Strain Lag for Equivalent 3.8 kPa (80 psf) Live Loading

Hairline cracking occurred parallel to the length of the center beam during service-level loading. Throughout the various load cycles, additional hairline cracks were observed. As mentioned, the transverse reinforcement across the center beam had a decreased spacing of 152 mm (6 in.) to help control the width of these cracks. Concrete strain in the transverse direction was recorded throughout the tests. For an equivalent area load of 3.8 kPa (80 psf), the average tensile strain in the transverse concrete gauges was around 40 microstrain. One of the strain gauges had a measured strain of roughly 180 microstrain. However, this was a localized measurement as the strain gauges near that gauge measured strain values that were close to the average. During the various loading scenarios, additional cracking appeared along the center beam when the floor system was loaded in different areas. The transverse reinforcement controlled the width of the cracks, and the stiffness of the floor system was not affected.

Throughout Tests 1-8, the shallow-depth floor system performed well during service loading. The response of the floor system was elastic, and the flexural stiffness was greater than the theoretical because more concrete contributes than the theoretical effective width. The service testing indicated that shallow-depth composite floor systems are a viable option for buildings with long beam lengths and large beam spacings. Furthermore, minimizing the floor depth is possible in these systems, and good performance can be achieved by developing composite action through bond between the steel and concrete.

Ultimate Loading

The ultimate capacity of the shallow-depth composite floor system was evaluated by connecting the test frames together and loading over the center beam. This concentrated the load directly over the center beam and loaded the section in four-point bending (Test 9 in Figure F-17). Loading for the ultimate system-level test was conducted in three stages similar to the component-level beam test and is shown in Figure F-21. A few load cycles were conducted at lower load levels in stage one. The main load cycle (stage two) consisted of loading the floor system until 127 mm (5 in.) of deflection was reached. Two additional reload cycles were conducted in stage three until the load plateaued and the midspan displacement of the center beam was approximately 185 mm (7.3 in.). To understand the magnitude of the applied moment, the A-shape's plastic moment $\left(M_{sp}\right)$ is indicated with a dashed line. Additionally, the composite section was analyzed for the standard effective width for a composite section. The partial composite strength (M_{nc}) was determined using the linear interpolation method (recommended for design), as well as the full composite strength $\left(M_{ncp}\right)$. Strength analysis for the composite section is discussed in Ottmers et al. (2025a). As shown in the concrete strain plot from Test 2 (Figure F-20), more concrete width contributes to the flexural capacity than the assumed effective width. Similar results were observed during the ultimate load testing. This explains why the floor system was able to reach nearly 125% of the full composite strength. This indicates that the theoretical effective width produces a conservative estimate for the composite capacity.

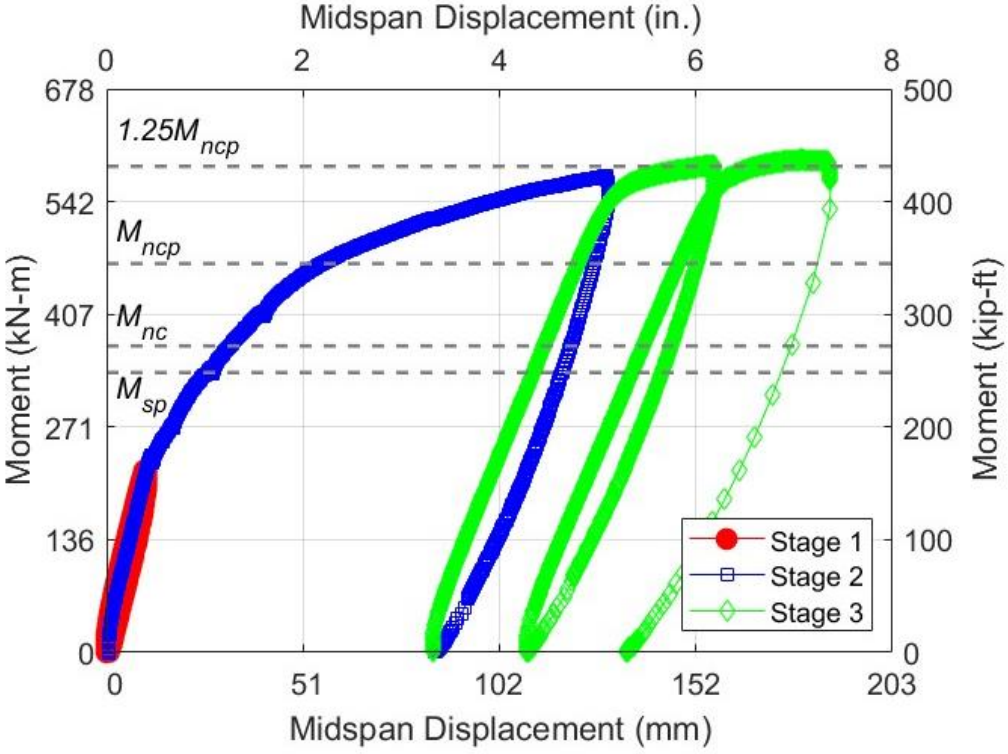

Figure F-21: Moment-Displacement Time History for Ultimate Loading

A system-level test adds complexity to the analysis due to load distribution to the other beams. To minimize the load distribution, the load was applied directly over the center beam during the final test. The load distribution was quantified using the midspan displacement of each beam (Grids A3, C3, and E3) and comparing the deflection of the center beam to the sum of the midspan displacements. The applied moment in Figure F-21 is calculated using only 80% of the applied load. In other words, this is saying that 10% of the load is being distributed to each of the edge beams. The load distribution changes throughout the test, and initially, the center beam is the only beam deflecting due to the load location. However, the edge beams start to resist load as the applied load is increased. The load distribution for the center beam plateau's around 80% when using midspan displacements. As a result, 80% of the load is assumed to be applied to the center beam during the entire test.

The displacement field for the maximum load during stage three is shown in Figure F-22. The floor system had great ductility and was able to resist significant load. During stage three, minor cracking occurred in the slab close to the stub columns due to the floor system bending in a large bowl-like shape. However, the cracking was hairline throughout the entire test. The flexural stiffness of the floor system was compared to the theoretical moment of inertia values, transforming the concrete into an equivalent steel width. For the system-level test, the gross moment of inertia was calculated using the theoretical effective width (I_{gross}) and two times the effective width $(I_{gross,2Be})$. To be consistent with the component-level test, the cracked moment of inertia $(I_{cracked})$ and equivalent moment of inertia (I_{equiv}) were also determined. The theoretical flexural rigidity (EI) is compared to stage one and part of stage two loading in Figure F-23. The floor system is stiffer than the theoretical flexural rigidity using two times the standard effective width. The behavior is linear during the lower-level loading with a high degree of flexural stiffness. This further shows that a large concrete width contributes to the flexural behavior of the shallow-depth floor system. During stage two, a crack formed around 230 kN-m (170 kip-ft), which softened the floor system. The stiffness of the softened floor system is similar to the flexural rigidity using the equivalent moment of inertia. However, the gross moment of inertia would be a conservative estimate for the stiffness for applied moments less than the partial composite strength (M_{nc}). At moment demands encountered for service analysis, the flexural rigidity of shallow-depth floor systems determined with two times the standard effective width is conservative.

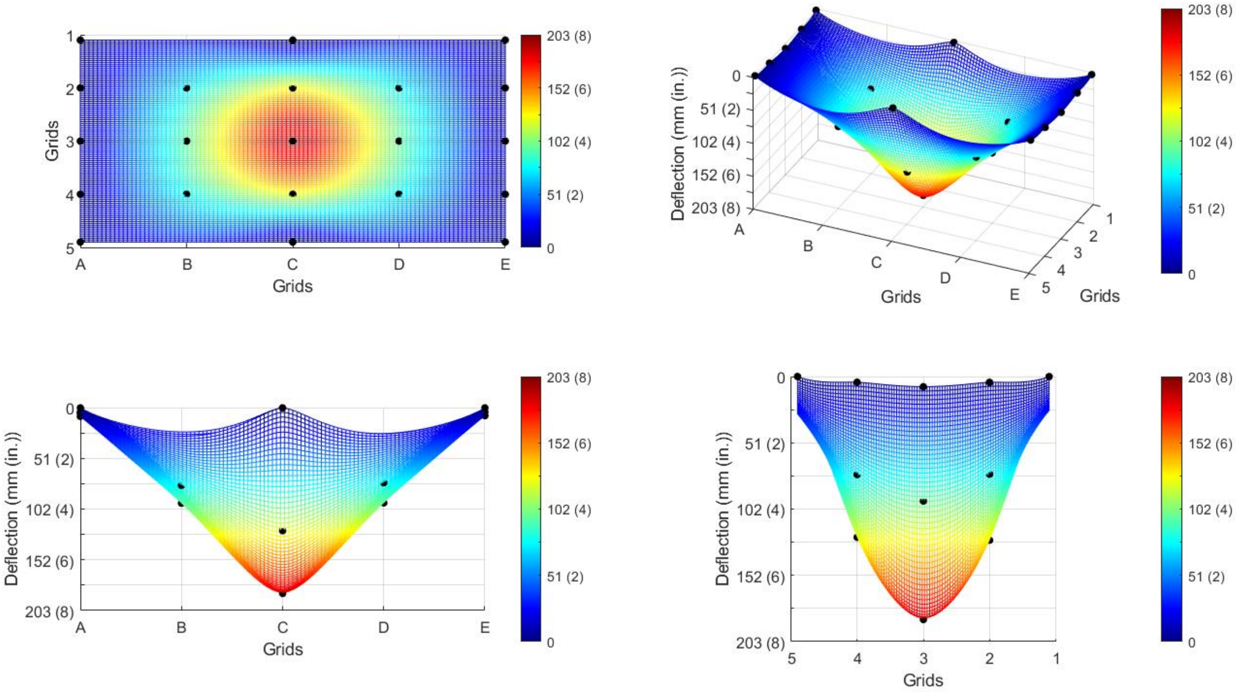

Figure F-22: Displacement Field for Maximum Load

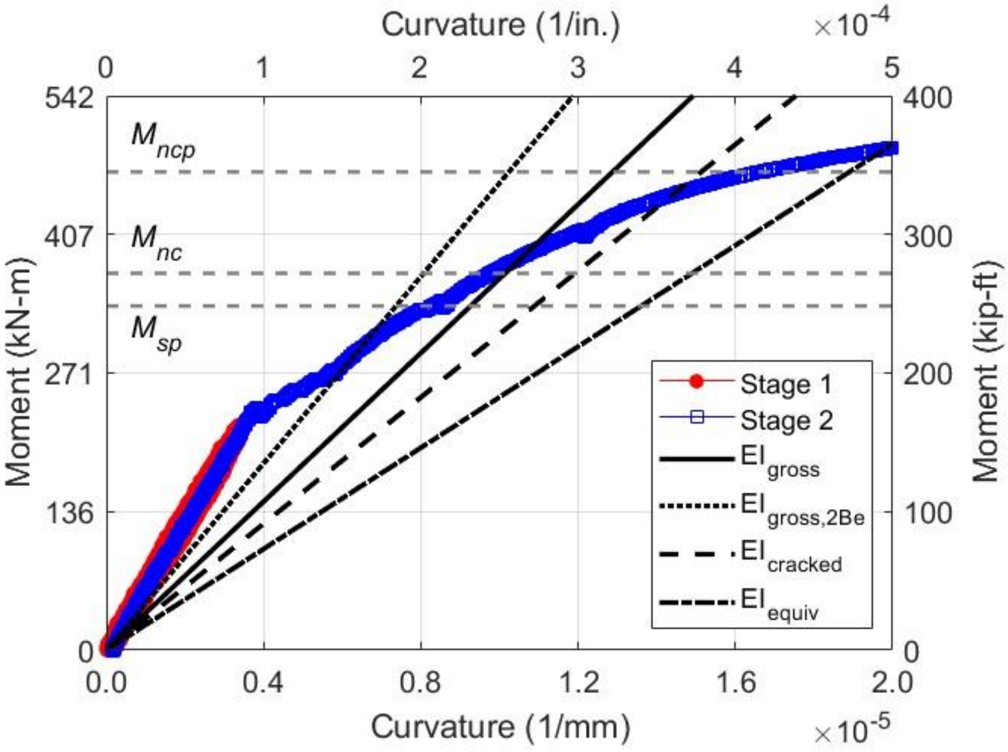

Figure F-23: Moment-Curvature Relationship during Ultimate Loading

The experimental strain was examined for varying load levels for the system test. A best-fit line was established through the experimental strain on the bottom flange and the top of the concrete. The encased gauges on the top flange and web were damaged after the concrete pour; therefore, these gauges were discarded from the data analysis. The depth of the experimental neutral axis varies less than 13 mm (0.5 in.) and is in the top flange for the selected moments in Figure F-24. The neutral axis depth aligns closely with the plastic neutral axis (PNA) of the full composite section determined with the theoretical effective width. The elastic neutral axis (ENA) depth of the gross composite section was determined for a section using the theoretical and two times the theoretical effective width. The bottom flange has just started to yield at midspan when the full composite moment (M_{ncp}) is reached. This further indicates that more concrete is being utilized than the theoretical effective width, reducing the strains at the extreme fibers of the cross-section. Since there is minor movement of the neutral axis and a significant moment was applied during the test, this reveals that the section is acting compositely due to bond stress forming between the steel and concrete. The ultimate load testing further shows the viability of shallow-depth floor systems. Analyzing the cross-section using the theoretical effective width provides conservative results for both the composite strength and stiffness.

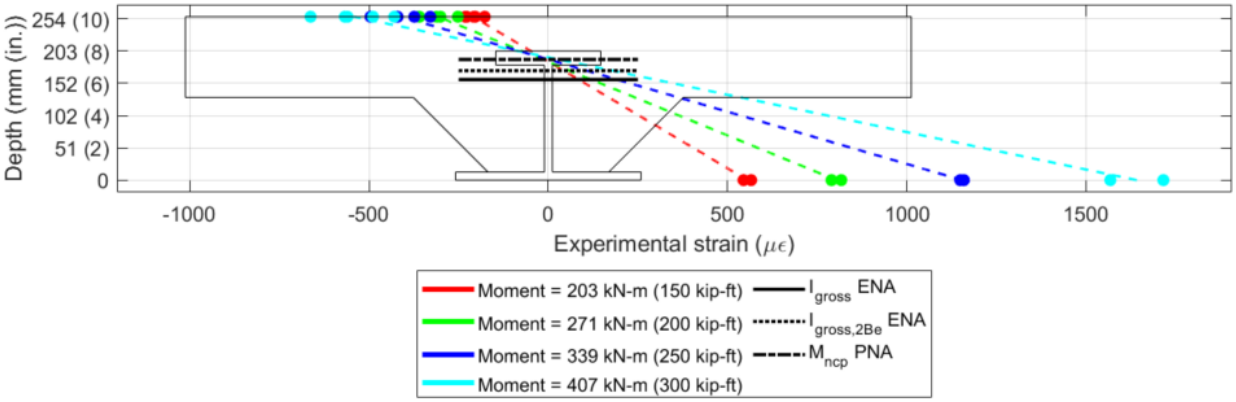

Figure F-24: Experimental Strain during Ultimate Loading

Comparison of Component-Level and System-Level Tests

A major difference between component-level and system-level testing is the complexity of the analysis. Composite beam testing at the component-level is a lot easier to understand the behavior due to the beam having a finite slab width. Furthermore, component-level testing provides conservative results when analyzing the flexural strength and stiffness compared to the system test (Figure F-8 and Figure F-23, respectively). On the other hand, system-level testing allows for an understanding of a full-scale floor system in several aspects that can't be analyzed with a component-level test. This includes the behavior during construction, vibration characteristics/performance, multiple service loading scenarios to simulate live loads around the slab, and the ultimate capacity of a composite section in a floor system.

The component-level and system-level testing performed in this study utilized similar cross-sections that had slightly different span lengths and concrete strengths. The component-level test had an idealized pin and roller support, whereas the system-level test used double clip angle shear connections. When comparing the experimental results to theoretical values for the composite strength and stiffness, the system-level test performs better in both metrics, as expected. The flexural stiffness of the component-level test can be reasonably estimated with the gross moment of inertia (Figure F-8). Whereas the flexural stiffness of the system-level test has a higher flexural stiffness than two times the effective width (Figure F-23). The component-level test reached the full composite strength whereas the system-level test slightly exceeded 125% of the full composite strength, utilizing the standard effective width. The bottom flange of the component-level test starts to yield at an applied moment of 76% of full composite strength (Figure F-7). On the contrary, the bottom flange does not start to yield in the system-level test until 96% of the full composite strength is applied (Figure F-24). The strain in the bottom flange is reduced throughout the system-level test because a large width of the concrete is contributing to the flexural stiffness of the composite section. Both tests proved that shallow-depth composite floor systems are ductile, have robust behavior, and exhibit similar performance after several significant load cycles (shown in Figure F-6 and Figure F-21).

Conclusions

Full-scale tests, both on a component and system-level, were conducted to understand the behavior of A-shapes in shallow-depth floor systems during construction and in-service. To achieve this, a component-level beam test was performed with a similar span length and concrete strength as the system-level test. The focus of the component-level test was to analyze the flexural strength and stiffness of a composite section gained purely through bond interaction between the steel and concrete. The system-level test consisted of constructing and testing two bays of a building using prototype A-shapes, New Millennium deep decking, and a concrete slab. System behavior was analyzed for the floor system during construction loading, in-service testing included vibration and service-level load testing, and the ultimate capacity of the floor system was evaluated.

Quantifying the composite stiffness of shallow-depth floor systems using the component-level test proved to be conservative. The experimental composite stiffness was compared to the theoretical moment of inertia quantified using (1) the gross composite section, (2) the cracked section, which ignores concrete below the neutral axis, and (3) an equivalent method that iterates between the steel and gross composite section based on the amount of load transfer that occurs between the steel and concrete in the composite section. The component-level test indicated that all three methods would provide reasonable and conservative results for service loading. The system-level test displayed a much stiffer response since a large width of concrete is available to resist bending of the floor system. The longitudinal strain at the top of the concrete was significant for two times the theoretical effective width. The system-level response was compared to the same three methods in the component-level response, as well as the gross moment of inertia determined with two times the theoretical effective width. For service-level loads, the system-level behavior is stiffer than the gross section with twice the effective width. The gross moment of inertia determined for a standard effective concrete width based on a quarter of the span length provides a conservative response until the applied moment exceeds the partial composite moment capacity.

Furthermore, both tests proved that significant composite strength can be achieved in shallow-depth floor systems by gaining composite action through steel-concrete bond interaction. Additionally, both tests showed that these composite sections have ductile and robust behavior from having similar response after significant loading. The component-level test reached 99% of the full-composite strength of the cross-section, which was determined with a plastic analysis. When comparing the component-level response to the partial composite strength, which is recommended for design, the beam reached 112%. Analysis was performed for the system-level test using a standard effective width for concrete in the composite cross-section. Using the obtained value, the system-level composite strength reached 125% of the full-composite strength and 161% of the partial composite strength (recommended for design) during the ultimate capacity test. This further indicates that a larger effective width of concrete is being utilized in the system response. The partial composite strength is recommended for design because composite action is developed through bond interaction between the steel and concrete.

Finally, A-shapes performed well during construction in terms of constructability and structural behavior. The floor system had acceptable live load deflections during service loading. Additionally, the vibration characteristics of the shallow-depth floor system were analyzed for a floor system in the constructed state. The floor system had two dominant frequencies, 8.1 Hz and 9.3 Hz, which are the two main bending modes of the floor system. The component-level and system-level testing performed on a full-scale shallow-depth composite floor system indicates that these systems are a viable option for buildings. Furthermore, these systems can improve the steel building economy, speed, and efficiency by increasing the speed of construction, reducing the cross-section depth, and providing relatively long beam lengths and wide beam spacings.

Future Research

Another important limit state for floor systems is fire and shallow-depth composite floor systems have an inherent fire resistance. This is attributed to the steel section being mostly encased in concrete, where the bottom flange is the only steel that would be exposed to a fire. As a result, a significant temperature gradient was observed during the experimental testing of these floor systems. Therefore, the section can still develop some composite strength and resist load during an extreme event. Some shallow-depth floor systems can achieve a 1-hour fire rating (or greater) without bottom flange protection. To improve the composite strength, fire reinforcement can be placed close to the web at the bottom of the concrete encasement to increase the flexural capacity. Shallow-depth floor systems using A-shapes could be fire tested to analyze the fire performance of a composite section gained purely through bond between the steel and concrete.

The acceleration data recorded during the vibration tests of shallow-depth floor systems with A-shapes will be further analyzed by Dr. Brad Davis and the authors. Furthermore, the walking data recorded during the testing will be analyzed. Evaluating shallow-depth floor systems with the criteria outlined in AISC's Design Guide 11 will be completed. This analysis will further analyze the viability of shallow-depth floor systems in buildings.

Data Availability Statement

Some or all data, models, or codes that support the findings of this study are available from the corresponding author upon reasonable request.

Acknowledgements

The authors are grateful to AISC for supporting this study through the Milek Fellowship. Any opinions, findings, conclusions, or recommendations expressed in this material are those of the authors and do not necessarily reflect the views of AISC. The authors thank the project industry panel for all their insight and support. This panel is comprised of three US steel mills (Nucor, Gerdau, and Steel Dynamics), fabricators, erectors, designers, and members of AISC (Devin Huber and Margaret Matthew). The authors would also like to thank New Millennium for providing the deep decking and their guidance during the design of the experiment, specifically Alex Therien and Marty Williams. Furthermore, the authors appreciate the support from the Advanced Structural Engineering Laboratory at Auburn University, which includes Rob Crosby and Caleb Fleming. Finally, the authors thank Dr. Brad Davis for his guidance and analysis of the vibration data. The authors appreciate Joshua McLeod's time and effort in assisting with data collection for the vibration testing.

References

AISC. 2022. Specification for S*tructural Steel Buildings*. *ANSI/AISC 360-22.* Chicago, IL: AISC.

AISC. 2023. *Steel Construction Manual*. 16th ed. Chicago, IL: AISC.

AISC. 2024. "Need for Speed." Accessed October 1, 2023. https://www.aisc.org/why-steel/innovative-systems/need-for-speed/.

ArcelorMittal. 2017. *Slim-Floor: An Innovative Concept for Floors*. Luxembourg: ArcelorMittal Commercial Sections.

ArcelorMittal. 2023b. "Slim Floor System." Accessed May 1, 2023. https://sections.arcelormittal.com/products_and_solutions/Our_Specialties/Slim_floor/EN.

Bandelt, M. J., S. P. Gross, D. W. Dinehart, J. R. Yost, and J. D. Pudleiner. 2019. "Flexural Behavior of a Composite Steel and Precast Concrete Open Web Dissymmetric Framing System." *Engineering Structures*, 198.

Davis, B., D. Lie, and T. Murray. 2014. "Simplified Experimental Evaluation of Floors Subject to Walking-Induced Vibration." *Journal of Performance of Constructed Facilities*, 28(5).

Davis, S. 2022. "Full-Scale Floor System Testing for Future Hot-Rolled Asymmetric Steel I-beams." Master Thesis, Texas A&M Univ.

Davis, S., E. Stoddard, and M. T. Yarnold. 2023. "Full-Scale Floor System Testing for Future Hot-Rolled Asymmetric Steel I-beams." *Journal of Structural Engineering*, 149(2).

DELTABEAM Technical Manual. 2019. *DELTABEAM Slim Floor Structure*. Lebanon, PA: Peikko.

Fahmy, Y. G. M., and A. N. M. Sidky. 2012. "An Experimental Investigation of Composite Floor Vibration due to Human Activities: A Case Study." *HBRC Journal*, 2012(8).

Girder-Slab Technologies. 2016. *The GIRDER-SLAB System Design Guide v3.3*. Cherry Hill, NJ: Girder-Slab Technologies

Hanagan, L. M., C. H. Raebel, and M. W. Trethewey. 2003. "Dynamic Measurements of In-Place Steel Floors to Assess Vibration Performance." *Journal of Performance of Constructed Facilities*, 17(3).

Hechler, O., M. Braun, R. Obiala, U. Kuhlmann, F. Eggert, and G. Hauf. 2016. "CoSFB - Composite Slim-Floor Beam: Experimental Test Campaign and Evaluation." *Composite Construction in Steel and Concrete*, 7.

Hicks, S. J., R. E. McConnel, and M. D. Weerasinghe. 2012. "The Testing of a Full-Scale Stub-Girder Floor Beam using 'Slimdek' Construction." *Composite Construction in Steel and Concrete*, IV(April).

Huber, D., and A. Varma. 2008. "Final Report for the AISC Fellowship Project." *Development of Long Span Floor Systems for Multi-Story Residential Structures*. AISC, Chicago, IL.

IBC. 2018. *International Building Code*. Country Club Hills, IL: International Code Council.

Ju, Y. K., S.-C. Chun, and S.-D. Kim. 2009. "Flexural Test of a Composite Beam using Asymmetric Steel Section with Web Openings." *Journal of Structural Engineering*, 135(4).

Ju, Y. K., S.-W. Kang, S.-C. Chun, Y.-K. Lee, S.-D. Kim, D.-H. Kim, K.-R. Chung, and S.-W. Yoon. 2004. "Experimental Assessment of Floor Vibration using iTECH Composite Beam." *Proceedings of the CTBUH International Conference on Tall Buildings*.

Kloeckner Metals. 2020. The Cellular Beam Pocket Guide Entrusted to Design and Deliver Metal Solutions. Leeds, UK: Kloeckner Metals UK.

Kloeckner Metals. 2023. "Ultra Shallow Floor Beam." Accessed June 1, 2023. https://www.kloecknermetalsuk.com/en/westok/products/ultra-shallow-floor-beam.html.

Kuhlmann, U., R. M. Lawson, O. Vassart, D. Lam, R. Zandonini, and E. Hendrickx. 2021. "Slim-Floor Beams Preparation of Application rules in view of improved safety, functionality and LCA (SlimAPP)." Project No. RFSR-CT-2015-00020. European Union, Luxembourg.

Lawson, R. M., and J. W. P. M. Brekelmans. 1999. "Design Recommendations for Shallow Floor Construction to Eurocodes 3 and 4.". European Commission.

Lawson, R. M., D. L. Mullet, and J. W. Rackham. 1997. *Design of Asymmetric Slimflor Beams using Deep Composite Decking*. *SCI P175.* Ascot, UK: The Steel Construction Institute.

Lawson, R. M., D. L. Mullett, and J. W. Rackham. 1998. "Design of Asymmetric Slimflor Beams." *Journal of Constructional Steel Research*, 46(1-3).

Liu, D., and B. Davis. 2015. "Walking Vibration Response of High-Frequency Floors Supporting Sensitive Equipment." *Journal of Structural Engineering*, 141(8).

Murray, T. M., D. E. Allen, E. E. Ungar, and D. B. Davis. 2016. Steel Design Guide 11: Vibrations of Steel-Framed Structural Systems due to Human Activity. Steel Design Guide Series. Chicago, IL: AISC.

New Millennium. 2019. Long-Span Composite Systems Featuring Deep-Dek Composite.

New Millennium. 2021a. Design Guide Deep-Dek Composite.

Ottmers, C., R. W. Alemayehu, and M. Yarnold. 2025a. "Evaluating the Composite Behavior developed through Bond in the Steel-Concrete Interface for Future Hot-Rolled Asymmetric Steel I-beams." *Engineering Structures*, 322.

Ottmers, C., E. Stoddard, and M. Yarnold. 2025b. "Establishment of Future A-Shape Geometry for Residential Construction." *Journal of Structural Engineering*.

Ottmers, C. E. 2025. "Full-Scale Testing and Numerical Evaluation of Hot-Rolled Asymmetric I-beams in Shallow-Depth Composite Floor Systems." Ph.D. Thesis, Texas A&M Univ.

Peikko. 2023. "DELTABEAM Slim Floor Structure for Open Spaces." Accessed June 1, 2023. https://www.peikko.com/products/deltabeam-slim-floor-structures/overview/.

Rackham, J. W., S. J. Hicks, and G. M. Newman. 2006. *Design of Asymmetric Slimflor Beams with Precast Concrete Slabs*. *SCI P342.* Ascot, UK: The Steel Construction Institute.

Sanchez, T. A., B. Davis, and T. Murray. 2011. "Floor Vibration Characteristics of Long Span Composite Slab Systems." *Structures Congress*, 2011.

Schorr, J., and U. Kuhlmann. 2019. "Design of Slim-Floors and their Connections between Steel and Concrete." *The 14th Nordic Steel Construction Conference, September 18-20, 2019, Copenhangen, Denmark.*

Seaburg, P. A., and C. J. Carter. 2003. Steel Design Guide 9: Torsional Analysis of Structural Steel Members. Steel Design Guide Series. Chicago, IL: AISC.

Sheehan, T., X. Dai, and D. Lam. 2018. "Flexural Behavior of Asymmetric Composite Beam with Low Degree of Shear Connection." *Journal of Constructional Steel Research*, 141(Feb).

Sheehan, T., X. Dai, J. Yang, K. Zhou, and D. Lam. 2019. "Flexural Behaviour of Composite Slim Floor Beams." *Structures*, 21.

Stoddard, E., and M. Yarnold. 2022. "Residual Stress and Global Deflection Limits for Future Hot-Rolled Steel Asymmetric I-beams." *Journal of Structural Engineering*, 148(1).

Stoddard, E. A. 2022. "Behavior of Hot-Rolled Asymmetric Steel I-beams: Concept to Construction." Ph.D. Thesis, Texas A&M Univ.

Yarnold, M. T., and E. Stoddard. 2020. "Future Hot-Rolled Asymmetric Steel I-beams." *Journal of Structural Engineering*, 146(9).

Appendix G – Floor Vibration Report

Appendix G is a supplemental analysis of the vibration data recorded for the full-scale validation test (Phase 5) discussed in Appendix F. The vibration analysis was conducted by Dr. Brad Davis at Davis Structural Engineering, LLC. Substantial vibration testing was performed, which included heel drop testing, jumping on the slab, walking at a specific pace to a metronome or at a random pace, and max excitation with up to ten people running and jumping on the slab. The vibration analysis presented in this appendix focused on a series of heel drop tests that were conducted in the same location for all tests while roving accelerometers across the slab. From this data, experimental modal shapes were established for the shallow-depth floor system.

Citation

The following work is not intended to be published separately. However, a condensed version is provided in the journal article presented in Appendix F, which has been submitted to the American Society of Civil Engineer's Journal of Structural Engineering and is currently under review.

Vibration Modes Summary Report

Brad Davis, Ph.D., S.E.[1]

[1]Davis Structural Engineering, LLC, BradD@DavisStructures.com,
P.O. Box 911142, Lexington, KY 40591, 859-490-8833, DavisStructures.com

Introduction

At the request of AISC and Dr. Matthew Yarnold of Auburn University, vibration measurements were analyzed in support of the ongoing research project "Behavior of Hot Rolled Asymmetric Steel I-beams." As part of this research, a long-span composite slab specimen with asymmetrical beams was built in the Auburn University Advanced Structural Engineering Laboratory. Auburn University personnel conducted experiments related to strength and stiffness, and performed vibration tests also.

The vibration tests should result in information that will be helpful for developing vibration serviceability design guidance for this type of floor. The purpose of the work reported herein is to assist in that effort. Two types of vibration tests were performed: heel-drop tests to determine natural modal properties and walking tests to determine accelerations due to walking. Heel-drop measurements, which were collected on 8/15/2024, were sent to me for processing. This report describes the heel-drop tests, analysis methods, and results.

Floor Specimen

Figure G-1 is a framing plan of the specimen. The slab is 9-5/8 in. thick (total), normal-weight concrete, with 4-5/8 in. deep deck. It spans between 8 in. deep steel beams with an 11-1/2 in. wide bottom flange and 6-1/2 in. wide top flange. The beams are spaced 20 ft center-to-center. The specimen was tested in the bare slab condition with no superimposed masses such as partitions.

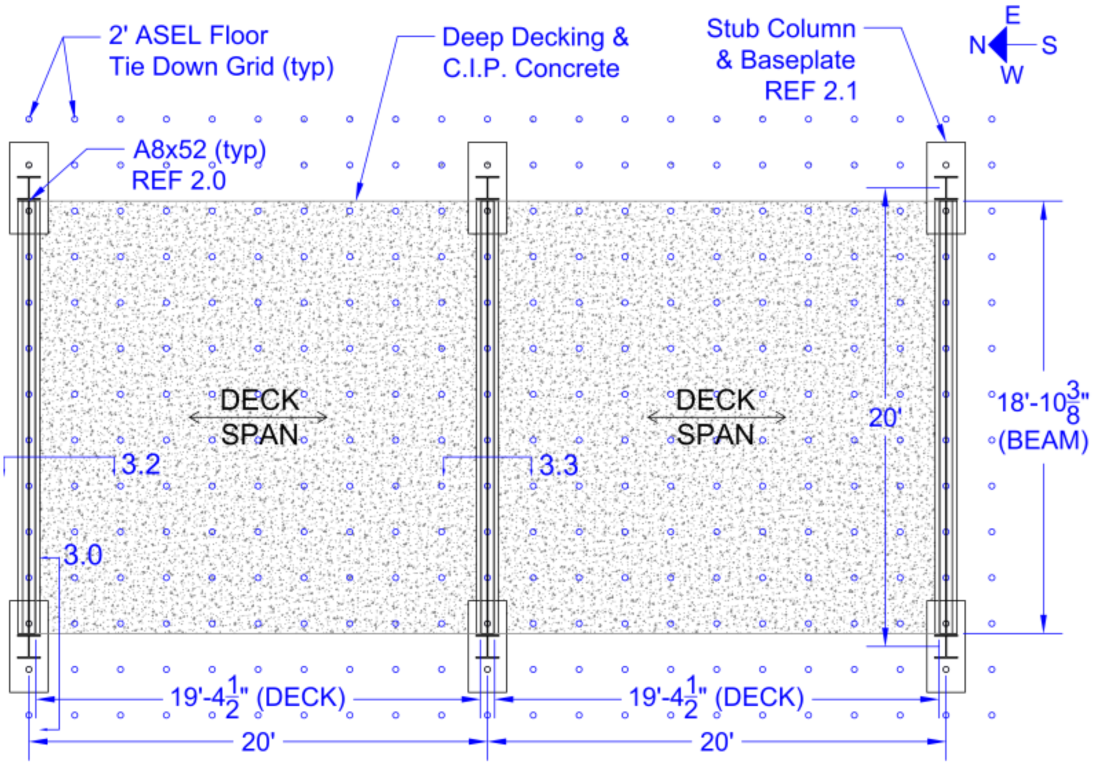

Figure G-1: Specimen Framing Plan

Heel-Drop Test Methods

Testing Methodology

Heel-drop tests are used to measure natural frequencies, mode shapes, and potentially estimate damping ratios.

As explained in Davis et al. (2014), during a heel-drop test, a measurement team member raises onto the balls of his feet and drops forcefully, once, onto the slab while floor vertical accelerations are measured. The heel-drop applies significant force in the frequency band of interest for floor vibration serviceability – approximately 2 Hz to 20 Hz. The acceleration waveform is Fourier transformed to an equivalent acceleration spectrum. Peaks in the spectrum indicate natural frequencies.

At each frequency in the spectrum, the acceleration is a complex quantity containing magnitude and phase information. When several accelerometers are used simultaneously, the phase information can be used to estimate the mode shape.

If the peaks are not closely spaced, the half-power bandwidth method can be used to coarsely estimate damping ratios.

Testing Specifics

During each test, the heel-drop was applied at the location pointed out on Figure G-2. This location was selected because it is not at a node in the theoretical fundamental mode shape or second mode shape for a two-span continuous beam with uniform mass, constant flexural rigidity, and rigid vertical supports.

Reference accelerometers A6 and A7 remained at grid coordinates R3-2 and R4-2, respectively, during each test. Five accelerometers, A1-A5, roved across the slab. In the first test, they were along R1 as shown in Figure G-2. In the test matrix in Table G-1, this is referred to as rove number "R1." For the second test, they were moved south to R2. This process was repeated to result in a simplified modal sweep across the entire specimen. Because A6 and A7 remained stationary, the series of tests could be linked to result in one data set for the specimen. A6 is near the node in the theoretical second mode shape mentioned above; A7 is not, so it was used as the reference during data processing. As shown in Table G-1, three heel-drop tests were performed for each rove number. During processing, the test for Heel-Drop Number 2 was used. Thus, the highlighted bold Test Numbers 2, 5, and so on, were processed.

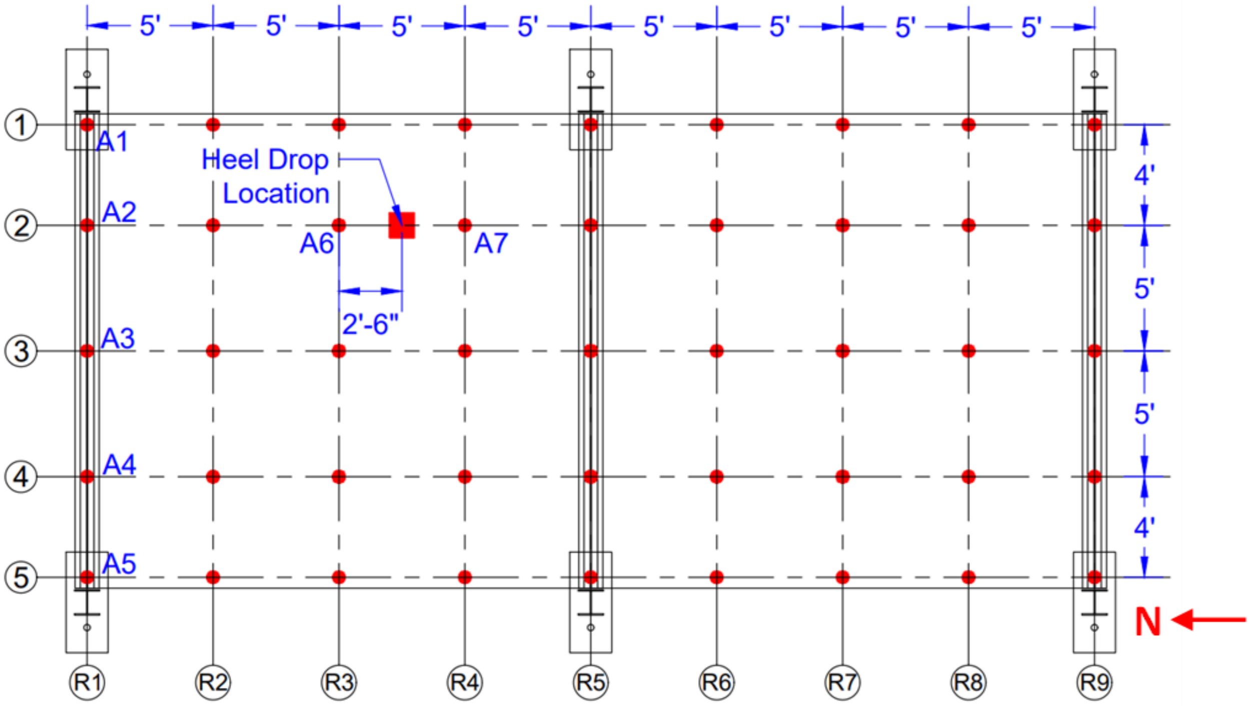

Figure G-2: Vibration Measurement Key Plan

Acceleration waveforms were measured at a 2048 Hz sampling frequency using seven PCB 352A24 accelerometers. Each waveform was approximately 30 seconds long. The first 20 seconds of each waveform was fast Fourier transformed to a spectrum with a frequency resolution of 0.05 Hz. Peaks in the spectral magnitude indicate natural frequencies. A separate plot of the magnitude with phase information included not only has peaks that indicate natural frequencies, but also reveals the relative directions and magnitudes of the synchronous motion – from that, the mode shapes can be inferred.

Table G-1: Heel-Drop Test Matrix

Test Number	Rove Number	Heel-Drop Number
1	R1	1
2		2
3		3
4	R2	1
5		2
6		3
7	R3	1
8		2
9		3
10	R4	1
11		2
12		3
13	R5	1
14		2
15		3
16	R6	1
17		2
18		3
19	R7	1
20		2
21		3
22	R8	1
23		2
24		3
25	R9	1
26		2
27		3

Results of Heel-Drop Tests

Example Test Result and Observations

Figure G-3 shows an example heel-drop test result, from Test 20. In this test, A6 and A7 were in the north span and A1 – A5 were in the south span.

The magnitude in Figure G-3(a) has two peaks that indicate natural frequencies of 8.10 Hz and 9.25 Hz. These plots are zoomed in for viewing of these two modes, which are of primary interest for floor vibration serviceability. Higher frequency modes are of lower interest, but might be useful for finite element model validation, so zoomed-out magnitudes are in Appendix G.1, and mode shapes are in Appendix G.2.

The 8.10 Hz and 9.25 Hz peaks are sufficiently widely spaced, so the half-power bandwidth method was used to estimate the following critical damping ratios for these two modes: 0.0095 and 0.0075. These ratios are slightly below the DG11 recommendation of 0.01 but are consistent with the writer's experience.

Figure G-3(b) is the plot of magnitude with phase information included.

In the 8.10 Hz mode, all accelerations are in phase, indicating that the north and south spans synchronously move in the same direction. In the south span, A1 and A5 accelerate the least, A2 and A4 accelerate significantly more, and A3 has the highest acceleration; this indicates the slab also bends transverse to the slab span direction.

In the 9.25 Hz mode, the synchronous motion has A6 and A7 accelerating in one direction while A1 – A5 accelerate in the opposite direction. A6 and A2 are in corresponding locations in the north and south span; these locations have approximately the same acceleration magnitudes. Thus, the slab bending mode has the same general shape as the theoretical fundamental natural mode for a two-span continuous beam. From observing the relative magnitudes of A1 – A5 as described in the previous paragraph, this mode also has bending transverse to the slab span direction.

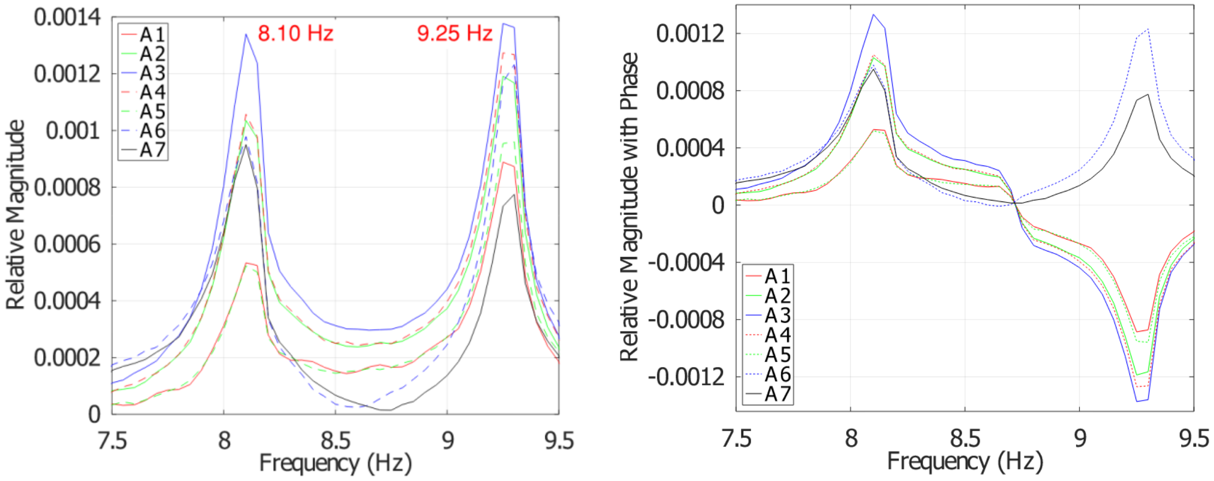

(a) Magnitudes

(b) Magnitudes with Phase Information Included

Figure G-3: Example Heel-Drop Test Results

Results for the Dataset

The series of tests were linked using the reference accelerometer to obtain unity-normalized mode shape values at each location shown in Figure G-2.

The 8.10 Hz mode shape is plotted in Figure G-4. The beams bend significantly and the slab is mostly bending transverse to its span. Thus, using AISC Design Guide 11 (Murray et al., 2016) Chapter 3 terminology, this mode corresponds to the beam bending mode.

Numerical values are summarized in Table G-2. These could be used to test finite element model accuracy in Modal Assurance Criterion calculations.

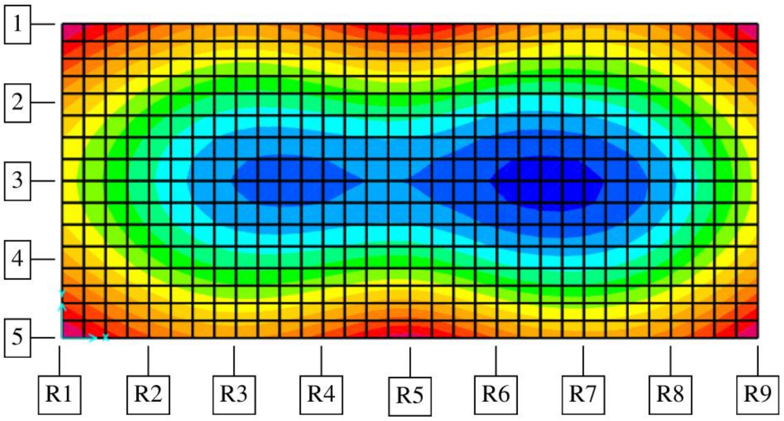

(a) Plan View

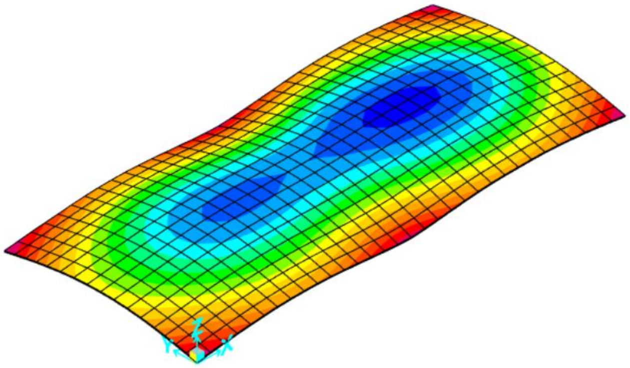

(b) 3D View

Figure G-4: 8.10 Hz Mode Shape

Table G-2: 8.10 Hz Mode Shape Numerical Values

		North-South								
		R1	**R2**	**R3**	**R4**	**R5**	**R6**	**R7**	**R8**	**R9**
East-West	**1**	0.0545	0.246	0.353	0.250	0.106	0.263	0.396	0.309	0.0478
	2	0.360	0.587	0.711	0.679	0.630	0.743	0.746	0.629	0.370
	3	0.523	0.757	0.917	0.930	0.913	0.988	1.000	0.858	0.537
	4	0.360	0.587	0.706	0.679	0.630	0.743	0.784	0.658	0.382
	5	0.0436	0.264	0.353	0.243	0.0920	0.282	0.373	0.298	0.0478

The 9.25 Hz mode shape is plotted in Figure G-5. There is virtually no vertical motion along R5 and slight motion along R1 and R9. Slab bending accounts for most of the motion. Thus, this mode corresponds to a slab bending mode. The shape is similar to the fundamental mode shape for a two-span continuous beam.

Numerical values are summarized in Table G-3. These could be used to test finite element model accuracy in subsequent Modal Assurance Criterion calculations.

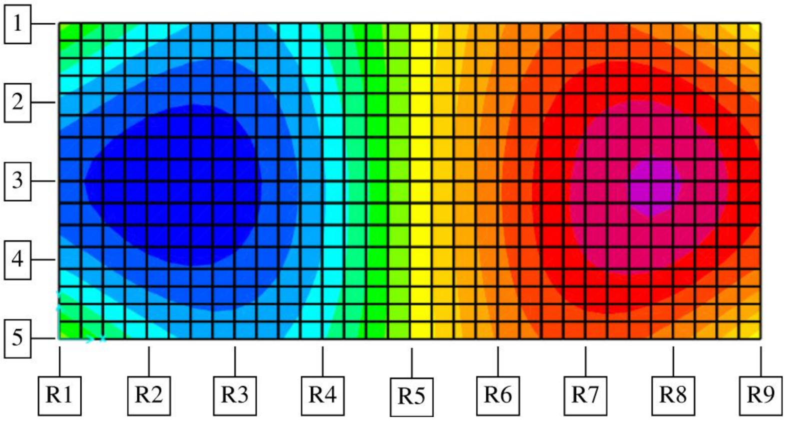

(a) Plan View

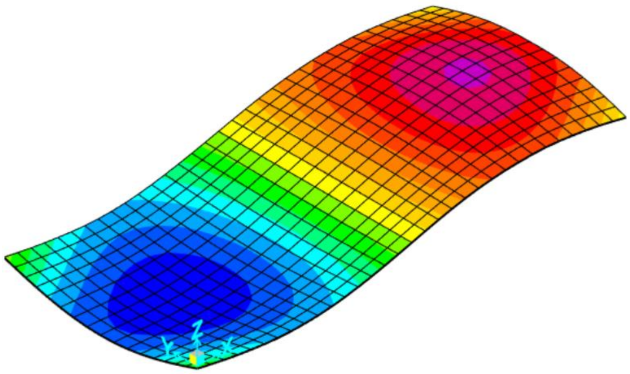

(b) 3D View

Figure G-5: 9.25 Hz Mode Shape

Table G-3: 9.25 Hz Mode Shape Numerical Values

		North-South								
		R1	**R2**	**R3**	**R4**	**R5**	**R6**	**R7**	**R8**	**R9**
East-West	**1**	-0.0774	-0.437	-0.591	-0.398	0.000	0.393	0.570	0.443	0.0649
	2	-0.536	-0.759	-0.788	-0.506	0.000	0.480	0.769	0.791	0.519
	3	-0.792	-0.956	-0.914	-0.579	0.000	0.541	0.884	1.000	0.714
	4	-0.548	-0.791	-0.806	-0.542	0.000	0.506	0.820	0.823	0.545
	5	-0.0774	-0.462	-0.619	-0.434	0.000	0.436	0.609	0.475	0.0649

Summary

A long span composite slab specimen was vibration tested as part of the ongoing research project "Behavior of Hot Rolled Asymmetric Steel I-beams" at Auburn University. The heel-drop test data was sent to me for further processing, resulting in estimated natural frequencies, damping ratios, and mode shapes.

The first vibration mode, at 8.10 Hz, has the shape shown in Figure G-6(a). This mode corresponds to a beam bending mode in Design Guide 11 Chapter 3. It has a critical damping ratio just under 0.01.

The second vibration mode, at 9.25 Hz, has the shape shown in Figure G-6(b). This mode would be categorized as a slab bending mode. It closely resembles the fundamental mode shape for a two-span continuous beam. Its critical damping ratio was 0.0075.

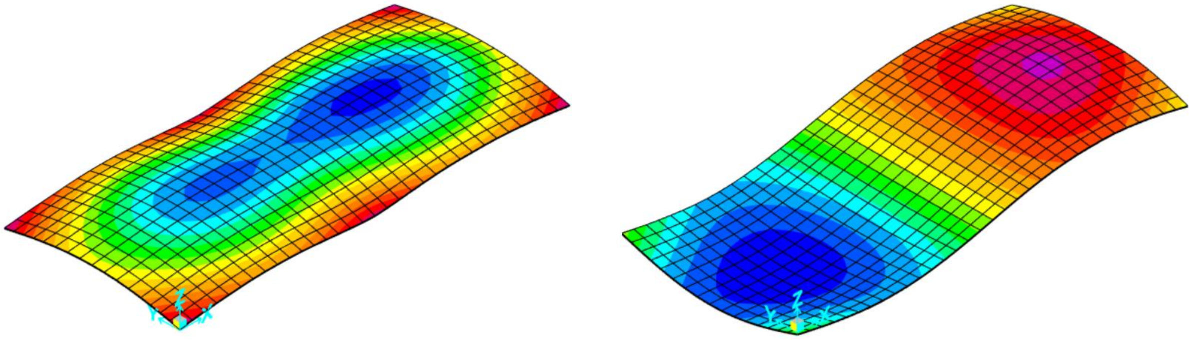

(a) 8.10 Hz Mode

(b) 9.25 Hz Mode

Figure G-6: Estimated Natural Mode Shapes

Brad Davis, Ph.D., S.E.

Davis Structural Engineering, LLC

References

Davis, B., Liu, D., and Murray, T.M. 2014. "Simplified Experimental Evaluation of Floors Subject to Walking Induced Vibration," *Journal of Performance of Constructed Facilities*, Vol. 28, No. 5.

Murray, T.M., Allen, D.E., Ungar, E.E., and Davis, D.B. 2016. *Vibrations of Steel-Framed Structural Systems Due to Human Activity*, American Institute of Steel Construction, Chicago, IL.

Appendix G.1 – Acceleration Spectral Magnitudes

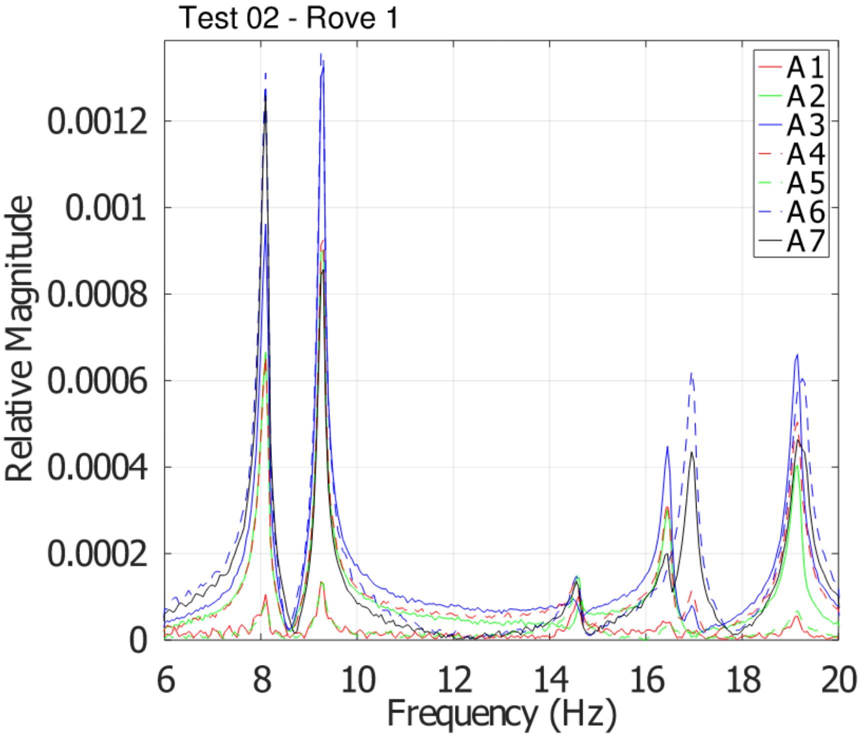

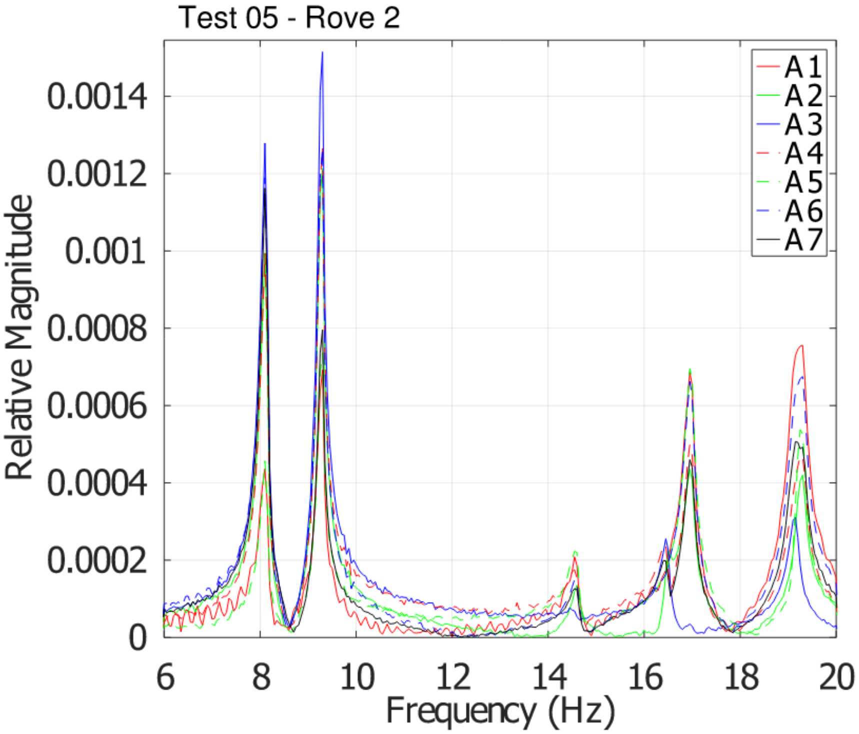

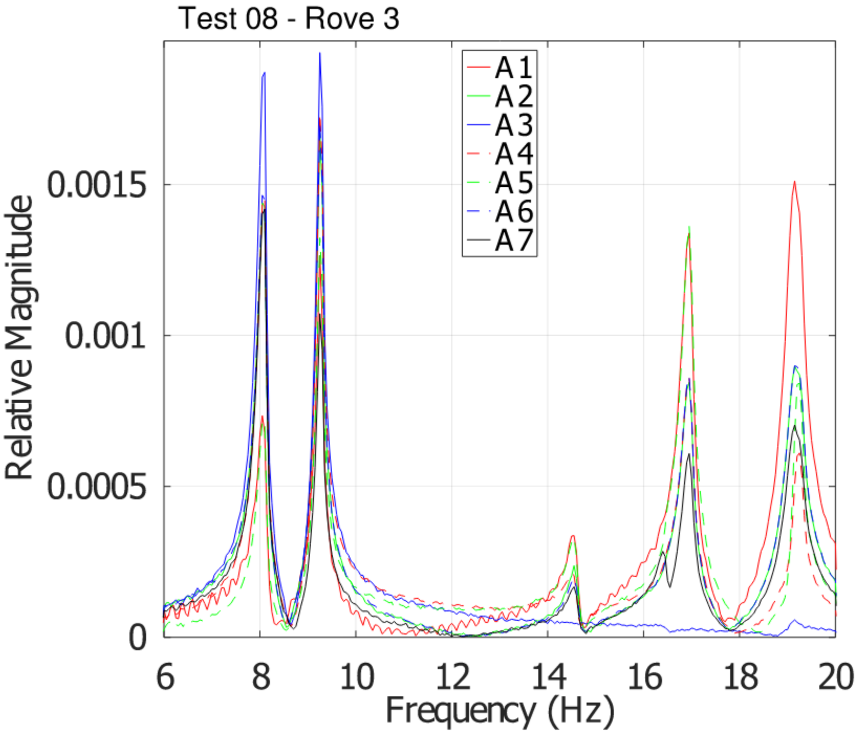
Test 08 - Rove 3
A1
A2
A3
A4
A5
A6
A7
Relative Magnitude
0.0015
0.001
0.0005
0
6
8
10
12
14
16
18
20
Frequency (Hz)

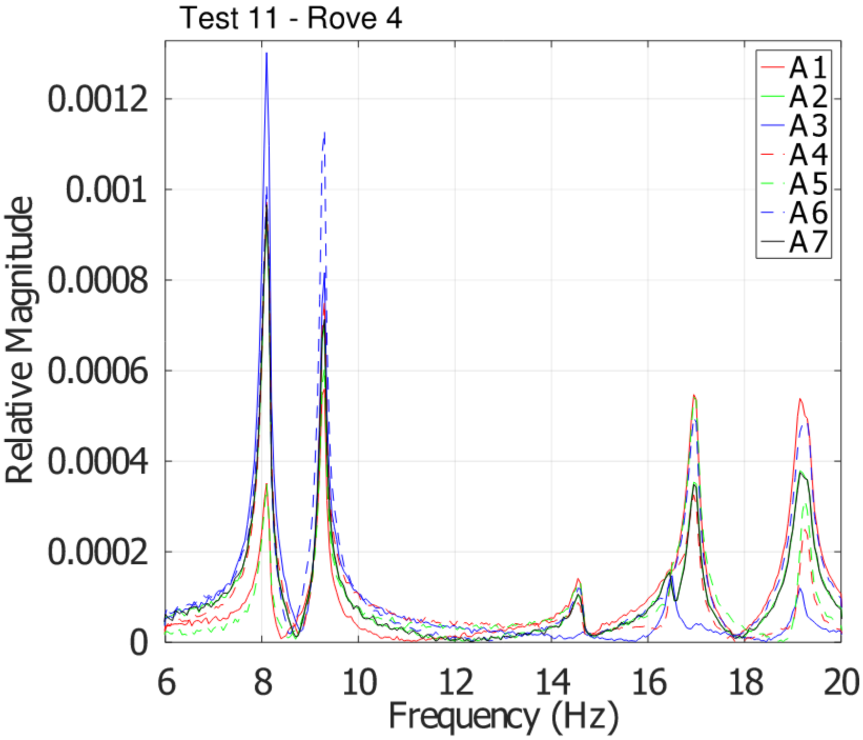
Test 11 - Rove 4
A1
A2
A3
A4
A5
A6
A7
Relative Magnitude
0.0012
0.001
0.0008
0.0006
0.0004
0.0002
0
6
8
10
12
14
16
18
20
Frequency (Hz)

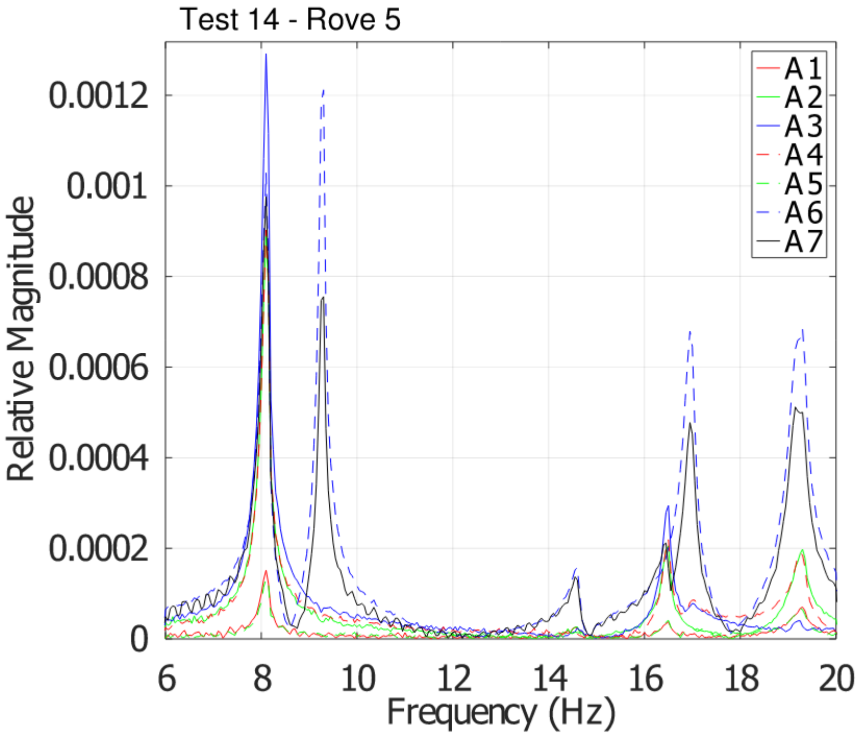
Test 14 - Rove 5
Relative Magnitude
0.0012
0.001
0.0008
0.0006
0.0004
0.0002
0
6
8
10
12
14
16
18
20
Frequency (Hz)
A1
A2
A3
A4
A5
A6
A7

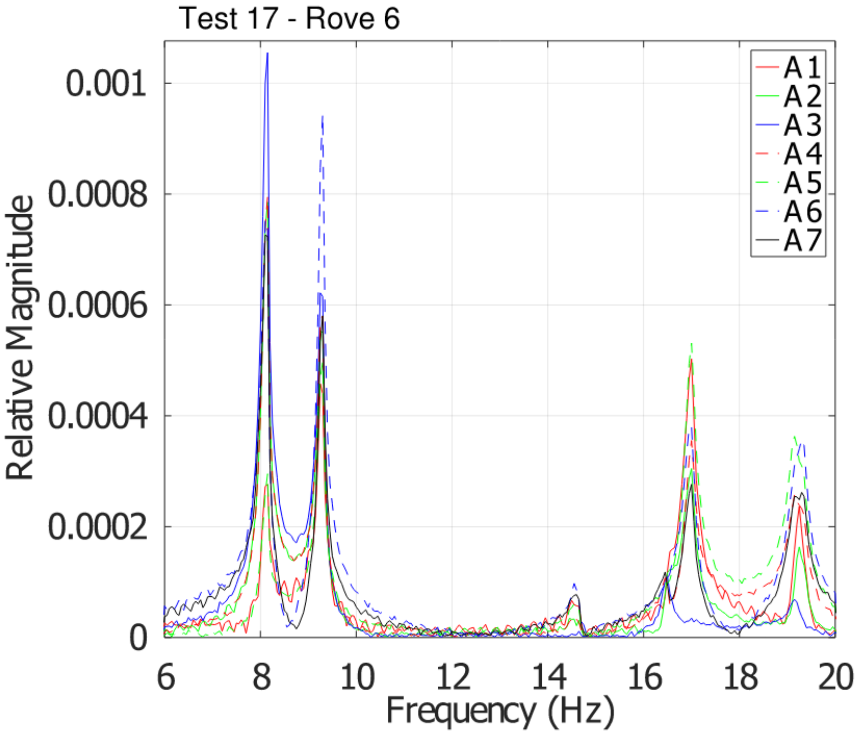
Test 17 - Rove 6
Relative Magnitude
0.001
0.0008
0.0006
0.0004
0.0002
0
6
8
10
12
14
16
18
20
Frequency (Hz)
A1
A2
A3
A4
A5
A6
A7

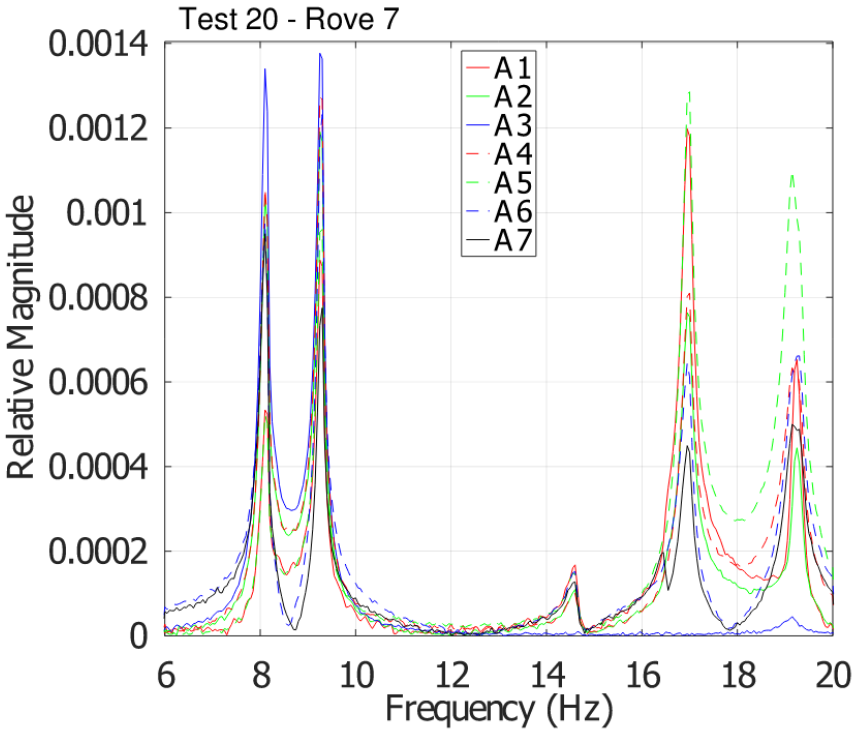
Test 20 - Rove 7
Relative Magnitude
0.0014
0.0012
0.001
0.0008
0.0006
0.0004
0.0002
0
6
8
10
12
14
16
18
20
Frequency (Hz)
A1
A2
A3
A4
A5
A6
A7

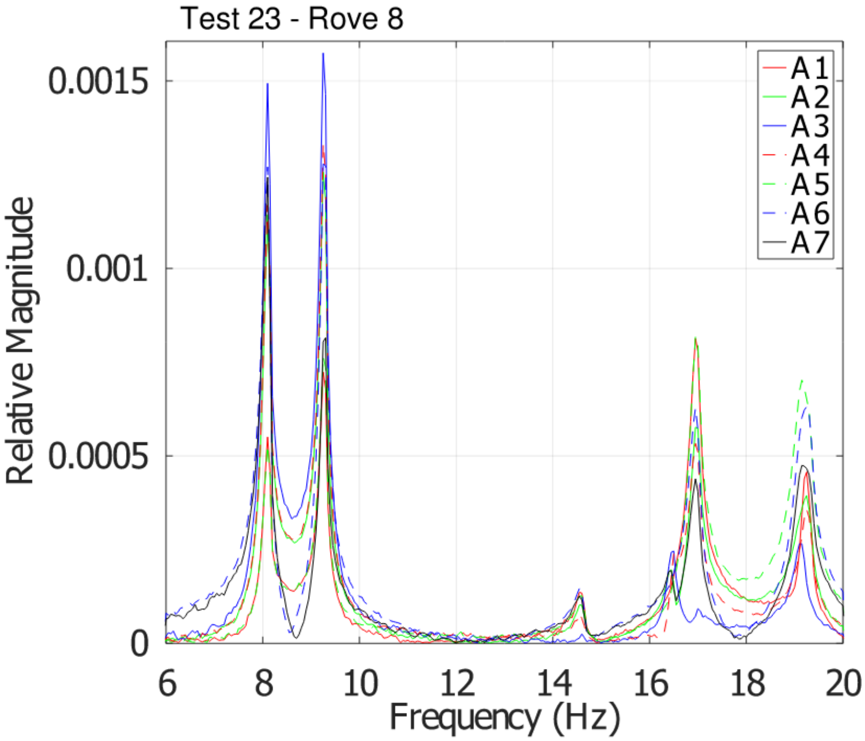
Test 23 - Rove 8
Relative Magnitude
0.0015
0.001
0.0005
0
6
8
10
12
14
16
18
20
Frequency (Hz)
A1
A2
A3
A4
A5
A6
A7

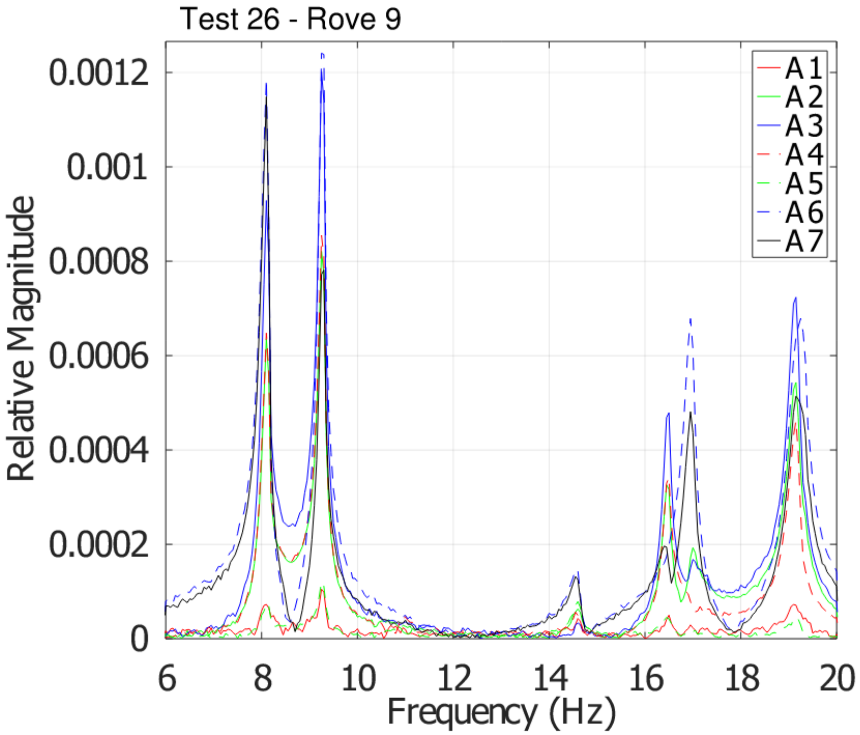
Test 26 - Rove 9
Relative Magnitude
0.0012
0.001
0.0008
0.0006
0.0004
0.0002
0
6
8
10
12
14
16
18
20
Frequency (Hz)
A1
A2
A3
A4
A5
A6
A7

Appendix G.2 – Higher Modes

14.6 Hz Mode

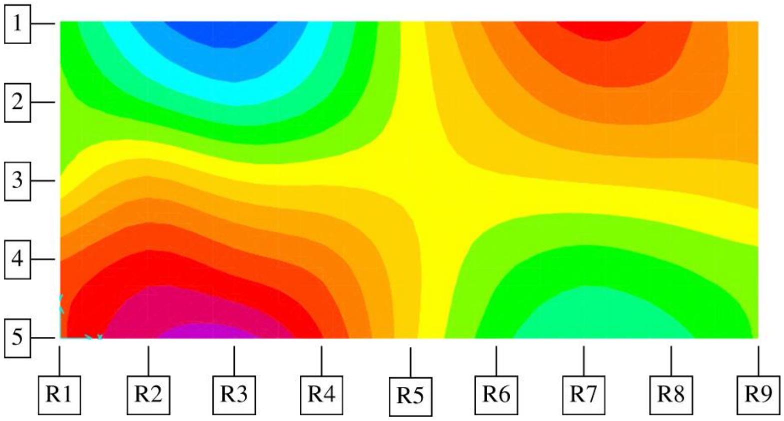

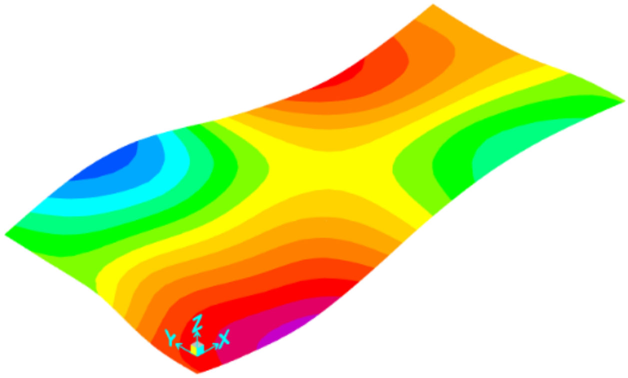

		North-South								
		R1	**R2**	**R3**	**R4**	**R5**	**R6**	**R7**	**R8**	**R9**
East-West	**1**	0.344	0.834	1.000	0.668	0.0885	-0.378	-0.659	-0.528	-0.151
	2	0.264	0.520	0.701	0.490	0.0947	-0.211	-0.421	-0.402	-0.224
	3	0.138	-0.187	0.00	0.0263	0.0442	0.0193	-0.017	-0.0512	-0.113
	4	-0.489	-0.687	-0.555	-0.408	-0.0508	0.263	0.395	0.319	0.217
	5	-0.571	-0.878	-0.970	-0.612	-0.0508	0.392	0.580	0.501	0.285

16.5 Hz Mode

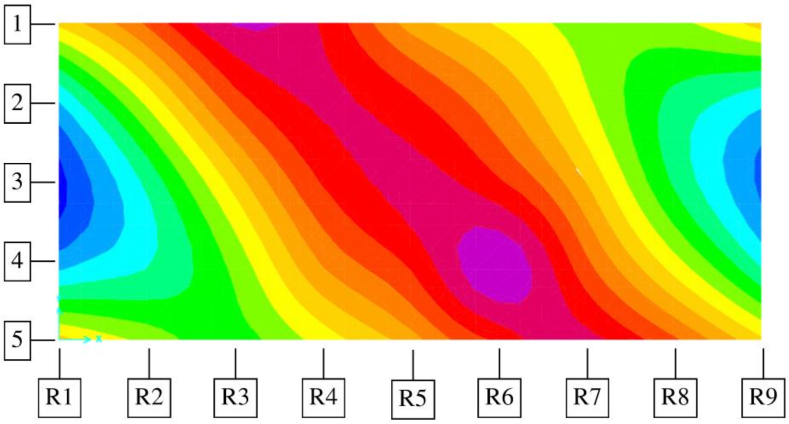

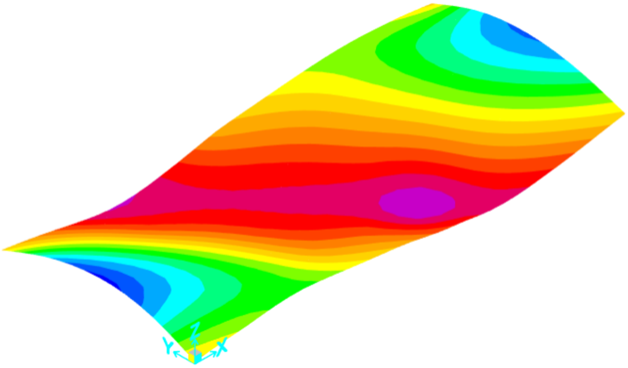

		North-South								
		R1	**R2**	**R3**	**R4**	**R5**	**R6**	**R7**	**R8**	**R9**
East-West	**1**	0.0818	-0.263	-0.613	-0.464	-0.0673	0.135	0.291	0.269	0.0574
	2	0.668	0.164	-0.338	-0.503	-0.372	-0.117	0.226	0.500	0.640
	3	1.000	0.570	0.0646	-0.373	-0.517	-0.377	0.000	0.497	0.868
	4	0.730	0.598	0.334	-0.112	-0.360	-0.718	-0.289	0.153	0.589
	5	0.0729	0.273	0.411	0.187	-0.0645	-0.385	-0.525	-0.267	0.0916

17.0 Hz Mode

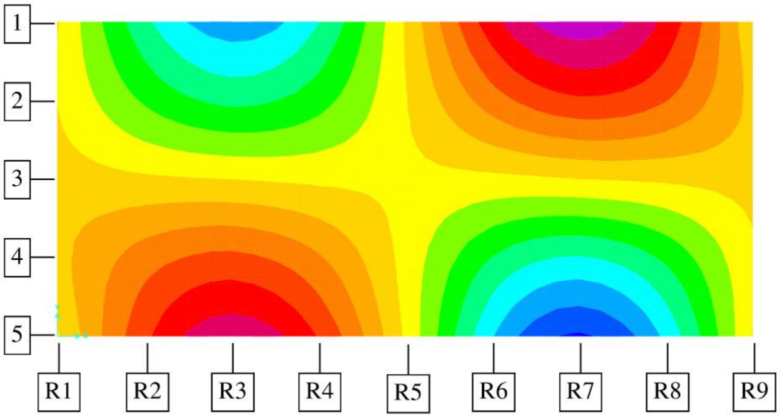

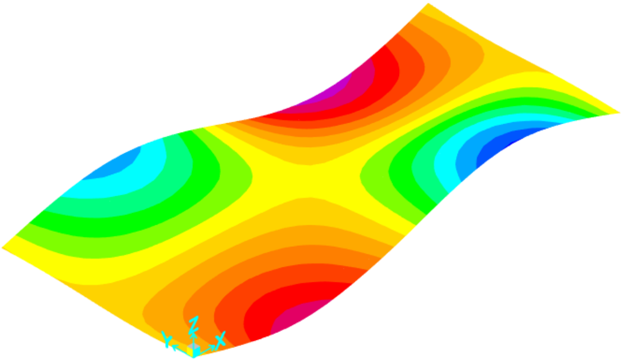

		North-South								
		R1	**R2**	**R3**	**R4**	**R5**	**R6**	**R7**	**R8**	**R9**
East-West	**1**	-0.0120	0.520	0.782	0.565	-0.00894	-0.651	-0.930	-0.662	-0.0184
	2	0.00396	0.327	0.497	0.364	0.00714	-0.389	-0.588	-0.463	-0.101
	3	-0.0645	-0.0233	0.00	0.0273	0.0301	0.0327	0.00	-0.0243	-0.0547
	4	-0.0942	-0.378	-0.502	-0.332	0.0438	0.461	0.628	0.428	0.0179
	5	0.0150	-0.524	-0.799	-0.555	0.0163	0.689	1.000	0.667	-0.00835

19.1 Hz Mode

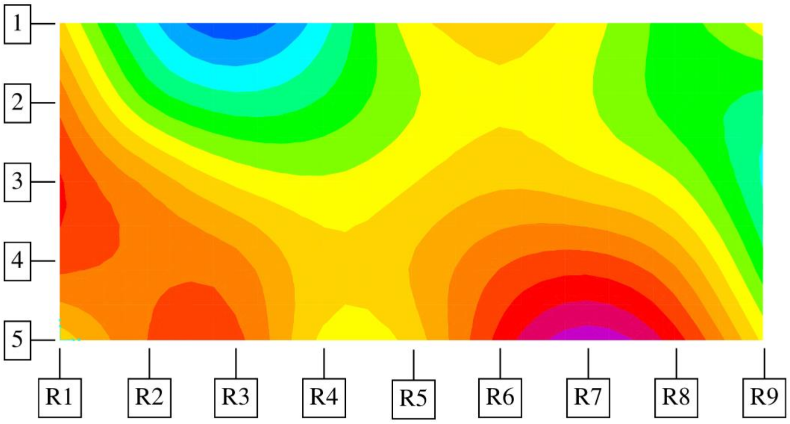

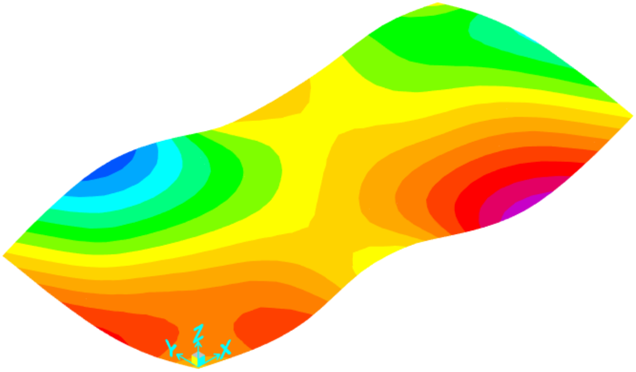

		North-South								
		R1	**R2**	**R3**	**R4**	**R5**	**R6**	**R7**	**R8**	**R9**
East-West	**1**	-0.0499	0.684	1.000	0.657	0.0643	-0.0634	0.0717	0.341	0.0638
	2	-0.368	0.372	0.591	0.459	0.178	0.0181	0.134	0.369	0.467
	3	-0.618	-0.268	0.0295	0.127	0.0106	-0.121	-0.0428	0.133	0.613
	4	-0.473	-0.421	-0.375	-0.0451	-0.160	-0.453	-0.571	-0.324	0.367
	5	-0.0638	-0.452	-0.501	0.0399	-0.0526	-0.648	-0.994	-0.674	0.0336

Appendix H – A-Shape Table

Appendix H provides the established cross-sectional geometry for seven A-shapes established in this research study. Section properties, both bending and torsional values, are provided for design guidance (Phase 6) of A-shapes within shallow-depth composite floor systems. Example calculations of the section properties are provided in Appendix I – Design Example (also a part of Phase 6). The section properties are used in Appendix J – Design Tables (third part of Phase 6).

Table 1-X. A-Shapes

The established cross-section geometries of A-shapes are provided in Table 1-X. The top flange dimensions have a 't' subscript (e.g., b_{ft}) and the bottom flange dimensions have a 'b' subscript (e.g., b_{fb}). The nominal weight of the A-shapes includes an estimate weight for fillets. Section properties are quantified for the A-shapes ignoring the contribution of the fillets and include both major and minor axis bending properties, as well as torsional properties for the A-shapes. The section properties include values for the top and bottom flange due to the asymmetry of the cross-section, e.g., S_{top} and S_{bot}, respectively.

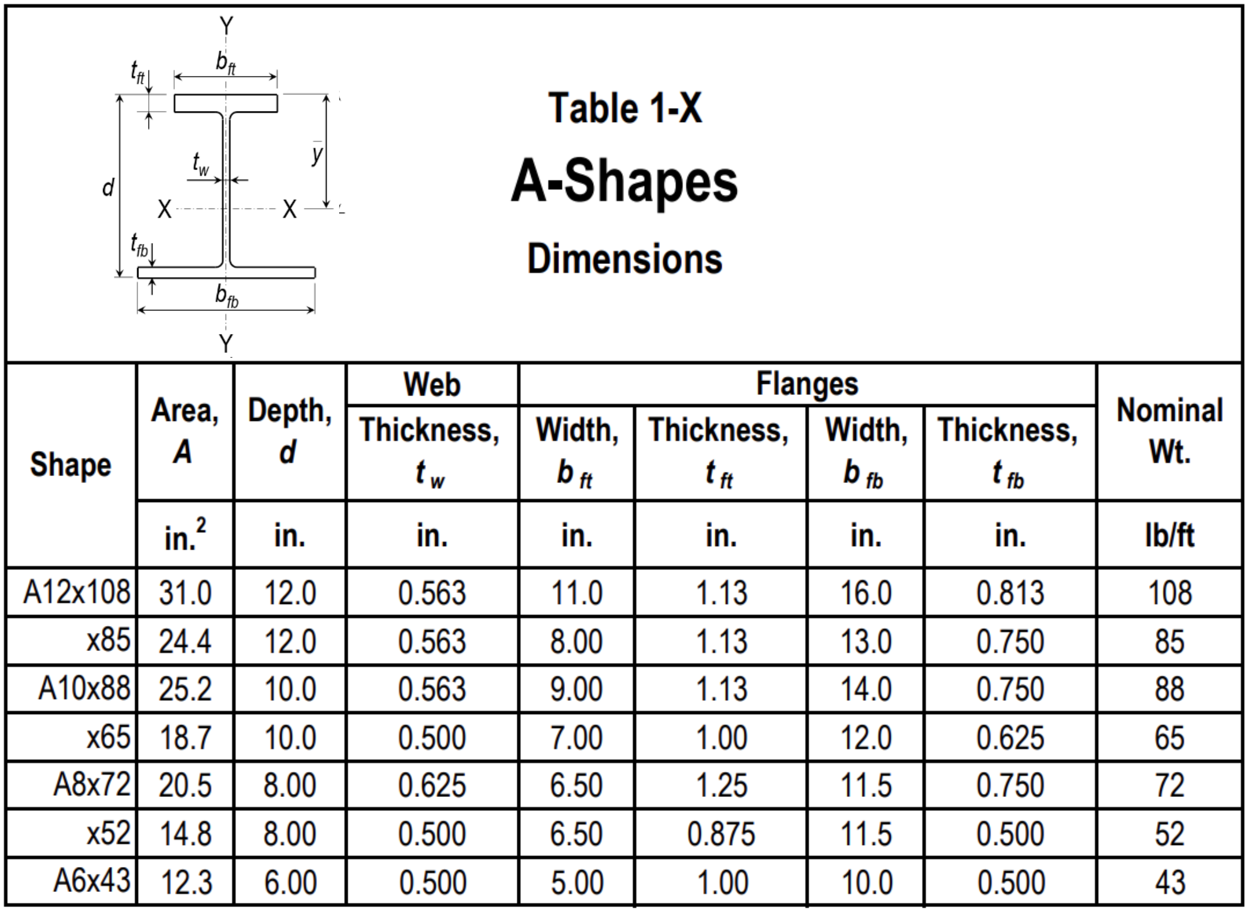

Table 1-X

A-Shapes

Dimensions

Shape	Area, A	Depth, d	Web Thickness, t_w	Flanges Width, b_{ft}	Flanges Thickness, t_{ft}	Flanges Width, b_{fb}	Flanges Thickness, t_{fb}	Nominal Wt.
	in.^{2}	in.	in.	in.	in.	in.	in.	lb/ft
A12x108	31.0	12.0	0.563	11.0	1.13	16.0	0.813	108
x85	24.4	12.0	0.563	8.00	1.13	13.0	0.750	85
A10x88	25.2	10.0	0.563	9.00	1.13	14.0	0.750	88
x65	18.7	10.0	0.500	7.00	1.00	12.0	0.625	65
A8x72	20.5	8.00	0.625	6.50	1.25	11.5	0.750	72
x52	14.8	8.00	0.500	6.50	0.875	11.5	0.500	52
A6x43	12.3	6.00	0.500	5.00	1.00	10.0	0.500	43

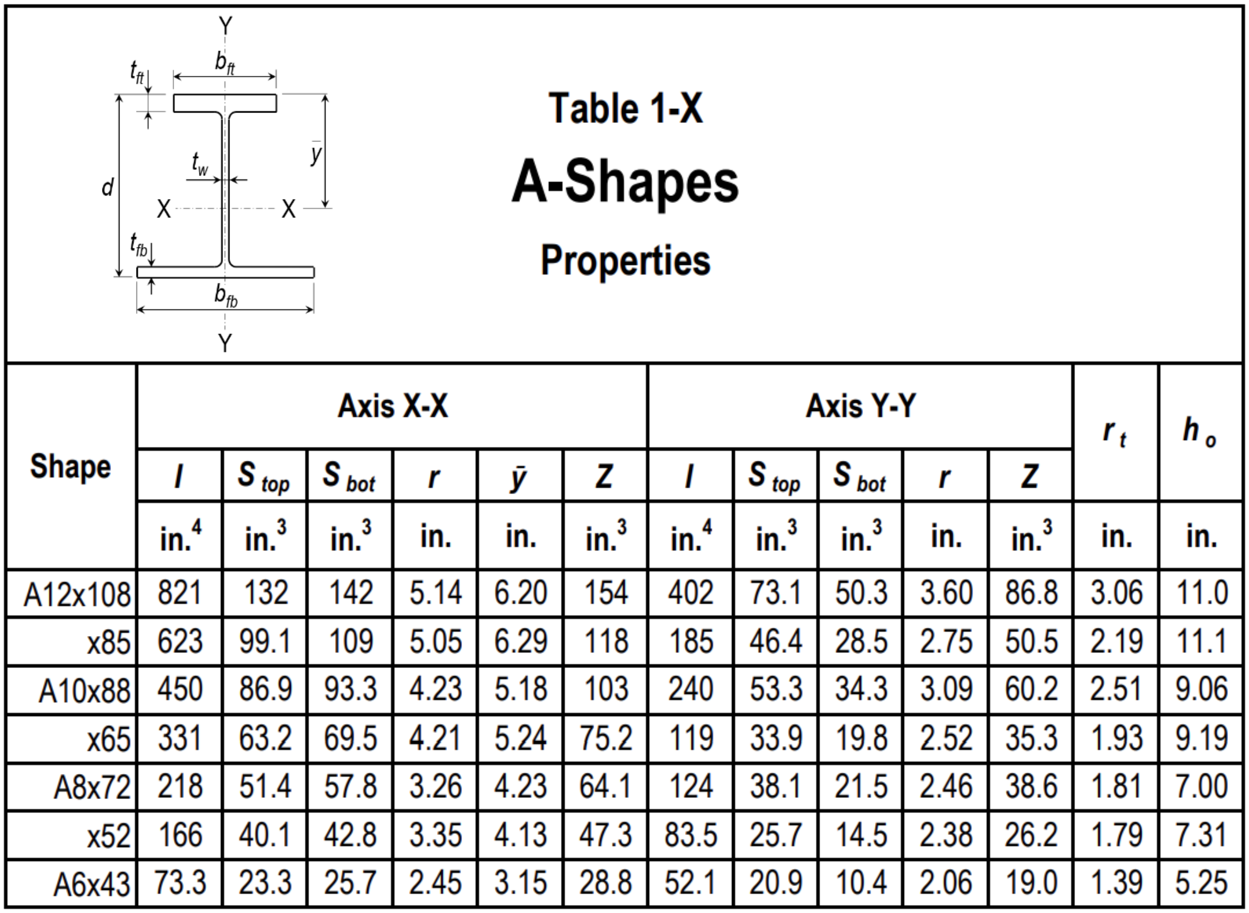

Table 1-X

A-Shapes

Properties

Shape	Axis X-X						Axis Y-Y					r_t	h_o
	I	S_{top}	S_{bot}	r	$\bar{y}$	Z	I	S_{top}	S_{bot}	r	Z		
	in.^{4}	in.^{3}	in.^{3}	in.	in.	in.^{3}	in.^{4}	in.^{3}	in.^{3}	in.	in.^{3}	in.	in.
A12x108	821	132	142	5.14	6.20	154	402	73.1	50.3	3.60	86.8	3.06	11.0
x85	623	99.1	109	5.05	6.29	118	185	46.4	28.5	2.75	50.5	2.19	11.1
A10x88	450	86.9	93.3	4.23	5.18	103	240	53.3	34.3	3.09	60.2	2.51	9.06
x65	331	63.2	69.5	4.21	5.24	75.2	119	33.9	19.8	2.52	35.3	1.93	9.19
A8x72	218	51.4	57.8	3.26	4.23	64.1	124	38.1	21.5	2.46	38.6	1.81	7.00
x52	166	40.1	42.8	3.35	4.13	47.3	83.5	25.7	14.5	2.38	26.2	1.79	7.31
A6x43	73.3	23.3	25.7	2.45	3.15	28.8	52.1	20.9	10.4	2.06	19.0	1.39	5.25

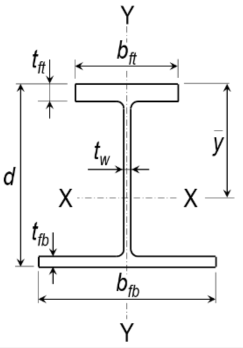

Table 1-X

A-Shapes

Torsional Properties

Shape	J	C_w	$W_{no,top}$	$W_{no,bot}$	$S_{w,top}$	$S_{w,bot}$	$Q_{f,top}$	$Q_{f,bot}$	Q_w
	in.^{4}	in.^{6}	in.^{2}	in.^{2}	in.^{4}	in.^{4}	in.^{3}	in.^{3}	in.^{3}
A12x108	8.74	10473	41.8	27.4	130	89.0	33.1	33.8	77.1
x85	6.28	4353	32.8	18.6	73.8	45.4	23.9	24.9	59.0
A10x88	6.78	4014	29.2	18.1	73.8	47.5	21.9	22.4	51.4
x65	3.69	1831	24.4	13.3	42.7	24.9	15.4	16.0	37.7
A8x72	6.42	1077	17.5	9.31	35.5	20.1	13.3	13.8	32.1
x52	2.24	814	18.1	10.1	25.7	14.5	9.69	9.95	23.7
A6x43	2.30	230	10.5	5.25	13.1	6.56	5.96	6.18	14.4

Appendix I - Design Example

Appendix I provides design guidance on A-shapes within shallow-depth composite floor systems (Phase 6). This includes analyzing the non-composite A-shape beam during construction and the composite section during in-service. Supplemental analysis is provided which includes fire resistance of an unprotected A-shape and alternative methods to calculate the partial composite strength. The design example was developed from the knowledge gained in the first five phases of the AISC Study on A-shape behavior.

Table of Contents

Headings Page

General Information

Non-Composite Analysis - Construction

Composite Analysis - In-Service

Design Summary

Supplemental Analysis

Back Matter

GENERAL INFORMATION

Description and Purpose of Design Example

The primary objective of this design example is to provide guidance on the design of hot-rolled asymmetric I-beams (termed A-shapes) within shallow-depth composite floor systems. Shallow-depth floor systems utilize asymmetric I-beams that support stay-in-place formwork (either precast concrete panels or steel deep decking) on the bottom flange. The aim is to reduce the overall floor depth of a steel-concrete composite floor system. Furthermore, these floor systems will help increase the speed of construction. The objective is to have long beam lengths and wide beam spacings to take advantage of the spanning capabilities of precast concrete panels and steel deep decking. This design example accompanies the research presented in the AISC Study - Behavior of Hot-Rolled Asymmetric Steel I-beams (Yarnold et al. 2024).

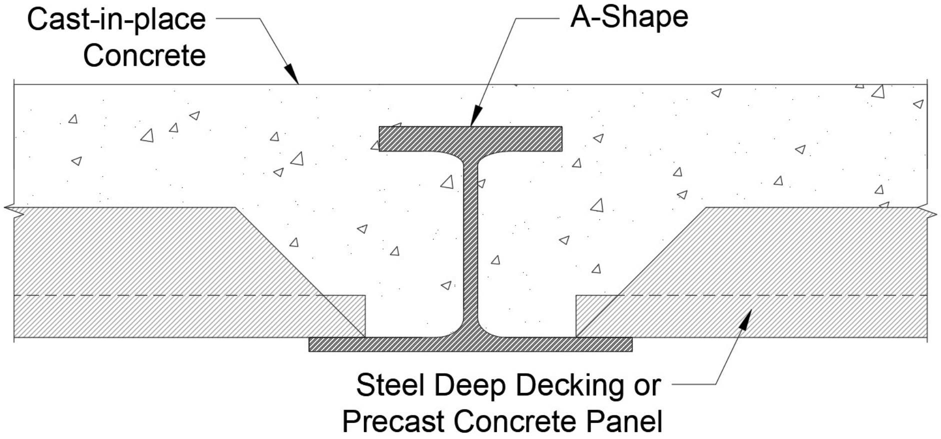

This design example includes the primary limit state calculations for the design of A-shapes within shallow-depth floor systems. Specifically, analysis during non-composite construction loading is performed, which incorporates a load height effect into the flexural capacity for the A-shape since load is applied to the bottom flange. The construction analysis includes torsion which is particularly important for large beam spacings. In-service composite analysis is provided, where composite action is developed through bond shear formation between the steel and concrete. No mechanical connectors, such as shear studs, are utilized to transfer load between the steel and concrete. Component and system-level experimental testing was conducted to evaluate the flexural strength and stiffness of the composite section. Knowledge on how to analyze the composite strength was gained and is implemented. Serviceability criteria, both deflection and vibration, are also analyzed for the composite section. Finally, supplemental analysis is presented for fire analysis of A-shapes without a protected bottom flange. Shallow-depth floor systems have an inherent fire resistance since only the bottom flange is exposed to fire. Concrete encasement around the top flange and web of the steel beam induce a significant temperature gradient over the beam depth (if the beam is unprotected). An analytical method was developed in literature and is implemented to quantify the fire resistance for A-shapes in shallow-depth floor systems.

Note, that all calculations required for a floor system are not conducted, such as A-shape shear (typically does not control), decking design, and connection design. Conventional analysis for these must be performed. Design aids for non-composite flexure, torsion, composite flexure, and beam selection for specific loading/geometry were developed to assist in the design. The approach shown herein was utilized for development of these design aids.

Building Grid Layout and Loading

Grid Layout

$L := 20\ ft$	beam length
$S := 20\ ft$	beam spacing

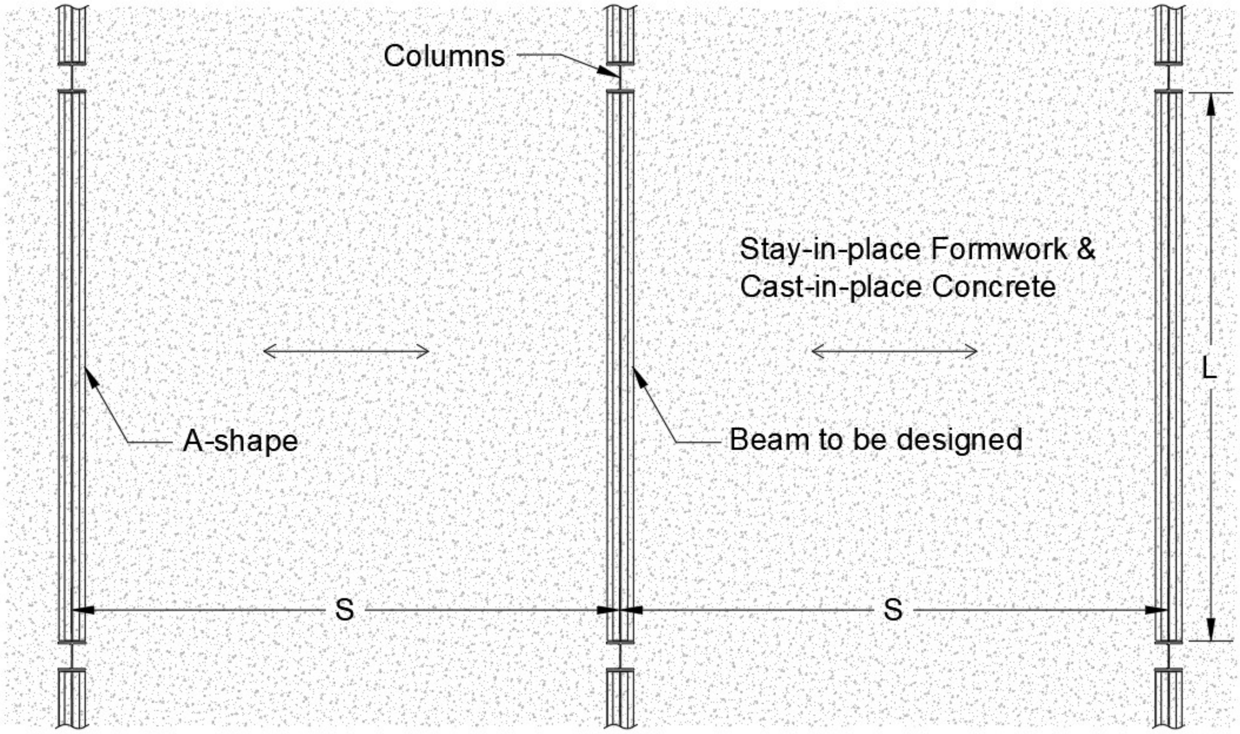

Defining Loads

$q_{conc} := 79\ psf$	concrete weight - Deep-Dek Design Guide (New Millennium 2021)
$q_{deck} := 4.1\ psf$	deck weight - NM Deep-Dek Design Guide
$q_D := q_{conc} + q_{deck} = 83\ psf$	total construction dead load
$q_{SDL} := 10\ psf$	superimposed dead load (e.g., MEP)
$q_{CL} := 20\ psf$	construction live load
$q_{Lo} := 40\ psf$	live load
$q_P := 15\ psf$	partition load

Reducing live load per ASCE 7 - 22, Section 4.7

$K_{LL} := 2$	Table 4.7-1 (ASCE 7-22)
$A_T := L \cdot S = 400\ ft^2$	tributary area
$K_{LL} \cdot A_T = 800\ ft^2$	

$$q_L := \max\left(q_{Lo} \cdot \left(0.25 + \frac{15 \cdot ft}{\sqrt{K_{LL} \cdot A_T}}\right), 0.5 \cdot q_{Lo}\right) = 31\ psf$$ reduced live load

NON-COMPOSITE ANALYSIS - CONSTRUCTION

Two main construction cases are evaluated for the non-composite A-shape, which include the following: (1) concentric loading from the full slab pour and (2) eccentric loading from slab pour of one bay. This section quantifies section properties of the asymmetric steel section, evaluates the non-composite flexural capacity, and the torsional response of the A-shape.

Cross-Section Geometry

Steel Beam: A8x52

$d := 8\ in$	full depth
$b_{ft} := 6.5\ in$	top flange width
$t_{ft} := 0.875\ in$	top flange thickness
$b_{fb} := 11.5\ in$	bottom flange width
$t_{fb} := 0.5\ in$	bottom flange thickness
$t_w := 0.5\ in$	web thickness
$h := d - t_{ft} - t_{fb} = 6.63\ in$	web height
$h_o := h + 0.5 \cdot t_{ft} + 0.5 \cdot t_{fb} = 7.31\ in$	distance between the center of flanges

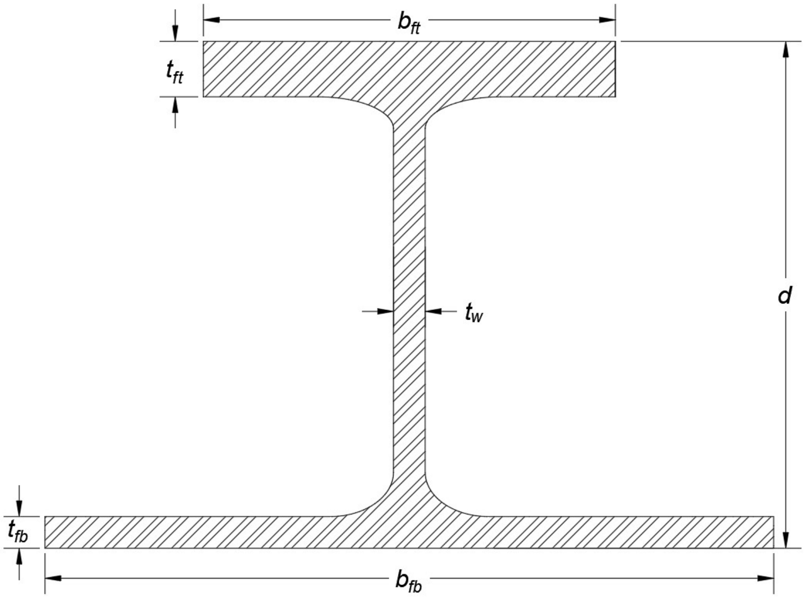

$A_t := b_{ft} \cdot t_{ft} = 5.69\ in^2$	top flange area
$A_w := h \cdot t_w = 3.31\ in^2$	web area
$A_b := b_{fb} \cdot t_{fb} = 5.75\ in^2$	bottom flange area
$A_{tot} := A_t + A_w + A_b = 14.8\ in^2$	cross section area
$F_y := 50\ ksi$	steel yield strength
$E := 29000\ ksi$	Young's modulus of steel
$G := 11200\ ksi$	Shear modulus of steel
$w_{beam} := 52\ \dfrac{lbf}{ft}$	estimated beam weight per foot

Steel Beam Section Properties

Centroid of each component

$$y_{ft} := d - \frac{t_{ft}}{2} = 7.56\ in$$

$$y_w := \frac{h}{2} + t_{fb} = 3.81\ in$$

$$y_{fb} := \frac{t_{fb}}{2} = 0.25\ in$$

distance to the centroid of the top flange, web, and bottom flange, measured from the bottom of the cross section

Elastic Neutral Axis

$$y_{bar\_bot} := \frac{A_t \cdot y_{ft} + A_w \cdot y_w + A_b \cdot y_{fb}}{A_{tot}} = 3.87\ in$$

ENA from the bottom

$$y_{bar\_top} := d - y_{bar\_bot} = 4.13\ in$$

ENA from the top

Moment of Inertia

$$I_x := \frac{1}{12}\ b_{ft} \cdot {t_{ft}}^3 + A_t \cdot \left(y_{ft} - y_{bar\_bot}\right)^2 + \frac{1}{12}\ t_w \cdot h^3 + A_w \cdot \left(y_w - y_{bar\_bot}\right)^2 + \frac{1}{12}\ b_{fb} \cdot {t_{fb}}^3 + A_b \cdot \left(y_{fb} - y_{bar\_bot}\right)^2 = 166\ in^4$$

$$I_y := \frac{1}{12}\ t_{ft} \cdot {b_{ft}}^3 + \frac{1}{12}\ h \cdot {t_w}^3 + \frac{1}{12}\ t_{fb} \cdot {b_{fb}}^3 = 83\ in^4$$

Section Modulus

$$S_{x\_top} := \frac{I_x}{y_{bar\_top}} = 40.1\ in^3$$

$$S_{x\_bot} := \frac{I_x}{y_{bar\_bot}} = 42.8\ in^3$$

Polar Moment of Inertia

$$J := \frac{1}{3}\ b_{ft} \cdot {t_{ft}}^3 + \frac{1}{3}\ h_o \cdot {t_w}^3 + \frac{1}{3}\ b_{fb} \cdot {t_{fb}}^3 = 2.24\ in^4$$

Plastic Section Modulus

$$A_{half} := \frac{A_{tot}}{2} = 7.38\ in^2$$

$$y_p := \left\| \begin{array}{l} \text{if } A_{half} > A_b \\ \quad \left\| \dfrac{A_{half} - A_b}{t_w} + t_{fb} \right. \\ \text{else} \\ \quad \left\| \dfrac{A_{half}}{b_{fb}} \right. \end{array} \right. = 3.75\ in$$

PNA location from the bottom of the section

PNA is located in the web:

$$UPWA := \left(d - t_{ft} - y_p\right) \cdot t_w = 1.69\ in^2$$

upper plastic web area
aka web area in compression

$$LPWA := A_w - UPWA = 1.63\ in^2$$

lower plastic web area
aka web area in tension

Calculate areas/centroids of compression and tension based on PNA location:

$$AC := A_t + UPWA = 7.38\ in^2$$

compression area

$$AT := A_b + LPWA = 7.38\ in^2$$

tension area

$$yC := \frac{\left(UPWA \cdot \dfrac{d - t_{ft} - y_p}{2}\right) + \left(A_t \cdot \left(d - \dfrac{t_{ft}}{2} - y_p\right)\right)}{AC} = 3.33\ in$$

distance to centroid
of compression area
from PNA

$$yT := \frac{\left(LPWA \cdot \dfrac{y_p - t_{fb}}{2}\right) + \left(A_b \cdot \left(y_p - \dfrac{t_{fb}}{2}\right)\right)}{AT} = 3.09\ in$$

distance to centroid of
tension area from PNA

Plastic Section Modulus

$$Z_x := \left(AC \cdot yC\right) + \left(AT \cdot yT\right) = 47.3\ in^3$$

$$Z_y := \frac{t_{ft} \cdot b_{ft}^{\ 2}}{4} + \frac{t_{fb} \cdot b_{fb}^{\ 2}}{4} + \frac{h \cdot t_w^{\ 2}}{4} = 26.2\ in^3$$

Torsional Properties

Weak moment of inertia of top and bottom flange

$$I_{yt} := \frac{1}{12}\ t_{ft} \cdot {b_{ft}}^{3} = 20\ \boldsymbol{in}^{4} \qquad I_{yb} := \frac{1}{12}\ t_{fb} \cdot {b_{fb}}^{3} = 63.4\ \boldsymbol{in}^{4}$$

Warping constant

$$C_w := {h_o}^{2} \cdot \frac{I_{yt} \cdot I_{yb}}{I_{yt} + I_{yb}} = 814\ \boldsymbol{in}^{6}$$

Normalized warping constant for top and bottom flange (Heins 1975)

$$\alpha := \frac{{b_{fb}}^{3} \cdot t_{fb}}{{b_{ft}}^{3} \cdot t_{ft} + {b_{fb}}^{3} \cdot t_{fb}} \cdot h_o = 5.56\ \boldsymbol{in}$$

shear center depth, referenced
from centroid of top flange

$$W_{no\_top} := \frac{\alpha \cdot b_{ft}}{2} = 18.1\ \boldsymbol{in}^{2}$$

$$W_{no\_bot} := \frac{h_o - \alpha}{2} \cdot b_{fb} = 10.1\ \boldsymbol{in}^{2}$$

Warping statical moment for top and bottom flange

$$S_{wt} := \frac{W_{no\_top} \cdot b_{ft} \cdot t_{ft}}{4} = 25.7\ \boldsymbol{in}^{4}$$

$$S_{wb} := \frac{W_{no\_bot} \cdot b_{fb} \cdot t_{fb}}{4} = 14.5\ \boldsymbol{in}^{4}$$

Statical moment of the top and bottom flange and the web

$$Q_{ft} := \left(\frac{\left(b_{ft} - t_w\right)}{2} \cdot t_{ft}\right) \cdot \left(y_{bar\_top} - \frac{t_{ft}}{2}\right) = 9.69\ \boldsymbol{in}^{3}$$

$$Q_{fb} := \left(\frac{\left(b_{fb} - t_w\right)}{2} \cdot t_{fb}\right) \cdot \left(y_{bar\_bot} - \frac{t_{fb}}{2}\right) = 9.95\ \boldsymbol{in}^{3}$$

$$A_{w2} := \left(y_{bar\_top} - t_{ft}\right) \cdot t_w = 1.63\ \boldsymbol{in}^{2}$$

$$Q_w := \left(A_t + A_{w2}\right) \cdot \frac{\left(A_t \cdot \left(y_{bar\_top} - \frac{t_{ft}}{2}\right) + A_{w2} \cdot \frac{y_{bar\_top} - t_{ft}}{2}\right)}{A_t + A_{w2}} = 23.7\ \boldsymbol{in}^{3}$$

A-shape Moment Capacity (per AISC F4)

Compression Flange Yielding (AISC F4.1)

$S_{xc} := S_{x\_top} = 40.1\ in^3$	elastic section modulus of compression flange
$S_{xt} := S_{x\_bot} = 42.8\ in^3$	elastic section modulus of tension flange
$M_{yc} := F_y \cdot S_{xc} = 167\ kip \cdot ft$	yield moment in compression flange
$M_p := F_y \cdot Z_x = 197\ kip \cdot ft$	plastic moment capacity
$h_c := \left(y_{bar\_top} - t_{ft}\right) \cdot 2 = 6.51\ in$	h_c & h_p equations from AISC Table B4.1b
$h_p := \left(d - y_p - t_{ft}\right) \cdot 2 = 6.75\ in$	

$$\lambda := \frac{h_c}{t_w} = 13$$

λ_{web} equations (Table B4.1b - Case 16)

$$\lambda_{rw} := 5.70 \cdot \sqrt{\frac{E}{F_y}} = 137 \qquad \lambda_{pw} := min\left(\frac{\frac{h_c}{h_p} \cdot \sqrt{\frac{E}{F_y}}}{\left(0.54 \cdot \frac{M_p}{M_{yc}} - 0.09\right)^2}, \lambda_{rw}\right) = 78$$

$$I_{yc} := \frac{1}{12} \cdot t_{ft} \cdot b_{ft}^{\ 3} = 20\ in^4 \qquad \frac{I_{yc}}{I_y} = 0.24$$

```
$R_{pc} :=$ if $\frac{I_{yc}}{I_y} > 0.23$
                if $\lambda \le \lambda_{pw}$
                    $\frac{M_p}{M_{yc}}$
                else
                    $min\left(\frac{M_p}{M_{yc}} - \left(\frac{M_p}{M_{yc}} - 1\right) \cdot \left(\frac{\lambda - \lambda_{pw}}{\lambda_{rw} - \lambda_{pw}}\right), \frac{M_p}{M_{yc}}\right)$
            else
                1.0
         $= 1.18$
```

Compression Flange Yielding Moment Capacity (F4.1)

$$M_n := R_{pc} \cdot M_{yc} = 197\ kip \cdot ft$$

$$\phi M_{n\_4\_1} := 0.9 \cdot M_n = 177\ kip \cdot ft$$

Lateral Torsional Buckling (AISC F4.2)

$L_b := L = 20\ ft$ unbraced length

$C_{b\_UDL} := 1.14$ lateral-torsional buckling modification factor for UDL, per Table 3-1 (AISC 2023)

Note, the load is applied to the bottom flange which improves the LTB behavior. Structural stability textbooks show that the critical buckling load is the greatest when load is applied to the bottom flange (Chen and Lui 1987). This is due to a restoring moment generated when the beam starts to twist if the load is applied to the bottom flange. This can be implemented using the load height effect and calculating C_b* (Helwig et al. 1997). Refer to Ottmers et al. (2025b) for more information.

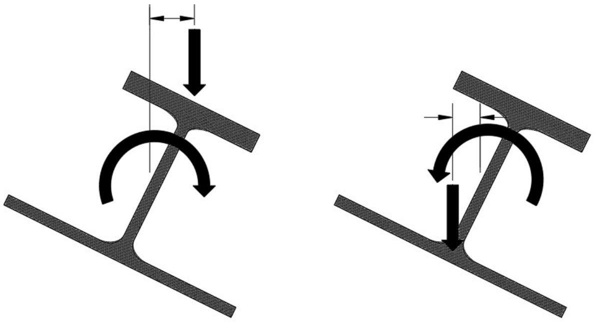

Illustration of restoring moment for load applied on bottom flange.

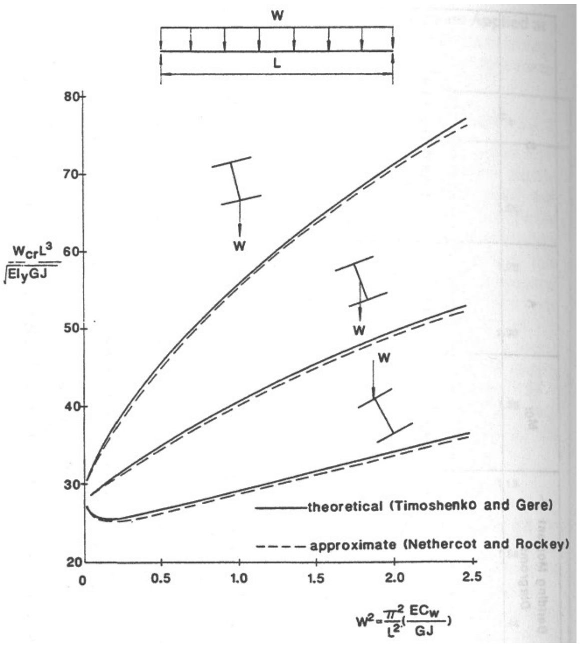

Structural Stability, Chen and Lui (1987)

$y := \frac{d}{2} - t_{fb} = 0.29\ ft$ distance from top flange to mid-depth

$W := \frac{\pi}{L_b} \cdot \sqrt{\frac{E \cdot I_y \cdot {h_o}^2}{4 \cdot G \cdot J}} = 0.47$ warping stiffness parameter (Helwig et al. 1997)

$B := 1 - 0.154 \cdot W^2 + 0.535 \cdot W = 1.22$ parameter that depends on warping stiffness and loading (assumed UDL) (Helwig et al. 1997)

$C_{b\_star} := C_{b\_UDL} \cdot B^{2 \cdot \frac{y}{h_o}} = 1.38$ load height modified lateral-torsional buckling modification factor (Helwig et al. 1997)

$$r_t := \frac{b_{ft}}{\sqrt{12\left(1+\frac{h_c \cdot t_w}{6 \cdot b_{ft} \cdot t_{ft}}\right)}} = 1.79\ in$$

effective radius of gyration

$$L_p := 1.1 \cdot r_t \cdot \sqrt{\frac{E}{F_y}} = 4\ ft$$

limiting unbraced length for yielding

```
$F_L :=$ if $\frac{S_{xt}}{S_{xc}} \geq 0.7$
            $0.7 \cdot F_y$
         else
            $F_y \cdot \frac{S_{xt}}{S_{xc}}$
$= 35\ ksi$
```

nominal compression flange stress

$$L_r := 1.95 \cdot r_t \cdot \frac{E}{F_L} \cdot \sqrt{\frac{J}{S_{xc} \cdot h_o} + \sqrt{\left(\frac{J}{S_{xc} \cdot h_o}\right)^2 + 6.76\left(\frac{F_L}{E}\right)^2}} = 30\ ft$$

limiting unbraced length for inelastic LTB

$$F_{cr} := \frac{C_{b\_star} \cdot \pi^2 \cdot E}{\left(\frac{L_b}{r_t}\right)^2} \cdot \sqrt{1 + 0.078 \cdot \frac{J}{S_{xc} \cdot h_o}\left(\frac{L_b}{r_t}\right)^2} = 75\ ksi$$

critical stress

Lateral-Torsional Buckling Moment Capacity (F4.2)

```
$M_n :=$ if $L_b \leq L_p$
            $R_{pc} \cdot M_{yc}$
         else if $L_p < L_b \leq L_r$
            $min\left(C_{b\_star} \cdot \left(R_{pc} \cdot M_{yc} - \left(R_{pc} \cdot M_{yc} - F_L \cdot S_{xc}\right)\left(\frac{L_b - L_p}{L_r - L_p}\right)\right), R_{pc} \cdot M_{yc}\right)$
         else if $L_b > L_r$
            $min\left(F_{cr} \cdot S_{xc}, R_{pc} \cdot M_{yc}\right)$
```

$$M_n = 197\ kip \cdot ft$$

$$\phi M_{n\_4\_2} := 0.9 \cdot M_n = 177\ kip \cdot ft$$

Compression Flange Local Buckling (AISC F4.3)

$$\lambda := \frac{b_{ft}}{2 \cdot t_{ft}} = 3.7$$

$$k_c := min\left(\max\left(0.35, \frac{4}{\sqrt{\frac{h}{t_w}}}\right), 0.76\right) = 0.76$$

λ_{flange} equations (Table B4.1b - Case 11)

$$\lambda_{pf} := 0.38 \cdot \sqrt{\frac{E}{F_y}} = 9.2 \qquad \lambda_{rf} := 0.95 \cdot \sqrt{\frac{k_c \cdot E}{F_L}} = 24$$

$\lambda < \lambda_{pf} = 1$ if 1 (compact flange) --> Section F4.3 does not apply

Tension Flange Yielding (AISC F4.4)

$S_{xt} \geq S_{xc} = 1$ if 1 (compression flange yields first) --> Section F4.4 does not apply

Non-Composite Flexural Strength

$$\phi M_n := min\left(\phi M_{n\_4\_1}, \phi M_{n\_4\_2}\right) = 177\ kip \cdot ft$$

Demand - Concentric Construction Loading

$$w_u := 1.2 \cdot \left(q_D \cdot \frac{S}{2} + w_{beam}\right) + 1.6 \cdot q_{CL} \cdot \frac{S}{2} = 1.38\ \frac{kip}{ft}$$

$$M_{uNC} := \frac{w_u \cdot L^2}{8} = 69\ kip \cdot ft$$

Note, the tributary width is S/2 due to shoring deep decking (DD) at midspan. The full beam spacing, S, would be used for unshored construction (precast concrete panels (PCP)).

Capacity vs Demand

$$\frac{\phi M_n}{M_{uNC}} = 2.57$$

A-shape is adequate for flexure during construction if > 1.0

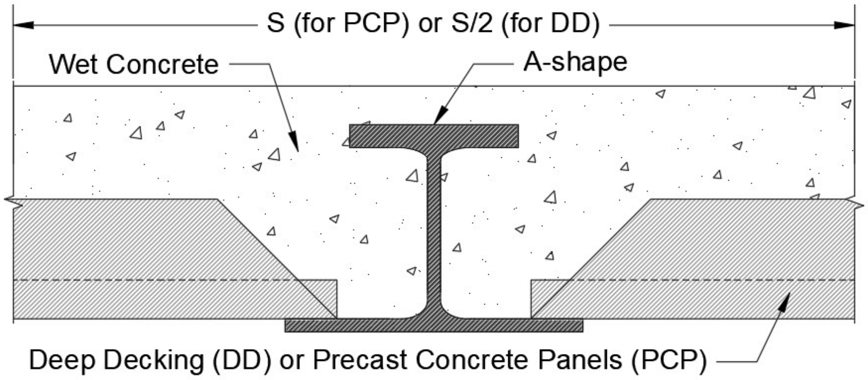

Torsion Analysis (per AISC Design Guide 9)

Demand - Eccentric Construction Loading

$s := \frac{1}{2} \cdot \frac{S}{2} = 5\ ft$ tributary width for torsion, this width assumes shoring at decking midspan - reducing the tributary width by an additional 1/2

note that for unshored precast panels, half of the tributary width should be utilized for torsion analysis

$b_{bearing} := 2\ in$ bearing width of stay-in-place formwork on bottom flange

$e := \frac{b_{fb}}{2} - \frac{b_{bearing}}{2} = 4.75\ in$ eccentricity to center of deck bearing on bottom flange

$w_u := 1.2 \cdot \left(q_D \cdot s + w_{beam}\right) + 1.6 \cdot q_{CL} \cdot s = 0.72\ \frac{kip}{ft}$ uniformly distributed load on beam for torsion

$V_u := w_u \cdot \frac{L}{2} = 7.2\ kip$ maximum shear demand

$M_u := \frac{w_u \cdot L^2}{8} = 36\ kip \cdot ft$ bending moment at midspan

$t_u := w_u \cdot e = 0.29\ \frac{kip \cdot in}{in}$ uniform torsional moment along beam length

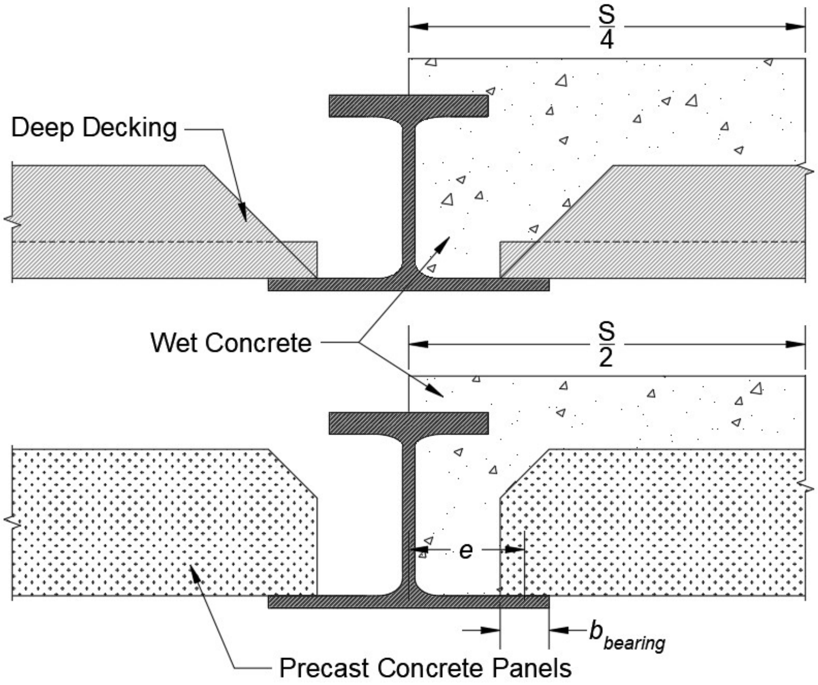

Note, torsional analysis for this design example assumes that the decking and concrete is only on one side of the beam (for simplicity). Due to the decking being shored (the tributary width is S/4) and most of the construction load is from the concrete, torsion is not a major concern. However, stay-in-place formwork installed on both sides of the beam before the slab pour is likely to occur.

If precast concrete panels are utilized (the tributary width is S/2 since unshored), torsion could be a controlling limit state. However, precast panels will likely be installed on both sides of the beam, meaning that the concrete is the only torsional load being applied to the A-shape. Larger in-plane bending would occur from the precast panels but a smaller torsional demand would be present. Including this scenario in the torsional analysis would be beneficial.

Bending Stresses at Midspan (Normal and Shear)

Bending stress: top and bottom flange

$$\sigma_{bx\_top} := \frac{-M_u}{S_{x\_top}} = -10.8\ \mathit{ksi}$$

Bending normal stress, DG9 - Eq 4.5

$$\sigma_{bx\_bot} := \frac{M_u}{S_{x\_bot}} = 10.1\ \mathit{ksi}$$

Shear stress: web, top and bottom flange

$$\tau_{b\_web} := \frac{V_u \cdot Q_w}{I_x \cdot t_w} = 2.1\ \mathit{ksi}$$

Bending shear stress, DG9 - Eq 4.6

$$\tau_{b\_top} := \frac{V_u \cdot Q_{ft}}{I_x \cdot t_{ft}} = 0.5\ \mathit{ksi}$$

$$\tau_{b\_bot} := \frac{V_u \cdot Q_{fb}}{I_x \cdot t_{fb}} = 0.9\ \mathit{ksi}$$

Torsional Stresses at Midspan (Normal)

$$a := \sqrt{\frac{E \cdot C_w}{G \cdot J}} = 30.7\ \mathit{in}$$

Section property, DG9 - Eq 3.6

$$\frac{L}{a} = 7.8$$

Use Case 4 in Appendix B (Distributed Torsional Moment)
or θ equation in Appendix C

Determine second derivatives of rotation @ Midspan (z/L = 0.5)

$z := 0.5 \cdot L$

$$\theta''_m := \frac{d^2}{dz^2}\left(\frac{t_u \cdot a^2}{G \cdot J}\left(\frac{L^2}{2 \cdot a^2} \cdot \left(\frac{z}{L} - \frac{z^2}{L^2}\right) \hookleftarrow \\ + \cosh\left(\frac{z}{a}\right) - \tanh\left(\frac{L}{2 \cdot a}\right) \cdot \sinh\left(\frac{z}{a}\right) - 1.0\right)\right) = -1.1 \cdot 10^{-5}\ \frac{\mathit{rad}}{\mathit{in}^2}$$

Normal Stresses due to Warping at Midspan, top and bottom flange

$$\sigma_{w\_top} := E \cdot W_{no\_top} \cdot \theta''_m = -5.7\ \mathit{ksi}$$

Warping normal stress, DG9 - Eq 4.3a

$$\sigma_{w\_bot} := E \cdot W_{no\_bot} \cdot \theta''_m = -3.2\ \mathit{ksi}$$

Torsional Stresses at Support (Shear)

Determine derivatives of rotation @ Support (z/L = 0)

$z := 0 \cdot L$

$$\theta'_s := \frac{d}{dz}\left(\frac{t_u \cdot a^2}{G \cdot J}\left(\begin{array}{l}\frac{L^2}{2 \cdot a^2} \cdot \left(\frac{z}{L} - \frac{z^2}{L^2}\right) + \cosh\left(\frac{z}{a}\right) \hookleftarrow \\ -\tanh\left(\frac{L}{2 \cdot a}\right) \cdot \sinh\left(\frac{z}{a}\right) - 1.0\end{array}\right)\right) = \left(1.0 \cdot 10^{-3}\right) \frac{rad}{in}$$

$$\theta'''_s := \frac{d^3}{dz^3}\left(\frac{t_u \cdot a^2}{G \cdot J}\left(\begin{array}{l}\frac{L^2}{2 \cdot a^2} \cdot \left(\frac{z}{L} - \frac{z^2}{L^2}\right) + \cosh\left(\frac{z}{a}\right) \hookleftarrow \\ -\tanh\left(\frac{L}{2 \cdot a}\right) \cdot \sinh\left(\frac{z}{a}\right) - 1.0\end{array}\right)\right) = -3.7 \cdot 10^{-7} \frac{rad}{in^3}$$

Shear Stresses due to Pure Torsion at Support

$\tau_{t\_web} := G \cdot t_w \cdot \theta'_s = 5.7\ ksi$ Pure torsion shear stress, DG9 - Eq 4.1

$\tau_{t\_top} := G \cdot t_{ft} \cdot \theta'_s = 10\ ksi$

$\tau_{t\_bot} := G \cdot t_{fb} \cdot \theta'_s = 5.7\ ksi$

Shear Stresses due to Warping at Support

$\tau_{w\_top} := \frac{-E \cdot S_{wt} \cdot \theta'''_s}{t_{ft}} = 0.3\ ksi$ Warping shear stress, DG9 - Eq 4.2a

$\tau_{w\_bot} := \frac{-E \cdot S_{wb} \cdot \theta'''_s}{t_{fb}} = 0.3\ ksi$

Combined Stresses

Critical Normal Stresses at Midspan:

$f_{un\_top} := \left|\sigma_{bx\_top}\right| + \left|\sigma_{w\_top}\right| = 16.5\ ksi$ Combining normal stress for max compression and tension, DG9 - Eq 4.8a

$f_{un\_bot} := \left|\sigma_{bx\_bot}\right| + \left|\sigma_{w\_bot}\right| = 13.3\ ksi$

Critical Shear Stresses at Support:

$f_{uv\_top} := \left|\tau_{b\_top}\right| + \left|\tau_{w\_top}\right| + \left|\tau_{t\_top}\right| = 10.8\ ksi$ Combining shear stress, DG9 - Eq 4.9a

$f_{uv\_bot} := \left|\tau_{b\_bot}\right| + \left|\tau_{w\_bot}\right| + \left|\tau_{t\_bot}\right| = 6.9\ ksi$

$f_{uv\_web} := \left|\tau_{b\_web}\right| + \left|\tau_{t\_web}\right| = 7.8\ ksi$

Stress Checks

Capacity vs Demand

A-shape is adequate if > 1.0

Yielding at Midspan: DG 9 - Eq 4.12

$$f_{un\_top} = 16.5\ \mathit{ksi} \quad <= \quad 0.9 \cdot F_y = 45\ \mathit{ksi} \qquad \frac{0.9 \cdot F_y}{f_{un\_top}} = 2.72$$

$$f_{un\_bot} = 13.3\ \mathit{ksi} \quad <= \quad 0.9 \cdot F_y = 45\ \mathit{ksi} \qquad \frac{0.9 \cdot F_y}{f_{un\_bot}} = 3.38$$

Shear Yielding at Support: DG 9 - Eq 4.13

$$f_{uv\_top} = 10.8\ \mathit{ksi} \quad <= \quad 0.9 \cdot 0.6 \cdot F_y = 27\ \mathit{ksi} \qquad \frac{0.9 \cdot 0.6 \cdot F_y}{f_{uv\_top}} = 2.51$$

$$f_{uv\_bot} = 6.9\ \mathit{ksi} \quad <= \quad 0.9 \cdot 0.6 \cdot F_y = 27\ \mathit{ksi} \qquad \frac{0.9 \cdot 0.6 \cdot F_y}{f_{uv\_bot}} = 3.92$$

$$f_{uv\_web} = 7.8\ \mathit{ksi} \quad <= \quad 0.9 \cdot 0.6 \cdot F_y = 27\ \mathit{ksi} \qquad \frac{0.9 \cdot 0.6 \cdot F_y}{f_{uv\_web}} = 3.48$$

Buckling at Midspan: DG 9 - Eq 4.14

$$F_{cr} := \frac{\pi^2 \cdot E}{\left(\frac{L_b}{r_t}\right)^2} \cdot \sqrt{1 + 0.078 \cdot \frac{J}{S_{xc} \cdot h_o} \left(\frac{L_b}{r_t}\right)^2} = 55\ \mathit{ksi}$$

critical stress for
buckling check

$$f_{un\_top} = 16.5\ \mathit{ksi} \quad <= \quad 0.85 \cdot F_{cr} = 46\ \mathit{ksi} \qquad \frac{0.85 \cdot F_{cr}}{f_{un\_top}} = 2.81$$

Twist at Midspan

$$t_{serv} := \left(q_D \cdot s + q_{CL} \cdot s\right) \cdot e = 0.2\ \frac{\mathit{kip} \cdot \mathit{in}}{\mathit{in}}$$

torsional moment along beam
length for twist check

$$z := 0.5 \cdot L$$

$$\theta_m := \frac{t_{serv} \cdot a^2}{G \cdot J} \left(\frac{L^2}{2 \cdot a^2} \cdot \left(\frac{z}{L} - \frac{z^2}{L^2}\right) + \cosh\left(\frac{z}{a}\right) - \tanh\left(\frac{L}{2 \cdot a}\right) \cdot \sinh\left(\frac{z}{a}\right) - 1.0 \right) = 2.9\ \mathit{deg}$$

$$\theta_m = 2.9\ \mathit{deg} \quad <= \quad \theta_{max} := 5\ \mathit{deg} \qquad \frac{\theta_{max}}{\theta_m} = 1.7$$

Note, this twist check is for constructability. Engineering judgement should be used for the allowable twist. The analysis conducted above assumes that all dead load is applied to one side of the beam. Due to the decking being shored at midspan, the torsional demand is minimal. However, for precast concrete panels, it would likely be the case that the panels are on both sides of the beam, and the only torsional load is the wet concrete. A more refined analysis could be conducted based on the figure above.

COMPOSITE ANALYSIS - IN-SERVICE

The shallow-depth composite floor system with A-shapes is evaluated in this section for in-service loading. As observed in experimental testing of a composite beam, the section did not reach full composite strength. The Linear Interpolation Method provided conservative results compared to the experimental results and is implemented to quantify the partial composite strength. In addition, serviceability criteria is analyzed to ensure deflection and vibration will be acceptable for the floor system.

Composite Section Properties

$f'_c := 4000\ psi$	concrete strength
$E_c := 57000\ psi \cdot \sqrt{f'_c \cdot \frac{1000}{ksi}} = 3605\ ksi$	Young's modulus of concrete
$D_c := 2.125\ in$	depth of concrete above steel section
$D_{tot} := d + D_c = 10.1\ in$	total depth of cross section
$D_d := 4.625\ in$	depth of stay-in-place formwork (deep deck)
$D_s := D_{tot} - t_{fb} - D_d = 5\ in$	depth of concrete over deep deck
$A_{slab} := D_s \cdot S = 8.33\ ft^2$	total slab area
$n := \frac{E}{E_c} = 8$	modular ratio
$y_e := y_{bar\_top} = 4.13\ in$	distance to ENA of steel section from top of steel
$B_e := min\left(S, \frac{L}{4}\right) = 5\ ft$	effective width per AISC (2022)
$A_{c1} := D_s \cdot B_e - A_t = 294\ in^2$	area of concrete slab for composite calculation
$A_{c2} := \left(b_{fb} - 2 \cdot b_{bearing} - t_w\right) \cdot D_d = 32\ in^2$	area of concrete by steel web

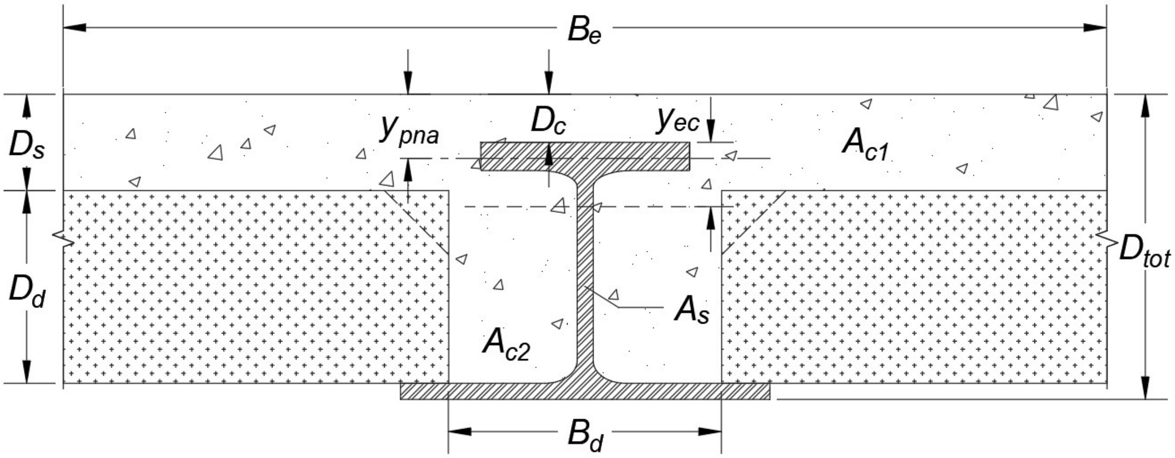

Elastic neutral axis of the composite section

$$y_{ec} := \frac{A_{tot} \cdot y_e + \left(\frac{A_{c2}}{n} \cdot \left(d - \left(0.5 \cdot D_d \right) - t_{fb} \right) \right) + \left(\frac{A_{c1}}{n} \cdot \left(0.5 \cdot D_s - D_c \right) \right)}{A_{tot} + \frac{A_{c2} + A_{c1}}{n}} = 1.73\ \mathit{in}$$

ENA ref's the top of the steel beam

Distances to top of concrete, top of steel, bottom of steel from ENA

$y_{ec\_top\_conc} := y_{ec} + D_c = 3.85\ \mathit{in}$ distance from ENA to top of concrete

$y_{ec\_top\_steel} := y_{ec} = 1.73\ \mathit{in}$ distance from ENA to top of steel beam

$y_{ec\_bot\_steel} := d - y_{ec\_top\_steel} = 6.27\ \mathit{in}$ distance from ENA to bottom of steel beam

Composite moment of inertia - gross

$$I_{x\_comp} := I_x + A_{tot} \cdot \left(y_e - y_{ec} \right)^2 + \frac{A_{c1}}{n} \cdot \left(0.5 \cdot D_s - D_c - y_{ec} \right)^2 + \frac{A_{c1}}{n} \cdot \frac{{D_s}^2}{12} \hookleftarrow = 449\ \mathit{in}^4$$
$$+ \frac{A_{c2}}{n} \cdot \left(d - 0.5 \cdot D_d - t_{fb} - y_{ec} \right)^2 + \frac{A_{c2}}{n} \cdot \frac{{D_d}^2}{12}$$

Find S_x for top of concrete, top of steel, and bottom of steel

$S_{xc\_tod} := \frac{I_{x\_comp}}{y_{ec\_top\_conc}} = 117\ \mathit{in}^3$ section modulus - top of concrete

$S_{xc\_tos} := \frac{I_{x\_comp}}{y_{ec\_top\_steel}} = 260\ \mathit{in}^3$ section modulus - top of steel

$S_{xc\_bos} := \frac{I_{x\_comp}}{y_{ec\_bot\_steel}} = 72\ \mathit{in}^3$ section modulus - bottom of steel

Full Composite Moment Capacity

Plastic neutral axis depth - referenced from the top of slab

$y_{PNA} := 2.49\ in$ iterate depth until T and C values on next page are in equilibrium

Width functions for concrete and steel

$$b_c(y) := \left\| \begin{array}{l} \text{if } y \le D_c \\ \quad \| B_e \\ \text{else if } D_c < y \le min\left(y_{PNA}, D_c + t_{ft}\right) \\ \quad \| B_e - b_{ft} \\ \text{else if } y \le min\left(y_{PNA}, D_s\right) \\ \quad \| B_e - t_w \\ \text{else if } D_s < y \le y_{PNA} \\ \quad \| b_{fb} - 2 \cdot b_{bearing} - t_w \end{array} \right\|$$

width of concrete as a function of depth, referenced from the top of slab

$$b_s(y) := \left\| \begin{array}{l} \text{if } y \le D_c \\ \quad \| 0\ in \\ \text{else if } D_c < y \le D_c + t_{ft} \\ \quad \| b_{ft} \\ \text{else if } y \ge D_{tot} - t_{fb} \\ \quad \| b_{fb} \\ \text{else} \\ \quad \| t_w \end{array} \right\|$$

width of steel as a function of depth, referenced from the top of slab

Plot of steel (blue) and concrete (black) width, and the PNA (red)

$y_h := 0\ in, 0.01\ in .. D_{tot}$

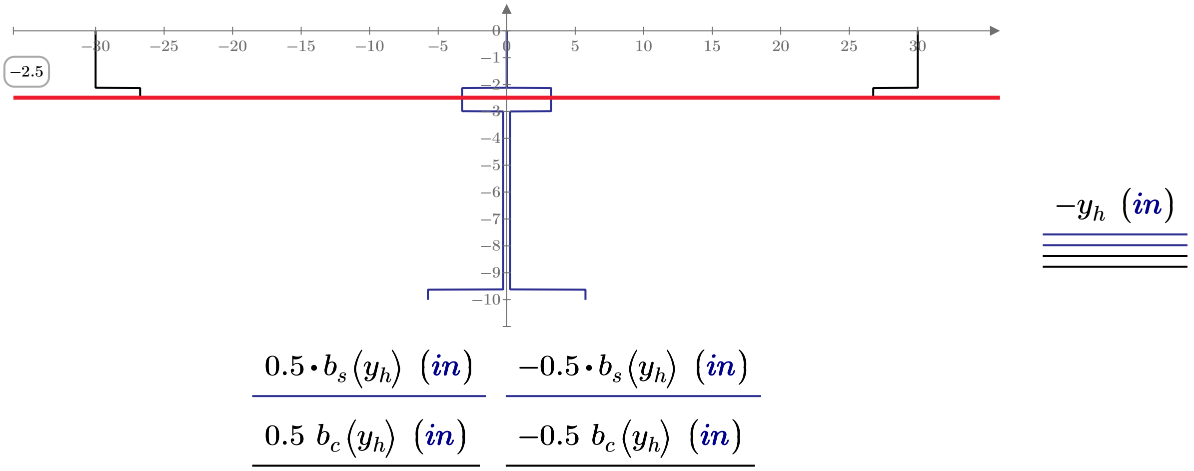

Everything above the PNA is in compression (steel and concrete) and must be in equilibrium with the steel below the PNA (ignoring concrete in tension). The concrete is assumed to be at 0.85*f'$_c$ and the steel is assumed to be at F$_y$ (both in compression and tension).

Sum of forces in concrete and steel

$$C_c := \int_{0}^{y_{PNA}} 0.85 \cdot f'_c \cdot b_c(y)\, \mathrm{d}y = 500\ \mathbf{kip}$$

sum of concrete compression forces

$$C_s := \int_{D_c}^{y_{PNA}} F_y \cdot b_s(y)\, \mathrm{d}y = 119\ \mathbf{kip}$$

sum of steel compression forces

$$C := C_c + C_s = 619\ \mathbf{kip}$$

total compression force

$$T := \int_{y_{PNA}}^{D_{tot}} F_y \cdot b_s(y)\, \mathrm{d}y = 619\ \mathbf{kip}$$

sum of steel tension forces

$$T - C = 0.35\ \mathbf{kip}$$

Check equilibrium. Iterate the plastic neutral axis depth until T-C ~ 0

Assumed stress distribution for full composite strength

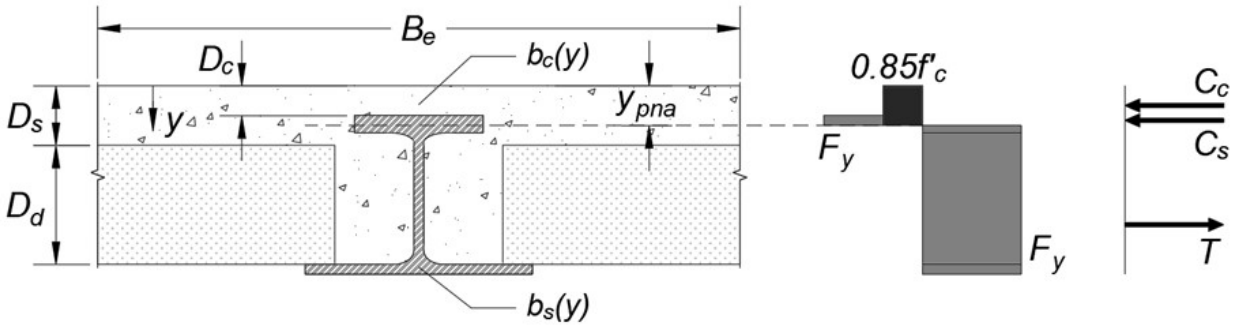

Full composite moment capacity

$$M_{ncp} := \int_{0}^{y_{PNA}} 0.85 \cdot f'_c \cdot b_c(y) \cdot \left(y_{PNA} - y\right) \mathrm{d}y \hookleftarrow = 288\ \mathbf{kip} \cdot \mathbf{ft}$$
$$+ \int_{D_c}^{D_{tot}} F_y \cdot b_s(y) \cdot \left|y_{PNA} - y\right| \mathrm{d}y$$

Note, full composite strength might not be achieved since mechanical connectors are not utilized to transfer load between the steel and concrete. The degree of composite action depends on the load transfer developed through bond shear between steel and concrete due to encasement. The partial composite strength is determined in the next set of calculations.

Partial Composite Strength - Linear Interpolation

Lower and Upper Bounds for Linear Interpolation

$M_s := R_{pc} \cdot M_{yc} = 197\ \text{kip} \cdot \text{ft}$ compression flange yielding of steel section

$M_{ncp} = 288\ \text{kip} \cdot \text{ft}$ full composite moment capacity

Max shear force that can be transferred from elastic bond shear

$p_{bs} := 2 \cdot \left(b_{ft} + y_{ec\_top\_steel}\right) - t_w = 16\ \text{in}$ bond shear perimeter that can transfer the longitudinal shear - above composite ENA only

$f_{bs} := 100\ \text{psi}$ bond shear strength: established from component-level beam tests (Ottmers et al. 2025a)

$F_{bs} := f_{bs} \cdot p_{bs} \cdot \dfrac{L}{4} = 96\ \text{kip}$ predicted max shear transfer force assuming elastic shear flow - UDL

The elastic bond shear is quantified by calculating the area under the shear diagram. The bond perimeter is assumed to act only above the elastic neutral axis of the composite section. The bond shear strength was established by conducting eight component beam tests that developed composite action through bond shear between the steel beam and concrete (Ottmers et al. 2025a).

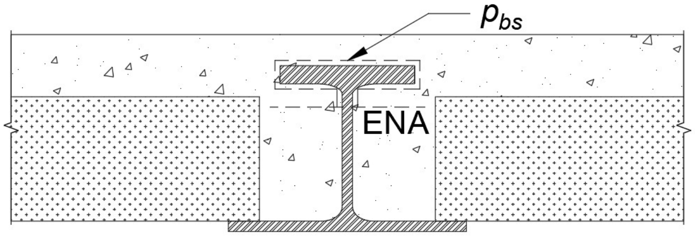

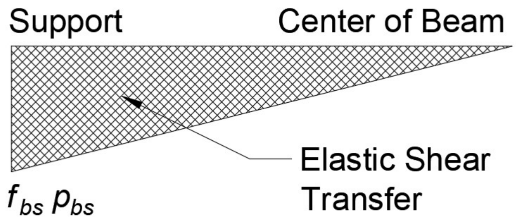

Max concrete compressive force

$C_c = 500\ \text{kip}$ max force that could form in the concrete when determining the full composite moment capacity

Partial composite moment capacity

$M_{nc\_linear} := M_s + \dfrac{F_{bs}}{C_c} \cdot \left(M_{ncp} - M_s\right) = 214\ \text{kip} \cdot \text{ft}$ linear interpolation between non-composite and full composite moment capacities

$\phi M_{nc} := 0.9 \cdot M_{nc\_linear} = 193\ \text{kip} \cdot \text{ft}$

Percent beyond steel moment capacity

$$\frac{F_{bs}}{C_c} = 19\%$$

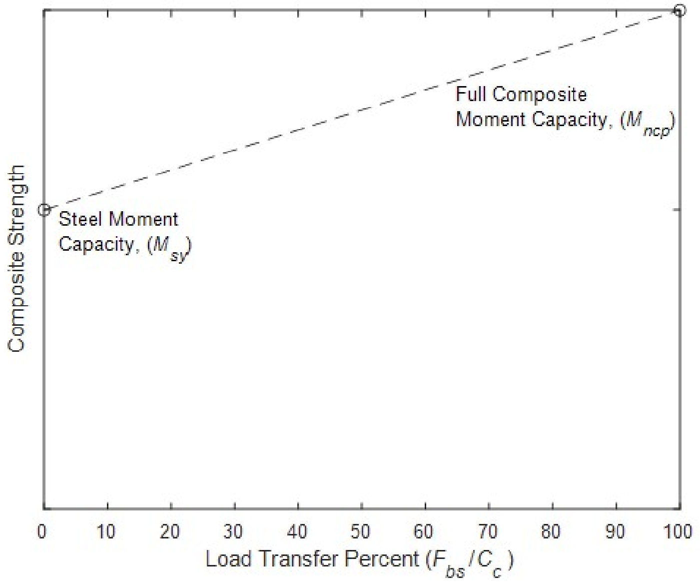

Partial composite action percentage

$$\frac{M_{nc\_linear}}{M_{ncp}} = 75\%$$

Demand

$$w_u := 1.2 \cdot \left(\left(q_D + q_{SDL}\right) \cdot S + w_{beam}\right) + 1.6 \cdot \left(q_L + q_P\right) \cdot S = 3.78 \ \frac{kip}{ft}$$

$$M_{uComp} := \frac{w_u \cdot L^2}{8} = 189 \ kip \cdot ft$$

Capacity vs Demand

$$\frac{\phi M_{nc}}{M_{uComp}} = 1.02$$ composite section is adequate for flexure if > 1.0

Note, two other methods to calculate the partial composite strength are shown at the end of the design example (see Supplemental Analysis Section). These include partial plastic stress distribution and strain compatibility. The composite strength gained through bond shear was validated in experimental testing, both on the component-level and system-level. The partial composite strength determine with linear interpolation provides a conservative estimate of the composite strength gained through bond interaction between the steel and concrete. Refer to Ottmers et al. (2025a) and Ottmers et al. (2025c) for experimental results and further discussion on calculating the composite strength.

Serviceability - Deflection

Live Load Deflection - Composite Section (Live and Partition Load)

$$w_L := \left(q_L + q_P\right) \cdot S = 0.92 \ \frac{kip}{ft}$$

live and partition load

$$\Delta_{Live} := \frac{5 \cdot w_L \cdot L^4}{384 \cdot E \cdot I_{x\_comp}} = 0.3 \ in$$

live load deflection assuming simply supported beam

Capacity vs Demand

$$\Delta_{Live\_Allow} := \frac{L}{360} = 0.7 \ in$$

allowable live load deflection per IBC (2018)

$$\frac{\Delta_{Live\_Allow}}{\Delta_{Live}} = 2.61$$

adequate for live load deflection if > 1.0

Dead Load Deflection - A-shape (Concrete and Beam Weight)

$$w_D := q_D \cdot S + w_{beam} = 1.71 \ \frac{kip}{ft}$$

dead load during construction

$$\Delta_{Dead} := \frac{5 \cdot w_D \cdot L^4}{384 \cdot E \cdot I_x} = 1.3 \ in$$

dead load deflection

$$\Delta_{Allow\_Camber} := 0.8 \cdot \Delta_{Dead} = 1 \ in$$

allowable camber (based on 80% of the dead load)

$$\Delta_{Camber} := 0.75 \ in$$

selected camber to implement for the A-shape

Superimposed Dead Load Deflection - Composite Section

$$w_{SDL} := q_{SDL} \cdot S = 0.2 \ \frac{kip}{ft}$$

superimposed dead load

$$\Delta_{SDL} := \frac{5 \cdot w_{SDL} \cdot L^4}{384 \cdot E \cdot I_{x\_comp}} = 0.1 \ in$$

SDL deflection

Capacity vs Demand

$$\Delta_{Total} := \Delta_{Dead} - \Delta_{Camber} + \Delta_{SDL} + \Delta_{Live} = 0.8 \ in$$

total deflection

$$\Delta_{Live\_plus\_Dead\_Allow} := \frac{L}{240} = 1 \ in$$

allowable dead + live load deflection per IBC (2018)

$$\frac{\Delta_{Live\_plus\_Dead\_Allow}}{\Delta_{Total}} = 1.18$$

adequate for total deflection if > 1.0

Serviceability - Vibration Analysis (per AISC Design Guide 11)

Assumed Loads for Vibration

$q_D = 83\ \mathit{psf}$	weight of concrete and metal deck - New Millennium design guide
$q_{SDL\_DG11} := 4\ \mathit{psf}$	estimate of actual dead load (e.g., MEP) - Section 3.3 of DG11
$q_{L\_DG11} := 6\ \mathit{psf}$	recommended live load for residences - Table 3-1 in DG11
$w := q_D + q_{SDL\_DG11} + q_{L\_DG11} = 93\ \mathit{psf}$	estimated supported weight per unit area - Section 4.1.2 DG11

Note, vibration response is the greatest for lightly loaded floors, therefore DG11 suggests to use expected day-to-day dead and live loads. The structure weight, estimate of actual superimposed dead load, and estimated live load for residences are utilized.

Composite Section Properties for Vibration

$n_{DG11} := \dfrac{E}{1.35 \cdot E_c} = 6$	modular ratio for dynamic response - Section 3.2 DG11
$y_e := y_{bar\_top} = 4.13\ \mathit{in}$	distance to ENA of steel section from top of steel
$D_d = 4.63\ \mathit{in}$	depth of stay-in-place formwork
$D_s = 5\ \mathit{in}$	depth of concrete slab over void
$D_c = 2.13\ \mathit{in}$	depth of concrete above steel section
$B_{e\_DG11} := min\left(S, 0.4 \cdot L\right) = 8\ \mathit{ft}$	effective width - Section 3.2 DG11
$A_{c1\_DG11} := D_s \cdot B_{e\_DG11} - A_t = 474\ \mathit{in}^2$	area of concrete slab for composite calculation
$A_{c2\_DG11} := A_{c2} = 32\ \mathit{in}^2$	area of concrete by steel web

Elastic neutral axis from the top of the steel for Vibration

$$y_{e\_DG11} := \frac{A_{tot} \cdot y_e + \left(\dfrac{A_{c2\_DG11}}{n_{DG11}} \cdot \left(d - \left(0.5 \cdot D_d\right) - t_{fb}\right)\right) + \left(\dfrac{A_{c1\_DG11}}{n_{DG11}} \cdot \left(0.5 \cdot D_s - D_c\right)\right)}{A_{tot} + \dfrac{A_{c2\_DG11} + A_{c1\_DG11}}{n_{DG11}}} = 1.19\ \mathit{in}$$

Composite moment of inertia (gross) for Vibration

$$I_{xc\_DG11} := I_x + A_{tot} \cdot \left(y_e - y_{e\_DG11}\right)^2 + \frac{A_{c1\_DG11}}{n_{DG11}} \cdot \left(0.5 \cdot D_s - D_c - y_{e\_DG11}\right)^2 + \frac{A_{c1\_DG11}}{n_{DG11}} \cdot \frac{D_s^2}{12} + \frac{A_{c2\_DG11}}{n_{DG11}} \cdot \left(d - 0.5 \cdot D_d - t_{fb} - y_{e\_DG11}\right)^2 + \frac{A_{c2\_DG11}}{n_{DG11}} \cdot \frac{D_d^2}{12} = 608\ in^4$$

Composite moment of inertia for deep deck

$I_{x\_deck} := 97.17\ \frac{in^4}{ft}$ uncracked moment of inertia of slab section transformed to steel - NM deck guide

Deflection calculation for beam and deck slab

$\Delta_{beam} := \frac{5 \cdot \left(w \cdot S + w_{beam}\right) \cdot L^4}{384 \cdot E \cdot I_{xc\_DG11}} = 0.4\ in$ deflection of beam, assuming simply supported for the estimated day-to-day load

$\Delta_{deck} := \frac{5 \cdot w \cdot L^4}{384 \cdot E \cdot I_{x\_deck}} = 0.1\ in$ deflection of deck slab, assuming simply supported for the estimated day-to-day load

Natural frequency of floor system

$g := 386\ \frac{in}{s^2}$ acceleration of gravity

$f_n := 0.18 \cdot \sqrt{\frac{g}{\Delta_{beam} + \Delta_{deck}}} = 5\ Hz$ fundamental frequency of the floor system - Section 3.1 DG11

Effective Panel Weight for Beam Panel Mode - Section 4.1.2 DG11

$C_j := 2$

beams in most areas - DG11

$D_{s\_DG11} := I_{x\_deck} = 97.2\ \frac{in^4}{ft}$

slab transformed moment of inertia - New Millennium Deep-Dek design guide

$D_j := \frac{I_{xc\_DG11}}{S} = 30.4\ \frac{in^4}{ft}$

beam moment of inertia per unit width - Eq 4-3a, DG11

$B_j := C_j \cdot \left(\frac{D_{s\_DG11}}{D_j}\right)^{0.25} \cdot L = 53\ ft$

effective panel width - Eq 4-3, DG11
note, the building is assumed to have a floor width > 1.5B_j per B_j definition

$W := w \cdot B_j \cdot L = 99578\ lbf$

effective panel weight for beam - Eq 4-2, DG11

$\beta := 0.03$

assumed damping ratio for structural system + ceiling and ductwork + finishes - Table 4-2 in DG11

Walking Criterion for Low - Frequency Floors

$P_o := 65\ lbf$

amplitude of the driving force - Section 4.1.1 DG11

$a_{p\_g} := \frac{P_o \cdot e^{-0.35 \cdot \frac{f_n}{Hz}}}{\beta \cdot W} = 0.004$

peak acceleration normalized by gravity due to walking - Eq 4-1 DG11

Max Tolerance Limit - Table 4-1 (DG11)

$a_{p\_g\_max} := 0.005$

Capacity vs Demand

$\frac{a_{p\_g\_max}}{a_{p\_g}} = 1.3$

adequate for
vibration if > 1.0

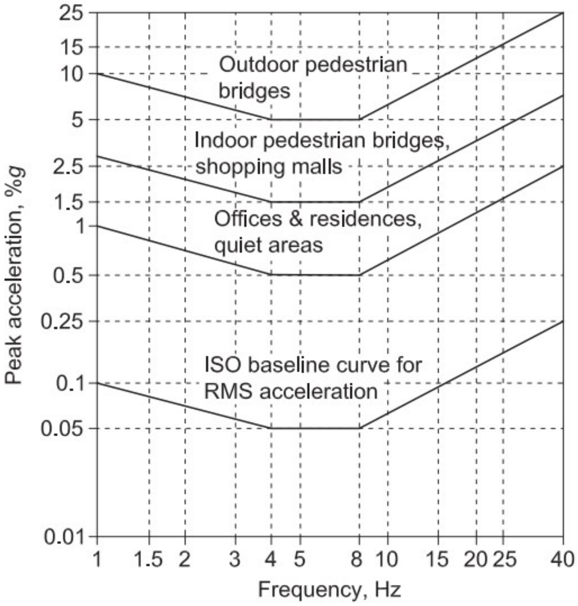

Fig 2-1. Tolerance Limits (DG11)

DESIGN SUMMARY

A design summary is provided in this section which includes the beam length and spacing, assumed loading for construction and in-service. The material strengths assumed in the analysis and an overview of the floor system is provided. Capacity to demand ratios are quantified for the primary limit states that were analyzed for the loading and grid layout. All primary limit states analyzed for the shallow-depth composite floor system are satisfactory.

Building Layout, Loads, Material Strengths, and Cross-Section

Grid Layout

$L=20\ ft$	beam length
$S=20\ ft$	beam spacing

Loads

$q_{conc}=79\ psf$	concrete weight - New Millennium Deep-Dek Design Guide
$q_{deck}=4.1\ psf$	deck weight - NM Deep-Dek Design Guide
$q_D=83\ psf$	total construction dead load
$q_{SDL}=10\ psf$	superimposed dead load (e.g., MEP)
$q_{CL}=20\ psf$	construction live load
$q_{Lo}=40\ psf$	live load (reducible)
$q_P=15\ psf$	partition load

Material Strengths

$F_y=50\ ksi$	steel yield strength
$f'_c=4\ ksi$	concrete strength

Floor System Cross - Section

A8x52	steel beam size
$d=8\ in$	steel beam depth
Deep−Dek 4.5, 18 ga	deep decking callout
$D_c=2.13\ in$	concrete depth above steel beam
$D_s=5\ in$	concrete slab thickness above deep decking
$D_d=4.63\ in$	deep decking actual depth
$D_{tot}=10.1\ in$	total depth of the composite floor system

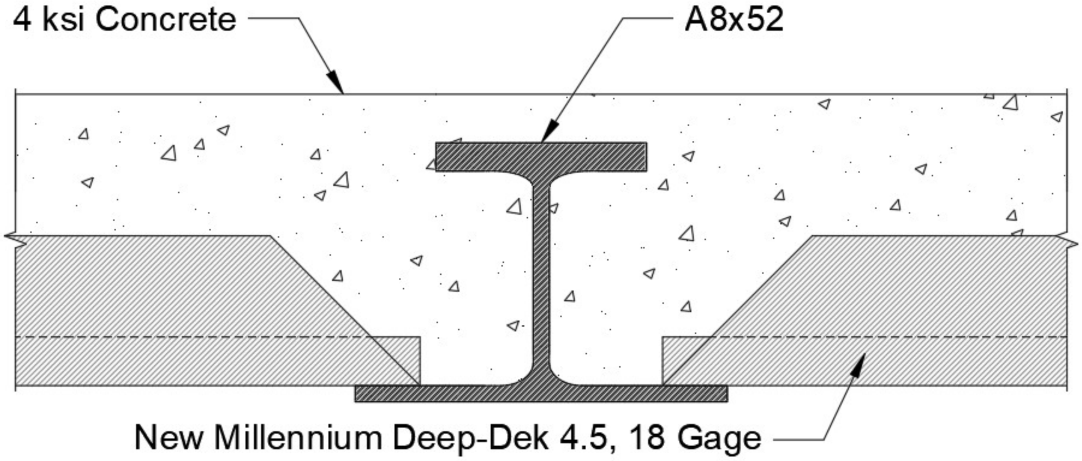

Capacity to Demand Ratios

Non-Composite Flexure

$$\frac{\phi M_n}{M_{uNC}}=2.57$$

Non-Composite Torsion - Stresses

$$\frac{0.9 \cdot F_y}{f_{un\_top}}=2.72 \qquad \frac{0.9 \cdot 0.6 \cdot F_y}{f_{uv\_top}}=2.51 \qquad \frac{0.9 \cdot 0.6 \cdot F_y}{f_{uv\_web}}=3.48$$

$$\frac{0.9 \cdot F_y}{f_{un\_bot}}=3.38 \qquad \frac{0.9 \cdot 0.6 \cdot F_y}{f_{uv\_bot}}=3.92 \qquad \frac{0.85 \cdot F_{cr}}{f_{un\_top}}=2.81$$

Non-Composite Torsion - Twist

$$\frac{\theta_{max}}{\theta_m}=1.7$$

Composite Flexure

$$\frac{\phi M_{nc}}{M_{uComp}}=1.02$$

Deflection

$$\frac{\Delta_{Live\_Allow}}{\Delta_{Live}}=2.61$$

$$\frac{\Delta_{Live\_plus\_Dead\_Allow}}{\Delta_{Total}}=1.18$$

Vibration

$$\frac{a_{p\_g\_max}}{a_{p\_g}}=1.3$$

Based on the capacity to demand ratios above, the controlling limit state for this design example is composite flexure. The capacity to demand ratio table for a similar construction dead load in Appendix J for a beam length and spacing of 20 ft is 1.01 (discrepancy due to slightly higher specified loads). The analysis conducted above is completed in the design aids to assist in design of A-shapes in shallow-depth composite floor systems.

SUPPLEMENTAL ANALYSIS

The supplemental analysis section quantifies the fire resistance of shallow-depth composite floor systems. The fire resistance utilizes a partial plastic stress distribution with varying steel strength due to the significant temperature gradient over the beam depth. Three methods for quantifying the temperature gradient are quantified in this section. In addition, two alternative methods are implemented to quantify the partial composite strength during ambient conditions. A comparison of the composite moment capacity is also provided.

Fire Resistance of Composite Section - Unprotected Bottom Flange

Material properties

$F_y = 50\ \mathbf{ksi}$	steel yield strength
$f'_c = 4\ \mathbf{ksi}$	concrete compressive strength
$F_{yr} := 60\ \mathbf{ksi}$	rebar yield strength
$z_r := 2\ \mathbf{in}$	height of rebar above the bottom side of the bottom flange
$d_r := 1\ \mathbf{in}$	size of rebar
$A_{fr} := 2 \cdot 0.79\ \mathbf{in}^2 = 1.58\ \mathbf{in}^2$	total area of rebar: 2 - #8's

Select Fire Exposure Duration

$R := 1\ \mathbf{hr}$	select fire exposure: 0.5, 1, 1.5, or 2 hours
$R\_col := \left\| \begin{array}{l} \text{if } R = 0.5\ \mathbf{hr} \\ \quad \| 0 \\ \text{else if } R = 1\ \mathbf{hr} \\ \quad \| 1 \\ \text{else if } R = 1.5\ \mathbf{hr} \\ \quad \| 2 \\ \text{else if } R = 2\ \mathbf{hr} \\ \quad \| 3 \end{array} \right\| = 1$	fire exposure column to determine coefficients to use for temperature gradient

Quantify Temperature Gradients

Coefficients for bottom flange temperature (per Zaharia and Franssen 2012)

$$A_{i\_table} := \begin{bmatrix} 0.113 & 0.130 & 0 & 0 \end{bmatrix}$$

$$B_{i\_table} := \begin{bmatrix} -12.80 & -11.80 & -2.60 & -1.25 \end{bmatrix}$$

$$C_{i\_table} := \begin{bmatrix} 760 & 980 & 990 & 1025 \end{bmatrix}$$

$$A_i := A_{i\_table}(0, R\_col) = 0.13$$

$$B_i := B_{i\_table}(0, R\_col) = -11.8$$

$$C_i := C_{i\_table}(0, R\_col) = 980$$

These coefficients are for a second-order best-fit function per Zaharia and Franssen (2012) for the temperature of the bottom flange. The coefficients were established using a numerical finite element model to analyze the temperature of the bottom flange for varying flange thicknesses and fire duration exposure. The coefficients were established for the ISO 834 fire curve which is very similar to the ASTM E119 fire curve.

Coefficients for web temperature (per Zaharia and Franssen 2012)

$$A_{w\_table} := \begin{bmatrix} -140.7 & -103.8 & -108.6 & -70.44 \end{bmatrix}$$

$$B_{w\_table} := \begin{bmatrix} 832.42 & 968.6 & 1146.7 & 1124.4 \end{bmatrix}$$

$$C_{w\_table} := \begin{bmatrix} 0.00317 & 0.00232 & 0.00198 & 0.00158 \end{bmatrix}$$

$$D_{w\_table} := \begin{bmatrix} -0.023 & -0.0182 & -0.0154 & -0.0134 \end{bmatrix}$$

$$A_w := A_{w\_table}\left(0, R\_col\right) = -103.8$$

$$B_w := B_{w\_table}\left(0, R\_col\right) = 968.6$$

$$C_w := C_{w\_table}\left(0, R\_col\right) = 0.0023$$

$$D_w := D_{w\_table}\left(0, R\_col\right) = -0.02$$

These coefficients are for an exponential best-fit function per Zaharia and Franssen (2012) for the temperature of the web. In shallow-depth floor systems, the web temperature has a significant gradient due to concrete encasement. The coefficients were established using a numerical finite element model to analyze the temperature of the web for varying bottom flange thicknesses and fire duration exposure. The coefficients were established for the ISO 834 fire curve which is very similar to the ASTM E119 fire curve.

Coefficients for longitudinal reinforcement temperature (per Hanus et al. 2017)

$$A_{r\_table} := \begin{bmatrix} 0 & 0.0954 & 0.0548 & 0.0381 \end{bmatrix}$$

$$B_{r\_table} := \begin{bmatrix} 0 & -19.254 & -15.13 & -12.797 \end{bmatrix}$$

$$C_{r\_table} := \begin{bmatrix} 300 & 1105.4 & 1135.9 & 1138.1 \end{bmatrix}$$

$$A_r := A_{r\_table}\left(0, R\_col\right) = 0.1$$

$$B_r := B_{r\_table}\left(0, R\_col\right) = -19.254$$

$$C_r := C_{r\_table}\left(0, R\_col\right) = 1105.4$$

These coefficients are for a second-order best-fit function per Hanus et al. (2017) for the temperature of the longitudinal fire reinforcement. Note, the coefficients were updated in Zanon et al. (2021) after a corrigendum was communicated to them by Hanus et al. (2017). The coefficients were established by Hanus et al. (2017) performing numerical modeling and analyzing the floor system for the ISO 823 fire curve (similar to ASTM E119).

The previous coefficients are used in the second-order and exponential best-fit functions to analyze the temperature of the A-shape and longitudinal fire reinforcement. Three methods are implemented for the temperature gradient: (1) Zaharia and Franssen 2012, (2) Zanon et al. 2021, and (3) Romero et al. 2019. Temperature gradient (1) is the most accurate compared to experimental measurements from fire tests. Gradients (2) and (3) implement different methods for an average web temperatures to simplify the analysis.

Temperature of bottom flange (per Zaharia and Franssen 2012)

$$t_{fb\_mm} := \frac{t_{fb}}{in} \cdot 25.4 = 12.7$$

bottom flange thickness in mm

$$T_{fb} := A_i \cdot {t_{fb\_mm}}^2 + B_i \cdot t_{fb\_mm} + C_i = 851$$

bottom flange temperature in $°C$

Temperature of web (per Zaharia and Franssen 2012)

$n := 500$

number of fiber slices to break web up into

$$dh_w := \frac{h}{n} = 0.0133\ in$$

thickness of fiber slices

$ii := 0..n-1$

index of vector

$$x_{ii} := ii \cdot \frac{h}{in \cdot n} + \frac{h}{in \cdot 2 \cdot n} = \begin{bmatrix} 0.007 \\ 0.02 \\ 0.033 \\ \vdots \end{bmatrix}$$

centroid of fiber slice in in

$$z_{ii} := x_{ii} \cdot 25.4 = \begin{bmatrix} 0.2 \\ 0.5 \\ 0.8 \\ \vdots \end{bmatrix}$$

centroid of fiber slice in mm to evaluate temperature of web for each fiber

$$T_w := \left(A_w \cdot \ln\left(t_{fb\_mm}\right) + B_w\right) \cdot \exp\left(\left(C_w \cdot \ln\left(t_{fb\_mm}\right) + D_w\right) \cdot z\right) = \begin{bmatrix} 703 \\ 700 \\ 698 \\ \vdots \end{bmatrix}$$

web temp in $°C$

Temperature of top flange (per Zaharia and Franssen 2012)

$n_{tf} := 200$

number of fiber slices to break top flange up into

$$dh_{tf} := \frac{t_{ft}}{n_{tf}} = \left(4.38 \cdot 10^{-3}\right)\ in$$

thickness of fiber slices

$ii := 0..n_{tf}-1$

index of vector

$$x_{ii} := ii \cdot \frac{t_{ft}}{in \cdot n_{tf}} + \frac{t_{ft}}{in \cdot 2 \cdot n_{tf}} + \frac{h}{in} = \begin{bmatrix} 6.63 \\ 6.63 \\ 6.64 \\ \vdots \end{bmatrix}$$

centroid of fiber slice in in

$$z_{tf_{ii}} := x_{ii} \cdot 25.4 = \begin{bmatrix} 168 \\ 168 \\ 169 \\ \vdots \end{bmatrix}$$

centroid of fiber slice in mm to evaluate temperature of top flange for each fiber

$$T_{ft} := \left(A_w \cdot \ln\left(t_{fb\_mm}\right) + B_w\right) \cdot \exp\left(\left(C_w \cdot \ln\left(t_{fb\_mm}\right) + D_w\right) \cdot z_{tf}\right) = \begin{bmatrix} 89 \\ 89 \\ 89 \\ \vdots \end{bmatrix}$$

top flange temp in $°C$

Temperature of web @ h/4 (per Zanon et al. 2021)

$$z_{25h} := 0.25 \cdot \frac{h}{in} \cdot 25.4 = 42$$

25% of the height of web from top of bottom flange in mm

$$T_{w\_25h} := \left(A_w \cdot \ln\left(t_{fb\_mm}\right) + B_w\right) \cdot \exp\left(\left(C_w \cdot \ln\left(t_{fb\_mm}\right) + D_w\right) \cdot z_{25h}\right) = 420$$

web temp @ 25% of h $°C$

Find height where temperature of web = 400 $°C$ (per Romero et al. 2019)

$$z_{400\_table} := \begin{bmatrix} 11.5 & 46 & 75 & 92 \end{bmatrix}$$

$$z_{400} := z_{400\_table}\left(0, R\_col\right) = 46$$

height mm where temp of web is 400 $°C$

$$T_{w\_400} := \left(A_w \cdot \ln\left(t_{fb\_mm}\right) + B_w\right) \cdot \exp\left(\left(C_w \cdot \ln\left(t_{fb\_mm}\right) + D_w\right) \cdot z_{400}\right) = 400$$

web temp = 400 $°C$

Temperature of top flange at mid thickness of top flange (average)

$$z_{tf\_avg} := \frac{h}{in} \cdot 25.4 + \frac{t_{ft}}{2 \cdot in} \cdot 25.4 = 179$$

$$T_{ft\_avg} := \left(A_w \cdot \ln\left(t_{fb\_mm}\right) + B_w\right) \cdot \exp\left(\left(C_w \cdot \ln\left(t_{fb\_mm}\right) + D_w\right) \cdot z_{tf\_avg}\right) = 78$$

temp of top flange in $°C$

Temperature of web: lower and upper portions (per Romero et al. 2019)

$$T_{w\_upper} := 0.5\ \left(400 + T_{ft}(0)\right) = 244$$

$$T_{w\_lower} := 0.5\ \left(400 + T_w(0)\right) = 552$$

temp of upper and lower web in $°C$

Temperature of longitudinal reinforcement (per Hanus et al. 2017)

$$k_{cbf} := 1$$

coefficient for percentage of concrete covering top surface of bottom flange, always 1.0 for this floor system

$$u_{eq} := min\left(45, 25 + \frac{t_{fb\_mm}}{2}\right) + \frac{5}{k_{cbf}} = 36.4$$

equivalent rebar distance in mm (conservative value to estimate rebar temp per Hanus et al. 2017)

$$T_r := A_r \cdot {u_{eq}}^2 + B_r \cdot u_{eq} + C_r = 532$$

longitudinal fire reinforcement temperature in $°C$

Temperature gradient over cross section depth for plot comparison

(1) Zaharia and Franssen 2012

$$T_{all} := \text{stack}\left(T_{fb}, T_{fb}, T_w, T_{ft}\right) = \begin{bmatrix} 851 \\ 851 \\ 703 \\ 700 \\ \vdots \end{bmatrix}$$

temperature over entire steel section depth in °C

$$z_{plot} := \frac{\text{stack}\left(0, t_{fb\_mm}, z + t_{fb\_mm}, z_{tf} + t_{fb\_mm}\right)}{25.4} = \begin{bmatrix} 0 \\ 0.5 \\ 0.5 \\ 0.5 \\ \vdots \end{bmatrix}$$

height of cross section in *in*

(2) Zanon et al. 2021

$$T_{all\_Zan} := \text{stack}\left(T_{fb}, T_{fb}, T_{w\_25h}, T_{w\_25h}, T_{ft\_avg}, T_{ft\_avg}\right) = \begin{bmatrix} 851 \\ 851 \\ 420 \\ 420 \\ 78 \\ 78 \end{bmatrix}$$

temperature of bottom flange, web, and top flange in °C

$$t_{ft\_bot} := t_{fb\_mm} + \frac{h}{in} \cdot 25.4 = 181$$

bottom of top flange in *mm*

$$d_{mm} := \frac{d}{in} \cdot 25.4 = 203$$

top of steel section in *mm*

$$z_{plot\_Zan} := \frac{\text{stack}\left(0, t_{fb\_mm}, t_{fb\_mm}, t_{ft\_bot}, t_{ft\_bot}, d_{mm}\right)}{25.4} = \begin{bmatrix} 0 \\ 0.5 \\ 0.5 \\ 7.1 \\ 7.1 \\ 8 \end{bmatrix}$$

height of cross section at changing thickness in *in*

(3) Romero et al. 2019

$$T_{all\_Rom} := \text{stack}\left(T_{fb}, T_{fb}, T_{w\_lower}, T_{w\_lower}, T_{w\_upper}, T_{w\_upper}, T_{ft\_avg}, T_{ft\_avg}\right)$$

$$T_{all\_Rom} = \begin{bmatrix} 851 \\ 851 \\ 552 \\ \vdots \end{bmatrix}$$

temperature of bottom flange, lower and upper web, and top flange in °C

$t_{ft\_bot} := t_{fb\_mm} + \frac{h}{in} \cdot 25.4 = 181$ bottom of top flange in mm

$d_{mm} := \frac{d}{in} \cdot 25.4 = 203$ top of steel section in mm

$z_{web\_400} := z_{400} + t_{fb\_mm} = 59$ web steel section in mm when T = 400 $°C$

$z_{web\_400\_in} := \frac{z_{web\_400} \cdot in}{25.4} = 2.31\ in$

$$z_{plot\_Rom} := \frac{\text{stack}\left(0, t_{fb\_mm}, t_{fb\_mm}, z_{web\_400}, z_{web\_400}, t_{ft\_bot}, t_{ft\_bot}, d_{mm}\right)}{25.4} = \begin{bmatrix} 0 \\ 0.5 \\ 0.5 \\ 2.3 \\ \vdots \end{bmatrix}$$

height of cross section at changing thickness in in

Plot of temperature gradients for $R = 1\ hr$

Red line = (1) Zaharia and Franssen 2012 (varying temperature gradient)

Blue line = (2) Zanon et al. 2021 (average web temperature gradient)

Green line = (3) Romero et al. 2019 (average temperature gradient w/ 2 web portions)

Black point = Hanus et al. 2017 (reinforcement temperature)

Horizontal axis is the temperature of the cross-section in $°C$

Vertical axis is the height of the steel cross-section in in

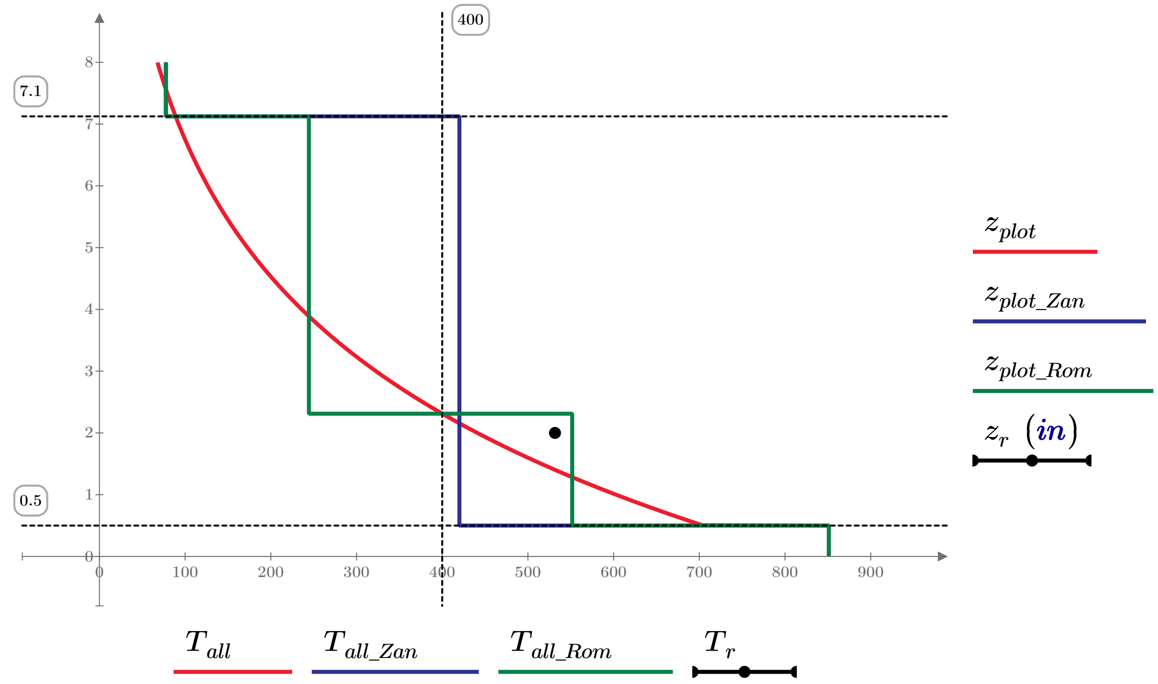

Select Temperature Gradient for Analysis

$temp\_model := 1$

1 = Zaharia and Franssen 2012
2 = Zanon et al. 2021
3 = Romero et al. 2019

$$z_{cent} := \frac{\text{stack}\left(0.5 \cdot t_{fb\_mm}, z + t_{fb\_mm}, z_{tf} + t_{fb\_mm}\right) \cdot in}{25.4} = \begin{bmatrix} 0.25 \\ 0.507 \\ 0.52 \\ \vdots \end{bmatrix} in$$

$i := 0 .. \text{rows}\left(z_{cent}\right) - 1$

```
$T_{beam_i} :=$
    if $temp\_model = 1$
        if $z_{cent_i} < t_{fb}$
            $T_{fb}$
        else if $z_{cent_i} > t_{fb} + h$
            $T_{ft_{i-1-n}}$
        else
            $T_{w_{i-1}}$
    else if $temp\_model = 2$
        if $z_{cent_i} < t_{fb}$
            $T_{fb}$
        else if $z_{cent_i} > t_{fb} + h$
            $T_{ft\_avg}$
        else
            $T_{w\_25h}$
    else if $temp\_model = 3$
        if $z_{cent_i} < t_{fb}$
            $T_{fb}$
        else if $z_{cent_i} > t_{fb} + h$
            $T_{ft\_avg}$
        else if $z_{cent_i} < z_{web\_400\_in}$
            $T_{w\_lower}$
        else
            $T_{w\_upper}$
```

$$= \begin{bmatrix} 851 \\ 703 \\ 700 \\ \vdots \end{bmatrix}$$

Temperature of the cross-section in $°C$ based on selected temperature gradient model

$temp\_model = 1$ --> 1 = Zaharia and Franssen 2012
2 = Zanon et al. 2021
3 = Romero et al. 2019

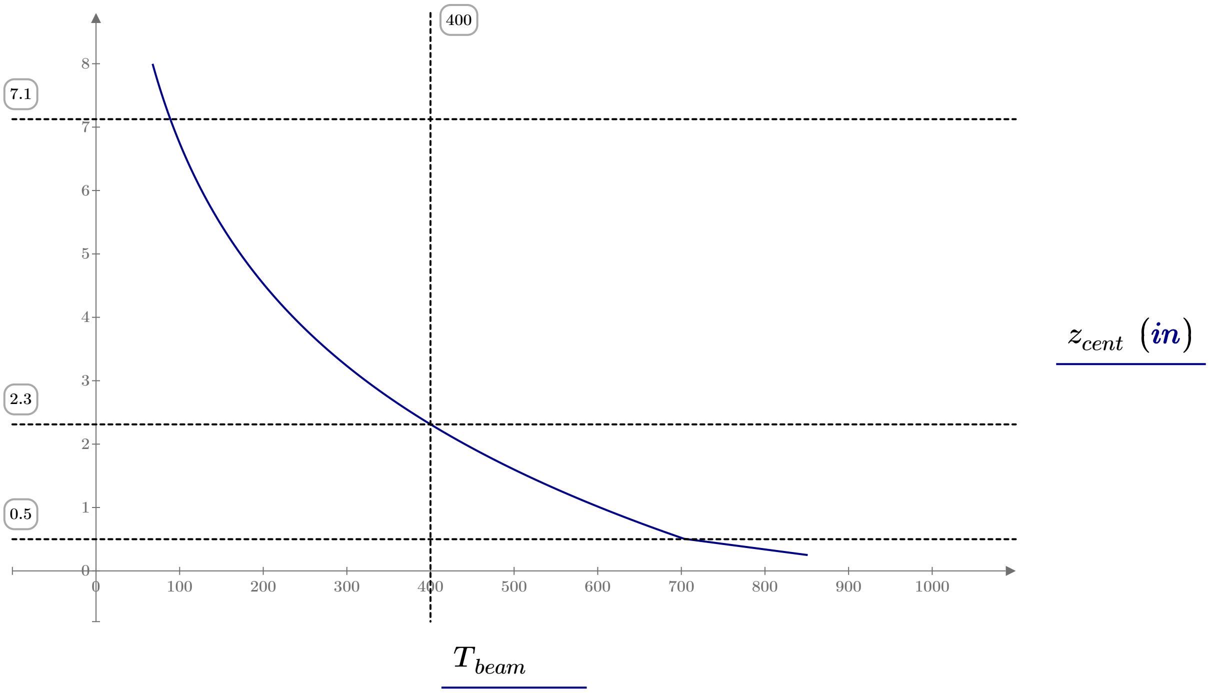

Temperature of the cross-section in $°C$

Note:
Bottom dashed line is the top of the bottom flange
Middle dashed line is where the temperature is $T \le 400\ °C$ - strength is unaffected
Top dashed line is the bottom of the top flange
Vertical dashed line is 400 $°C$

Strength Reduction Factors

Table A-4.2.1: Properties of Steel at Elevated Temperatures (AISC 2022)

T_{steel_AISC}	k_{y_AISC}
20	1
93	1
200	1
320	1
400	1
430	0.94
540	0.66
650	0.35
760	0.16
870	0.07
980	0.04
1100	0.02
1200	0

The strength of steel degrades with elevated temperatures. Appendix 4 in the AISC Specification for Structural Steel Buildings has strength reduction factors for the strength of steel at elevated temperatures.

Temperature is listed in $°C$ since temperature gradients are determined in $°C$

k_{y_AISC} is a strength reduction factor ratio of the steel strength at ambient temperature (20 $°C$ or 68 $°F$) and at the elevated temperature

Plot of strength reduction factors

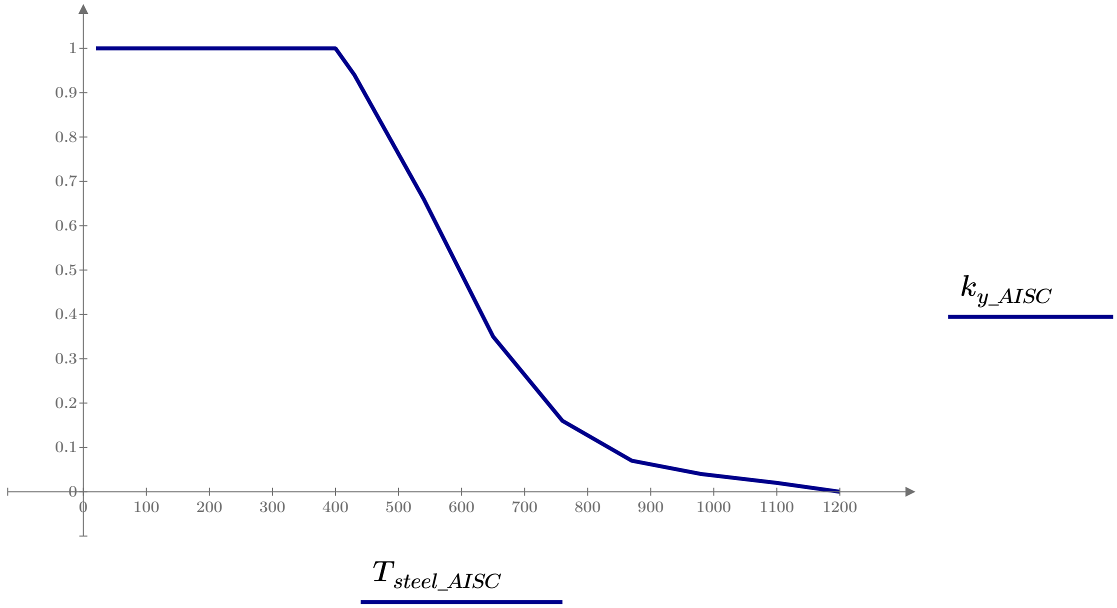

Temperature in $°C$

Obtain reduction factors for beam's temperature gradient

$$k_{y\_beam_i} := \text{linterp}\left(T_{steel\_AISC}, k_{y\_AISC}, T_{beam_i}\right) = \begin{bmatrix} 0.09 \\ 0.26 \\ 0.26 \\ \vdots \end{bmatrix}$$

steel yield strength reduction factors

$$k_{y\_rebar} := \text{linterp}\left(T_{steel\_AISC}, k_{y\_AISC}, T_r\right) = 0.68$$

rebar strength reduction factor

Plot reduction factor based on temperature gradient over the beam depth

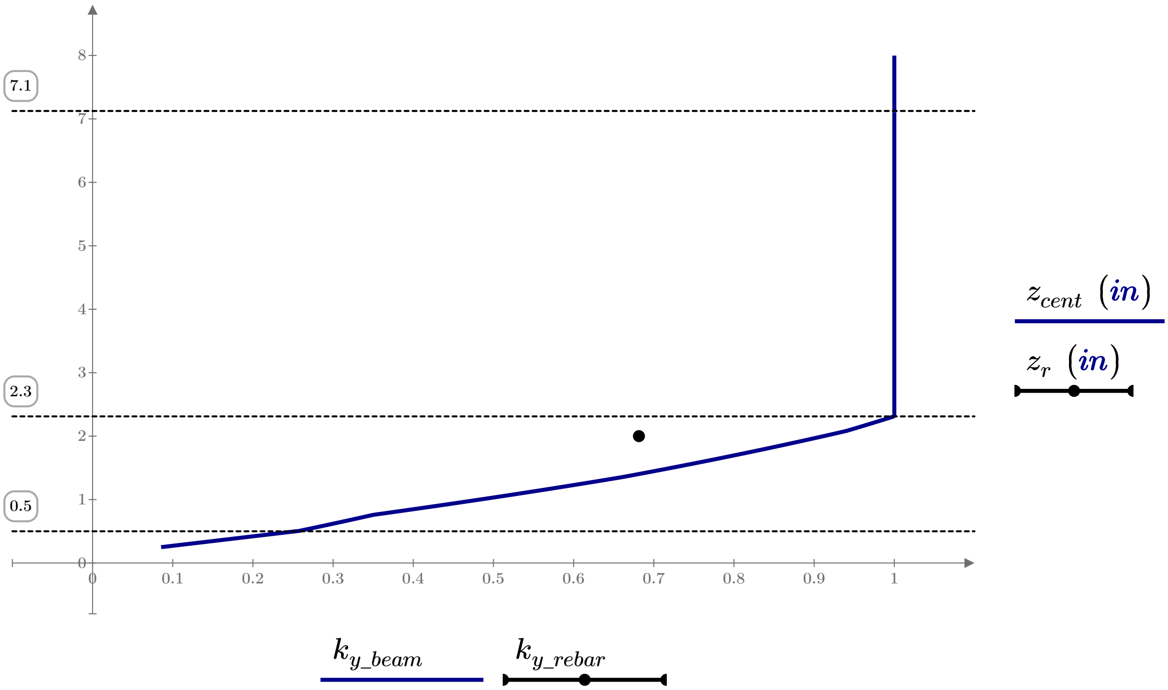

Bottom dashed line is the top of the bottom flange
Middle dashed line is where the temperature is 400 °C - strength is unaffected
Top dashed line is the bottom of the top flange

Bottom flange is assumed to be a constant temperature; however, plot is connecting k_y at the centroid of each fiber

Width and Thickness Functions

Thickness function for each fiber

$$dh_{beam_i} := \left\| \begin{array}{l} \text{if } z_{cent_i} < t_{fb} \\ \quad \left\| \, t_{fb} \right. \\ \text{else if } z_{cent_i} > t_{fb} + h \\ \quad \left\| \, dh_{tf} \right. \\ \text{else} \\ \quad \left\| \, dh_w \right. \end{array} \right\| = \begin{bmatrix} 0.5 \\ 0.01 \\ 0.01 \\ \vdots \end{bmatrix} in$$

Bottom flange is treated as one fiber because constant temperature is utilized for entire bottom flange. The web and top flange thickness is defined above when analyzing temperature gradients.

Width function for each fiber

$$b_{beam_i} := \left\| \begin{array}{l} \text{if } z_{cent_i} < t_{fb} \\ \quad \left\| \, b_{fb} \right. \\ \text{else if } z_{cent_i} > t_{fb} + h \\ \quad \left\| \, b_{ft} \right. \\ \text{else} \\ \quad \left\| \, t_w \right. \end{array} \right\| = \begin{bmatrix} 11.5 \\ 0.5 \\ 0.5 \\ \vdots \end{bmatrix} in$$

Assumed stress distribution for partial plastic stress distribution for fire

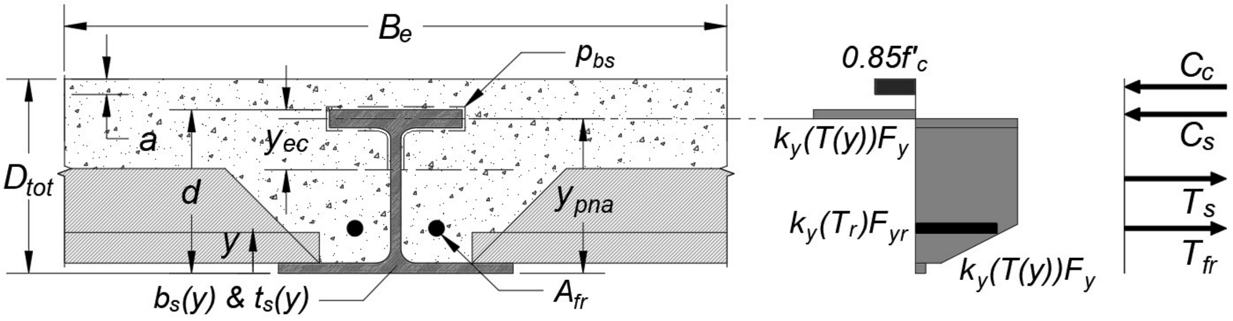

A partial plastic stress distribution with varying steel strength is implemented to analyze the fire resistance of A-shapes in shallow-depth floor systems. The concrete force is limited by elastic shear transfer from bond shear. The strength reduction factors based on the temperature gradient are multiplied by the yield strength to determine the steel strength throughout the steel section. The reduced strength of the fire reinforcement is quantified in a similar approach. The partial composite strength during a fire event is evaluated below.

Partial Moment Capacity when exposed to Fire - with Fire Reinforcement

Compressive force limited by elastic bond shear transfer

$f_{bs}=100\ psi$ — bond strength: established during component beam tests (Ottmers et al. 2025a)

$p_{bs}=16\ in$ — bond perimeter - above ENA of composite section

$F_{bs}:=f_{bs}\cdot p_{bs}\cdot\frac{L}{4}=96\ kip$ — elastic shear transfer strength from bond strength - UDL

$a:=\frac{F_{bs}}{0.85\cdot f'_c\cdot B_e}=0.5\ in$ — depth of concrete stress block due to elastic bond transfer

$C_c:=F_{bs}=96\ kip$ — max concrete force based on bond strength shear transfer

Determine PNA of composite section

$PNA_{fire}:=7.345\ in$ — guess PNA for composite section during fire and iterate until equilibrium

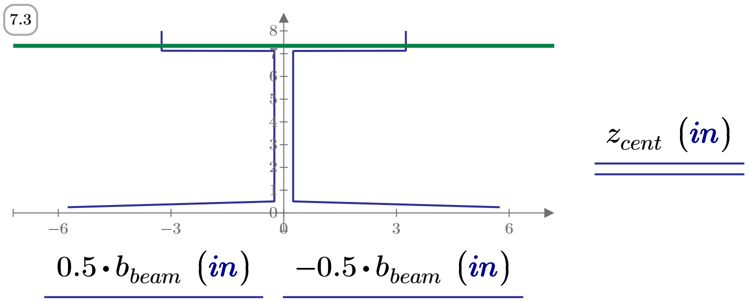

Plot steel beam width (green line is PNA_fire) for partial comp section to be in equilibrium.

$PNA_{index}:=\text{match}\left(PNA_{fire},z_{cent},\text{“near”}\right)_0=550$ — index of row that is closest to the PNA guess value

$z_{cent_{PNA_{index}}}=7.34\ in$ — centroid value that is closest to PNA guess

Check equilibrium in composite section

$$C_s:=\sum_{i=PNA_{index}}^{\text{rows}(z_{cent})-1}k_{y\_beam_i}\cdot F_y\cdot dh_{beam_i}\cdot b_{beam_i}=215\ kip$$

summation of compressive force above PNA_{fire}

$C_c=96\ kip$ — compressive force in slab

$$T:=\sum_{i=0}^{PNA_{index}}k_{y\_beam_i}\cdot F_y\cdot dh_{beam_i}\cdot b_{beam_i}=246\ kip$$

tension force below PNA_{fire}

$T_{fr}:=k_{y\_rebar}\cdot F_{yr}\cdot A_{fr}=65\ kip$ — tension force in rebar

$C_c+C_s-T-T_{fr}=0\ kip$ — check equilibrium of partial composite section during fire

Partial composite strength when exposed to fire

Concrete contribution

$$M_{Cc} := C_c \cdot \left(D_c - \frac{a}{2} + d - PNA_{fire}\right) = 20\ \boldsymbol{kip \cdot ft}$$

Steel compressive contribution

$$M_{Cs} := \sum_{i=PNA_{index}}^{\text{rows}\left(z_{cent}\right)-1} k_{y\_beam_i} \cdot F_y \cdot dh_{beam_i} \cdot b_{beam_i} \cdot \left(z_{cent_i} - PNA_{fire}\right) = 6\ \boldsymbol{kip \cdot ft}$$

Steel tension contribution

$$M_T := \sum_{i=0}^{PNA_{index}} k_{y\_beam_i} \cdot F_y \cdot dh_{beam_i} \cdot b_{beam_i} \cdot \left(PNA_{fire} - z_{cent_i}\right) = 56\ \boldsymbol{kip \cdot ft}$$

Rebar contribution

$$M_{Tr} := k_{y\_rebar} \cdot F_{yr} \cdot A_{fr} \cdot \left(PNA_{fire} - z_r\right) = 29\ \boldsymbol{kip \cdot ft}$$

Total partial moment capacity

$$M_{c\_fire} := M_{Cc} + M_{Cs} + M_T + M_{Tr} = 111\ \boldsymbol{kip \cdot ft}$$

$$R = 1\ \boldsymbol{hr}$$

Moment demand

$$w_u := 1.2 \cdot \left(\left(q_D + q_{SDL}\right) \cdot S + w_{beam}\right) + 0.5 \cdot \left(q_L + q_P\right) \cdot S = 2.76\ \frac{\boldsymbol{kip}}{\boldsymbol{ft}}$$

factored distributed load per ASCE 7

$$M_u := \frac{w_u \cdot L^2}{8} = 138\ \boldsymbol{kip \cdot ft}$$

moment demand

$$\frac{M_{c\_fire}}{M_u} = 0.8$$

if <1.0, then the bottom flange needs to be protected to reduce temperature in cross-section

Note, this is an analytical method based on temperature gradients from literature that were developed using finite element models that were validated using experimental results of similar cross-sections. The specific cross-section has not been fire tested.

Alternative Partial Composite Strength - Partial Plastic Distribution

The first alternative method to analyze the partial composite strength utilizes a partial plastic stress distribution. The partial plastic stress distribution assumes that the steel is at yield in both compression and tension. The force that can develop in the concrete is limited by the maximum load that can be transferred from the steel to the concrete. For shallow-depth composite floor systems, this is based on the elastic shear transfer developed through bond shear. This is the same method that is utilized in the AISC Specification for conventional composite floor systems, but has been implemented for shallow-depth composite floor systems.

Max shear force that can be transferred from elastic bond shear

$$\Sigma Q_n := f_{bs} \cdot p_{bs} \cdot \frac{L}{4} = 95.7 \; kip$$

elastic shear transfer strength from bond strength - UDL

$$a := \frac{\Sigma Q_n}{0.85 \cdot f'_c \cdot B_e} = 0.5 \; in$$

height of concrete stress block due to elastic bond transfer at nominal

Determine partial PNA (Y1)

$$Y1 := 2.33 \; in$$

Iterate partial PNA (Y1) until T-C ~ 0. Y1 is referenced from top of the steel beam

Width function for steel beam and plot the beam with partial PNA (green line)

$$b_{so}(y) := \begin{cases} b_{ft} & \text{if } y \le t_{ft} \\ b_{fb} & \text{else if } y \ge d - t_{fb} \\ t_w & \text{else} \end{cases}$$

width function from top of steel - depth of steel only

$$y_h := 0 \; in, 0.01 \; in .. d$$

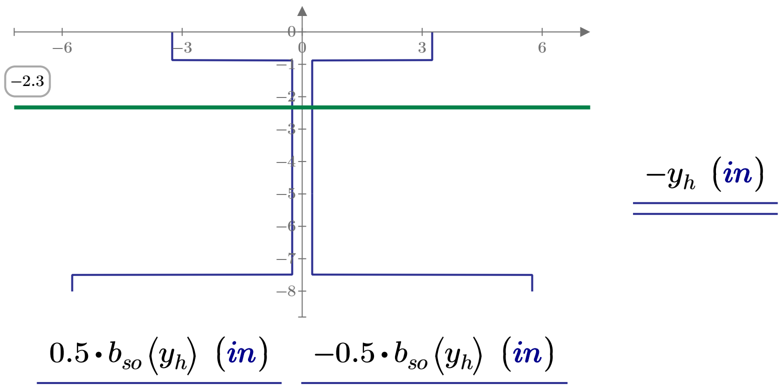

Assumed stress distribution for partial plastic stress distribution

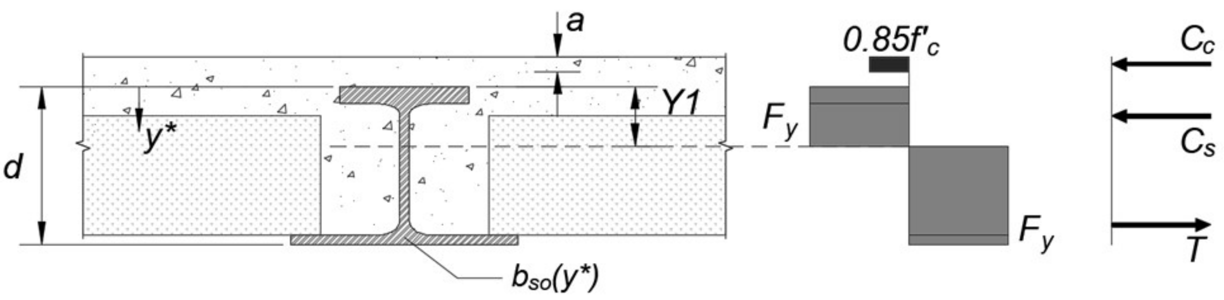

$C_c := \Sigma Q_n = 95.7\ \mathit{kip}$	max concrete force based on bond strength shear transfer
$C_s := \int_0^{Y1} F_y \cdot b_{so}(y)\, \mathrm{d}y = 321\ \mathit{kip}$	steel in compression above Y1 at yield
$C := C_c + C_s = 416\ \mathit{kip}$	total compressive force
$T := A_{tot} \cdot F_y - C_s = 417\ \mathit{kip}$	remainder of steel in tension below Y1 at yield
$T - C = 0.3\ \mathit{kip}$	check equilibrium of partial comp section

Partial comp strength taking moments about partial composite PNA

$$M_{nc\_partial} := C_c \cdot \left(D_c - \frac{a}{2} + Y1\right) + \int_0^{d} F_y \cdot b_{so}(y) \cdot \left|Y1 - y\right| \mathrm{d}y = 238\ \mathit{kip} \cdot \mathit{ft}$$

Partial comp strength with formula in AISC Commentary I3.2a

Note, the same result as above can be obtained using the formula in the AISC commentary (C-I3-10). This method determines the centroids of the compression and tension forces for each component.

$d_1 := D_c - \frac{a}{2} = 1.89\ \mathit{in}$	centroid of concrete force - ref top of steel
$d_2 := \frac{A_t \cdot \left(\frac{t_{ft}}{2}\right) + t_w \cdot \left(Y1 - t_{ft}\right) \cdot \left(\frac{Y1 - t_{ft}}{2} + t_{ft}\right)}{A_t + t_w \cdot \left(Y1 - t_{ft}\right)} = 0.57\ \mathit{in}$	centroid of compression steel - ref top of steel
$d_3 := y_e = 4.13\ \mathit{in}$	centroid of steel section - ref top of steel

$$M_{nc\_partial\_C\_I3\_10} := C_c \cdot \left(d_1 + d_2\right) + A_{tot} \cdot F_y \cdot \left(d_3 - d_2\right) = 238\ \mathit{kip} \cdot \mathit{ft}$$

Alternative Partial Composite Strength - Strain Compatibility

The second alternative method utilizes strain compatibility. Strain compatibility assumes a linear strain profile over the depth of the composite section. As a result, constitutive models must be utilized for steel and concrete. An elastic perfectly plastic model was used for steel and the Hognestad model was implemented for concrete. Observed in experimental testing of these composite sections, the strain profile is linear throughout the test before yielding occurs in the bottom flange. Therefore, the bottom flange strain was set to yield and the concrete strain was iterated until equilibrium was established, assuming the linear strain profile.

Steel constitutive model - Elastic Perfectly Plastic

$F_y = 50\ ksi$ yield stress

$\varepsilon_y := \frac{F_y}{E} = 0.0017$ yield strain

$$f_s(\varepsilon) := \begin{array}{l} \text{if } \varepsilon < 0 \\ \quad \max(\varepsilon \cdot E, -F_y) \\ \text{else if } \varepsilon \geq 0 \\ \quad min(\varepsilon \cdot E, F_y) \end{array}$$

steel constitutive model

$\varepsilon_x := -0.005, -0.0049 .. 0.005$ evaluate constitutive model at given strains

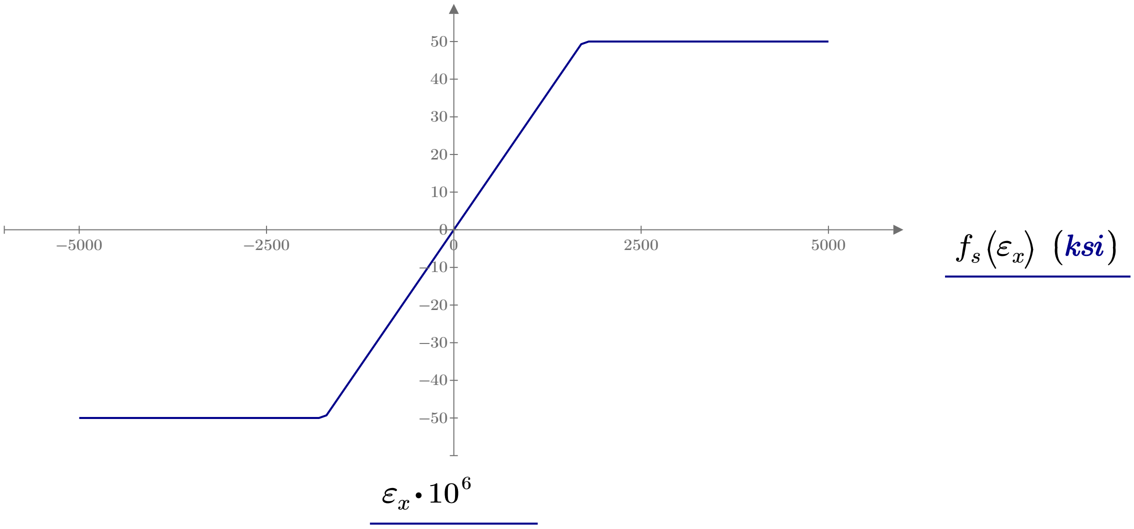

Concrete constitutive model - Hognestad

$$f'_c = 4\ ksi$$

$$\varepsilon_0 := \frac{2 \cdot 0.85 \cdot f'_c}{E_c} = 0.0019$$

$$\varepsilon_{cu} := 0.004$$

$$f_c(\varepsilon) := \begin{Vmatrix} \text{if } \varepsilon \le \varepsilon_0 \\ \quad \left\Vert f'_c \cdot \left(2 \cdot \frac{\varepsilon}{\varepsilon_0} - \left(\frac{\varepsilon}{\varepsilon_0}\right)^2\right) \right. \\ \text{else if } \varepsilon_0 \le \varepsilon \le \varepsilon_{cu} \\ \quad \left\Vert f'_c \cdot \left(1 - \frac{\varepsilon - \varepsilon_0}{\varepsilon_{cu} - \varepsilon_0} \cdot 0.15\right) \right. \end{Vmatrix}$$

tensile strength in concrete is ignored

$$\varepsilon_x := 0, 0.0001 .. 0.005$$

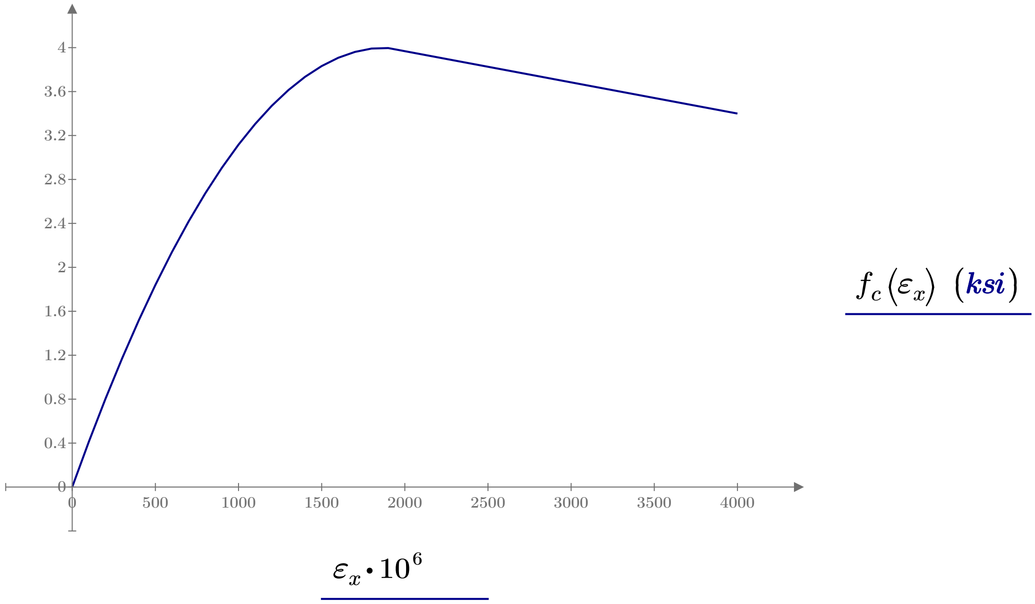

Linear strain profile in concrete and steel per AISC I1.2b

$\varepsilon_{max\_conc} := 0.00087$	concrete strain - iterate this value till equilibrium
$\varepsilon_{max\_bf} := -\varepsilon_y = -0.0017$	steel bottom flange strain
$c_{NA} := \left(\frac{\varepsilon_{max\_conc}}{\varepsilon_{max\_conc} - \varepsilon_{max\_bf}}\right) \cdot D_{tot} = 3.4\ in$	depth of NA, ref from top of slab
$\phi := \frac{\varepsilon_{max\_conc}}{c_{NA}} = \left(2.56 \cdot 10^{-4}\right) \frac{1}{in}$	curvature
$\varepsilon(y) := \varepsilon_{max\_conc} - \phi \cdot y$	strain profile as a function of depth (comp is + due to constitutive model function)
$y_h := 0\ in, 0.01\ in .. D_{tot}$	$D_{tot} = 10.13\ in$

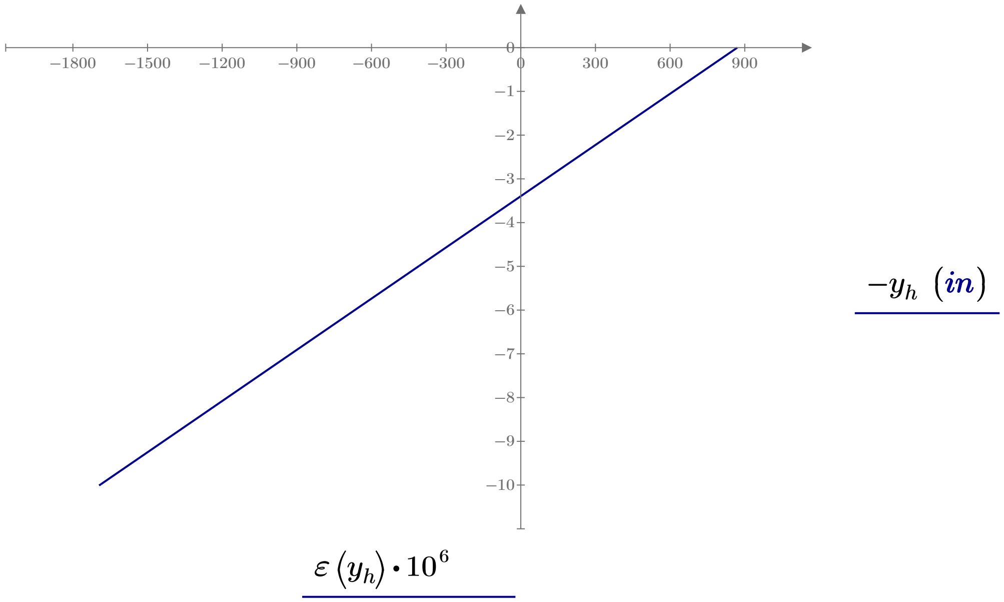

Strain check:

$\varepsilon(0\ in) = 0.0009$	concrete
$\varepsilon(D_c) = 0.0003$	top flange
$\varepsilon(D_{tot}) = -0.0017$	bottom flange

Width functions for concrete and steel

$$b_c(y) := \left\| \begin{array}{l} \text{if } y \le D_c \\ \quad \| B_e \\ \text{else if } D_c < y \le min\left(c_{NA}, D_c + t_{ft}\right) \\ \quad \| B_e - b_{ft} \\ \text{else if } y \le min\left(c_{NA}, D_s\right) \\ \quad \| B_e - t_w \\ \text{else if } D_s < y \le c_{NA} \\ \quad \| b_{fb} - 2 \cdot b_{bearing} - t_w \end{array} \right.$$

$$b_s(y) := \left\| \begin{array}{l} \text{if } y \le D_c \\ \quad \| 0\ in \\ \text{else if } D_c < y \le D_c + t_{ft} \\ \quad \| b_{ft} \\ \text{else if } y \ge D_{tot} - t_{fb} \\ \quad \| b_{fb} \\ \text{else} \\ \quad \| t_w \end{array} \right.$$

width of concrete as a function of depth from the top of slab

width of steel as a function of depth referenced from the top of slab

Plot of steel (blue) and concrete (black) width, and the NA (red)

$$y_h := 0\ in, 0.01\ in .. D_{tot}$$

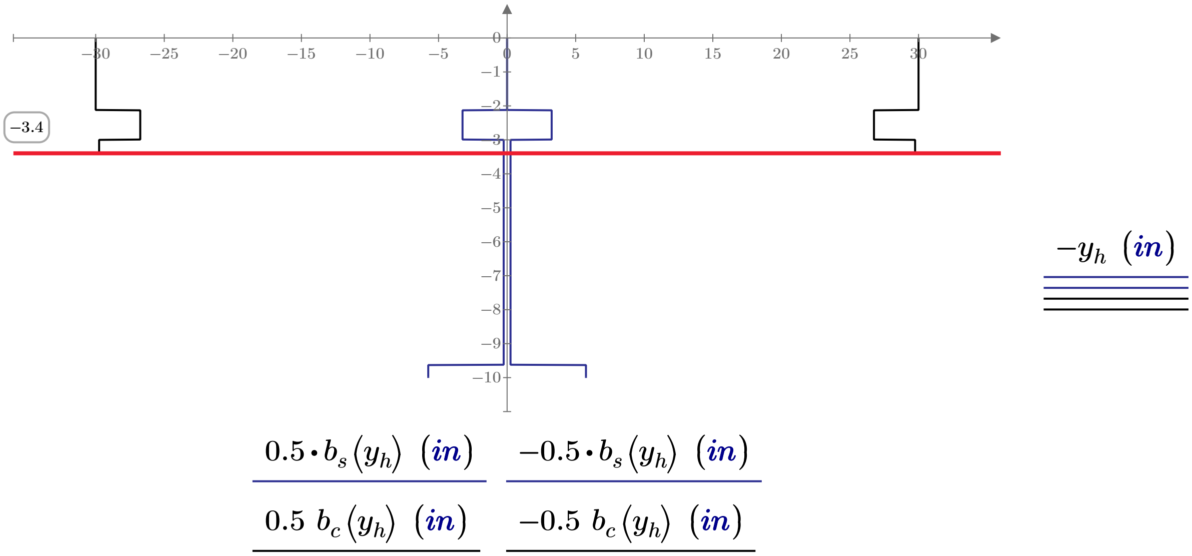

Assumed stress distribution for strain compatibility

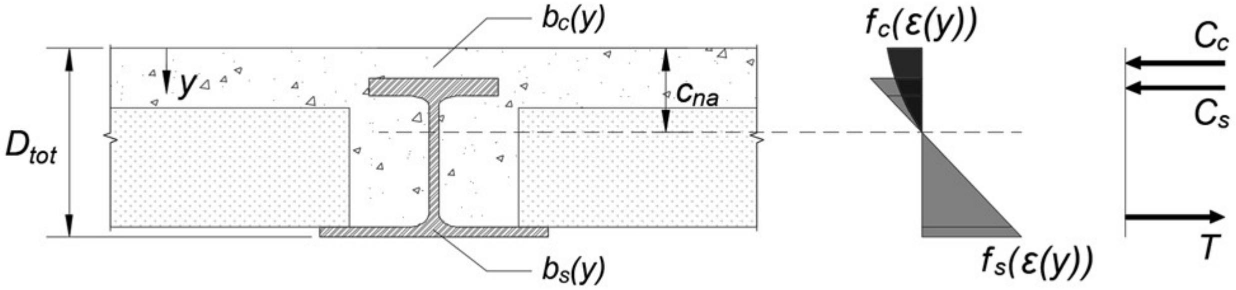

Sum of forces in concrete and steel

$$C_c := \int_0^{c_{NA}} f_c(\varepsilon(y)) \cdot b_c(y)\, \mathrm{d}y = 313\ \mathbf{kip}$$

sum of concrete forces (however, it is greater than F_{bs})

$$C_s := \int_{D_c}^{c_{NA}} f_s(\varepsilon(y)) \cdot b_s(y)\, \mathrm{d}y = 35\ \mathbf{kip}$$

sum of steel compression forces

$$C := C_c + C_s = 349\ \mathbf{kip}$$

total compression force

$$T := \int_{c_{NA}}^{D_{tot}} f_s(\varepsilon(y)) \cdot b_s(y)\, \mathrm{d}y = -349\ \mathbf{kip}$$

sum of steel tension forces

$$T + C = -0.19\ \mathbf{kip}$$

check equilibrium - good when ~ 0

Resultant moment about the NA

$$M_{nc\_strain} := \int_0^{c_{NA}} f_c(\varepsilon(y)) \cdot b_c(y) \cdot (c_{NA} - y)\, \mathrm{d}y \ \hookleftarrow = 235\ \mathbf{kip} \cdot \mathbf{ft}$$
$$+ \int_{D_c}^{D_{tot}} f_s(\varepsilon(y)) \cdot b_s(y) \cdot (c_{NA} - y)\, \mathrm{d}y$$

Comparison of Composite Moment Capacity

Full Composite Strength

$M_{ncp} = 288\ kip \cdot ft$

Partial Composite Strength - Linear Interpolation

$M_{nc\_linear} = 214\ kip \cdot ft$

Partial Composite Strength - Partial Plastic Stress Distribution

$M_{nc\_partial} = 238\ kip \cdot ft$

Partial Composite Strength - Strain Compatibility

$M_{nc\_strain} = 235\ kip \cdot ft$

Note, the recommended method for analyzing the composite strength for shallow-depth floor systems using A-shapes is the *linear interpolation method* . The reason for this is it provides the most conservative estimate for the composite strength since composite action is developed through bond interaction between the steel and concrete.

BACK MATTER

References

AISC. 2022. *Specification for Structural Steel Buildings. ANSI/AISC 360-22*. Chicago, IL: AISC.

AISC. 2023. *Steel Construction Manual*. 16th ed. Chicago, IL: AISC.

ASCE. 2022. *Minimum Design Loads and Associated Criteria for Buildings and Other Structures*. ASCE/SEI 7-22. Reston, VA: ASCE.

Chen, W. F., and E. M. Lui. 1987. *Structural Stability - Theory and Implementation*. New York, NY: Elsevier Science Publishing Co., Inc.

Hanus, F., D. Zaganelli, L.-G. Cajot, and M. Braun. 2017. "Analytical Methods for the Prediction of Fire Resistance of "Reinforced" Slim Floor Beams." *ce/papers*, 1(2).

Heins, C. P. (1975). Bending and Torsional Design in Structural Members. Lexington Books.

Helwig, T. A., K. H. Frank, and J. A. Yura. 1997. "Lateral-Torsional Buckling of Singly Symmetric I-beams." *Journal of Structural Engineering*, 123(9).

IBC. 2018. *International Building Code*. Country Club Hills, IL: International Code Council.

Murray, T. M., D. E. Allen, E. E. Ungar, and D. B. Davis. 2016. *Steel Design Guide 11: Vibrations of Steel-Framed Structural Systems due to Human Activity. Steel Design Guide Series*. Chicago, IL: AISC.

New Millennium. 2021. *Design Guide Deep-Dek Composite*.

Ottmers, C., R. W. Alemayehu, and M. Yarnold. 2025a. "Evaluating the Composite Behavior developed through Bond in the Steel-Concrete Interface for Future Hot-Rolled Asymmetric Steel I-beams." *Engineering Structures*, 322.

Ottmers, C., E. Stoddard, and M. Yarnold. 2025b. "Establishment of Future A-Shape Geometry for Residential Construction." *Journal of Structural Engineering*.

Ottmers, C., R. W. Alemayehu, and M. Yarnold. 2025c. "Full-Scale System Testing for Asymmetric Steel I-beams in Shallow-Depth Composite Floor Systems." *Under Review*.

Romero, M. L., V. Albero, A. Espinos, and A. Hospitaler. 2019. "Fire Design of Slim-Floor Beams." *Stahlbau*, 88(7).

Seaburg, P. A., and C. J. Carter. 2003. *Steel Design Guide 9: Torsional Analysis of Structural Steel Members*. *Steel Design Guide Series*. Chicago, IL: AISC.

Yarnold, M., C. Ottmers, R. Alemayehu, E. Stoddard, and S. Davis. 2024. *Behavior of Hot-Rolled Asymmetric Steel I-beams. AISC Milek Fellowship Final Report.* Chicago, IL: AISC.

Zaharia, R., and J. M. Franssen. 2012. "Simple Equations for the Calculation of the Temperature within the Cross-Section of Slim Floor Beams under ISO Fire." *Steel and Composite Structures*, 13(2).

Zanon, R., S. Yildiz, R. Obiala, and M. Braun. 2021. "Shallow Composite Floor Beams - Proposal of a Simplified Analytical Method for Standard Fire Rating." *ce/papers*, 4.

Appendix J – Design Tables

Appendix J provides design guidance (Phase 6) on A-shapes within shallow-depth floor systems. Guidance is provided with design tables that were developed through the knowledge gained in the previous research phases. The design tables include non-composite flexural strength and maximum torsional load applied to an A-shape to assist with the design for limit states during construction. Composite strength is quantified for each of the established A-shapes to assist with in-service analysis. The final design table consists of minimum capacity-to-demand ratios for an array of beam length and spacing combinations for assumed loading. The capacity-to-demand ratio table has several assumptions embedded but will give a sense of what shape to use for a given load scenario and building grid layout.

Table 3-X. Flexural Strength – A-Shapes

The available major axis flexural strength, ϕM_n, of A-shapes is tabulated as a function of the unbraced length, L_b, with $F_y = 50$ ksi (ASTM 2022). The flexural strength is quantified utilizing AISC Specification Section F4 (AISC 2022). Two tables are shown with C_b (lateral-torsional buckling modification factor) taken as unity, and the second table implements a load height effect, C_b^*. Flexural strengths were determined with load and resistance factor design (LRFD) only.

The main application of A-shapes is within shallow-depth floor systems where the bottom flange supports precast concrete panels or steel deep decking. As a result, the load will be transferred to the A-shape through the bottom flange. Structural stability books have shown that applying load to the bottom flange increases the critical uniformly distributed load (UDL) to cause lateral-torsional buckling (Chen and Lui 1987; Ziemian 2010). This can be visually observed by analyzing the direction of a moment that is generated when the beam starts to twist. An additive moment is generated with load applied to the top flange; however, a restoring moment is produced when load is applied to the bottom flange (Figure J-1). The load height effect can be applied by modifying the C_b factor, and the equation depends on the warping stiffness of the cross-section (W) and the load distribution along the beam length. The load distribution effect is quantified with the parameter (B) and the equation shown is for a UDL. The load height effect modification, C_b^*, is determined in Equations (J-1) through (J-3) per Helwig et al. (1997). The C_b factor in Equation (J-3) can be taken as 1.14 for a UDL.

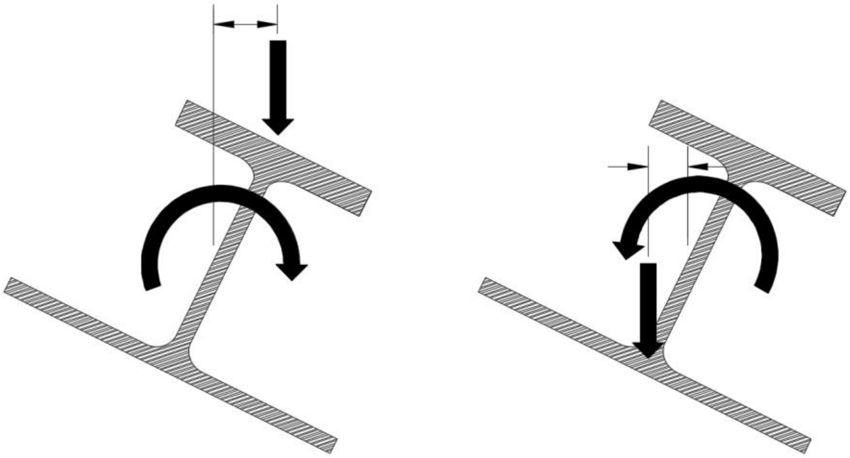

Figure J-1: Load Height Effect for Loading Applied to the Top Flange and Bottom Flange

$$W = \frac{\pi}{L_b}\sqrt{\frac{E_s I_y h_o^2}{4GJ}} \tag{J-1}$$

$$B = 1 - 0.154W^2 + 0.535W \tag{J-2}$$

$$C_b^* = BC_b \tag{J-3}$$

The available shear strength, $\phi_v V_n$, of A-shapes are given at the bottom of the table per AISC Specification Section G2 (AISC 2022) with $F_y = 50$ ksi (ASTM 2022) using LRFD.

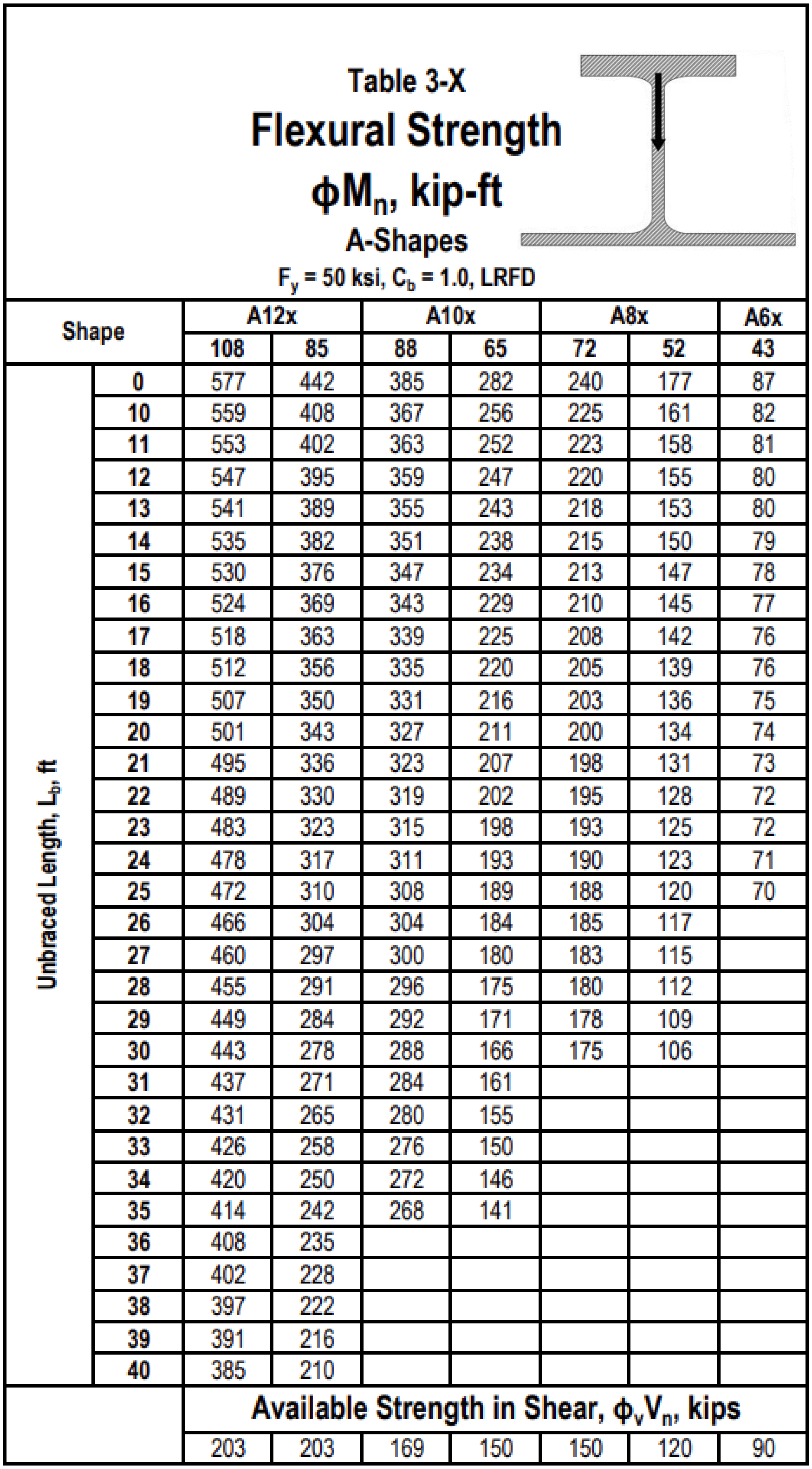

Table 3-X

Flexural Strength

ϕM_n, kip-ft

A-Shapes

$F_y = 50$ ksi, $C_b = 1.0$, LRFD

Shape		A12x		A10x		A8x		A6x
		108	85	88	65	72	52	43
Unbraced Length, L_b, ft	0	577	442	385	282	240	177	87
	10	559	408	367	256	225	161	82
	11	553	402	363	252	223	158	81
	12	547	395	359	247	220	155	80
	13	541	389	355	243	218	153	80
	14	535	382	351	238	215	150	79
	15	530	376	347	234	213	147	78
	16	524	369	343	229	210	145	77
	17	518	363	339	225	208	142	76
	18	512	356	335	220	205	139	76
	19	507	350	331	216	203	136	75
	20	501	343	327	211	200	134	74
	21	495	336	323	207	198	131	73
	22	489	330	319	202	195	128	72
	23	483	323	315	198	193	125	72
	24	478	317	311	193	190	123	71
	25	472	310	308	189	188	120	70
	26	466	304	304	184	185	117	
	27	460	297	300	180	183	115	
	28	455	291	296	175	180	112	
	29	449	284	292	171	178	109	
	30	443	278	288	166	175	106	
	31	437	271	284	161			
	32	431	265	280	155			
	33	426	258	276	150			
	34	420	250	272	146			
	35	414	242	268	141			
	36	408	235					
	37	402	228					
	38	397	222					
	39	391	216					
	40	385	210					
		Available Strength in Shear, $\phi_v V_n$, kips						
		203	203	169	150	150	120	90

Table 3-X

Flexural Strength

ϕM_n, kip-ft

A-Shapes

F_y = 50 ksi, $C_b = C_b^*$, LRFD

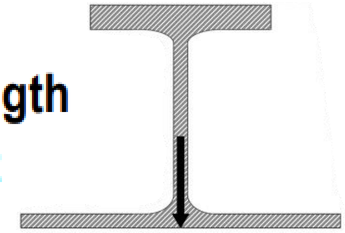

Shape		A12x		A10x		A8x		A6x
		108	**85**	**88**	**65**	**72**	**52**	**43**
Unbraced Length, L_b, ft	**0**	577	442	385	282	240	177	87
	10	577	442	385	282	240	177	87
	11	577	442	385	282	240	177	87
	12	577	442	385	282	240	177	87
	13	577	442	385	282	240	177	87
	14	577	442	385	282	240	177	87
	15	577	442	385	282	240	177	87
	16	577	442	385	282	240	177	87
	17	577	442	385	282	240	177	87
	18	577	442	385	282	240	177	87
	19	577	442	385	282	240	177	87
	20	577	442	385	282	240	177	87
	21	577	442	385	282	240	177	87
	22	577	442	385	280	240	174	87
	23	577	442	385	272	240	169	87
	24	577	442	385	265	240	165	87
	25	577	431	385	257	240	160	87
	26	577	420	385	249	235	156	
	27	577	409	385	242	231	151	
	28	577	398	385	235	228	147	
	29	577	387	385	228	224	143	
	30	577	376	383	221	220	139	
	31	577	366	376	213			
	32	577	355	370	205			
	33	577	344	363	198			
	34	575	332	356	191			
	35	565	321	350	185			
	36	555	311					
	37	545	301					
	38	535	292					
	39	525	283					
	40	516	275					
		Available Strength in Shear, $\phi_v V_n$, kips						
		203	203	169	150	150	120	90

Table 3-X. Max Torsional Load – A-Shapes

The maximum LRFD uniformly distributed torsional load applied to an A-shape is tabulated as a function of the beam span length, L, per AISC Design Guide 9 (Seaburg and Carter 2003). The steel properties of the A-shapes are assumed to be $F_y = 50$ ksi (ASTM 2022), $E = 29{,}000$ ksi, and $G = 11{,}200$ ksi. The bottom flange supports stay-in-place formwork, either precast concrete panels or steel deep decking that has a bearing width of 2 in. on the bottom flange. Therefore, the uniformly distributed load (w_u) is assumed to be applied eccentrically to the beam at the center of the bearing width, i.e., 1.0 in. away from the edge of the bottom flange (Figure J-2).

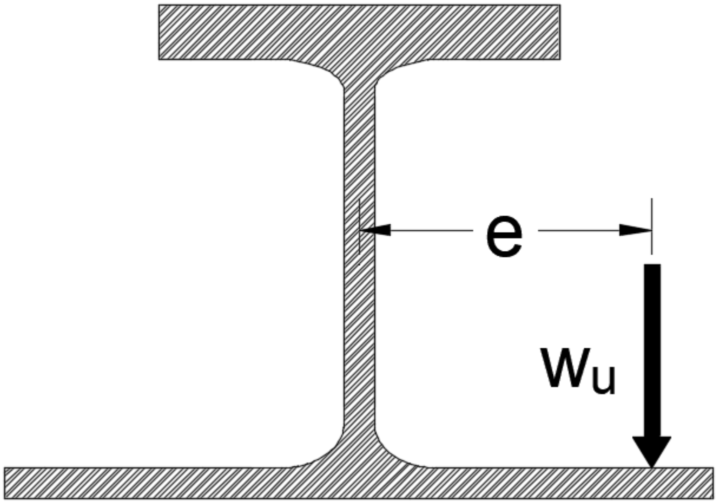

Figure J-2: Torsional Load Applied to A-shape

The maximum distributed load is quantified by evaluating torsional limit states of yielding under normal and shear stresses, and buckling per AISC Design Guide 9 (Seaburg and Carter 2003). In addition, a construction twist limit of 5° is implemented to ensure the constructability of shallow-depth floor systems (Figure J-3). The beam is assumed to be pinned – pinned supported for flexure and torsion.

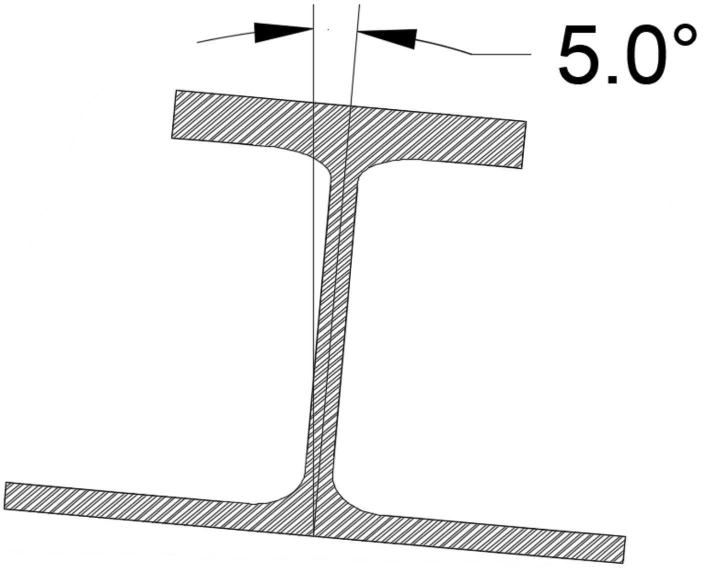

Figure J-3: Twist Limit for Constructability

The values in the table are quantified assuming that the distributed load is applied to one side of the beam, as shown in Figure J-2. This scenario would be the case if precast concrete panels are placed all on one side of the beam during construction. Precast panels utilize unshored construction, meaning that the A-shapes must support half of the beam spacing, S, for the tributary width. Deep decking panels are significantly lighter than precast panels; therefore, analyzing torsion due to deck placement is not a major concern. The more torsional demanding load case for deep decking is during the concrete pour; however, the deep decking is usually shored at midspan with larger beam spacings. If the decking is shored, the torsional demand on the A-shape has a tributary width of $S/4$. The torsional load case during the slab pour is shown for precast panels and deep decking in Figure J-4. As mentioned, the analysis performed in the tables assumes that load is applied only on one side of the beam.

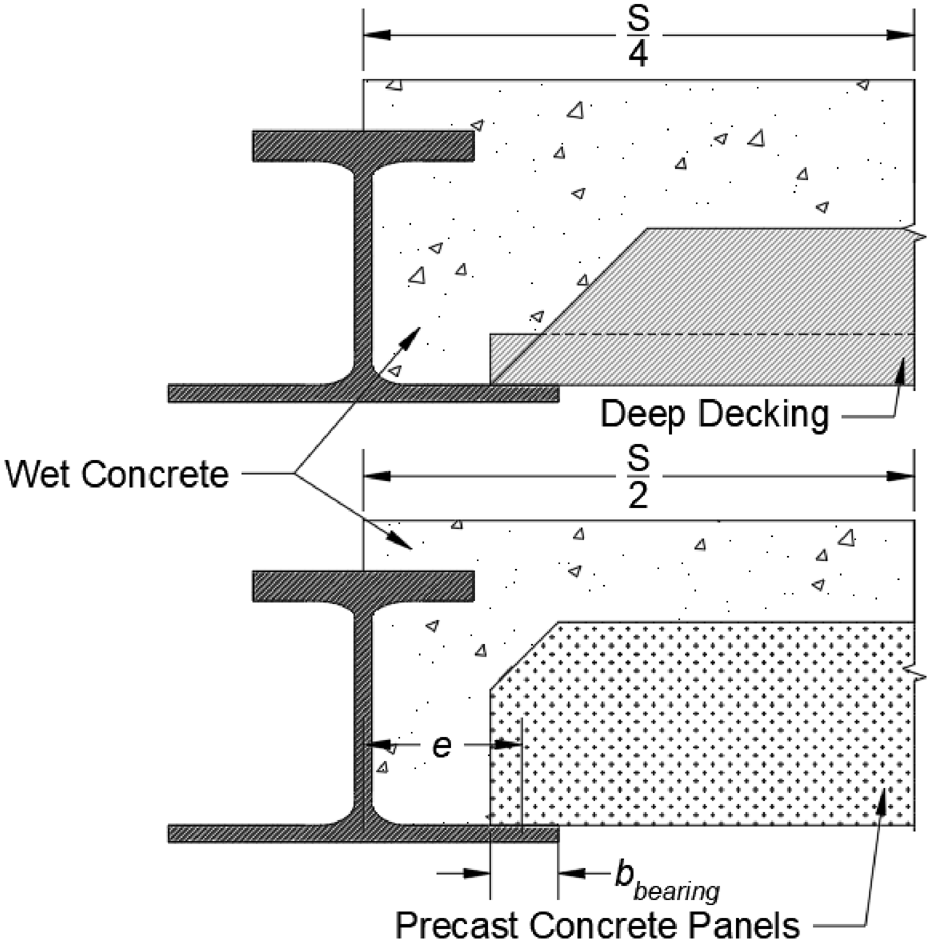

Figure J-4: Torsional Load Case during Slab Pour

Note, precast concrete panels will likely be installed on both sides of the beam during the concrete pour. In doing so, the torsional demand is only from the topping slab, and the precast panels induce in-plane bending only. Torsional analysis for shallow-depth floor systems will need to consider plausible construction scenarios resulting in torsional demand.

Table 3-X

Max Torsional Load

w_u, kip/ft

A-Shapes

F_y = 50 ksi, e = $0.5b_{fb}$ - 1 in., LRFD

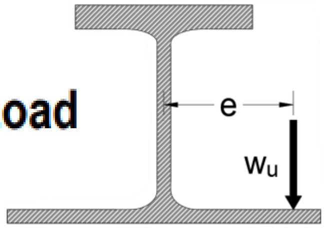

Shape		A12x		A10x		A8x		A6x
		108	85	88	65	72	52	43
Beam Span Length, L, ft	10						4.60	3.20
	11						4.10	2.30
	12						3.65	1.70
	13						3.05	1.30
	14						2.50	1.00
	15				3.60	4.55	2.15	0.75
	16				3.05	4.20	1.80	0.60
	17				2.65	3.90	1.55	0.50
	18				2.30	3.65	1.35	0.40
	19				2.00	3.25	1.20	0.30
	20		2.95	2.85	1.80	2.90	1.05	0.25
	21		2.60	2.50	1.60	2.60	0.95	
	22		2.35	2.25	1.40	2.35	0.85	
	23		2.10	2.00	1.30	2.15	0.80	
	24		1.90	1.85	1.15	1.95	0.70	
	25	2.10	1.75	1.65	1.05	1.80	0.65	
	26	1.90	1.60	1.50	0.95	1.65	0.60	
	27	1.75	1.45	1.40	0.90	1.55	0.55	
	28	1.60	1.35	1.30	0.80	1.40	0.50	
	29	1.45	1.20	1.20	0.75	1.30	0.45	
	30	1.35	1.15	1.10	0.70	1.25	0.45	
	31	1.25	1.05	1.00				
	32	1.15	1.00	0.95				
	33	1.05	0.90	0.90				
	34	1.00	0.85	0.85				
	35	0.95	0.80	0.80				
	36	0.85						
	37	0.80						
	38	0.75						
	39	0.75						
	40	0.70						

Table 3-X. Composite Strength – Shallow-Depth Floor System with A-Shapes

The composite flexural strength of a shallow-depth composite floor system with A-shapes is tabulated as a function of the beam span length, L. Composite action is gained in shallow-depth composite floor systems through bond shear forming between the unpainted steel and concrete. The effective width, B_e, for the concrete slab is $L/4$ per AISC Specification Section I3 (AISC 2022) for a standard interior beam with large beam spacings, S. The material strengths for steel and concrete are $F_y = 50$ ksi (ASTM 2022) and $f'_c = 4$ ksi, respectively. The concrete depth above the top of the steel section is assumed to be 1.5 in. However, the composite strength does not vary significantly (only a few kip-ft) for different concrete topping thicknesses, 1.5 – 2.5 in., and concrete strengths of 4 – 5 ksi. A generalized composite section is shown in Figure J-5.

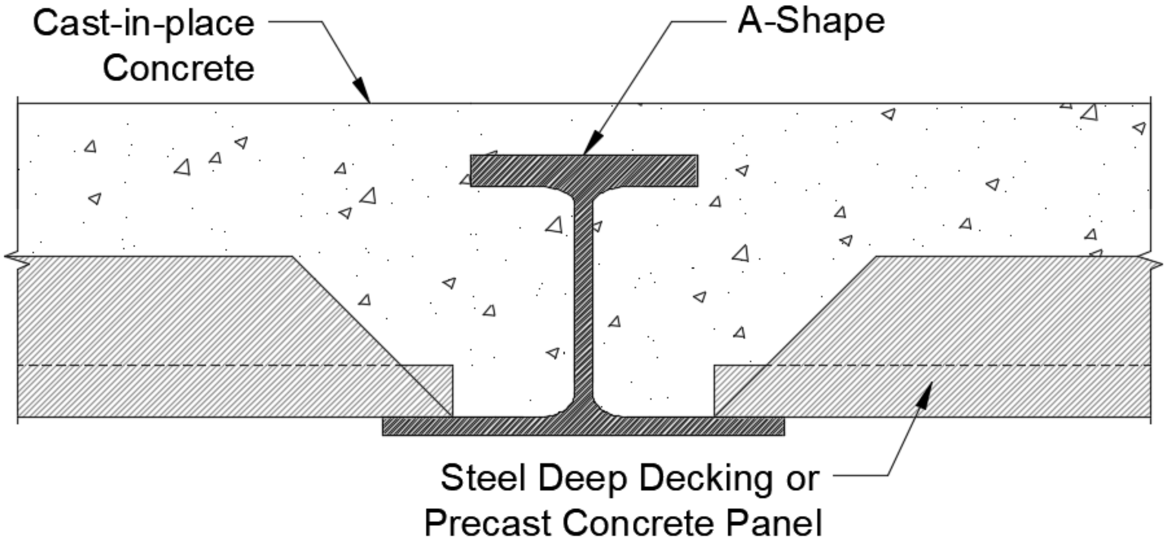

Figure J-5: Shallow-Depth Composite Floor System

Due to the fact that no mechanical connectors are utilized to transfer load between the steel and concrete, full composite action might not be achieved. Therefore, the partial composite strength, M_{nc}, is quantified with linear interpolation between the fully braced ($L_b = 0$ ft) steel moment capacity, M_{sy}, and the full composite capacity, M_{ncp}, utilizing a plastic analysis. The degree of partial composite strength is quantified by the ratio of the elastic shear transfer developed through bond stress between the unpainted steel and concrete, F_{bs}, and the concrete force developed in the full composite section, C_c. The partial composite strength is quantified in Equation (J-4) and Figure J-6. The strength reduction factor, ϕ, is assumed to be 0.9 for the composite section. Through experimental testing (Ottmers et al. 2025a; Ottmers et al. 2025c), the shallow-depth floor system had great ductility with composite action gained through bond shear.

$$M_{nc} = M_{sy} + \frac{F_{bs}}{C_c}\left(M_{ncp} - M_{sy}\right) \tag{J-4}$$

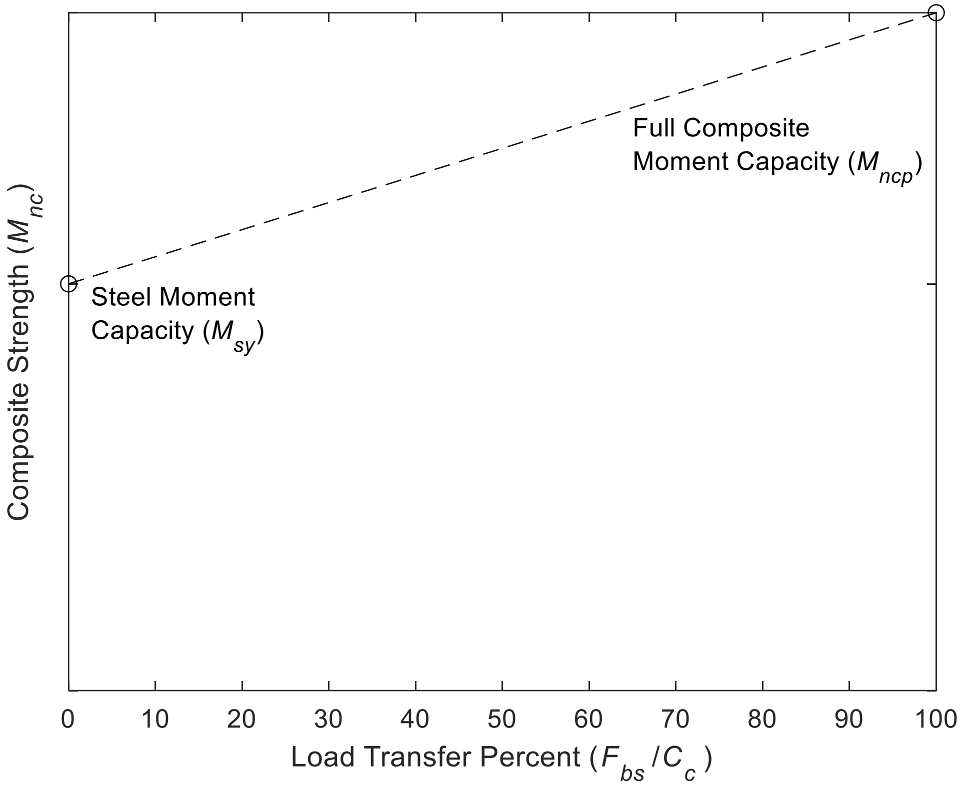

Figure J-6: Linear Interpolation for Partial Composite Strength

Elastic shear transfer is quantified using a constant bond stress, f_{bs}, of 100 psi, which acts around a bond perimeter, p_{bs}, that is assumed to act above the elastic neutral axis (ENA) of the composite section. The bond stress was determined through experimental testing of eight unpainted component-level beam tests (Ottmers et al. 2025a). The unit bond shear, $p_{bs}f_{bs}$, acts over an effective length, which depends on the load. For uniformly distributed loads, the effective length is $L/4$ due to the area under the shear diagram being triangular. See Equations (J-5) and (J-6) and Figure J-7 for quantifying and an illustration of the elastic shear transfer.

$$p_{bs} = 2\left(b_{ft} + y_{ec}\right) - t_w \tag{J-5}$$

$$F_{bs} = p_{bs}f_{bs}\frac{L}{4} \tag{J-6}$$

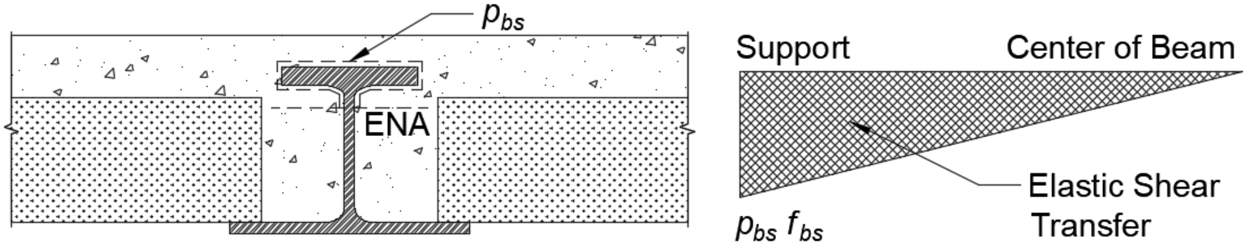

Figure J-7: Bond Shear Action in Shallow-Depth Composite Floor Systems

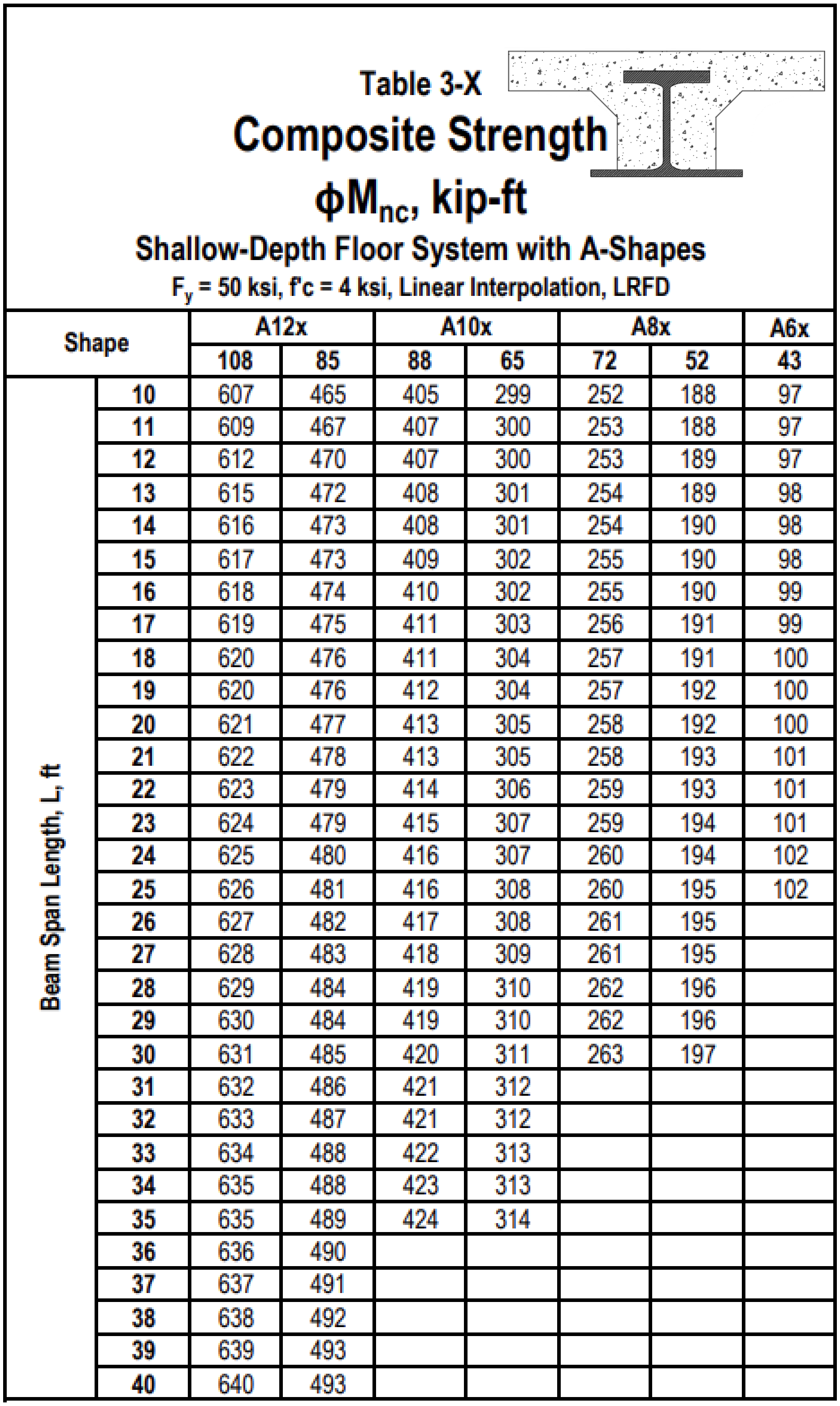

Table 3-X

Composite Strength

ϕM_{nc}, kip-ft

Shallow-Depth Floor System with A-Shapes

F_y = 50 ksi, f'c = 4 ksi, Linear Interpolation, LRFD

Shape		A12x		A10x		A8x		A6x
		108	**85**	**88**	**65**	**72**	**52**	**43**
Beam Span Length, L, ft	**10**	607	465	405	299	252	188	97
	11	609	467	407	300	253	188	97
	12	612	470	407	300	253	189	97
	13	615	472	408	301	254	189	98
	14	616	473	408	301	254	190	98
	15	617	473	409	302	255	190	98
	16	618	474	410	302	255	190	99
	17	619	475	411	303	256	191	99
	18	620	476	411	304	257	191	100
	19	620	476	412	304	257	192	100
	20	621	477	413	305	258	192	100
	21	622	478	413	305	258	193	101
	22	623	479	414	306	259	193	101
	23	624	479	415	307	259	194	101
	24	625	480	416	307	260	194	102
	25	626	481	416	308	260	195	102
	26	627	482	417	308	261	195	
	27	628	483	418	309	261	195	
	28	629	484	419	310	262	196	
	29	630	484	419	310	262	196	
	30	631	485	420	311	263	197	
	31	632	486	421	312			
	32	633	487	421	312			
	33	634	488	422	313			
	34	635	488	423	313			
	35	635	489	424	314			
	36	636	490					
	37	637	491					
	38	638	492					
	39	639	493					
	40	640	493					

Table X-X. Minimum Capacity-to-Demand Ratio – Shallow-Depth Floor System with A-Shapes

The minimum capacity-to-demand (C/D) ratio for varying beam length, L, and beam spacing, S, combinations are shown in Table X-X. There are multiple tables with different A-shape cross-sections and varying live and dead loads. These tables should be utilized to initially select an A-shape for a building grid layout or vice versa. The C/D tables utilize the prior design aids (and assumptions explained for each design table) to evaluate a cross-section for several beam length and spacing combinations. The tables are generalized and include the minimum C/D ratio for both types of construction, deep decking and precast concrete panels. The one exception is the A6 table assumes deep decking (shored) construction only.

Several load cases are analyzed to develop this table. The load cases include (1) precast panel placement on one side of the beam, (2a) full slab pour, (2b) slab pour on one side of the beam and panels on both sides, and (3) in-service analysis (see Figure J-8). Precast panel construction is an unshored system. The same load cases are assumed for deep decking construction; however, the deck panels are significantly lighter. Therefore, deck placement on one side of the beam (case 1) wouldn't be a controlling limit state. Furthermore, the decking is likely shored at midspan during construction. Therefore, the analysis conducted for these tables assumes that the tributary width is half of the beam spacing for deep decking. If shoring is not utilized and large construction loads are present, torsional analysis must be analyzed as it could control during construction.

A large portion of the C/D ratios are equal for both deep decking and precast panels due to the controlling limit state being composite flexure. Composite flexure is analyzed using linear interpolation between the steel and full composite moment capacity (see discussion for Table 3-X. Composite Strength). Some of the building grid layouts are controlled by dead plus live load deflection. The deflection check assumes the beam is cambered to help satisfy the deflection limit state. Limit states that are not included are vibration and fire resistance. Analysis for these limit states should be completed separately. Furthermore, analysis of the deep decking or precast concrete panels is not conducted in these tables.

The limit states that are analyzed for the A-shape minimum C/D ratio tables are below. Limit states that need to be checked but that are not included in the analysis are italicized in the following list.

- Load Case 1 and 2b:
    - Torsion – Stress and Twist
    - Non-composite Flexure
    - Shear
- Load Case 2a:
    - Non-composite Flexure
    - Shear
- Load Case 3:
    - Composite Flexure and Longitudinal Shear
    - Deflection (Live Load only and Dead plus Live Load)
    - Shear
    - *Vibration*
    - *Fire Resistance*

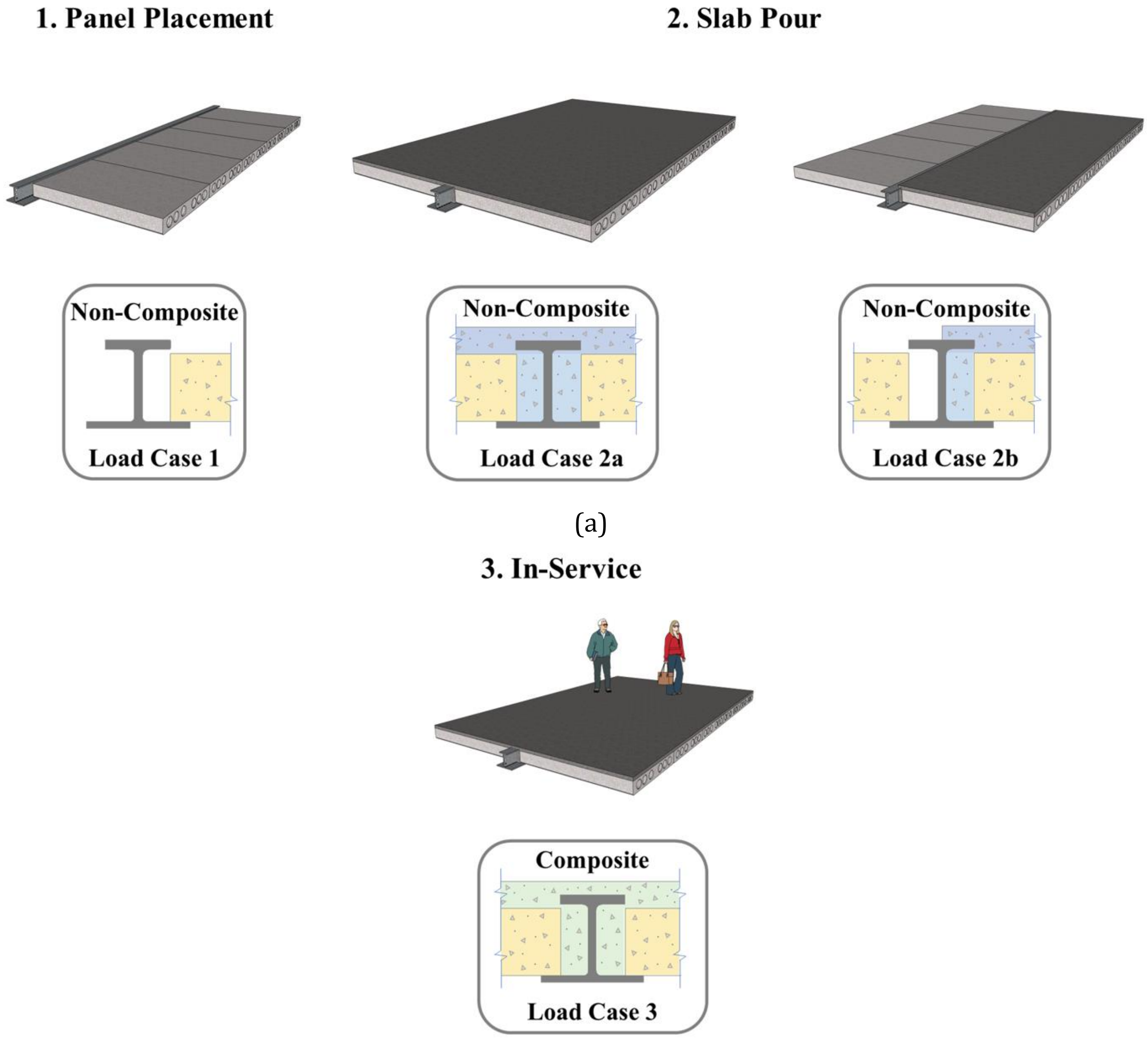

(a)

(b)

Figure J-8: Structural Load Cases (a) Construction and (b) In-Service

Note that these tables are for initial design consideration only when selecting a beam size for a given building grid layout. Analysis should be conducted for limit states during construction (flexure, shear, torsion, connection design, etc.) and in-service (flexure, deflection, vibration, fire, etc.). Plausible load scenarios during construction and in-service need to be considered by the designer. The C/D ratio can change due to different loading assumptions. Therefore, an analysis must be completed by the engineer on record to ensure that the designed floor system is adequate for the specific scenario.

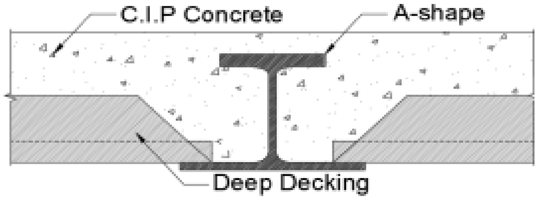

Table X-X

Minimum Capacity-to-Demand Ratio

Shallow-Depth Floor System with A-Shapes - A6x43

F_y = 50 ksi, f'c = 4 ksi, 40 psf Live, 15 psf Partition, 65 psf Dead, 10 psf SDL

		Beam Length (ft)										
		10	**11**	**12**	**13**	**14**	**15**	**16**	**17**	**18**	**19**	**20**
Beam Spacing (ft)	**10**	4.21	3.48	2.70	2.13	1.72	1.40	1.46	1.16	0.93	0.76	0.63
	11	3.83	3.18	2.46	1.95	1.57	1.28	1.34	1.06	0.86	0.70	0.57
	12	3.52	2.92	2.27	1.79	1.44	1.57	1.24	0.98	0.79	0.65	0.53
	13	3.26	2.70	2.10	1.66	1.33	1.46	1.15	0.92	0.74	0.60	0.49
	14	3.03	2.51	1.95	1.54	1.24	1.37	1.07	0.86	0.69	0.56	0.46
	15	2.83	2.35	1.83	1.44	1.17	1.28	1.01	0.80	0.65	0.53	0.43
	16	2.66	2.20	1.71	1.36	1.40	1.21	0.95	0.76	0.61	0.50	0.41
	17	2.50	2.08	1.62	1.29	1.33	1.14	0.90	0.72	0.58	0.47	0.39
	18	2.37	1.96	1.54	1.22	1.26	1.08	0.85	0.68	0.55	0.45	0.37
	19	2.24	1.87	1.46	1.16	1.21	1.03	0.81	0.65	0.52	0.42	0.35
	20	2.13	1.79	1.39	1.11	1.15	1.00	0.77	0.61	0.50	0.40	0.33
	21	2.05	1.71	1.33	1.06	1.11	0.94	0.74	0.59	0.47	0.39	0.32
	22	1.97	1.64	1.28	1.22	1.06	0.90	0.71	0.56	0.45	0.37	0.30
	23	1.89	1.57	1.22	1.17	1.02	0.86	0.68	0.54	0.43	0.35	0.29
	24	1.82	1.51	1.18	1.13	0.98	0.83	0.65	0.52	0.42	0.34	0.28
	25	1.76	1.46	1.13	1.09	0.95	0.79	0.62	0.50	0.40	0.33	0.27

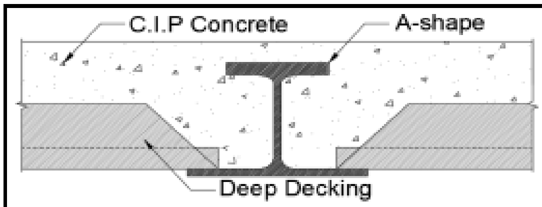

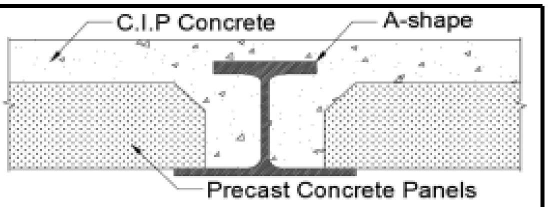

Table X-X

Minimum Capacity-to-Demand Ratio

Shallow-Depth Floor System with A-Shapes - A8x52

F_y = 50 ksi, f'c = 4 ksi, 40 psf Live, 15 psf Partition, 65 psf Dead, 10 psf SDL

		Beam Length (ft)															
		10	**11**	**12**	**13**	**14**	**15**	**16**	**17**	**18**	**19**	**20**	**21**	**22**	**23**	**24**	**25**
Beam Spacing (ft)	**10**	4.58	4.58	4.58	4.49	3.61	2.95	2.44	2.04	1.73	1.48	1.27	1.91	1.75	1.62	1.50	1.39
	11	4.58	4.58	4.58	4.10	3.30	2.70	2.23	1.87	1.58	1.35	1.93	1.76	1.62	1.49	1.38	1.28
	12	4.58	4.58	4.58	3.77	3.04	2.48	2.05	1.72	1.46	1.25	1.79	1.64	1.50	1.39	1.28	1.19
	13	4.58	4.58	4.41	3.49	2.81	2.30	1.91	1.60	1.36	1.84	1.67	1.53	1.40	1.29	1.20	1.11
	14	4.58	4.58	4.10	3.25	2.62	2.15	1.78	1.50	1.27	1.72	1.57	1.43	1.32	1.21	1.12	1.04
	15	4.58	4.55	3.84	3.04	2.46	2.02	1.67	1.41	1.19	1.63	1.48	1.35	1.24	1.14	1.06	0.98
	16	4.58	4.28	3.60	2.87	2.32	1.90	1.58	1.33	1.14	1.54	1.40	1.28	1.17	1.08	1.00	0.93
	17	4.58	4.03	3.40	2.71	2.19	1.80	1.49	1.26	1.61	1.46	1.33	1.21	1.11	1.02	0.95	0.88
	18	4.58	3.81	3.24	2.58	2.08	1.71	1.42	1.19	1.53	1.39	1.26	1.15	1.06	0.97	0.90	0.84
	19	4.35	3.63	3.08	2.45	1.98	1.63	1.35	1.13	1.46	1.32	1.20	1.10	1.01	0.93	0.86	0.79
	20	4.14	3.48	2.94	2.34	1.89	1.55	1.29	1.08	1.40	1.27	1.15	1.05	0.96	0.89	0.82	0.76
	21	3.95	3.34	2.82	2.24	1.81	1.48	1.23	1.49	1.34	1.21	1.10	1.01	0.92	0.85	0.79	0.72
	22	3.77	3.21	2.70	2.14	1.73	1.42	1.18	1.43	1.29	1.16	1.06	0.97	0.89	0.82	0.75	0.69
	23	3.61	3.08	2.59	2.06	1.66	1.36	1.13	1.38	1.24	1.12	1.02	0.93	0.85	0.78	0.72	0.66
	24	3.47	2.97	2.49	1.98	1.60	1.31	1.09	1.32	1.19	1.08	0.98	0.89	0.82	0.76	0.70	0.63
	25	3.33	2.87	2.40	1.91	1.54	1.26	1.05	1.28	1.15	1.04	0.94	0.86	0.79	0.73	0.67	0.61
	26	3.20	2.77	2.31	1.84	1.48	1.22	1.02	1.23	1.11	1.00	0.91	0.83	0.76	0.70	0.65	0.59
	27	3.09	2.67	2.24	1.78	1.43	1.17	1.34	1.19	1.07	0.97	0.88	0.81	0.74	0.68	0.63	0.56
	28	2.98	2.58	2.16	1.72	1.39	1.14	1.29	1.16	1.04	0.94	0.85	0.78	0.71	0.66	0.61	0.53
	29	2.88	2.49	2.09	1.66	1.34	1.10	1.25	1.12	1.01	0.91	0.83	0.75	0.69	0.64	0.59	0.50
	30	2.78	2.41	2.03	1.61	1.30	1.06	1.22	1.09	0.98	0.88	0.80	0.73	0.67	0.62	0.57	0.47

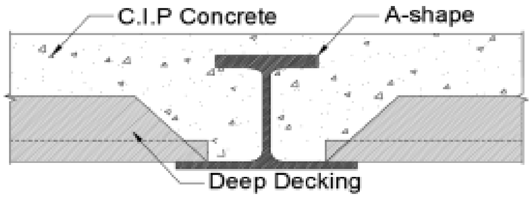

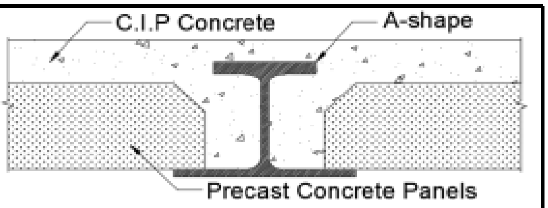

Table X-X

Minimum Capacity-to-Demand Ratio

Shallow-Depth Floor System with A-Shapes - A8x52

F_y = 50 ksi, f'c = 4 ksi, 40 psf Live, 15 psf Partition, 85 psf Dead, 10 psf SDL

	Beam Length (ft)															
Beam Spacing (ft)	10	11	12	13	14	15	16	17	18	19	20	21	22	23	24	25
10	4.58	4.58	4.58	3.83	3.08	2.51	2.08	1.74	1.47	1.25	1.85	1.69	1.55	1.43	1.32	1.22
11	4.58	4.58	4.42	3.49	2.81	2.29	1.90	1.59	1.34	1.23	1.70	1.56	1.43	1.32	1.22	1.13
12	4.58	4.58	4.07	3.21	2.58	2.11	1.74	1.46	1.24	1.74	1.58	1.44	1.32	1.22	1.13	1.05
13	4.58	4.58	3.76	2.97	2.39	1.95	1.62	1.36	1.24	1.62	1.47	1.35	1.23	1.14	1.05	0.97
14	4.58	4.31	3.50	2.77	2.23	1.82	1.51	1.27	1.16	1.52	1.38	1.26	1.16	1.07	0.98	0.91
15	4.58	4.02	3.28	2.59	2.09	1.71	1.42	1.19	1.58	1.43	1.30	1.19	1.09	1.00	0.93	0.86
16	4.39	3.78	3.08	2.44	1.97	1.61	1.34	1.12	1.49	1.35	1.23	1.12	1.03	0.95	0.87	0.81
17	4.14	3.56	2.90	2.30	1.86	1.52	1.26	1.14	1.41	1.28	1.16	1.06	0.97	0.90	0.83	0.77
18	3.91	3.36	2.75	2.19	1.76	1.45	1.20	1.50	1.34	1.22	1.11	1.01	0.93	0.85	0.79	0.73
19	3.71	3.21	2.62	2.08	1.68	1.37	1.14	1.43	1.28	1.16	1.05	0.96	0.88	0.81	0.75	0.70
20	3.53	3.05	2.50	1.98	1.60	1.31	1.09	1.36	1.22	1.11	1.01	0.92	0.84	0.78	0.72	0.66
21	3.36	2.91	2.39	1.90	1.53	1.25	1.12	1.30	1.17	1.06	0.96	0.88	0.81	0.74	0.69	0.63
22	3.21	2.78	2.29	1.82	1.46	1.20	1.07	1.25	1.12	1.02	0.92	0.84	0.77	0.71	0.66	0.59
23	3.08	2.66	2.20	1.74	1.41	1.15	1.35	1.20	1.08	0.98	0.89	0.81	0.74	0.68	0.63	0.54
24	2.95	2.55	2.11	1.67	1.35	1.11	1.30	1.16	1.04	0.94	0.85	0.78	0.71	0.66	0.61	0.50
25	2.83	2.45	2.03	1.61	1.30	1.06	1.25	1.12	1.00	0.91	0.82	0.75	0.69	0.63	0.59	0.46
26	2.73	2.36	1.96	1.55	1.25	1.03	1.21	1.08	0.97	0.87	0.79	0.72	0.66	0.61	0.56	0.43
27	2.63	2.28	1.89	1.50	1.21	1.00	1.17	1.04	0.94	0.85	0.77	0.70	0.64	0.59	0.53	0.40
28	2.54	2.20	1.83	1.45	1.17	1.03	1.13	1.01	0.91	0.82	0.74	0.68	0.62	0.57	0.49	0.38
29	2.45	2.12	1.77	1.40	1.13	1.00	1.09	0.98	0.88	0.79	0.72	0.66	0.60	0.55	0.46	0.36
30	2.37	2.05	1.71	1.36	1.09	1.20	1.06	0.95	0.85	0.77	0.70	0.64	0.58	0.54	0.43	0.34

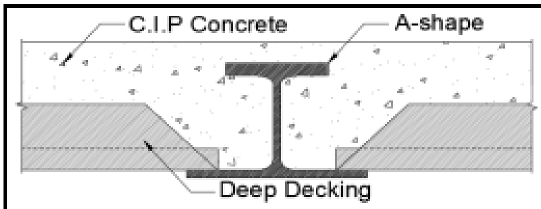

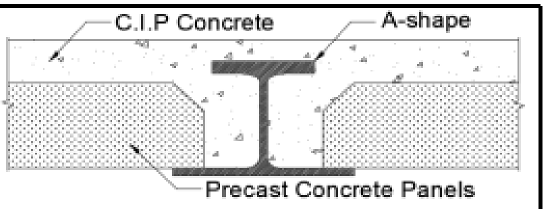

Table X-X

Minimum Capacity-to-Demand Ratio

Shallow-Depth Floor System with A-Shapes - A8x72

F_y = 50 ksi, f'c = 4 ksi, 40 psf Live, 15 psf Partition, 65 psf Dead, 10 psf SDL

	Beam Length (ft)															
Beam Spacing (ft)	**15**	**16**	**17**	**18**	**19**	**20**	**21**	**22**	**23**	**24**	**25**	**26**	**27**	**28**	**29**	**30**
10	3.77	3.12	2.61	2.21	1.89	1.62	1.41	2.32	2.06	1.98	1.75	1.71	1.59	1.37	1.31	1.23
11	3.45	2.85	2.39	2.02	1.73	1.49	1.30	2.14	1.97	1.83	1.69	1.53	1.47	1.38	1.29	1.21
12	3.18	2.63	2.21	1.87	1.60	1.38	2.17	1.99	1.84	1.68	1.57	1.46	1.31	1.24	1.15	1.04
13	2.95	2.44	2.06	1.74	1.49	1.29	2.03	1.77	1.71	1.59	1.47	1.37	1.28	1.19	1.12	1.00
14	2.75	2.29	1.92	1.63	1.40	2.08	1.90	1.75	1.61	1.49	1.38	1.28	1.16	1.11	1.05	0.99
15	2.59	2.15	1.81	1.54	1.31	1.96	1.79	1.65	1.52	1.40	1.30	1.21	1.13	1.06	0.97	0.85
16	2.45	2.03	1.71	1.45	1.24	1.86	1.70	1.56	1.43	1.33	1.23	1.14	1.07	1.00	0.93	0.74
17	2.32	1.93	1.62	1.37	1.19	1.76	1.61	1.48	1.36	1.26	1.17	1.09	1.01	0.95	0.86	0.66
18	2.20	1.83	1.54	1.30	1.85	1.68	1.53	1.41	1.30	1.20	1.11	1.03	0.96	0.90	0.75	0.59
19	2.10	1.74	1.46	1.24	1.76	1.60	1.46	1.34	1.24	1.14	1.06	0.98	0.92	0.86	0.68	0.53
20	2.00	1.66	1.40	1.18	1.68	1.53	1.40	1.28	1.18	1.09	1.01	0.94	0.88	0.80	0.61	0.49
21	1.92	1.59	1.34	1.13	1.61	1.47	1.34	1.23	1.13	1.05	0.97	0.90	0.84	0.72	0.56	0.45
22	1.84	1.52	1.28	1.71	1.55	1.41	1.29	1.18	1.09	1.00	0.93	0.86	0.81	0.65	0.51	0.42
23	1.76	1.46	1.23	1.65	1.49	1.35	1.24	1.13	1.04	0.96	0.89	0.83	0.77	0.60	0.48	0.39
24	1.70	1.41	1.18	1.59	1.44	1.30	1.19	1.09	1.01	0.93	0.86	0.80	0.72	0.55	0.44	0.37
25	1.63	1.36	1.14	1.53	1.38	1.26	1.15	1.05	0.97	0.90	0.83	0.77	0.66	0.51	0.41	0.35
26	1.58	1.31	1.10	1.48	1.34	1.22	1.11	1.02	0.94	0.86	0.80	0.74	0.61	0.48	0.39	0.33
27	1.52	1.26	1.06	1.43	1.29	1.18	1.07	0.98	0.91	0.84	0.77	0.72	0.57	0.45	0.37	0.31
28	1.47	1.22	1.54	1.39	1.25	1.14	1.04	0.95	0.88	0.81	0.75	0.70	0.53	0.42	0.35	0.29
29	1.43	1.18	1.49	1.34	1.21	1.10	1.01	0.92	0.85	0.78	0.73	0.65	0.50	0.40	0.33	0.28
30	1.38	1.15	1.45	1.30	1.18	1.07	0.98	0.89	0.82	0.76	0.70	0.61	0.47	0.38	0.31	0.27

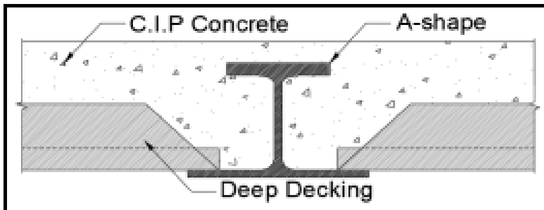

Table X-X

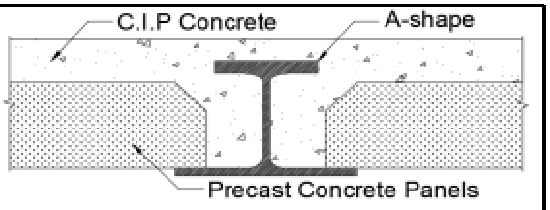

Minimum Capacity-to-Demand Ratio

Shallow-Depth Floor System with A-Shapes - A8x72

F_y = 50 ksi, f'c = 4 ksi, 40 psf Live, 15 psf Partition, 85 psf Dead, 10 psf SDL

		Beam Length (ft)															
		15	**16**	**17**	**18**	**19**	**20**	**21**	**22**	**23**	**24**	**25**	**26**	**27**	**28**	**29**	**30**
Beam Spacing (ft)	**10**	3.19	2.64	2.21	1.87	1.59	1.37	2.24	1.97	1.89	1.75	1.62	1.51	1.41	1.32	1.23	1.15
	11	2.92	2.41	2.02	1.71	1.46	1.38	2.06	1.89	1.74	1.61	1.49	1.39	1.27	1.21	1.14	1.07
	12	2.68	2.22	1.86	1.58	1.35	1.28	1.91	1.76	1.62	1.49	1.39	1.29	1.20	1.12	1.02	0.89
	13	2.49	2.06	1.73	1.47	1.26	1.96	1.79	1.64	1.51	1.39	1.29	1.20	1.12	1.05	0.98	0.75
	14	2.32	1.93	1.62	1.37	1.29	1.83	1.67	1.54	1.41	1.31	1.21	1.13	1.05	0.98	0.84	0.65
	15	2.18	1.81	1.52	1.29	1.22	1.73	1.58	1.45	1.33	1.23	1.14	1.06	0.99	0.92	0.73	0.57
	16	2.06	1.71	1.43	1.22	1.80	1.63	1.49	1.37	1.26	1.16	1.08	1.00	0.93	0.84	0.64	0.51
	17	1.95	1.62	1.36	1.27	1.70	1.55	1.41	1.30	1.19	1.10	1.02	0.95	0.88	0.74	0.57	0.46
	18	1.85	1.53	1.29	1.21	1.62	1.47	1.34	1.23	1.13	1.05	0.97	0.90	0.84	0.65	0.51	0.42
	19	1.76	1.46	1.22	1.15	1.54	1.40	1.28	1.17	1.08	1.00	0.92	0.86	0.78	0.59	0.47	0.38
	20	1.68	1.39	1.17	1.63	1.48	1.34	1.22	1.12	1.03	0.95	0.88	0.82	0.70	0.53	0.43	0.36
	21	1.60	1.33	1.12	1.56	1.41	1.28	1.17	1.07	0.99	0.91	0.85	0.79	0.63	0.49	0.40	0.33
	22	1.54	1.28	1.18	1.50	1.36	1.23	1.12	1.03	0.95	0.87	0.81	0.75	0.57	0.45	0.37	0.31
	23	1.48	1.22	1.14	1.44	1.30	1.18	1.08	0.99	0.91	0.84	0.78	0.70	0.53	0.42	0.34	0.29
	24	1.42	1.18	1.09	1.39	1.25	1.14	1.04	0.95	0.88	0.81	0.75	0.64	0.49	0.39	0.32	0.27
	25	1.37	1.13	1.49	1.34	1.21	1.10	1.00	0.92	0.84	0.78	0.72	0.58	0.45	0.37	0.30	0.26
	26	1.32	1.09	1.44	1.29	1.17	1.06	0.97	0.89	0.81	0.75	0.70	0.54	0.42	0.34	0.29	0.25
	27	1.27	1.05	1.39	1.25	1.13	1.02	0.93	0.86	0.79	0.73	0.67	0.50	0.40	0.33	0.27	0.23
	28	1.23	1.13	1.35	1.21	1.09	0.99	0.90	0.83	0.76	0.70	0.62	0.47	0.38	0.31	0.26	0.22
	29	1.19	1.09	1.30	1.17	1.06	0.96	0.88	0.80	0.74	0.68	0.58	0.44	0.35	0.29	0.25	0.21
	30	1.15	1.06	1.26	1.13	1.02	0.93	0.85	0.78	0.72	0.66	0.54	0.42	0.34	0.28	0.24	0.20

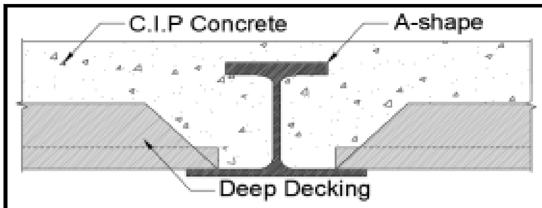

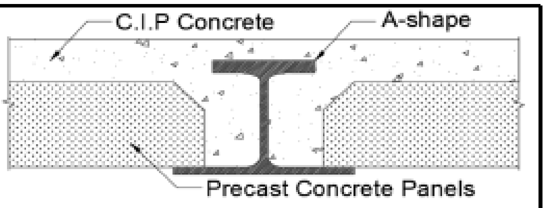

Table X-X

Minimum Capacity-to-Demand Ratio

Shallow-Depth Floor System with A-Shapes - A10x65

F_y = 50 ksi, f'c = 4 ksi, 40 psf Live, 15 psf Partition, 75 psf Dead, 10 psf SDL

		Beam Length (ft)															
		15	**16**	**17**	**18**	**19**	**20**	**21**	**22**	**23**	**24**	**25**	**26**	**27**	**28**	**29**	**30**
Beam Spacing (ft)	**10**	4.86	4.40	3.69	3.12	2.66	2.29	1.99	1.74	1.53	2.16	1.93	1.72	1.55	1.39	1.26	1.14
	11	4.86	4.02	3.37	2.85	2.44	2.10	1.83	1.60	2.20	1.98	1.76	1.58	1.41	1.28	1.15	1.05
	12	4.48	3.70	3.10	2.63	2.25	1.94	1.69	1.48	2.04	1.82	1.62	1.45	1.30	1.18	1.06	0.96
	13	4.15	3.44	2.89	2.45	2.10	1.81	1.57	2.07	1.90	1.69	1.51	1.35	1.21	1.09	0.99	0.89
	14	3.87	3.22	2.70	2.29	1.96	1.69	1.47	1.94	1.78	1.58	1.40	1.26	1.13	1.02	0.92	0.83
	15	3.64	3.02	2.54	2.15	1.84	1.59	1.38	1.83	1.67	1.48	1.32	1.18	1.06	0.95	0.86	0.78
	16	3.43	2.85	2.40	2.03	1.74	1.50	1.88	1.73	1.57	1.39	1.24	1.11	0.99	0.90	0.81	0.73
	17	3.25	2.70	2.27	1.92	1.64	1.42	1.78	1.64	1.48	1.31	1.17	1.04	0.94	0.85	0.76	0.69
	18	3.09	2.56	2.15	1.82	1.56	1.34	1.70	1.56	1.40	1.24	1.11	0.99	0.89	0.80	0.72	0.66
	19	2.94	2.44	2.05	1.74	1.48	1.77	1.62	1.48	1.33	1.18	1.05	0.94	0.84	0.76	0.69	0.62
	20	2.80	2.33	1.95	1.66	1.42	1.69	1.55	1.42	1.26	1.12	1.00	0.89	0.80	0.72	0.65	0.59
	21	2.68	2.22	1.87	1.58	1.35	1.62	1.48	1.36	1.21	1.07	0.95	0.85	0.77	0.69	0.62	0.57
	22	2.57	2.13	1.79	1.52	1.30	1.56	1.42	1.30	1.15	1.02	0.91	0.81	0.73	0.66	0.60	0.54
	23	2.46	2.05	1.72	1.45	1.24	1.50	1.37	1.25	1.10	0.98	0.87	0.78	0.70	0.63	0.57	0.52
	24	2.37	1.97	1.65	1.40	1.59	1.44	1.31	1.20	1.06	0.94	0.84	0.75	0.67	0.61	0.55	0.50
	25	2.28	1.89	1.59	1.35	1.53	1.39	1.27	1.15	1.02	0.90	0.80	0.72	0.65	0.58	0.53	0.48
	26	2.20	1.83	1.53	1.30	1.48	1.34	1.22	1.11	0.98	0.87	0.77	0.69	0.62	0.56	0.51	0.46
	27	2.12	1.76	1.48	1.25	1.43	1.30	1.18	1.07	0.95	0.84	0.75	0.67	0.60	0.54	0.49	0.44
	28	2.05	1.70	1.43	1.21	1.38	1.25	1.14	1.03	0.91	0.81	0.72	0.65	0.58	0.52	0.47	0.43
	29	1.99	1.65	1.38	1.17	1.34	1.22	1.11	1.00	0.88	0.78	0.70	0.62	0.56	0.50	0.46	0.41
	30	1.93	1.60	1.34	1.44	1.30	1.18	1.08	0.97	0.85	0.76	0.67	0.60	0.54	0.49	0.44	0.40

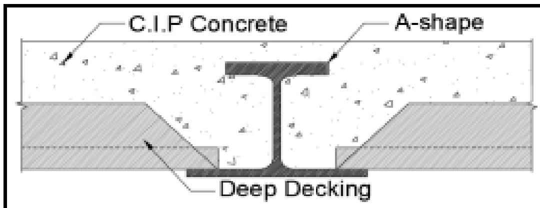

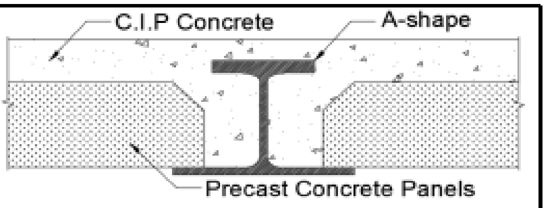

Table X-X

Minimum Capacity-to-Demand Ratio

Shallow-Depth Floor System with A-Shapes - A10x65

F_y = 50 ksi, f'c = 4 ksi, 40 psf Live, 15 psf Partition, 95 psf Dead, 10 psf SDL

		Beam Length (ft)															
		15	**16**	**17**	**18**	**19**	**20**	**21**	**22**	**23**	**24**	**25**	**26**	**27**	**28**	**29**	**30**
Beam Spacing (ft)	**10**	4.57	3.78	3.16	2.67	2.28	1.96	1.70	1.48	2.12	1.90	1.69	1.52	1.36	1.23	1.11	1.01
	11	4.17	3.45	2.88	2.44	2.08	1.79	1.56	1.47	1.95	1.74	1.55	1.39	1.25	1.12	1.02	0.92
	12	3.84	3.17	2.66	2.25	1.92	1.66	1.44	1.97	1.81	1.60	1.43	1.28	1.15	1.03	0.94	0.85
	13	3.55	2.94	2.47	2.09	1.79	1.54	1.44	1.83	1.67	1.48	1.32	1.18	1.06	0.96	0.87	0.79
	14	3.32	2.75	2.31	1.95	1.67	1.44	1.87	1.72	1.56	1.38	1.23	1.10	0.99	0.89	0.81	0.73
	15	3.11	2.58	2.17	1.83	1.57	1.35	1.76	1.62	1.46	1.30	1.15	1.03	0.93	0.84	0.76	0.69
	16	2.93	2.43	2.04	1.73	1.48	1.37	1.66	1.53	1.37	1.22	1.09	0.97	0.87	0.79	0.71	0.65
	17	2.77	2.30	1.93	1.63	1.40	1.73	1.58	1.45	1.29	1.15	1.02	0.92	0.82	0.74	0.67	0.61
	18	2.63	2.18	1.83	1.55	1.32	1.64	1.50	1.37	1.23	1.09	0.97	0.87	0.78	0.70	0.64	0.58
	19	2.50	2.08	1.74	1.47	1.36	1.57	1.43	1.31	1.16	1.03	0.92	0.82	0.74	0.67	0.60	0.55
	20	2.39	1.98	1.66	1.40	1.30	1.49	1.36	1.25	1.11	0.98	0.88	0.78	0.70	0.63	0.57	0.52
	21	2.28	1.89	1.58	1.34	1.58	1.43	1.31	1.20	1.06	0.94	0.83	0.75	0.67	0.61	0.55	0.50
	22	2.18	1.81	1.52	1.28	1.51	1.37	1.25	1.14	1.01	0.90	0.80	0.71	0.64	0.58	0.52	0.48
	23	2.09	1.74	1.46	1.23	1.45	1.32	1.20	1.09	0.97	0.86	0.76	0.68	0.61	0.55	0.50	0.46
	24	2.01	1.67	1.40	1.28	1.40	1.27	1.16	1.05	0.93	0.82	0.73	0.66	0.59	0.53	0.48	0.44
	25	1.94	1.61	1.35	1.23	1.35	1.22	1.11	1.01	0.89	0.79	0.70	0.63	0.57	0.51	0.46	0.42
	26	1.87	1.55	1.30	1.19	1.30	1.18	1.08	0.97	0.86	0.76	0.68	0.61	0.55	0.49	0.45	0.40
	27	1.80	1.49	1.25	1.39	1.26	1.14	1.04	0.94	0.83	0.73	0.65	0.59	0.53	0.47	0.43	0.39
	28	1.74	1.44	1.21	1.35	1.21	1.10	1.01	0.90	0.80	0.71	0.63	0.56	0.51	0.46	0.41	0.37
	29	1.68	1.40	1.17	1.30	1.18	1.07	0.97	0.87	0.77	0.68	0.61	0.55	0.49	0.44	0.40	0.35
	30	1.63	1.35	1.23	1.26	1.14	1.03	0.94	0.84	0.75	0.66	0.59	0.53	0.47	0.43	0.39	0.33

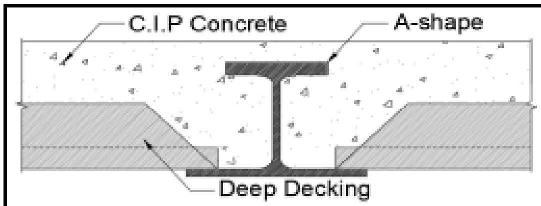

Table X-X

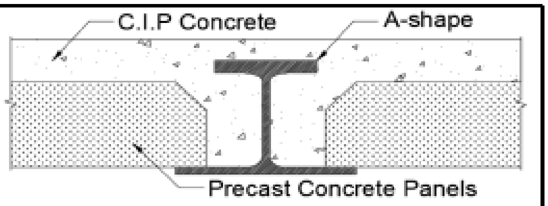

Minimum Capacity-to-Demand Ratio

Shallow-Depth Floor System with A-Shapes - A10x88

F_y = 50 ksi, f'c = 4 ksi, 40 psf Live, 15 psf Partition, 75 psf Dead, 10 psf SDL

	Beam Length (ft)															
Beam Spacing (ft)	20	21	22	23	24	25	26	27	28	29	30	31	32	33	34	35
15	2.10	1.82	1.59	2.25	2.08	1.93	1.79	1.67	1.56	1.46	1.37	1.29	1.22	1.15	1.09	1.01
16	1.98	1.72	1.50	2.13	1.97	1.83	1.70	1.58	1.48	1.38	1.30	1.22	1.15	1.09	1.03	0.88
17	1.87	1.63	1.42	2.02	1.87	1.73	1.61	1.50	1.40	1.31	1.23	1.16	1.09	1.03	0.98	0.78
18	1.78	1.54	2.09	1.92	1.78	1.65	1.53	1.43	1.33	1.25	1.17	1.10	1.04	0.98	0.86	0.70
19	1.69	1.47	1.99	1.84	1.69	1.57	1.46	1.36	1.27	1.19	1.12	1.05	0.99	0.93	0.77	0.63
20	1.62	1.40	1.91	1.75	1.62	1.50	1.39	1.30	1.21	1.14	1.07	1.00	0.95	0.88	0.70	0.58
21	1.55	1.35	1.83	1.68	1.55	1.44	1.34	1.24	1.16	1.09	1.02	0.96	0.90	0.79	0.64	0.53
22	1.48	1.91	1.75	1.61	1.49	1.38	1.28	1.19	1.11	1.04	0.98	0.92	0.87	0.72	0.59	0.50
23	1.42	1.84	1.68	1.55	1.43	1.33	1.23	1.15	1.07	1.00	0.94	0.89	0.83	0.66	0.55	0.46
24	1.37	1.77	1.62	1.49	1.38	1.28	1.19	1.10	1.03	0.97	0.91	0.85	0.76	0.61	0.51	0.43
25	1.32	1.71	1.56	1.44	1.33	1.23	1.14	1.06	0.99	0.93	0.87	0.82	0.70	0.57	0.48	0.41
26	1.28	1.65	1.51	1.39	1.28	1.19	1.10	1.03	0.96	0.90	0.84	0.79	0.65	0.53	0.45	0.38
27	1.75	1.59	1.46	1.34	1.24	1.15	1.07	0.99	0.93	0.87	0.81	0.76	0.61	0.50	0.42	0.36
28	1.69	1.54	1.41	1.30	1.20	1.11	1.03	0.96	0.90	0.84	0.79	0.71	0.57	0.47	0.40	0.35
29	1.64	1.49	1.37	1.26	1.16	1.08	1.00	0.93	0.87	0.81	0.76	0.66	0.53	0.45	0.38	0.33
30	1.59	1.45	1.33	1.22	1.13	1.04	0.97	0.90	0.84	0.79	0.74	0.62	0.50	0.42	0.36	0.31
31	1.54	1.41	1.29	1.19	1.09	1.01	0.94	0.88	0.82	0.77	0.72	0.58	0.48	0.40	0.35	0.30
32	1.50	1.37	1.25	1.15	1.06	0.98	0.91	0.85	0.79	0.74	0.69	0.55	0.45	0.38	0.33	0.29
33	1.46	1.33	1.22	1.12	1.03	0.96	0.89	0.83	0.77	0.72	0.65	0.52	0.43	0.37	0.32	0.28
34	1.42	1.29	1.19	1.09	1.01	0.93	0.86	0.81	0.75	0.70	0.61	0.49	0.41	0.35	0.30	0.27
35	1.38	1.26	1.15	1.06	0.98	0.91	0.84	0.78	0.73	0.69	0.58	0.47	0.39	0.34	0.29	0.26

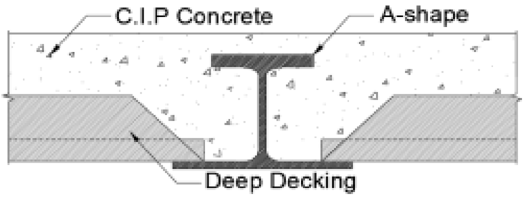

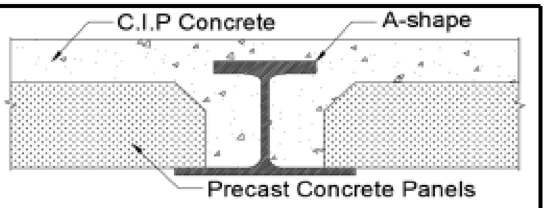

Table X-X

Minimum Capacity-to-Demand Ratio

Shallow-Depth Floor System with A-Shapes - A10x88

F_y = 50 ksi, f'c = 4 ksi, 40 psf Live, 15 psf Partition, 95 psf Dead, 10 psf SDL

		Beam Length (ft)															
		15	**16**	**17**	**18**	**19**	**20**	**21**	**22**	**23**	**24**	**25**	**26**	**27**	**28**	**29**	**30**
Beam Spacing (ft)	**15**	4.11	3.41	2.86	2.43	2.07	1.79	1.55	1.47	2.00	1.84	1.71	1.59	1.48	1.38	1.29	1.21
	16	3.88	3.22	2.70	2.29	1.96	1.68	1.46	2.05	1.89	1.74	1.61	1.50	1.40	1.30	1.22	1.15
	17	3.67	3.05	2.55	2.16	1.85	1.59	1.50	1.94	1.79	1.65	1.53	1.42	1.32	1.24	1.16	1.09
	18	3.48	2.89	2.42	2.05	1.76	1.51	1.43	1.85	1.70	1.57	1.45	1.35	1.26	1.17	1.10	1.03
	19	3.32	2.75	2.31	1.95	1.67	1.44	1.36	1.76	1.62	1.49	1.38	1.29	1.20	1.12	1.05	0.98
	20	3.16	2.62	2.20	1.86	1.59	1.37	1.84	1.68	1.55	1.43	1.32	1.23	1.14	1.07	1.00	0.94
	21	3.02	2.51	2.10	1.78	1.52	1.43	1.76	1.61	1.48	1.37	1.27	1.17	1.09	1.02	0.96	0.90
	22	2.90	2.40	2.01	1.71	1.46	1.37	1.69	1.54	1.42	1.31	1.21	1.13	1.05	0.98	0.92	0.86
	23	2.78	2.31	1.93	1.64	1.40	1.31	1.62	1.48	1.36	1.26	1.17	1.08	1.01	0.94	0.88	0.83
	24	2.67	2.22	1.86	1.57	1.34	1.71	1.56	1.43	1.31	1.21	1.12	1.04	0.97	0.91	0.85	0.79
	25	2.57	2.13	1.79	1.51	1.29	1.65	1.50	1.38	1.26	1.17	1.08	1.00	0.93	0.87	0.82	0.77
	26	2.48	2.06	1.72	1.46	1.36	1.59	1.45	1.33	1.22	1.13	1.04	0.97	0.90	0.84	0.79	0.72
	27	2.40	1.99	1.66	1.41	1.31	1.54	1.40	1.28	1.18	1.09	1.01	0.94	0.87	0.81	0.76	0.67
	28	2.32	1.92	1.61	1.36	1.27	1.49	1.36	1.24	1.14	1.05	0.97	0.90	0.84	0.79	0.74	0.62
	29	2.24	1.86	1.56	1.32	1.59	1.44	1.31	1.20	1.10	1.02	0.94	0.88	0.82	0.76	0.71	0.58
	30	2.17	1.80	1.51	1.28	1.54	1.40	1.27	1.17	1.07	0.99	0.91	0.85	0.79	0.74	0.69	0.55
	31	2.10	1.74	1.46	1.24	1.49	1.35	1.23	1.13	1.04	0.96	0.89	0.82	0.77	0.72	0.65	0.52
	32	2.04	1.69	1.42	1.20	1.45	1.32	1.20	1.10	1.01	0.93	0.86	0.80	0.74	0.70	0.61	0.49
	33	1.98	1.64	1.38	1.27	1.41	1.28	1.17	1.07	0.98	0.91	0.84	0.78	0.72	0.68	0.57	0.46
	34	1.93	1.60	1.34	1.24	1.37	1.24	1.13	1.04	0.95	0.88	0.81	0.76	0.70	0.66	0.54	0.44
	35	1.88	1.56	1.30	1.20	1.34	1.21	1.10	1.01	0.93	0.86	0.79	0.74	0.69	0.64	0.52	0.42

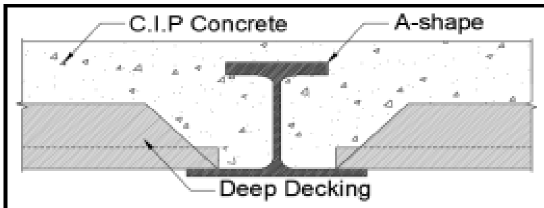

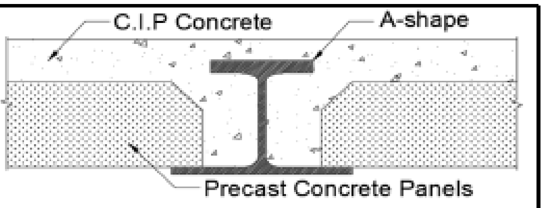

Table X-X

Minimum Capacity-to-Demand Ratio

Shallow-Depth Floor System with A-Shapes - A12x85

F_y = 50 ksi, f'c = 4 ksi, 40 psf Live, 15 psf Partition, 95 psf Dead, 10 psf SDL

		Beam Length (ft)															
		15	**16**	**17**	**18**	**19**	**20**	**21**	**22**	**23**	**24**	**25**	**26**	**27**	**28**	**29**	**30**
Beam Spacing (ft)	**15**	4.78	4.35	3.65	3.09	2.64	2.27	1.97	1.72	1.65	2.11	1.88	1.69	1.52	1.37	1.24	1.13
	16	4.59	4.10	3.44	2.91	2.49	2.14	1.86	1.62	1.56	1.99	1.77	1.59	1.43	1.29	1.17	1.06
	17	4.33	3.88	3.25	2.75	2.35	2.02	1.76	1.53	2.06	1.88	1.67	1.50	1.35	1.22	1.10	1.00
	18	4.10	3.68	3.09	2.61	2.23	1.92	1.67	1.59	1.96	1.78	1.58	1.42	1.28	1.15	1.04	0.95
	19	3.89	3.50	2.93	2.48	2.12	1.83	1.58	1.51	1.87	1.69	1.50	1.35	1.21	1.09	0.99	0.90
	20	3.71	3.34	2.80	2.37	2.02	1.74	1.51	1.94	1.78	1.61	1.43	1.28	1.15	1.04	0.94	0.86
	21	3.54	3.19	2.67	2.26	1.93	1.66	1.44	1.86	1.71	1.53	1.37	1.22	1.10	0.99	0.90	0.82
	22	3.38	3.05	2.56	2.17	1.85	1.59	1.51	1.78	1.64	1.46	1.31	1.17	1.05	0.95	0.86	0.78
	23	3.24	2.92	2.46	2.08	1.77	1.53	1.45	1.71	1.57	1.40	1.25	1.12	1.01	0.91	0.82	0.75
	24	3.11	2.81	2.36	2.00	1.70	1.47	1.80	1.65	1.51	1.35	1.20	1.08	0.97	0.87	0.79	0.72
	25	2.98	2.70	2.27	1.92	1.64	1.41	1.73	1.59	1.46	1.29	1.15	1.03	0.93	0.84	0.76	0.69
	26	2.87	2.60	2.19	1.85	1.58	1.49	1.67	1.53	1.40	1.25	1.11	1.00	0.90	0.81	0.73	0.67
	27	2.77	2.50	2.11	1.79	1.53	1.44	1.62	1.48	1.35	1.20	1.07	0.96	0.86	0.78	0.71	0.64
	28	2.67	2.42	2.04	1.73	1.47	1.39	1.56	1.43	1.31	1.16	1.03	0.93	0.83	0.75	0.68	0.62
	29	2.58	2.33	1.97	1.67	1.43	1.34	1.51	1.39	1.26	1.12	1.00	0.90	0.81	0.73	0.66	0.60
	30	2.50	2.26	1.91	1.62	1.38	1.58	1.46	1.34	1.22	1.08	0.97	0.87	0.78	0.70	0.64	0.58
	31	2.42	2.19	1.85	1.57	1.34	1.53	1.42	1.30	1.18	1.05	0.94	0.84	0.76	0.68	0.62	0.56
	32	2.35	2.12	1.80	1.52	1.30	1.49	1.37	1.27	1.15	1.02	0.91	0.81	0.73	0.66	0.60	0.54
	33	2.28	2.06	1.75	1.48	1.38	1.44	1.33	1.23	1.11	0.99	0.88	0.79	0.71	0.64	0.58	0.53
	34	2.21	2.00	1.70	1.44	1.34	1.40	1.29	1.20	1.08	0.96	0.86	0.77	0.69	0.62	0.56	0.51
	35	2.15	1.94	1.65	1.40	1.31	1.36	1.26	1.17	1.05	0.93	0.83	0.75	0.67	0.61	0.55	0.50

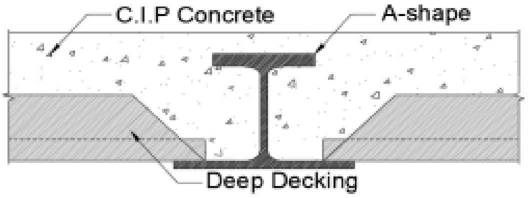

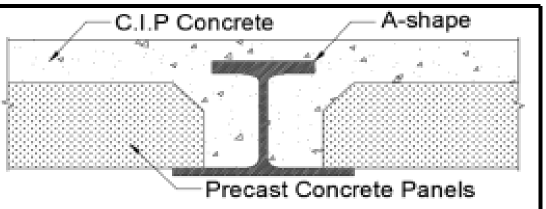

Table X-X

Minimum Capacity-to-Demand Ratio

Shallow-Depth Floor System with A-Shapes - A12x108

F_y = 50 ksi, f'c = 4 ksi, 40 psf Live, 15 psf Partition, 95 psf Dead, 10 psf SDL

	Beam Length (ft)															
Beam Spacing (ft)	**20**	**21**	**22**	**23**	**24**	**25**	**26**	**27**	**28**	**29**	**30**	**31**	**32**	**33**	**34**	**35**
20	2.26	1.96	1.71	1.63	2.13	1.97	1.83	1.71	1.59	1.49	1.37	1.27	1.18	1.10	1.02	0.96
21	2.16	1.87	1.63	1.56	2.03	1.89	1.75	1.63	1.52	1.42	1.31	1.21	1.12	1.04	0.98	0.91
22	2.07	1.79	1.56	2.09	1.95	1.81	1.68	1.57	1.46	1.35	1.25	1.15	1.07	1.00	0.93	0.87
23	1.98	1.72	1.50	2.00	1.87	1.74	1.62	1.50	1.40	1.29	1.19	1.10	1.02	0.95	0.89	0.83
24	1.91	1.65	1.57	1.92	1.79	1.67	1.55	1.45	1.35	1.24	1.14	1.06	0.98	0.91	0.85	0.78
25	1.83	1.59	1.51	1.84	1.72	1.61	1.50	1.39	1.29	1.19	1.10	1.02	0.94	0.88	0.82	0.72
26	1.77	1.53	1.91	1.78	1.66	1.55	1.45	1.35	1.24	1.14	1.05	0.98	0.91	0.84	0.79	0.67
27	1.71	1.48	1.84	1.71	1.60	1.50	1.40	1.30	1.20	1.10	1.02	0.94	0.87	0.81	0.76	0.62
28	1.65	1.43	1.78	1.65	1.54	1.44	1.35	1.26	1.16	1.06	0.98	0.91	0.84	0.78	0.71	0.59
29	1.60	1.51	1.72	1.60	1.49	1.40	1.31	1.22	1.12	1.03	0.95	0.88	0.81	0.76	0.66	0.55
30	1.55	1.46	1.66	1.55	1.44	1.35	1.27	1.18	1.08	0.99	0.91	0.85	0.79	0.73	0.62	0.52
31	1.50	1.42	1.61	1.50	1.40	1.31	1.23	1.14	1.04	0.96	0.88	0.82	0.76	0.71	0.59	0.49
32	1.45	1.68	1.56	1.45	1.36	1.27	1.19	1.10	1.01	0.93	0.86	0.79	0.74	0.68	0.56	0.47
33	1.41	1.63	1.52	1.41	1.32	1.23	1.15	1.07	0.98	0.90	0.83	0.77	0.71	0.64	0.53	0.45
34	1.37	1.59	1.47	1.37	1.28	1.20	1.12	1.04	0.95	0.87	0.81	0.75	0.69	0.60	0.50	0.43
35	1.46	1.54	1.43	1.33	1.24	1.16	1.09	1.01	0.92	0.85	0.78	0.73	0.67	0.57	0.48	0.41
36	1.42	1.50	1.39	1.30	1.21	1.13	1.06	0.98	0.90	0.83	0.76	0.71	0.65	0.54	0.46	0.39
37	1.38	1.46	1.36	1.26	1.18	1.10	1.03	0.95	0.87	0.80	0.74	0.69	0.63	0.52	0.44	0.38
38	1.35	1.42	1.32	1.23	1.15	1.07	1.01	0.93	0.85	0.78	0.72	0.67	0.60	0.50	0.42	0.36
39	1.50	1.39	1.29	1.20	1.12	1.05	0.98	0.91	0.83	0.76	0.70	0.65	0.57	0.48	0.40	0.35
40	1.46	1.35	1.26	1.17	1.09	1.02	0.96	0.88	0.81	0.74	0.69	0.63	0.55	0.46	0.39	0.34

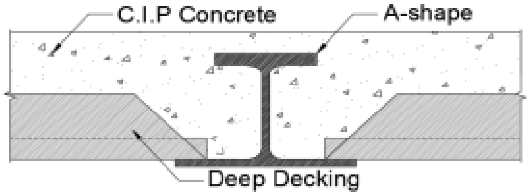

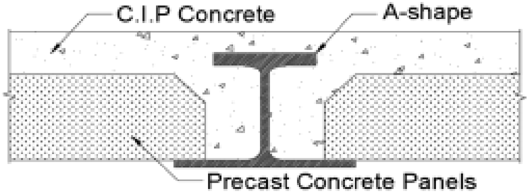

Table X-X

Minimum Capacity-to-Demand Ratio

Shallow-Depth Floor System with A-Shapes - A8x72

F_y = 50 ksi, f'c = 4 ksi, 100 psf Live, 65 psf Dead, 10 psf SDL

		Beam Length (ft)															
		10	**11**	**12**	**13**	**14**	**15**	**16**	**17**	**18**	**19**	**20**	**21**	**22**	**23**	**24**	**25**
Beam Spacing (ft)	**10**	4.82	4.19	3.69	3.30	2.97	2.70	2.48	2.20	1.86	1.59	1.37	1.20	1.69	1.57	1.45	1.33
	11	4.38	3.81	3.36	3.00	2.70	2.46	2.25	2.01	1.70	1.46	1.27	1.11	1.57	1.46	1.35	1.26
	12	4.02	3.49	3.08	2.75	2.48	2.25	2.06	1.85	1.58	1.36	1.18	1.57	1.48	1.37	1.27	1.18
	13	3.71	3.22	2.84	2.54	2.29	2.08	1.93	1.74	1.48	1.28	1.11	1.50	1.39	1.29	1.19	1.11
	14	3.45	2.99	2.64	2.35	2.12	1.97	1.85	1.63	1.40	1.20	1.49	1.42	1.31	1.21	1.13	1.05
	15	3.22	2.79	2.46	2.20	2.02	1.88	1.77	1.54	1.32	1.13	1.43	1.35	1.24	1.15	1.07	0.99
	16	3.01	2.62	2.31	2.09	1.94	1.81	1.70	1.46	1.25	1.08	1.37	1.28	1.18	1.10	1.02	0.95
	17	2.84	2.46	2.19	2.01	1.86	1.74	1.63	1.39	1.19	1.02	1.32	1.23	1.13	1.04	0.97	0.90
	18	2.68	2.33	2.11	1.94	1.80	1.68	1.57	1.33	1.13	1.33	1.27	1.17	1.08	1.00	0.93	0.86
	19	2.54	2.24	2.04	1.88	1.74	1.62	1.50	1.27	1.08	1.28	1.22	1.12	1.04	0.96	0.89	0.83
	20	2.41	2.17	1.98	1.82	1.68	1.57	1.43	1.21	1.03	1.24	1.18	1.08	0.99	0.92	0.85	0.79
	21	2.34	2.10	1.92	1.76	1.63	1.52	1.38	1.16	1.00	1.20	1.13	1.04	0.96	0.88	0.82	0.76
	22	2.27	2.04	1.86	1.71	1.58	1.47	1.32	1.12	1.23	1.17	1.09	1.00	0.92	0.85	0.79	0.73
	23	2.21	1.99	1.81	1.66	1.54	1.43	1.27	1.08	1.19	1.13	1.05	0.97	0.89	0.82	0.76	0.71
	24	2.15	1.93	1.76	1.61	1.49	1.39	1.23	1.04	1.16	1.10	1.02	0.93	0.86	0.79	0.74	0.68
	25	2.10	1.88	1.71	1.57	1.46	1.36	1.19	1.00	1.13	1.07	0.99	0.90	0.83	0.77	0.71	0.66
	26	2.04	1.84	1.67	1.53	1.42	1.32	1.15	0.97	1.10	1.04	0.95	0.88	0.81	0.74	0.69	0.64
	27	1.99	1.79	1.63	1.50	1.38	1.29	1.11	0.94	1.07	1.01	0.93	0.85	0.78	0.72	0.67	0.62
	28	1.95	1.75	1.59	1.46	1.35	1.26	1.08	1.11	1.05	0.99	0.90	0.82	0.76	0.70	0.65	0.60
	29	1.91	1.71	1.56	1.43	1.32	1.23	1.04	1.08	1.02	0.96	0.87	0.80	0.74	0.68	0.63	0.59
	30	1.86	1.67	1.52	1.40	1.29	1.20	1.01	1.06	1.00	0.93	0.85	0.78	0.72	0.66	0.61	0.57

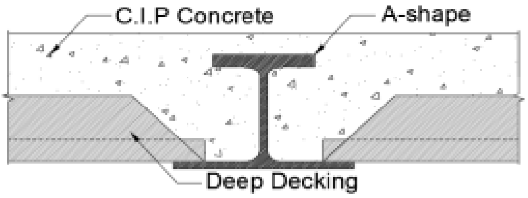

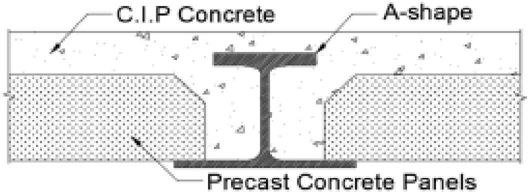

Table X-X

Minimum Capacity-to-Demand Ratio

Shallow-Depth Floor System with A-Shapes - A10x65

F_y = 50 ksi, f'c = 4 ksi, 100 psf Live, 75 psf Dead, 10 psf SDL

		Beam Length (ft)															
		10	**11**	**12**	**13**	**14**	**15**	**16**	**17**	**18**	**19**	**20**	**21**	**22**	**23**	**24**	**25**
Beam Spacing (ft)	**10**	4.86	4.86	4.86	4.55	4.09	3.71	3.39	3.11	2.64	2.25	1.94	1.69	1.49	1.31	1.64	1.53
	11	4.86	4.86	4.65	4.14	3.72	3.38	3.09	2.83	2.41	2.07	1.79	1.57	1.37	1.65	1.53	1.42
	12	4.86	4.85	4.26	3.79	3.41	3.09	2.83	2.62	2.24	1.92	1.67	1.45	1.28	1.54	1.43	1.33
	13	4.86	4.48	3.94	3.50	3.15	2.86	2.65	2.45	2.09	1.80	1.56	1.36	1.57	1.45	1.34	1.25
	14	4.81	4.16	3.66	3.25	2.92	2.70	2.53	2.30	1.96	1.69	1.46	1.28	1.48	1.37	1.27	1.18
	15	4.49	3.88	3.41	3.04	2.78	2.59	2.42	2.17	1.85	1.59	1.38	1.20	1.40	1.29	1.20	1.12
	16	4.21	3.64	3.20	2.89	2.67	2.48	2.32	2.06	1.75	1.51	1.31	1.45	1.33	1.23	1.14	1.06
	17	3.96	3.43	3.03	2.78	2.57	2.39	2.23	1.95	1.66	1.43	1.24	1.38	1.27	1.17	1.09	1.01
	18	3.74	3.24	2.93	2.68	2.48	2.30	2.13	1.86	1.58	1.36	1.18	1.32	1.21	1.12	1.04	0.97
	19	3.54	3.12	2.83	2.59	2.39	2.23	2.04	1.78	1.51	1.30	1.38	1.26	1.16	1.07	0.99	0.92
	20	3.37	3.02	2.74	2.51	2.32	2.15	1.96	1.70	1.45	1.24	1.32	1.21	1.11	1.03	0.95	0.89
	21	3.27	2.93	2.65	2.43	2.24	2.09	1.89	1.63	1.39	1.19	1.27	1.16	1.07	0.99	0.92	0.85
	22	3.17	2.84	2.58	2.36	2.18	2.02	1.82	1.56	1.33	1.14	1.22	1.12	1.03	0.95	0.88	0.82
	23	3.08	2.76	2.50	2.29	2.12	1.97	1.76	1.50	1.28	1.10	1.18	1.08	1.00	0.92	0.85	0.79
	24	3.00	2.69	2.44	2.23	2.06	1.91	1.70	1.45	1.23	1.25	1.14	1.04	0.96	0.89	0.82	0.76
	25	2.93	2.62	2.37	2.17	2.00	1.84	1.64	1.40	1.19	1.21	1.10	1.01	0.93	0.86	0.80	0.74
	26	2.85	2.55	2.31	2.12	1.95	1.79	1.59	1.35	1.15	1.17	1.07	0.98	0.90	0.83	0.77	0.72
	27	2.79	2.49	2.26	2.07	1.91	1.73	1.55	1.31	1.11	1.14	1.04	0.95	0.87	0.81	0.75	0.69
	28	2.72	2.44	2.21	2.02	1.86	1.68	1.50	1.26	1.08	1.10	1.01	0.92	0.85	0.78	0.72	0.67
	29	2.66	2.38	2.16	1.97	1.82	1.64	1.45	1.23	1.04	1.07	0.98	0.89	0.82	0.76	0.70	0.65
	30	2.60	2.33	2.11	1.93	1.78	1.59	1.41	1.19	1.15	1.04	0.95	0.87	0.80	0.74	0.68	0.64

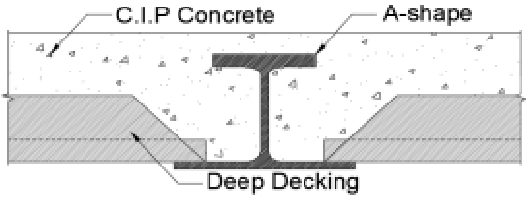

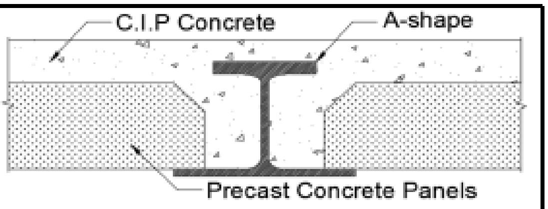

Table X-X

Minimum Capacity-to-Demand Ratio

Shallow-Depth Floor System with A-Shapes - A10x88

F_y = 50 ksi, f'c = 4 ksi, 100 psf Live, 75 psf Dead, 10 psf SDL

		Beam Length (ft)															
		15	**16**	**17**	**18**	**19**	**20**	**21**	**22**	**23**	**24**	**25**	**26**	**27**	**28**	**29**	**30**
Beam Spacing (ft)	**15**	3.46	2.89	2.43	2.07	1.78	1.54	1.34	1.37	1.74	1.61	1.50	1.40	1.31	1.23	1.15	1.09
	16	3.27	2.73	2.30	1.96	1.68	1.46	1.27	1.30	1.65	1.53	1.43	1.33	1.24	1.17	1.10	1.03
	17	3.11	2.59	2.19	1.86	1.60	1.38	1.41	1.24	1.58	1.46	1.36	1.27	1.18	1.11	1.04	0.98
	18	2.96	2.47	2.08	1.77	1.52	1.31	1.34	1.63	1.51	1.40	1.30	1.21	1.13	1.06	1.00	0.94
	19	2.83	2.36	1.99	1.69	1.45	1.25	1.28	1.56	1.44	1.34	1.24	1.16	1.08	1.02	0.95	0.90
	20	2.70	2.25	1.90	1.61	1.39	1.20	1.22	1.50	1.38	1.28	1.19	1.11	1.04	0.97	0.91	0.86
	21	2.59	2.16	1.82	1.55	1.33	1.35	1.57	1.44	1.33	1.23	1.15	1.07	1.00	0.94	0.88	0.83
	22	2.49	2.07	1.75	1.48	1.27	1.29	1.51	1.39	1.28	1.19	1.10	1.03	0.96	0.90	0.85	0.80
	23	2.39	1.99	1.68	1.43	1.22	1.24	1.46	1.34	1.24	1.15	1.07	0.99	0.93	0.87	0.82	0.74
	24	2.31	1.92	1.62	1.37	1.18	1.20	1.41	1.29	1.20	1.11	1.03	0.96	0.90	0.84	0.79	0.68
	25	2.22	1.85	1.56	1.33	1.14	1.16	1.36	1.25	1.16	1.07	0.99	0.93	0.87	0.81	0.76	0.63
	26	2.15	1.79	1.51	1.28	1.29	1.44	1.32	1.21	1.12	1.04	0.96	0.90	0.84	0.79	0.74	0.58
	27	2.08	1.73	1.46	1.24	1.25	1.40	1.28	1.18	1.09	1.01	0.93	0.87	0.81	0.76	0.69	0.55
	28	2.01	1.68	1.41	1.20	1.21	1.35	1.24	1.14	1.05	0.98	0.91	0.84	0.79	0.74	0.64	0.51
	29	1.95	1.62	1.37	1.16	1.17	1.32	1.21	1.11	1.02	0.95	0.88	0.82	0.77	0.72	0.60	0.48
	30	1.89	1.58	1.33	1.13	1.14	1.28	1.17	1.08	0.99	0.92	0.86	0.80	0.74	0.70	0.57	0.46
	31	1.84	1.53	1.29	1.09	1.11	1.25	1.14	1.05	0.97	0.90	0.83	0.78	0.72	0.68	0.53	0.43
	32	1.79	1.49	1.25	1.25	1.33	1.21	1.11	1.02	0.94	0.87	0.81	0.75	0.71	0.64	0.50	0.41
	33	1.74	1.45	1.22	1.22	1.30	1.18	1.08	1.00	0.92	0.85	0.79	0.74	0.69	0.60	0.48	0.39
	34	1.69	1.41	1.18	1.19	1.27	1.15	1.06	0.97	0.90	0.83	0.77	0.72	0.67	0.57	0.46	0.38
	35	1.65	1.37	1.15	1.16	1.24	1.13	1.03	0.95	0.87	0.81	0.75	0.70	0.65	0.54	0.43	0.36

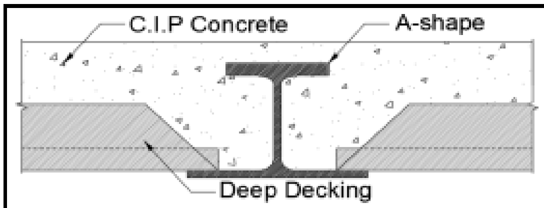

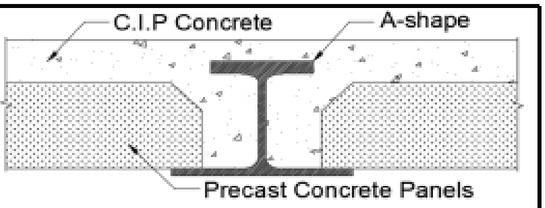

Table X-X

Minimum Capacity-to-Demand Ratio

Shallow-Depth Floor System with A-Shapes - A12x85

F_y = 50 ksi, f'c = 4 ksi, 100 psf Live, 95 psf Dead, 10 psf SDL

		Beam Length (ft)															
		15	**16**	**17**	**18**	**19**	**20**	**21**	**22**	**23**	**24**	**25**	**26**	**27**	**28**	**29**	**30**
Beam Spacing (ft)	**15**	3.59	3.34	3.12	2.83	2.53	2.19	1.91	1.67	1.59	1.41	1.57	1.47	1.37	1.28	1.20	1.13
	16	3.45	3.21	2.98	2.69	2.40	2.07	1.80	1.70	1.50	1.61	1.49	1.39	1.30	1.22	1.14	1.06
	17	3.32	3.08	2.84	2.56	2.27	1.97	1.71	1.62	1.43	1.53	1.42	1.32	1.24	1.16	1.09	1.00
	18	3.20	2.97	2.71	2.45	2.16	1.87	1.63	1.54	1.36	1.46	1.36	1.26	1.18	1.10	1.04	0.95
	19	3.09	2.87	2.60	2.35	2.06	1.78	1.67	1.47	1.51	1.40	1.30	1.21	1.13	1.06	0.99	0.90
	20	2.99	2.78	2.49	2.25	1.97	1.70	1.60	1.40	1.45	1.34	1.24	1.16	1.08	1.01	0.94	0.86
	21	2.90	2.68	2.40	2.16	1.89	1.63	1.53	1.35	1.39	1.29	1.19	1.11	1.04	0.97	0.90	0.82
	22	2.81	2.58	2.31	2.08	1.81	1.57	1.47	1.29	1.34	1.24	1.15	1.07	1.00	0.94	0.86	0.78
	23	2.73	2.49	2.23	2.01	1.74	1.51	1.42	1.40	1.29	1.19	1.11	1.03	0.96	0.90	0.82	0.75
	24	2.66	2.40	2.15	1.94	1.68	1.57	1.36	1.35	1.24	1.15	1.07	0.99	0.93	0.87	0.79	0.72
	25	2.59	2.32	2.08	1.88	1.62	1.51	1.32	1.30	1.20	1.11	1.03	0.96	0.90	0.84	0.76	0.69
	26	2.52	2.25	2.01	1.82	1.56	1.46	1.27	1.26	1.16	1.08	1.00	0.93	0.87	0.81	0.73	0.67
	27	2.45	2.18	1.95	1.76	1.51	1.41	1.33	1.22	1.13	1.04	0.97	0.90	0.84	0.78	0.71	0.64
	28	2.38	2.12	1.89	1.71	1.46	1.37	1.29	1.18	1.09	1.01	0.94	0.87	0.82	0.75	0.68	0.62
	29	2.31	2.06	1.84	1.65	1.50	1.32	1.25	1.15	1.06	0.98	0.91	0.85	0.79	0.73	0.66	0.60
	30	2.25	2.00	1.79	1.60	1.46	1.28	1.22	1.12	1.03	0.95	0.88	0.82	0.77	0.70	0.64	0.58
	31	2.19	1.94	1.74	1.56	1.42	1.25	1.18	1.09	1.00	0.93	0.86	0.80	0.75	0.68	0.62	0.56
	32	2.13	1.89	1.70	1.51	1.38	1.21	1.15	1.06	0.98	0.90	0.84	0.78	0.73	0.66	0.60	0.54
	33	2.08	1.85	1.65	1.47	1.35	1.23	1.12	1.03	0.95	0.88	0.82	0.76	0.71	0.64	0.58	0.53
	34	2.03	1.80	1.61	1.43	1.31	1.20	1.09	1.01	0.93	0.86	0.79	0.74	0.69	0.62	0.56	0.51
	35	1.98	1.76	1.57	1.39	1.28	1.17	1.07	0.98	0.90	0.84	0.78	0.72	0.67	0.61	0.55	0.50

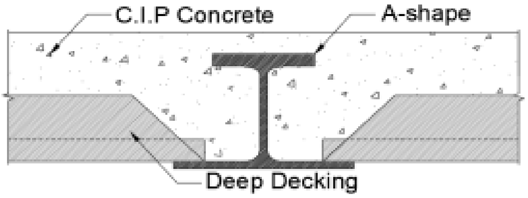

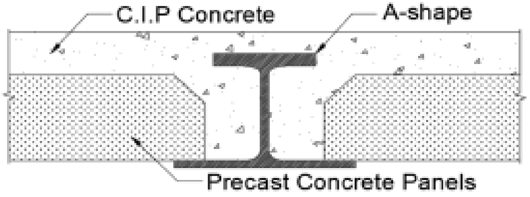

Table X-X

Minimum Capacity-to-Demand Ratio

Shallow-Depth Floor System with A-Shapes - A12x108

F_y = 50 ksi, f'c = 4 ksi, 100 psf Live, 95 psf Dead, 10 psf SDL

		Beam Length (ft)															
		15	**16**	**17**	**18**	**19**	**20**	**21**	**22**	**23**	**24**	**25**	**26**	**27**	**28**	**29**	**30**
Beam Spacing (ft)	**20**	3.48	3.48	3.24	2.92	2.52	2.18	1.90	1.66	1.59	1.41	1.61	1.50	1.40	1.31	1.23	1.16
	21	3.48	3.47	3.11	2.81	2.42	2.09	1.82	1.72	1.52	1.67	1.55	1.44	1.35	1.26	1.18	1.11
	22	3.48	3.34	3.00	2.70	2.32	2.01	1.75	1.66	1.46	1.60	1.49	1.39	1.29	1.21	1.14	1.07
	23	3.48	3.23	2.89	2.60	2.23	1.93	1.68	1.59	1.41	1.55	1.43	1.34	1.25	1.17	1.10	1.03
	24	3.48	3.12	2.79	2.51	2.15	1.86	1.62	1.54	1.35	1.49	1.39	1.29	1.20	1.13	1.06	0.99
	25	3.39	3.02	2.70	2.42	2.07	1.79	1.69	1.48	1.56	1.44	1.34	1.25	1.16	1.09	1.02	0.96
	26	3.28	2.92	2.62	2.34	2.00	1.73	1.63	1.43	1.51	1.40	1.30	1.21	1.13	1.05	0.99	0.93
	27	3.18	2.83	2.54	2.26	1.94	1.67	1.58	1.38	1.46	1.35	1.25	1.17	1.09	1.02	0.96	0.90
	28	3.09	2.75	2.46	2.19	1.88	1.62	1.53	1.34	1.42	1.31	1.22	1.13	1.06	0.99	0.93	0.87
	29	3.00	2.67	2.39	2.12	1.82	1.57	1.48	1.30	1.38	1.27	1.18	1.10	1.03	0.96	0.90	0.85
	30	2.92	2.60	2.32	2.06	1.76	1.52	1.44	1.45	1.34	1.24	1.15	1.07	1.00	0.93	0.87	0.82
	31	2.84	2.53	2.26	2.00	1.71	1.61	1.40	1.41	1.30	1.20	1.12	1.04	0.97	0.91	0.85	0.80
	32	2.77	2.46	2.20	1.94	1.66	1.56	1.36	1.37	1.27	1.17	1.09	1.01	0.94	0.88	0.83	0.78
	33	2.70	2.40	2.15	1.89	1.62	1.52	1.32	1.34	1.23	1.14	1.06	0.99	0.92	0.86	0.81	0.76
	34	2.63	2.34	2.09	1.84	1.58	1.48	1.29	1.31	1.20	1.11	1.03	0.96	0.90	0.84	0.79	0.74
	35	2.57	2.28	2.04	1.79	1.54	1.44	1.25	1.27	1.17	1.09	1.01	0.94	0.87	0.82	0.77	0.72
	36	2.51	2.23	2.00	1.75	1.50	1.41	1.35	1.24	1.15	1.06	0.98	0.91	0.85	0.80	0.75	0.70
	37	2.45	2.18	1.95	1.71	1.46	1.37	1.32	1.21	1.12	1.03	0.96	0.89	0.83	0.78	0.73	0.69
	38	2.40	2.13	1.91	1.66	1.55	1.34	1.29	1.19	1.09	1.01	0.94	0.87	0.81	0.76	0.71	0.67
	39	2.35	2.09	1.87	1.63	1.51	1.31	1.26	1.16	1.07	0.99	0.92	0.85	0.80	0.74	0.70	0.66
	40	2.30	2.04	1.83	1.59	1.48	1.28	1.24	1.14	1.05	0.97	0.90	0.83	0.78	0.73	0.68	0.64

References

AISC. 2022. Specification for Structural Steel Buildings. ANSI/AISC 360-22. Chicago, IL: AISC.

ASTM. 2022. Standard Specification for Structural Steel Shapes. ASTM A992. West Conshohcocken, PA: ASTM.

Chen, W. F., and E. M. Lui. 1987. Structural Stability - Theory and Implementation. New York, NY: Elsevier Science Publishing Co., Inc.

Helwig, T. A., K. H. Frank, and J. A. Yura. 1997. "Lateral-Torsional Buckling of Singly Symmetric I-beams." Journal of Structural Engineering, 123(9).

Ottmers, C., R. W. Alemayehu, and M. Yarnold. 2025a. "Evaluating the Composite Behavior developed through Bond in the Steel-Concrete Interface for Future Hot-Rolled Asymmetric Steel I-beams." Engineering Structures, 322.

Ottmers, C., R. W. Alemayehu, and M. Yarnold. 2025c. "Full-Scale System Testing for Asymmetric Steel I-beams in Shallow-Depth Composite Floor Systems." Under Review.

Seaburg, P. A., and C. J. Carter. 2003. Steel Design Guide 9: Torsional Analysis of Structural Steel Members. Steel Design Guide Series. Chicago, IL: AISC.

Ziemian, R. D. 2010. Guide to Stability Design Criteria for Metal Structures, 6th Edition. Hoboken, NJ: John Wiley & Sons, Inc.

130 E Randolph St, Ste 2000
Chicago, IL 60601
312.670.2400
www.aisc.org

Research Report No. AISC-MILEK-2025-01AISC-MILEK-2025-01